Fluid flow and heat transfer in unconventional tube bundle arrangements in crossflow

Castiglia, Davide

FLUID FLOW AND HEAT TRANSFER IN UNCONVENTIONAL TUBE BUNDLE ARRANGEMENTS IN CROSSFLOW

Davide CASTIGLIA

Thesis submitted for the degree of Doctor of Philosophy in the University of London

King's College London
Department of Mechanical Engineering
Experimental and Computational Laboratory for the Analysis of Turbulence (ECLAT)

July 2002

To

my family

Dino, Isabella,

Domenico and Daniele

Abstract

This thesis is concerned with experimental investigations of non-conventional tube bundles in steady and pulsating cross-flow of water. LDA and flow visualisation were used to study the velocity and vortex shedding characteristics of three tube bundles, two in-line arrays with elliptic and drop-shaped tubes respectively and an asymmetric array with circular tubes. A thermocouple heat transfer measurement technique was developed to determine surface temperature measurements in the asymmetric and in-line arrays with circular and elliptic cylinders respectively.

The results showed that the in-line array with elliptic cylinders of axis ratio 1:2 is characterised by low turbulence and poor lateral mixing compared to circular cylinder arrays. A weak flow periodicity rows with a constant Strouhal number of 0.11 was detected in downstream rows. The occurrence of lock-on of the natural vortex shedding at half of the superimposed pulsation frequency was observed in all rows. The flow visualisation study confirmed the lack of any significant vortex activity behind the first row and the occurrence of lock-on of the natural vortex shedding at half of the superimposed pulsation frequency.

The results of the investigation on the asymmetric tube array with circular cylinders indicated that the configuration studied generates less turbulence than a staggered array (with the same longitudinal and transverse spacing) with circular cylinders. A vortex shedding activity was detected, but it was not as well defined as in the in-line arrays with elliptic and circular cylinders respectively. The Strouhal number was found to be approximately equal to 0.22 in inner rows. The only significant effect of the pulsations on the turbulence of the flow was observed in the wake of the first cylinder. The flow visualisation study confirmed the findings of the LDA measurements and in particular the lack of a well-defined and unique vortex shedding frequency.

The study on the flow around the in-line array with drop-shaped cylinders showed that differences of turbulence levels between the in-line arrays with elliptic and drop-

shaped cylinders respectively can be observed only in the cylinder wakes, particularly behind the first one. A vortex shedding activity could be observed behind all rows, but a well defined vortex shedding frequency was detected only downstream of the second one. The Strouhal number was found to be equal to 0.16 in inner rows. The only significant effect of the pulsations on the turbulence of the flow was observed behind the first cylinder, as in the in-line and asymmetric arrays with elliptic and circular cylinders respectively. Lock-on of the natural vortex shedding at either the superimposed pulsation frequency, or at half of its value - depending on the reduced amplitude of pulsations upstream of the tube bundle - was observed.

An experimental investigation was carried out on the heat transfer over circular and elliptic cylinders of an asymmetric and in-line array respectively in both steady and pulsating flow. The results showed that the heat transfer rates in the asymmetric array in steady flow are low around the first row cylinder and they increase in subsequent rows. The heat transfer rates at the exit of the bundle, that is row 6, are also similar to the rates measured in row 2. A comparison of the heat transfer rates between steady and pulsating flow clearly shows that the heat transfer is enhanced when the flow is pulsed. The flow conditions adopted were such that vortex shedding was promoted and locked at the pulsation frequency. The study on the in-line array with elliptic cylinders indicated that the heat transfer rates are low around the first row cylinder and they increase in subsequent rows. The heat transfer augmentation due to pulsations increases with the relative amplitude of pulsations A_o as already observed in the asymmetric array. Finally, it was found that the heat transfer of the in-line array is considerably lower than that of the staggered array in all rows.

The results indicated that both the tube arrangement and tube shape affect significantly the vortex shedding characteristics of the tube bundle. The superimposition of a sinusoidal periodic component onto the approaching flow caused the vortex shedding frequency to lock on at the pulsation frequency or its sub-harmonics on all the arrangements investigated. Lock-on modified the flow and turbulence in the wakes of the cylinders and also increased the heat transfer in the arrays.

Acknowledgements

Not enough words are ever spent to thank those we are indebted to or those we love.

I would like to acknowledge all those who have assisted and supported me during the course of my PhD study.

I would like to thank Prof. Yianneskis for giving me the opportunity to live this extraordinary experience. I would also thank him for his continuous support, guidance and criticism, his understanding and respect.

I am deeply obliged to Dr Balabani for her constant and patient supervision. A few days before her twins were born she was still revising my thesis. I have no words to describe my gratefulness. I wish the twins a joyful and successful life.

I am indebted to Dr Lee who (together with Dr Balabani) introduced me to the experimental techniques and helped me with several computing related issues. His continuous suggestions and assistance were greatly appreciated.

I need to thank Mr Alex Heaney and Mr Ray Moslin for the construction of the rig and the test sections used in this work. I was never denied their help and support. I would also like to thank Mr Julian Greenberg for his constant help with any problem.

My friends and colleagues Dr E. Konstantinidis, N. St. Hill, Dr S. Sirivedin and A. Boheimer made my life during this project enjoyable.

To Pichai, who gave me the wisdom and warmth of an older brother. Thank you for your help in my studies and your support.

A note of thank goes to Sandro and his father, Prof. Baldi, Andrea, Martina, Loukia, James, Wonsirk, Michail and Dr Hann for their friendship, the shared smiles and cheerfulness.

Jo. You accompanied me during my first steps into this adventure.

I need to thank Blanca, Kozue and Gigi. I have never showed them enough gratefulness for their friendship. Blanca, I will never forget the time you spent next to my bed at the hospital and during my convalescence at Nutford House. The smile always painted on your face was my strength during those difficult moments.

I am grateful to the English surgeons who operated me on my leg. It is due to their professionalism that I could walk again and continue my thesis. I am also obliged to the Italian doctors who operated me on my hand, so skilfully that I could work again after few weeks.

Angela. Love and patience, warmth and understanding. You sacrificed so much of your life and time to support me through these years that I could never return what I owe you.

I thank my parents, Dino and Isabella, and my brothers, Domenico and Daniele. Their Love is a distant and warm~~th~~ embrace that supports me throughout the years. This thesis is dedicated to them and to the memory of my grandmother. I also thank all the members of my numerous family, who always encouraged me to continue and be successful.

I thank God for His love and forgiveness. He was behind all, at the beginning and at the end.

Table of Contents

Nomenclature

Roman characters

a	semi-long axis of the elliptic cylinders, m
A	cylinder heat transfer area, m^2
A_o	relative amplitude of pulsation
b	semi-short axis of the elliptic cylinders, m
b_o	laser beam diameter, m
b_w	laser beam waist at $1/e^2$ intensity, m
b_x	diameter of measuring volume, m
b_y	length of measurement volume, m
d	diameter of circular cylinders, m
d_e	equivalent diameter of elliptic cylinders, equal to the diameter of an equivalent circular cylinder, whose circumferential length is equal to that of the present elliptic cylinder, m
d_p	particle diameter, m
d_x	longitudinal length of the drop-shaped cylinders, m
d_y	transversal length of the drop-shaped cylinders, m
d^*	characteristic length, m
e	2.718...
e	cylinder eccentricity, m
E_U, $E_{r.m.s.}$	percentage error in the mean and r.m.s. velocities respectively
f_1, f_2, f_3	focal lengths of lenses of anemometer, m
f_s	vortex shedding frequency when $f_d \neq 0$, Hz
f_{so}	natural vortex shedding frequency when $f_d = 0$, Hz
f_d	flow pulsation (or driving) frequency, Hz
g	acceleration due to gravity, ms^{-2}
h	sampling time interval, s
h	projected height of an elliptic cylinder, m
H	height of test sections, m
I	electric current through the cartridge, A
k	order of the diffracted beams
k_c	thermal conductivity, $Wm^{-1}K^{-1}$
Kr	kurtosis of velocity p.d.f.
L	longitudinal spacing between vortices, m; also cylinder length, m
L_F	vortex formation length, m
n	number of line in grating
N	number of cycles in a signal burst; also number of transverse rows in a tube bundle
N_G	rotational speed of diffraction grating, Hz
N_n, P_n	anticlockwise and clockwise shed vortices respectively; n is an integer which indicates the order of succession of vortices

N_{na}, P_{na}	anticlockwise and clockwise shed vortices respectively relative to the sequence of frames (a); n is an integer which indicates the order of succession of vortices
N_{nb}, P_{nb}	anticlockwise and clockwise shed vortices respectively relative to the sequence of frames (b); n is an integer which indicates the order of succession of vortices
N_{na}^{*}, P_{na}^{*}	anticlockwise and clockwise vortices respectively formed by the separation of the flow over the tip of the downstream cylinder and relative to the sequence of frames (a); n is an integer which indicates the order of succession of vortices
N_{nb}^{*}, P_{nb}^{*}	anticlockwise and clockwise vortices respectively formed by the separation of the flow over the tip of the downstream cylinder and relative to the sequence of frames (b); n is an integer which indicates the order of succession of vortices
Q	electrical power dissipated in the cartridge heater, W
s	line spacing of the diffraction grating, m
Sk	skewness of velocity p.d.f.
S_L	longitudinal spacing, m
S_T	transverse spacing, m
S_L'	centre-to-centre diagonal distance between two cylinders in adjacent transverse rows, m
t_a, t_a	observation time relative to the frame sequences (a) and (b) respectively, s
T	vortex shedding period, s; also time taken by a particle to travel the distance λ^{*} (fringe spacing), s
T_s	surface temperature, K
Tu	turbulence intensity
T_∞	bulk temperature, K
u	instantaneous velocity in x-direction, ms^{-1}
u'	r.m.s. velocity in x-direction, ms^{-1}
u'_{max}	maximum r.m.s. velocity on the wake centreline, ms^{-1}
u'_p	r.m.s. velocity in x-direction under pulsating flow conditions, ms^{-1}
u'_s	r.m.s. velocity in x-direction under steady flow conditions, ms^{-1}
u'_{ups}	r.m.s. velocity in x-direction measured upstream of the bundle at a reference location, ms^{-1}
U	mean velocity in x-direction, ms^{-1}
U_{fs}	freestream velocity, ms^{-1}
U_g	gap velocity, ms^{-1}
U_{osc}	instantaneous oscillatory velocity component, ms^{-1}
$U_{particle}$	velocity component of particle crossing the measuring volume, m
U_{puls}	instantaneous pulsating velocity component, ms^{-1}
U_s	settling velocity of a spherical particle, ms^{-1}
U*	characteristic velocity, m/s
U_∞	upstream bulk velocity, ms^{-1}
V	radial mean velocity in y-direction, ms^{-1}; also voltage, V
V_v	streamwise vortex velocity, ms^{-1}
V_{k4}	thermocouple amplified signal, arbitrary units

v'	radial r.m.s. velocity in y-direction, ms^{-1}
v'_{ups}	r.m.s. velocity in y-direction measured upstream of the bundle at a reference location, ms^{-1}
W	lateral spacing between vortices, m; also test section width, m
x, y, z	co-ordinates in three orthogonal directions, m
x_c	distance downstream from the centre of the cylinder along the centreline, m
x_i, y_i, z_i	cylinder local co-ordinates in three orthogonal directions, m
Zc	function of confidence level
$\Re$	wavenumber, m^{-1}

Abbreviations

2-D	2-dimensional
CNC	computer numerically controlled
CCD	charge-coupled device
d.c.	direct current, A
DC	downstream cylinder
FFT	fast-Fourier transform
LDA	laser Doppler anemometry
PSD	power spectral density
p.d.f.	probability density function
r.m.s.	root mean square
UC	upstream cylinder

Greek symbols

α	angle of attack, ^{o}
ΔU	amplitude of pulsation, m/s
$\Delta\tau_N$	duration of a number N of cycles in a signal burst, s
ε	reduced amplitude of flow pulsations
ε_c	timing error
θ	angle of intersection of laser beams, ^{o}
λ	wavelength, m
λ^*	fringe spacing, m
ν	kinematic viscosity of the fluid, m^2s^{-1}; also frequency, Hz
ν_c	Nyquist frequency, Hz
ν_d	Doppler frequency, Hz
ν_s	frequency shift, Hz
ν_T	clock frequency shift, Hz
ρ_p	particle density, kg/m^3
ρ	fluid density, kg/m^3
σ_b	r.m.s. due to broadening contribution, ms^{-1}
σ_d	total measured r.m.s., ms^{-1}
σ_f	r.m.s. broadening contributions due to small scale velocity fluctuations within the measurement volume, ms^{-1}
σ_g	r.m.s. broadening contributions due to velocity gradient, ms^{-1}

σ_i	r.m.s. broadening contributions due to finite instrument bandwidth, ms^{-1}
σ_t	r.m.s. broadening contributions due to finite transit time, ms^{-1}
σ_v	r.m.s. due to the flow turbulence, ms^{-1}
φ	angular distance from front stagnation point, ^{o}
φ_k	angle of beams emerging from diffraction grating, ^{o}

Dimensionless numbers

Le	Lewis number
Nu	Nusselt number
Nu_p	Nusselt number in pulsating flow
Nu_s	Nusselt number in steady flow
Nu_m	mean Nusselt number
Re	Reynolds number
Sh	Sherwood number
St	Strouhal number

List of Figures

List of Tables

CHAPTER 1

Introduction

1.1 Background

Tube bundles are found in the nuclear and process industries, and are the most common geometry used in heat exchangers. These heat exchangers consist normally of a bundle of tubes contained within a cylindrical cell. The efficiency and performance of such heat exchangers depends on the fluid flow and heat transfer characteristics of the tube bundle, which in turn depend on the geometry of the tube bundle, that is the arrangement of the tubes, and the flow conditions.

Fouling of heat exchangers is an important constraint with respect to the use of such equipment. It increases the heat transfer resistance and therefore causes the efficiency of such apparatus to drop. In the worst case fouling leads to total failure of the heat exchanger with probably enormous economical consequences. The most common type of fouling encountered in heat recovery systems is gas-side particulate fouling, meaning that particulate matter present in the gas stream deposits on the heat transfer surface.

Flow periodicities are also present in tube bundles which may incite tube vibrations. Four excitation mechanisms have been identified: turbulent buffeting, vorticity shedding, fluid elastic instability and acoustic resonance. The first two mechanisms are relevant to the present work. Vortex shedding excitation is attributed either to shed vortices or to instabilities of the flow between tubes. The problem of flow induced vibration is handled empirically in industry. The approach involves the mismatching of the vortex shedding frequencies and the tube natural frequencies or the acoustic natural frequencies of the heat exchanger shell. An exhaustive review on flow-induced vibration can be found in Païdoussis (1983) and Weaver and Fitzpatrick (1988).

A great amount of effort has been directed towards effective ways of enhancing heat transfer. Both active (flow perturbations) and passive methods (asymmetric and non-circular tube arrangements) of heat transfer augmentation and minimisation of heat exchanger fouling are investigated. Results in the published literature suggest that flow perturbations can lead to increased heat transfer rates while a rearrangement of the tubes or a redesign of the tube shape, can lead to reduced deposition rates (Bergeles et al, 2000).

This thesis is concerned with experimental investigations of unconventional tube bundles in steady and pulsating cross-flow of water. Three configurations were investigated: two in-line arrays with elliptic and drop-shaped tubes respectively and an asymmetric array with circular tubes. The work is mainly concerned with the velocity characteristics of tube bundle flows which were quantified by laser Doppler anemometry. Laser sheet flow visualisation was also employed to provide qualitative information on the flows under investigation and a thermocouple heat transfer measurement technique was developed to determine surface temperature.

The present study is an extension of a previous experimental work by Balabani (1996) on the flow characteristics in conventional tube bundles and is part of an on-going research programme carried out at King's College London on heat exchanger tube bundle flows. The objectives of the present experimental work are to study the effects of asymmetric tube arrangements and non-circular tubes under steady and pulsating flow conditions on the flow and heat transfer characteristics of cylinder arrays.

Finally, the data collected were used to validate the numerical models developed as part of the research program for the prediction of the flow and heat transfer in the geometries investigated.

1.2 Literature review

Most of the published literature deals with flows in conventional tube bundles, that is, tube bundles with circular cylinders arranged either in an in-line or a staggered configuration. In the first arrangement the tubes are aligned to the direction of the upstream velocity and in the second one they are staggered in alternating rows (Figure 1.1). Both configurations have a symmetrical arrangement of the tubes. The parameters that describe the geometry of such arrays are the tube diameter, d, the transverse, S_T, and longitudinal, S_L, spacings between tubes. On the ground of dimensional analysis and geometric similarity these three parameters are grouped into two others (non-dimensional spacings): S_T/d, and S_L/d

Only in recent years, tube bundles with streamlined tubes (tubes with a cross section whose eccentricity, e[1], is different from zero, or equally, whose axis ratio, b/a, is different from one) as well as tube bundles with asymmetric arrangements of the tubes have been considered for cross-flow heat exchangers.

This chapter provides a review of the most pertinent literature on the flow and heat transfer phenomena in tube bundles as an exhaustive review of all related works cannot be given.

Although this thesis is concerned with unconventional tube bundles, a brief account of the main characteristics of the flow past a single cylinder is given as it helps to understand more complicated flows as in tube bundles. The flow and heat transfer in conventional tube bundles is also briefly reviewed for comparison.

1.2.1 Single cylinder in cross-flow

The regimes of the flow past a single cylinder can be mainly characterised in terms of the range of Reynolds numbers in which they occur. Balabani (1996) summarised the

[1] $e = (1-b^2/a^2)^{1/2}$, where a and b are the semi-long and semi-short axis of the elliptic cylinder respectively.

different flow regimes that have been identified for different Re according to the corresponding boundary layer behaviour.

Re < 1.0	The inertia forces are negligible and the flow is potential in nature.
2.0 < Re 30	Two symmetrical vortices are formed behind the cylinder and the flow is laminar and steady. The vortices become more elongated with increasing Re.
40 < Re < 70	A periodical oscillation of the wake is observed.
90 < Re < 300	Vortices are shed periodically and alternately from each side of the wake, forming two rows of vortices.
Re > 300	The subcritical regime is established characterised by boundary layer separation at about 80°-85° from the front stagnation point. The cylinder wake is larger than the cylinder diameter (Roshko, 1961).
Re > 200,000 (critical Re)	A transition of the boundary layer from laminar to turbulent occurs. This regime is characterised by laminar separation bubbles followed by turbulent reattachment and delayed final separation (140°).

At higher Re the supercritical regime is established, characterised by the fact that transition occurs closer to the front stagnation point and the separation moves upstream. For Re > 3.5×10^6 transition occurs so close to the front stagnation point that the flow is independent of Re. This regime is known as transcritical regime.

The transition between the different flow regimes in real flows depends on several parameters such as the free-stream turbulence, blockage ratio, surface roughness, cylinder aspect ratio (length/diameter) and so on.

Numerous investigations are concerned with the fluid dynamics, flow periodicities and geometrical characteristics of the cylinder near-wake (Gerrard, 1966; Williamson, 1996). The near wake flow of a cylinder in the subcritical regime can be characterised by four characteristic lengths, all depending on the Reynolds number: the length of the separated laminar shear layer, the vortex formation length, the length of the recirculation bubble and the diffusion length. The vortex formation length is defined as the "distance downstream of the cylinder axis to a point where the r.m.s. velocity fluctuations are maximised on the wake centreline" (Williamson, 1996). It is an indication of the distance at which the first vortex appears. Gerrard (1966) has shown that the vortex formation length is a relevant length scale for the distribution of fluctuating velocity close to the body. The vortex that is formed on one side of the cylinder is continuously fed by the circulation from the shear layer until it becomes strong enough to draw the opposite shear layer into the wake. The approach of vorticity of opposite sign may cut off further supply of circulation to the vortex, which ceases to increase in strength. Gerrard suggests that this stage corresponds to the actual shedding of the vortex. The diffusion length is defined as the thickness (Gerrard, 1966) of the shear layer at the end of the formation region where the layer is drawn across the wake.

For Re ranging between 50 and 10^6, and even for higher values, vortices are shed periodically and alternatively from each side of the cylinder as a result of the interaction between the separating shear layers, base pressure, diffusion and distribution of vorticity through the flow field (Konstantinidis, 2001). As a consequence of the shedding of vortices, low-pressure zones are generated on the downstream side of the cylinder. These alternating zones cause the body to move towards the low-pressure zone perpendicularly to the direction of the flow. The nature of the vortex shedding can be disruptive when the natural shedding frequency, f_{so}, matches the resonant frequency of the cylinder. It should be noted that the oscillations excited by the vortex shedding on a flexible and lightly damped, or rigid and flexibly mounted bluff body are usually transverse to the direction of the oncoming flow as the generated lift force is larger than the drag force.

It was Strouhal (1878) who discovered the systematic process of vortex shedding for flow past a single cylinder. By scaling the shedding frequency with the free stream

velocity and the cylinder diameter, he established a non-dimensional flow parameter that identifies consistent physics downstream of the cylinder over a broad range of Reynolds numbers. This fundamental parameter, widely known as the Strouhal number, and its validity for specific combinations of flow and geometric conditions has been under investigation for well over 100 years (Snarski and Jordan, 2001). In the subcritical range, the Strouhal number, St (= f_{so} d*/U*, where d* is the characteristic length of the cylinder and U* the characteristic velocity of the oncoming flow), remains at an almost constant value of 0.2, which implies a linear relationship between the vortex shedding and the velocity. The relative constancy of the Strouhal number is attributed (Gerrard, 1966) to the fact that the two major frequency-determining factors (vortex formation length and diffusion length) tend to change the frequency in opposite directions as the Reynolds number is altered. When the free-stream turbulence is increased at constant Re, the vortex formation length decreases, but the diffusion length presumably increases to such an extent that the two opposite effects balance.

Vortex shedding can be dramatically changed when a cylinder is oscillating in a steady flow or, equally, when the flow past a rigid cylinder has an oscillatory component. In fact, for certain ranges of amplitude and frequency of the oscillations, the cylinder motion or the oscillating flow can take control of the instability mechanism and consequently of the frequency of the vortex shedding. This coincidence or resonance of the vortex and vibration frequencies is commonly termed "lock-on", "lock-in" or "synchronisation".

Vortex excited oscillations have a tremendous engineering significance. They could result in large aerodynamics forces and induced stresses, increased fatigue or even lead to structural damage or have destructive consequences.

1.2.2 Conventional tube bundles in cross-flow

Numerous experimental studies have been carried out on the fluid flow and heat transfer in conventional tube bundles due to their wide applications in heat exchangers. Conventional tube bundles used in practical applications of heat

exchangers have two generic configurations: in one, circular cylinders are arranged *in-line* with the flow direction and in the other, they are *staggered* in alternating rows. By displacing one or more cylinders in either direction or adopting cylinders of non-circular shape more complex configurations, here termed "unconventional", can be produced.

Flow regimes

The cross-flow around a cylinder inside a bundle can be significantly different from that around an isolated cylinder due to the interference from the adjacent cylinders. Furthermore, the interference flows may become more complex as the number of cylinders in cross-flow increases. However, various flow regimes can be identified in tube bundles in cross-flow depending on the Reynolds number. The transition between these regimes depends on the arrangement, geometrical parameters of the tube bundle and the roughness of the tubes. Table 1.1 summarises the different flow regimes distinguished by Žukauskas (1989).

Table 1.1. Summary of flow regimes identified in tube bundles in cross-flow.

Flow regime	Re
predominantly laminar	Re < 1,000
mixed or subcritical	Re < 200,000
predominantly turbulent or critical	Re > 200,000
supercritical flow	Re > 400,000

Flow periodicity

As previously mentioned, flow induced vibration in tube bundles may be excited by one or more of the following mechanisms: 1. turbulent buffeting (or simply turbulence), 2. vorticity shedding (or Strouhal periodicity), 3. fluid elastic instability and 4. acoustic resonance.

The buffeting refers to unsteady forces developed on a body exposed to a highly turbulent flow. Weaver and Fitzpatrick (1988) observed in fact that the tubes in a tube-and-shell heat exchangers act as generators of turbulence, and, consequently, at all practical Re, they will be subjected to broad band turbulent buffeting, that is random fluctuating forcing. The action is one way, from fluid to solid cylinder, and the amplitude of the incited vibrations is small and rarely built up to large amplitudes (Moretti, 1993)

Vortex shedding refers instead to the fact that even when a cylinder is exposed to a uniform, non-turbulent oncoming flow, the cylinder wake develops an instability leading to fluctuating lift and drag forces on the body (Savkar, 1977). The vorticity shedding excitation was found to originate from alternate vortex shedding occurring in the first rows of staggered arrays (Weaver et al, 1991, 1993) and symmetrical or anti-symmetrical jet instabilities in in-line arrays (Ziada and Oengören, 1991). Weaver and Fitzpatrick (1988) define the Strouhal periodicity as "a narrow band (essential periodic) phenomenon that occurs at a constant Strouhal number". It should be noted that the possibility of vortex shedding in closely spaced tube arrays has been a subject of debate for several years. For example, Fitzpatrick and Donaldson (1980) found a transitional nature of the turbulence beyond the fourth row in in-line arrays. This transition was attributed to the existence of a buffeting frequency in tube banks, according to the theory of Owen (1965), who argued that vortex shedding could not occur deep inside closely spaced tube arrays.

Ziada and Oengören (1991) tested an in-line tube array with circular tubes and intermediate tube spacings in both a wind and water tunnel in order to reveal the nature of the vorticity shedding excitation. Measurements were taken behind the second and third rows. Velocity fluctuations seemed to occur at a well-defined (single) frequency, which decreased linearly as the gap velocity decreased. The correspondent Strouhal number of the flow periodicity in both cases (air and water) was similar and equal to St = 0.15. This led the author to the conclusion that the nature of the flow instabilities must be the same for both cases. This value is substantially lower than those given by Fitz-Hugh (1973) and Chen (1984), that are 0.24 and 0.28 respectively, although Chen's chart gives an additional subharmonic component of 0.14. Ziada and Oengören argue that the disagreement is due to the fact

that both Fitz-Hugh and Chen's charts were obtained from acoustic resonance cases, whose corresponding Strouhal number differs from the one of the flow periodicity. Rae and Wharmby (1987) constructed a Strouhal chart based on non-resonant data which gave value of St = 0.15, much closer to the one obtained by Ziada and Oengören. The same authors argued that a direct comparison with charts (see Weaver et al (1987)) relative to standard in-line geometries (square in-line arrays) are not possible.

A large amount of published Strouhal number data exists for various tube bundle geometries (Chen, 1977; Weaver et al, 1987; Oengöeren and Ziada, 1995). However, St is strongly dependent on the tube arrangement, the spacing between tubes, the Reynolds number, the location within the array and even the tube shape. Armstrong et al (1986) investigated the flow over three bluff bodies of different shape: a circular cylinder, a D-shaped cylinder, with front face flat, and a flat plate. The cylinders were horizontal and perpendicular to the free-stream direction. Both the Strouhal number and the base pressure were evaluated. Their variation with Reynolds number was negligible. The Strouhal number for the circular cylinder was approximately equal to 0.21 and higher than for the flat and D-shaped tubes, St ≅ 0.16 and 0.15 respectively.

Furthermore, there is evidence of multiple Strouhal numbers for certain arrays. Consequently, the scatter in the published data is considerable.

Velocity measurements

A brief account of the velocity characteristics in cylinder arrays is given below. A more extensive review can be found in Balabani and Yianneskis (1996), Balabani (1996) and Žukauskas (1972). As Konstantinidis (2001) has noted, probably the most complete published study of the mean and fluctuating velocity fields in cylinder arrays is that of Balabani and Yianneskis (1996). They studied an in-line (S_L/d x S_T/d = 2.1 x 3.6) and two staggered arrays (S_L/d x S_T/d = 2.1 x 3.6 and S_L/d x S_T/d = 1.6 x 3.6) in water cross-flow. They found that the staggered array produces higher turbulence levels and the flow develops in fewer rows than in the in-line array with

the same spacing. The staggered array with larger longitudinal spacing showed lower r.m.s velocities and longer recirculation regions.

Halim and Turner (1986) studied the velocity characteristics of a normal triangular array. They found that the flow is fully developed after the third row. A pronounced recirculation was observed behind the first row with negative velocities up to 40% of the mean velocity within the bank. The mean recirculation region extended one diameter downstream of the centre of the first row.

Heat transfer

An extensive review of the earlier work on the heat transfer from arrays in cross-flow, including the case of a single cylinder can be found in Žukauskas (1972).

The variation of the heat transfer around a tube in a bundle is determined by the flow pattern, which in turn depends strongly on the arrangement and number of tubes. Furthermore, it greatly depends on the Reynolds number and on the physical properties of the fluid.

Žukauskas (1972) compared the heat transfer variation in inner rows of in-line and staggered arrangements with that of a single cylinder. In both arrays a higher turbulence intensity in the flow causes the heat transfer to increase at the front and at rear part of the cylinder.

The heat transfer around a cylinder in the first row of a staggered array resembles that of a single cylinder. As the fluid flows through the first row it is disturbed. The heat transfer in downstream rows increases up to the third one, downstream of which no further increase is observed.

The same author compared published experimental data for the staggered and in-line arrangements. The comparison showed that at low Re the heat transfer in the in-line array is significantly lower than that in the staggered one. The heat transfer of both arrays increases with Re, but that in the in-line array increases more rapidly and at high Re approaches the heat transfer intensity of the staggered array.

The free stream turbulence was also found to increase the heat transfer, mainly in the first rows where the heat transfer coefficient increases with Re and turbulence level (Stephan and Traub, 1986; Traub, 1990). The increase was found to be more pronounced in in-line arrangements than in staggered ones. Žukauskas (1972) observed also a significant increase of the heat transfer in the transition from subcritical to critical flow. No effect of surface roughness on heat transfer was instead observed in subcritical and transcritical regimes, as while the roughness reduces the critical Re it anticipates the heat transfer enhancement at lower Re. An increase of the heat transfer was instead detected in the critical and supercritical regimes. This was more pronounced in the staggered arrangement.

1.2.3 Flow and heat transfer in unconventional tube bundle geometries.

Both the asymmetric array with circular tubes and the in-line ones with elliptic and drop-shaped tubes respectively investigated in the present work are novel and therefore there are very few relevant publications which are discussed below.

Effect of the shape of the tubes

The advantages of adopting a streamlined configuration can be significant. It has been found, for instance (Ota et al, 1984), that elliptic-shaped tubes have a drag coefficient, which, at small angles of attack, is lower than that of a circular cylinder. As a result, heat exchangers with such tubes will require less pumping power on the shell-side. Moreover, for a given pumping power requirement the overall design of a tube bundle with elliptic tubes is expected to be more compact.

Modi and Wiland (1970) studied experimentally the aerodynamics of a set of two-dimensional elliptic cylinders with eccentricity of 0.8 and 0.6 respectively, at various angles of attack. The Reynolds number based on the major axis of the ellipse and the freestream velocity, U_{fs}, ranged from 20,000 to 100,000. Data on Strouhal number, unsteady pressures and wake geometry were presented as a function of the angle of

attack during static conditions of the models. For the thicker ellipse (of eccentricity, *e*, equal to 0.6) a slow rise in the projected height of the cylinder, h[2] (see Figure 1.2), with a small drop in shedding frequency led to an almost uniform Strouhal number in the Reynolds range investigated. On the other hand, for the thinner ellipse the very sharp drop in shedding frequency offset the relatively greater rise in projected height thus leading to a decrease in Strouhal number. Basing the Strouhal number on the projected height of the cylinder, h, appeared to reduce its dependence on the angle of attack.

Modi and Dikshit (1974) studied the near wake aerodynamics of two-dimensional elliptic cylinders with eccentricities, varying from 0.44 to 0.98, at various angles of attack. Four elliptic cylindrical models were arranged side by side. The Reynolds number was 68,000 ($Re = U_{fs}\, 2a/\nu$, ν being the kinematic viscosity of the fluid). Wake geometry characteristics, such longitudinal spacing (L), vortex velocity (V_v), lateral spacing (W), wake geometry ratio, (W/L), and vortex formation length were determined from measurements of the fluctuating pressure of the field associated with the vortex shedding from the elliptic cylinders.

The recorded r.m.s. values of the pressure signal gave a set of curves, each having two peaks near the vortex centreline. The distance between these maxima, at a given downstream station, was taken to be a measure of the lateral spacing, W, between the two rows of vortices at that station. The location of the peak fluctuation was taken approximately as the position of the vortex core. The longitudinal spacing between consecutive vortices, L, showed an increase with increasing the angle of attack, the larger change being associated with high eccentricity ellipses; that is, at a given station, L increases, as the cylinder becomes more slender. The vortex velocity, V_v, was deduced from the relation, $V_v = L \times f_{so}$, with L being the longitudinal spacing and f_{so} the natural vortex shedding frequency respectively. Although V_v showed a similar trend to the longitudinal spacing, it was found to depend less on the cylinder eccentricity. It is apparent that for zero angle of attack, $\alpha = 0$, the wake width, W, was found to diminish with increasing the cylinder eccentricity; however, the wake

---

[2] $h = 2(a^2\sin^2\alpha + b^2\cos^2\alpha)^{1/2}$, where a and b are the semi-long and semi-short axis of the elliptic cylinder respectively and α is the angle of attack.

geometry ratio (W/L) increased suggesting a greater reduction in longitudinal spacing.

Finally, although a decrease in the eccentricity showed a slight increase of the formation length no conclusive remarks on the effect of eccentricity at a given angle of attack were made.

Ota et al (1983) investigated the heat transfer characteristics of an elliptic cylinder with an axis ratio of 1:2. The working fluid was air and the Reynolds number ranged from about 5,000 to 90,000. The angle of attack was varied from 0° and 90°. The Re number range tested fell within the subcritical regime number region and as a result the heat transfer coefficient showed no substantial change with Re.

The results for $\alpha = 0$ showed clear symmetry of the local Nusselt number distribution on the upper and lower surfaces of the cylinder around its centreline at all the Re numbers investigated. Nu attains the highest value at the leading edge and decreases steeply as a laminar boundary layer develops on the upstream face. In the separated flow region, Nu, increases again with downstream location and reaches a relative maximum at the trailing edge. At very low Reynolds numbers Nu shows no essential change therein, probably due to a very stagnant flow in the near wake.

The mean Nusselt number over the whole circumference of the elliptic cylinder was estimated by a graphical integration and was found to increase linearly with the Reynolds number in logarithmic scale at all angles of attack studied. In order to compare the heat transfer characteristics of the elliptic cylinder with that of a circular one the diameter of a circular cylinder of equal circumferential length was selected as a suitable characteristic length for both Re and Nu.

The empirical formula of Hilpert was used to calculate the mean Nusselt number for a circular cylinder in the region 4,000 - 40,000. Even the lowest value of the mean Nusselt for an elliptic cylinder was found to be higher than that for the circular cylinder. Therefore the elliptic cylinder of axis ratio 1:2 exhibited a superior heat transfer performance.

Ota et al (1986) investigated the local and overall heat transfer characteristics of two elliptic cylinders of axis ratio 1:2 in tandem arrangement. The working fluid was air and the Reynolds number based on the major axis of the tubes, 2a, ranged from 15,000 to 80,000. The angle of attack was varied from 0° to 90° and the transverse spacing, S_T, from 1.25 to 4.00 times the major axis of the cylinders.

It was noted that the local Nu distribution showed no essential dependence upon the Reynolds number in the range investigated. It was also observed that for $\alpha = 0°$, the local Nusselt number on the upstream surface of the upstream cylinder (UC) exhibits no dependence on $S_T/2a$. On the other hand, it was strongly affected by the cylinder spacing in the downstream separated region. Nu increased with increasingly $S_T/2a$ from 1.25 to 1.5, then decreased discontinuously up to $S_T/2a = 2.00$. A further increase of the cylinder spacing did not bring any essential change in the Nu distribution. This sudden variation was attributed to the jumping-phenomena, that is, when the spacing between the cylinders is large enough (critical spacing), a vortex street is formed behind the upstream cylinder producing a higher heat transfer rate therein. A similar, but greater sudden variation of the local Nusselt number was observed for the downstream cylinder (DC), whose Nu varies remarkably on the whole of the cylinder surface with the cylinder spacing. It is interesting that the sudden change of the local heat transfer rate of the DC occurred between $S_T/2a = 2.00$ and 2.5, that is, at higher values than for the UC.

Merker and Hanke (1986a) measured both the mass transfer coefficients and the static pressure distribution along the shell-side of oval-shaped tubes in cross-flow heat exchangers. Two staggered arrays were investigated. Both arrays had a transverse pitch ratio, $S_T/2b$, equal to 2.63 and longitudinal pitch ratios, $S_L/2a$, equal to 1 and 0.67 respectively. The axis ratio of the tubes was about 4:1. The working fluid was air and the Reynolds number ranged from 19,890 to 26,000. The heat transfer coefficients were determined with the aid of the analogy between heat and mass transfer. The velocity distribution along the arclength was determined from static pressure measurements using Bernoulli's equation.

It was observed that for the bank with $S_L/2a = 1.00$ the velocity profiles at all rows were quite similar to that of a single cylinder. Furthermore the location of the separation point did not change significantly from row to row. However, in the bank with $S_L/2a = 0.67$ the velocity profiles in the first two rows differ substantially and were characterised by late and early separation respectively. The velocity profiles for the third and sixth row were found to be similar indicating that the flow becomes fully developed after the third row.

The local Nusselt number (Nu) distributions along the arclength of the first and sixth rows showed that there was good agreement between the Nusselt distribution of a single cylinder and that of the first tube of the bank with $S_L/2a = 1.00$. The distributions showed an exponential decrease of Nu from the front edge of the cylinder to the rear one.

In a following paper (1986b) the same authors reported mass transfer and pressure drop measurements on staggered tube banks with oval-shaped tubes having longitudinal and transverse pitch ratios in the range of 0.67 - 1.00 and 1.97 - 3.16 respectively. Measured mass transfer coefficients, expressed in terms of a Sherwood number, were calculated for each row and converted into Nu numbers using the analogy between heat and mass transfer ($Nu = Sh \times Le^{-n}$). Measurements were taken for Re in the range of 1,390 to 42,740 in the tube bank with $S_L/2a = 1.00$ and $S_T/2b = 1.97$.

For Reynolds numbers lower than 3,000, the Sh number had approximately the same value for each row. When the Re was increased up to 20,000, the Sh increased in the first and up to the third row, decreased in the fifth and sixth row and increased again up to the last row. By taking into account the scattering of the experimental data the Sh number was considered fairly constant from the fourth or fifth row up to the last, which implied that the entrance region was restricted to the first three or four rows of the bank.

The Sherwood-Reynolds number dependence (evaluated as the arithmetic mean value between the Sh measured in rows four to seven) was also given for eight banks having different longitudinal and transverse pitches and a single tube. The Sh number

increased almost linearly with the Reynolds number for all the designs investigated. The Sh numbers for banks with the same longitudinal pitch were very close together, i.e., the transverse pitch had a very weak influence. Furthermore, comparing the empirical correlations representing the data for the tube banks and a single tube, it was clear that the average mass transfer coefficient is higher for tube banks with small longitudinal pitches. An opposite trend was observed only for sufficiently high Reynolds numbers.

The authors also made a comparison between tubular cross flow heat exchangers having circular or oval-shaped tubes. The dependence of the ratio of the thermal power per unit temperature to the pumping power on the mass flow rate was investigated. The ratio is greater the larger the frontal area of the shell side is. In general, the oval-shaped tube banks have small frontal areas on the shell side compared to those with circular tubes. This is evidently advantageous when the available pumping power is restricted.

Li et al (1997) investigated the heat transfer and pressure drop of tube banks with elliptic tubes having an axis ratio of 1:2. In-line configurations with different longitudinal and transverse pitch were tested. The longitudinal pitch ranged from 1.5 to 3.0 and the transverse one from 2.0 to 2.8. The experimental results showed that the average Nusselt number increases linearly with the Reynolds number independently of the geometrical parameters of the bank. Conversely, the smaller the transverse spacing or the higher the longitudinal spacing the higher the pressure drop. A comparison between in-line and staggered tube banks with elliptic tubes with corresponding banks with circular cylinders was made. Configurations with circular tubes showed a higher mean Nusselt number at all the Reynolds number investigated; Nu was slightly higher for the in-line arrangement at high Reynolds numbers only. The staggered configuration with elliptic cylinders exhibited the lowest Nu values. With regard to the pressure drop, the in-line configuration with elliptic cylinders showed the lowest resistance to the flow, whereas the staggered configuration with circular tubes the highest one, as expected.

Nair and Sengupta (1997) investigated the flow past elliptic cylinders for different Reynolds number and angles of attack by 2-D direct numerical simulation. Two axis

ratio combinations (1:10 and 1:4) along with three angle of attack cases ($\alpha = 10^{\circ}$, $\alpha = 12^{\circ}$, $\alpha = 30^{\circ}$) were investigated. Comparing the two axis ratios investigated, it can be seen that for the ellipse with axis ratio b/a = 0.1, the flow behaves more like a conventional airfoil. The separation point, which is near the leading edge for b/a = 0.1, is either absent or is located further downstream for b/a = 0.25. The number of secondary vortices increases with an increase in the axis ratio for the same α. The strength of the vortices shed increases with b/a. This results in an increased movement of the front stagnation point and the deflection of the wake. The average lift is higher for smaller axis ratio at the same α, even though the maximum lift is higher for the ellipse with b/a = 0.25 wake. For b/a = 0.25 negative values of the lift were obtained, due to the significant movement of the front stagnation point and the formation of alleyways. This negative lift tells that the larger the axis ratio the more the ellipse behaves like a bluff body for the same α.

Effect of the arrangement of the tubes

Katinas and Tumosa (1992) studied experimentally the effect of transverse displacement on heat transfer and fluid dynamics of a staggered tube bundle with transverse and longitudinal pitch ratios of 1.15 and 0.98 respectively. The Re ranged from 10^3 to 6×10^5. The experiments showed significant alterations to the local Nu distributions around the displaced tube followed by changes in the vortex shedding frequencies and the locations of impact and separation points. The alterations were more pronounced at larger displacements. The average heat transfer was found to increase by 25% at large displacements as a result of the shift in the locations of the impact and separation points. The maximum heat transfer augmentation was observed at displacements equal to approximately 0.1 d, but as the displacement increased further the average heat transfer decreased.

However, Wung et al (1986) reported that both the heat transfer rates and the pressure drop of non-standard arrays resulting from various displacements of alternate or other rows in the transverse direction fell between the values for the corresponding in-line and staggered arrays. They concluded that heat transfer can not

be augmented more than that of a staggered array merely by shifting rows in the transverse direction.

Sharatchandra and Rhode (1997) predicted that small longitudinal displacements have little influence on the thermal and hydraulic characteristics of a closely spaced staggered tube bundle. However, disproportionate increases were observed for longitudinal displacements of the order of half the tube radius: the average Nu was found to improve moderately whereas the friction factor increased significantly suggesting no improvement on the overall efficiency of the tube bundle as a result of tube displacement. Local Nu distributions showed that as the tube displacement increases the Nu decreases at the front portion and increases significantly at the rear portion reaching a local maximum.

1.2.4 Pulsating flow

No standard terminology exists to distinguish between purely oscillatory flows (o) and flows with velocity oscillations superimposed to the flow (m). However, it has been suggested (Cooper et al, 1993) to use the term "oscillatory" to describe the first type of flow aforementioned (o) and "modulated" to describe the second one (m).

In the rest of the work the term *pulsating flow*, or *flow pulsations*, is used to describe an oscillatory flow superimposed to the steady non-zero mean flow. For the sake of easier analytical and numerical processing and/or modelling typical oscillatory flows are sinusoidal in time. Therefore, this survey focuses on periodic pulsating flow containing a well-defined or dominating single frequency. Oscillating flows are expected to affect appreciably the fluid-dynamical and thermal behaviour of the flow. Velocity fluctuations, in fact, may change the mechanism of the turbulent-energy production and therefore the turbulence structure of the flow, which controls the convective heat transfer process. Although, due to the thermal inertia, the temperature field cannot follow the velocity oscillation at high frequency, pulsating, or oscillating flow, at relatively high frequencies and high amplitudes may have a substantial effect on the heat transfer behaviour. Although our experimental

investigation on pulsating flow deals with low frequencies and relatively high amplitudes of pulsations this survey will cover a wider ranges of flow conditions.

It can be anticipated that, although, not much work has been published on the flow and heat transfer under pulsating conditions over a single cylinder as well over tube bundles, the conclusions are largely conflicting as to the effect seen.

1.2.4.1 Pulsation generators

A literature survey was conducted in order to identify the methods used to introduce flow pulsations in a steady mean flow.

Base et al (1981) generated an oscillating flow in the working section of a wind tunnel by oscillating the primary air supply through the air inducers and the secondary flow, the main one, was induced according to the primary flow. The oscillating primary air supply was obtained by means of a solenoid valve, which underwent an on/off operation according to the electrical signal supplied to the valve and controlled by a square wave signal generator. The frequency could be varied from 0.0025 to 25 Hz using a ten-turn dial.

Kotake and Aoki (1984) obtained large amplitude oscillations by changing the cross-sectional area of the flow passages. Two choked throats geometrically symmetrical were located at the outlets from the air storage tank of a wind tunnel. The cross-sectional area was changed in antiphase by a sliding motion of a wedge-shaped piece with the Scotch mechanism. This pulsation generator provided exactly sinusoidally oscillating flows of velocities from 0 to 60 m/s and amplitudes up to 80% at 3 Hz or 10% at 10 Hz.

Andraka and Diller (1985) produced pulsations by means of six rotating shutters mounted on parallel shafts in the settling chamber of a wind tunnel. The shutters provided a nearly sinusoidal waveform with at least 95% of the wave energy at the fundamental frequency. The wave relative amplitude, $\Delta U/U_{\infty}$ [3] = A_o, was varied

[3] ΔU is the pulsation amplitude.

between 4 and 25% of the mean flow. Armstrong et al (1986) similarly introduced pulsations by rotating a set of four shutters situated downstream of the test section. The shutters were rotated in phase by a variable d.c. motor through a belt drive. The perturbation amplitude was found to depend on both the mean flow velocity and perturbation frequency. For a given mean velocity and frequency the amplitude of pulsations was varied by changing the shutters' widths. Spectra of the perturbation velocity showed that its harmonics were small, although not quantified, compared with the fundamental frequency amplitude. When rotating shutters are used as pulsations generators (see also Wolochuk et al (1996)) the amplitude of the oscillations, therefore, depends on their frequency (which could, on the other hand, reach very high values) and increases linearly with the mean flow velocity.

Sung et al (1994) generated pulsations by means of a non-mechanical device. They, in fact, achieved pulsation of the free stream flow by placing a speaker in the settling chamber of a wind tunnel. The sinusoidal signal was produced by means of a function generator. The signal was passed through an audio amplifier and then sent to the speaker. High quality pulsations were produced in the free stream flow. Experiments were carried out with pulsation frequencies, f_d, and relative amplitudes, A_o, ranging between 10 and 40 Hz and between 0.08 and 0.23 respectively. Although this acoustic device produced high quality pulsations and led to a straightforward and simple experimental design it would be hardly applicable in a water tunnel.

Peacock et al (1998) superimposed on the main flow an oscillatory sine wave component provided by a Scotch yoke mechanism. The apparatus allowed them to control the mean and oscillatory components independently. Despite the straightforward design of the apparatus the maximum achievable frequency was equal to $f_d = 3$ Hz.

The pulsation generators described, therefore, present limitations either because of the restricted frequency or amplitude of the pulsations ranges that could be covered or because of construction difficulties. For the present investigation, therefore, a rotating valve, which will be described in Chapter 2, was chosen as pulsator mechanism. Its design as well as its accommodation into the water tunnel was straightforward, and high quality pulsations were achieved. The rotating valve

consisted of a full stainless steel cylinder with a slot cut along its longitudinal axis. The frequency of the associated velocity perturbation was twice that of the rotating valve as the time-varying blockage presented to the flow repeated itself every half turn of the rotating valve. The valve was driven by a variable speed motor, which could provide frequencies from 0 up to 100 Hz. The amplitude of the pulsations could be varied from 0 to 45% of the mean velocity by adjusting the flowrate through the valve and through a secondary parallel steady flow branch of the water tunnel. The amplitude of the pulsations depended on the flowrate through both the steady flow brunch and the rotating valve one as well as on their combination.

1.2.4.2 Effect of pulsations on the flow and heat transfer over bluff bodies

Flow pulsations have been shown to enhance process-engineering characteristics in many applications such as mixing, heat and mass transfer. They also offer the advantage of controlling process conditions via the amplitude and frequency of oscillations. There is an enormous amount of literature on pulsating flows and their applications. A comprehensive review of the fluid mechanics of such flows and the associated applications can be found in Cooper et al (1993).

Pulsating flows over single cylinders and in particular vortex shedding lock-on have attracted considerable attention due to their practical significance in the design of offshore structures (Armstrong et al, 1986, 1987; Barbi et al, 1986; Telionis et al, 1992). It is well known that at large Reynolds numbers one of the major properties of the flow is the shedding of vortices from the body into the wake. The vortex shedding gives rise to a fluctuating lift and drag force whose frequencies are equal and twice the shedding frequency respectively. As a response the cylinder could vibrate transversally to the flow and eventually, if the body is slightly damped, the amplitude of this vibration could become large enough for the vibrational frequency of the cylinder to lock-on to the frequency of the shedding frequency. As a consequence both the lift and drag forces would have a substantial increase leading, eventually, to a failure of the bluff structures and/or structures having bluff components (Armstrong et al, 1986).

Investigations on in-line vibrating cylinders in steady flow have shown that for Reynolds number between 80 and 4,000, lock-on was found, in which the vortex shedding frequency remained at half the cylinder frequency over a range of cylinder frequencies which was twice that of a vortex shedding from the cylinder when it was not vibrated. Little work has been done on cylinders vibrating in-line with the flow and even less on the related case when the cylinder is steady and the oncoming velocity has superimposed an oscillatory perturbation. Armstrong et al (1986) pointed out as these two cases are completely equivalent when the acoustic wavelength is large compared with the diameter of the cylinder. In Armstrong's experimental apparatus this condition was satisfied. Three bluff bodies were used in this investigation: a circular cylinder, a D-shaped cylinder, with front face flat, and a flat plate. The cylinders were horizontal and perpendicular to the free-stream direction. The velocity perturbation was produced by rotating a set of four shutters that were situated at the downstream end of the test section. The authors found that the shedding frequency locked on half the driving frequency, that is the frequency of the flow pulsations, over a range of velocities. The lock-on region was also found to increase with the amplitude of the pulsations. The base pressure was observed to decrease with lock-on and its minimum decreased as well as the pulsation amplitude increased. The effect of lock-on on the base pressure was smaller for the D-shaped cylinder and the flat plate, which have fixed separation points.

Averaged wake velocity measurements by Armstrong et al (1987) indicated that pulsations increased the vortex strength by 29% and decreased the separation of the vortices by 25%. As a result the mean velocity profiles in the wake remained unaltered but the velocity fluctuations in the wake centreline increased. The amount of shed vorticity was estimated to be 12% higher with lock-on and the remaining increase in the vortex strength was accounted for by a decrease in the amount of shed vorticity destroyed in the vortex formation process.

Barbi et al (1986) carried out an experimental investigation of a circular cylinder in steady and oscillatory flow with non-zero mean velocity up to Re = 40,000. Their findings showed that the shedding frequency may vary smoothly with the driving frequency before locking on half the driving (or pulsation) frequency. Furthermore,

they observed that that at the lowest limit of lock-on (which was found to depend on both the amplitude and frequency of the oscillations and on Re), vortices are shed simultaneously on both side of the cylinder.

Telionis et al (1992) found that lock-on occurred for driving frequencies near the natural shedding frequency or its first harmonic and it was most pronounced in the second case. It was observed that lock-on produces a number of effects such an increase in the strength of the vortices and a decrease in the mean base pressure, which are associated with a change in the wake structure.

A number of studies have also been published on the effects of flow pulsations on the heat transfer from a single stationary cylinder but they are not conclusive as to whether flow pulsations augment heat transfer rates. Kim et al (1983) studied experimentally the response of incompressible flow and heat transfer to natural and forced pulsations of the incoming stream over a circular cylinder. The effect of oscillation on the mean heat transfer at the stagnation point of the single cylinder was evaluated. As expected, an increase in the mean velocity corresponded to an increase in the heat transfer, but the dimensionless heat transfer $Nu/\sqrt{Re}$ remained constant. Correspondence was found between the velocity and heat transfer fluctuations. Moreover the fluctuating component of heat transfer decreased with frequency, a decrease which corresponds to an increase in the amplitude of pulsations if one inspects the experimental data the authors provide in their paper. Significant is the fact that no measured effect of oscillations on the mean heat transfer was observed.

Kotake and Aoki (1984) investigated the heat transfer of a cylinder in large-amplitude oscillating wake flows. A wind tunnel was equipped to supply airflow with exactly sinusoidal oscillation of velocity at relatively low frequencies and high amplitudes. One cylinder was located in the oscillating airflow and another cylinder in its wake flow. The cylinder wall was wrapped into a stainless steel foil heated electrically by an alternating current. The surface temperature of the foil was measured circumferentially by rotating the cylinder with a copper-constantan thermocouple soldered to the foil. The mean Reynolds number based on the bulk velocity and a mean cylinder diameter was $Re \cong 16{,}000$.

It was found that the mean-time surface temperature as well as the amplitude of the surface temperature oscillation (heat transfer coefficient and its relative amplitude of oscillation) takes a minimum (maximum) value at the reattachment point of the shear flow separated from the first cylinder, and larger (smaller) values at the forward stagnation and rearward separation points, although it is hardly affected by the mean flow oscillations. With an increase in the frequency of the main flow oscillation, the amplitude of the surface temperature (heat transfer coefficient) decreased. The latter, contrarily, increased with an increase in the amplitude of the velocity oscillations. At slightly staggered positions of the second cylinder with respect to the first one the circumferential distribution of the surface temperature shifted towards the staggered direction. At larger staggers than half of the cylinder radius it tended to coincide with the one of the single cylinder.

1.3 Main findings

The main findings of the preceding literature review can be summarised as follows:

- Four excitation mechanisms have been identified in tube bundles: turbulent buffeting, vorticity shedding, fluid elastic instability and acoustic resonance.

- A large amount of published Strouhal number data exists for various tube bundle geometries (Chen, 1977; Weaver et al, 1987; Oengören and Ziada, 1995). However, St is strongly dependent on the tube arrangement, the spacing between tubes, the Reynolds number, the location within the array and even the tube shape. Furthermore, there is evidence of multiple Strouhal numbers for certain arrays. As a result, the scatter in the published data is considerable.

- In the subcritical range, the Strouhal number, St, remains at an almost constant value of 0.2, which implies a linear relationship between the vortex shedding and the velocity.

- The near wake flow of a cylinder in the subcritical regime can be characterised by four characteristic lengths, all depending on the Reynolds number: the length of

the separated laminar shear layer, the vortex formation length, the length of the recirculation bubble and the diffusion length.

- The relative constancy of the Strouhal number is attributed (Gerrard, 1996) to the fact that the two major frequency-determining factors (vortex formation length and diffusion length) tend to change the frequency in opposite directions as the Reynolds number is altered.

- Although relatively little work has been published on the heat transfer of asymmetric arrays as well as of arrays with non-circular tubes, the conclusions reached are largely conflicting as to observed phenomena. However, the smaller frontal area of the elliptic tubes allows for a more compact design and is also beneficial in terms of particulate fouling of the outer surface.

- Pulsating flow around a single cylinder may cause lock-on of the shedding frequency. Armstrong et al (1986) pointed out that the case of cylinder vibrating in-line with the flow and the case of a steady cylinder in pulsating flow are completely equivalent when the acoustic wavelength is large compared with the diameter of the cylinder.

- Lock-on can cause considerable changes in the wake structure and forces acting on the cylinder.

- There is evidence in the literature that pulsating the flow in heat exchangers enhances heat transfer, although there is disagreement on this point. It should be noted that several investigators have only considered a small number of variables in their studies, which furthermore were confined to relatively narrow ranges.

1.4 Objectives of the present investigation

Most of the published literature on the cross-flow past cylinder arrays has dealt with conventional tube bundles. The in-line array with drop-shaped tubes investigated in the present work is novel and not much work has been published on the flow and

heat transfer over asymmetric arrays or in-line ones with elliptic tubes. Furthermore, to the best knowledge of the author no data are available on the flow and heat transfer over these configurations under pulsating flow.

In view of the above consideration and the main findings of the literature survey, the objectives of the present investigation are:

1. Obtaining accurate velocity data in the three selected tube bundle configurations under steady flow conditions.

2. Identifying flow periodicities and quantify their effects on the measured quantities.

3. Determining the effect of pulsations on the velocity characteristics of the flow.

4. Identifying the occurrence of lock-on.

5. Providing qualitative information on the flows under investigation using Laser sheet flow visualisation.

6. Developing and applying a thermocouple measurement technique for the measurement of surface temperature distributions in the asymmetric array and in the in-line one with elliptic cylinders.

1.5 Outline of the thesis

The reminder of this thesis is divided into six chapters. The following chapter describes the tube bundle configurations and the experimental techniques used for the present investigation. Chapter 3 presents the flow measurements taken in the arrangement with elliptic cylinders under steady and pulsating flow conditions. The flow and vortex shedding characteristics of an asymmetric tube array with circular cylinders are studied in Chapter 4 so that the effect of the tube arrangement can be studied. Chapter 5 examines the flow and vortex shedding characteristics of an in-

line array with drop-shaped cylinders. Chapter 6 examines the heat transfer characteristics of both the in-line and the asymmetric array with elliptic and circular cylinders respectively. All measurements were taken in both steady and pulsating flow. The study was carried out in order to evaluate the effect of the mean flow and turbulence characteristics on the heat transfer. The findings of the entire investigation are summarised in Chapter 7, where recommendations for future work are also made.

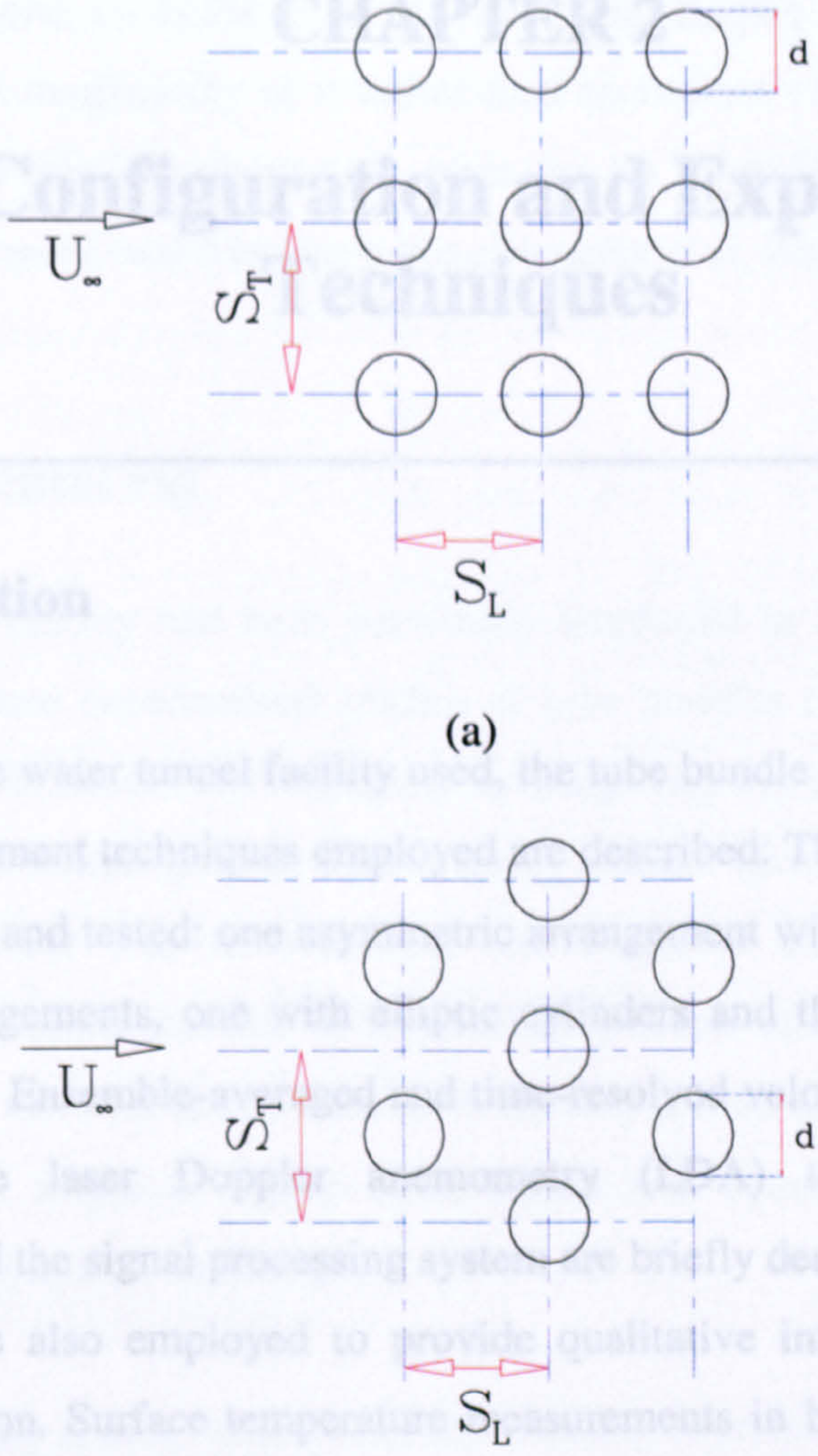

(a)

(b)

Figure 1.1. In-line (a) and staggered (b) tube bundle geometries.

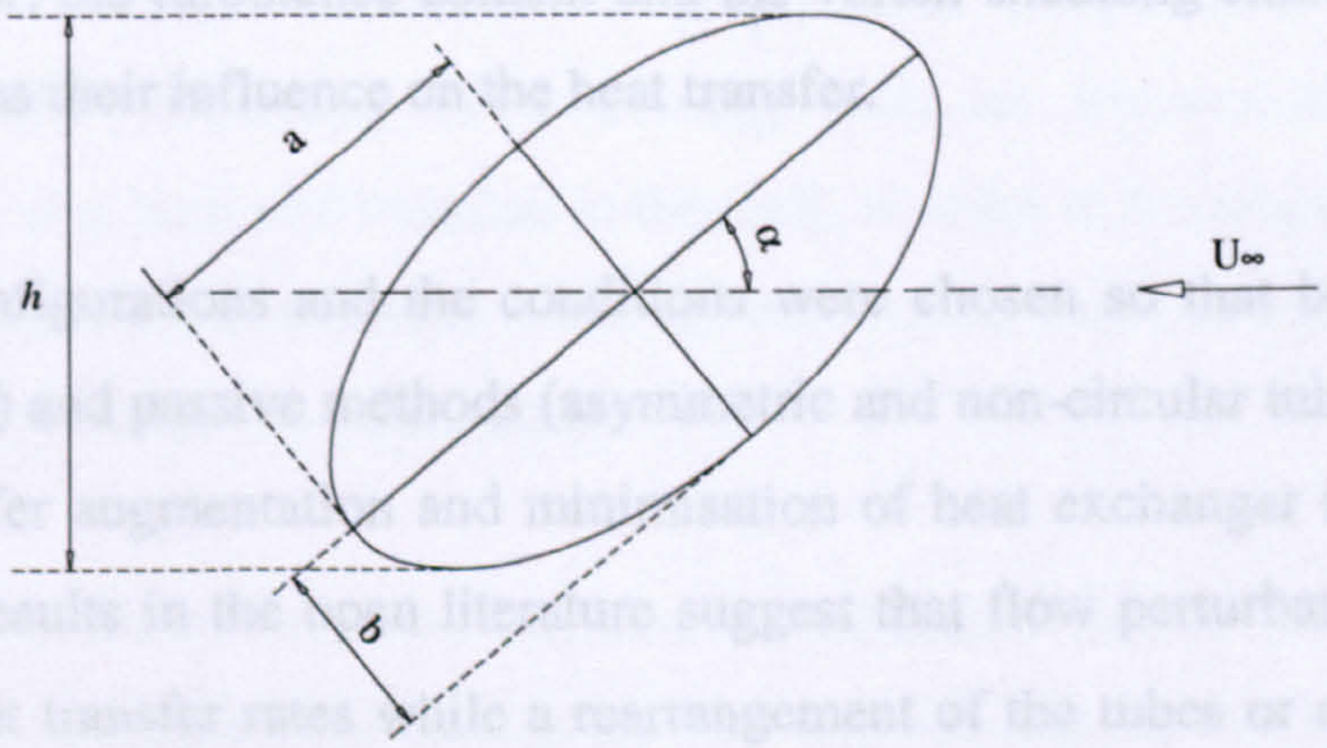

Figure 1.2. Cross-section of an elliptic cylinder in cross-flow. α is the angle of attack and h the projected height.

CHAPTER 2

Flow Configuration and Experimental Techniques

2.1 Introduction

In this chapter the water tunnel facility used, the tube bundle models investigated and the flow measurement techniques employed are described. Three tube bundle models were constructed and tested: one asymmetric arrangement with circular cylinders and two in-line arrangements, one with elliptic cylinders and the other one with drop-shaped cylinders. Ensemble-averaged and time-resolved velocity measurements were taken using the laser Doppler anemometry (LDA) technique. The optical configuration and the signal processing system are briefly described. Laser sheet flow visualisation was also employed to provide qualitative information on the flows under investigation. Surface temperature measurements in both the asymmetric test section with circular cylinders and the in-line one with elliptic cylinders were taken using a thermocouple measurement technique also described in this chapter. All measurements were taken in both steady and pulsating flow. Pulsations were introduced in the flow approaching the tube bundle in order to study their effect on the mean flow, the turbulence content and the vortex shedding characteristics of the flow as well as their influence on the heat transfer.

The flow configurations and the conditions were chosen so that both active (flow perturbations) and passive methods (asymmetric and non-circular tube arrangements) of heat transfer augmentation and minimisation of heat exchanger fouling could be examined. Results in the open literature suggest that flow perturbations can lead to increased heat transfer rates while a rearrangement of the tubes or a redesign of the tube shape, can lead to reduced deposition rates. The alternative shapes for the tubes were designed and constructed on the basis of numerical findings which showed that an in-line tube bundle with elliptic-shaped tubes exhibits the lowest particle

deposition rates and pressure drop and that drop-shaped tubes help the fouling particles to travel tangentially to it rather than to impact and possibly stick on the surface, reducing thus the deposition rates by up to 81% in comparison to the standard in-line bundle with circular tubes (Bergeles et al, 2000).

2.2 Experimental rig

An experimental facility had been previously employed in ECLAT, King's College London, to facilitate experimental studies of tube bundles in crossflow as part of a previous JOULE II Research Programme investigating the effects of fouling on the efficiency of heat exchangers in lignite utility boilers (Bergeles et al, 1996). This experimental facility was re-assembled and modified to accommodate a flow pulsating mechanism. It consists of a closed-loop water tunnel designed so that the flow entering the test section has a uniform velocity profile and a Re similar to that of a tube bundle in a typical lignite boiler under real operating conditions so that dynamic similarity can be achieved.

A centrifugal pump is used to circulate the working fluid (water) from a tank. A by-pass valve is installed to regulate the flowrate, which is monitored with two precision-bore flowmeters (KGD model 2000). The working fluid flows downward through a straightening section to the test section. The flow straightener utilises a piece of a hexagonal cell honeycomb made of aluminium for the effective removal of lateral mean velocity variations. A proportional temperature control system (Eurotherm 818) consisting of a cooling coil, an immersion heater and a thermocouple was built and installed in the tank, in order to maintain the temperature of the working fluid to within ± 0.05 °C. A solenoid valve is used to control the water flowrate through the cooling coil.

After careful consideration of the literature on pulsating flows, it was decided that the best method to generate pulsations in the flow approaching the test sections would be to replace one of the existing valves in the rig with a rotating valve driven by a variable speed motor. The rotating valve was positioned downstream of one of the flowmeters and upstream of the test section. The frequency of the pulsation could be

controlled by varying the speed of the motor and the amplitude could be adjusted by varying the flowrate through the rotameter connected to the rotating valve while maintaining the total flowrate the same. Alternatively, the size of the aperture in the rotating valve could be adjusted to provide additional means of modifying the amplitude of the pulsations but this was not necessary in the present investigation. A schematic diagram of the flow rig is shown in Figure 2.1. The pipework, fluid tank and all components of the rig were arranged with their axes vertical. The experimental rig has a maximum capacity of 290 lit/min corresponding to a maximum upstream bulk velocity, U_∞, equal to 0.93 m/s with tap water at 25 °C used as working fluid. Measurements were carried out upstream of the first row of the tube bundles at $x/S_L = -1.0$ in order to ensure that the approaching flow was uniform. The two-dimensionality of the flow was established both upstream and inside the bundle (at $x/S_L = -1.0$ and 1.33 respectively) by measuring mean velocity profiles at three different z-planes (z = -6.0, 0.0, 6.0 mm).

2.3 Flow configuration

2.3.1 Tube bundle models

In shell-and-tube heat exchangers, the tubes are arranged in rows. The rows perpendicular to the shell-side flow are called transverse rows; the rows parallel to the flow are called longitudinal rows (or columns). There are two typical tube bundle arrangements:

1. *In-line arrangements*, in which the tubes in adjacent transverse rows are in-line with each other and the direction of the flow. The centre-to-centre distance between tubes in adjacent transverse rows is the longitudinal spacing S_L. The centre-to-centre distance between the longitudinal rows is the transverse spacing S_T. There are two types of in-line arrangements: a square in-line arrangement, in which $S_L = S_T$ and a rectangular in-line arrangement, in which $S_L \neq S_T$. In in-line arrangements the minimum cross-section presented to the flowing stream occurs between the longitudinal rows and is equal to S_T - d, where d is the diameter of the tubes.

2. *Staggered arrangements*, in which the tubes in adjacent transverse rows are not in line with the direction of the flow. The distance S_T is the centre-to-centre spacing of tubes in the transverse rows, while S_L is the centre-to-centre spacing of longitudinal rows. The centre-to-centre diagonal distance between two tubes in adjacent transverse rows, S_L', is related to S_L and S_T by:

$$S_L' = \sqrt{S_L^2 + \left(\frac{S_T}{2}\right)^2} \qquad (2.1)$$

The following types of staggered arrangements can be found:

a: Staggered triangular arrangement, in which $S_T \neq S_L'$. When $S_T < S_L'$, the minimum cross section of flow occurs between the longitudinal rows and is equal to $S_T - d$, while if $S_T > S_L'$, the minimum cross section of flow occurs along the diagonal $S_L' - d$. The staggered square arrangement (or rotated square) is a special case of the staggered triangular arrangement in which $S_L' = S_T/\sqrt{2}$.

b: Staggered equilateral-triangular arrangement, in which $S_L' = S_T$.

3. *Asymmetric (or semi-staggered) arrangements*, which are intermediate configurations between in-line and staggered arrangements and asymmetric with respect to the centreline (vertical axis). They are constructed by shifting the even rows in an in-line tube bundle in the transverse direction.

The tube bundle models investigated comprised an in-line arrangement with elliptic cylinders, an asymmetric arrangement with circular cylinders and an in-line arrangement with drop-shaped cylinders. The in-line arrangement with elliptic cylinders had pitch ratios of $S_T/2b = 5.5$ and $S_L/2a = 1.6$, where 2b and 2a were the minor and major axes of the elliptic cross-section of the cylinders. The bundles consisted of 6 rows and 3 columns of tubes. The axis ratio of the cylinders, b:a, was 1:2. A detailed drawing of the cross-section of the elliptic configuration is shown in Figure 2.2 (a).

The asymmetric arrangement, constructed by shifting the even rows in the in-line tube arrangement by one diameter in the positive transverse direction, had a

longitudinal pitch ratio, S_L/d, of 2.1 and a transverse pitch ratio, S_T/d, of 3.6. It consisted of 6 rows and 5 columns of tubes. A detailed drawing of its cross section is given in Figure 2.2 (b). The in-line arrangement with drop-shaped tubes had a longitudinal pitch ratio, S_L/d_x, of 1.6 and a transverse pitch ratio, S_T/d_y, of 5.8, where d_x is the height of the drop-shaped cylinders and d_y the diameter of the bottom circular half of the cylinders. It consisted of 6 rows and 3 columns of tubes. A detailed drawing of the cross-section of the drop-shaped configuration is shown in Figure 2.2 (c).

All the three models had a square cross-section (72 mm x 72 mm) and were manufactured from transparent acrylic material (poly-methyl methacrylate – Perspex). The elliptic cylinders had a major axis of 13 mm and a minor axis of 6.5 mm. These axes were chosen so that the circumferential length of the elliptic cylinders was the same as that of the circular ones employed in the asymmetric arrangement. The circular cylinders were 10 mm in diameter. The drop-shaped cylinders were manufactured by joining half a cylinder of radius of 3.08 mm with a parabolically-shaped one described by the equation:

$$y_i = \pm \sqrt{\frac{0.0036}{3.8}(0.01 + x_i)}\ ^{1} \quad [m] \tag{2.2}$$

where x_i (varying between 0 and -0.01 m) and y_i refer to a local co-ordinate system, (see Figure 2.2 (c)). The total cross-sectional longitudinal, d_x, and transversal lengths, d_y, of the cylinders were 13.08 mm and 6.16 mm respectively, the latter corresponding to the diameter of the semi-circular cylinder. Again, these dimensions were chosen so that the circumferential length of the drop-shaped tubes, and therefore the heat transfer area, is the same as that of both the circular and the elliptic ones. All cylinders were also manufactured from Perspex. Two of the tube columns in the test sections comprised half cylinders which were fixed along the wall – in alternate rows in the asymmetric arrangement and in each row in the in-line ones – to simulate an infinite tube bundle and minimise wall boundary layer effects. The

---

[1] When $x_i = 0 \Rightarrow y_i = \pm \sqrt{\frac{0.0036}{3.8}0.01} = \pm 3.08\ 10^{-3}$ [m]; $y_i = 0$ when $x_i = -0.01$ [m].

Perspex cylinders were fixed horizontally in the test section and they were rigidly mounted by pressing them tightly into holes drilled on the Perspex plates to eliminate possible resonance effects that might interfere with the flow parameters measured. Table 2.1 summarises the dimensions and geometrical parameters of the tube bundle models investigated.

Table 2.1. Dimensions and geometrical parameters of the tube bundle models.

Arrangement		In-line with elliptic cylinders	Asymmetric with circular cylinders	In-line with drop-shaped cylinders
Dimensions, L x W x H (mm x mm x mm)		72x72x196	72x72x196	72x72x196
Cylinder diameter, d (mm)		*	10	*
Major axis, 2a / height, d_x (mm)		13	*	13.08
Minor axis, 2b / diameter, d_y (mm)		6.5	*	6.16
Transverse spacing, S_T (mm)		36	36	36
Longitudinal spacing, S_L (mm)		21	21	21
Transverse pitch, $S_T/2b$, S_T/d, S_T/d_y		5.5	3.6	5.8
Longitudinal pitch, $S_L/2a$, S_L/d, S_L/d_x		1.6	2.1	1.6
No. rows, N		6	6	6
No. columns		3	5	3
Aspect ratio	L/2b	11.08	*	*
	L/d	*	7.2	*
	L/d_y	*	*	11.7

2.3.2 Co-ordinate system and flow conditions

The co-ordinate system employed is shown in Figure 2.3. All measurements were taken at the plane of symmetry, z = 0.0 mm, a plane that crosses the cylinders at midspan. The measurement locations are described in terms of normalised co-ordinates, x/S_L, y/S_T, where S_L and S_T are the longitudinal and transvers spacings respectively, which are the same for all three arrangements.

The pulsation waveforms generated by the rotating valve were nearly sinusoidal, with at least 95 % of the pulsation energy at the fundamental frequency. The oncoming velocity was thus approximately given by:

$$u = U_\infty[1 + A_0\sin(2\pi f_d t)] + u' \qquad (2.3)$$

where u is the instantaneous flow velocity, U_∞ the upstream bulk velocity, A_o and f_d the pulsation relative amplitude (defined as the ratio between the pulsation amplitude and the upstream bulk velocity, $\Delta U/U_\infty$) and frequency respectively, t the time and u' the fluctuating velocity component. By introducing the velocity term U_{osc}, defined as:

$$U_{osc} = U_\infty[1 + A_0\sin(2\pi f_d t)] = U_\infty + U_{puls} \qquad (2.4)$$

where $U_{puls} = U_\infty A_0\sin(2\pi f_d t) = \Delta U\sin(2\pi f_d t)$, equation (2.3) can be rewritten as follows:

$$u = U_{osc} + u' \qquad (2.5)$$

Figure 2.4 (a) shows a typical time trace of the oncoming instantaneous velocity ($x/S_L = -1$, $y/S_T = 0.0$), u, in pulsating flow (f_d = 10 Hz, Re = 1,755). Figures 2.4 (b) and (c) show the corresponding oscillatory velocity component, U_{osc}[3], and the superimposition of u and U_{osc} respectively.

---

[2] Note that the mean of the oscillatory component of the velocity is equal to the upstream bulk velocity, that is $\overline{U_{osc}} = U_\infty$.

[3] The oscillatory velocity component, U_{osc}, was obtained by notch-filtering in the frequency domain the instantaneous velocity (u) spectrum. The *notch* filter is a well known filtering technique designed to remove only a narrow frequency band around a specific frequency (Balabani, 1996).

Another important parameter that will be used in the following chapters to characterise the pulsations is the *reduced amplitude*, ε, defined as:

$$\varepsilon = \Delta U/2\pi f_d d^* \qquad (2.6)$$

where d* is a characteristic length of the cylinders (see also Chapter 3, paragraph 3.3.1).

Errors in the estimation of both the driving frequency, f_d, and the amplitude of pulsation, ΔU, which define the pulsation waveform, can arise from the accuracy of the device employed to generate pulsations, that is the rotating valve driven by the variable speed motor. The motor speed, measured by means of a tachometer, was accurate within ± 10 rev/minute, that is ± 0.15 Hz, during the measuring period. The cycle-to-cycle variation pulsation amplitude was evaluated by analysing the oscillatory velocity component waveform (see Figure 2.4 (b)). The deviation from the mean pulsation amplitude (given by the amplitude spectrum) averaged over a comparatively high number of cycles/measuring period was estimated to be within 5 %.

Table 2.2, given below, summarises the flow conditions adopted in the present investigation for all the arrangements tested.

The Reynolds number for the asymmetric array with circular cylinders was defined using the cylinder diameter, d, as characteristic dimension and the gap velocity, U_g, as characteristic velocity, that is, $Re = U_g\, d/\nu$. The Reynolds number for the in-line array with elliptic cylinders was instead defined using the minor axis of the elliptic cylinder, 2b, as characteristic dimension and the gap velocity, U_g, as characteristic velocity, that is, $Re = U_g\, 2b/\nu$. Finally, the Reynolds number for the in-line array with drop-shaped cylinders was defined using the diameter of the bottom circular half of the cylinders, d_y, as characteristic dimension and the gap velocity, U_g, as characteristic velocity, that is, $Re = U_g\, d_y/\nu$.

Table 2.2. Experimental conditions studied.

Arrangement	Asymmetric with circular cylinders	In-line with elliptic cylinders	In-line with drop-shaped cylinders
Working fluid	water	water	water
Re	638-12,858	638-6,760	638-6,760
Fluid temperature (°C)	25	25	25
Flow pulsation frequency, f_d (Hz)	7-14	7-14	7-14

2.4 Flow measurement techniques

2.4.1 Flow visualisation

Flow visualisation is a powerful tool of investigation in fluid mechanics. In the present investigation it was adopted with the objective of examining the flow field in the wake of the tubes and in the near region around the separation points and to complement the LDA measurements. It differs from other experimental methods in that it renders certain properties of a flow field directly observable by visual inspection. By visualising the flow, therefore, an idea of the whole development of the flow could be attained, and the insight into the physical processes under investigation improved.

Due to the fact that most of the fluids used for experiments are transparent media, their motion remains invisible to direct observation. The techniques by which the flow is made visible are called "*flow-visualisation techniques*". As for the LDA technique, they can be non-intrusive, that is, they do not interfere with the flow. Several methods of flow visualisation can be identified (Merzkirch, 1987). This thesis will be concerned with the technique by which tracer particles are inserted into the flow and made visible by illumination; if the particles are small enough, it can be assumed that they follow the flow, both in direction and magnitude; what is

observed, therefore, is not the fluid itself but the motion of the inserted tracers. The main concern with flow visualisation studies using tracer particles is whether the particles themselves follow the flow. Although generally this is not the case, actions can be taken in order to reduce the deviation in velocity magnitude and direction between the particles and the fluid flow. The particles should, therefore, fulfil two contradictory characteristics: high visibility and minimisation of slip between particles and fluid flow. The first, in fact, increases with particle size, while the smaller the particle the better it follows the flow. For the second requirement to be fulfilled it is necessary that the particle is neutrally buoyant. In order to evaluate this last characteristic the expression for the settling velocity of a spherical particle, assuming Stokes' law, is given below:

$$U_s = (g d_p^2 / 18\nu)\{(\frac{\rho_p}{\rho}) - 1\} \qquad (2.6)$$

where ν is the kinematic viscosity of the fluid, d_p the particle diameter, ρ_p and ρ the density of the particle and of the fluid, respectively. A particle is neutrally buoyant if $U_s = 0$. If the condition $\frac{\rho_p}{\rho} = 1$ cannot be achieved, that is, if the density of the particle is not the same as that of the fluid, then neutral buoyancy can be approached by using extremely small particles (micron-sized). Tracer particles of about 100 μm are often used. In the present investigation hollow glass particles, with a diameter of 15 μm, were used. These were spherical borosilicate glass particles whose density, ρ_p, was equal to 1.1 kg/m^3. The density ratio, $\frac{\rho_p}{\rho}$, and the actual sedimentation velocity, calculated for the conditions of the present investigation, were equal to 1.1 and 12 x 10^{-6} m/s, respectively. These values show that the buoyancy of the particles could be neglected and eventually particles of bigger size could be considered, to increase visibility. However, preference was given to the minimisation of the velocity slip between fluid and particle velocities and finally the 15 μm diameter particles were adopted throughout the whole investigation.

The most common illumination method is the light sheet with which the particles in a thin plane in the flow can be illuminated (Véret, 1987). The light sheet can be

produced by either a lamp or by expanding a laser beam into a light sheet by means of a cylindrical lens. In the present investigation both a 1000 W white lamp and a 1.2 W output Argon-Iron laser (model: Spectra Physics - 164) operating at a wavelength of 514 nm were used in a comparative preliminary study. The laser-sheet technique proved to give a better resolution of the recorded photographs and was finally adopted. Video recordings of the flow were taken by means of a CCD video camera with a zoom lens. Finally, a video grabber was used in order to obtain individual frames from the video. The laser sheet was several centimetres high and about 1 mm thick. The tracer particles were observed and photographed in a direction approximately perpendicular to the illuminated plane. The light sheet enables visualisation of the motions in one plane and therefore allows us to recognise the vortical structures present in the flow. The time exposure in the present experimental set up, as in most flow visualisation studies adopting the same technique, was controlled by the mechanical shutter provided by the video camera (alternatively a pulse light source can be utilised). With this arrangement each particle appears like a streak whose length is proportional to the average local velocity. The control of the exposure time is crucial to the quality of the image. The video camera could provide shutter speeds of 50, 120, 250, 1000 frames per second. Considering that in the present experimental conditions the velocity did not vary over a wide range (as the higher the velocity the shorter the exposure time should be), in most recordings a shutter speed, or frequency, of 50 frames per second, that is recording a frame every 0.02 seconds, was adopted.

2.4.2 Laser Doppler anemometry

Velocity measurements were taken by employing a single component dual-beam laser Doppler anemometer (LDA) operating in forward scatter, which made use of a 10 mW He-Ne laser (Spectra Physics model 106). Laser Doppler anemometry (LDA) is a well-established optical technique, which allows the measurement of the local instantaneous velocity of small particles suspended or introduced into the flow. Since it is non-intrusive and does not disturb the flow it is advantageous in turbulent and recirculating flows such as those in tube bundles investigated here. However, optical access to the transparent fluid and light-scattering particles are required. The LDA is

based on the measurements of the Doppler shift of laser light scattered from particles carried with the fluid, which are sufficiently small to follow the flow faithfully. The most common LDA systems are the "reference beam", the "two-scattered beam" and the "dual beam" or "fringe" types. The basic principle of the latter method, which was employed in this investigation, is briefly summarised below.

The fringe-type method system makes use of two crossing laser beams of equal intensity to produce an interference fringe pattern within their volume of intersection (control or measurement volume). Single particles have to pass through this volume in order to produce beat signals providing information on the velocity of the particles. When a particle crosses the fringes, it scatters light, the intensity of which increases or decreases at a rate proportional to its velocity. The regions of intensity maxima and minima are referred to as "bright" and "dark" fringes, respectively. If the amplitudes of the two intersecting light waves are equal, as in the present LDA arrangement, the "fringe visibility" is large, that is the dark fringes are completely black. The fringe spacing, λ^*, that is the spacing between pairs of light and dark bands, is given by the following expression:

$$\lambda^* = \frac{\lambda}{2\sin(\theta/2)} \tag{2.7}$$

where λ and θ are the wavelength of the laser light and the angle of intersection of the laser beams respectively. The time T taken by a particle to travel the distance λ^* is:

$$T = \lambda^*/U_{particle} \tag{2.8}$$

so the frequency ν_d (Doppler frequency) of the intensity modulation of the scattered light is:

$$1/T = \nu_d = 2U_{particle}\frac{\sin(\theta/2)}{\lambda} \tag{2.9}$$

where $U_{particle}$ is the velocity component of the particle perpendicular to the fringes, which, if the particles are such that they follow the flow faithfully, represents also the fluid velocity component perpendicular to the fringes themselves.

This intensity modulation, resulting in a Doppler burst or signal, is detected by a photomultiplier, which transforms the optical signal into an electrical one. The latter signal is processed by suitable electronics systems in order to determine the Doppler frequency and, therefore the fluid flow velocity component. Extensive velocity measurements can be obtained by moving the control volume throughout the flow field of interest. A common problem to the signal analysis is posed by reverse flow, as found in turbulence or recirculating regions. The Doppler frequency, in fact, although related to the velocity, is independent of its direction. In order to overcome this limitation, frequency-shifting devices are used to eliminate this directional ambiguity. The frequencies of the two crossing beams are shifted with respect to each other and, as a consequence, the fringes move with respect to the optical axis at a speed proportional to the frequency shift ν_s. The Doppler frequency or velocity will depend on whether the particle is travelling in the same or opposite direction with the moving fringes (being higher in the latter case). Both the direction and magnitude of the particle velocity can be determined by the following expression:

$$U_{particle} = (\nu_d \pm \nu_s)\frac{\lambda}{\sin(\theta/2)} \qquad (2.10)$$

The frequency shifting was produced by means of a diffraction grating mounted perpendicularly to the direction of the incident light through which the laser beam was passed (see Figure 2.5) and driven by a bi-directional variable speed d.c. motor. The incident light wave is diffracted through the grating, and laser beams emerge at angles given by the following expression:

$$\varphi_K = \sin^{-1}\left(\frac{k\lambda}{s}\right) \qquad (2.11)$$

where k is the order of the diffraction beam and s is the line spacing. The diffraction grating can, therefore, be utilised also as a beam splitter. Through Doppler shift considerations it can be derived that the frequency of each of the diffracted beams will be shifted with respect to the incident wave by the quantity:

$$\nu_s = 2kn\frac{N_G}{60} \tag{2.12}$$

where N_G is the rotational speed of the grating in rev/min and n the number of radial lines etched on the grating.

The presence of scattering particles is essential in laser Doppler anemometry. These may be found occurring naturally in the fluid, or otherwise have to be added artificially. If the particles are too small the intensity of the scattered light might not be enough to exceed the noise level of the detection system, while if they are too large they might block the light completely. This is more important if the system works in forward scattering, that is, if the photodetector collects the light scattered in the direction of propagation of the incident wave. In the present investigation tap water was used as working fluid. It contained a sufficient concentration of impurities so that seeding of the flow was not necessary. The quality of the signal was very good (signal to noise ratios of around 30 were achieved) and the data rates high for both ensemble-averaged and time resolved measurements (≈ 1 kHz).

One of the major criteria in choosing the components of the LDA system is the selection of both the dimensions of the control volume and the angle between the beams. Since lasers in LDA always operated in their fundamental mode (TEM_{00}), their output beam has a Gaussian light intensity distribution. The measurement volume defined by the $1/e^2$ boundary of the maximum beam intensity is ellipsoidal in shape (see Figure 2.6). Its diameter is given by the following expression:

$$b_x = \frac{b_w}{\cos(\theta/2)} \tag{2.13}$$

and its length, by:

$$b_y = \frac{b_w}{\sin(\theta/2)} \tag{2.14}$$

where b_w is the waist of the focused laser beam in the measurement volume. The anemometer used in this study is described below.

2.4.3 Optical configuration

The fringe-type LDA system used in the present investigation is shown in Figure 2.7. In order to minimise errors in measurements taken in turbulent and recirculating flows characterised by steep velocity gradients, the control volume has to be as small as possible. This leads to a better signal to noise ratio and a decrease in the probability of overlapping bursts. The formulas shown above indicated that the dimensions of the control volume depend on the beam waist. The latter is expressed as a function of the focal lenses f_1, f_2 and f_3 of the lenses L_1, L_2, L_3 employed, as shown in the following expression:

$$b_w = \frac{4\lambda f_1 f_3}{\pi b_o f_2} \tag{2.15}$$

where b_o is the diameter of the beam emitted by the laser. The laser employed, operating at a wavelength of 632.8 nm (red light), had a beam diameter of 0.83 mm. The following combination of lenses was chosen. The laser beam was focused by a plano-convex lens with a focal lens, f_1, of 200 mm onto a 4000-line diffraction grating. This was used both to split and frequency-shift the beams. The grating was rotated at 12,000 revs/minute, its speed chosen on the basis of the expected flow velocity magnitude range. The grating could be rotated through 90° about the optical axis. The plane containing the crossing laser beams could be rotated accordingly, thus allowing two orthogonal velocity components to be measured. The axial (U, u') and radial (V, v') mean and r.m.s. velocities were measured with the beams' plane parallel to the x-z vertical plane and to the y-z horizontal plane respectively. All measurements were taken along the plane of symmetry, z = 0.0 mm. The corresponding frequency shift, calculated for the first order beams (which have

higher intensities than the higher order beams), was equal to 1.6 MHz. The pair of the beams emerging from the grating was collimated by a plano-convex lens, which was placed at one focal length, f_2 = 520 mm, from the grating. Finally a third plano-convex lens of focal length, f_3, of 135 mm, focused the two parallel beams in order to cross and produce the measurement volume. The ellipsoidal control volume was 50.6 μm and 502 μm in diameter and length respectively.

The scattered light from the particles crossing the control volume was collected by a photomultiplier (EMI 9658B) powered by a Brandenburg 10-2,000 Volts d.c. power supply. The characteristics of the LDA system used are summarised in Table 2.3.

Table 2.3. Characteristics of the LDA system used.

Laser (He-Ne)	
Wavelength, λ (nm)	632.8 (red)
Power (mW)	10
Beam diameter, b_0 (mm)	83
Lens	
f_1 (mm)	200
f_2 (mm)	520
f_3 (mm)	135
Diffraction grating	
Number of lines, n	4,000
Rotational speed of the grating, N_G (rev/min)	12,000
Frequency shift, ν_s (MHz)	1.6
Measurement volume dimensions (at $1/e^2$ intensity)	
Diameter, b_x (μm)	50.6
Length, b_y (μm)	502
Number of fringes (stationary)	16
Half angle of intersection, θ in air (°)	5.76
Fringe spacing, λ^* (μm)	3.15
Frequency to velocity conversion factor (m/s/MHz)	3.15

2.4.4 Signal processing and data acquisition

A frequency counting technique was used to perform both ensemble-averaged and time resolved measurements. An ensemble of a random process is an average over repeats of an experiment. In LDA measurements the "experiments" consist of measuring instantaneous velocities over a given number of Doppler bursts. By averaging the measured velocities, mean and r.m.s. velocities (ensemble-averages) at a point in the flow are determined. Time-resolved measurements involve the recording of instantaneous velocities at given time intervals over a period of time. The time intervals can be either equally or randomly spaced. The reciprocal of the time interval in equal-spaced data is called sampling rate (or frequency) and expresses the number of samples recorded per second. Equally spaced data are time series of velocity points which can be analysed to determine both frequency spectra (providing information on the characteristic frequencies of the flow) and autocorrelation functions (providing information on the time correlation between adjacent fluctuations in the flow).

Although most processing tools require equally spaced data, the instantaneous LDA velocity measurements are randomly distributed in time. Different interpolation techniques can be adopted (zero-order, linear, etc..). The most common one is the zero-order interpolation used to reconstruct the set of data in which the signal is sampled at the arrival time of each validated burst. Each velocity value so determined is held until another valid signal arrives. This procedure, adopted also in the present investigation, is known as hold-and-sample procedure and is recommended for high data rate and low burst density conditions. A flow with low data rates can be sampled randomly since there is no need to satisfy the Nyquist criterion as described below. Spectral analysis techniques are also available for randomly sampled data. The most important factors in taking time resolved measurements are, therefore, both the validated data rate and the sampling rate. Sampling at high frequencies will yield correlated and redundant data, while sampling at low frequencies will lead to confusion between high and low frequency components in the original data. In order to define a frequency component in the original signal two samples per cycle are necessary. Therefore, if h is the sampling time interval and 1/h the sampling rate, the

highest frequency that can be resolved is 1/2h Hz. The cut-off frequency can be defined as:

$$\nu_c = 1/2h \tag{2.16}$$

This frequency is called the Nyquist frequency. Frequencies above ν_c are aliased with those in the range $0 << \nu << \nu_c$. In order to overcome this limitation h is chosen sufficiently small so that no frequencies higher than the cut-off frequency will exist in the flow (cut-off frequency 1.5 - 2 times greater than the maximum anticipated frequency), or the data are filtered prior to sampling so that information above a maximum frequency of interest is "cut-off". According to Bendat and Piersol (1971) choosing $\nu_c = 1/2h$ would give accurate results for frequencies below ν_c.

Another limitation in the choice of the sampling frequency is the phase ambiguity noise, arising from the possibility that two or more particles could be crossing the control volume at a given time. The frequency at which phase ambiguity noise becomes a significant factor can be estimated (Kresta, 1991) from the wavenumber, $\Re$, as defined by Hinze (1975) and the diameter of the measurement volume, b_x, for measurements in the axial direction:

$$\Re = 2\pi\nu/U = 1/b_x \tag{2.17}$$

Above that frequency, the spectrum will be composed of white noise. In the present investigation the frequency estimated from the above formula was found to be higher than the corresponding sampling rates, at all the measurement locations, so that phase ambiguity noise was not expected to be significant.

In this investigation, both equally spaced and randomly distributed in time data were obtained and analysed. Equally spaced data were used to determine frequency spectra and to filter out periodical components, while randomly distributed ones were mainly used to analyse velocity probability distributions and to determine their skewness and kurtosis as well as to better re-construct time-velocity traces.

The Doppler signal from the photodetector was firstly pre-amplified and then fed to a TSI frequency counter, model 1990B. The counter was equipped with a built-in variable gain and band-pass filters and a fixed threshold level of 50 mV, for amplitude validation. The pre-amplified signal was fed to the counter where it was band-pass filtered for noise and pedestal removal and then amplified by the variable gain. The pedestal is a low frequency component of intensity variation that appears in addition to a burst of a differential Doppler frequency even when the signal quality is perfect (i.e. the particle passing through the centre of a fringe pattern produced by intersecting beams of equal intensity) and is associated with the particle size and path. The quality of the signal was monitored with a dual channel oscilloscope (Hitachi model V-525).

The counter operated in the "single measurement per burst" mode. In order to determine the Doppler frequency, the time taken to complete a prescribed number of fringes was measured. The timing was started when a threshold is exceeded and stops after a given number of cycles. In order to reject results whose accuracy was dubious a common counting validation technique, described here below, was adopted. Errors can arise if the signals are obtained by particles which do not pass through the control volume, if there are not enough cycles left in a burst after exceeding the threshold, if a second particle crosses the fringes during the timing period, or if the period starts in one cycle and ends in another. The validation procedure entailed comparison of two measurements of the period of the Doppler signal using different numbers of cycles. A measurement is considered valid when the time required for 5 cycles in the Doppler burst agrees with that for 8 cycles within a tolerance limit of 3%. The counter was interfaced to a PC with appropriate data acquisition software.

Data analysis

Blocks ranging between 5,000 and 15,000 samples of time-resolved measurement recordings were acquired at each location. A typical velocity recording in pulsating flow was shown in Figure 2.4. Two commercial software packages, MATHEMATICA and MATLAB, were used for the analysis of the data. Both applications are equipped with built-in functions for Fast Fourier Transforms, which is the principal tool in analysing time-resolved measurements.

Analysis of the data included the estimation of amplitude and power spectra[4] as well as the filtering of periodic components. A typical amplitude spectrum, corresponding to the velocity recording in Figure 2.4, is shown in Figure 2.8. The notch-filtering technique was selected to filter the frequency spectrum in order to remove any frequency associated with the variation of the mean flow. Fourier and inverse Fourier Transforms, amplitude and power spectra definitions as well as the notch-filtering technique are well known and can be found briefly described in Balabani (1996).

A numerical algorithm was also developed using MATLAB in order to determine the skewness and the kurtosis of the velocity probability function. The skewness (Sk) and kurtosis (Kr) are defined as follows:

$$Sk = \frac{1}{N}\frac{\sum_{i=1}^{N}(u_i - U)^3}{r.m.s.^3} \tag{2.18}$$

$$Kr = \frac{1}{N}\frac{\sum_{i=1}^{N}(u_i - U)^4}{r.m.s.^4} \tag{2.19}$$

The skewness is equivalent to the third central moment divided by the standard deviation cubed. Positive skewness indicates a distribution with a long right tail (skewed to the left), whereas negative skewness indicates a distribution with a long left tail (skewed to the right). Therefore, the skewness is a measure of symmetry, or more accurately, the lack of symmetry. A distribution, or data set, is symmetric if it looks the same to the left and right of the centre point. The skewness for a normal distribution is zero, and any symmetric data should have a skewness near zero.

The kurtosis is equivalent to the fourth central moment divided by the standard deviation to the power of four. It is a measure of whether the data are peaked or flat relative to a normal distribution. That is, data sets with a high kurtosis tend to have a

[4] The amplitude of the spectrum is defined in terms of the power spectral density (PSD) that is the distribution of power in each frequency interval. In the present investigation FFT procedures (a periodogram) were employed for the estimation of the PSD.

distinct peak near the mean, decline rather rapidly, and have long tails. Data sets with low kurtosis tend to have a flat top near the mean rather than a sharp peak. The kurtosis for a standard normal distribution is 3.

2.4.5 Measurement errors and uncertainty

A brief description of the major errors involved in the present experimental investigation is given below (see also Balabani, 1996).

2.4.5.1 Positional errors

A transverse mechanism was used to move the control volume throughout the tube bundle model and to measure its y and z co-ordinates. The x co-ordinate was instead measured by means of a linear encoder. Positional errors can arise from the accuracy of the transverse mechanism and the linear encoder in positioning the control volume, from the dimension of the control volume as well as from the accuracy in locating the measurement volume at a reference point.

The positional accuracy was 0.05 mm in the y and z directions, and 0.01 mm in the x direction respectively. Due to the fact that all measurements were taken on the same $z = 0$ plane, positional errors related to the reference point location were minimised by re-setting the latter only in the x-direction as each tube row encountered. The error associated with positioning the control volume at a reference position was estimated to be equal to 0.25 mm in the y direction, 0.42 mm in the z-direction and 0.025 mm in the x direction.

2.4.5.2 Frequency shifting

The frequency shifting needed to resolve directional ambiguities was produced by a diffraction grating, which, as already mentioned, was driven by a bi-directional d.c. motor. The variations in the rotational speed were minimised by "padding out" the potentiometer of the d.c. motor with resistances so that the control voltage range was

reduced. The motor speed was equal to 12,000 ± 6 rev/minute, with a maximum r.m.s speed variation of 0.05% and a maximum speed fluctuation of ± 1%. According to Melling (1977), the errors introduced by such variations on the r.m.s. velocities measured are negligible.

2.4.5.3 Bias effects

Due to the fact that more fast particles cross the measurement volume than slow particles in a given time, the velocity probability distribution will be skewed toward higher velocities, that is, the number of measurements at higher velocities will be greater than at low velocities. This will obviously bias the calculation of statistical quantities formed by ensemble-averaging the validated measurements: giving to all measurements the same weight will give a mean velocity that is too high. Therefore, the corrections to the velocity biased errors consist of determining the most appropriate quantity to weight the particle velocities with. For turbulent measurements especially of high intensity both residence, or transit time (Buchhave et al, 1979; George, 1975) and arrival time (Durâo et al, 1980), directly related to the transit time, were suggested and used as weights for the velocity data. The first method is implemented if the counter registers together with the Doppler frequency the residence time for each measurement. The counter used in the present investigation could not provide this information. Durâo and Whitelaw (1976) overcame the bias introduced by the correlation between arrival time and velocity by randomly sampling the already discretised sample. The method has the disadvantage that a great number of data is not processed.

Halim and Turner (1986) applied both the residence and arrival time weighting to the velocity measurements taken in a tube bundle in cross flow. The results of their investigation did not show clearly the benefit of the two techniques. Although Halim (1998) concluded that the arrival time weighting was a better method, due to the uncertainties associated with the effects of these errors and the type of bias correction to be used, the velocity data in the present investigation were not bias-corrected (Balabani, 1996). Another bias source, with opposite effect, that is, skewing the probability density function toward lower velocities, may occur due to the averaging

characteristics of the photomultiplier, which mitigates the velocity bias and reduces the overall bias effect (Yianneskis, 1982). However, Durâo et al (1980) showed that the errors introduced by both the velocity and photomultiplier effect may be insignificant for a large range of flow configurations. Thus, such bias effects are not expected to influence significantly the trends shown by the present data.

2.4.5.4 Broadening effects

Different effects can cause the p.d.f. of the Doppler frequency to be wider than that of the true velocity (broadening effect). The most usual sources of broadening are:

1. small scale velocity fluctuations within the measurements volume (σ_f^2)
2. gradients in the mean velocity (σ_g^2)
3. the finite time taken by scattering particles to cross the measurements volume (σ_t^2)
4. instrument broadening (σ_i^2)
5. brownian motion and laser linewidth

If the last effect (5) is neglected, as suggested by Durst et al (1976), the total mean square contribution of broadening errors, σ_b^2, is given by:

$$\sigma_b^2 = \sigma_f^2 + \sigma_g^2 + \sigma_t^2 + \sigma_i^2 \qquad (2.20)$$

The mean square of the fluctuations that is measured is, therefore, the sum of the actual flow velocity fluctuation σ_v^2 and the broadening contribution σ_b^2:

$$\sigma_d^2 = \sigma_v^2 + \sigma_b^2 \qquad (2.21)$$

Contributions (3) and (4), due to transit time and instrument broadening respectively, have been proved not to affect the measurements taken with a frequency counter, which was used in the present investigation for signal processing (Lee, 1995). We can therefore re-write equation (2.21) as follows:

$$\sigma_d^2 = \sigma_v^2 + \sigma_f^2 + \sigma_g^2 \qquad (2.22)$$

George and Lumley (1973) estimated the broadening contribution due to fluctuations in the velocity of a particle crossing the finite control volume as a function of the dissipation of turbulence energy and the standard deviation of the length of the measurement volume. The correction suggested therefore is subject to the estimation of these two terms and is consequently quite complex to evaluate. This broadening error was estimated by Melling (1975) to be of the same order of the velocity gradient broadening. The latter occurs when the control volume is located in a region of steep velocity gradients. Particles crossing the measurement volume through different sections will have different velocities; the steeper the velocity gradient and the larger the control volume, the higher the broadening and skewing of the Doppler frequency spectrum. Suen (1992) estimated the broadening effect in a flow with similar velocity gradients to be of the order of 2 % in most regions of the flow and 8 % in regions of highly non-linear gradients. However, due to the small dimensions of the control volume employed in this investigation, the error is expected to be minimal.

2.4.5.5 Count ambiguity

The frequency of a burst signal can be determined, as already mentioned, by measuring the duration, $\Delta\tau_N$, of a predetermined number N of cycles in a signal burst, according to $\nu_d = N/\Delta\tau_N$. A correct evaluation of the Doppler frequency presumes that the measurement of time is exact. However, an error arises when this time is measured by means of a counting technique. This error is called count ambiguity. The measurement is made by counting pulses generated by a clock of constant frequency, ν_t, within a gate started and closed between two zero crossings. The inherent resolution of these counters is ± 1 count error in counting the pulses for a large number of gate openings, due to the fact that the gate containing the pulse train could open and/or close missing one pulse. If an ideal sinusoidal signal of frequency ν_d is considered, in the time $\Delta\tau_1$ between two zero crossings the counter will generate $\Delta\tau_1\nu_t = N_{t1}$ pulses. The maximum timing error, ε_c, can therefore be calculated to be ± $1/\nu_t$, and the relative error, $\varepsilon_c/\Delta\tau_1$:

$$\varepsilon_c/\Delta\tau_1 = (1/\nu_\tau)/\Delta\tau_1 = \nu_d/\nu_\tau \tag{2.23}$$

which shows that the clock frequency has to be much higher than the burst frequency to minimise the error. For N zero crossings the relative counting error, $\varepsilon_{cN}/\Delta\tau_1$, is given by:

$$\varepsilon_{cN}/\Delta\tau_1 = \nu_d/(N\nu_\tau) \tag{2.24}$$

This relationship shows that in order to optimise the signal processing system and reduce the timing errors all possible signal cycles should be utilised within a burst and the frequency of the electronic clock enhanced (Durst et al, 1976). In the present study the measured frequencies were not higher than 4 MHz, while the frequency counter had a 500 MHz oscillator. The resulting relative error over 8 cycles calculated from Equation (2.24) was, therefore, less than 0.1%.

2.4.5.6 Statistical error

The default maximum number of samples that could be measured by the data acquisition software was 22,000. Ensemble-averages of mean and r.m.s velocities were calculated by averaging 5,000 to 15,000 samples, depending on the data rate and the flow regions measured. Averaging over a finite number of samples can introduce errors, which can be estimated by statistical analysis (Yanta, 1973) as shown below:

$$E_U(\%) = \sqrt{\frac{Z_C}{N}Tu^2}\ ;\ E_{rms}(\%) = \sqrt{\frac{Z_C}{N}} \tag{2.25}$$

where Z_C is a confidence level function which has values 2.58, 1.96 and 1.645 for confidence levels of 99%, 95%, 90% respectively and Tu the turbulence intensity. $E_U(\%)$ and $E_{rms}(\%)$ are the percentage errors in the mean and r.m.s. velocities respectively. Assuming a number of samples equal to 5,000, the errors on the mean and r.m.s. velocities were estimated to be about 1% and 2% respectively, assuming a turbulence level of 50% and a confidence level of 95%. Clearly, the errors are

smaller for larger samples. The accuracy and repeatability of the measurements were checked by repeating the measurements at least twice in every location.

As already stated, no correction techniques were employed in the present study, but the errors were shown to be minimised by using a comparatively and appropriately small control volume and a dense measurement grid in regions of steep velocity gradients. Cheung (1989) and Suen (1992) quantified the accuracy of a similar LDA system to the one in the present investigation and in flows with similar spatial and temporal velocity gradients by assessing an overall error on the mean and r.m.s. velocities of 1%-5% and 5%-8% respectively, the higher values occurring in regions of steep gradients. Although no correction techniques were employed for some of the errors their magnitude is expected to be negligible and their effect on the present results insignificant.

2.5 Heat transfer measurement technique

A thermocouple heat transfer measurement technique was developed to facilitate surface temperature measurements in both the asymmetric test section with circular tubes and the in-line one with elliptic tubes.

Asymmetric arrangement with circular tubes

The technique made use of a duraluminium cylinder, 10 mm in diameter, equipped with a thermocouple and a cartridge heater to allow temperature measurements to be made under constant heat flux conditions. A T-type thermocouple (Copper/Constantan), 0.25 mm in diameter, was embedded into a longitudinal groove machined along the surface of the circular cylinder with its junction at the midpoint, while a stainless steel cartridge, 5.90 mm in diameter, was fitted inside to supply heat to the inside surface of the cylinder. Thermal glue was used to ensure good contact between the thermocouple and the cylinder. The heater was powered by a variable voltage dc, power supply. Figure 2.9 shows a schematic of the instrumented cylinder. The instrumented cylinder was designed so that each time a Perspex cylinder in the tube bundle model investigated was replaced by the

instrumented one and the surface temperature distribution was obtained. Figure 2.10 shows the modifications made to the wall of the test section to accommodate the instrumented cylinder and ensure leak proof operation. The instrumented cylinder was rotated by means of a stepping motor, with a step angle of 1.8°, so that the thermocouple could be positioned at various angular positions from the front stagnation point. It allowed, therefore, 100 angular positions to be measured around half of the cylinder circumference i.e. from the front to the rear stagnation point. As the 0.25 mm thermocouple diameter corresponds to a circumferential angle of 2.86° and the stepping motor had an angle resolution of 1.8°, it was decided to take temperature measurements at 7.2 degree intervals along the cylinder perimeter as the corresponding 50 angular positions that could be measured were sufficient to obtain an accurate surface temperature distribution.

In-line arrangement with elliptic tubes

A similar technique was developed for the elliptic tube bundle model. The elliptic shape did not allow the thermocouple to be positioned by simply rotating the cylinder and an instrumented elliptic cylinder was constructed by embedding 4 T-type thermocouples (Copper/Constantan), 0.25 mm in diameter, along its surface. The number of thermocouples and their position in the elliptic cylinder were determined by the geometry and dimensions of the elliptic cylinders. The 4 thermocouples, positioned at 0, 25, 155 and 180 degrees respectively from the front stagnation point, allowed the temperature to be determined in 4 positions along the instrumented cylinder surface. A surface temperature profile was obtained by interpolation, assuming y-symmetry of the flow, and consequently, of the heat transfer field.

Both the asymmetric tube bundle with circular tubes and the in-line one with elliptic tubes were modified to allow easy insertion and removal of both the Perspex cylinders and the instrumented one without disassembling as shown in Figures 2.11 and 2.12. Figure 2.12 also shows the stepper motor attached to the instrumented cylinder for positioning. The thermocouple signal was firstly amplified and fed to a micro-controller interfaced to a PC. The micro-controller read the thermocouple

output and also controlled the stepper motor. The thermocouple was firstly calibrated by immersing it into a constant temperature bath and reading the corresponding amplified signal (V_{K4}) on the PC. Subsequently, it was similarly calibrated when embedded into the duraluminium cylinder and the resulting calibration curve was adopted to evaluate the surface temperature from the V_{K4} readings. The calibration curve is shown in Figure 2.13, from which it can be seen that in the temperature range investigated there is a linear dependence between V_{K4} and T. The uncertainties on both the bath temperature and the temperatures measured from V_{k4} amplified signal were ± 0.1 °C and 0.01 °C respectively. In order to minimise the axial heat loss due to conduction through the cylinder, the end of the instrumented cylinder was made of Teflon. The bulk temperature was kept constant at 20 °C using a temperature control system as explained earlier in this chapter and was measured by inserting a thermocouple at the outlet of the tube bundle. Due to both the relatively small dimensions of the experimental apparatus and the flowrate adopted, the bulk temperature difference between inlet and outlet of the test section could be neglected. Measurements were taken only when the bulk temperature had reached a steady value. A study was carried out in order to determine the response time of the thermocouple and to establish the minimum time interval between measurements at different angular positions. It was found that it was sufficient to allow 1 minute to lapse before moving the thermocouple into the next angular position and take a new measurement. Mean temperature values were evaluated by averaging 10,000 instantaneous temperature recordings.

The Nusselt number was calculated by using the following expression:

$$Nu = \frac{Qd}{k_c A(T_s - T_\infty)} \tag{2.26}$$

where Q is the electrical power dissipated in the cartridge heater[5], that is Q = IV, where I is the current through the cartridge and V the voltage applied to it. T_s and T_∞ are the measured surface and bulk temperatures respectively, k_c the thermal

[5] Q is also the heat flux provided by the cartridge heater if the axial heat loss due to conduction is neglected

conductivity of the fluid at T_∞, d the diameter of the circular instrumented cylinder as well as the equivalent diameter of the elliptic one[6]. A is the heat transfer area, equal to πdL, with L the longitudinal length of the cylinders. It should be noted that the circular cylinder of the asymmetric array and the elliptic cylinder of the in-line one had the same heat transfer area and the equivalent diameter is defined on the basis of this.

The uncertainty in the evaluation of the Nusselt number in the present study depends on several factors: manufacturing accuracy of the instrumented cylinders, positional error, uncertainties in the temperature measurements and in the estimation of the heat flux, Q/A. Positional errors as well as uncertainties in the temperature measurements can arise from the size of the thermocouples employed. However, the use of a comparatively small thermocouple with suitable characteristics (the diameter of the thermocouple subtended an angle of 2.86°), minimised the errors involved. The complex geometrical configuration of the instrumented cylinders, the heat losses, the imperfect matching between the thermocouple junctions, the thermal glue and the duraluminium thermal conductivities represent the main sources of uncertainty in the estimation of the heat flux and therefore of the Nusselt number. Despite the use of T-type thermocouples, a silver-epoxy glue (gap filling) to minimise thermal conductivity differences with the duraluminium cylinder and the use of the Teflon end cap to minimise the axial heat loss due to conduction, the uncertainty in the estimation of the heat flux remains the main source of uncertainty in the estimation of the Nusselt number.

Although the repeatability of the measured Nusselt number was within 1%-3%, depending on the measuring location (higher in the front stagnation point and lower in the rear one), the systematic error related to the estimation of the heat flux may be as high as 15% (Ota et al, 1986; Ruth, 1983; Scholten et al, 1998).

---

[6] The equivalent diameter is defined as the diameter of an equivalent circular cylinder whose circumferential length is equal to that of the present elliptic cylinder, that is, 10 mm.

2.6 Summary

The water tunnel facility used, the tube bundle models investigated and the flow measurement techniques employed were described. The experimental facility previously employed in ECLAT, King's College London, was re-assembled and modified in order to introduce an oscillating component to the flow approaching the tube bundle models to be investigated. The pulsation waveforms generated by the rotating valve were also analysed and proved to be nearly sinusoidal, with at least 95% of the pulsation energy at the fundamental frequency. The three unconventional tube bundle models constructed and tested were extensively described: one asymmetric arrangement with circular tubes and two in-line arrangements, one with elliptic tubes and the other with drop shaped tubes.

The LDA experimental technique was briefly described. The principal sources of uncertainties in the LDA system, varying with measurement location, number of samples and with the local characteristics of the flow field, were analysed. No correction techniques were employed in the present study, but the errors were minimised by using a comparatively small control volume and a dense measurement grid in regions of steep velocity gradients. The overall error on the mean and r.m.s. velocities was estimated to be of 1%-5% and 5%-8% respectively. Flow visualisation was adopted as an additional tool of investigation in the present study, mostly to complement the LDA measurements. The flow visualisation technique used was described. Finally a description of the heat transfer technique adopted for surface temperature measurements was given. Both the asymmetric test section and the in-line one with elliptic tubes were modified in order to accommodate an instrumented cylinder for surface temperature measurements. The overall error in the evaluation of the electric power, Q, was estimated to be as high as 15%.

The following chapter presents the flow measurements taken in the arrangement with elliptic cylinders using the techniques described above, i.e. LDA and flow visualisation.

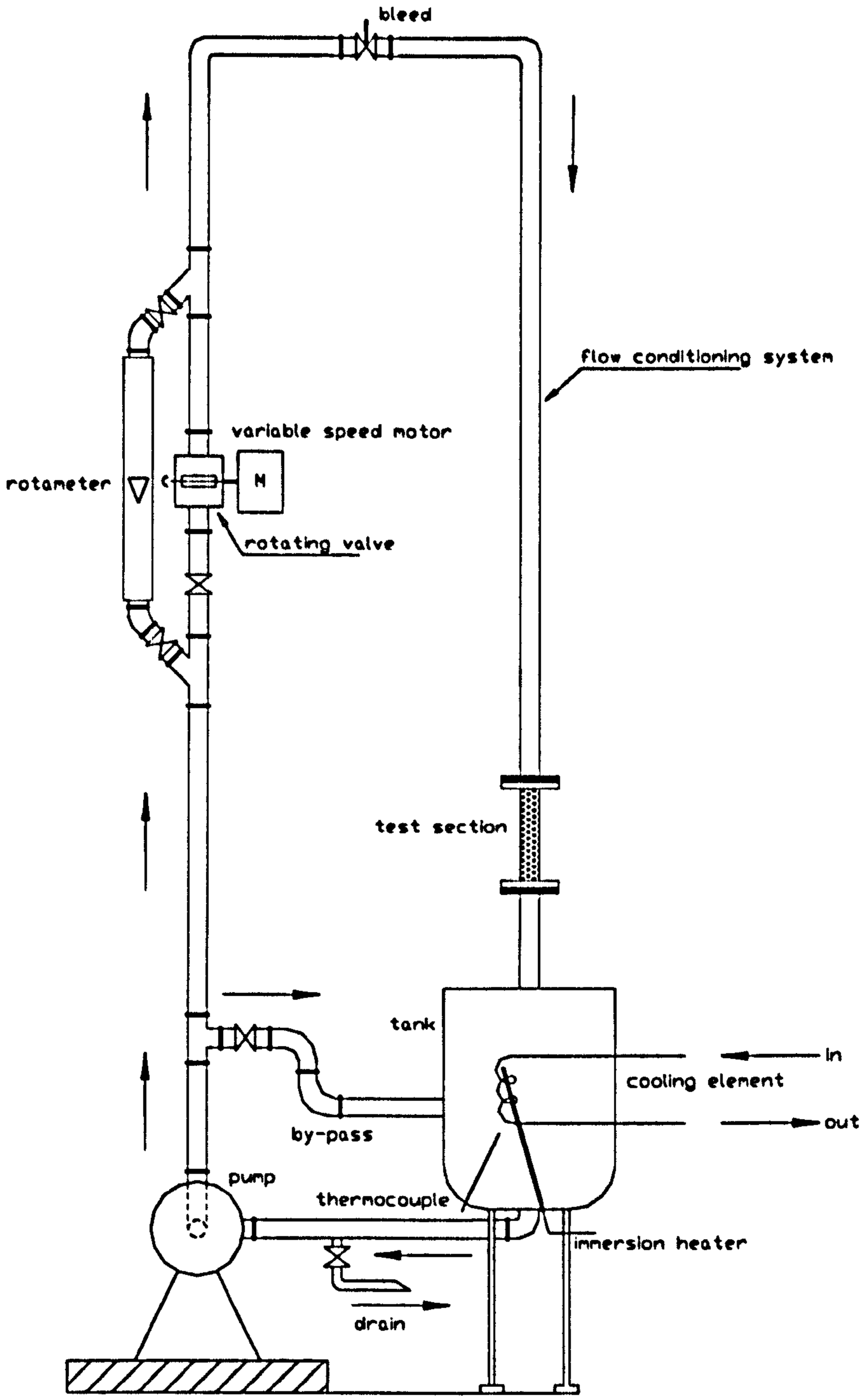

Figure 2.1. Schematic diagram of the experimental facility.

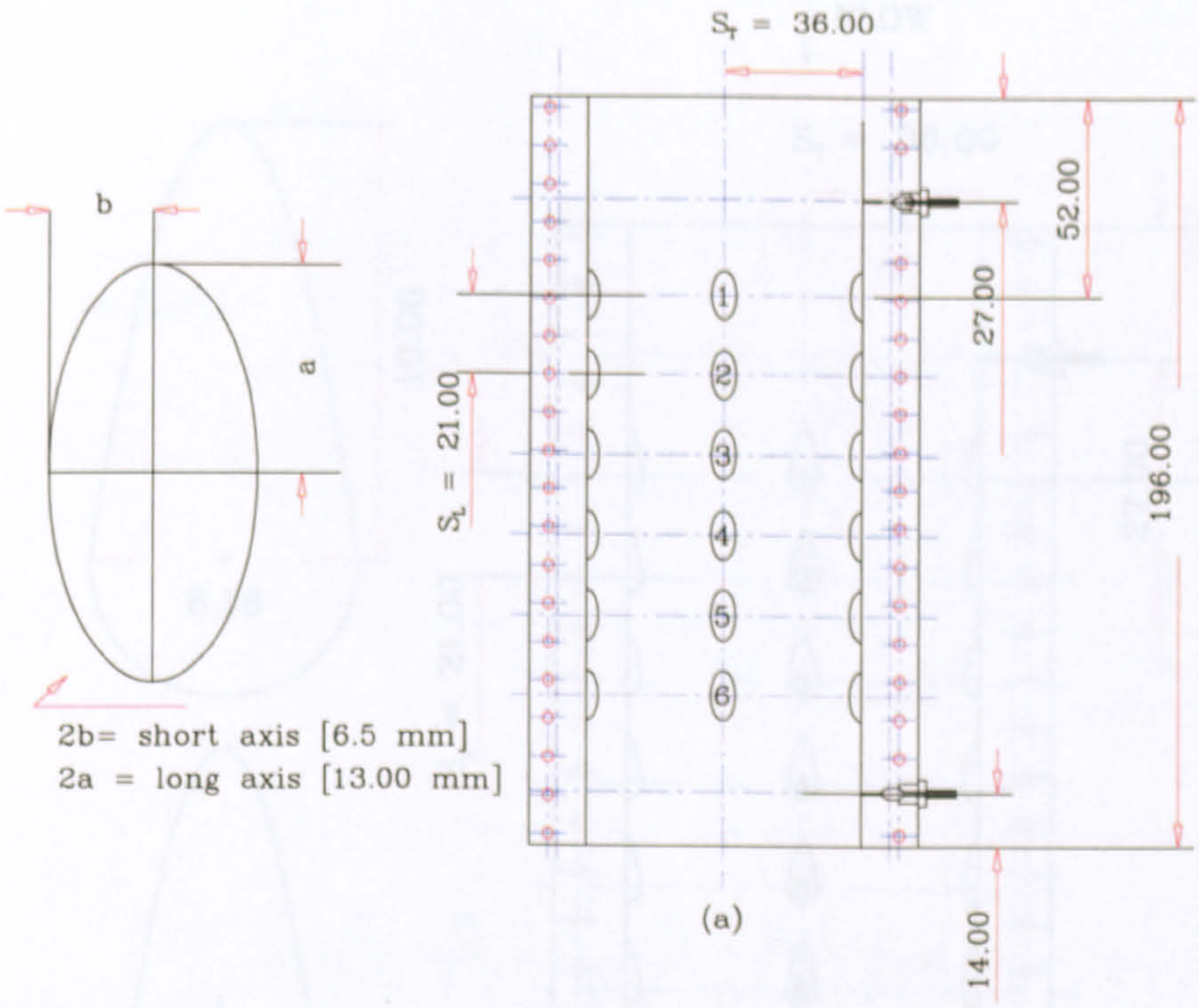

Figure 2.2 (a). Cross-section of the in-line tube bundle with elliptic tubes[1].

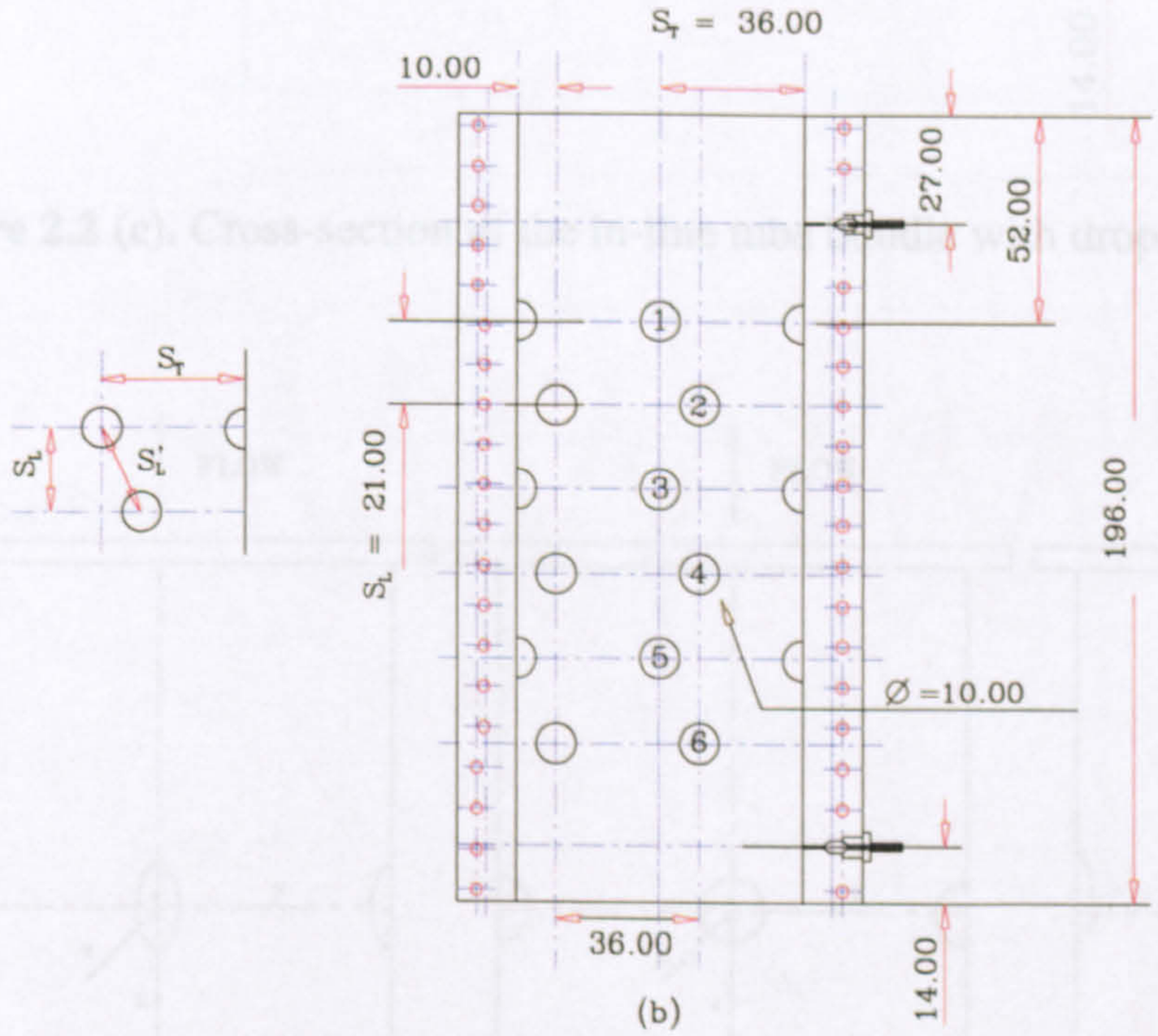

Figure 2.2 (b). Cross-section of the asymmetric tube bundle with circular tubes.

[1] All dimensions in Figures 2.2 (a)-(c) are expressed in mm.

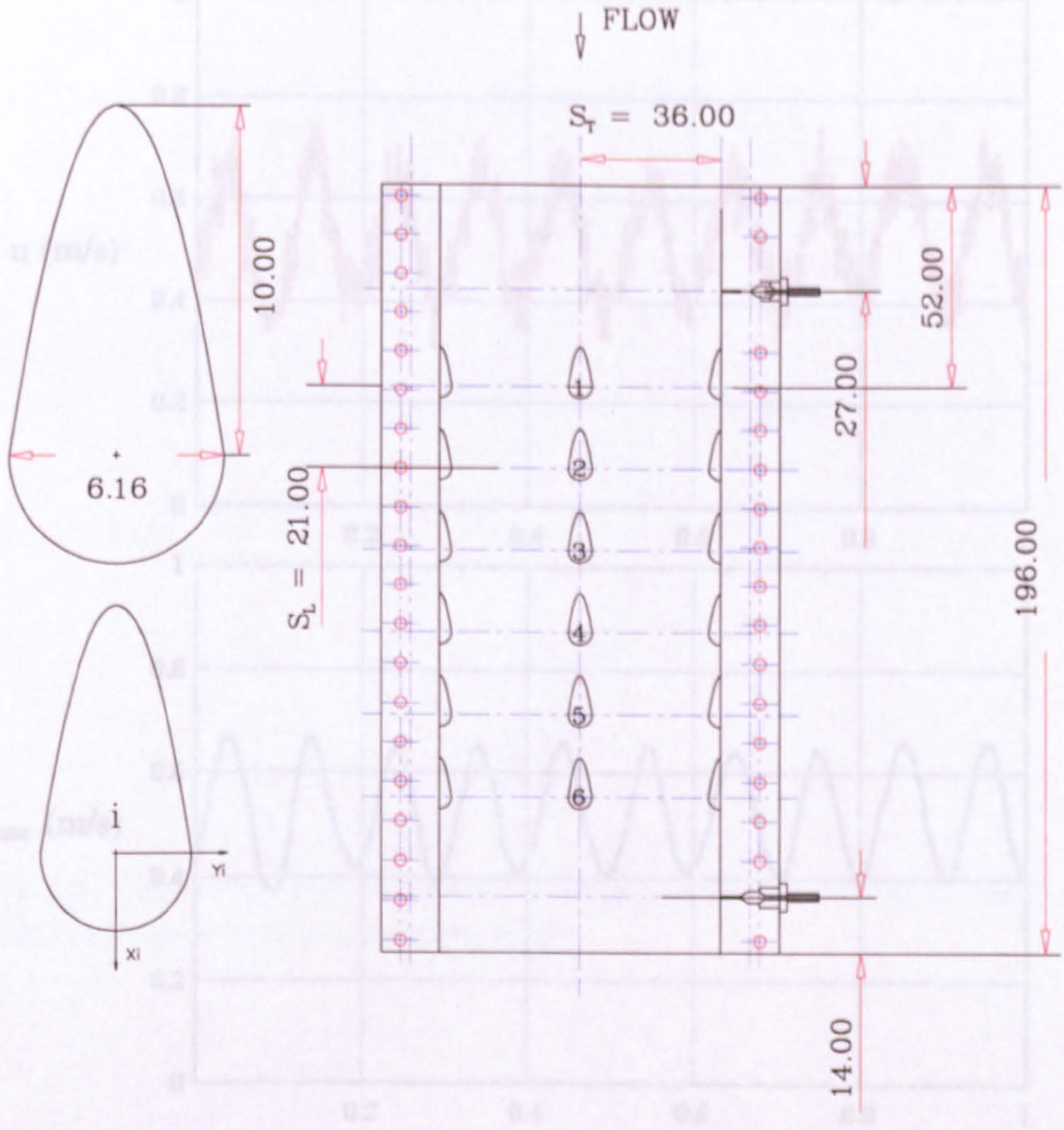

Figure 2.2 (c). Cross-section of the in-line tube bundle with drop-shaped tubes.

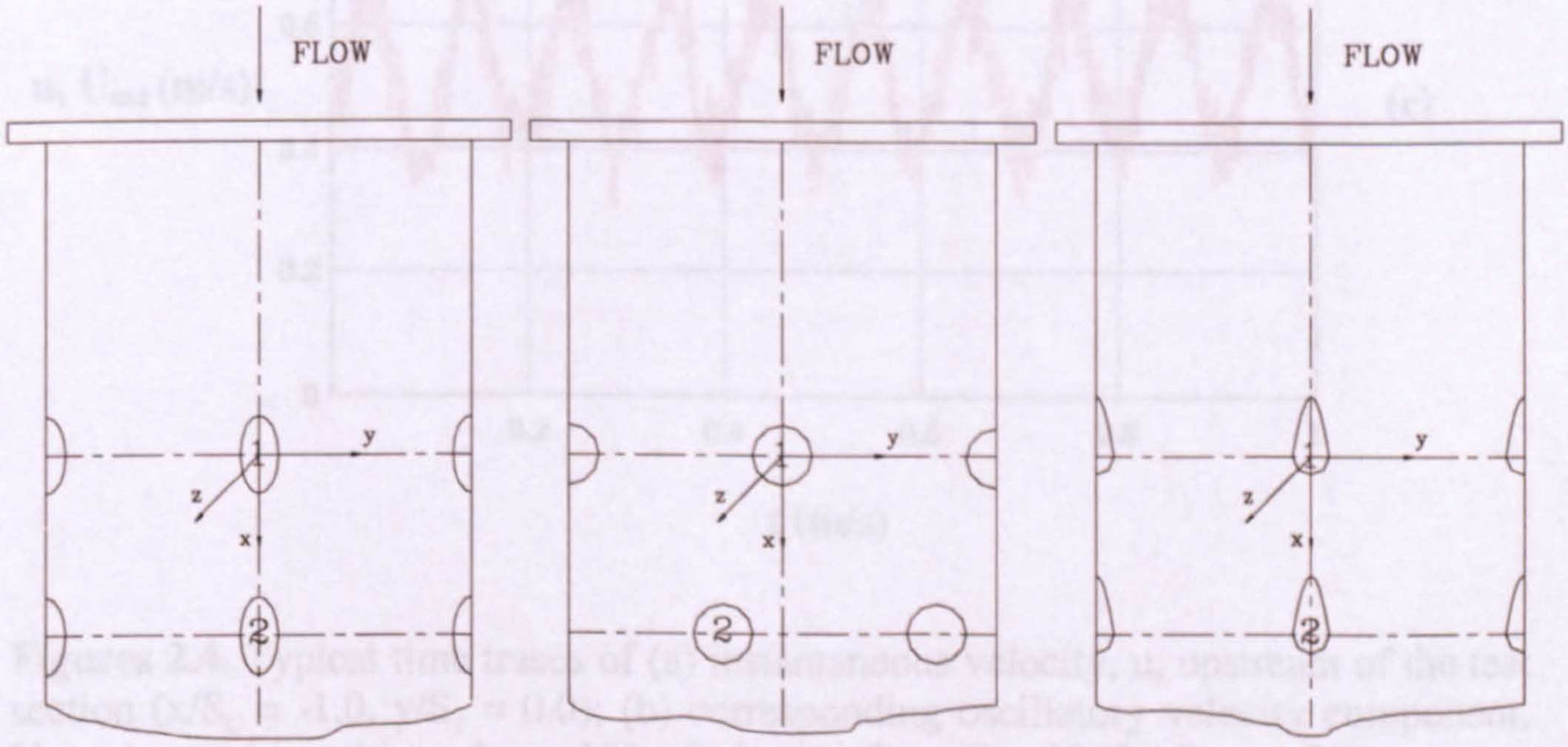

Figure 2.3. Co-ordinate system employed in the present study.

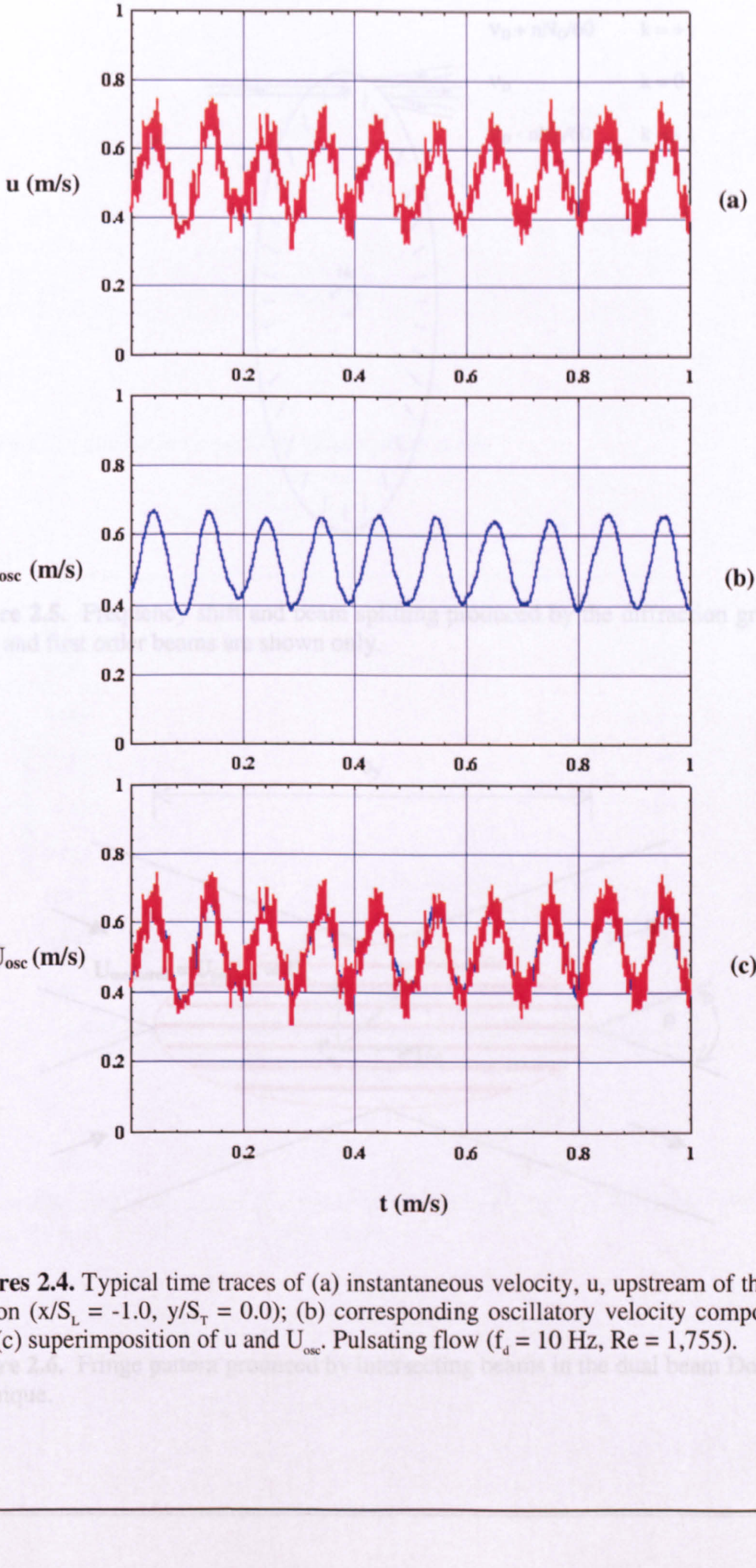

Figures 2.4. Typical time traces of (a) instantaneous velocity, u, upstream of the test section (x/S_L = -1.0, y/S_T = 0.0); (b) corresponding oscillatory velocity component, U_{osc}; (c) superimposition of u and U_{osc}. Pulsating flow (f_d = 10 Hz, Re = 1,755).

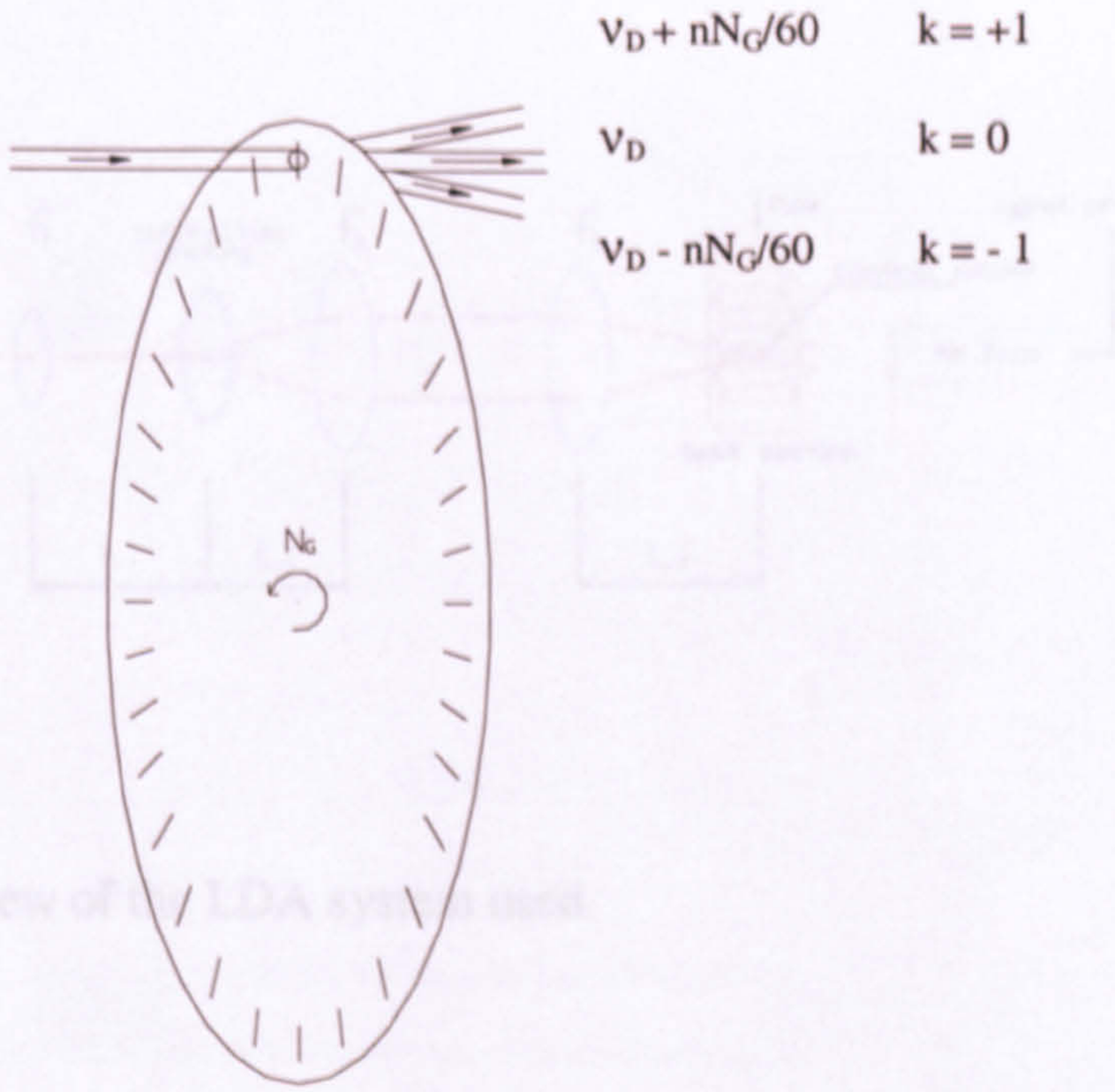

Figure 2.5. Frequency shift and beam splitting produced by the diffraction grating. Zero and first order beams are shown only.

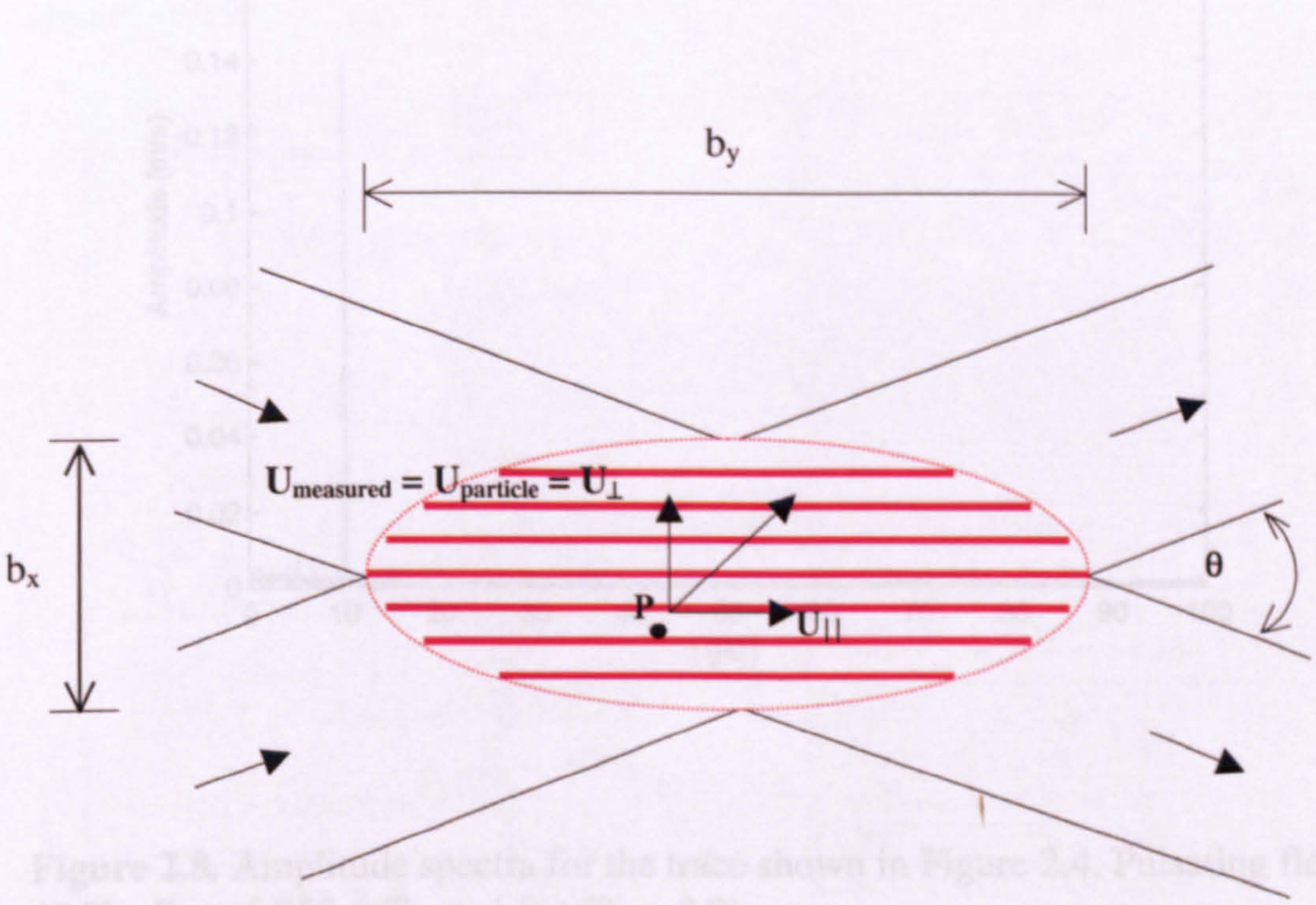

Figure 2.6. Fringe pattern produced by intersecting beams in the dual beam Doppler technique.

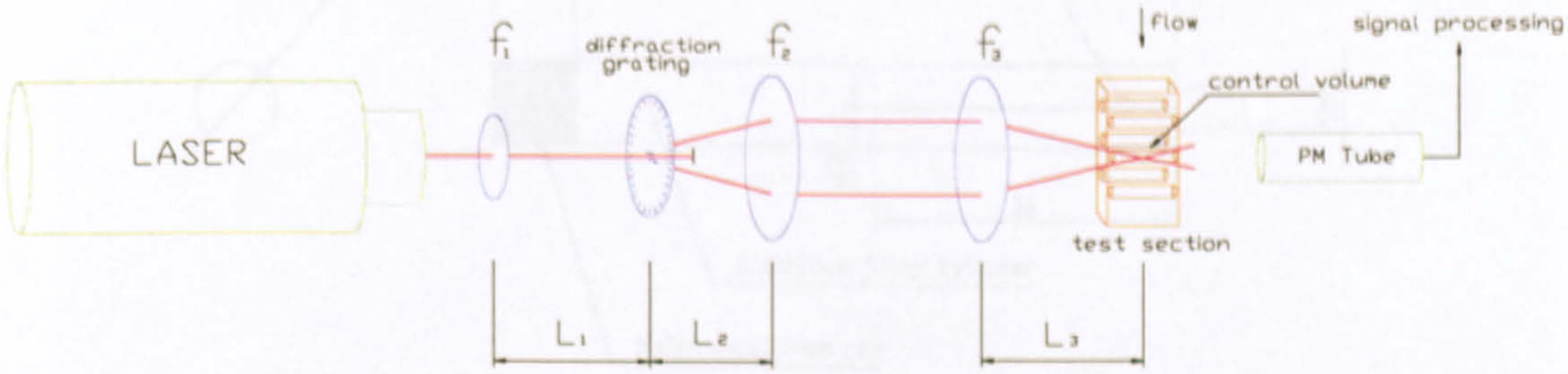

Figure 2.7. Schematic view of the LDA system used.

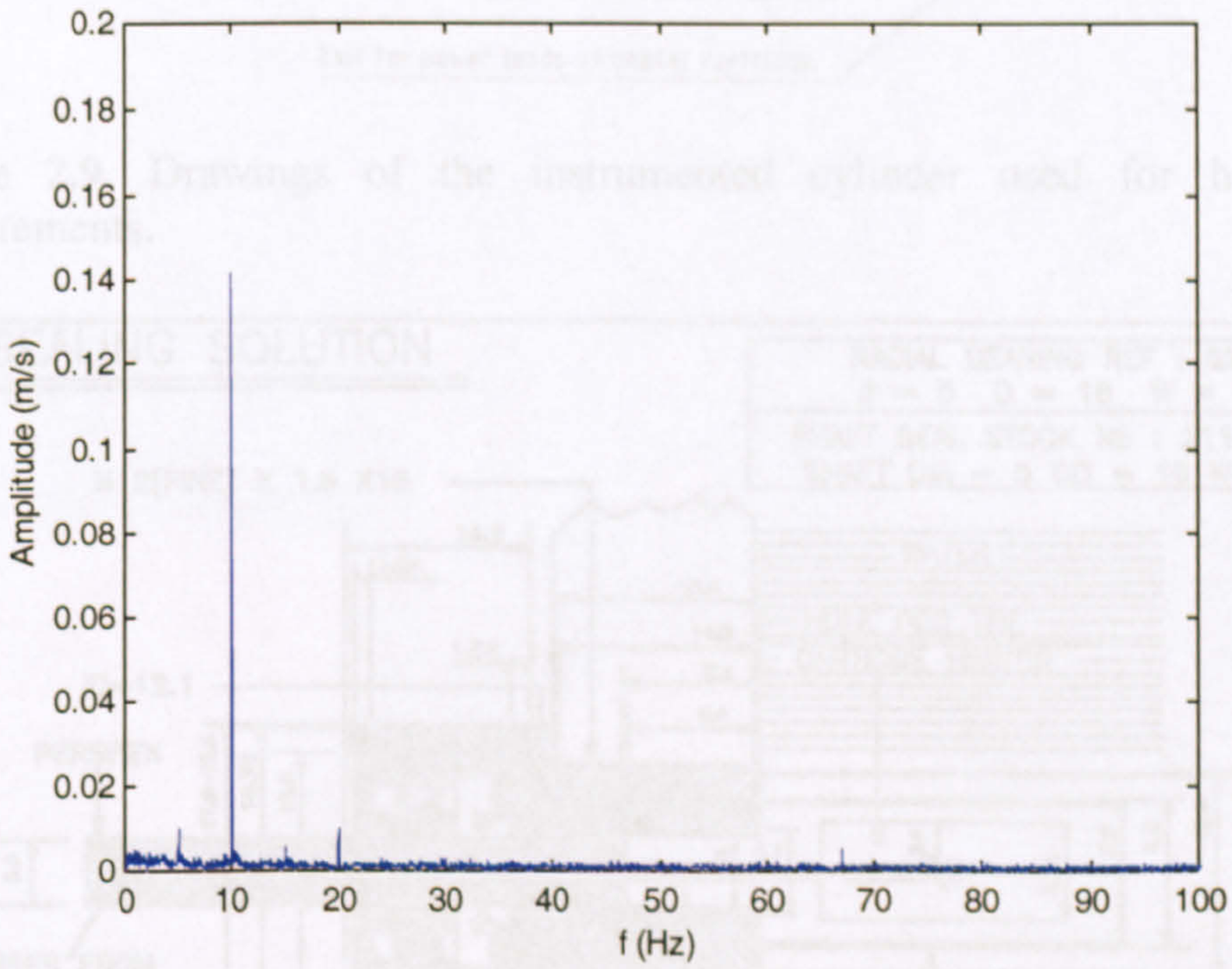

Figure 2.8. Amplitude spectra for the trace shown in Figure 2.4. Pulsating flow (f_d = 10 Hz, Re = 1,755; x/S_L = -1.0, y/S_T = 0.0).

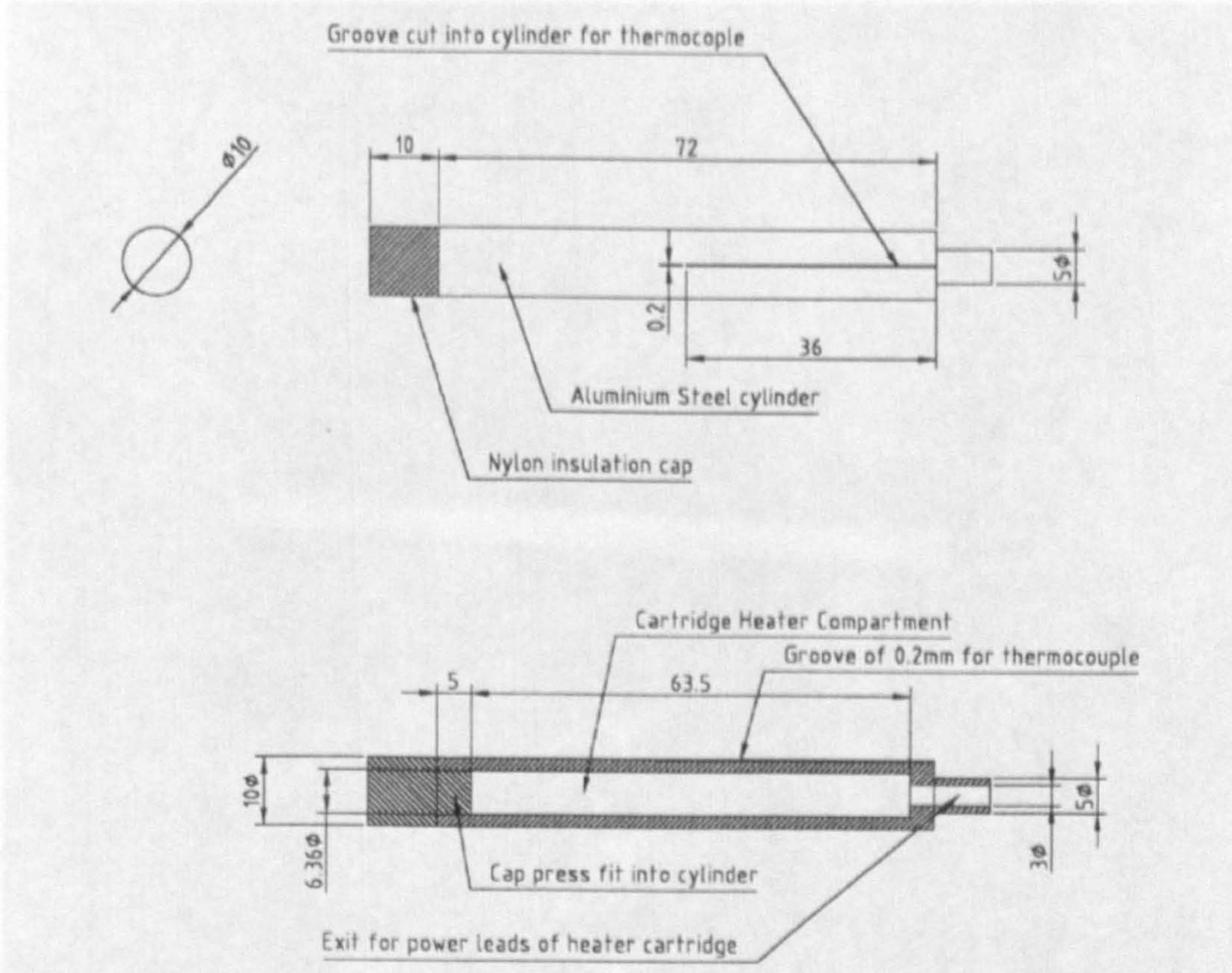

Figure 2.9. Drawings of the instrumented cylinder used for heat transfer measurements.

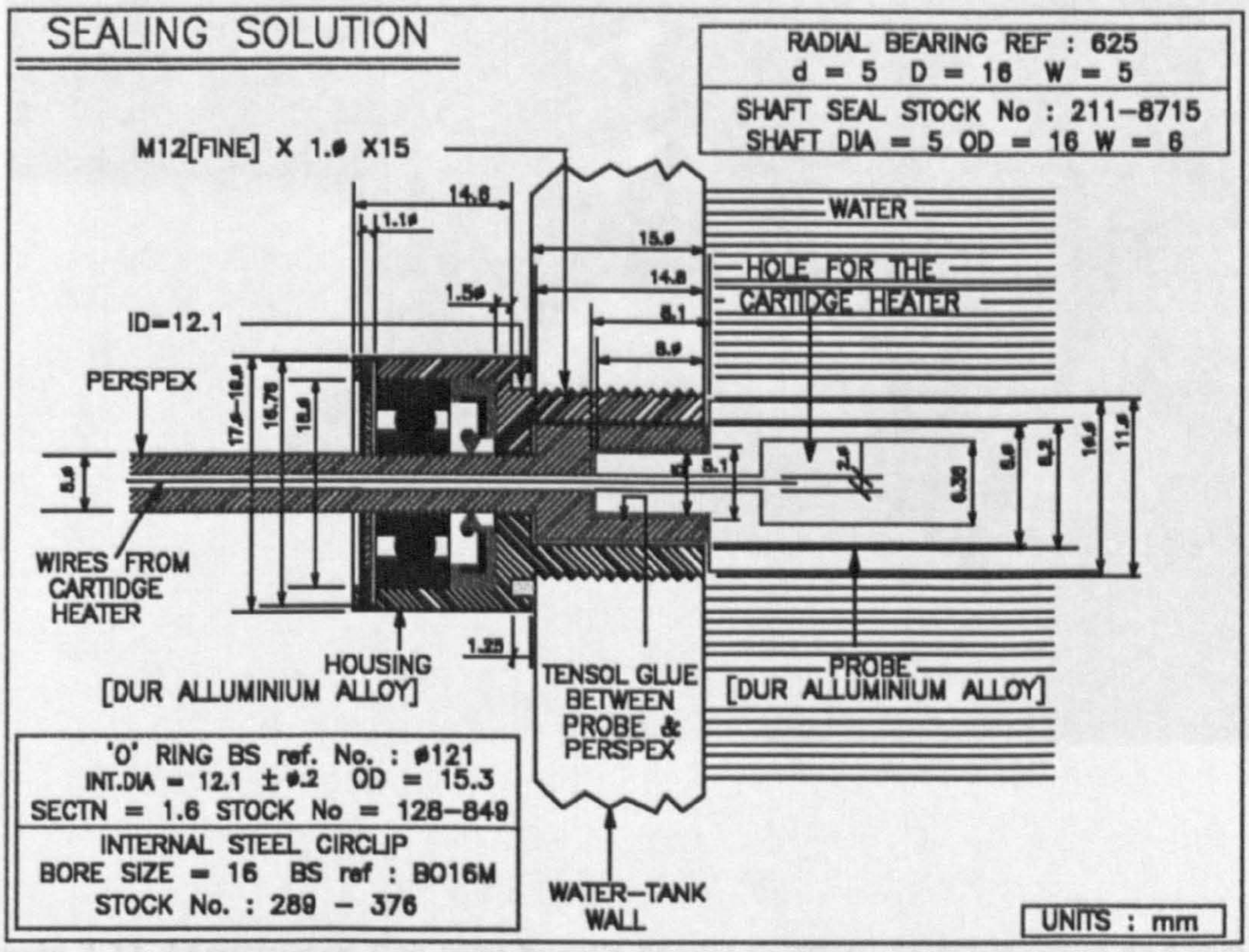

Figure 2.10. A schematic diagram of the modifications made to the tube bundle models to accommodate the instrumented cylinder.

Figure 2.11. Modified in-line tube bundle model to allow easy insertion and removal of both the Perspex cylinders and the instrumented one.

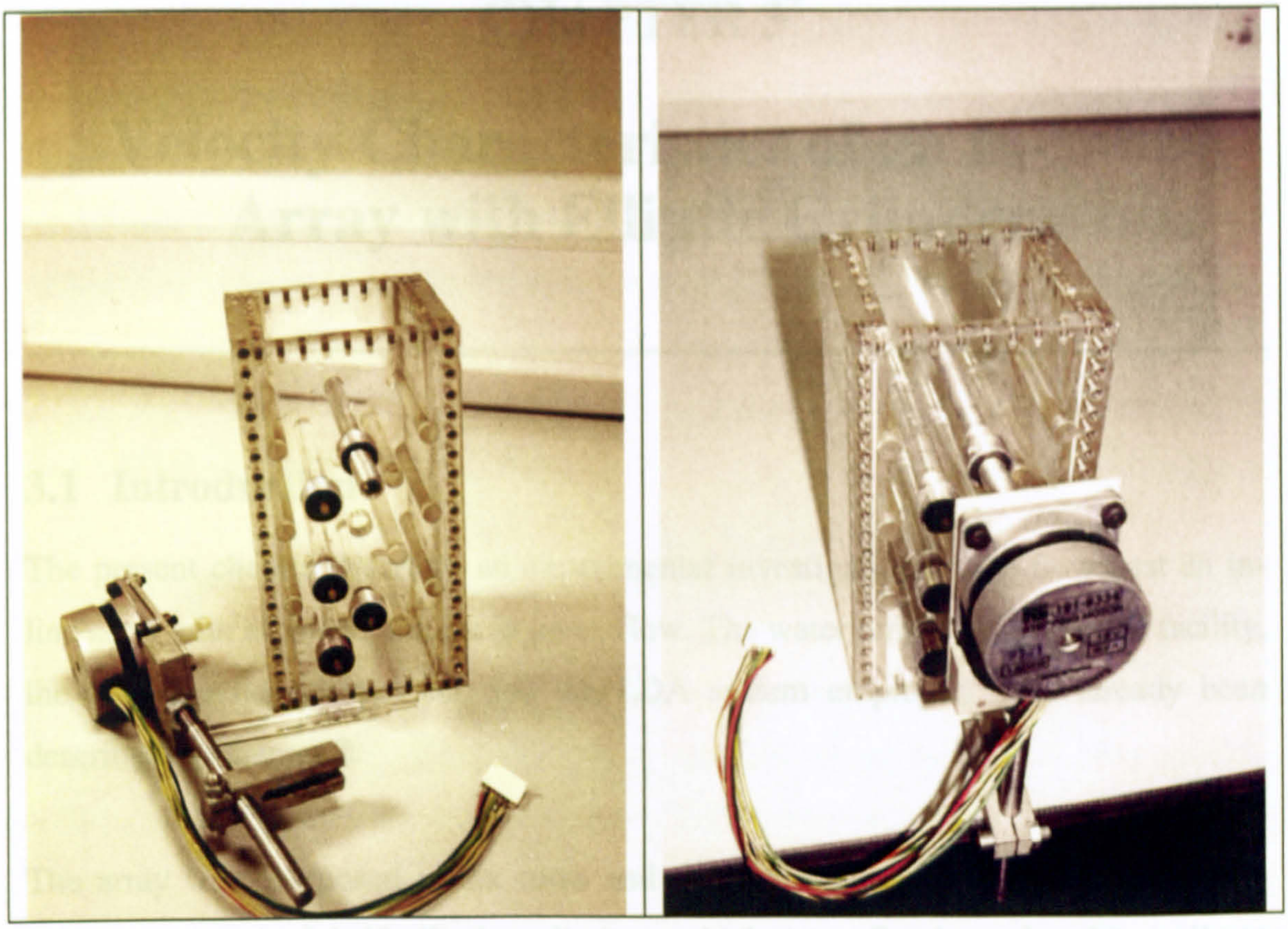

Figure 2.12. Photographs of the modified asymmetric tube bundle model. The stepper motor attached to the instrumented cylinder is also shown.

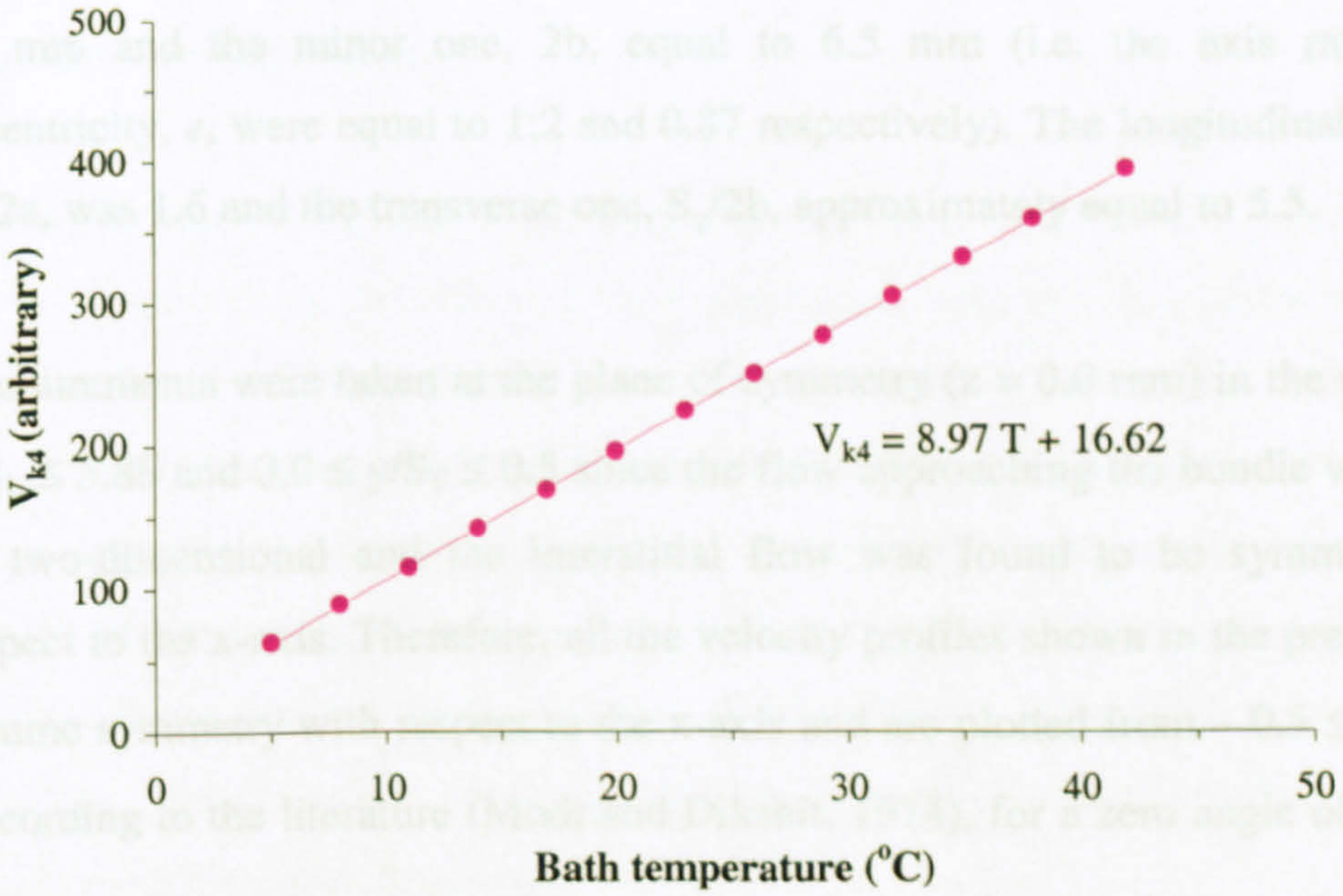

Figure 2.13. Calibration curve of the T-type thermocouple embedded into the duraluminium cylinder.

CHAPTER 3*

Velocity Characteristics of an In-Line Array with Elliptic Cylinders

3.1 Introduction

The present chapter describes an experimental investigation of the flow past an in-line array with elliptic cylinders in cross-flow. The water tunnel experimental facility, the tube bundle arrangement and the LDA system employed have already been described in Chapter 2.

The array was composed of six rows and three columns of cylinders. Two of the columns comprised half elliptic cylinders, which were fixed on the side walls to minimise boundary layer effects and simulate an infinite tube bundle. The elliptic cylinders were designed so that the heat transfer area is kept the same as that in the tube bundle models with circular tubes and were manufactured from cast acrylic material using a CNC machine. The major axis of the elliptic tubes, 2a, was equal to 13 mm and the minor one, 2b, equal to 6.5 mm (i.e. the axis ratio and the eccentricity, *e*, were equal to 1:2 and 0.87 respectively). The longitudinal pitch ratio, $S_L/2a$, was 1.6 and the transverse one, $S_T/2b$, approximately equal to 5.5.

Measurements were taken at the plane of symmetry (z = 0.0 mm) in the region $0.0 \leq x/S_L \leq 5.88$ and $0.0 \leq y/S_T \leq 0.5$ since the flow approaching the bundle was found to be two-dimensional and the interstitial flow was found to be symmetrical with respect to the x-axis. Therefore, all the velocity profiles shown in the present chapter assume symmetry with respect to the x-axis and are plotted from $-0.5 \leq y/S_T \leq 0.5$. According to the literature (Modi and Dikshit, 1974), for a zero angle of attack, $\alpha =$

---

* Some of the results shown in this chapter appear in: Castiglia, D., Balabani, S., Papadakis, G. and Yianneskis, M. (2001) "An experimental investigation and numerical study of the flow past elliptic cylinder arrays", Proceedings of IMechE, Part C, Vol. 215, pp. 1287-1301.

0, and a uniform upstream velocity profile, the wake behind an elliptic cylinder is symmetrical. Ensemble-averaged and time resolved measurements were taken in the above arrangement in both steady and pulsating flow conditions and a flow visualisation study was carried out for Reynolds number ranging from 638 to 6,760 and driving frequencies ranging from 7 Hz to 14 Hz.

3.2 Steady flow conditions

3.2.1 Mean velocity distributions (Re = 6,760)

Detailed ensemble-averaged measurements of the axial and radial mean velocities were taken at Re = 6,760. The bulk velocity upstream of the bundle, U_∞, was equal to 0.854 m/s and the working fluid was water. The corresponding Re and flowrate were 6,760 and 265 l/m respectively. Re is defined by the minor axis, 2b, and the maximum velocity at the gap between adjacent tubes in a row, U_g, which is equal to $1.22U_\infty$ (1.04 m/s) for the arrangement investigated. The equivalent Reynolds number defined by the upstream bulk velocity and the hydraulic diameter of the duct upstream of the bundle was 61,398. According to the literature (Žukauskas, 1972), under these conditions the flow regime is subcritical, characterised by laminar boundary layer separation.

In order to study the effect of the Reynolds number on the velocity characteristics of the array as well as the effect of flow pulsations, velocity measurements were also taken at Re = 1,755 behind each row. The mean velocity vectors are shown in Figure 3.1. It should be mentioned that due to optical access restrictions, the axial mean and r.m.s. velocity components, U and u' respectively, were measured at only one transverse plane behind each row and halfway between adjacent rows ($x_c/S_L = 0.5$, where x_c is the distance from the centre of the cylinder). Accordingly, the vector plots show the velocity vectors in those locations where both the mean (U, u') and radial (V, v') velocities were measured.

As expected, the flow field is characterised by areas of high and relatively uniform velocity at the flow passages between tube columns and low velocities in the

wake regions. Flow reversal is evident only behind the first row, at the plane x/S_L = 0.5. Although not clear from the vector plot, the outer edge of the shear layer separating from the second cylinder widens in the downstream direction and the radial component becomes more significant at an increasing distance from the centreline. Vectors are uniform and vertical on the entrance to the tube bank, and deflect slightly as the fluid passes through the gap between successive rows. At the exit of the tube bundle all the velocity vectors are directed inwards. The distribution of the axial mean velocities, U/U_∞, is shown in Figure 3.2 (a) and Figure 3.2 (b) as profiles and contours, respectively. Positive axial mean velocities indicate velocities in the downward direction. Figure 3.2 (a) shows that the axial mean velocity profile upstream of the tube bundle is uniform within 1% (x/S_L = - 1.0). The velocity profile in the free stream between tubes in the first row appears also to be uniform and consequently, due to the low speed region in the wake, a steep velocity gradient can be observed across the corresponding shear layer. Velocity gradients become progressively less steep in the downstream cylinders both because the turbulence generated in the wakes spreads to the rest of the flow domain, increasing the lateral mixing, and the recirculation becomes less pronounced. Figure 3.2 (b) shows the axial mean velocity distribution, U/U_∞, in contour plot form[1]. Velocities are approximately equal to the upstream bulk velocity, U_∞, in the free stream, indicating very little interference from the neighbouring tubes in the transverse direction. In other words, due to the large transverse spacing the flow is similar to the flow over a single column of elliptic tubes. Flow reversal is pronounced only behind the first row, where a steep velocity gradient can be observed as the shear layer separates; a weak flow reversal is observed again behind the second and third row.

Figure 3.3 shows a comparison of the axial mean velocity profile (normalised by the upstream bulk velocity U_∞) along the flow passage (y/S_T = 0.5) with that of an in-line array with circular cylinders[2] (Balabani, 1996; Balabani and Yianneskis, 1996). The profiles exhibit a similar trend; the magnitude of the velocities increases in the downstream direction with relative maxima in locations that lie between

[1] A small area adjacent to the cylinders was left undefined in all the contours shown since interpolation by assuming zero values at the wall led to an unrealistic representation of the distributions in that region.

[2] The two in-line arrays have the same longitudinal and transverse spacings. The diameter, d, of the circular cylinders was equal to 10 mm.

neighbouring cylinders in a row but is generally lower in the elliptic array than in the circular one, particularly behind the first, third and fourth rows. It is only behind the second row that the two arrays exhibit velocities of the same magnitude. Figure 3.4 (a) shows the comparison of the axial mean velocity profiles, U/U_∞, between the two arrays in the wake of the first cylinder. The profiles were plotted against y/d*, where d* corresponds to either the cylinder diameter (d = 10 mm) or the minor axis (2b = 6.5 mm) for the circular and elliptic cylinders respectively. It can be seen that when the transverse locations are normalised by d* the velocity distributions are very similar with both the maximum and minimum velocity magnitude occurring at approximately the same dimensionless locations. The velocity magnitude is slightly higher in the shear layer and the recirculation more pronounced in the circular cylinders than in the elliptic ones. Figures 3.4 (b)-(d) show the comparison of the axial mean velocity profiles, U/U_∞, between the two arrays downstream of the second, third and fourth rows respectively[3]. The velocity magnitude is generally slightly higher in the array with circular cylinders with the exception of the profile downstream of the second row. In contrast to the first cylinder, the recirculation is slightly more pronounced in the array with elliptic cylinders, but the difference is negligible and decreases in the downstream direction.

The distribution of the radial mean velocities, V/U_∞, is shown in Figure 3.5 (a) and Figure 3.5 (b) as profiles[4] and contours, respectively. Negative radial velocities indicate velocities in the inward direction. The profile on the entrance to the tube bundle (x/S_L = 0.0) shows a significant variation of the radial mean velocity magnitude along the transverse direction; a similar trend although with a smaller magnitude is observed at x/S_L = 0.11. The V/U_∞ profiles become more uniform in the downstream direction with the exception of those halfway between successive rows. These exhibit, in fact, a reverse trend. The radial mean velocity profiles exhibit a negative relative maximum, which increases in magnitude and occurs closer to the centreline in the downstream rows. The velocity profile downstream of the first row

[3] Two profiles for the circular cylinders are compared with one for the elliptic ones as measurements were not taken along the same x-planes. The two profiles for circular cylinders can be averaged to approximate the profile at the same x-plane as the one for the elliptic cylinders.

[4] Note that the normalised radial velocity, V/U_∞, in Figure 3.5 (a), was multiplied by a factor 6 in order to magnify the profile velocity gradients.

shows also a relative positive maximum at $y/S_T = 0.06$ ($y/2b = 0.33$) due to the strong recirculation in this region. The contours in Figure 3.5 (b) show that the transverse mean velocities have near zero values along the flow passages and generally low negative values in the vicinity of the tubes after each row is encountered. The radial velocity distribution appears slightly more uniform than in the configuration with circular tubes studied by Balabani (1996). In both cases low positive velocities were recorded on the shoulder of the penultimate row cylinder, but in the arrangement with circular tubes low positive values were also observed over the shoulder of the last row cylinder.

3.2.2 Turbulence level distributions (Re = 6,760)

In order to visualise the turbulence characteristics of the tube bundle the measured axial and radial normalised r.m.s. velocities, u'/U_∞, and v'/U_∞, have been plotted and are shown as both profiles in Figures 3.6-3.9, and as contours in Figure 3.10. Figures 3.6 (a) and 3.7 show the axial r.m.s. velocity profiles throughout the whole array and a comparison of the axial r.m.s. velocity profiles along the flow passage between the present in-line array with elliptic tubes and an in-line one with circular tubes respectively, whereas Figures 3.8 and 3.9 show a closer comparison of the axial r.m.s. velocity profiles obtained behind each row. The turbulence intensity[5] upstream of the test section ($x/S_L = -1.0$, $y/S_T < 0.5$, $z = 0.0$ mm) was nearly constant and equal to 0.058.

The radial r.m.s. velocity component, v', was measured only halfway between successive rows ($x_c/S_L = 0.5$), that is, the plane where u' could also be measured, due to optical access restrictions. In the present work, measurements were taken only at positive values of y/S_T and symmetry was assumed around the centreline.

The normalised axial r.m.s. velocities (Figure 3.6 (a)) are relatively low behind the first cylinder, but start rising downstream of the second row. The peak velocity fluctuation ($x/S_L = 0.5$) behind the first cylinder was recorded at a distance of $y/S_T = 0.11$ ($y/2b = 0.6$) from the centreline. Its location can be taken approximately as the

[5] The *turbulence intensity* here is defined as the ratio of the fluctuating component in the direction of the flow (u') to the local axial mean velocity (U), that is, $Tu = u'/U$.

position of the vortex core at that station. The r.m.s. peak occurred closer to the centreline in downstream locations. Behind the last cylinder this position was recorded at approximately $y/S_T = 0.055$-0.069 ($y/2b = 0.3$-0.38). This value is in very good agreement with the one extrapolated by the results of Modi and Dikshit (1974) for a single elliptic cylinder. The r.m.s. values behind the last row cylinder are significantly higher than those measured in previous rows. The normalised radial r.m.s. velocities (Figure 3.6 (b)) are also relatively low behind the first cylinder, but start increasing downstream of the second row. The radial r.m.s. velocity profile behind the first cylinder is very similar to that of the axial r.m.s. velocity. A peak velocity fluctuation was, in fact, recorded at the same location, that is $y/S_T = 0.11$ ($y/2b = 0.6$) and a relative minimum at $y/S_T = 0.0$. This trend is reversed in downstream rows: the r.m.s. velocity magnitude behind each row increases from $y/S_T = 0.5$ to $y/S_T = 0.0$ where it reaches a maximum. The magnitude of the maximum also increases in downstream locations.

Figure 3.7 shows a comparison of the axial r.m.s velocity profiles along the flow passages ($y/S_T = 0.5$), $(u'- u'_{ups})/U_\infty$, where u'_{ups} is the upstream axial r.m.s. velocity magnitude, with that of the in-line array with circular cylinders. The value of the upstream axial r.m.s. velocity was subtracted from the local one in order to take into account the different upstream turbulence levels between the two arrays. The turbulence levels remain nearly constant along the flow passages of the elliptic cylinder array in contrast to the gradual and significant increase of the r.m.s. velocity in the downstream direction in the array with circular cylinders. At this point, it is worth mentioning that in the wake of a bluff body two regions can be identified: 1) the immediate vicinity of the body where the separated shear layers undergo transition to turbulence and roll into vortices; 2) the far wake, where the vortices diffuse and dissipate forming a turbulent field; the first region is referred to here as the "near wake". It was not possible to identify a far wake behind the first five rows due to the presence of the downstream cylinders obstructing the flow. However, it was possible to identify, by averaging over a large time (compared to the shedding period), a "mean recirculation region" (Williamson, 1996) in the near wake, which is symmetric and closed. Its width (which will be referred to as *wake width*) is confined within the inner edge of the shear layer separating from the upstream cylinder and is defined by the lateral distance between the vortex centres on each side of the

centreline. According to the literature (Hooker, 1936), the maxima velocity fluctuations do not occur along the path of vortex centres but they rather develop in the neighbourhood of the core farthest from the centreline. As a result, the distance between the peaks on each side of the centreline overestimates the wake width, but the error is negligible. Figure 3.8 shows how the wake width decreases in downstream rows from about 8 mm behind the first row to about 3.5 mm behind the last one. Unfortunately the axial r.m.s. velocities were measured only at one station behind each row and therefore no additional information could be extracted about the wake geometry, such as the longitudinal (L) and lateral spacing (W) between vortices, the wake geometry ratio (W/L) and the vortex formation length. The flow region confined by the outer edge of the opposite shear layers enlarges consistently downstream in the tube bank. Figure 3.9 demonstrates how the turbulence levels increase in the downstream direction. The separation of the boundary layer from the cylinders and the vorticity generated on the upstream side of subsequent cylinders increase the turbulence intensity in the free stream of the subsequent rows. On the contrary, at the lower Reynolds number investigated (Re = 1,755), the r.m.s. distributions measured behind each row (not shown here for brevity) were found to be more uniform. The arrow in Figure 3.9 highlights how the regions of steep r.m.s. velocity gradients move further away from the centreline in downstream locations.

Figures 3.10 (a), (b) show the distribution of the axial, u'/U_∞, and radial, v'/U_∞, r.m.s. velocities respectively in contour form. The turbulence is generated primarily in the wake regions and spreads slowly to the rest of the flow domain. In general, the distributions look very similar for both components. Both the axial and radial r.m.s. velocities increase in the downstream rows. However the axial r.m.s. velocities are slightly higher than the radial ones as the flow passes over the shoulder of each elliptic cylinder. The radial r.m.s. velocities are slightly higher than the axial ones in the wakes of the first three rows cylinders but exhibit similar values further downstream. Turbulence can be considered fully developed from the fifth row onward. It is well known that the entrance effects reach more rows in in-line arrays than in staggered ones and this might be more pronounced in an in-line array with elliptic cylinders. In the wakes of the fifth and sixth rows both components reach a maximum value of $0.4U_\infty$. The above distributions indicate little turbulent mixing in the in-line configuration with elliptic tubes in comparison with the one with circular

tubes (Balabani, 1996). It should be noted however, that although the transverse spacing is the same for the two arrays, the elliptic cylinders have a smaller minor axis and therefore the free spacing between adjacent cylinders in a row is larger.

Figures 3.11 (a)-(d) show a comparison of the axial r.m.s. profiles, $(u'- u'_{ups})/U_\infty$, between the two arrays downstream of the first, second, third and fourth row cylinders respectively. The radial co-ordinate, y, is normalised by d*, which is equal to d for circular cylinders and 2b for elliptic ones. With this normalisation, the peak velocities occur at the same dimensionless location for both arrays in a manner similar to that observed in the mean velocity profiles. The peak r.m.s. velocity occurs at $y/d^* = 0.6$ behind the first row and shifts closer to the centreline further downstream in both arrays. Behind the first row the main differences between the axial r.m.s. velocities are concentrated in the wake region where the elliptic cylinders exhibit lower r.m.s. velocities by 20% on average. The r.m.s. velocities are in general lower than that of the circular cylinders further downstream. Behind the second row the magnitude of the peak r.m.s. velocity ($0.22U_\infty$) is 60% lower than that for the circular cylinders ($0.35U_\infty$). The slight shift of the r.m.s. velocity peaks towards the centreline in both arrays shows that there is a similar decrease of the wake width in downstream rows.

The distribution of the ratio of the r.m.s. velocities, $|v'- u'|/U_\infty$, plotted in Figure 3.12 assesses the degree of anisotropy in the turbulence generated by the tube bank. The difference of the two r.m.s. components is near zero over the whole flow domain indicating that the turbulence can be assumed highly isotropic. On the contrary, the turbulence in the wake regions of the in-line arrangement with circular tubes was found to be highly anisotropic, especially downstream of the third and fourth rows, where the two r.m.s. velocity components differed by up to $0.6U_\infty$ (Balabani, 1996).

Vortex formation length

The vortex formation length, L_F, behind the last cylinder was estimated at Re = 1,755 and 6,760. The spacing between cylinders in a longitudinal row is so small that there is not a sufficient number of measurements to estimate the vortex formation length or other wake characteristics behind other row cylinders. The vortex formation length is defined here as the "distance downstream of the cylinder axis to a point where the r.m.s. velocity fluctuations are maximised on the wake centreline, u'_{max}" (Williamson, 1996). It is a measure of the length of the mean recirculating region in the wake of the cylinder, or simply, an indication of the distance at which the first vortex appears. Figure 3.13 shows the axial r.m.s. velocity profile along the centreline for both the Reynolds numbers studied. The r.m.s. velocities are normalised with the peak r.m.s. velocity[6] and the distance x_c is measured from the cylinder axis and is normalised with the major axis of the cylinder.

It can be seen that the location of the maximum r.m.s. velocity and consequently the vortex formation length depends on the Reynolds number, as expected. The vortex formation length normalised with 2a, $L_F/2a$, is approximately equal to 1.035 for Re = 6,760 and to 1.04 for Re = 1,755, i.e. the vortex formation decreases as the Reynolds number increases. According to the literature, the vortex formation length also decreases when the turbulence levels increase. It is expected, therefore, that L_F will be greater in upstream cylinders for both Re since turbulence levels are lower. This causes a decrease in the size of the vortices shed further downstream and, consequently, a narrowing of the mean recirculating bubble in downstream locations (Ljungkrona et al, 1991). Figure 3.8 shown earlier illustrated this continuous change in the wake width (Re = 6,760), indicated by the closer spacing between the r.m.s. peaks, in downstream rows.

---

[6] u'_{max} was chosen as normalisation factor in order to have the same normalised r.m.s magnitude ($u'_{max}/u'_{max} = 1$) at the location along the centreline where $u' = u'_{max}$ for all flow conditions and behind all rows (see paragraph 4.2.2). The adoption of u'_{max} as normalisation factor facilitates therefore the comparison of the r.m.s relative variation along the centreline and of the vortex formation length with other authors (see Williamson (1996)) and between different rows of the same array.

3.2.3 Flow periodicity

Time resolved measurements were taken at one station behind each cylinder (x_c/S_L = 0.5 and y/S_T = 0.11). Velocity spectra were estimated for Re = 6,760 and 1,755 respectively in order to gain an understanding about the vortex shedding characteristics of the elliptic cylinders in the bundle. In order to evaluate the corresponding Strouhal number dependence on the Reynolds number, additional time resolved measurements were taken at $x_c/S_L = 0.5$ and $y/S_T = 0.125$ in the range 1,157 < Re < 5,206. Figure 3.14 shows typical power spectra behind each row at Re = 1,755 and steady flow conditions. It can be observed that there is not any distinct periodicity behind the first three rows of the bundle. A weak frequency peak with f_{so} = 4.7 Hz appears downstream of the fourth row. This peak is also detectable further downstream and its amplitude has increased significantly exhibiting a maximum value behind the fifth row. Figure 3.15 shows power velocity spectra obtained at exactly the same location for Re = 6,760. The spectra indicate that the vortex shedding frequency peak has shifted to a higher frequency, approximately equal to f_{so} = 17.5 Hz. However, the Strouhal number maintains the same value, i.e., St = 0.11, defined by the gap velocity and the minor axis of the elliptic cylinders, 2b. The spectra show similar characteristics with those obtained at the lower Reynolds number. However, the spectra in Figure 3.15 show a vortex shedding peak behind the third row implying that by increasing the Reynolds number the flow periodicity moves to upstream rows. The amplitude of the vortex shedding peak increases in downstream rows and reaches a maximum downstream of the fifth row, as in the case of lower Reynolds number. The absence of a vortex shedding peak in the front rows might be attributed to the fact that the shear layer separating from the cylinders reattaches on the downstream rows. This has been confirmed by flow visualisation.

Different characteristic lengths and velocities have been used in the literature to define the Strouhal number for elliptic cylinders. In Table 3.1 the Strouhal number values based on various definitions are given for both Re = 6,760 and 1,755. For comparison, the Strouhal numbers observed in an equivalent array with circular cylinders by Konstantinidis et al (2000) and in a single elliptic cylinder with an axis ratio b/a = 0.6 (i.e. slightly higher than the axis ratio of the cylinders used in the present investigation, b/a = 0.5) by Modi and Dikshit (1974) are also given.

The Strouhal number was defined by the minor axis of the elliptic cylinders, 2b, since in the present in-line array the flow was aligned with the major axis of the cylinders and therefore the minor axis was considered as their effective diameter (Modi and Dikshit (1974), Mittal and Balachandar (1996), Balachandar et al (1997)) and used as the reference length scale. This definition is useful since it can be used for comparison between flows over elliptic cylinders of various axis ratios. The lower Strouhal number value observed in the present array, in comparison to the St of a single elliptic cylinder and an equivalent array with circular cylinders, can be partly attributed to the relatively smaller free space between successive cylinders available for the vortices to be formed and shed. Table 3.1 shows that if the equivalent diameter d_e, defined in the same table, is chosen, as characteristic length, the Strouhal number is higher than that for an array with circular cylinders and equal to either St = 0.17 or St = 0.21, depending on the characteristic velocity adopted (U_g or U_∞, respectively). It is obvious, therefore, that the correct choice of the characteristic length to use in the definition of the Strouhal number is critical. As previously stated, the projected height of the cylinder, h, (i.e. the minor axis, for an ellipse at zero angle of attack) is commonly used by several authors as characteristic length to allow comparisons of St numbers between flows over elliptic cylinders of various axis ratio and angle of attacks; it is also used to define the Reynolds number (Mittal and Balachandar, 1996). Table 3.1 also shows that the Strouhal number for cylinders in an in-line array, is generally lower than that of single cylinders and this is true for both elliptic and circular cylinders.

Table 3.1. Strouhal number definitions and relative values for both Re = 6,760 and Re = 1,755 in the in-line array with elliptic cylinders.

	IN-LINE ARRAY WITH ELLIPTIC CYLINDERS	IN-LINE ARRAY WITH CIRCULAR CYLINDERS	SINGLE ELLIPTIC CYLINDER
Definition	St (Re = 6,760 and Re = 1,755) (present investigation)	St (Re^{**} = 2,800) (Konstantinidis et al, 2000)	St (Re^{***} = 34,000) (Modi and Dickshit, 1974)
$St = \frac{f_{so} d_e^{*}}{U_g}$	0.17	0.14	
$St = \frac{f_{so} d_e}{U_\infty}$	0.21	0.19	≈ 0.28
$St = \frac{f_{so} h^{****}}{U_g}$	0.11	0.14	
$St = \frac{f_{so} h}{U_\infty}$	0.14	0.19	≈ 0.21
$St = \frac{f_{so} d_e}{U_f^{*****}}$	0.16		
$St = \frac{f_{so} h}{U_f}$	0.10		

*d_e is defined as the diameter of an equivalent circular cylinder, whose circumferential length is equal to that of the present elliptic cylinder, that is, d_e = 10 mm.

** The Reynolds number, Re, was defined using the cylinder diameter of the circular cylinders (d = d_e = 10 mm) as characteristic dimension and the gap velocity, U_g, as characteristic velocity, that is, $Re = U_g\, d/\nu$.

*** The Reynolds number, Re, was defined using the minor axis of the elliptic cylinder as characteristic dimension and the bulk velocity, U_∞, as characteristic velocity, that is, $Re = U_\infty\, 2b/\nu$.

****The angle of attack in the present investigation was chosen equal to zero. By definition, the projected height, $h = 2b$ for the elliptic cylinders and h = d for the circular ones.

***** U_f is here defined as a freestream velocity evaluated at $x/S_L = 0$, $y/S_T = 0.5$.

Figures 3.16-3.20 show spectra obtained in other Reynolds numbers. The spectra in Figures 3.16 show no distinct peak associated with vortex shedding activity behind the first row. As the Reynolds number increases the number and amplitude of peaks increases. The same trend was observed behind the second row (the corresponding spectra are not shown for brevity). The spectra in Figures 3.17 to 3.20 (note that the scale of the spectra in Figures 3.19 and 3.20 is different due to the higher amplitude peaks) show the presence of a distinct peak whose frequency shifts as the Reynolds number increases. The amplitude of the peaks also increases with Reynolds number and a number of low frequency peaks make their appearance.

Although the spectra in Figures 3.17 and 3.20 exhibit similar trends, the variation of the amplitude of the vortex shedding peaks with the Reynolds number depends on the row depth. Figure 3.21 shows the variation of the peak amplitude versus Re in the wakes of the third, fourth, fifth and sixth rows. It can be observed that behind the third and fourth rows the amplitude increases smoothly with Re (the trend is approximately parabolic) in the range $1{,}157 < Re < 5{,}206$. The values of the amplitude are similar between the two rows up to about $Re = 2{,}300$. For $Re > 2{,}300$, the amplitude of the vortex shedding peak behind the fourth row becomes increasingly higher than that behind the third one. The amplitude of the peaks behind the fifth and sixth rows, instead, increases moderately up to approximately $Re = 2{,}300$. The amplitude values are similar behind these two rows but slightly higher than that observed in upstream rows. At higher Re there is a relatively abrupt increase of the peak amplitude behind the 5^{th} and 6^{th} rows; for example, from $Re = 2{,}300$ to $Re = 4{,}500$ it increases up to 25% in relation to that recorded behind the second and third rows. For Re above 4,500, the amplitude of the vortex shedding peak behind the fifth row remains approximately constant. On the contrary, the one behind the sixth row increases first steeply, as mentioned, and then slightly up to an asymptotic value (reached at about $Re = 5{,}200$) that is approximately 70% of the one recorded behind the fifth row at the same Re.

In general, at low Re the amplitude of the vortex shedding peaks increases moderately behind all rows examined and differences between rows are relatively small (they are almost negligible between the third and fourth rows). The differences in the amplitude of vortex shedding become significant at higher Reynolds number,

particularly between the first and the last row. Furthermore, at higher Re the amplitude of the peaks behind the fifth and sixth rows reach a constant value whereas amplitudes recorded behind the third and fourth rows, increase continuously in the Reynolds number range investigated.

Figure 3.22 compares the shedding frequency, f_s, obtained in the wake of the third, fourth, fifth and sixth rows (Figures 3.18-3.20) respectively as a function of the normalised gap velocity, $U_g/2b$. For this comparison the data set for the $x/S_L = 5.5$ case was reconstructed by averaging the primary and secondary frequency peaks[7] detected for $U_g/2b = 95.8$ (Re = 4,050) and $U_g/2b = 123.5$ (Re = 5,206) (see Figure 3.20). These frequencies were weight-averaged, the weight being their corresponding amplitude. A linear fit of all data was obtained and the following $f_s - U_g/2b$ relationship was determined:

$$f_s = -0.14 + 0.11\, U_g/2b \qquad (3.1)$$

Note that the slope of this equation is equal to the Strouhal number, that is St = 0.11. It should be noted that although Equation (3.1) does not apply to the first two rows, where prominent peaks could not be observed, it is valid for the rest of the bundle. It is interesting to note that the natural shedding frequencies estimated from Equation (3.1) for Re = 6,760 ($U_g/2b = 160$) and 1,755 ($U_g/2b = 41.5$) are very close to the ones determined experimentally[8]; the spectra showed frequencies of 17.5 Hz and 4.7 Hz respectively whereas Equation (3.1) yields frequencies of 17.4 Hz and 4.4 Hz. The difference between measured and estimated frequencies is slightly higher for the lower Reynolds number, probably due to the lower resolution in the spectra. In Figure 3.22 the shedding frequency for Re = 6,760 and Re = 1,755 is represented by black circles. The linearity of the Equation (3.1) confirms the existence of a constant Strouhal number as evidenced experimentally.

---

[7] The term "secondary frequency peaks" refers to peaks whose amplitude is lower than the dominant one.

[8] Note that the experimental data corresponding to Re = 6,760 ($U_g/2b = 160$) and 1,755 ($U_g/2b = 41.5$) were not used to obtain correlation (3.1).

3.3 Pulsating flow conditions

A sinusoidal pulsation, $U_{puls} = \Delta U \sin 2\pi f_d t$, was superimposed on the flow approaching the tube bundle, as explained in paragraph 2.3.2 in Chapter 2. The frequency, f_d, and the relative amplitude of the pulsation, $A_o = \Delta U/U_\infty$, varied from 7 Hz to 14 Hz and from 0.036 to 0.4 respectively. The Reynolds number was varied from 1,560 to 2,665. Detailed measurements were taken at f_d = 10 Hz, and the corresponding axial mean and r.m.s. velocity distributions are discussed below.

3.3.1 Mean velocity

Figure 3.23 shows a comparison between the axial mean velocity profiles in steady and pulsating flow (f_d = 10 Hz, Re = 1,755). The relative amplitude of the pulsation, A_o, was kept constant at 0.25 (ε[9] = $\Delta U/(2\pi f_d 2b) \approx 0.07$). The integral of the velocity profiles evaluated at each station varies within 1% between steady and pulsating flow. The superimposed pulsations appear to affect the wake of the first cylinder mainly. In the immediate vicinity of the cylinder there is a significant decrease of the mean velocity in pulsating flow, due to more pronounced flow reversal. This velocity deficit is compensated in the shear layer where the velocities for pulsating flow are higher than the ones in steady flow. In the downstream wakes, the velocity profiles are similar for steady and pulsating flow. The velocity deficit in the wake decreases and is smaller than that for steady flow and its compensation occurs at increasing distances from the centreline, but always within the region $-0.5 \leq y/S_T \leq 0.5$.

3.3.2 Turbulence level distributions

A comparison of the axial r.m.s. velocities measured in steady and pulsating flow is given in Figure 3.24. The r.m.s. values are based on the entire signal, and therefore

---

[9] The *reduced amplitude*, ε, for the case of a fixed cylinder in an oscillatory flow, is equivalent to the parameter $\Delta U/d^*$ for forced motion of a cylinder in a steady cross-flow (ΔU is the amplitude of the cylinder oscillations and d^* its characteristic length). ε is commonly employed by investigators of pulsating flows past single cylinders (see Barbi et al, 1986). The boundary zones of lock-on (see paragraph 3.3.3) are related to the reduced amplitude, ε, as reported by Griffin and Ramberg (1976).

include 'a pseudo-turbulence' contribution by the variation of the mean flow due to pulsations. As a result, the r.m.s. values appear to be consistently higher for pulsating flow throughout the flow-field. In order to estimate the actual effect of the pulsation on the turbulence levels, the periodic contribution of the pulsations was removed by filtering the signal. Figure 3.25 shows a typical time trace of the axial mean velocity at $x/S_L = 0.0$ and $y/S_T = 0.17$ for pulsating flow (10 Hz) and Re = 1,755 (blue line). Superimposed onto the time trace (red line) is an ideal sinusoidal waveform with a frequency $f_d = 10$ Hz and amplitude $\Delta U = 0.09$ m/s, corresponding to the frequency and mean amplitude of the pulsations introduced to the flow. This waveform can, therefore, be described by the equation $U_{puls} = 0.09 \sin(2\pi \times 10)$ (m/s)[10] and can be used to approximate the pulsations introduced to the flow by the rotating valve. It is this waveform that was subtracted from the velocity signal to filter out the pseudo-turbulence contribution by the flow pulsation.

It is well known that the r.m.s. of a sinusoidal signal is given by $\Delta U/\sqrt{2}$. In the present investigation this value is equal to 0.06. This value should therefore represent the pseudo-turbulence introduced by the pulsations. The numerical value obtained by adding this contribution to the "real turbulence" measured in steady flow at the same Reynolds number, coincided, within the experimental error, with the r.m.s. velocity of the unfiltered signal in pulsating flow[11] (at $x/S_L = 0.0$ and $y/S_T = 0.166$). Therefore, we can conclude that in the entrance region as well as upstream of the tube bundle there is no significant effect of the pulsations on the turbulence of the flow. The increase in the r.m.s. magnitude of the velocity fluctuations observed when flow pulsations were superimposed can be attributed only to the pseudo turbulence introduced. For example, the turbulence intensity, u'/U, increases by about 75% across the freestream at $x/S_L = 0.5$, but this is due to the variation of the mean velocities caused by the pulsations.

---

[10] Note that the amplitude of the pulsations was determined by the amplitude spectra (not shown for brevity) of the velocity periodic component, obtained by notch-filtering in the frequency domain the instantaneous velocity.

[11] $x/S_L = 0.5$, $y/S_T = 0.5$, Re = 1,755: recorded r.m.s. velocity in steady flow, r.m.s. = 0.04 m/s, calculated pseudo turbulence, r.m.s. = 0.06, recorded r.m.s. velocity in pulsating flow, r.m.s. = 0.07, therefore the r.m.s. unfilterd signal in pulsating flow = $\sqrt{0.04^2 + 0.06^2} \cong 0.07$.

The most significant effect of the pulsations on the turbulence of the flow can be observed in the wake of the first cylinder. Figure 3.26 shows a comparison between the r.m.s. of the unfiltered signal (1) in pulsating flow and the steady one (2) in the wake of the first cylinder. The filtered signal (3) is also shown in Figure 3.26. It can be seen clearly that even when the contribution of the pulsations to the velocity signal is removed by filtering, the r.m.s. velocities (3) are still higher than those in steady flow (2). The r.m.s. amplitude of the velocity fluctuations rises by about 170% when the flow is pulsed, but only 75% of this increase can be attributed to changes in the structure of the wake caused by the pulsations as will be discussed later in this chapter. The effect of pulsation seems to be negligible downstream in the tube bundle. Figure 3.26 also shows that at the station investigated the lateral spacing between vortices (wake width), W, has decreased from $W/S_T = 0.27$ ($W/2b = 1.5$) to $W/S_T = 0.11$ ($W/2b = 0.6$) in pulsating flow, as indicated by the peak r.m.s. velocity moving closer to the centreline. A similar decrease was already observed in steady flow and high Reynolds number between the first and last row of the bundle and the effect was related to the increased turbulence levels.

3.3.3 Vortex shedding characteristics

Velocity spectra were estimated in pulsating flow at the same locations as in steady flow. The spectra are shown in Figure 3.27. The frequency and amplitude of the pulsation were $f_d = 10$ Hz and $A_o \cong 0.25$ respectively. It can be seen that while the spectra obtained in the first three rows in steady flow were characterised by the absence of a vortex shedding frequency, in pulsating flow they contain two dominant peaks, one at the frequency of pulsation, 10 Hz, and the second at 5 Hz. It seems that the superimposed pulsations incite vortex shedding from the first three cylinders, which was suppressed in steady flow. The position of the vortex shedding peak is centred at half the frequency of pulsation indicating vortex shedding lock-on. A comparison of the amplitude of the peaks in pulsating flow with the ones obtained in steady flow at the same Reynolds number shows clearly an increase in the peak strength particularly in the first four cylinders (note that the scale in the graphs has been changed in relation to those in steady flow due to the higher amplitude of the peaks). In addition, it can be observed that the amplitude of the 5 Hz peak decreases

in the downstream direction while that of the peak at 10 Hz increases. This observation suggests that the vortex lock-on phenomenon in cylinder arrays is pronounced in the first row but diminishes with row depth. Velocity spectra were also estimated at pulsation frequencies varying from 7 Hz to 13.9 Hz behind the last row at Re = 1,560 (Figure 3.28), which shows amplitude velocity spectra). It can be seen that for pulsating frequencies from 11.8 to 13.9 Hz two peaks are detectable, one corresponding to the natural vortex shedding frequency (around 4 Hz) and the other to the pulsation frequency. For pulsating frequencies 7-10 Hz there is a coupling between the pulsation and the vortex shedding frequencies, and in particular the vortex shedding frequency seems to lock-on at half the pulsation frequency.

This suggests a competition between vortex shedding modes (natural shedding of vortices and lock-on). The transition between the two modes occurs in the frequency range 10 Hz < f_d < 11.8 Hz.

Figure 3.29 shows the variation of f_s/f_{so} with f_d/f_{so} at Re = 1,560. f_s is the vortex shedding frequency in pulsating flow and f_{so} the natural vortex shedding frequency (under steady flow conditions). The frequency of shedding is locked on the subharmonic of the driving frequency as indicated by the linear dependence of f_s/f_{so} on the ratio f_d/f_{so} for f_d ranging from 7 to 10 . The lock on region ends with a smooth transition before the vortices are shed again at the natural Strouhal frequency, f_{so} = 4.2 Hz (for f_d ranging from 11.8 Hz to 13.1 Hz). These findings are in agreement with Barbi et al (1986) who studied the lock-on phenomenon on a single cylinder. It should be mentioned that the relative amplitude of the pulsations upstream of the tube bundle was not kept constant, but varied between 0.4 at 7 Hz (2ε = 0.56) and 0.036 at 14Hz (2ε = 0.025). Figure 3.30 shows the variation of 2ε with f_d/f_{so} and the lock-on limits[12] under pulsating flow conditions. The lock-on region is the one within the curve (black line). It depends strongly on both ε and the ratio between the driving and the natural shedding frequencies. The red circles represent the same data as in Figure 3.28 and confirm the occurrence of lock-on for f_d

[12] The lock-on limits were obtained by interpolating the data recorded by Barbi et al (1986) and Griffin and Ramberg (1976) for a single circular cylinder. It is here assumed that the same curve applies to the sixth elliptic cylinder of the present array, which, due to the fact that it is not obstructed by cylinders downstream, shows similar features to those of a single elliptic cylinder.

ranging from 7 Hz to 10 Hz (Re = 1,650, f_{so} = 4.2). Note that if the relative amplitude of pulsation, ΔU (which is proportional to the reduced amplitude, ε, that is, $\Delta U \propto 2\varepsilon$), and the Reynolds number ($\propto f_{so}$) are increased, the lock-on region will occur for higher values of f_d (see dotted line in Figure 3.30, obtained for Re = 1,950 and pulsation amplitudes varying linearly with the driving frequency, f_d, $\Delta(\Delta U) \cong 0.09 f_d$, with respect to the cases represented by the red circles). The occurrence of lock-on for a driving frequency of 14 Hz and 2ε = 0.56 (ΔU = 0.08) was confirmed by the visualisation study.

The vortex shedding lock-on is also illustrated in Figure 3.31, which shows the spectra and the velocity traces obtained at the inlet of the tube bundle at two different transverse locations. The frequency of the pulsations was 10 Hz and the Reynolds number Re = 1,755. Two peaks at 10 Hz and 5 Hz respectively can be observed. The amplitude of the 5 Hz peak increases closer to the cylinder. The 5 Hz peak cannot be considered as a sub-harmonic of the pulsation frequency introduced by the spectra analysis since the time trace at y/d_e = 0.4 shows clearly both the 10 Hz and 5 Hz harmonics.

Finally, two power spectra (not shown for brevity) obtained at x/S_L = 3.5 and y/S_T = 0.278 (Re = 1,755) in steady and pulsating flow (10 Hz) respectively were compared. Both showed, at higher frequencies, the characteristic –5/3 slop typical of the inertia subrange region. As already stated, the turbulence in steady flow is nearly isotropic and it seemed not to be significantly affected by the pulsations.

3.4 Skewness and kurtosis in steady and pulsating flow

The skewness and the kurtosis[13] of the velocity probability function were also determined in both pulsating and steady flow at one station behind each row (x_c/S_L = 0.5) at Re = 2665. Selected results are shown in Figures 3.32 and 3.33.

[13] Skewness and kurtosis were defined in Chapter 2 as the third central moment divided by the standard deviation cubed and the fourth central moment divided by the standard deviation to the power of four respectively. They are, therefore, non-dimensional parameters.

Figure 3.32 shows the kurtosis distribution behind the first, second, and fourth rows in steady flow (Re = 2665). The kurtosis profile behind the first cylinder has a maximum (and this maximum is higher than 3, the value for a normal distribution) at about $y/S_T = 0.195$. The corresponding velocity distribution is, consequently, highly peaked around the mean local velocity. The profiles at $x/S_L = 1.5$ and $x/S_L = 3.5$, i.e. behind the second and fourth rows respectively, indicate that the peak moves away from the centreline (although this shift is not significant behind the second row) in agreement with the outward shifting of the shear layer position in downstream rows. In the wake of the cylinders the kurtosis values are much lower than in the shear layer meaning that very dissimilar velocity scales are locally recorded. Figure 3.33 shows a comparison between the skewness and kurtosis profiles behind the first row for steady and pulsating flow. A maximum negative is observed in the skewness profile in steady flow at $y/S_T = 0.195$, corresponding to the location of the maximum kurtosis. This implies that a low velocity region moves intermittently into a measuring location where high velocities are mostly present, i.e. on average the flow has large fluctuations below the mean more often than above it. The low velocity region, aforementioned, can be identified with low velocities intermittently recorded from the vortices shed from the first cylinder. It should be mentioned that flow visualisation showed that, although a corresponding well-defined shedding periodicity could not be observed, vortices are formed behind the first cylinder. Furthermore, Figure 3.33 shows that the kurtosis and skewness profiles in pulsating flow appear to be more uniform and they do not deviate significantly from a normal distribution, although relative peaks in the kurtosis profiles are observed in the same locations as in the steady flow case. In downstream rows the differences in the skewness and kurtosis profiles between steady and pulsating flow were less significant since the effect of pulsations was less pronounced than in the first row.

3.5 Flow visualisation

The objective of the visualisation study was to examine the flow field in the wake of the tubes and in the near region around the separation point and complement the LDA measurements.

Selected visualisation pictures obtained behind the first, fourth and sixth cylinders in steady flow are shown in Figures 3.34 to 3.37. Selected frames for pulsating flow behind the first cylinder are also shown in Figures 3.38 and 3.39 for driving frequencies of 10 and 14 Hz respectively. The time interval between frames, ΔT_F, was determined by the shutter frequency of the video camera and it was equal to 1/50 frames per second, that is 20 ms. Consequently, only flow periodicities whose frequency range varies from a minimum frequency, f_{smin}, equal to $1/(N_F \times \Delta T_F)$ Hz, with N_F being the number of frames, to a maximum theoretical frequency, f_{smax}, of $1/(2 \times \Delta T_F) = 25$ Hz (two is the minimum number of frames required to complete a cycle), could be detected. The first frame of each sequence of images was arbitrarily chosen to correspond to the observation time t = 0 ms. In the sequence of frames, time increases from left to right and from top to bottom.

Anticlockwise vortices shed on the left hand side of the cylinders, i.e. on the left hand side of the frames, will be called "negative vortices" and indicated with the suffix N_n, with n being an integer number indicating the order of succession of vortices; conversely, the vortices shed on the opposite side will be called "positive vortices" (clockwise) and indicated with the suffix P_n.

Figure 3.34 shows selected flow visualisation pictures obtained behind the first row at Re = 638. No clear vortex shedding activity can be observed. (No periodical vortex shedding could be observed also at higher Reynolds numbers). The wake regions seem stagnant. Despite of the low Reynolds numbers, the flow visualisation behind the fourth and sixth rows shows clearly shedding of vortices. The Reynolds number and the natural vortex shedding were equal to 638 and 1.7 Hz respectively. Figures 3.35 (a)-(f) and 3.37 (a)-(c) show two complete cycles of vortex shedding behind these rows.

A grid was superimposed to the first frame in Figure 3.35 (a), t = 0 ms, in order to provide spatial information. The distance between the lower edge of the upper cylinder (row 4) and the upper edge of the second one (row 5) is equal to 8 mm. Therefore, the vertical and horizontal dimensions of the grid cells are approximately equal to 0.73 mm. The first frame (t = 0 ms) of Figure 3.35 shows two vortices, P_1

(clockwise, termed "positive") and N_1 (anticlockwise, termed "negative"), shed by the fourth cylinder and convected downstream. The phase difference[14] between the two vortices, evaluated by visual inspection, is approximately equal to 5.11 mm. From t = 0 ms to t = 100 ms the positive vortex, P_1, grows slightly in size and moves downstream towards the centreline, although the distance travelled is negligible. That means that in this time interval P_1 can be considered "standing" (virtually stationary) in the wake with an approximate diameter (we refer to "vortex" as the largest close fluid loop) ranging from 2.73 mm (t = 0 ms) to 4 mm (t = 100 ms), that is about 0.21 and 0.31 times the major axis of the elliptic cylinder respectively. The "positive" shear layer, that is the one adjacent to P_1, is violently drawn into the wake. It partly rolls up into the interior of the formation region, partly entrained by P_1, partly by N_1 bearing vorticity of opposite sign, and also by the "negative" (that is, separating from the left hand side of the cylinder) irrotational shear layer upstream of N_1. At $t \cong 40$ ms N_1 impacts against the downstream cylinder and dissipates. A similar description of the mechanics of the formation region was given by Gerrard (1966) for a single bluff body. In the present case, however, differences arise due to the presence of the downstream cylinder. The latter has the double effect of deflecting the entrained shear layer and blocking the downstream convection of vortices without preventing their formation. From t = 0 ms to t = 100 ms, P_1 is, therefore, "constricted" by the accelerated shear layer drawn into the wake and deflected by the downstream cylinder. With the disappearance of N_1 ($t \geq 100$ ms) the positive shear layer, after crossing the wake axis, rolls downward along the shoulder of the downstream cylinder. As a consequence, P_1 (Figure 3.35 (b)) initially grows in size and move towards the centreline ($120 < t\ (ms) < 140$). At t = 120 ms a second negative vortex is forming (it is not clearly shown in the picture, as in the video recording, but its formation can be inferred by the successive ones), N_2, bearing vorticity of the same sign as that of N_1. The irrotational negative shear layer is drawn into the wake by the action of both vortices. It may be assumed that the time frame, t = 280 ms, is the one at which the flow, drawn by N_2, begins to cross the wake axis. The crossing point is defined (Gerrard, 1966) as the end of the formation region. The vortex formation length can be therefore graphically estimated; an approximate evaluation gives $L_F/2a$

[14] The phase difference is here defined as the difference, expressed in mm, between the x-co-ordinates of the centres of the vortices.

≅ 1.00. This value is in agreement with the LDA findings for the sixth row of the present in-line array, which gave values of $L_r/2a = 1.035$ and $L_r/2a = 1.04$ for Re = 6,760 and 1,780 respectively.

At t = 300 ms (Figure 3.35 (c)) finally the first half-cycle ends; N_2 has grown in size entraining fluid from the irrotational negative shear layer and from P_1, which has meanwhile dissipated. It can be seen from the subsequent frames (300 < t (ms) < 600) that although the anticlockwise vortex, N_2, is formed and shed by the upstream cylinder the overall wake characteristics are not exactly the same as for the first half-cycle. The main difference is in that the negative shear layer drawn by N_2 is obstructed by P_1 and only a thin layer (for instance, see t = 320 ms) is drawn into the wake and deflected over the shoulder of the downstream cylinder. Once P_1 is dissipated, N_2 can grow in size and at t = 380 ms it almost occupies the entire wake region, slightly off-centre towards the positive side of the wake. The vortex axis is also slightly inclined with respect to the centreline in contrast to P_1 whose axis was vertical and, therefore, parallel to the centreline. At t = 600 ms the cycle is completed with a new clockwise vortex shed from the upstream cylinder while N_2 is convected downstream and impacts against the downstream cylinder. Although the initial conditions are restored at the end of the cycle and repeat over the next cycles, i.e., the flow in the wake is periodic, the two half cycles are not entirely symmetrical over one period. However, symmetry between the two half-cycles is achieved over a larger number of periods. These half-to-half cycle variations are probably due to both the turbulence of the flow and minor non-uniformities (the upstream mean velocity profile is uniform within 1%) in the mean flow. A major difference between the present configuration and closely packed in-line arrays is that vortex shedding occurs in an anti-symmetric mode. The present visualisation study shows that the shed vortices occupy a large portion of the wake region, which together with the substantial mass transfer across the wake necessitates anti-symmetrical vortex shedding in the wake (see also Ziada and Oengören, 1991).

Figure 3.36 shows two zoomed images of the flow past the sixth cylinder. The separation point can be located by direct observation at approximately 90 degrees from the front stagnation point.

Figures 3.37 (a)-(c) show selected flow visualisation pictures obtained behind the sixth row at Re = 638 so that a comparison between the near wake fluid dynamics, flow periodicities and wake characteristics of the fourth and sixth rows can be made. It was also important to confirm the LDA finding that the natural shedding frequency, f_{so}, is the same for all the rows of the tube bundle and, in particular, that the vortex shedding was periodical with the same period for the fourth and sixth rows. A similar investigation was carried out for the third and fifth rows (the corresponding visualisation pictures are not shown for brevity) showing that the conclusion drawn for the fourth cylinder can be extended to the third and fifth. It should be noted that some unique features may be attributed to the flow field past the sixth row due to the fact that there are no rows downstream of it that obstruct the flow.

The first frame (t = 0 ms) of Figure 3.37 (a) shows three vortices, P_1 and P_2 (that is forming - although not clear from the picture), clockwise, and N_1, anticlockwise, shed by the sixth cylinder and convected downstream. As with the fourth row the wake of the sixth row shows an anti-symmetric vortex pattern. The main differences between the two arise from the fact that there is not a downstream cylinder to obstruct the flow as already mentioned earlier. The vortex patterns therefore resemble more closely those for single cylinders. Moreover the accelerated and deflected shear layer does not impinge on downstream cylinders. It is therefore free to flap across the wake and its oscillations are characterised by a large amplitude. This can be seen when the second frame of the sequence, t = 20 ms, is compared with the tenth one, t = 320 ms ($t \equiv T/2$) (Figure 3.37 (b)). The latter shows also the direction of the negative and positive shear layers near the cylinder wall at t = 20 ms (dotted line) for comparison. The angle between the two directions is approximately equal to 50 degrees. The same large amplitude oscillations could not be observed behind the fourth row where the shear layer separating from the upstream row was partially deflected towards the inner wake by the downstream row and partly impacted on it. It should be noted that since the flapping is related to the formation and convection/diffusion of the vortices, it occurs at approximately the same frequency as the natural vortex shedding one (compare the first frame of Figure 3.37, t = 0 ms, with the one at t = 560 ms). The cycle is complete after about 600 ms corresponding to a frequency of $f_{so} \cong 1/600$ ms $\cong$ 1.7 Hz as for the fourth row.

Figure 3.38 shows a complete cycle of vortex shedding behind the first cylinder under pulsating flow conditions (f_d = 10 Hz, 2ε = 0.25, Re = 1,560). The corresponding natural vortex shedding frequency observed in steady flow in downstream rows was equal to 4.2 Hz. However, as already stated, no vortex shedding was observed or detected behind the first row. The sequence of pictures shows clearly that the superimposed pulsations have triggered the shedding of vortices. The sequence of frames shows that the flow pattern at t = 0 repeats after 200 ms. This corresponds to a flow periodicity (vortex shedding) with a frequency, f_s, of 1/200 ms = 5 Hz; the pulsations have therefore triggered vortex shedding at half the driving frequency in agreement with the LDA findings. The first frame (t = 0 ms) shows two vortices, P_2 and N_2 shed by the upstream cylinder and two others, P_1 and N_1, convected downstream and impacting against the downstream one. It can be noticed that the anti-symmetrical vortex pattern observed in steady flow is suppressed and symmetrical vortex shedding is promoted. P_2 and N_2, in fact, are shed alternatively, but the phase difference is now negligible. It is also evident that the pulsations strongly modify the quasi-stagnant "steady" wake, increase the turbulence of the flow and decrease the formation length to the proximity of the rear stagnation point of the upstream cylinder (see frame at t = 80 ms and also refer to the description of Figure 3.35). It is interesting to note that the width of the wake is larger in pulsating flow than in steady flow during the shedding phase (see t = 80-100 ms) and slightly smaller after the vortices dissipate (see t = 140+160). In addition the increased vortex activity in pulsating flow is not limited to the proximity of the upstream cylinder, but extends to the downstream one and generally to the neighbourhood of the cylinders' wall from the front to the rear stagnation point. This may suggest that flow pulsations can lead to a substantial increase in the heat transfer rate in tube bundles not only because the turbulence levels eventually increase (we refer to the "real" turbulence and not to the pseudo one introduced by the pulsations), but also, and probably most importantly, because of the substantial change in the mean flow; the cylinder walls in pulsating flow are swept by the fluid in the region which was stagnant in steady flow. This assumption was confirmed by the heat transfer findings described in Chapter 6.

Figure 3.39 shows a complete cycle of vortex shedding behind the first cylinder for different pulsating conditions (at f_d = 14 Hz, 2ε = 0.56 and Re = 1,950). The sequence shows that the flow pattern at t = 0 ms repeats after 140 ms. This corresponds to a flow periodicity whit a frequency, f_s, equal to 1/140 ms = 7 Hz, that is half the pulsation frequency. It should be noted that the LDA results did not show lock-on for f_d =14 Hz. However, both the reduced amplitude and the Reynolds number were lower (2ε = 0.025 and Re = 1,560) than in the present case (2ε = 0.56 and Re = 1,950). As stated in paragraph 3.3.3, the lock-on region will occur for higher values of f_d if the amplitude of pulsation, ΔU ($\propto 2\varepsilon$), and the Reynolds number are increased (see Figure 3.30). The first frame of Figure 3.39 shows two vortices, P_1 and N_1, which have grown in size considerably and are convected downstream. The vortices are nearly identical in size and orientation and symmetrical with respect to the centreline and occupy a significant portion of the wake region. Their diameter is approximately equal to 5.5 mm, that is about 84% (42%) of the minor (major) axis of the elliptic cylinders. Because of the higher shedding frequency compared to the case described above and therefore the smaller time scales involved, the wake width does not exhibit the same large variations. A comparison between the first frames in Figures 3.38 and 3.39 shows the effect of the relative amplitude and the frequency of the pulsations on the vortex shedding. The symmetry of the vortex pattern increases and so the size and the convection velocity of the shed vortices. The degree of symmetry as well as the size of the vortices, however, do not increase proportionally to the relative amplitude of pulsations, due mainly to the presence of the downstream cylinder which contributes to increased symmetry in the wake flow (as it acts as a barrier to the mass transfer across the wake) and limits the growth of the vortices.

3.6 Conclusions

An experimental investigation was carried out on the flow around an in-line array with elliptic cylinders of axis ratio 1:2. LDA and flow visualisation were used to study the velocity and vortex shedding characteristics in both steady and pulsating flow. The results showed that the tube bundle configuration investigated generates less turbulence than an equivalent (with the same longitudinal and transverse spacing) in-line array with circular tubes. The turbulence levels remain nearly constant along the flow passages indicating negligible interference between adjacent columns. The difference of the two r.m.s. components, u'/U_∞ and v'/U_∞, is near zero over the whole flow domain indicating that the turbulence might be assumed to be highly isotropic. On the contrary, the turbulence in the wake regions of the in-line arrangement with circular tubes was found to be highly anisotropic, especially downstream of the third and fourth rows (Balabani, 1996). A weak vortex shedding activity was detected. The correspondent Strouhal number, defined by the gap velocity and the minor axis of the elliptic cylinders, 2b, was found to be equal to 0.11. The only significant effect of the pulsations on the turbulence of the flow was observed in the wake of the first cylinder. The occurrence of lock-on of the natural vortex shedding at half of the superimposed pulsation frequency was observed in all rows. Behind the first row, where no vortex shedding activity was observed in steady flow, the superimposed pulsations triggered the shedding of vortices and its frequency locked at half of the driving frequency.

The flow visualisation study confirmed the findings of the LDA measurements. In particular, it showed the lack of any significant vortex activity behind the first row, and confirmed the occurrence of lock-on of the natural vortex shedding at half of the superimposed pulsation frequency.

The chapter that follows examines the flow and vortex shedding characteristics of an asymmetric tube array with circular cylinders.

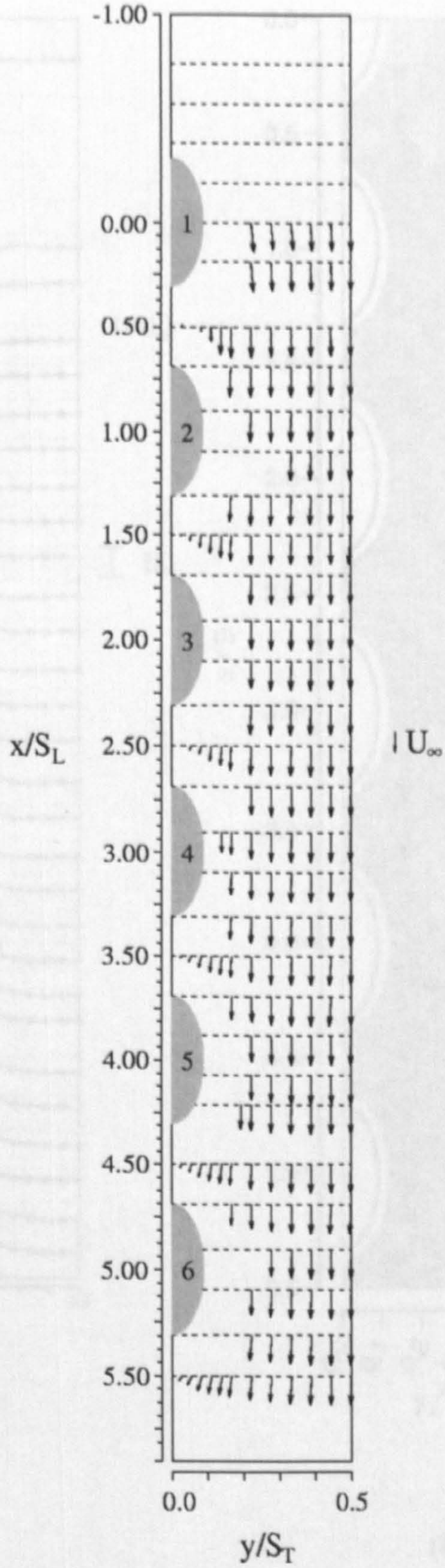

Figure 3.1. Velocity vectors in the in-line bundle with elliptic cylinders (steady flow, Re = 6,760).

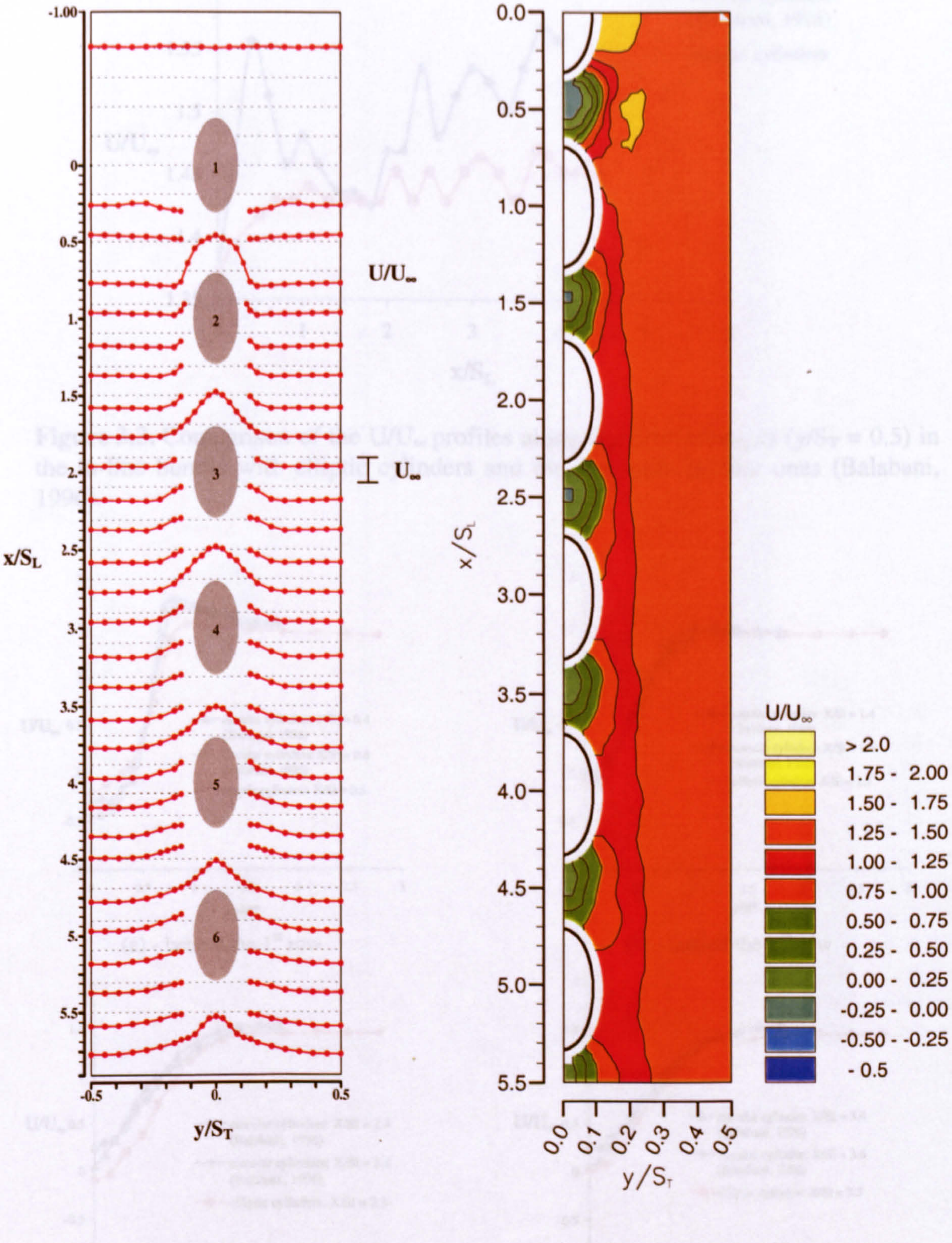

(a) (b)

Figure 3.2. Distribution of U/U_∞ as profiles (a) and contours (b), in the in-line bundle with elliptic cylinders (steady flow, Re = 6,760).

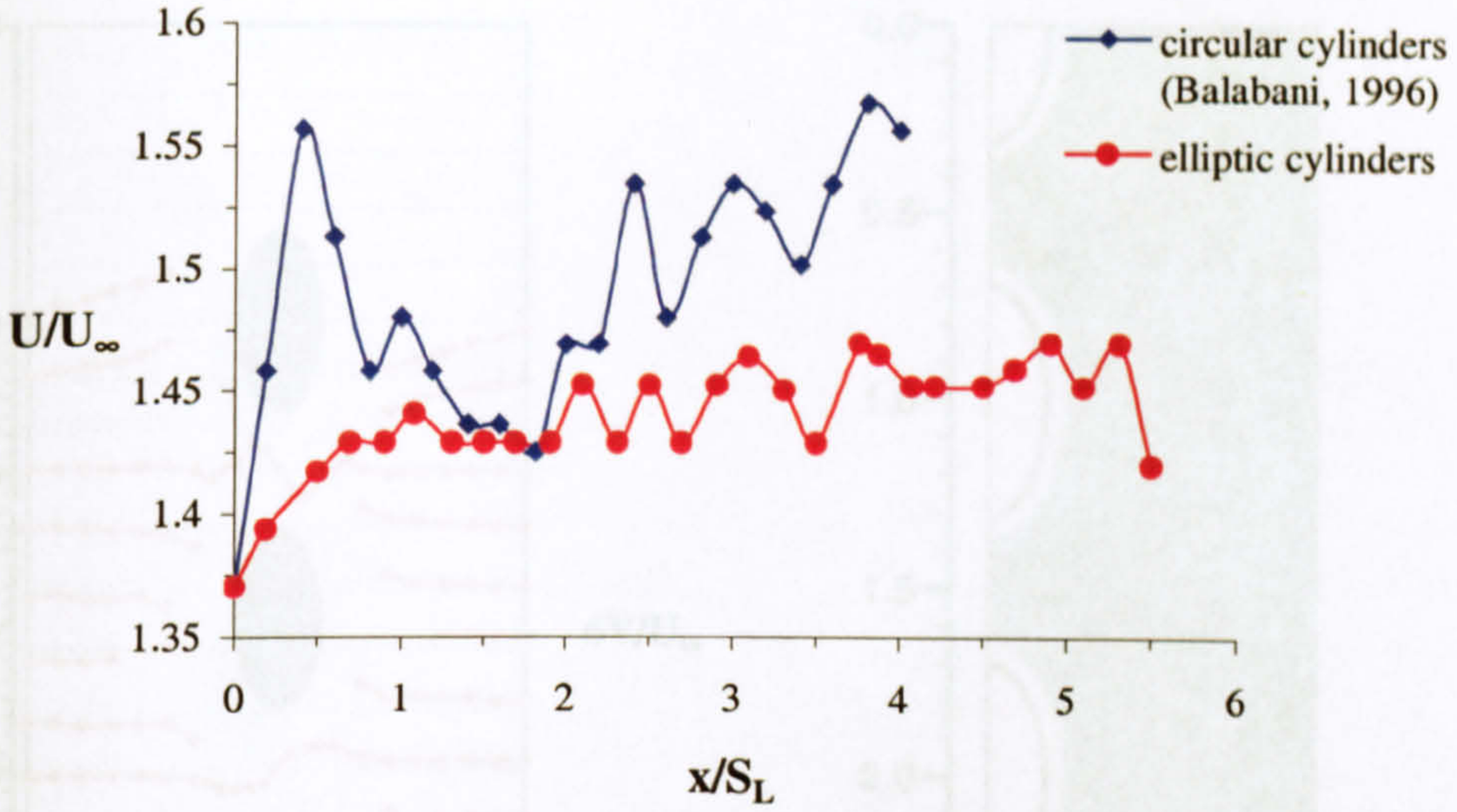

Figure 3.3. Comparison of the U/U_∞ profiles along the flow passages ($y/S_T = 0.5$) in the in-line bundle with elliptic cylinders and the one with circular ones (Balabani, 1996).

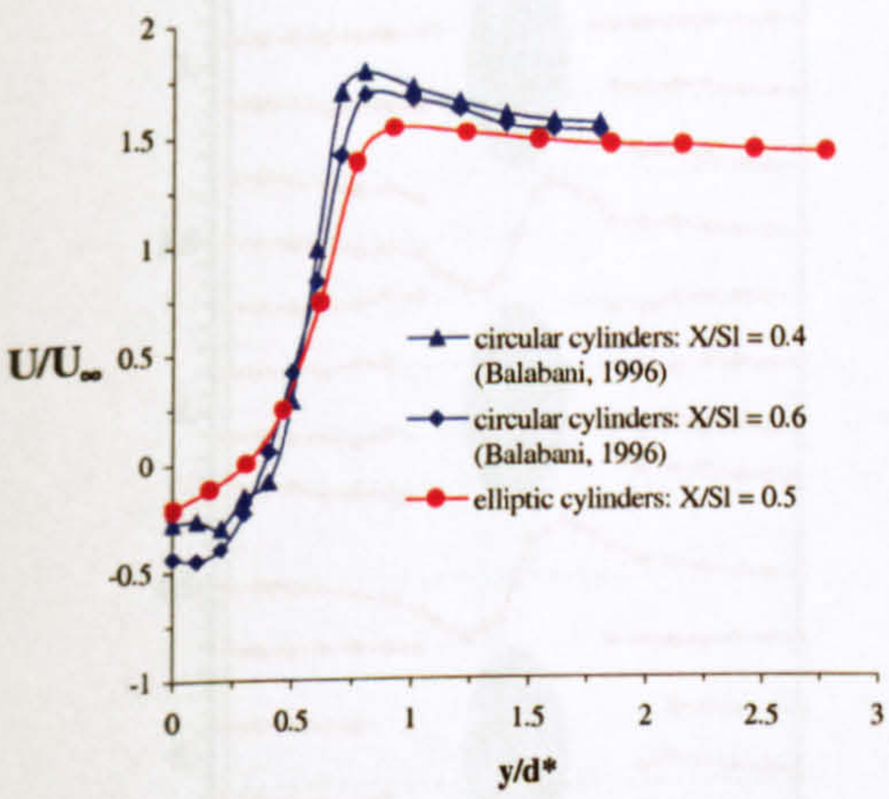

(a) - behind the 1st row

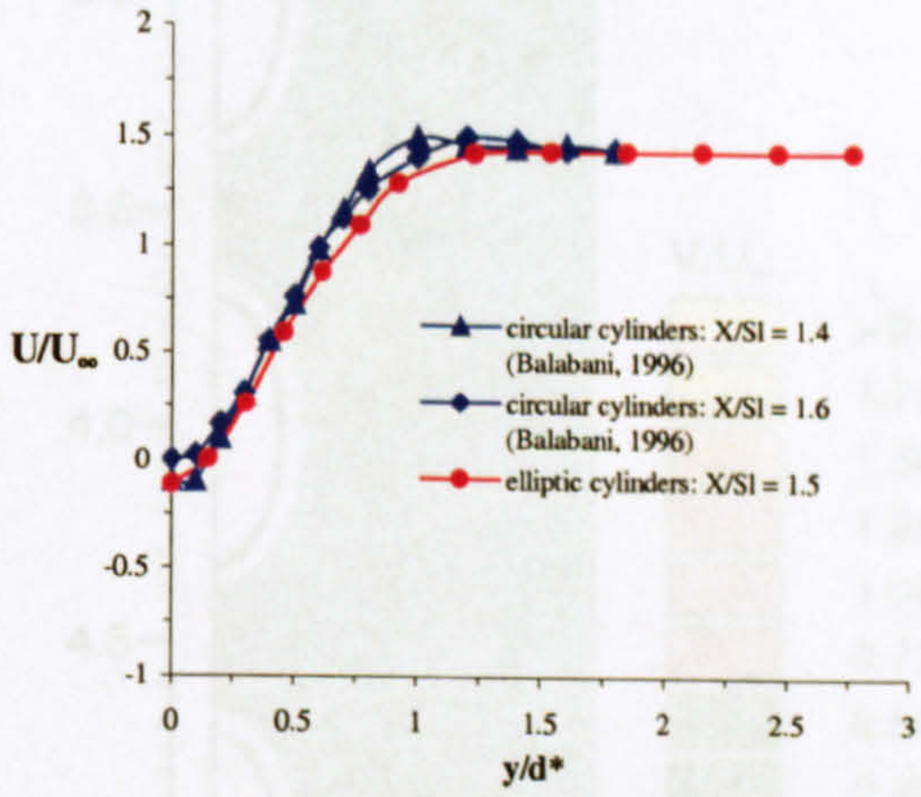

(b) - behind the 2nd row

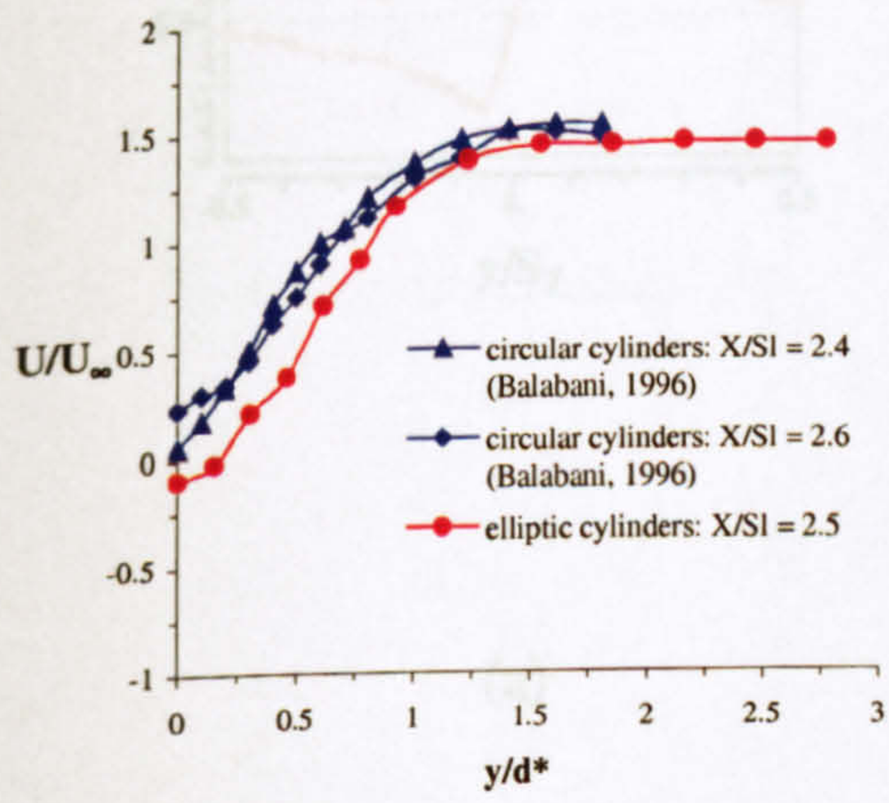

(c) - behind the 3rd row

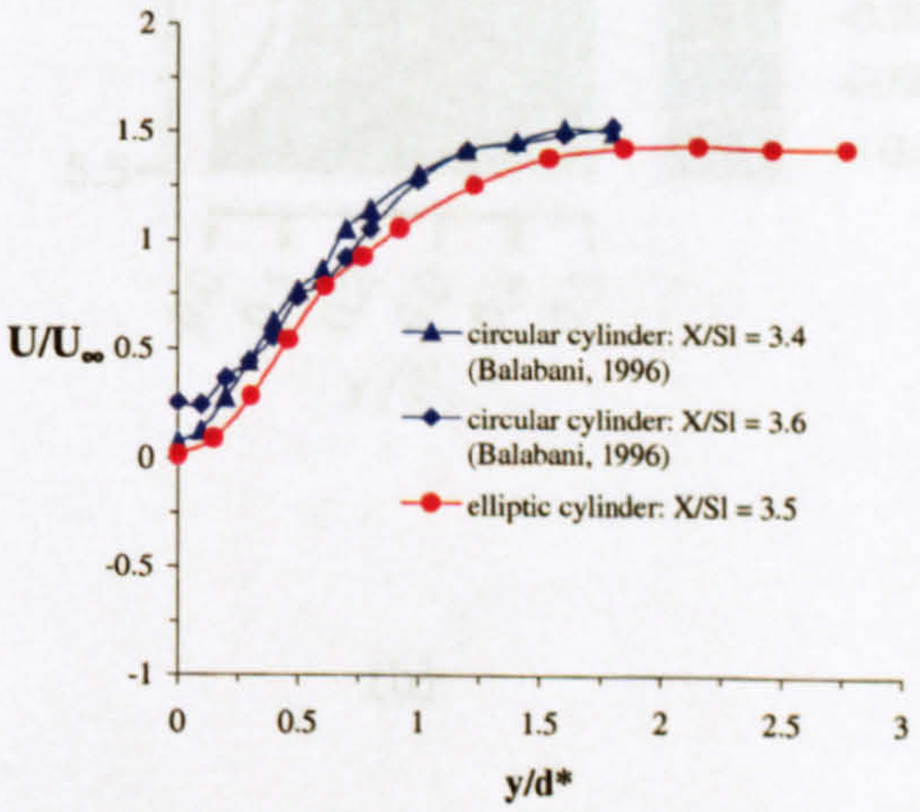

(d) - behind the 4th row

Figure 3.4. Comparison of the U/U_∞ profiles along wake centrelines in the in-line bundle with elliptic cylinders and the one with circular cylinders (Balabani, 1996).

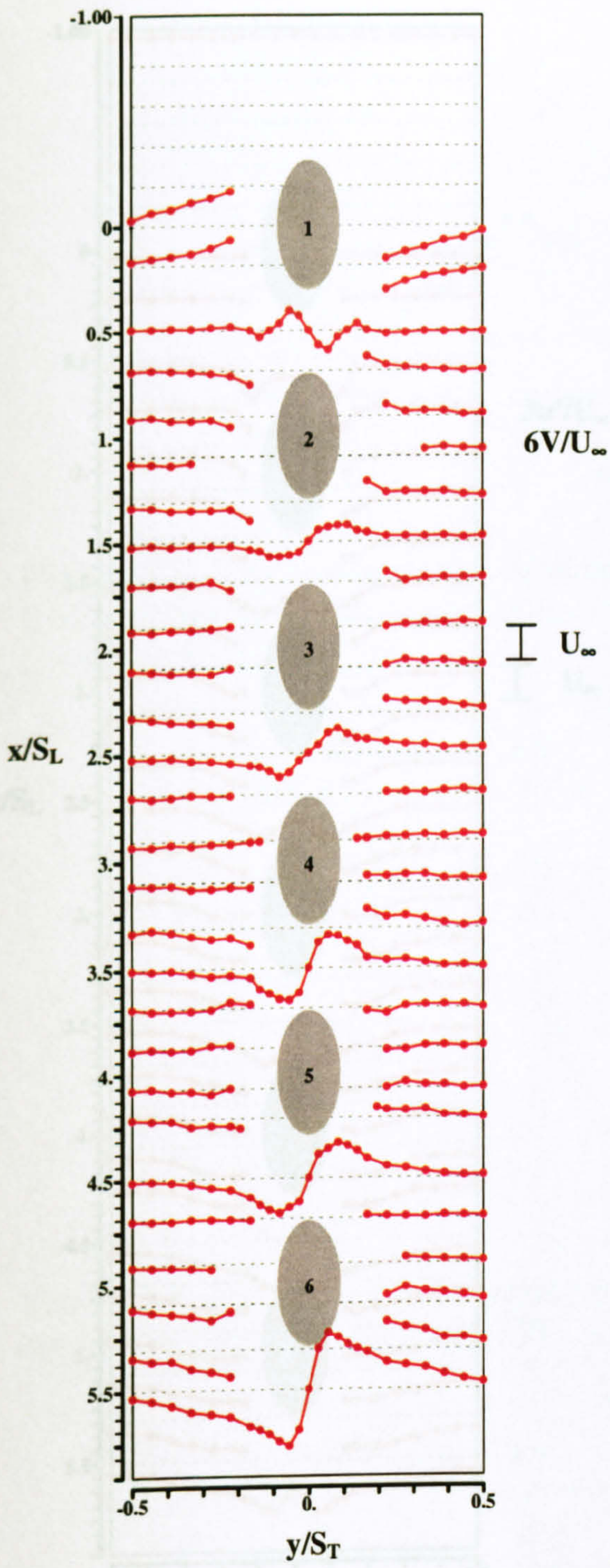

(a)

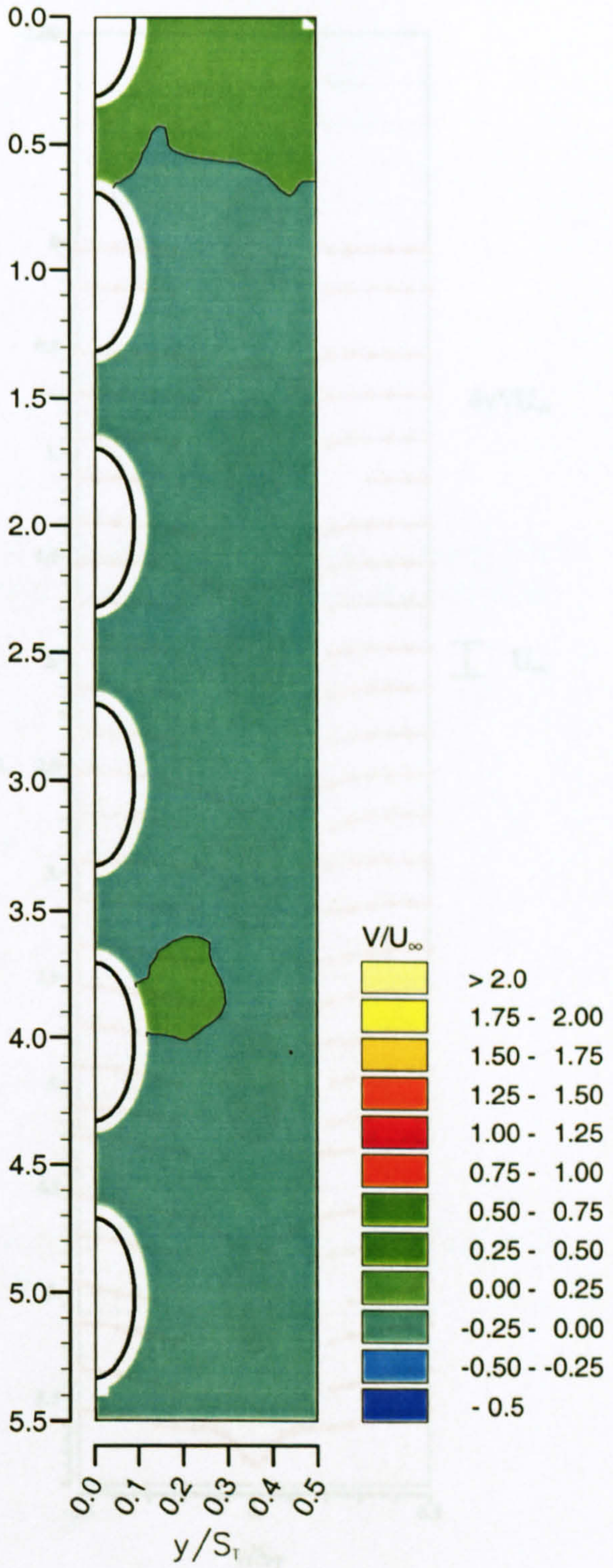

(b)

Figure 3.5. Distribution of V/U_∞ as profiles (a) and contours (b), in the in-line bundle with elliptic cylinders (steady flow, Re = 6,760).

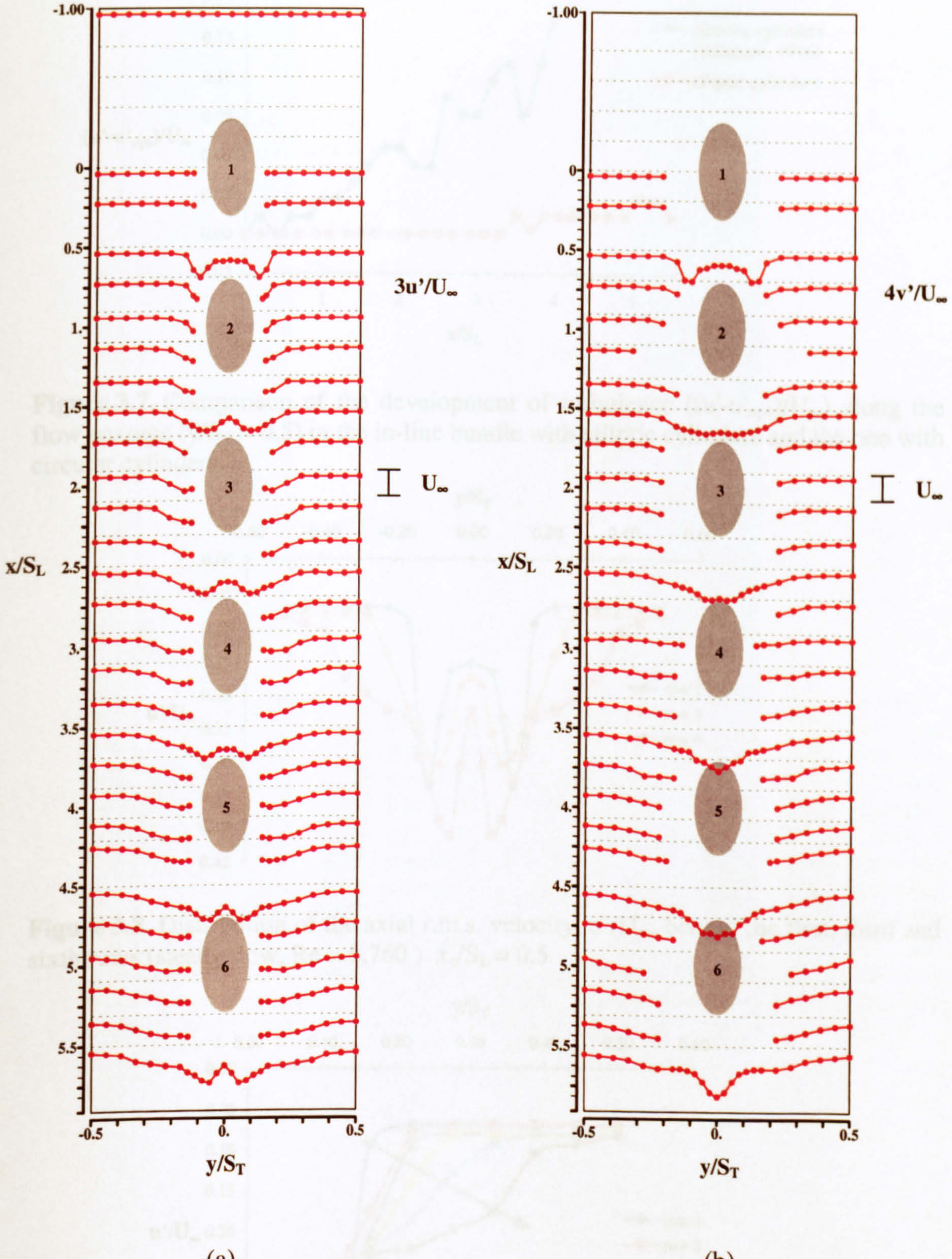

(a) (b)

Figure 3.6. Distribution of u'/U_∞, (a), and v'/U_∞, (b), in the in-line bundle with elliptic cylinders (steady flow, Re = 6,760).

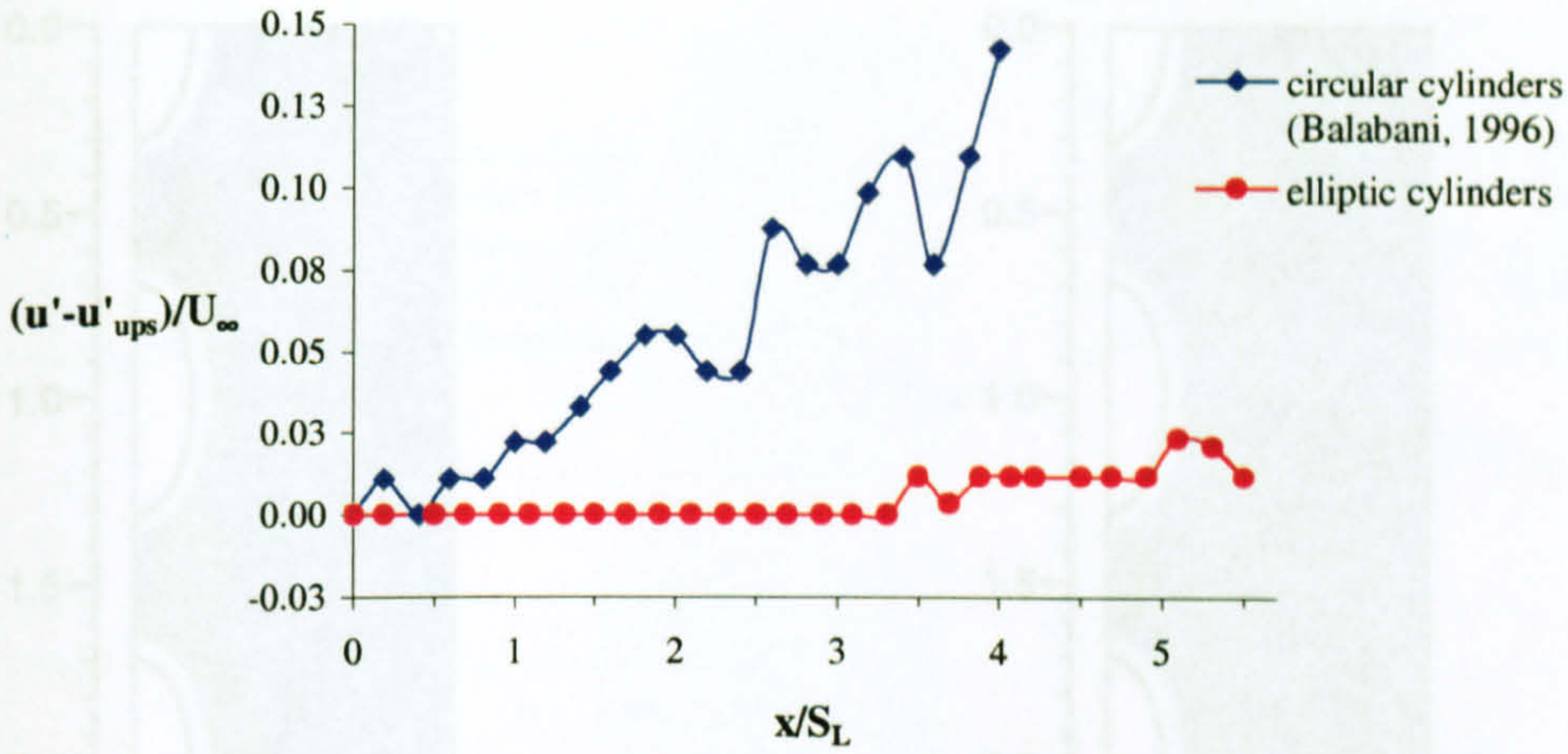

Figure 3.7. Comparison of the development of turbulence ($(u'-u'_{ups})/U_\infty$) along the flow passage ($y/S_T = 0.5$) in the in-line bundle with elliptic cylinders and the one with circular cylinders.

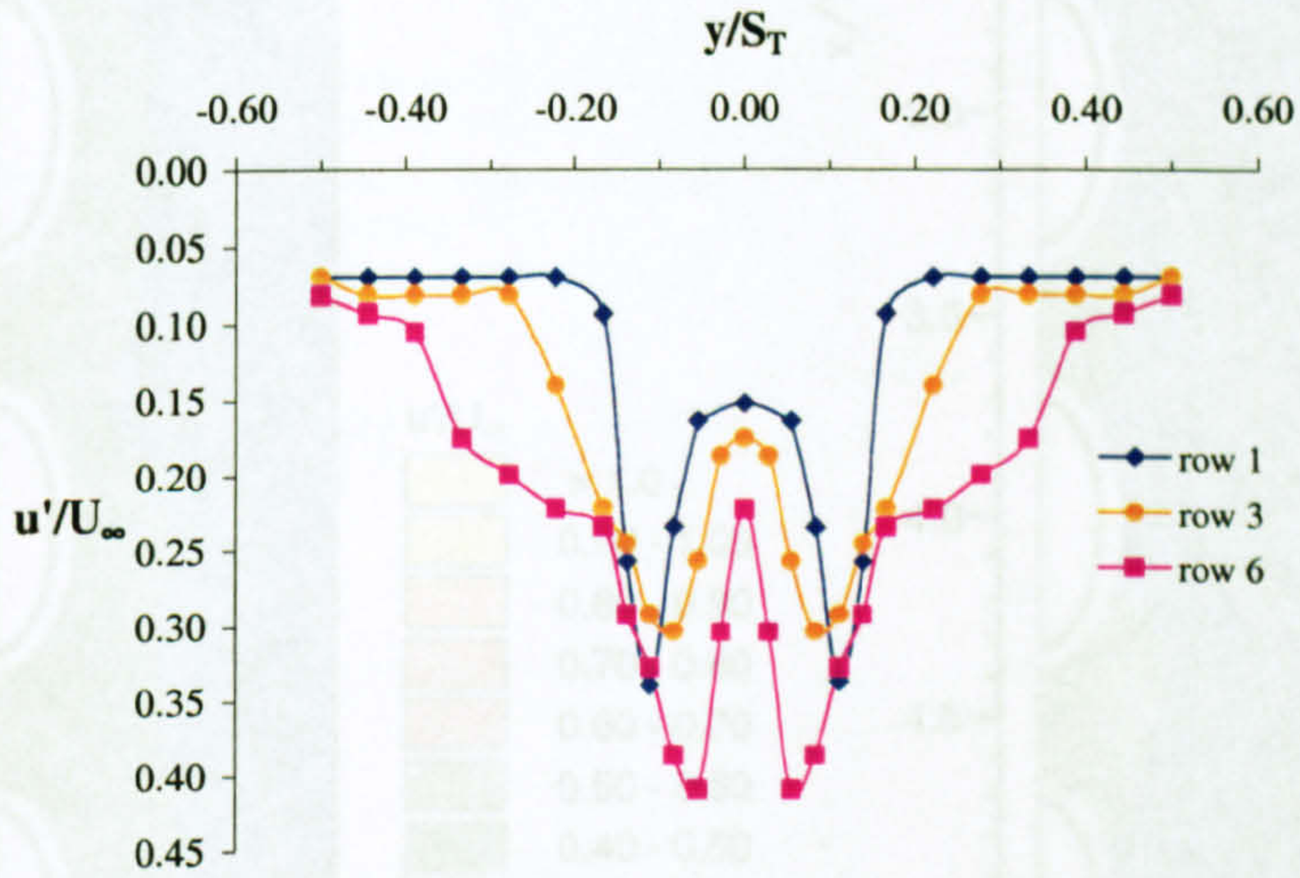

Figure 3.8. Distribution of the axial r.m.s. velocity, u'/U_∞, behind the first, third and sixth rows (steady flow, Re = 6,760). $x_c/S_L = 0.5$.

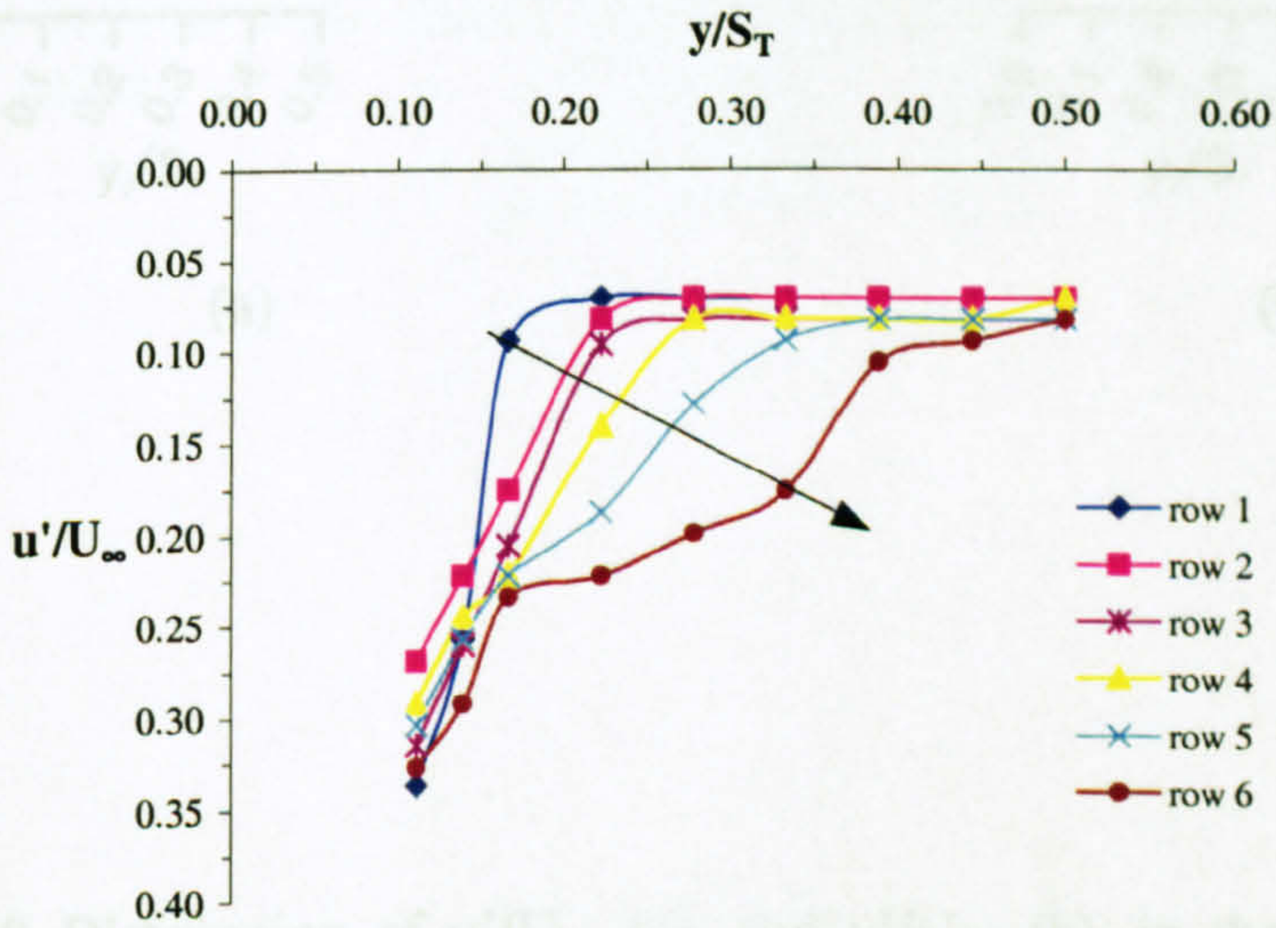

Figure 3.9. Distribution of the axial r.m.s. velocity, u'/U_∞, behind each row (steady flow, Re = 6,760) for $y/S_T > 0.11$ and $x_c/S_L = 0.5$.

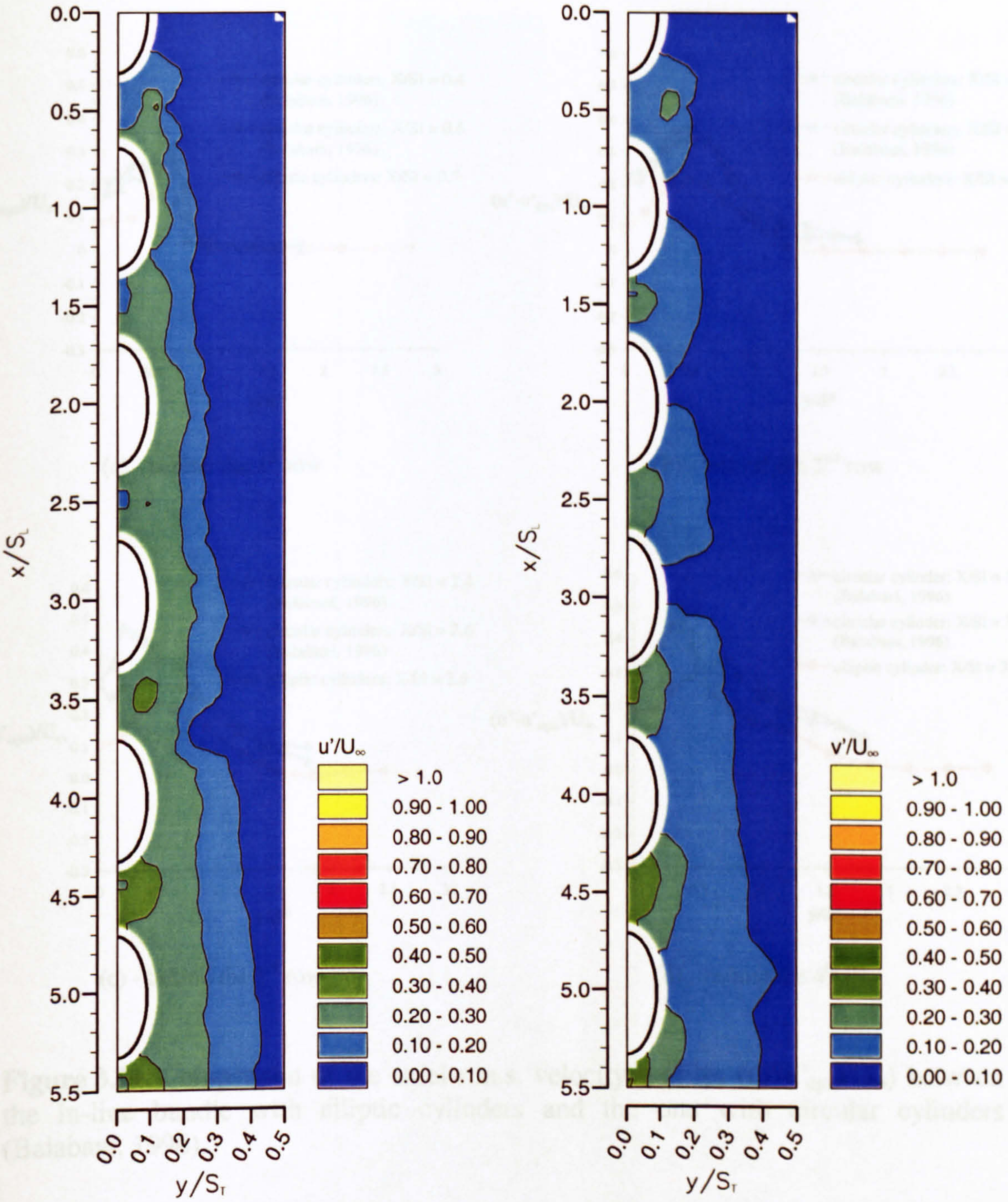

Figure 3.10. Distribution of u'/U_∞, (a), and v'/U_∞, (b), in the in-line bundle with elliptic cylinders (steady flow, Re = 6,760).

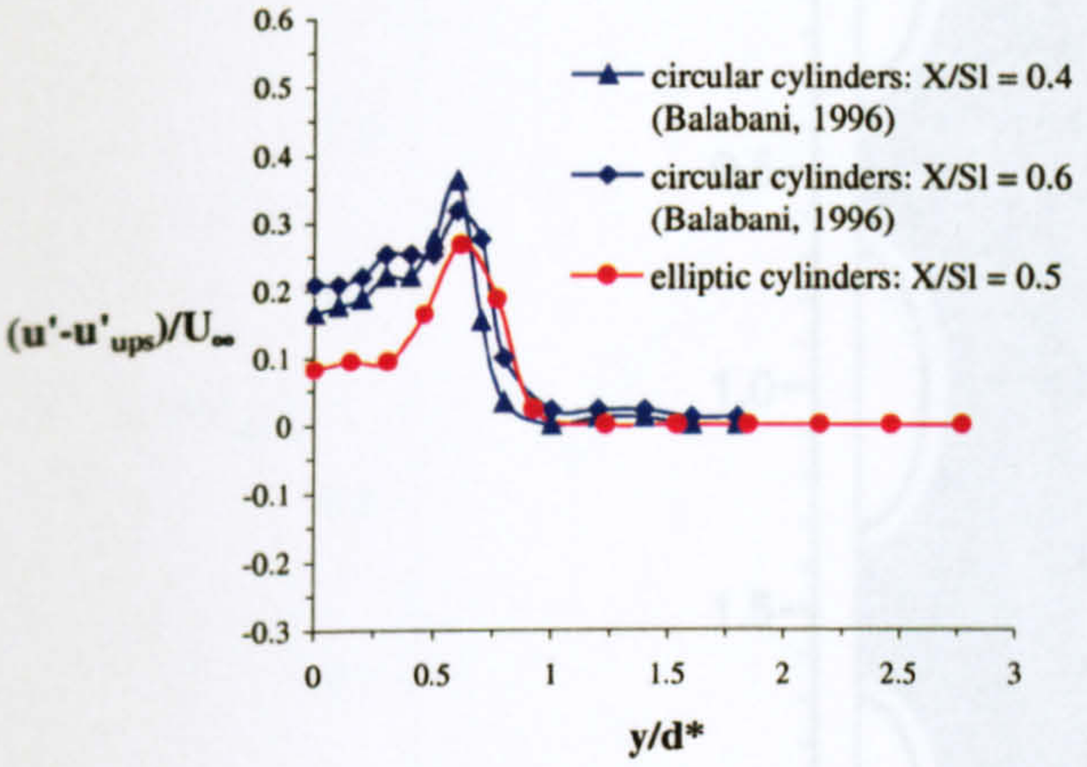

(a) - behind the 1st row

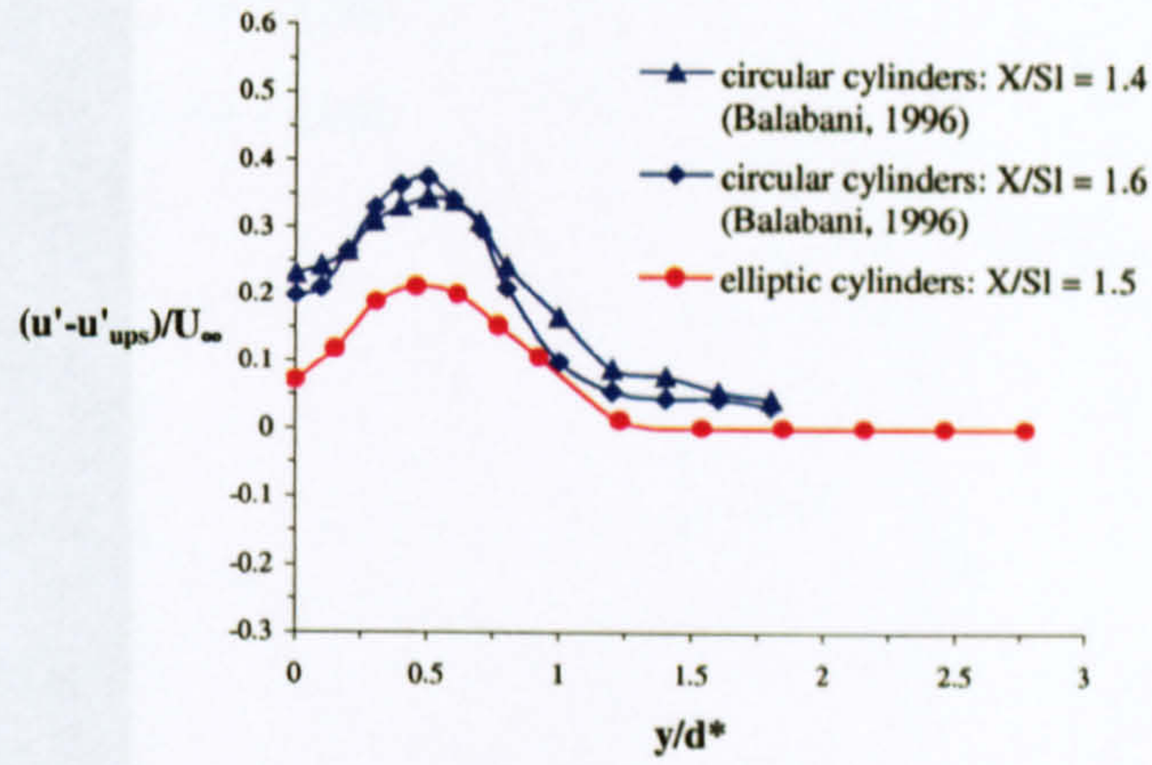

(b) - behind the 2nd row

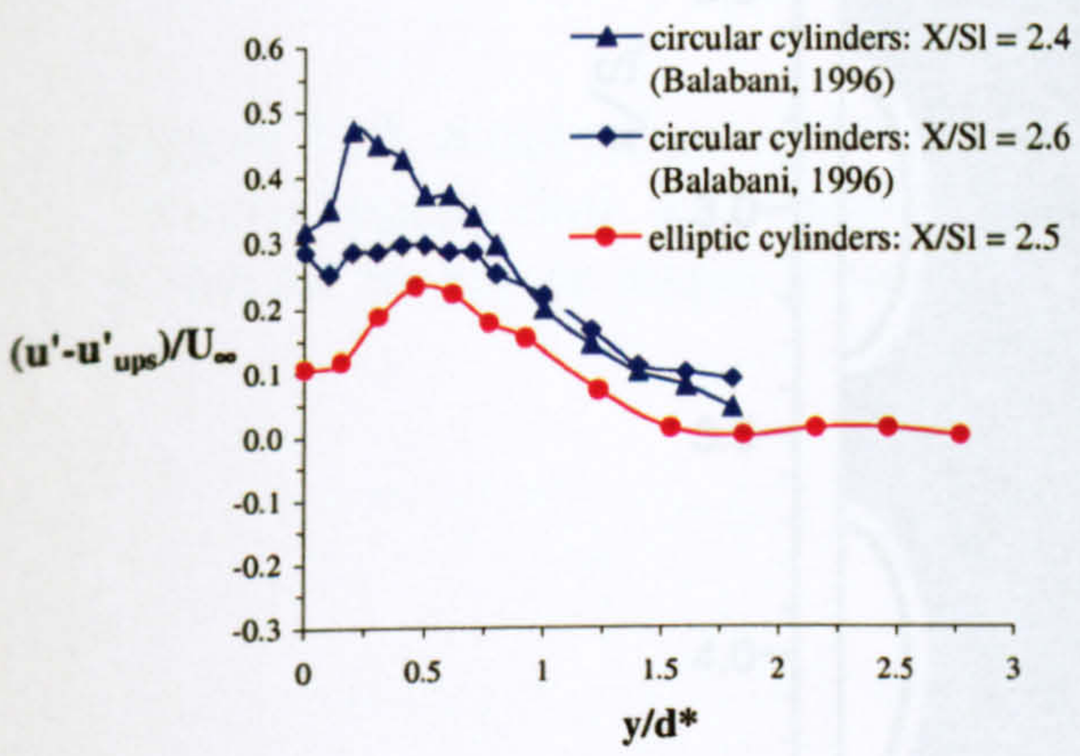

(c) - behind the 3rd row

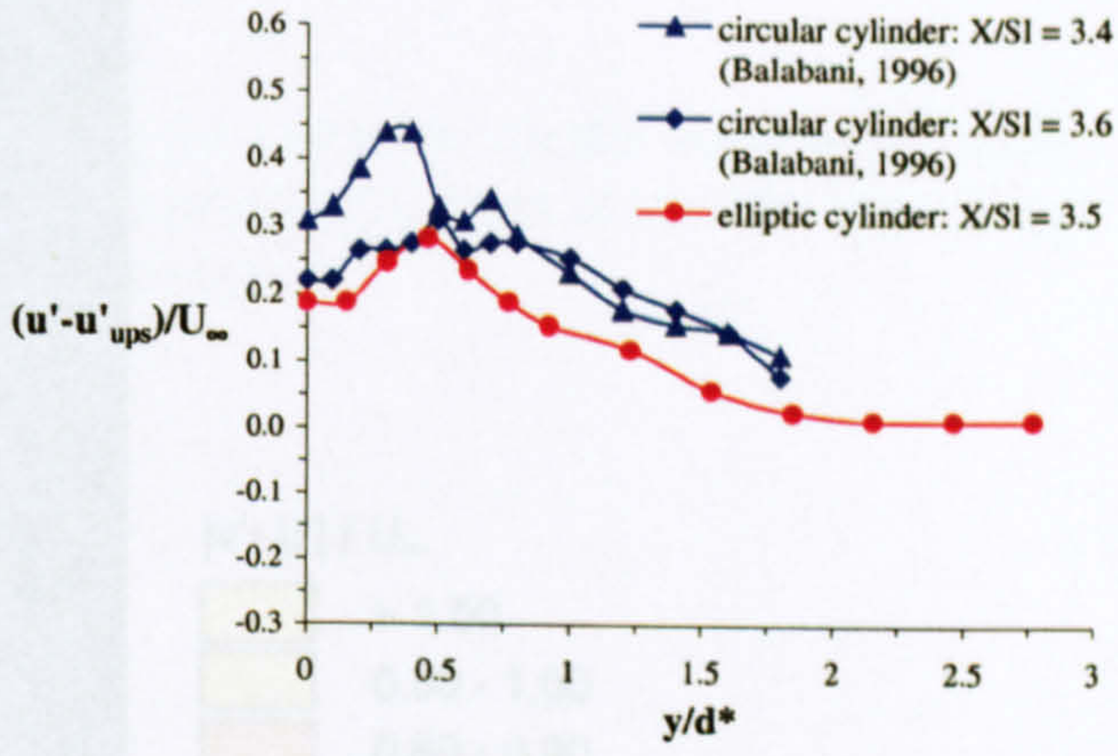

(d) - behind the 4th row

Figure 3.11. Comparison of the axial r.m.s. velocity profiles ($(u'-u'_{ups})/U_\infty$) between the in-line bundle with elliptic cylinders and the one with circular cylinders (Balabani, 1996).

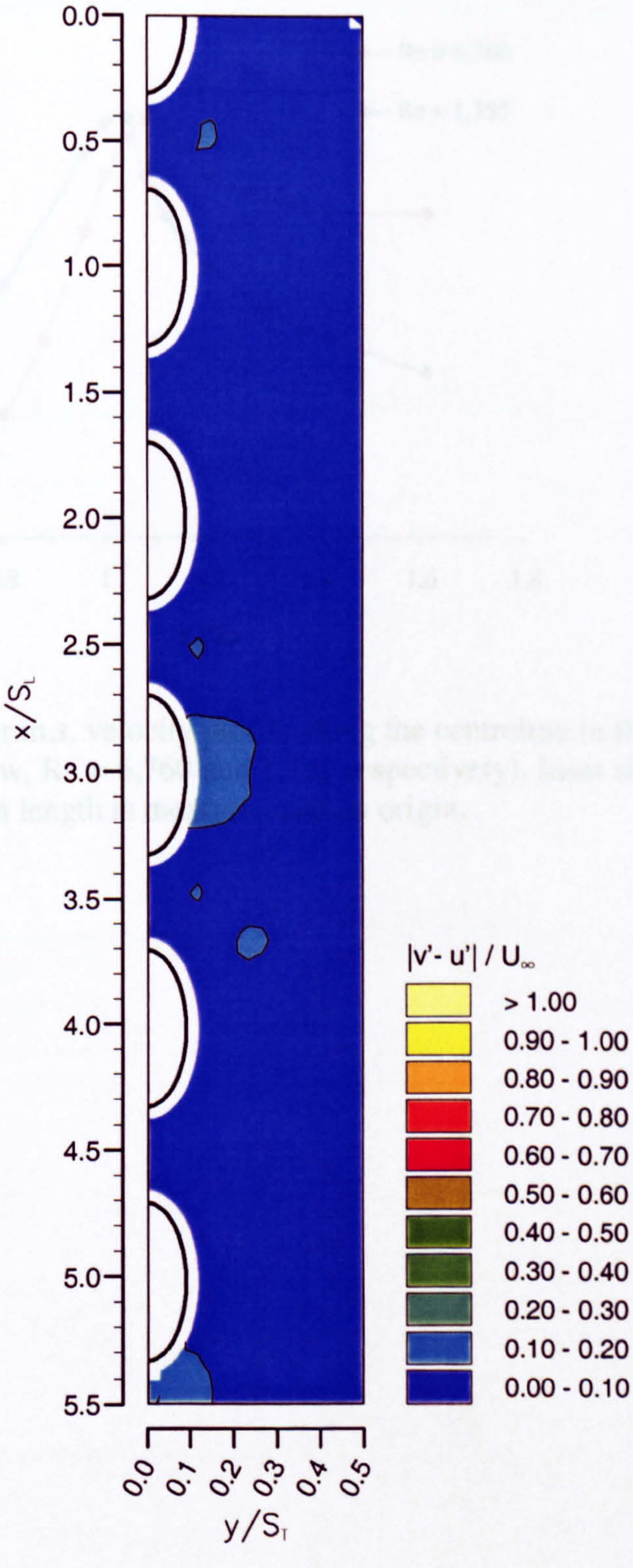

Figure 3.12. Distribution of $|v'-u'|/U_\infty$, in the in-line bundle with elliptic cylinders (steady flow, Re = 6,760).

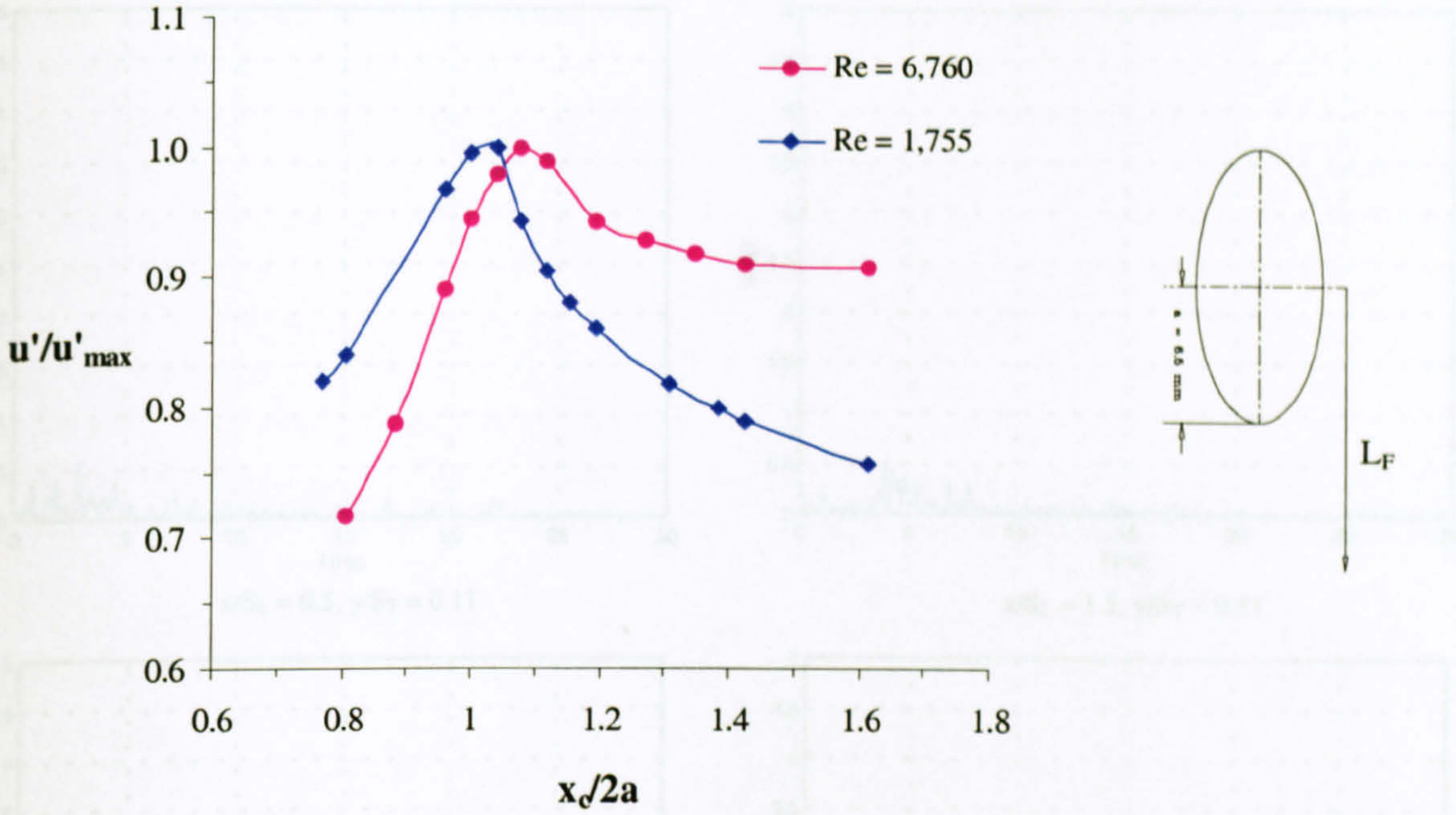

Figure 3.13. Axial r.m.s. velocity profile along the centreline in the wake of the sixth cylinder (steady flow, Re = 6,760 and 1,755 respectively). Inset shows the axis along which the formation length is measured and its origin.

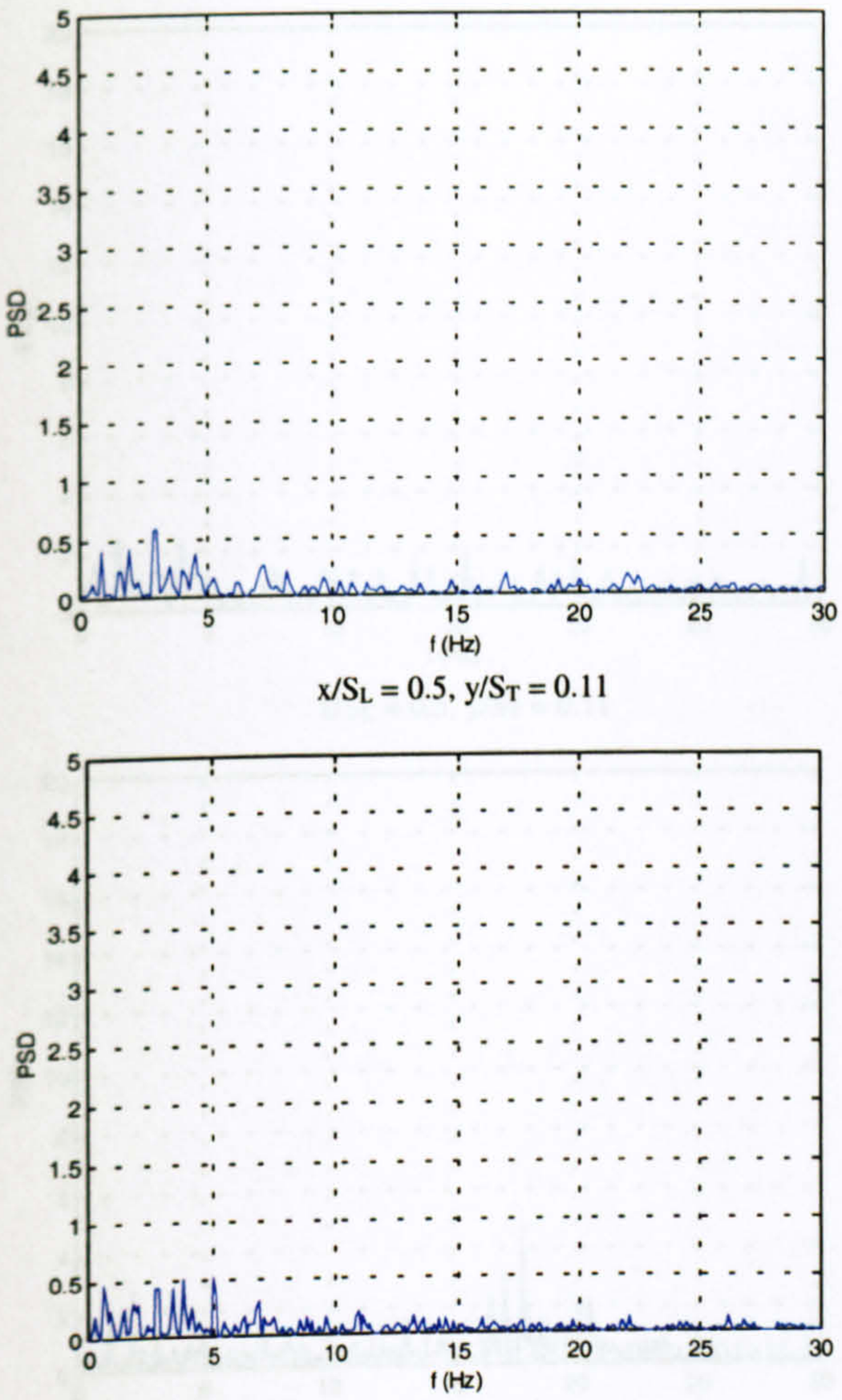

Figure 3.14. Power spectra behind each row in the in-line bundle with elliptic cylinders (steady flow, Re = 1,755).

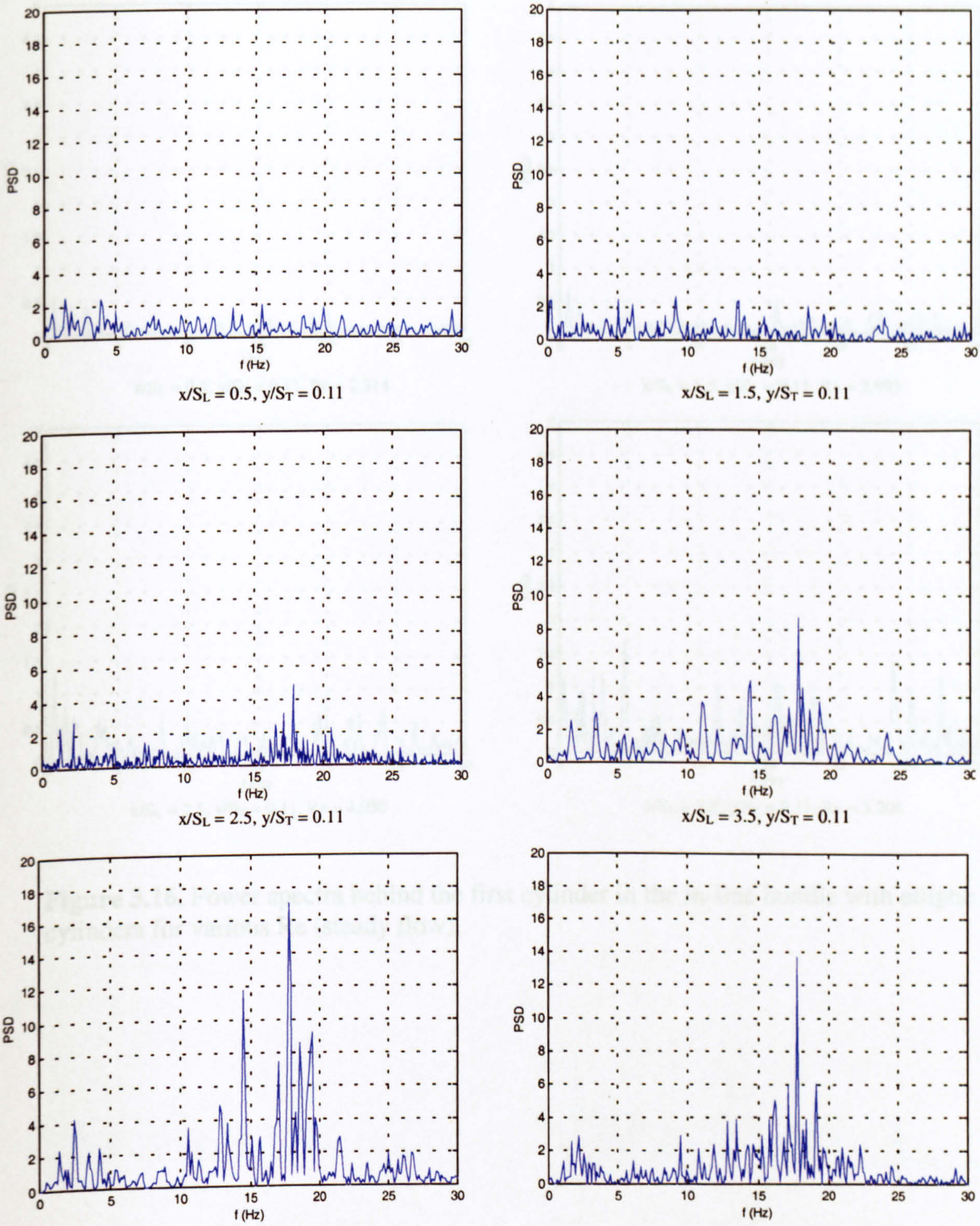

Figure 3.15. Power spectra in the in-line bundle with elliptic cylinders (steady flow, Re = 6,760).

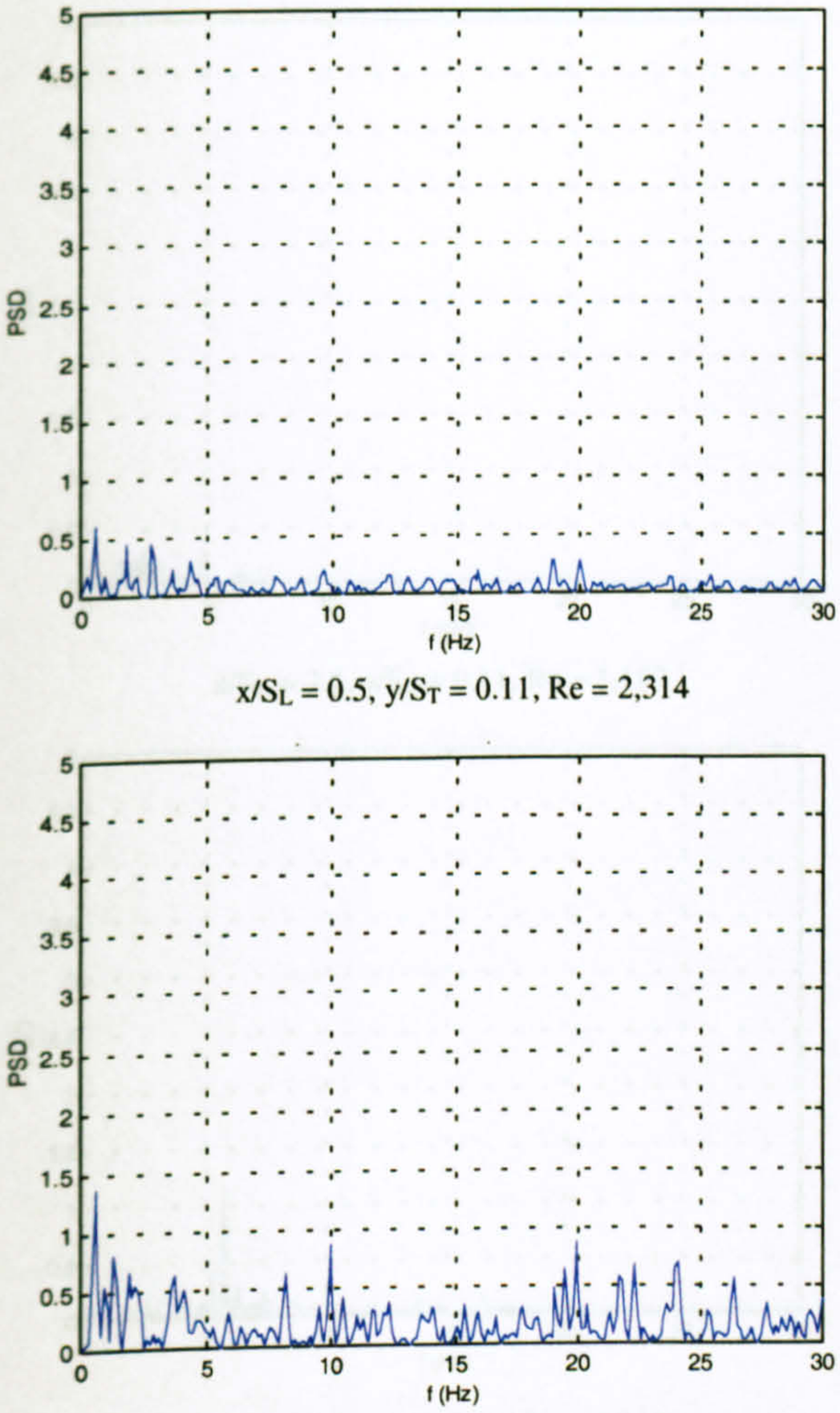

Figure 3.16. Power spectra behind the first cylinder in the in-line bundle with elliptic cylinders for various Re (steady flow).

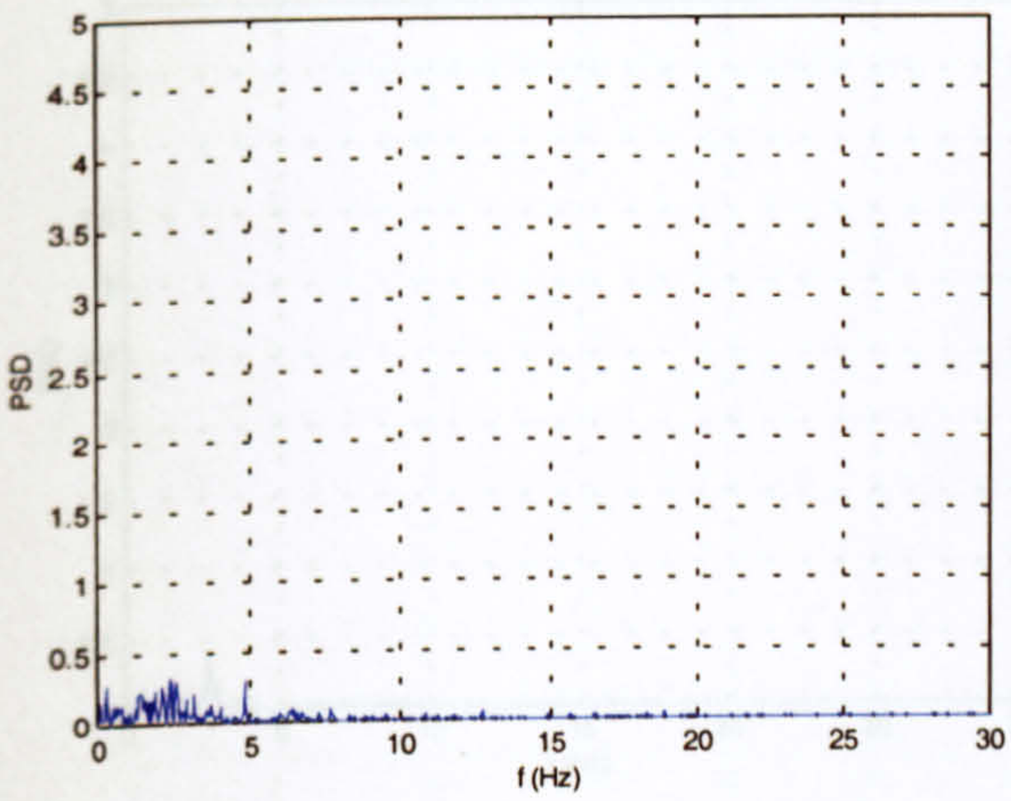

$x/S_L = 2.5$, $y/S_T = 0.11$, Re = 1,157

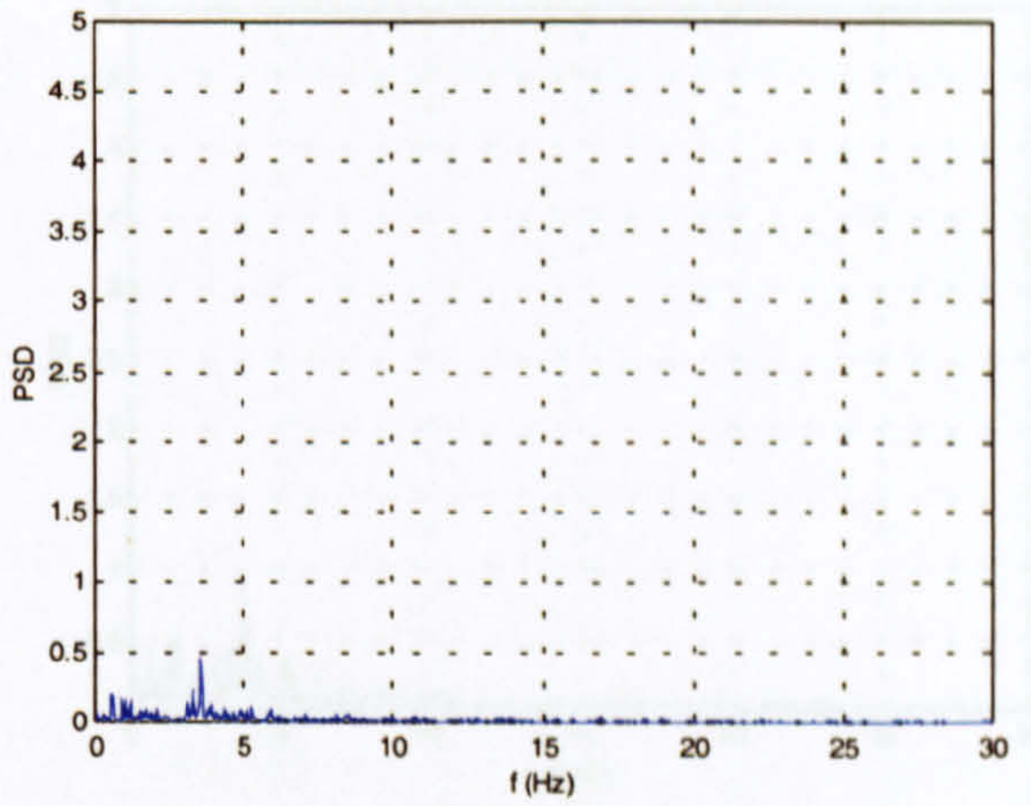

$x/S_L = 2.5$, $y/S_T = 0.11$, Re = 1,703

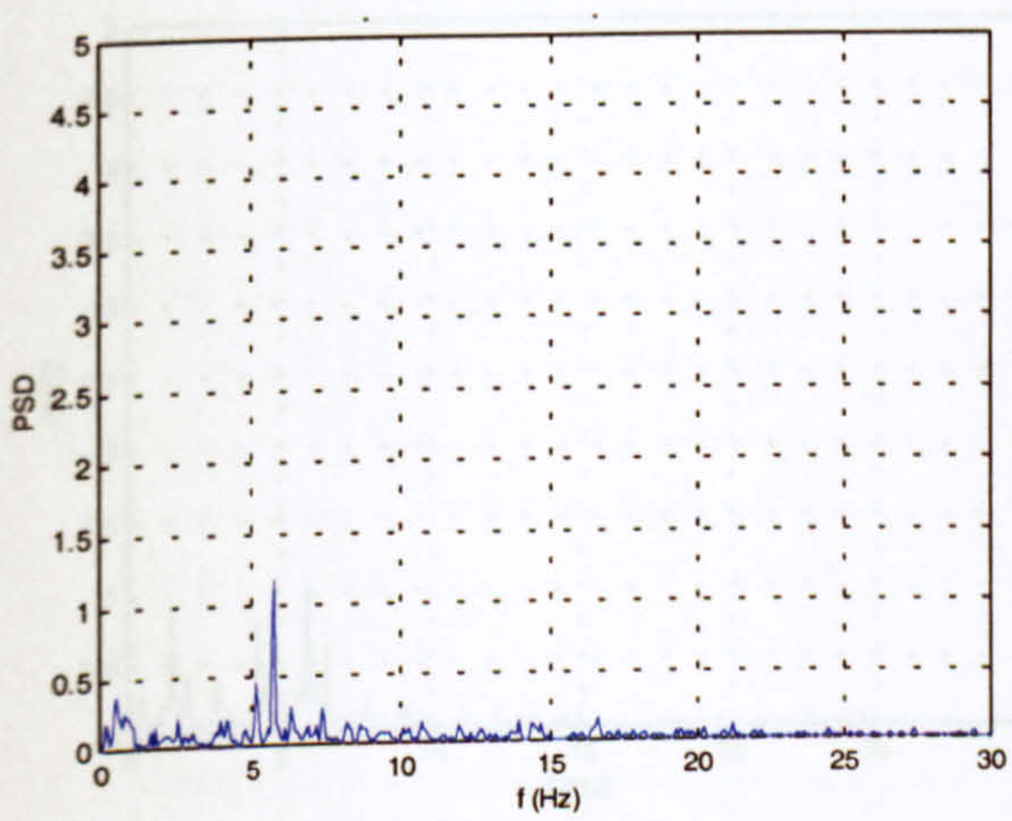

$x/S_L = 2.5$, $y/S_T = 0.11$, Re = 2,314

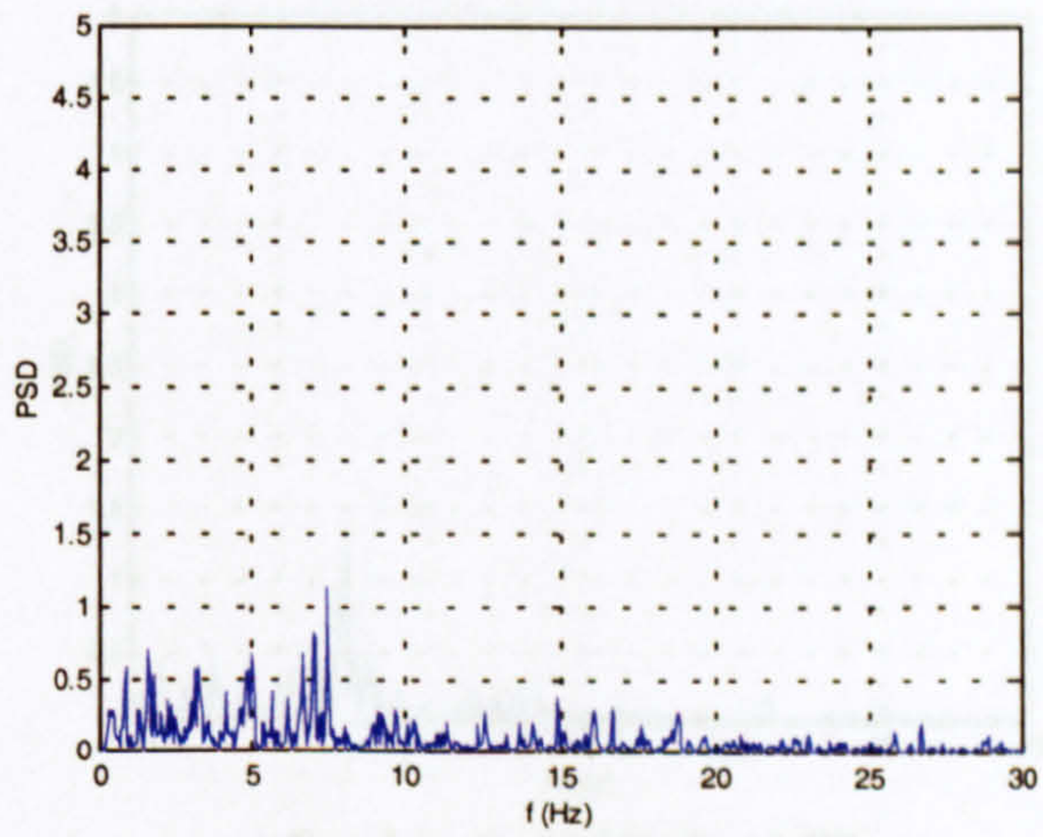

$x/S_L = 2.5$, $y/S_T = 0.11$, Re = 2,892

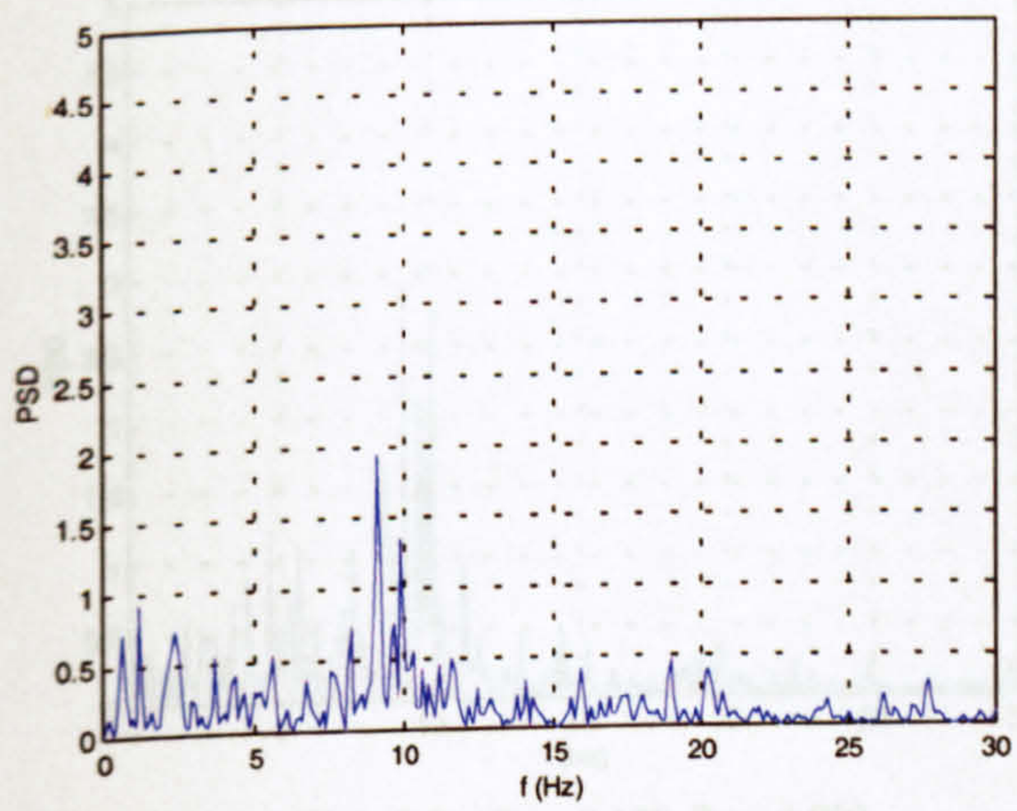

$x/S_L = 2.5$, $y/S_T = 0.11$, Re = 4,050

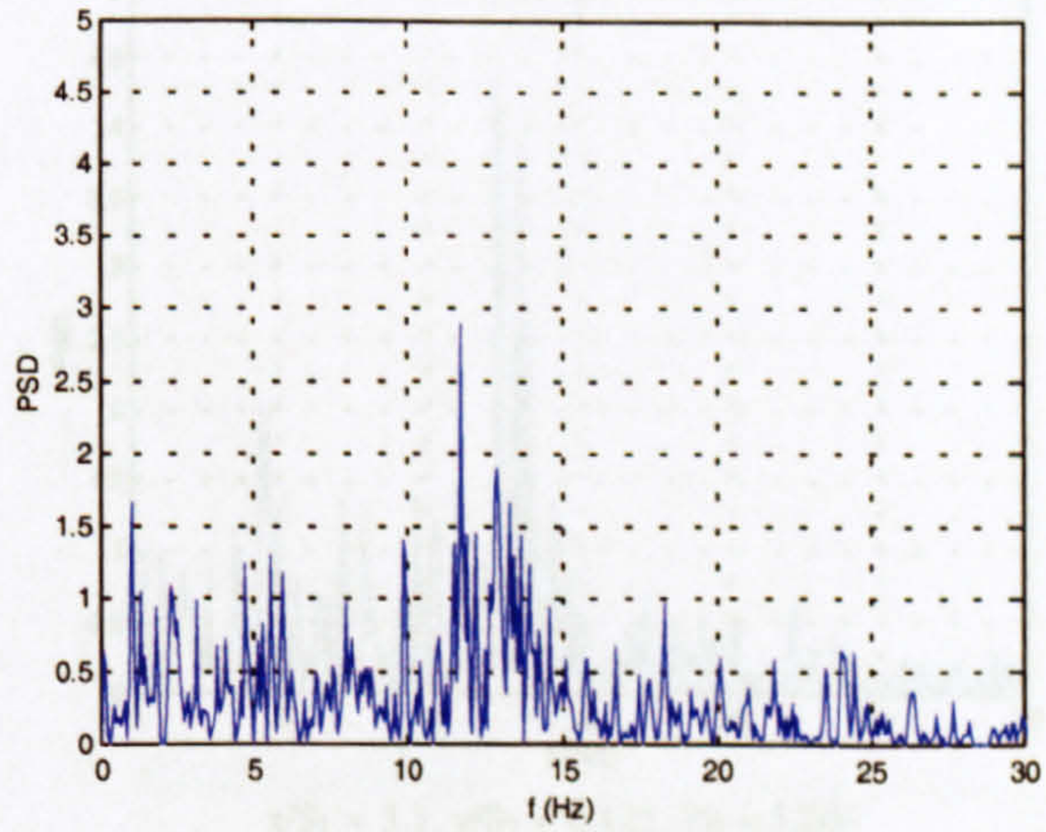

$x/S_L = 2.5$, $y/S_T = 0.11$, Re = 5,206

Figure 3.17. Power spectra behind the third cylinder in the in-line bundle with elliptic cylinders for various Re (steady flow).

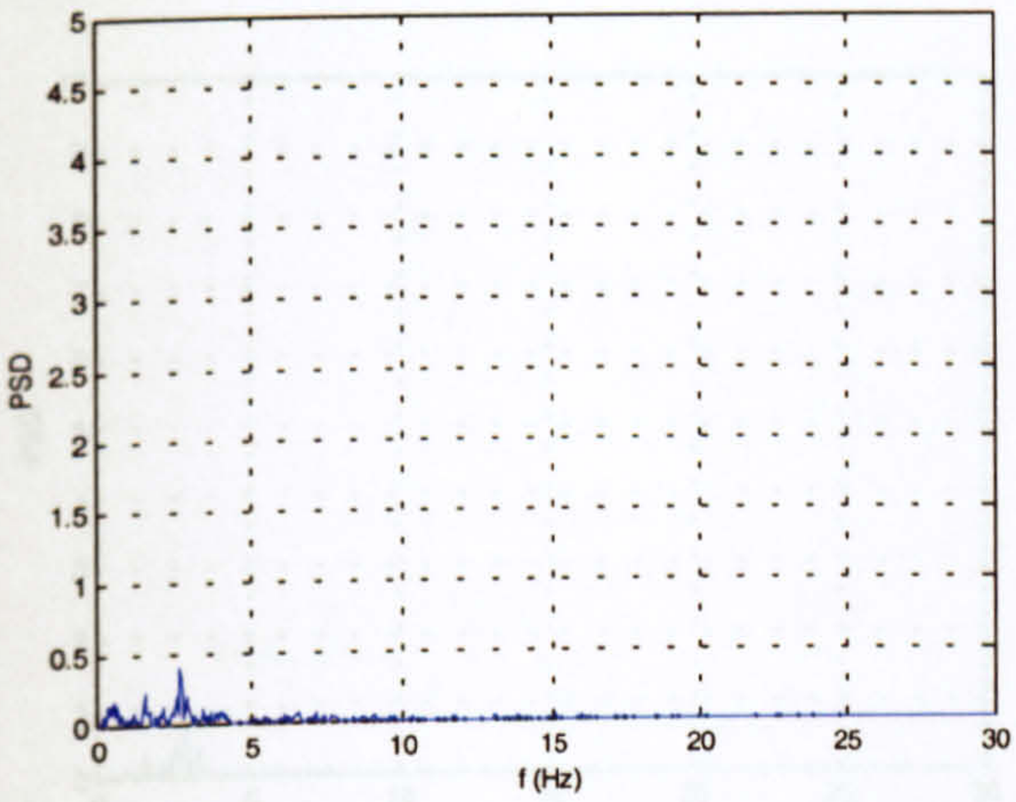

$x/S_L = 3.5$, $y/S_T = 0.125$, Re = 1,157

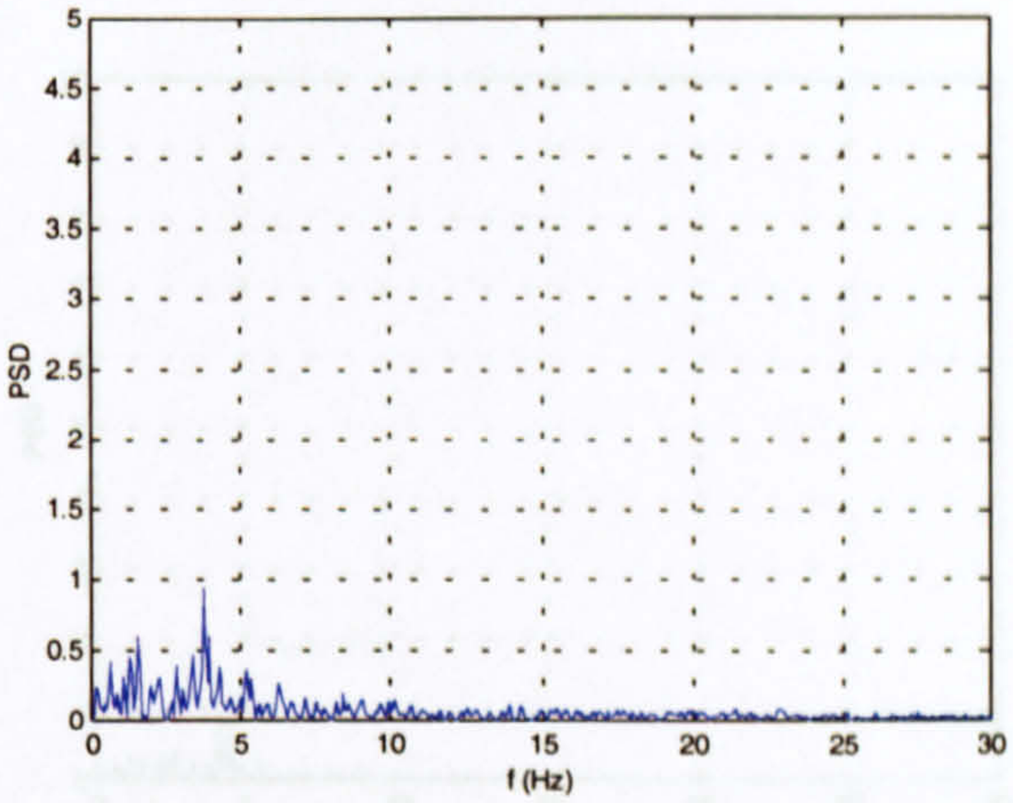

$x/S_L = 3.5$, $y/S_T = 0.125$, Re = 1,703

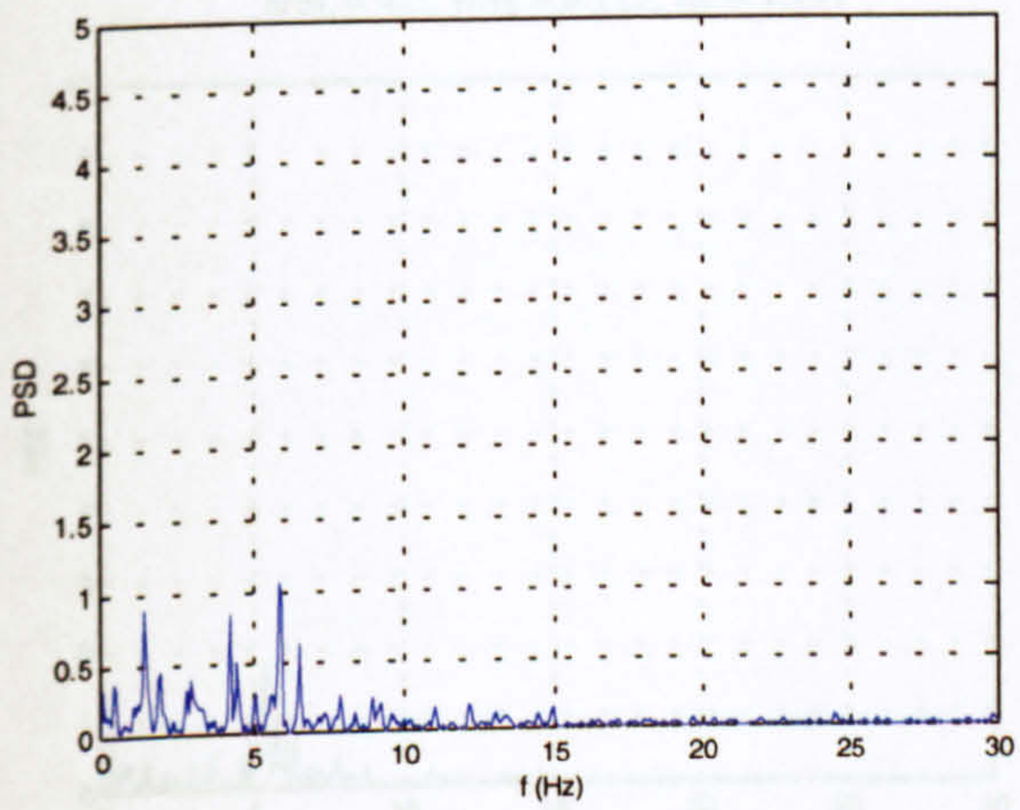

$x/S_L = 3.5$, $y/S_T = 0.125$, Re = 2,314

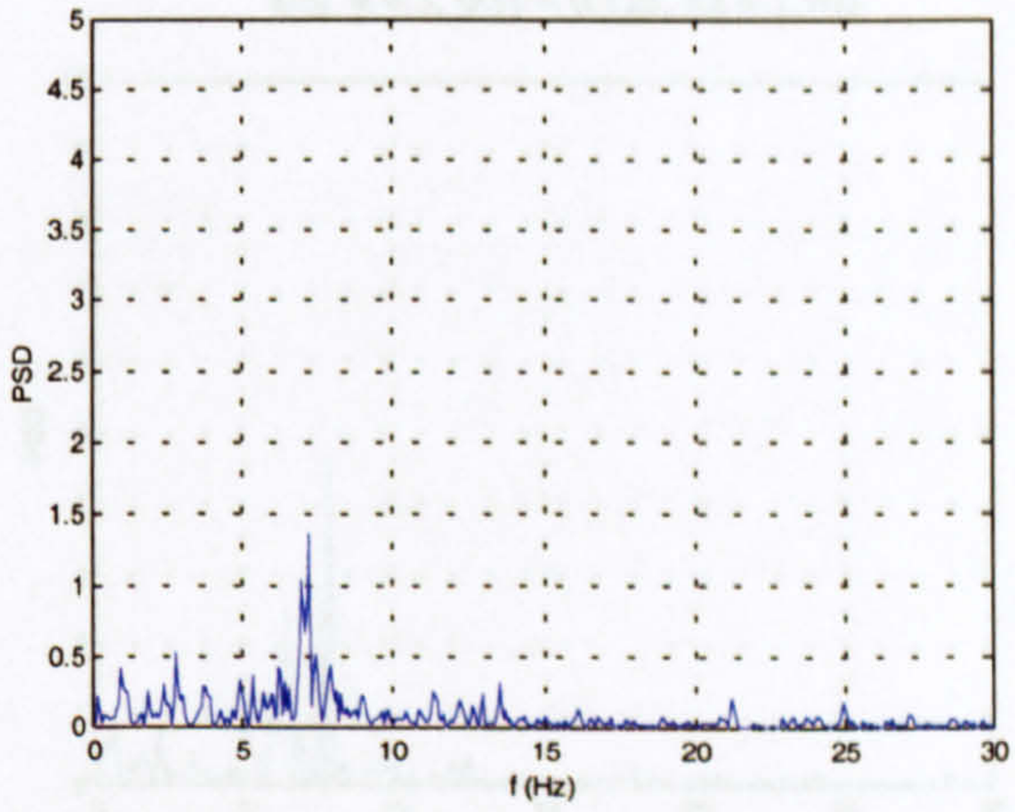

$x/S_L = 3.5$, $y/S_T = 0.125$, Re = 2,892

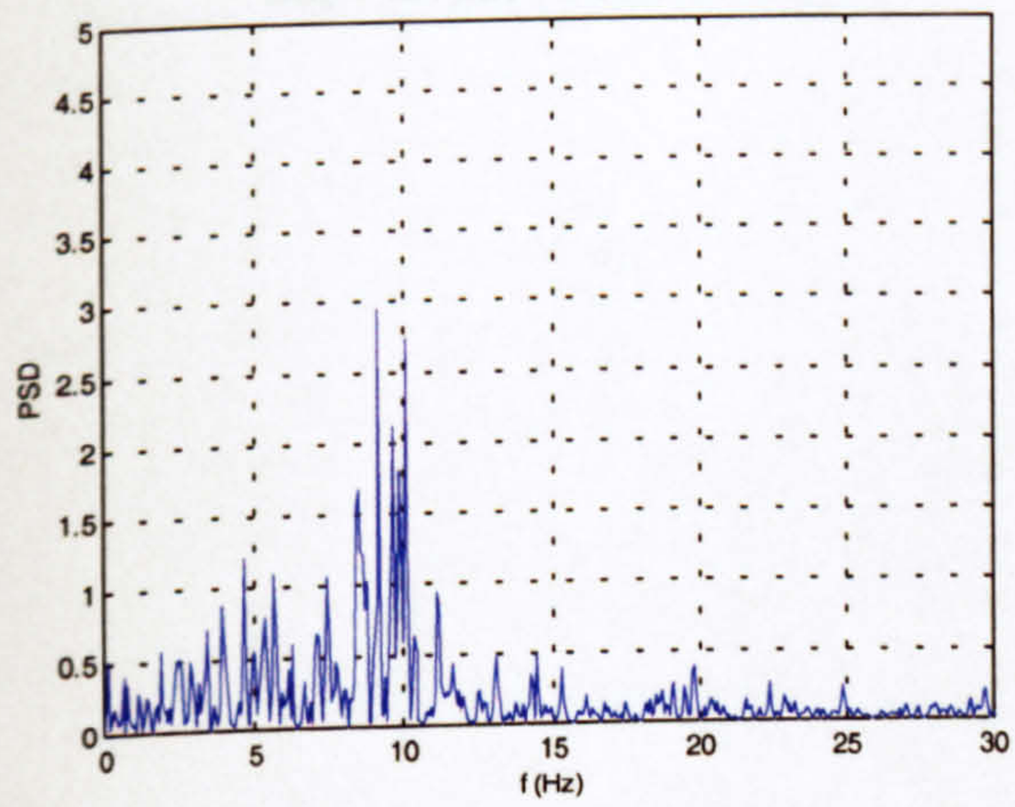

$x/S_L = 3.5$, $y/S_T = 0.125$, Re = 4,050

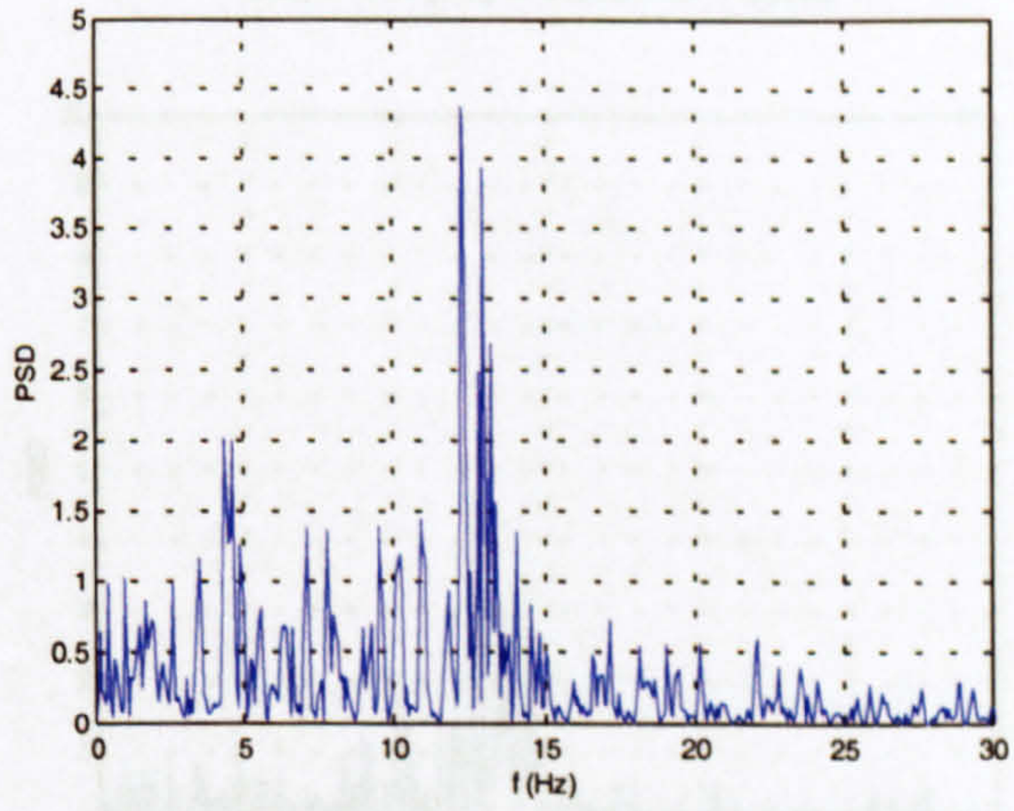

$x/S_L = 3.5$, $y/S_T = 0.125$, Re = 5,206

Figure 3.18. Power spectra behind the fourth cylinder in the in-line tube bundle with elliptic cylinders for various Re (steady flow).

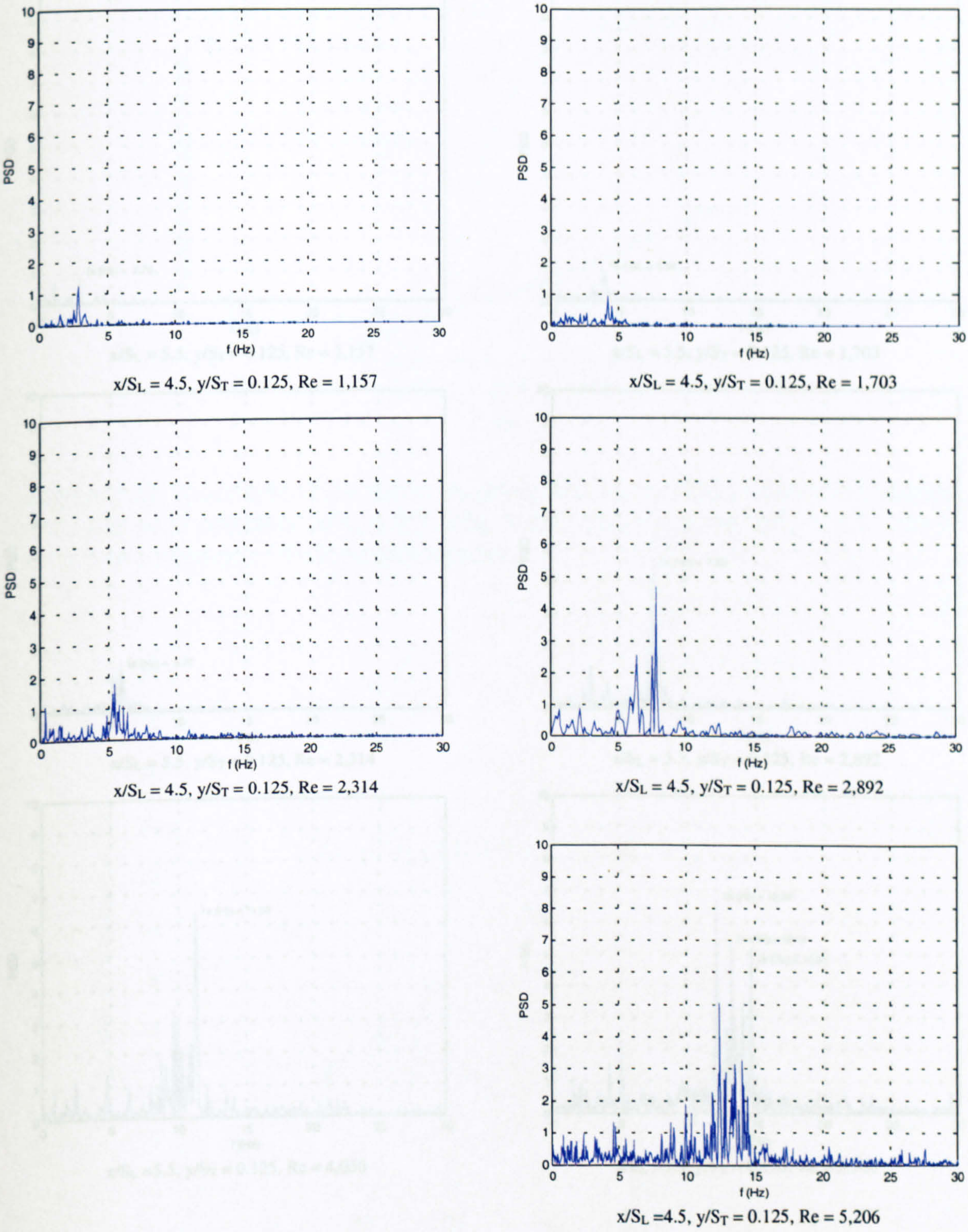

Figure 3.19. Power spectra behind the fifth cylinder in the in-line tube bundle with elliptic cylinders for various Re (steady flow).

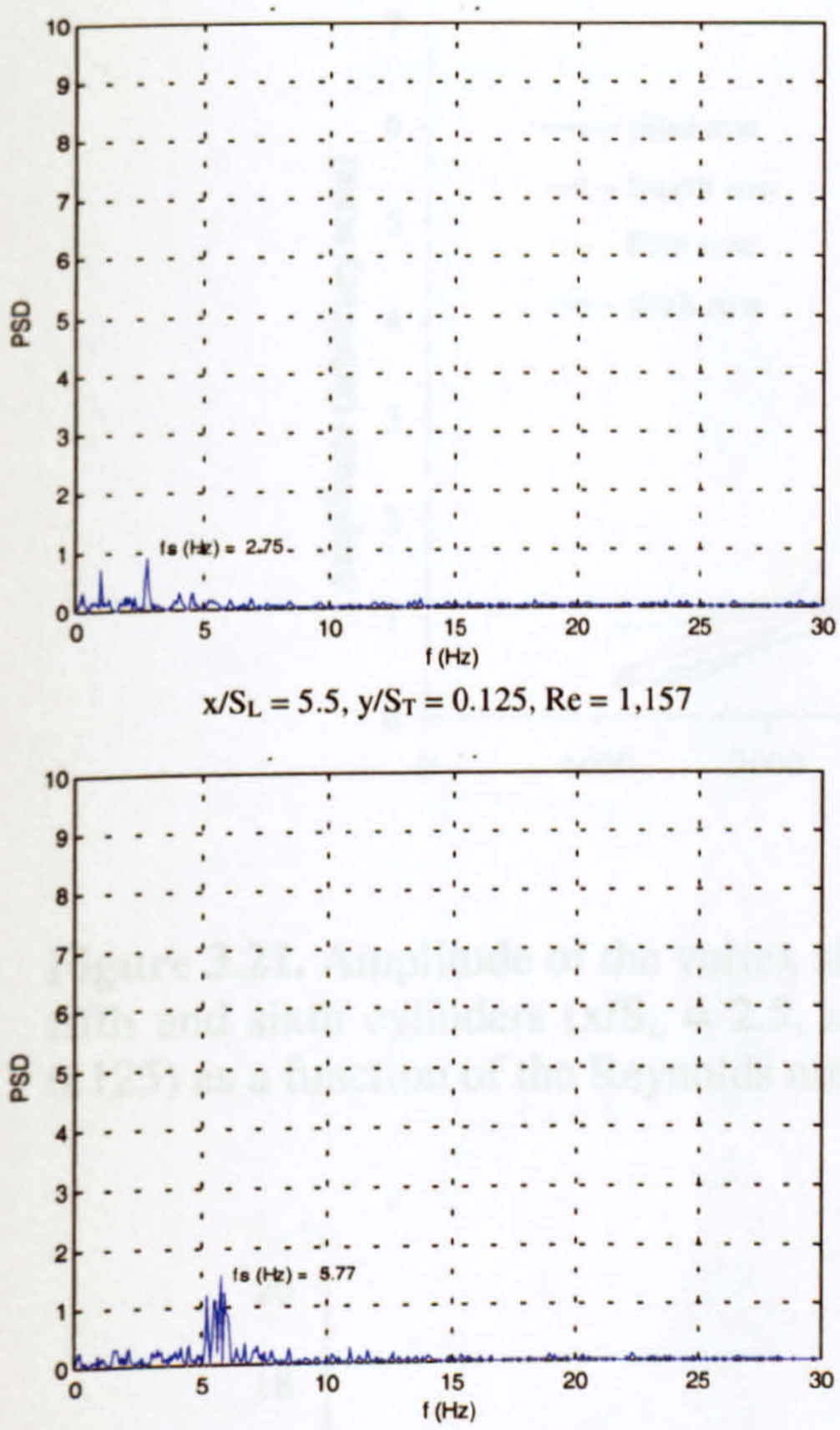

$x/S_L = 5.5, y/S_T = 0.125, Re = 1,157$

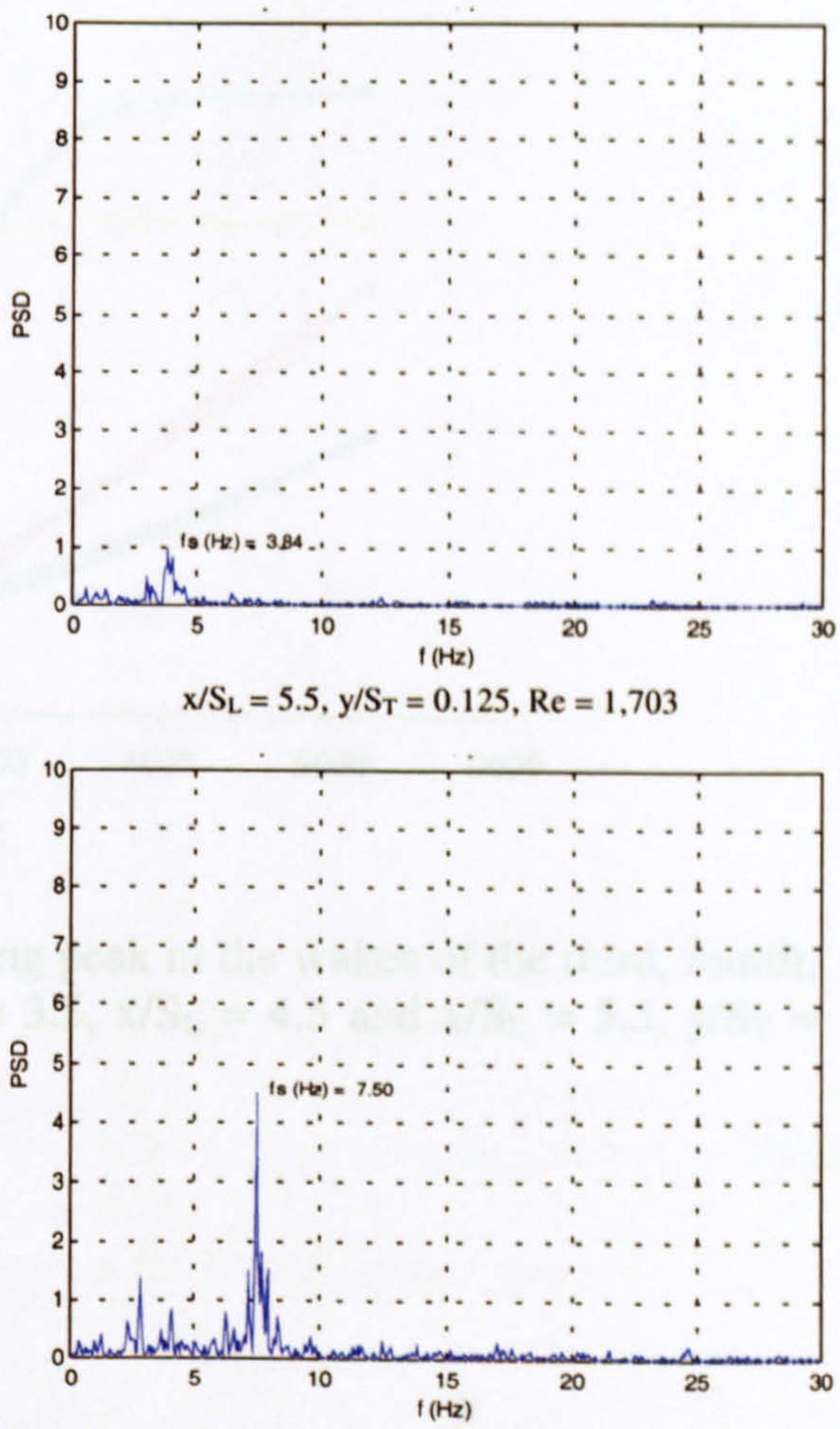

$x/S_L = 5.5, y/S_T = 0.125, Re = 1,703$

$x/S_L = 5.5, y/S_T = 0.125, Re = 2,314$

$x/S_L = 5.5, y/S_T = 0.125, Re = 2,892$

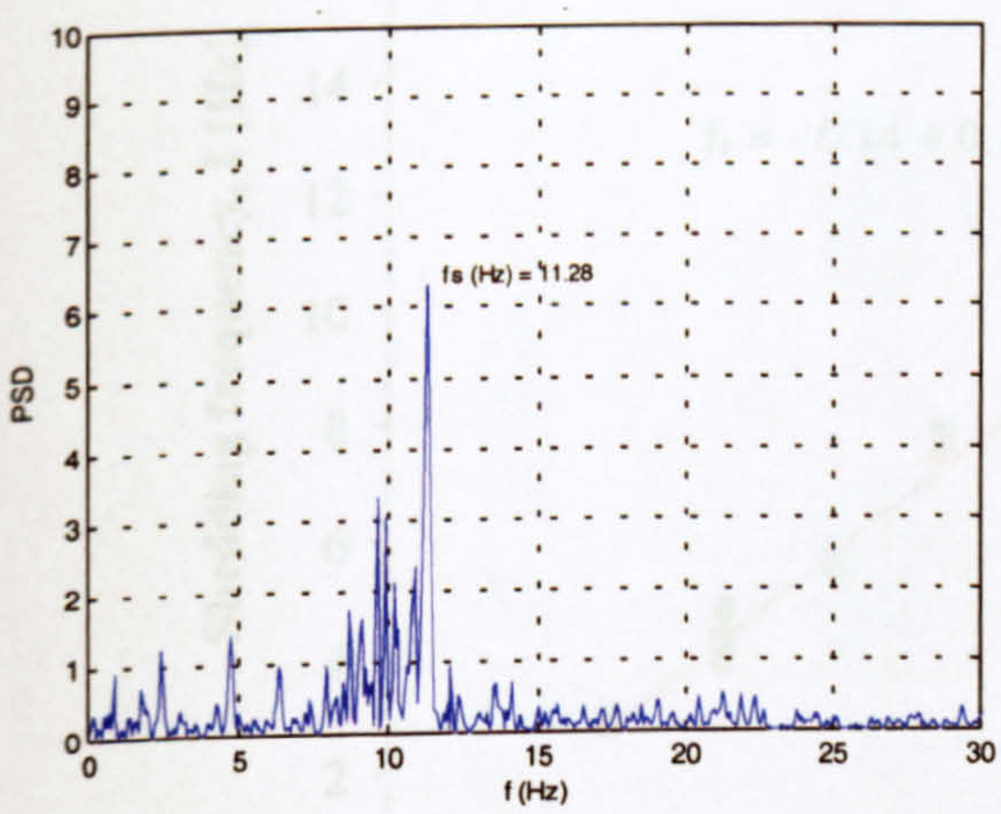

$x/S_L = 5.5, y/S_T = 0.125, Re = 4,050$

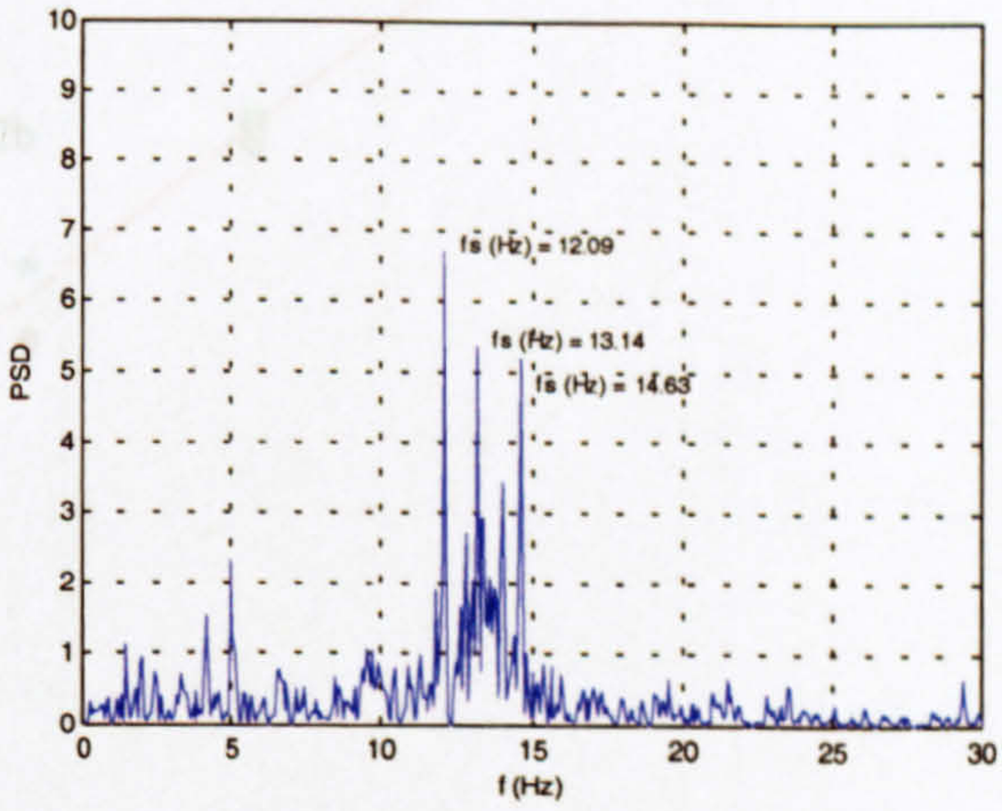

$x/S_L = 5.5, y/S_T = 0.125, Re = 5,206$

Figure 3.20. Power spectra behind the sixth cylinder in the in-line tube bundle with elliptic cylinders for various Re (steady flow).

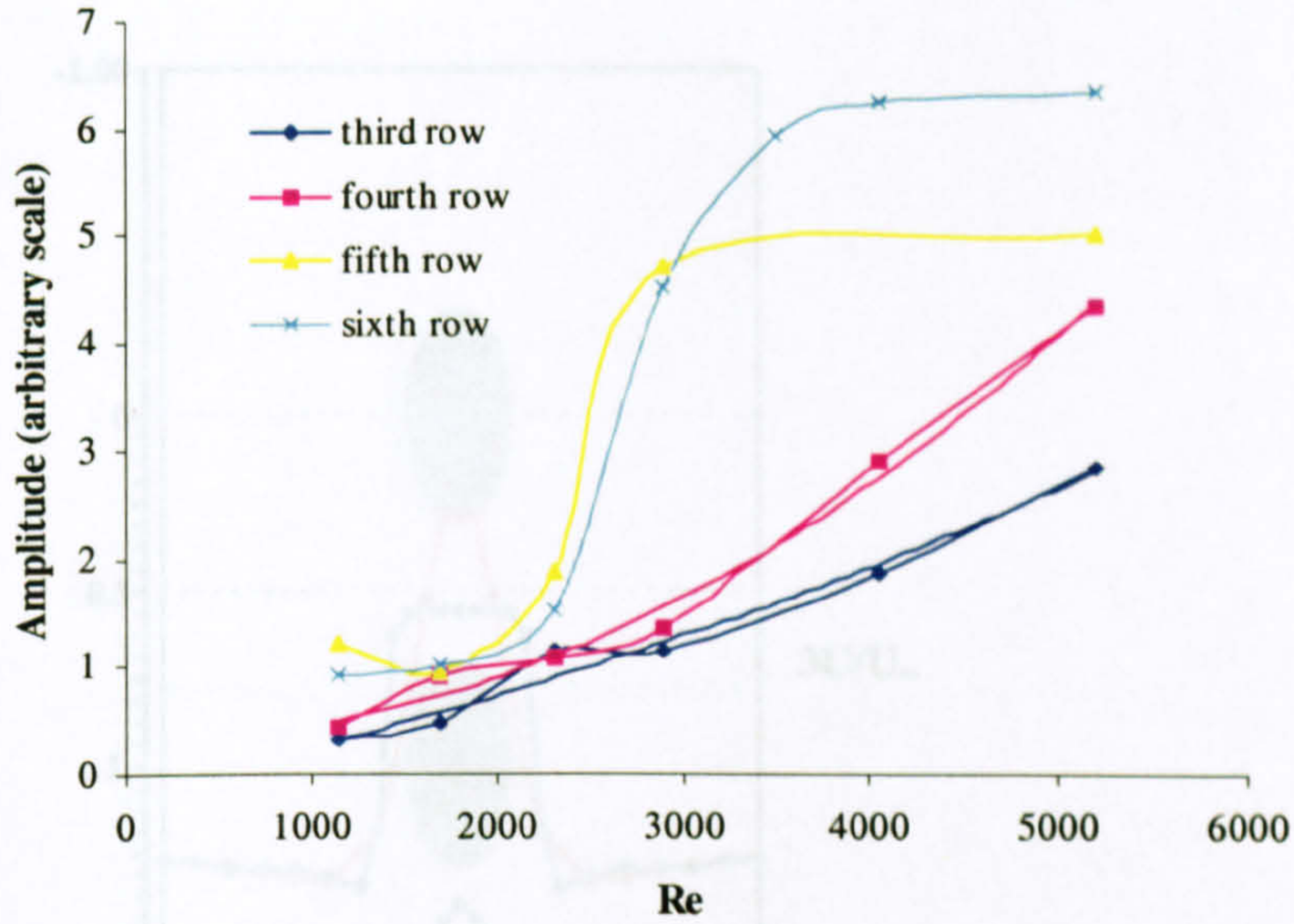

Figure 3.21. Amplitude of the vortex shedding peak in the wakes of the third, fourth, fifth and sixth cylinders ($x/S_L = 2.5$, $x/S_L = 3.5$, $x/S_L = 4.5$ and $x/S_L = 5.5$, $y/S_T = 0.125$) as a function of the Reynolds number.

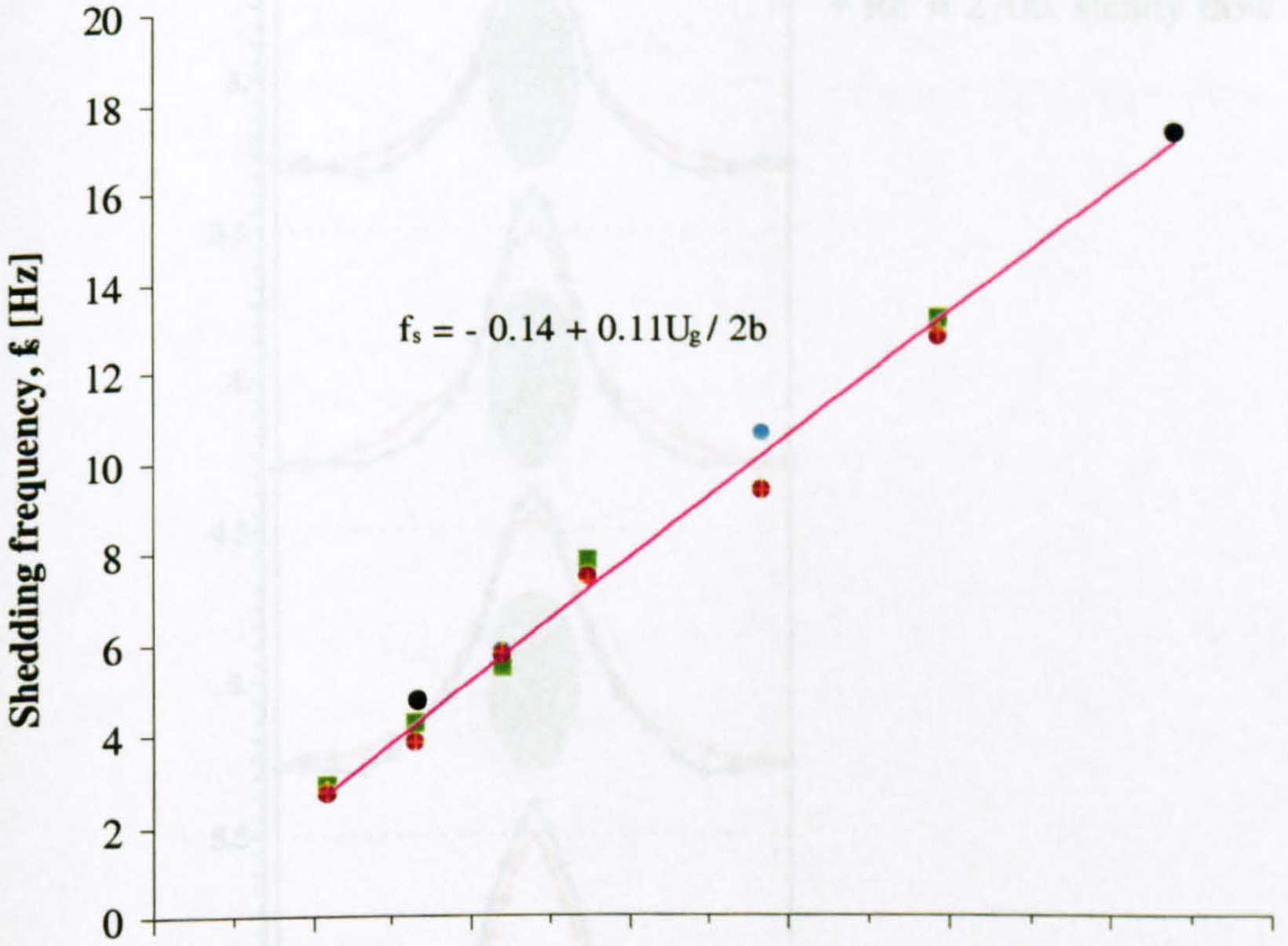

Figure 3.22. Shedding frequencies measured in the wakes of the third, fourth, fifth and sixth cylinders ($x/S_L = 2.5$, $x/S_L = 3.5$, $x/S_L = 4.5$ and $x/S_L = 3.5$, $y/S_T = 0.125$) as a function of $U_g/2b$.

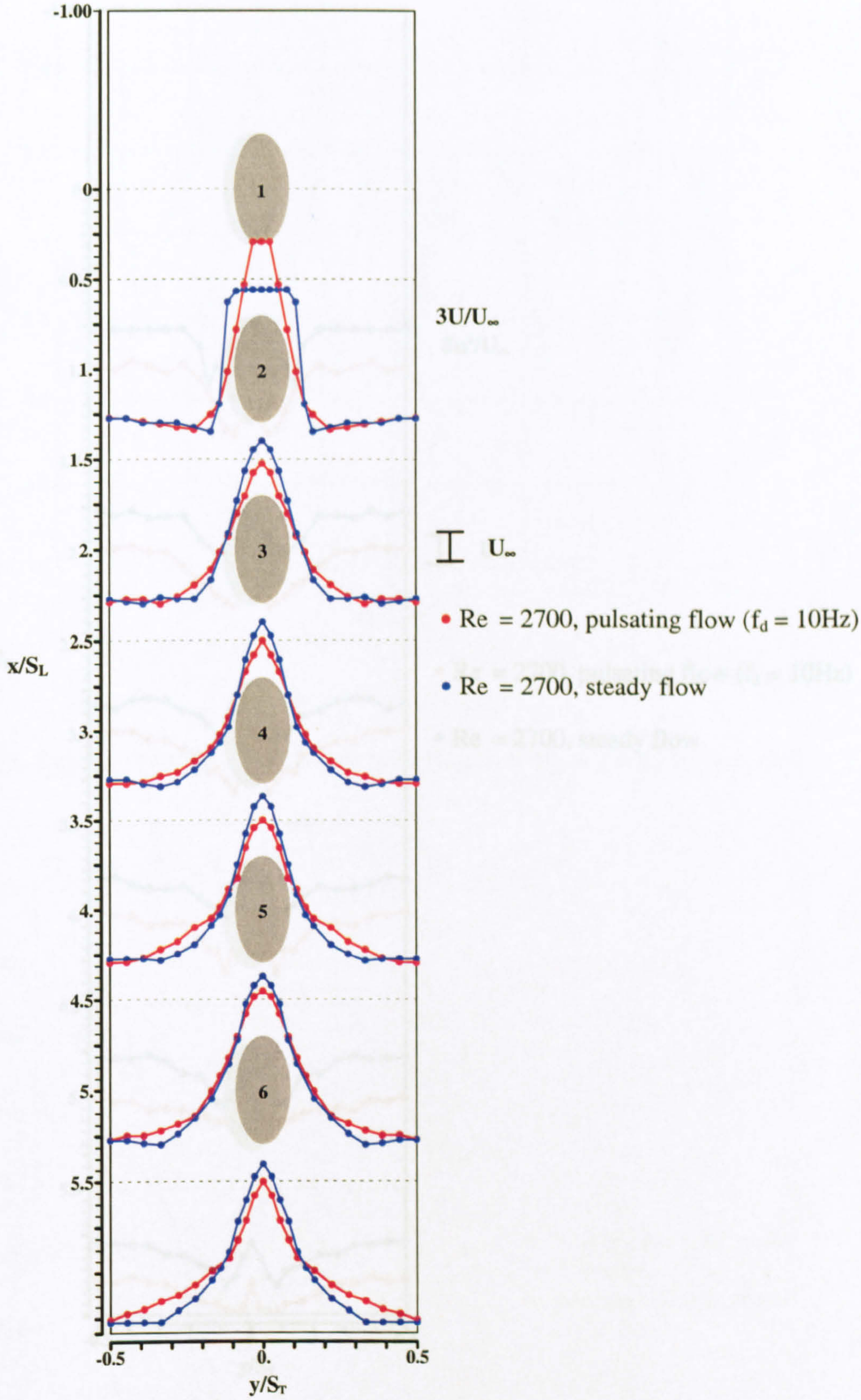

Figure 3.23. Comparison of the axial mean velocity profiles, U/U_{∞},, obtained in steady and pulsating flow (f_d = 10 Hz, Re = 1,755).

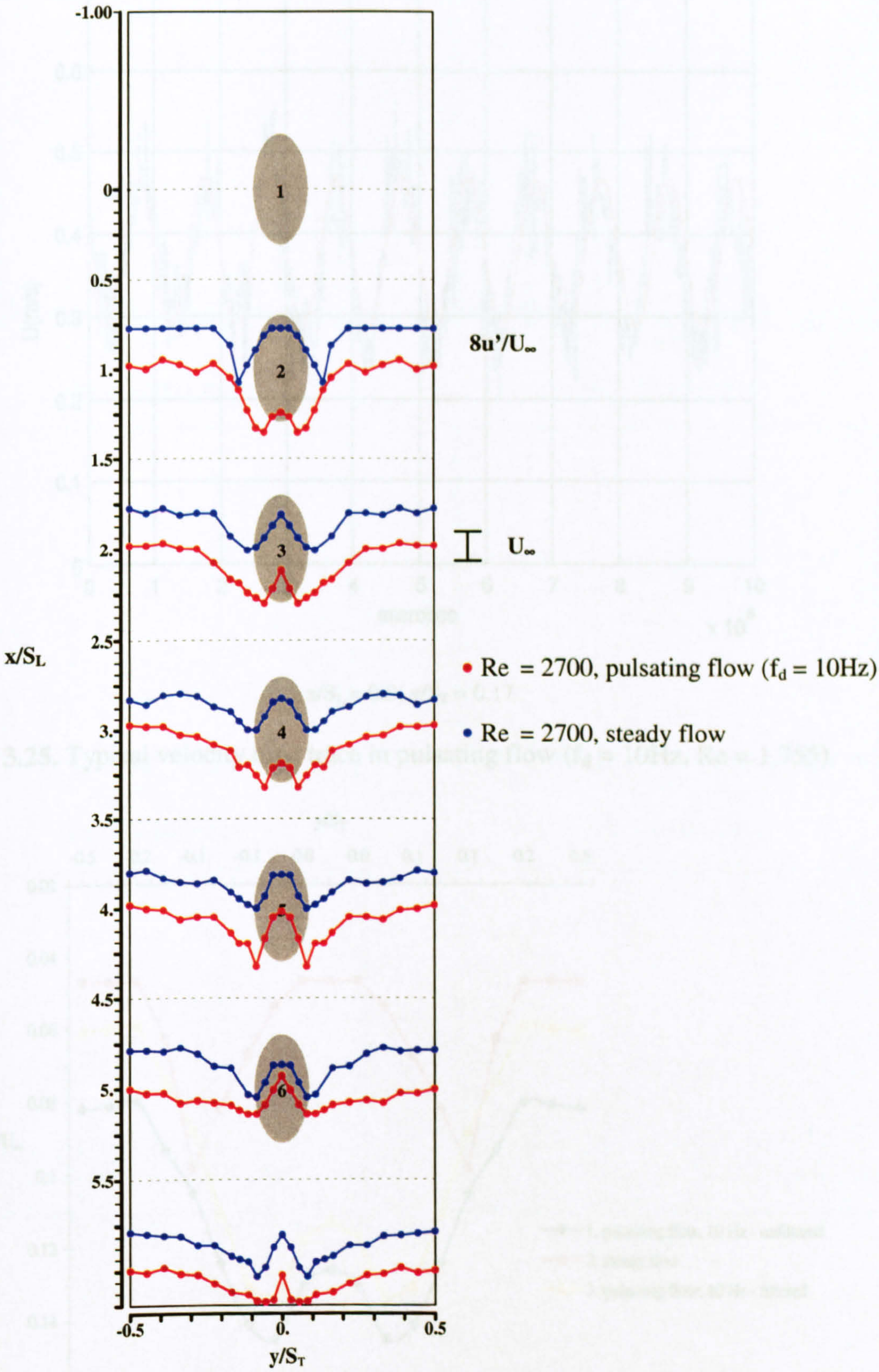

Figure 3.24. Comparison of the axial r.m.s. velocity profiles, u'/U_∞, obtained in steady and pulsating flow (f_d = 10 Hz, Re = 1,755).

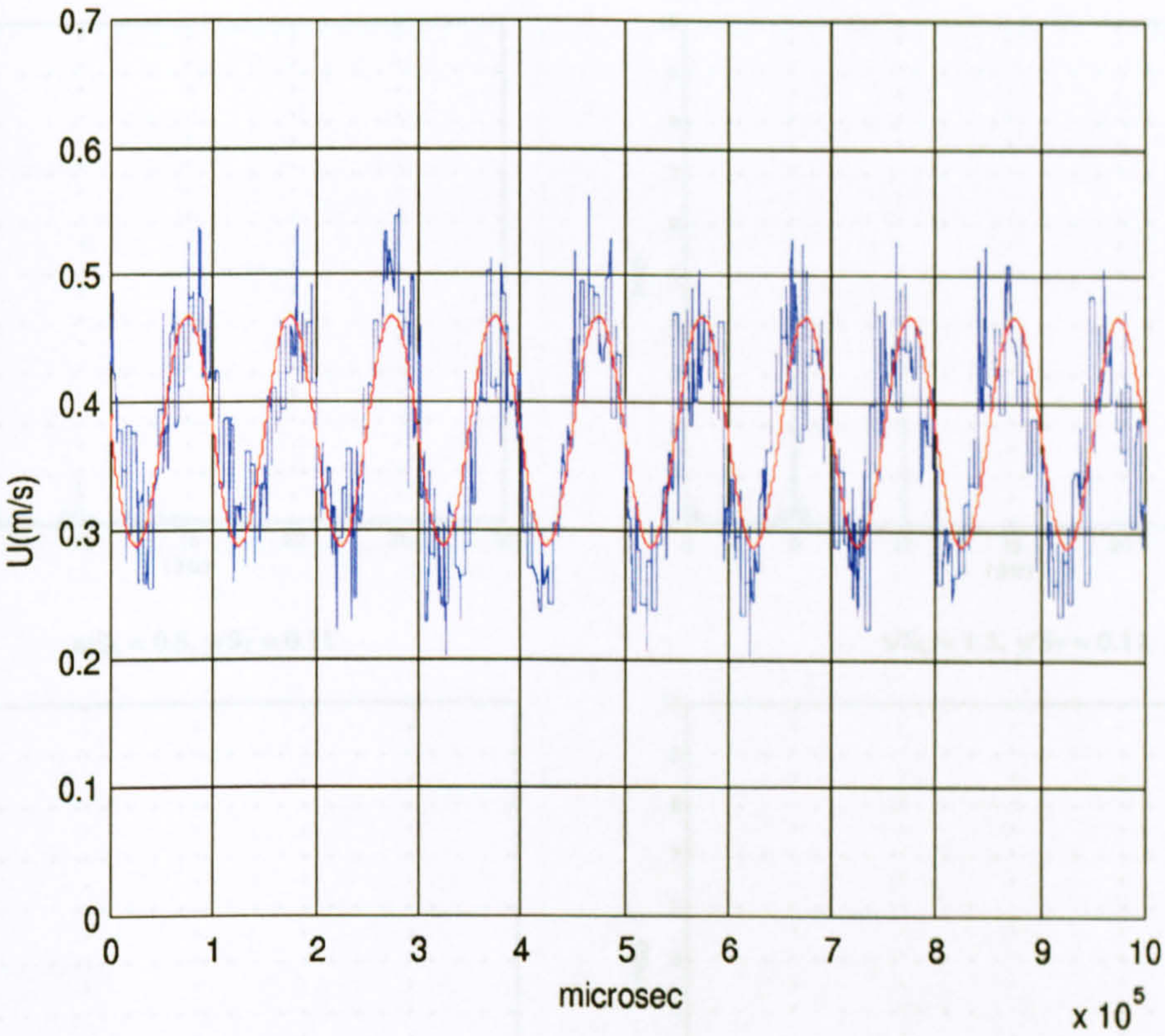

$x/S_L = 0.0$; $y/S_T = 0.17$

Figure 3.25. Typical velocity time trace in pulsating flow (f_d = 10Hz, Re = 1,755).

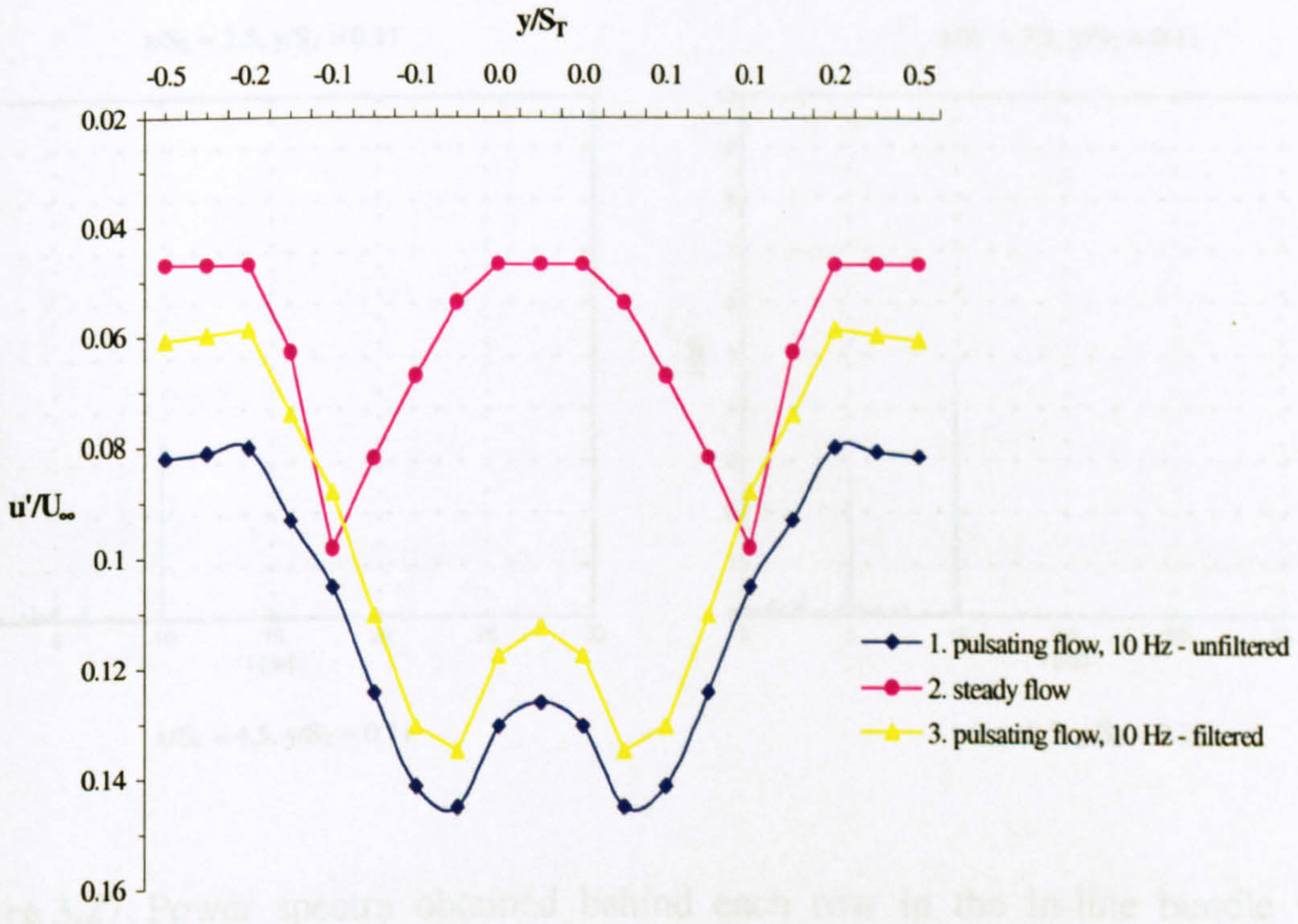

Figure 3.26. Comparison of the axial r.m.s. velocity profiles downstream of the first row in steady and pulsating flow (f_d = 10 Hz, Re = 1,755).

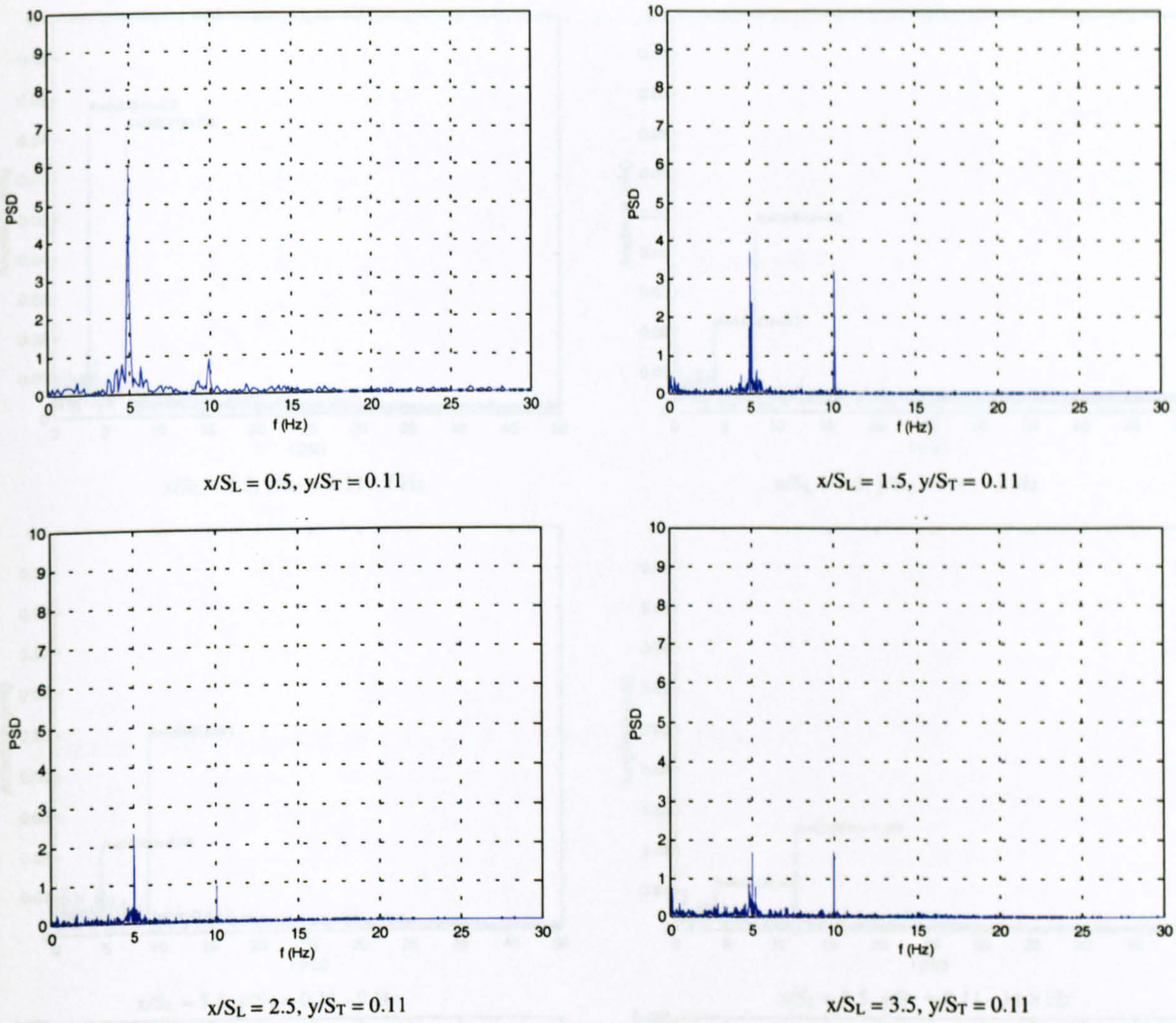

Figure 3.27. Power spectra obtained behind each row in the in-line bundle with elliptic cylinders under pulsating flow conditions (Re = 1,755, f_d = 10 Hz).

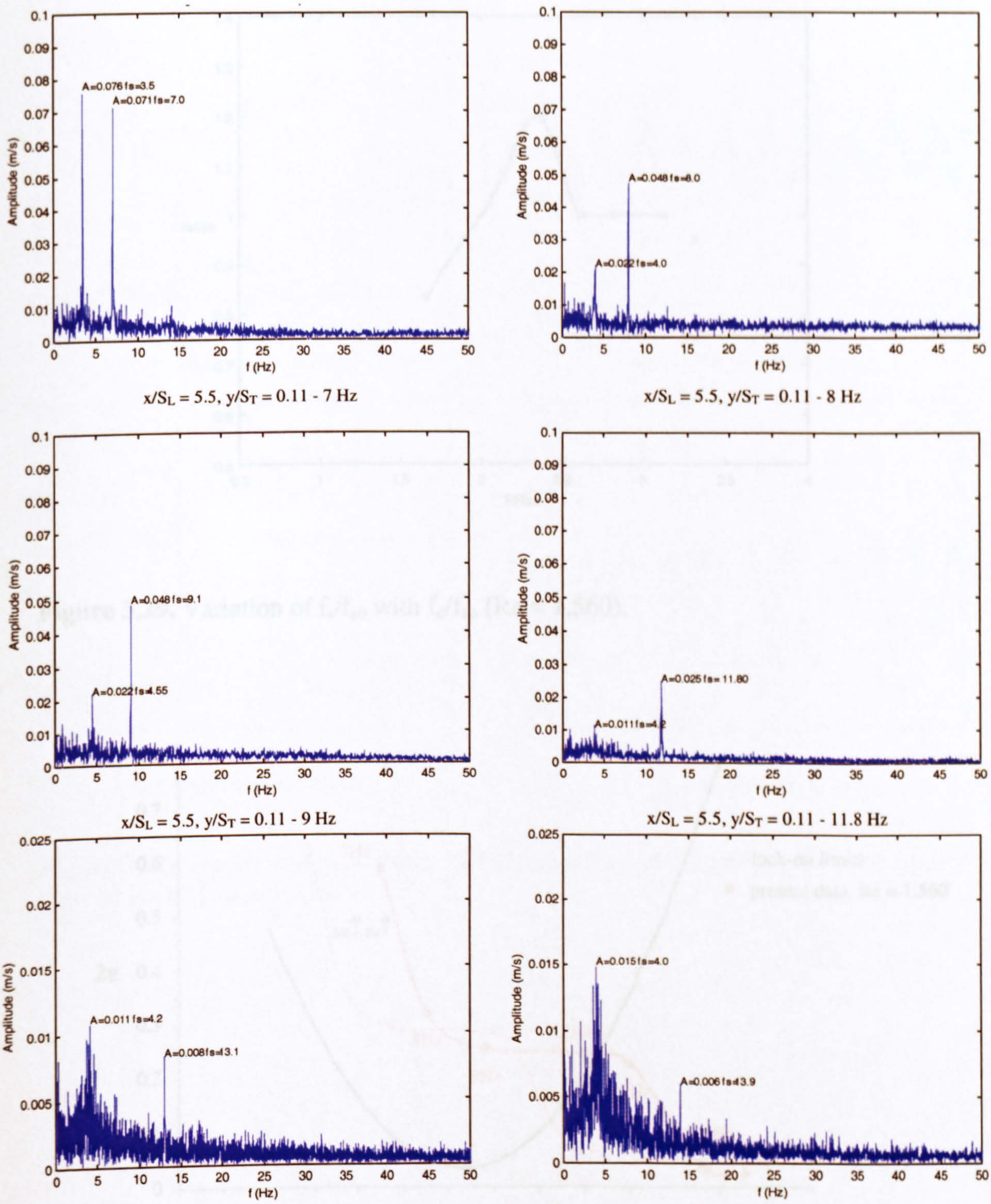

Figure 3.28. Velocity amplitude spectra obtained behind the last cylinder in the in-line tube bundle with elliptic cylinders under pulsating flow conditions and frequencies varying between 7 Hz and 13.9 Hz (Re = 1,560).

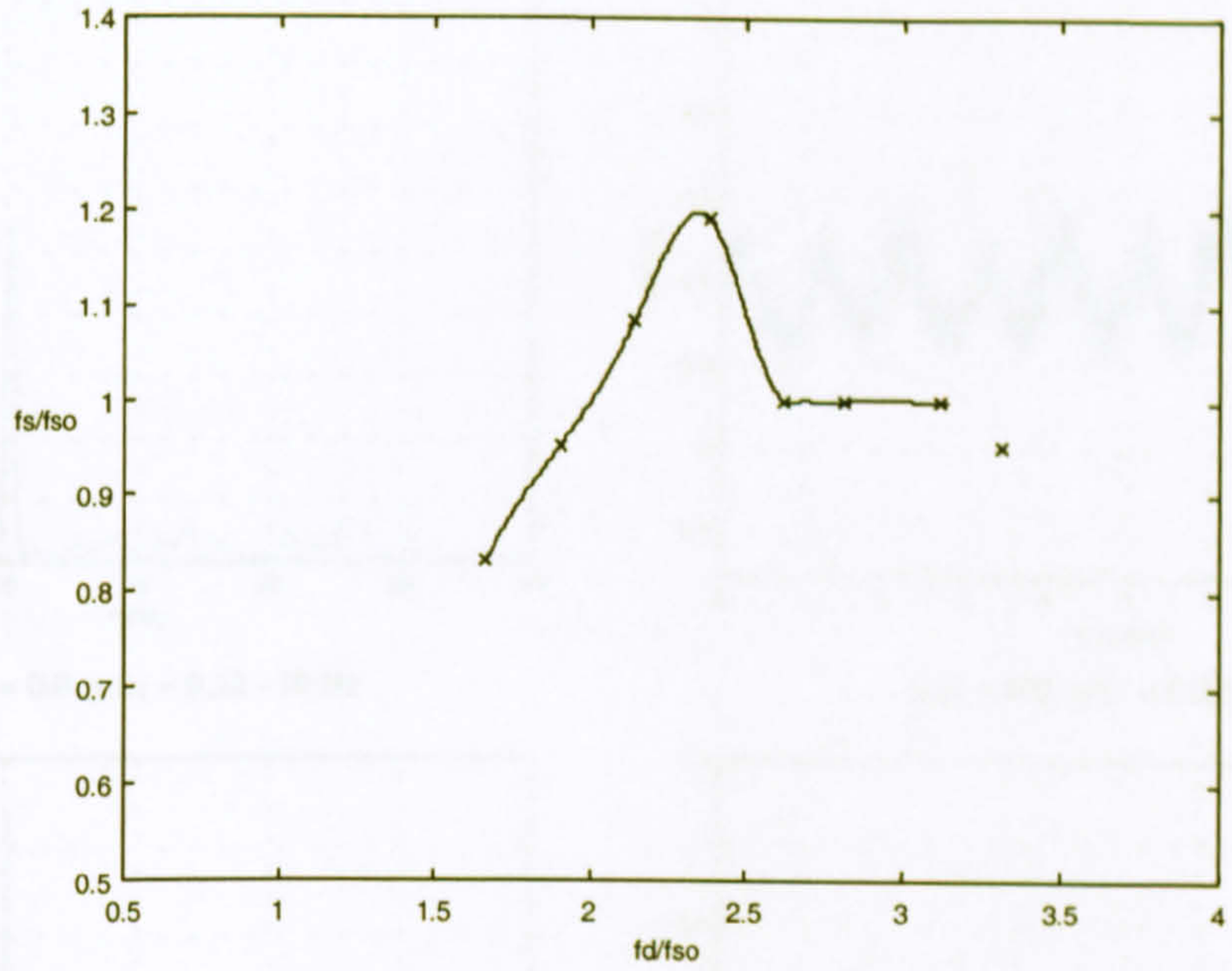

Figure 3.29. Variation of f_s/f_{so} with f_d/f_{so} (Re = 1,560).

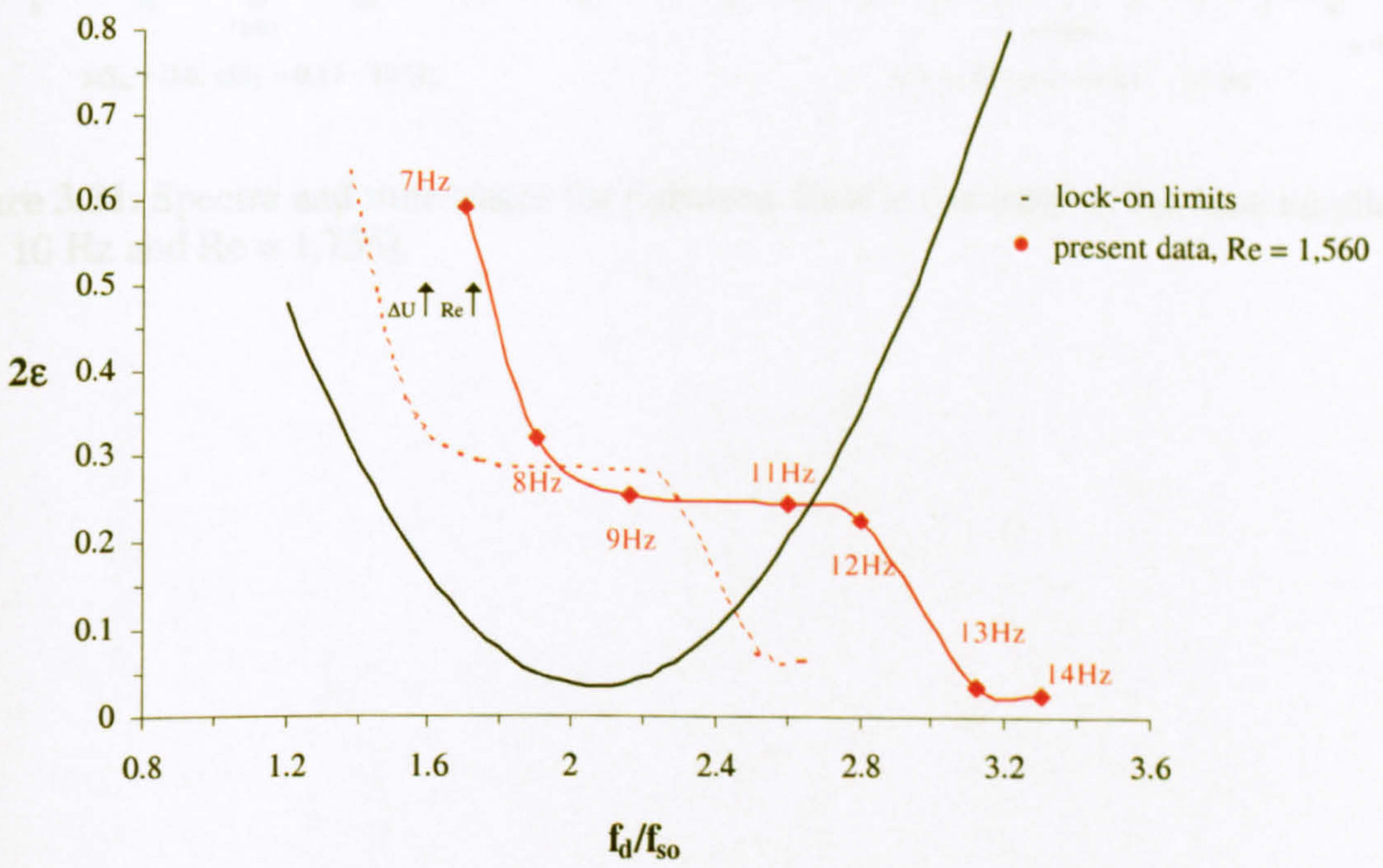

Figure 3.30. Variation of 2ε with f_d/f_{so} and lock-on limits in the in-line tube bundle with elliptic tubes under pulsating flow conditions.

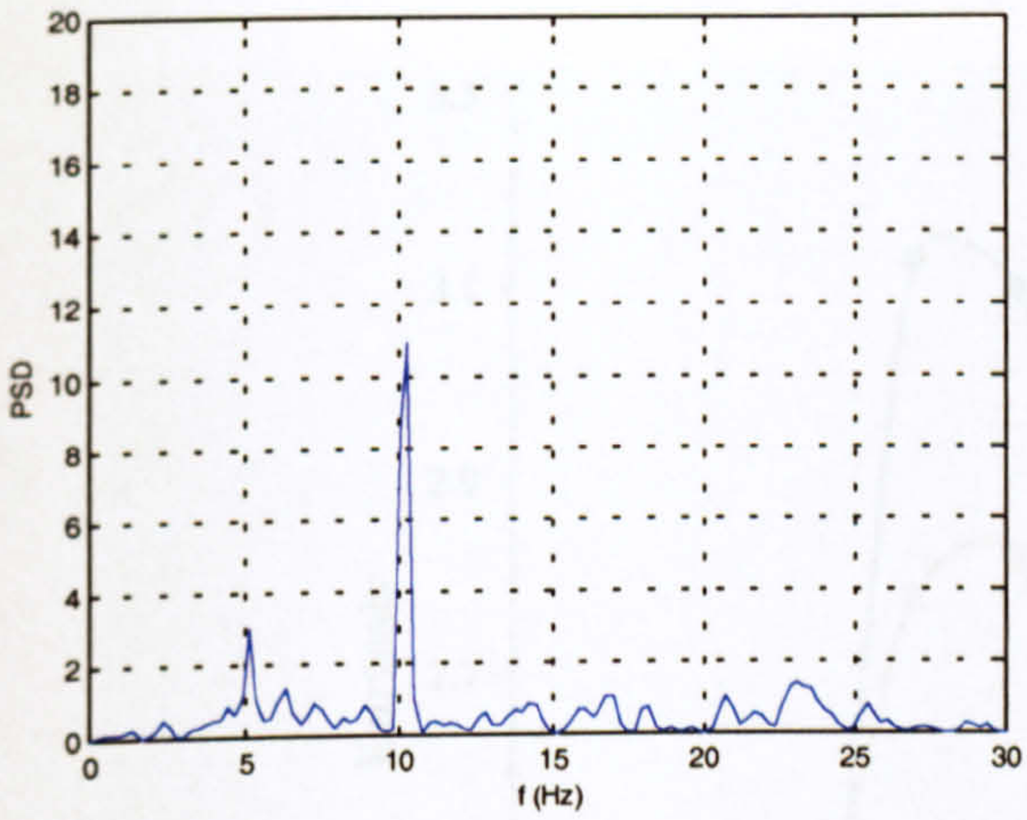

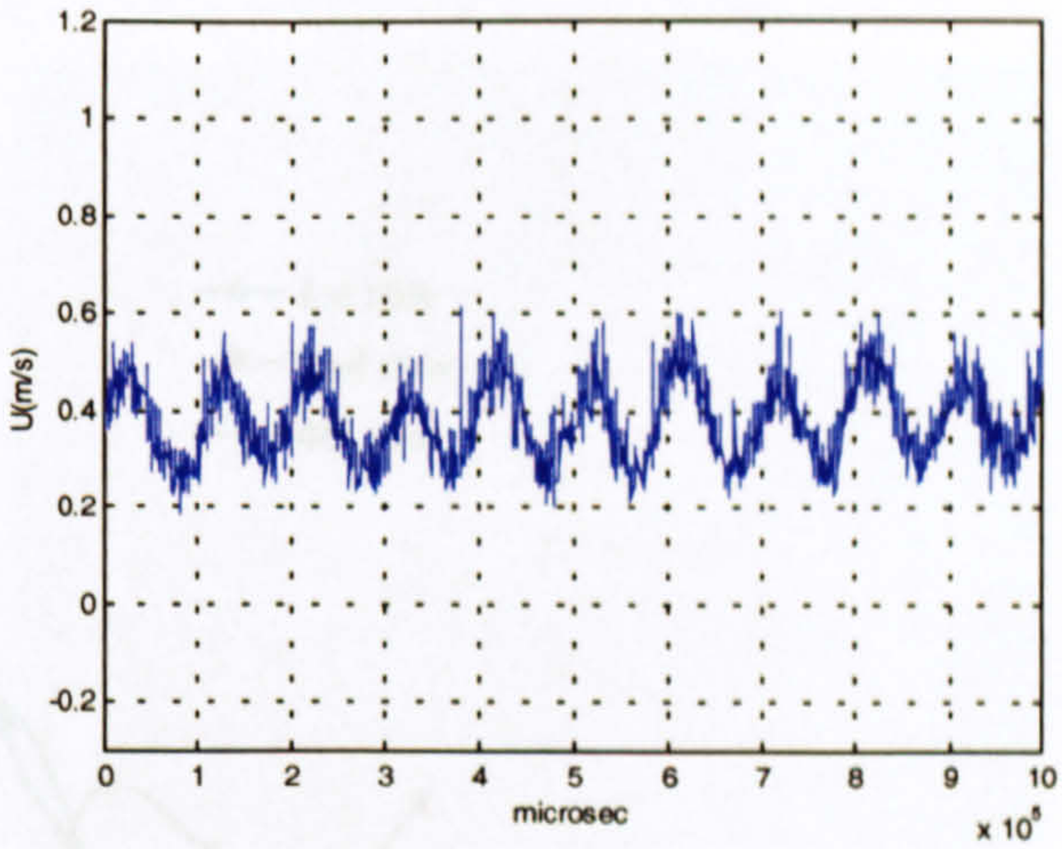

$x/S_L = 0.0$, $y/S_T = 0.22$ - 10 Hz

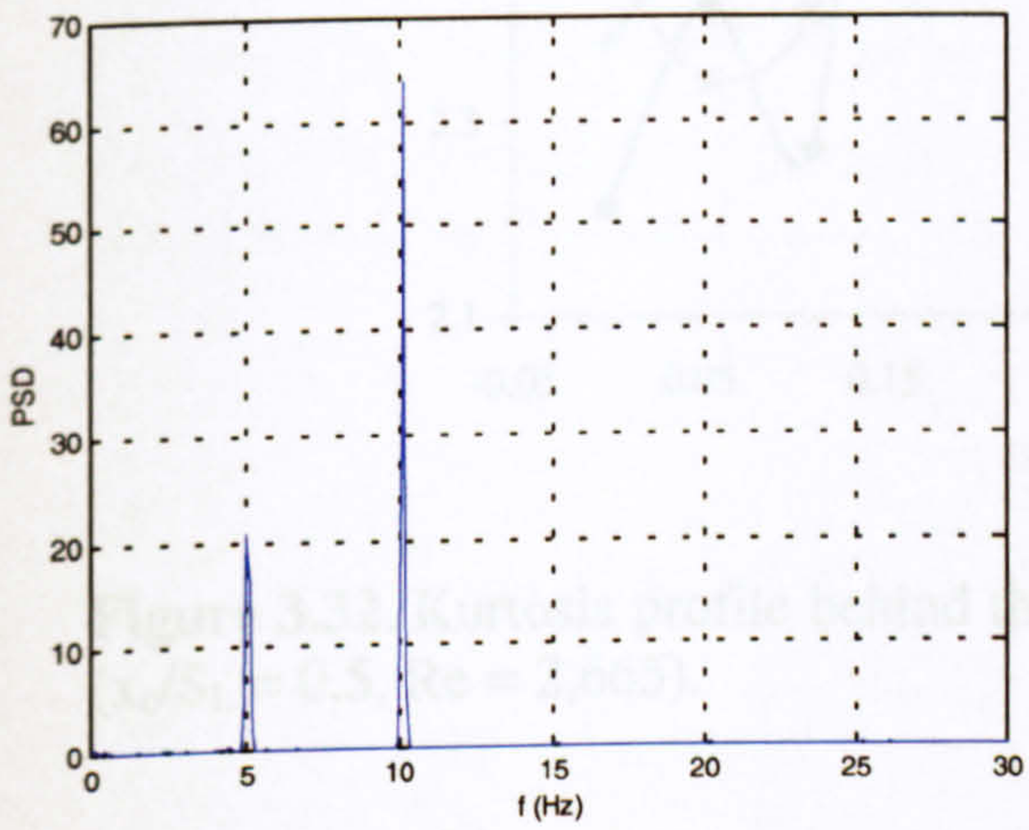

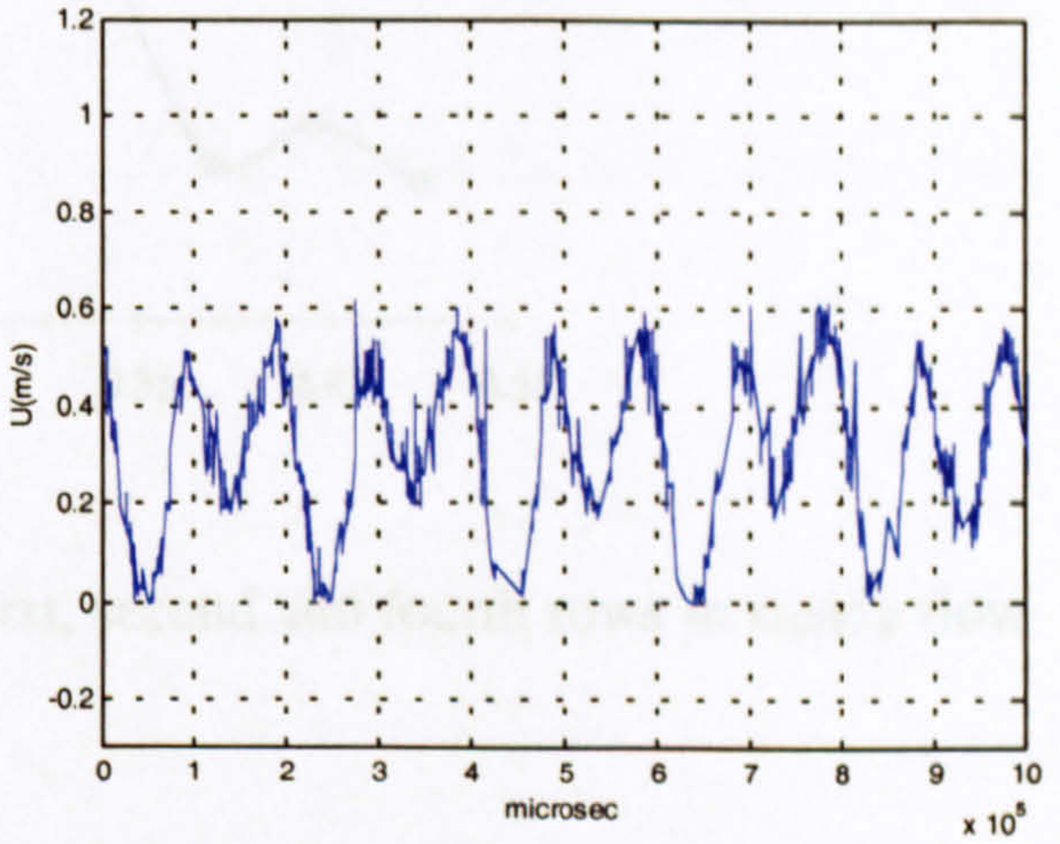

$x/S_L = 0.0$, $y/S_T = 0.11$ - 10 Hz

$x/S_L = 0.0$, $y/S_T = 0.11$ - 10 Hz

Figure 3.31. Spectra and time traces for pulsating flow at the inlet of the tube bundle (f_d = 10 Hz and Re = 1,755).

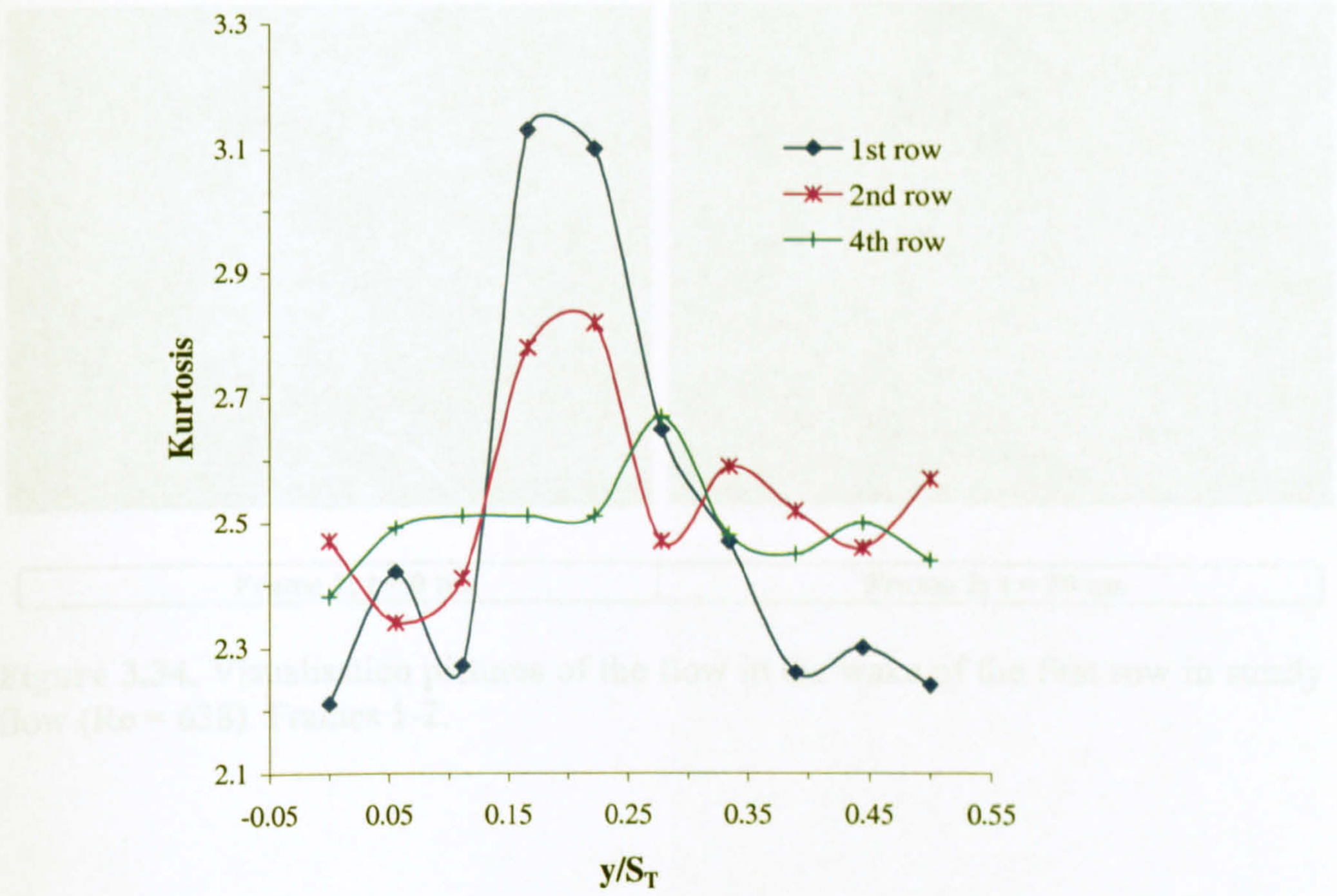

Figure 3.32. Kurtosis profile behind the first, second and fourth rows in steady flow ($x_c/S_L = 0.5$, Re = 2,665).

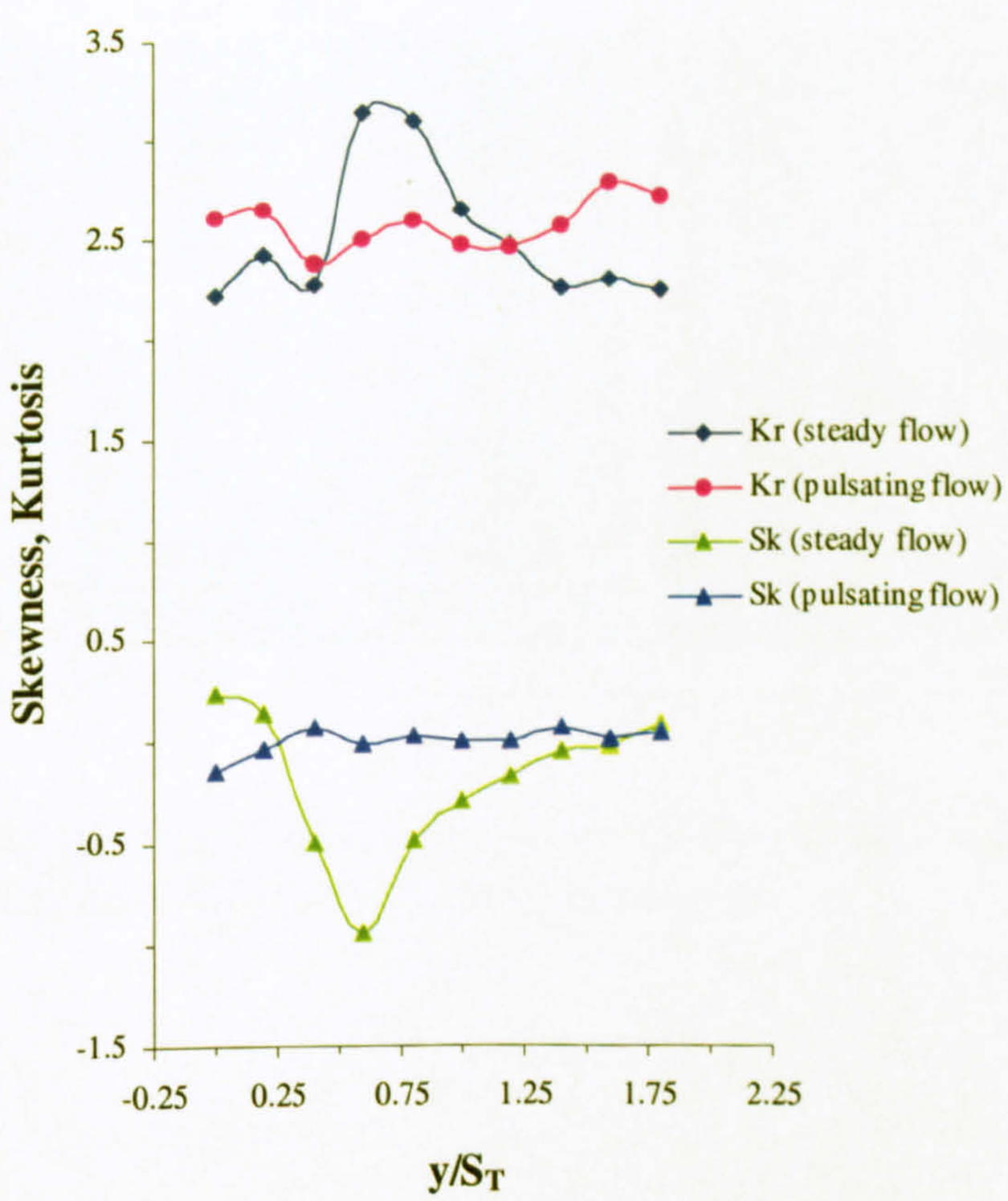

Figure 3.33. Skewness and kurtosis profiles behind the first row ($x/S_L = 0.5$, Re = 2,665) in both steady and pulsating flow past the elliptic cylinder array.

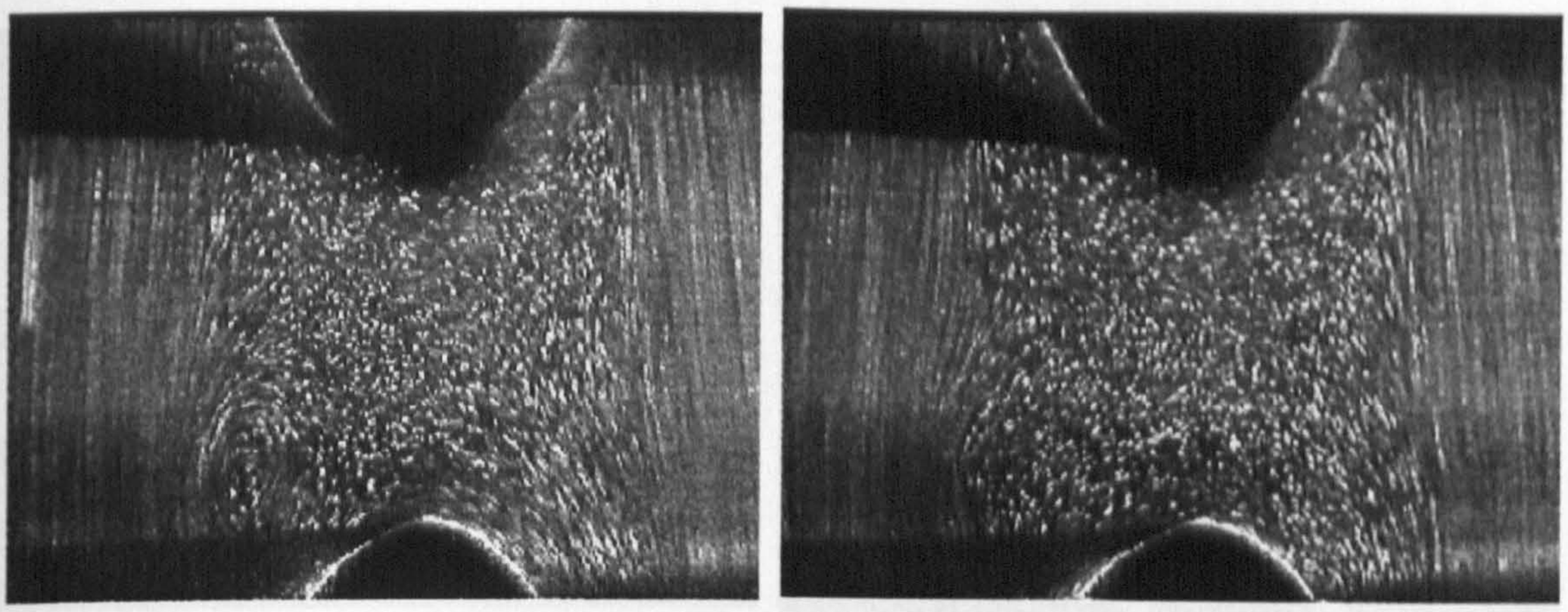

Frame 1; t = 0 ms	Frame 2; t = 20 ms

Figure 3.34. Visualisation pictures of the flow in the wake of the first row in steady flow (Re = 638). Frames 1-2.

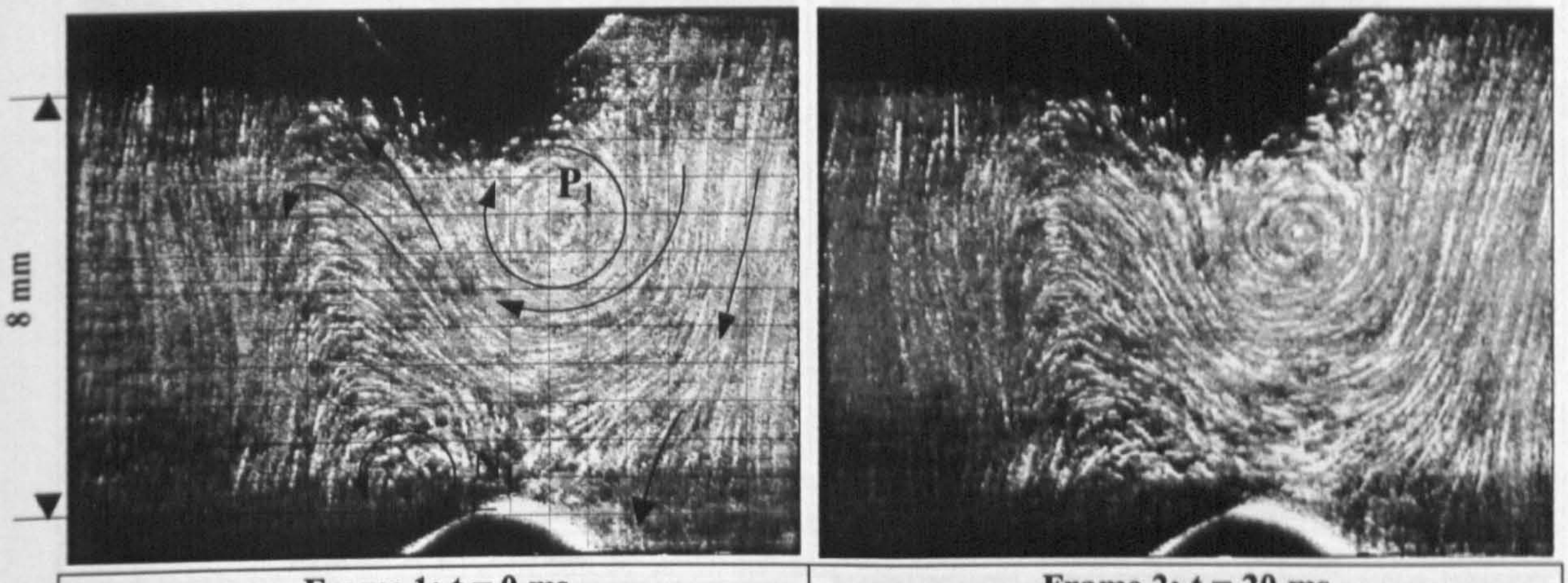

Frame 1; t = 0 ms	Frame 2; t = 20 ms
Frame 3; t = 40 ms	Frame 4; t = 60 ms
Frame 5; t = 80 ms	Frame 6; t = 100 ms

Figure 3.35 (a). Visualisation pictures of the flow in the wake of the fourth cylinder (steady flow, Re = 638, f_{so} = 1.7 Hz). Frames 1-6.

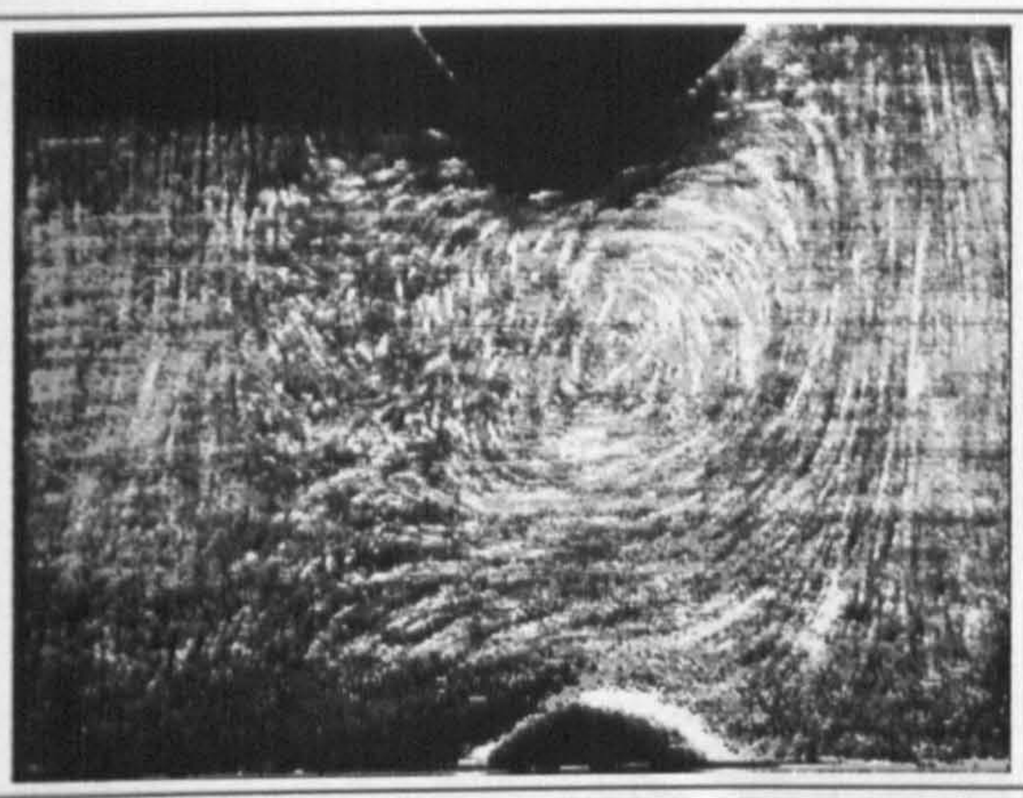

Frame 7; t = 120 ms

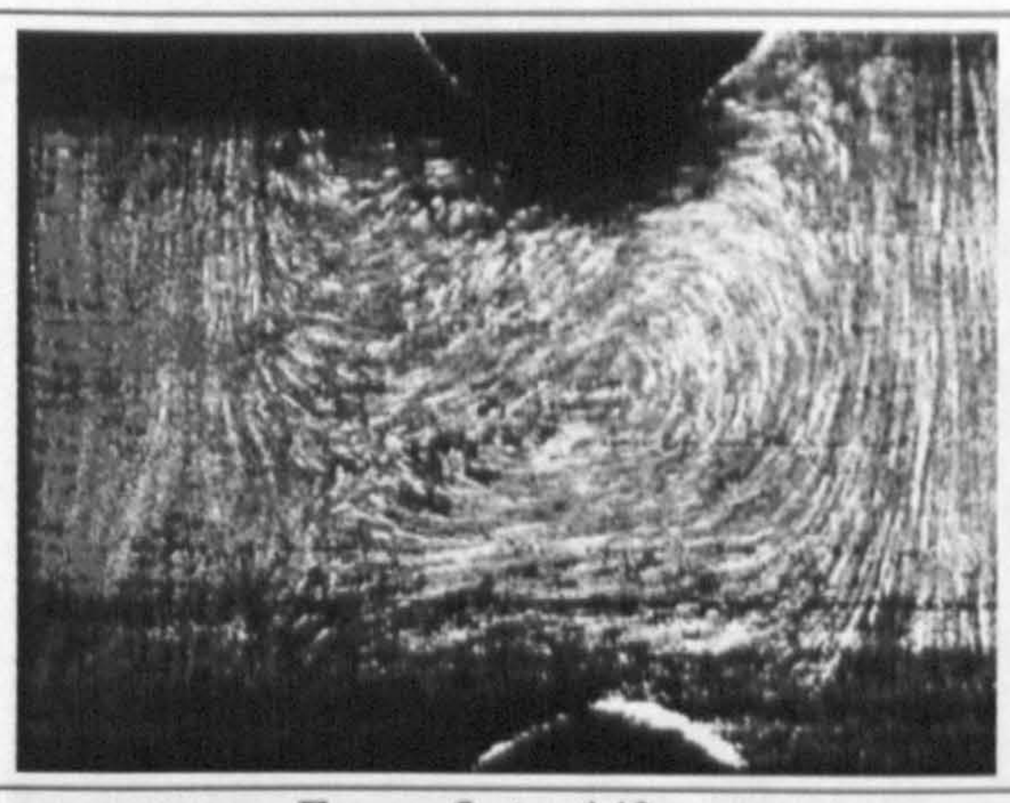

Frame 8; t = 140 ms

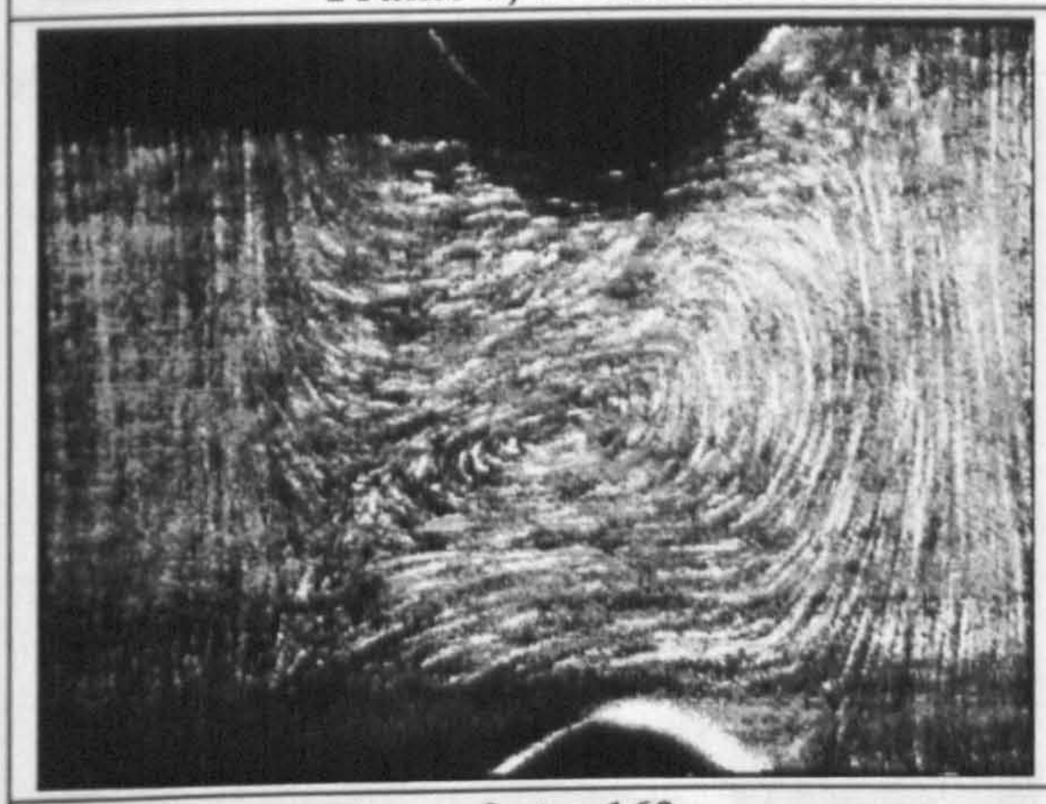

Frame 9; t = 160 ms

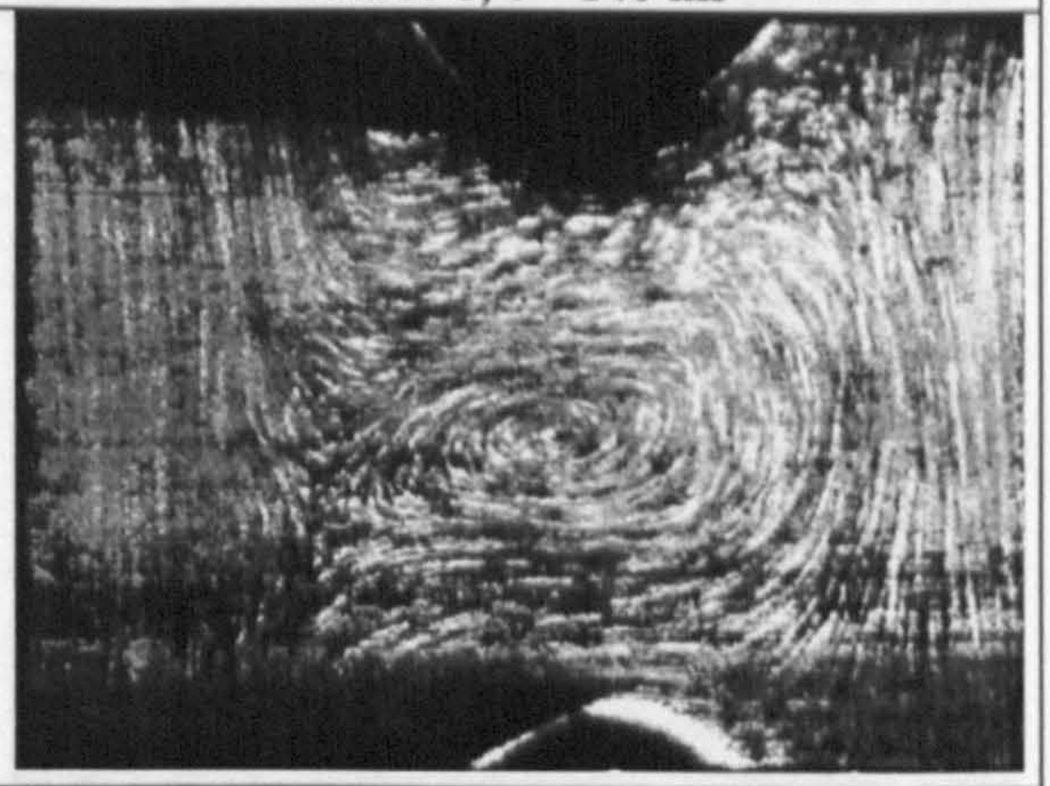

Frame 10; t = 180 ms

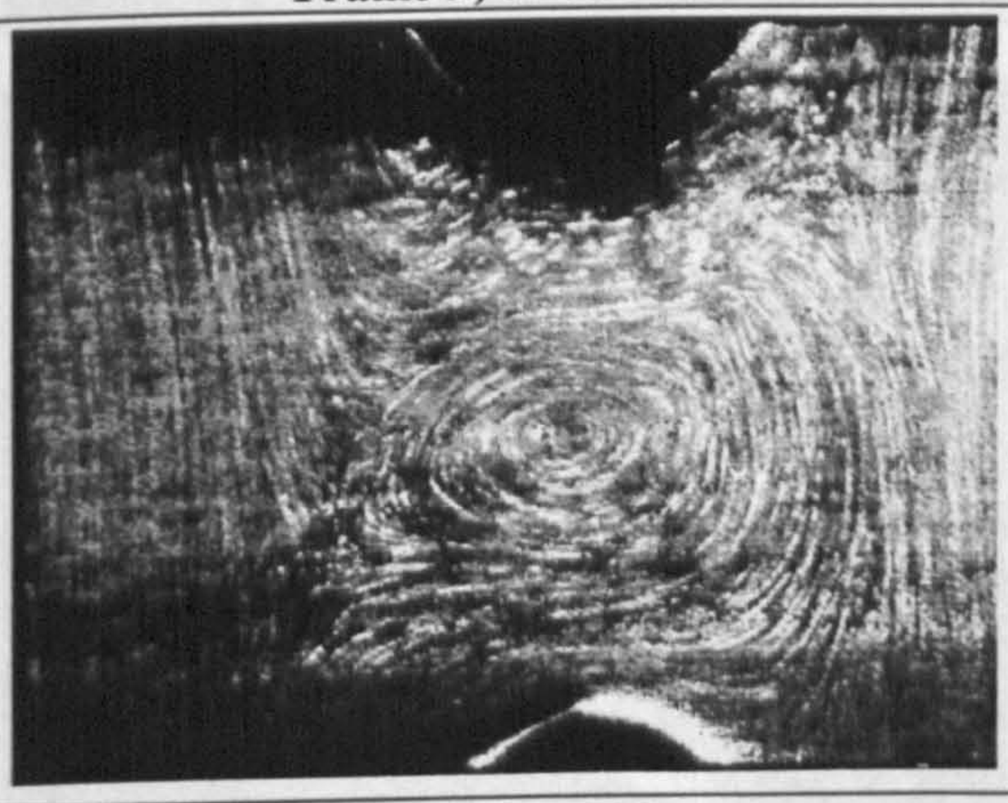

Frame 11; t = 200 ms

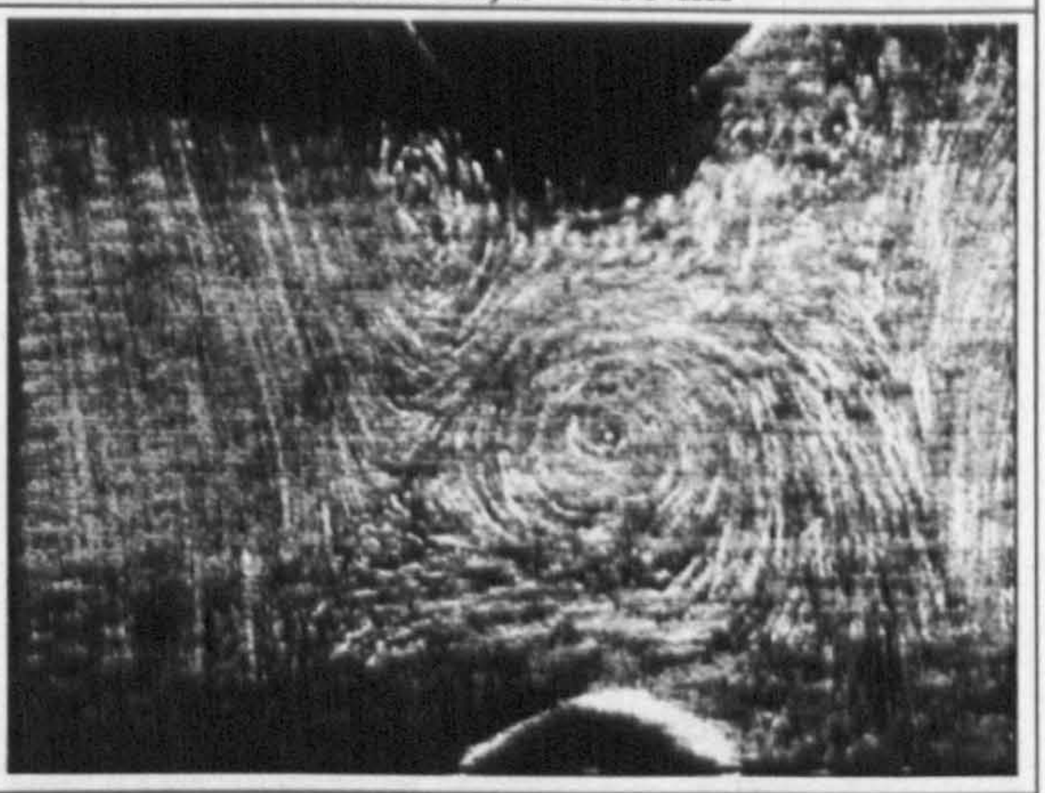

Frame 12; t = 220 ms

Figure 3.35 (b). Visualisation pictures of the flow in the wake of the fourth cylinder (steady flow, Re = 638, f_{so} = 1.7 Hz). Frames 7-12.

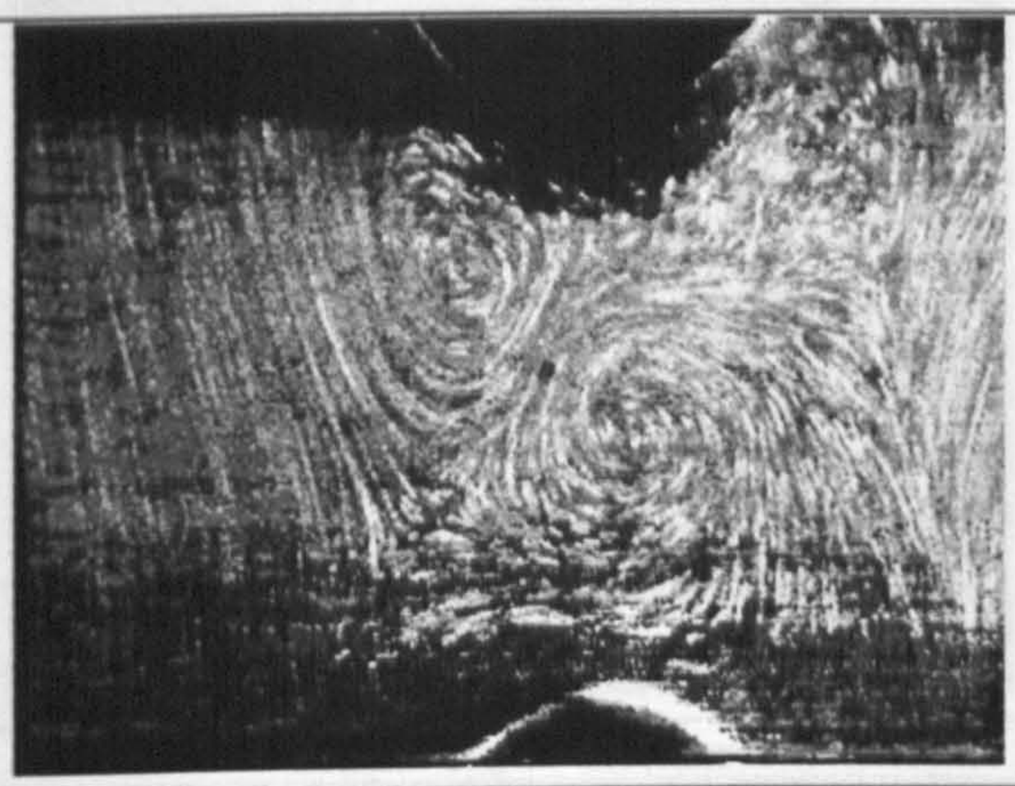

Frame 13; t = 240 ms

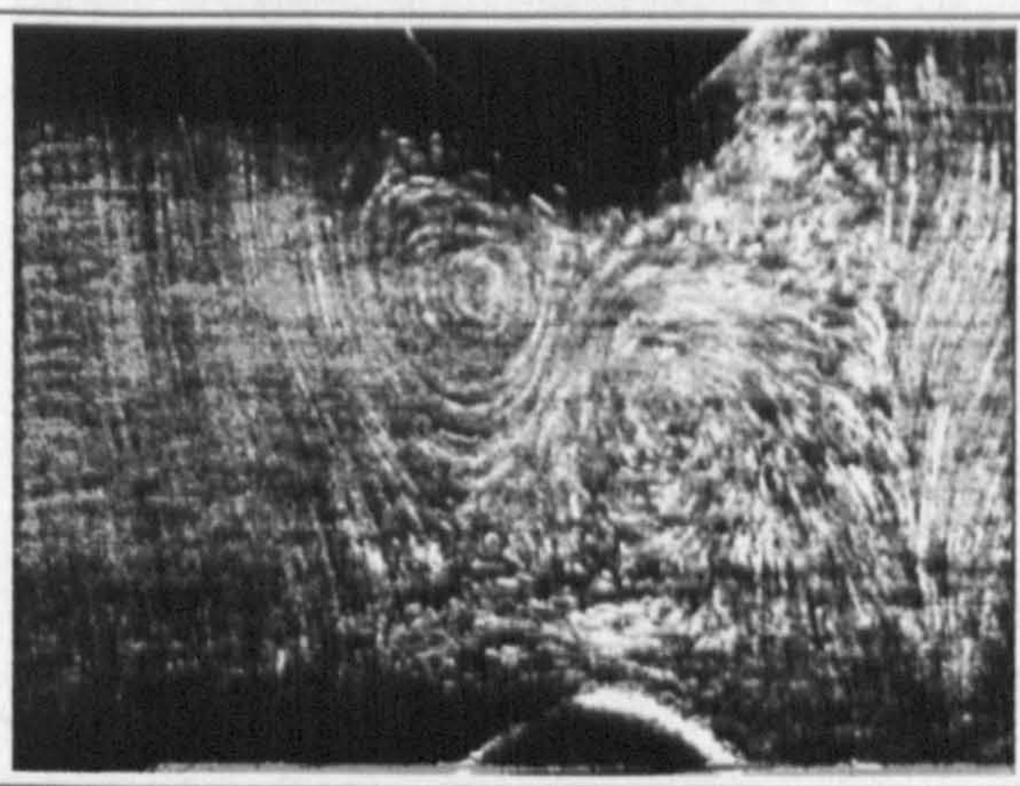

Frame 14; t = 260 ms

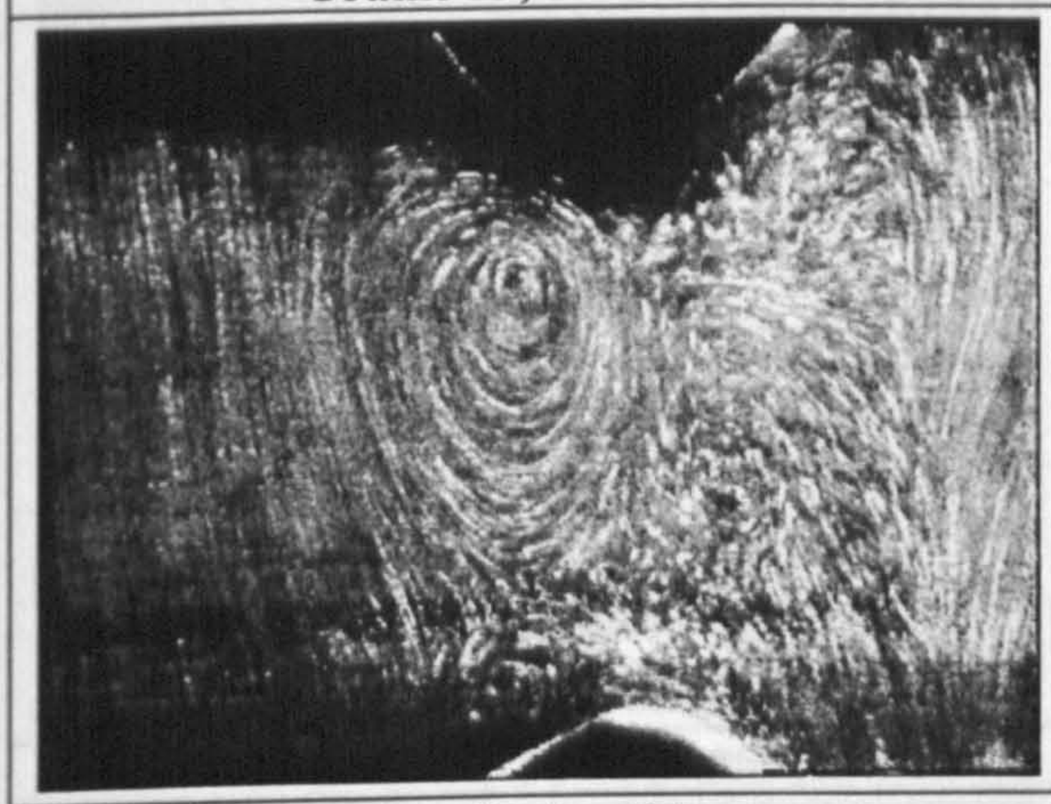

Frame 15; t = 280 ms

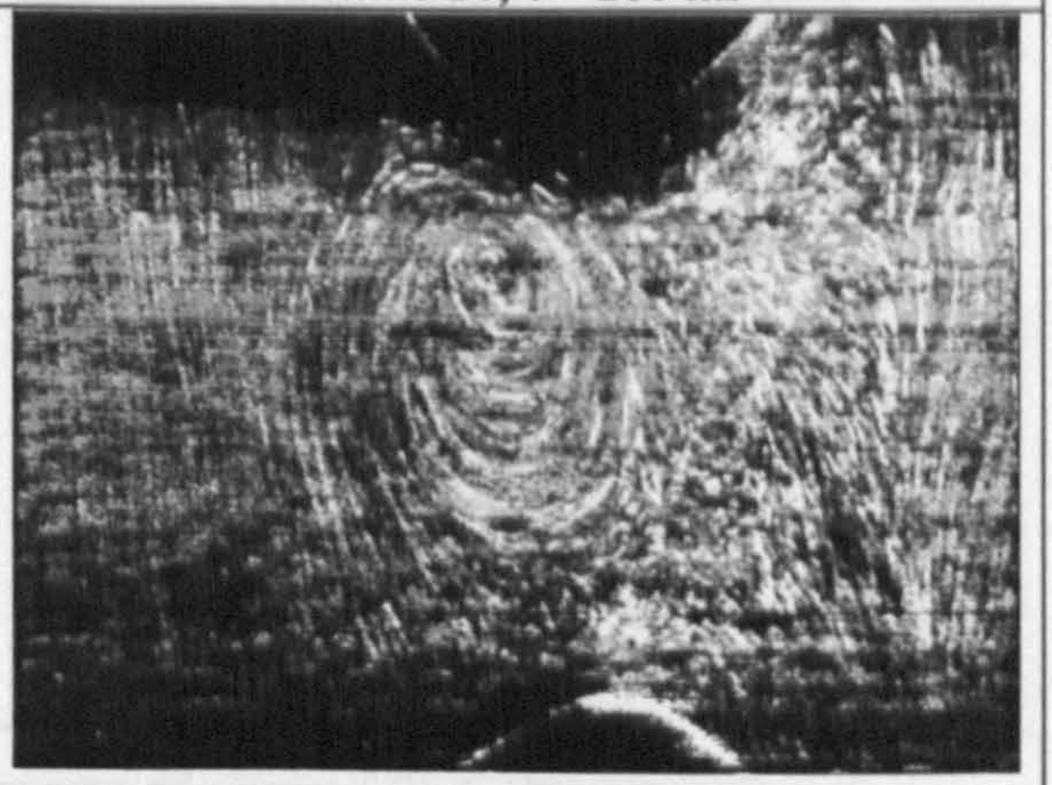

Frame 16; t = 300 ms

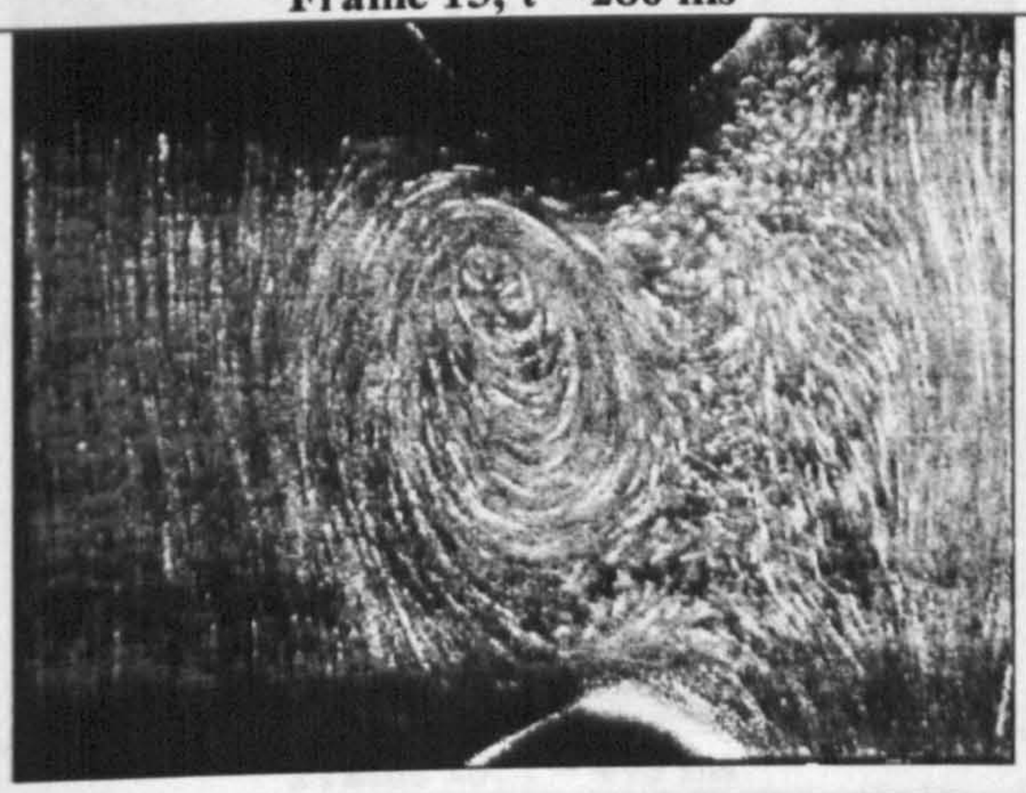

Frame 17; t = 320 ms

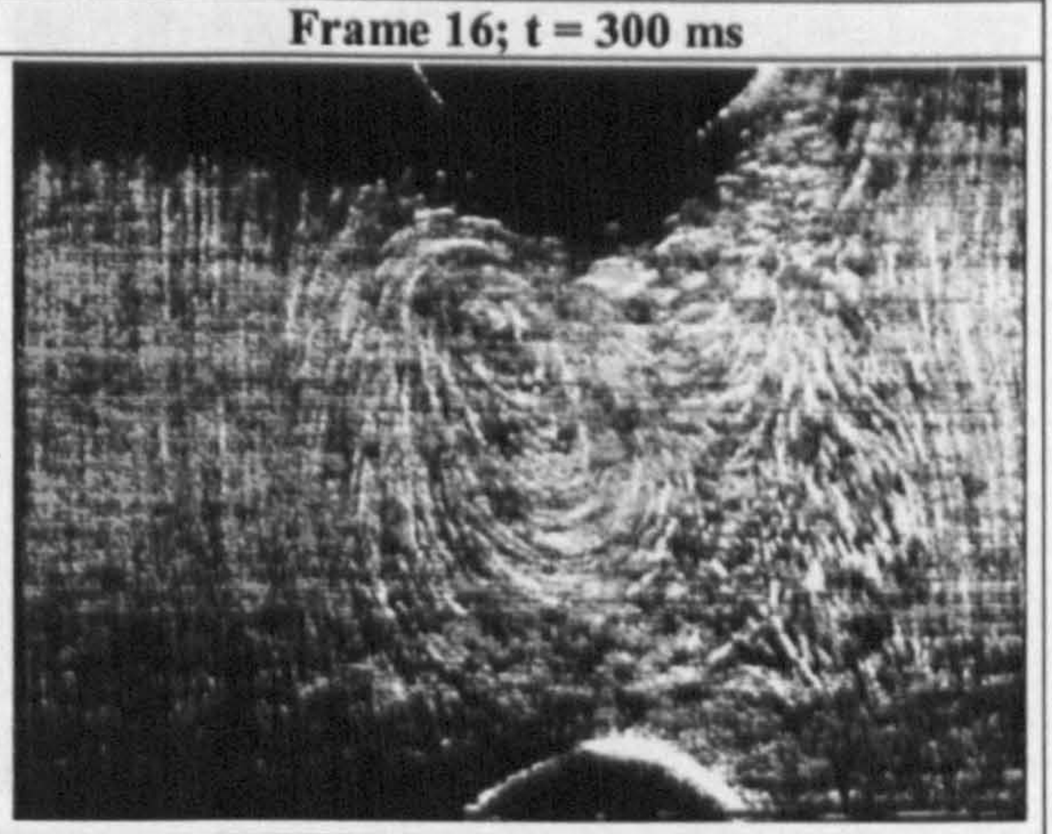

Frame 18; t = 340 ms

Figure 3.35 (c). Visualisation pictures of the flow in the wake of the fourth cylinder (steady flow, Re = 638, f_{so} = 1.7 Hz). Frames 13-18.

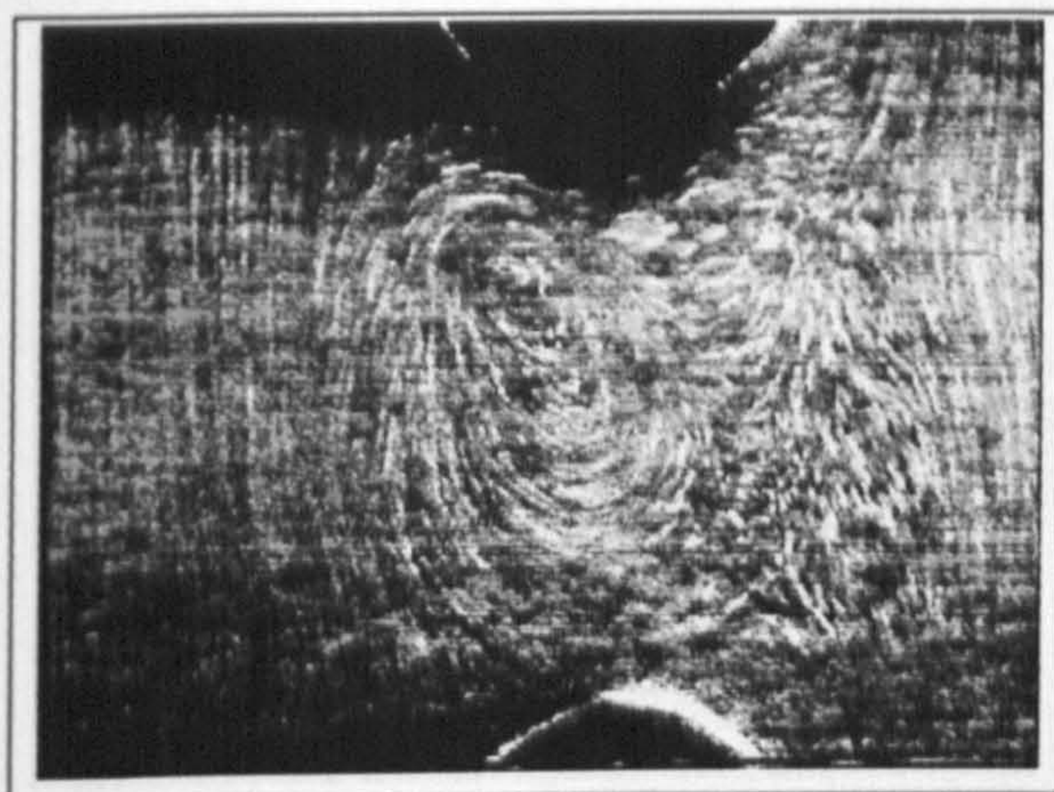

Frame 19; t = 360 ms

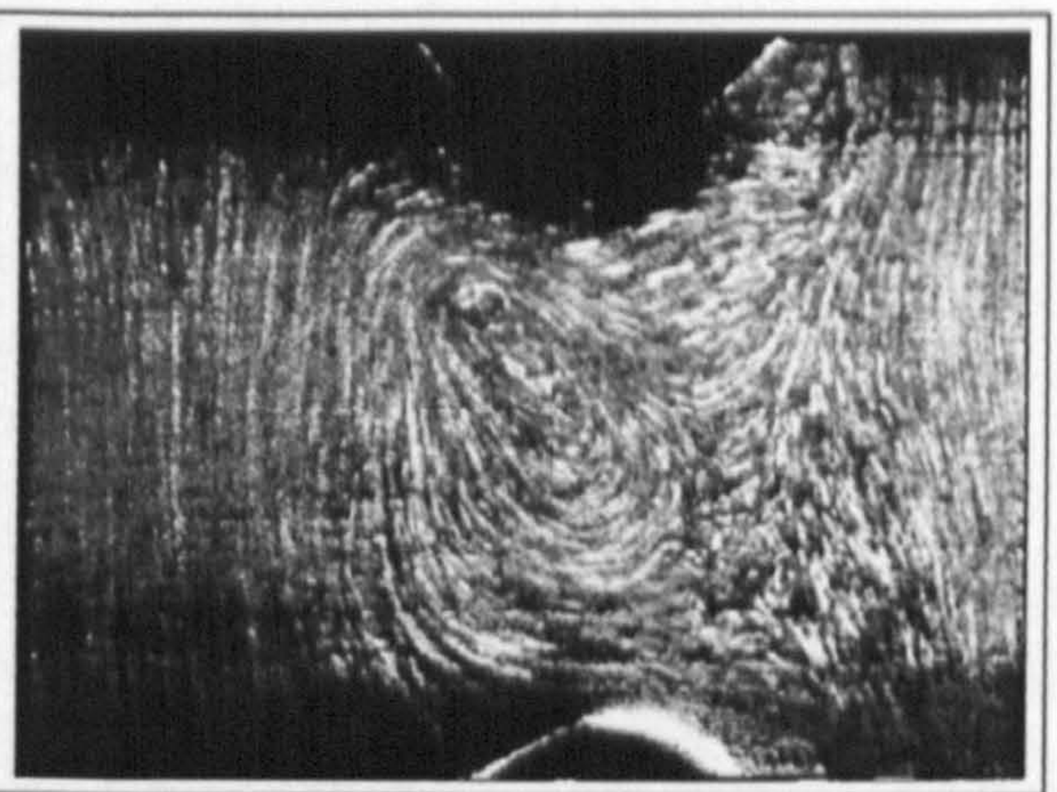

Frame 20; t = 380 ms

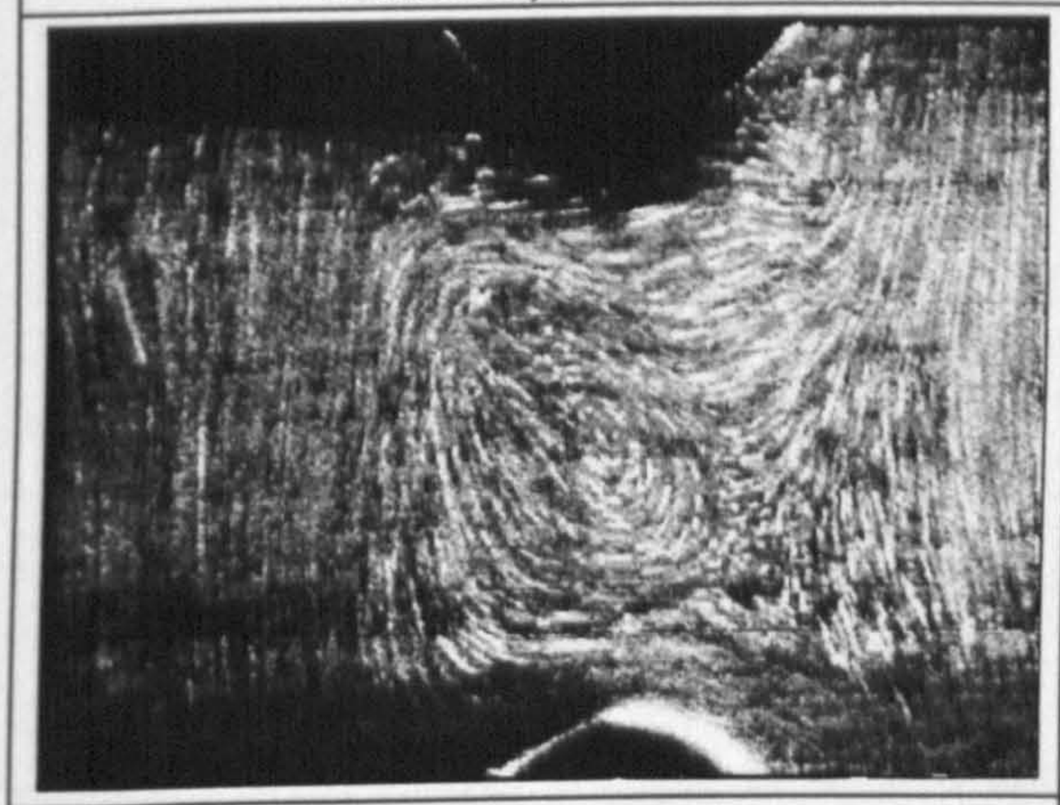

Frame 21; t = 400 ms

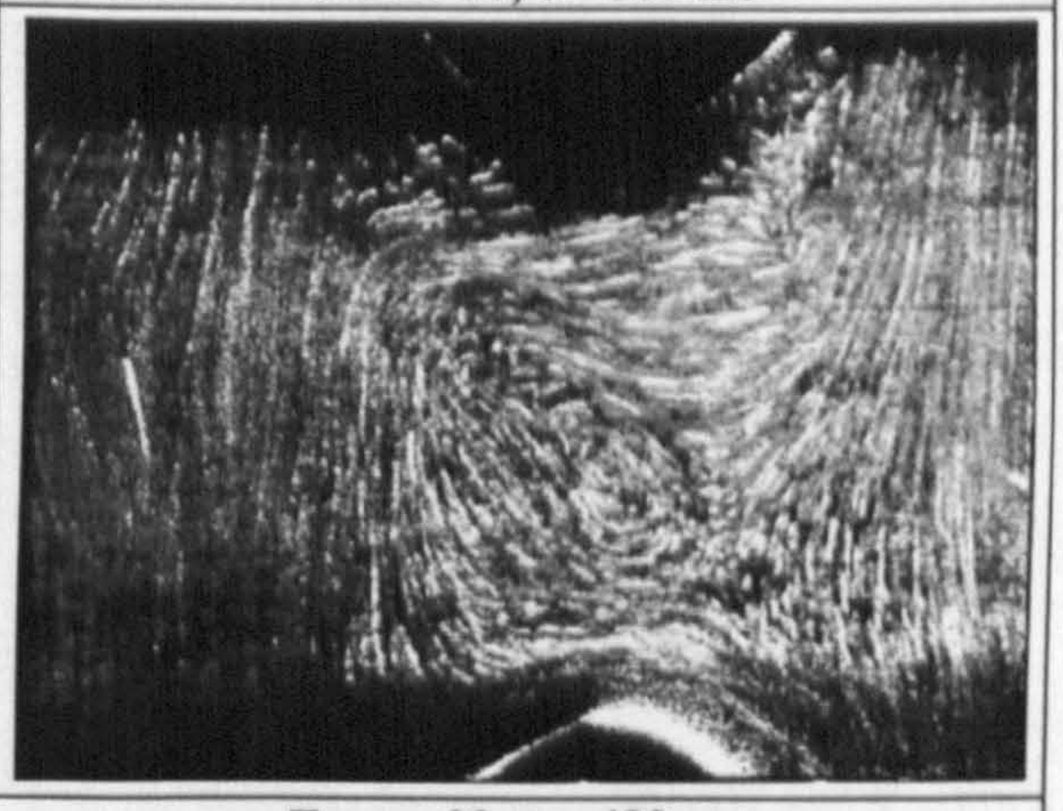

Frame 22; t = 420 ms

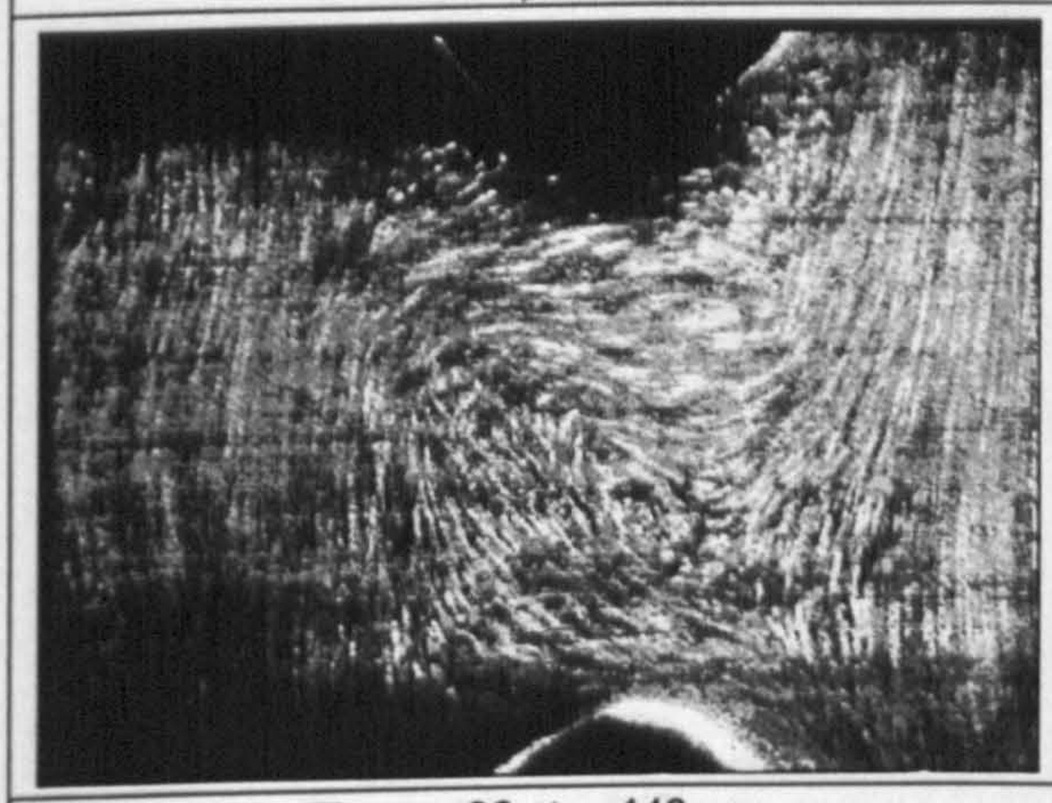

Frame 23; t = 440 ms

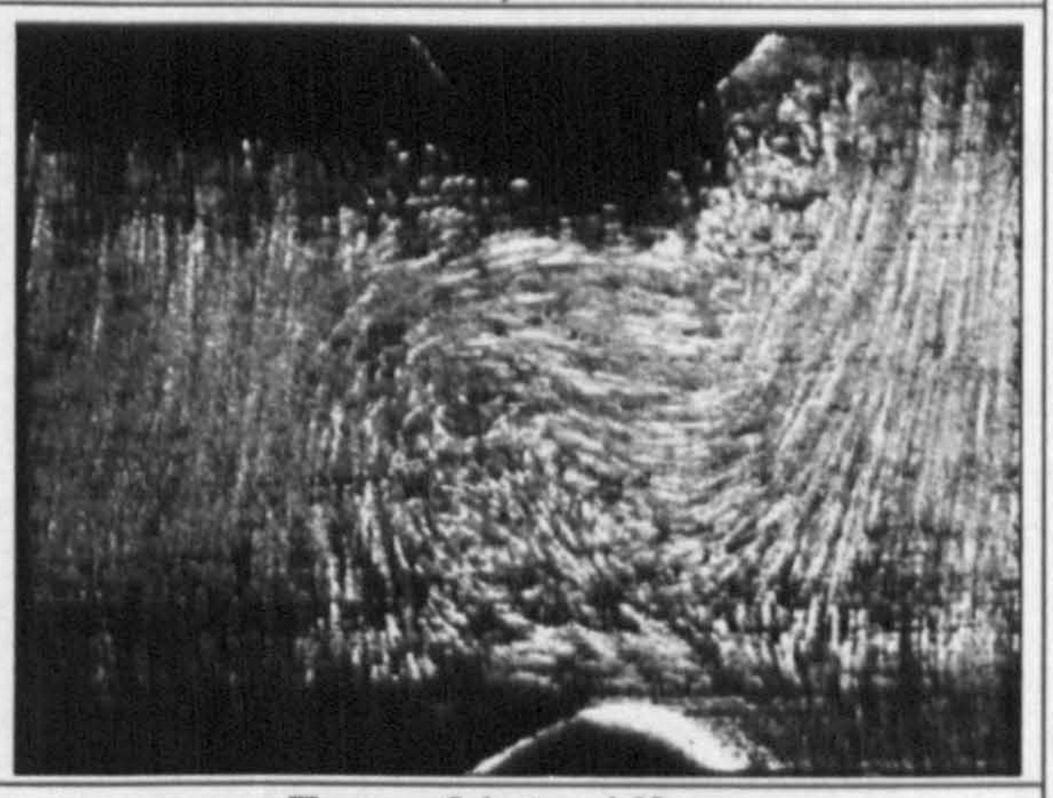

Frame 24; t = 460 ms

Figure 3.35 (d). Visualisation pictures of the flow in the wake of the fourth cylinder (steady flow, Re = 638, f_{so} = 1.7 Hz). Frames 19-24.

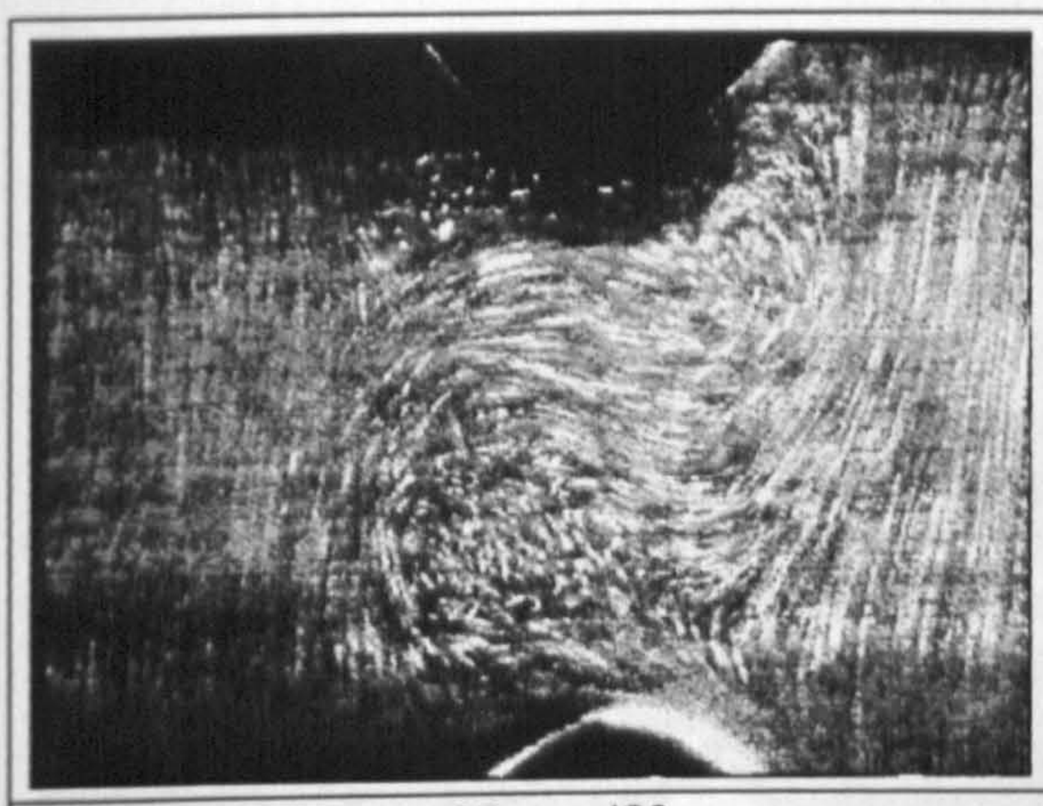

Frame 25; t = 480 ms

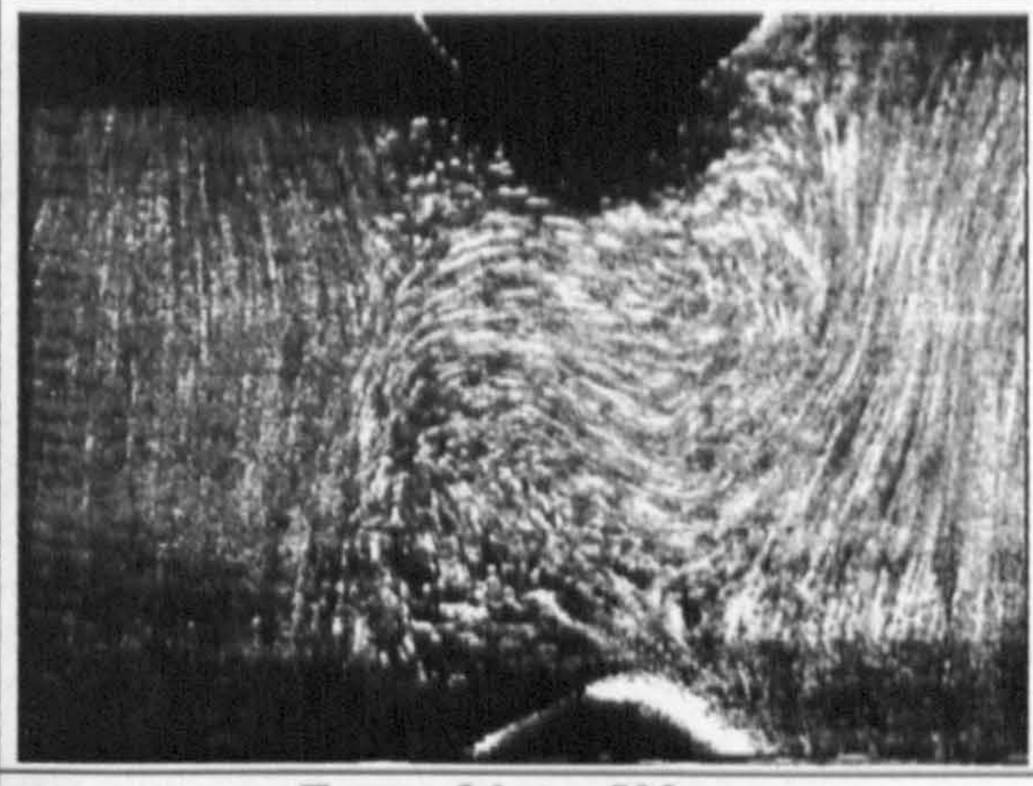

Frame 26; t = 500 ms

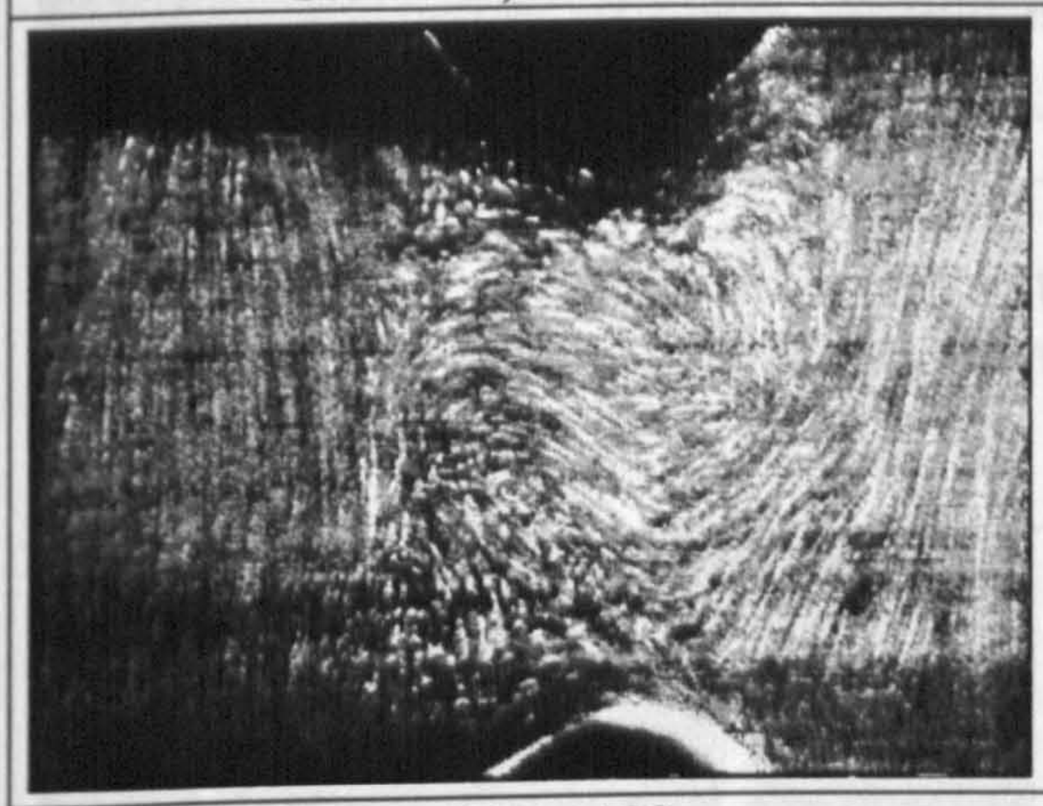

Frame 27; t = 520 ms

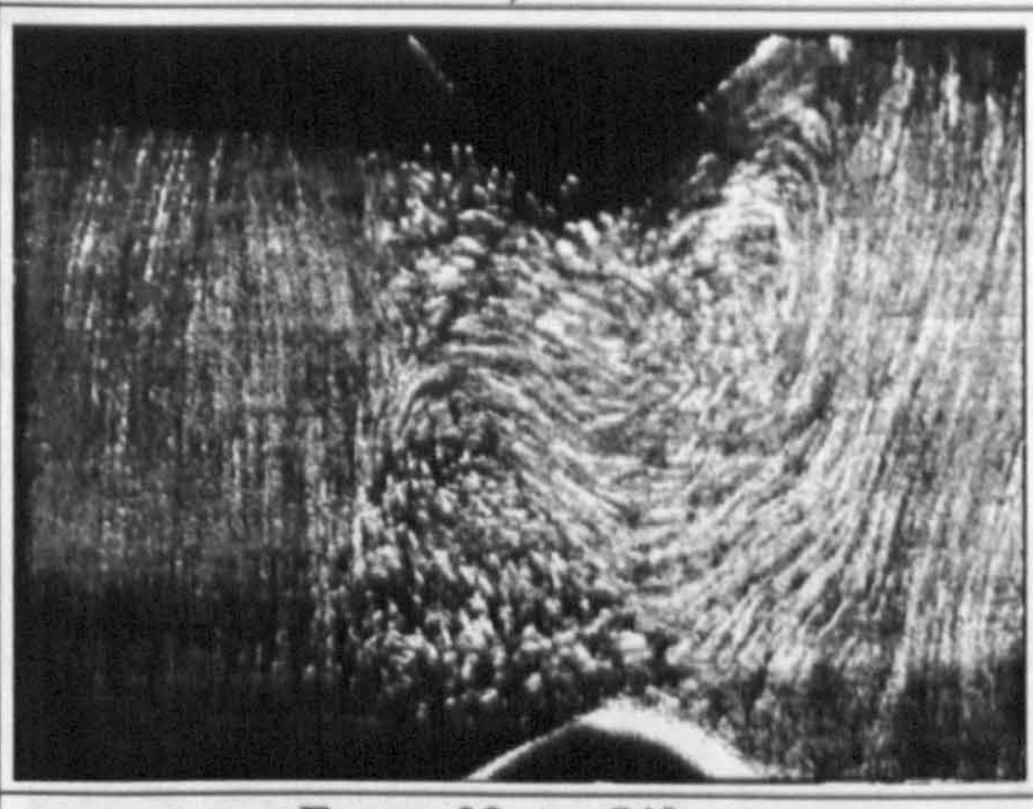

Frame 28; t = 540 ms

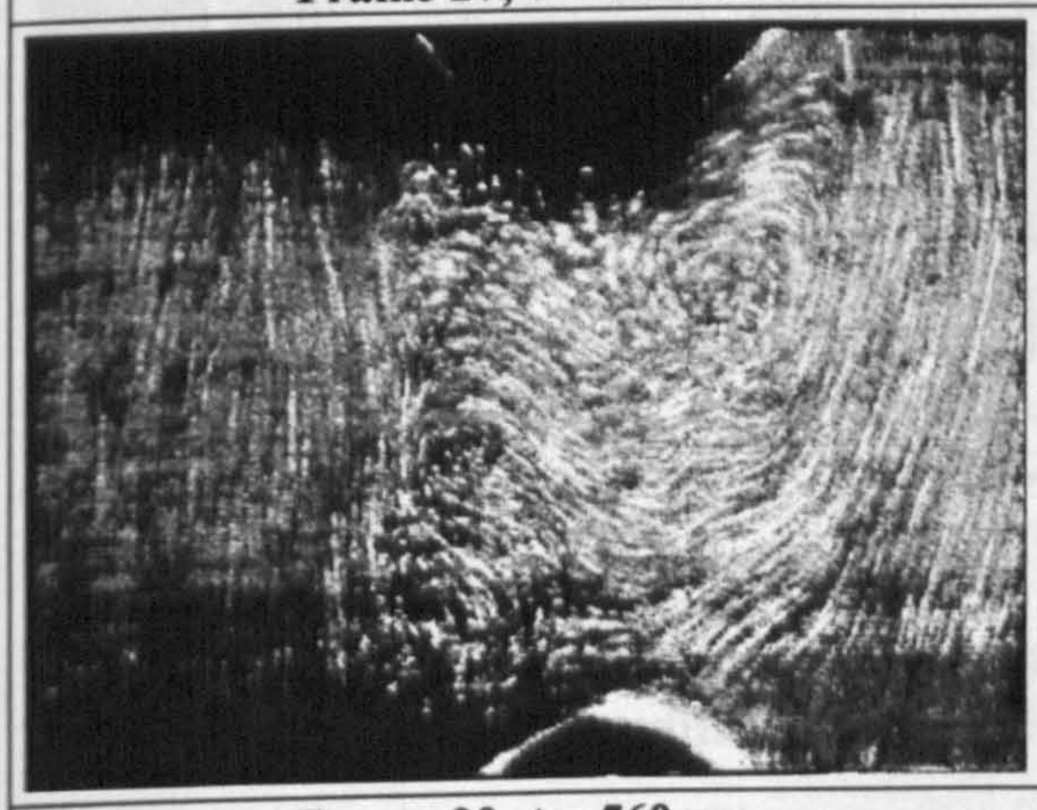

Frame 29; t = 560 ms

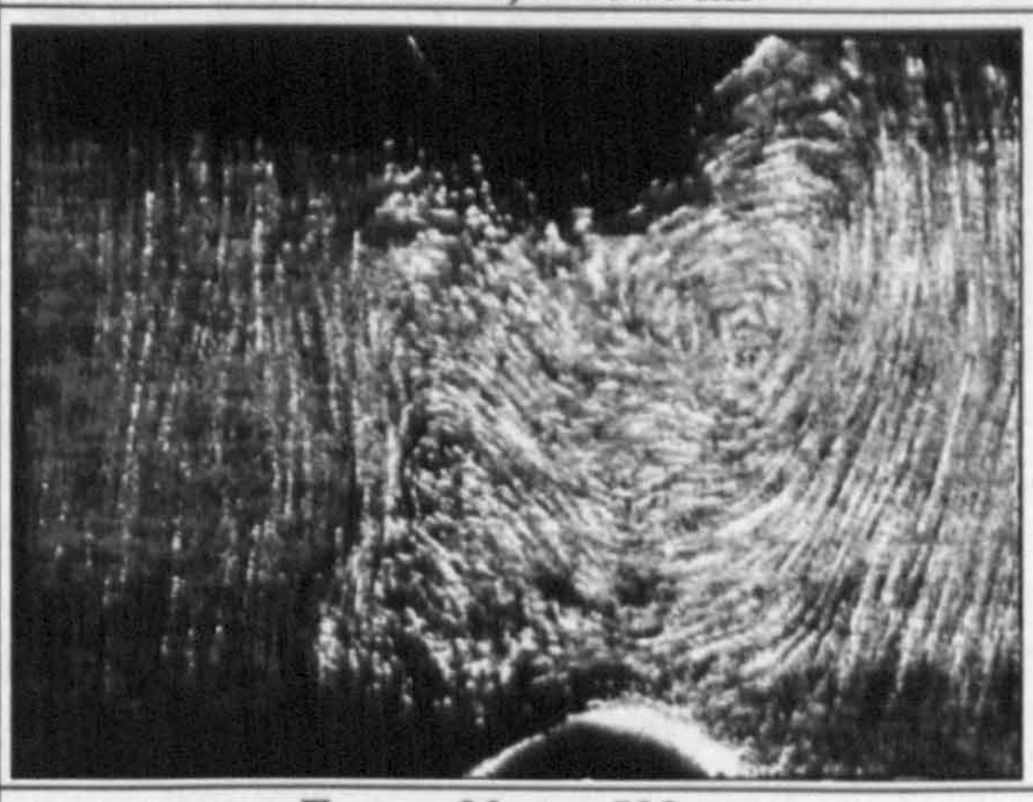

Frame 30; t = 580 ms

Figure 3.35 (e). Visualisation pictures of the flow in the wake of the fourth cylinder (Re = 638, f_{so} = 1.7 Hz). Frames 25-30.

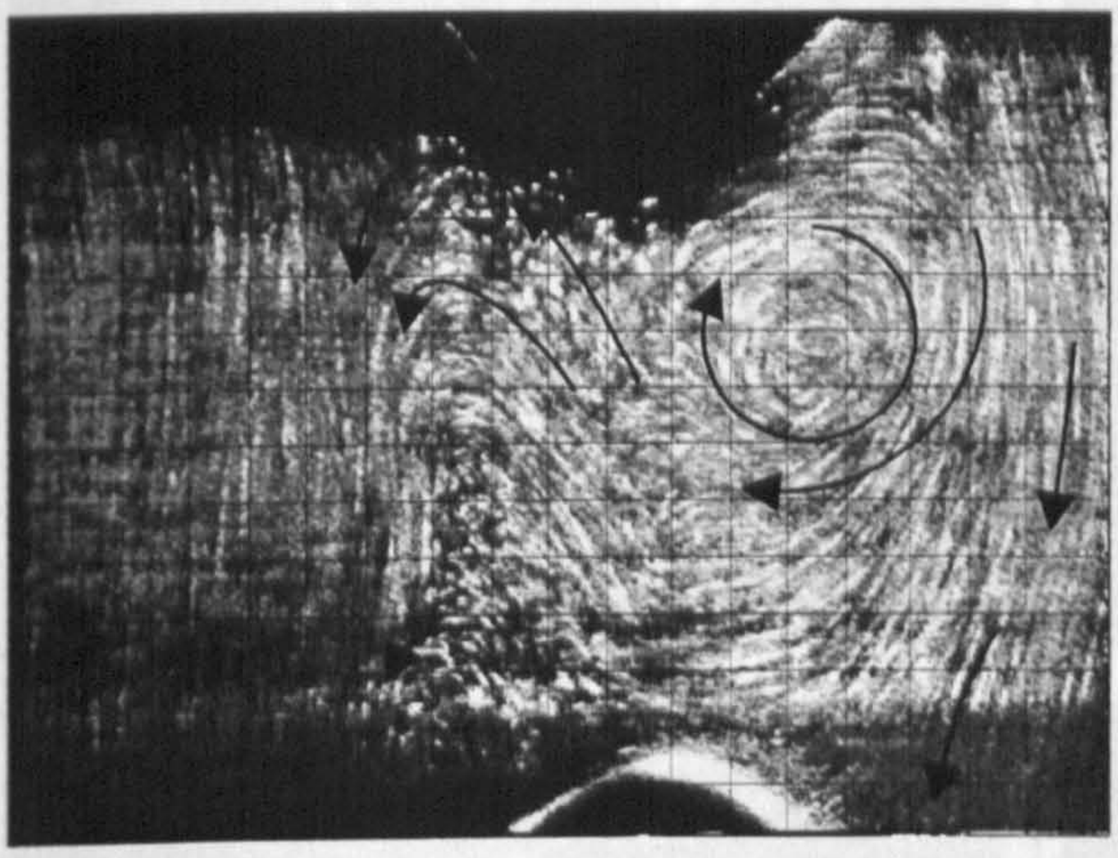

Frame 31; t = 600 ms ≅ T

Figure 3.35 (f). Visualisation picture of the flow in the wake of the fourth cylinder (steady flow, Re = 638, f_{so} = 1.7 Hz). Frame 31.

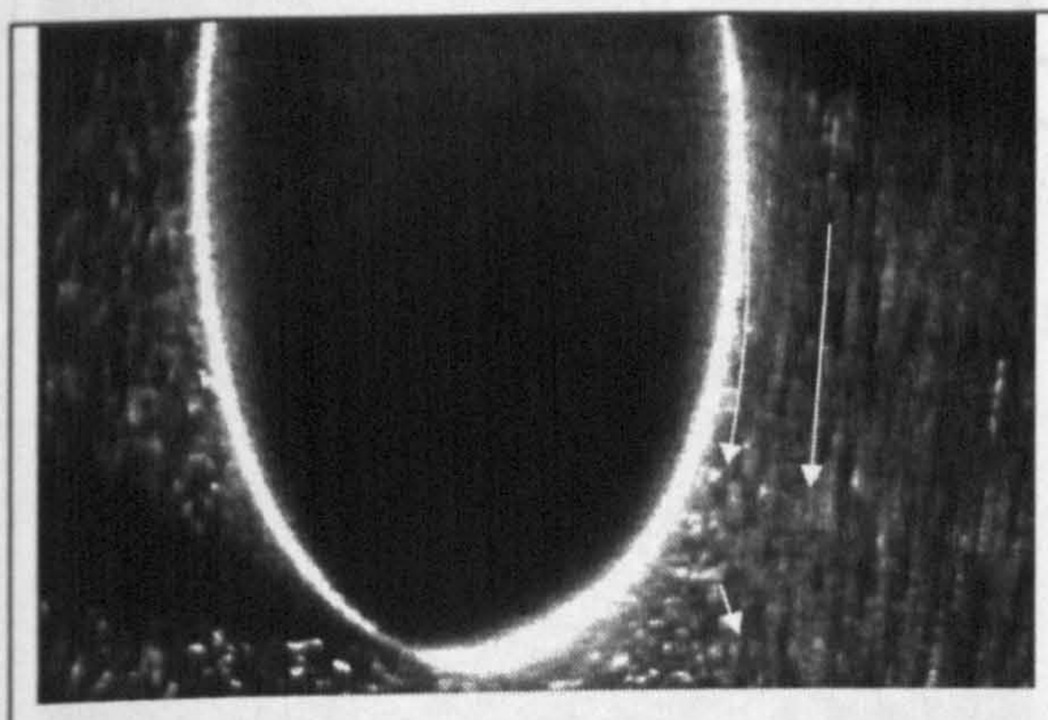

Frame 1; t = 0 ms

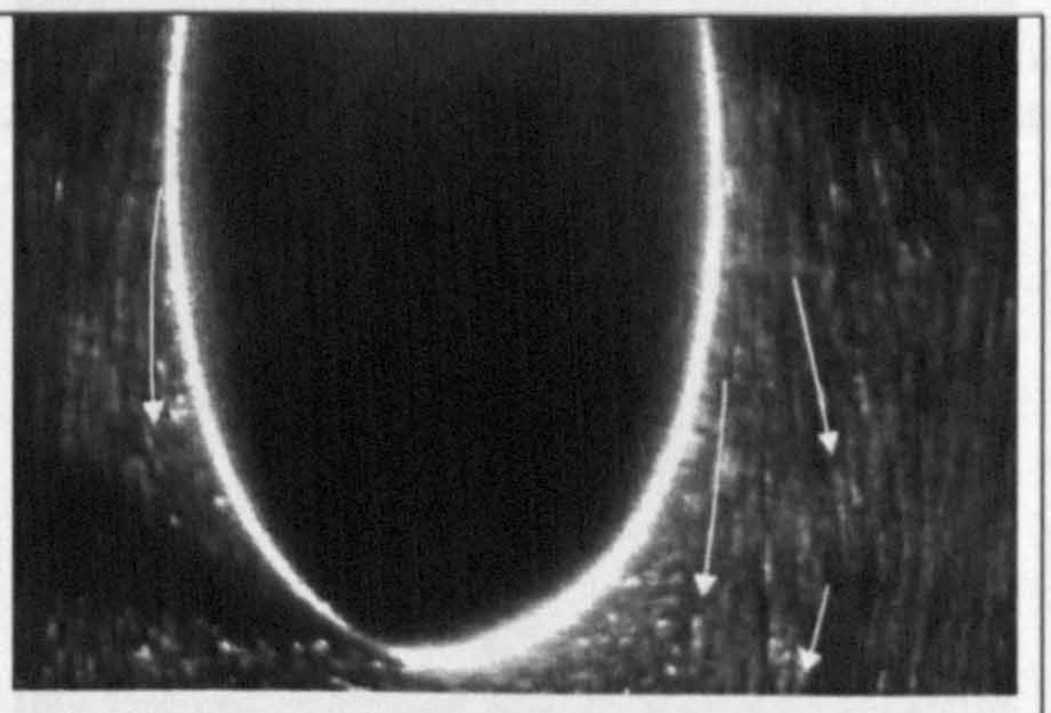

Frame 8; t = 140 ms

Figure 3.36. Visualisation pictures focusing on the separation points of the steady flow past the sixth row cylinder (Re = 638, f_{so} = 1.7 Hz). Frames 1 and 8.

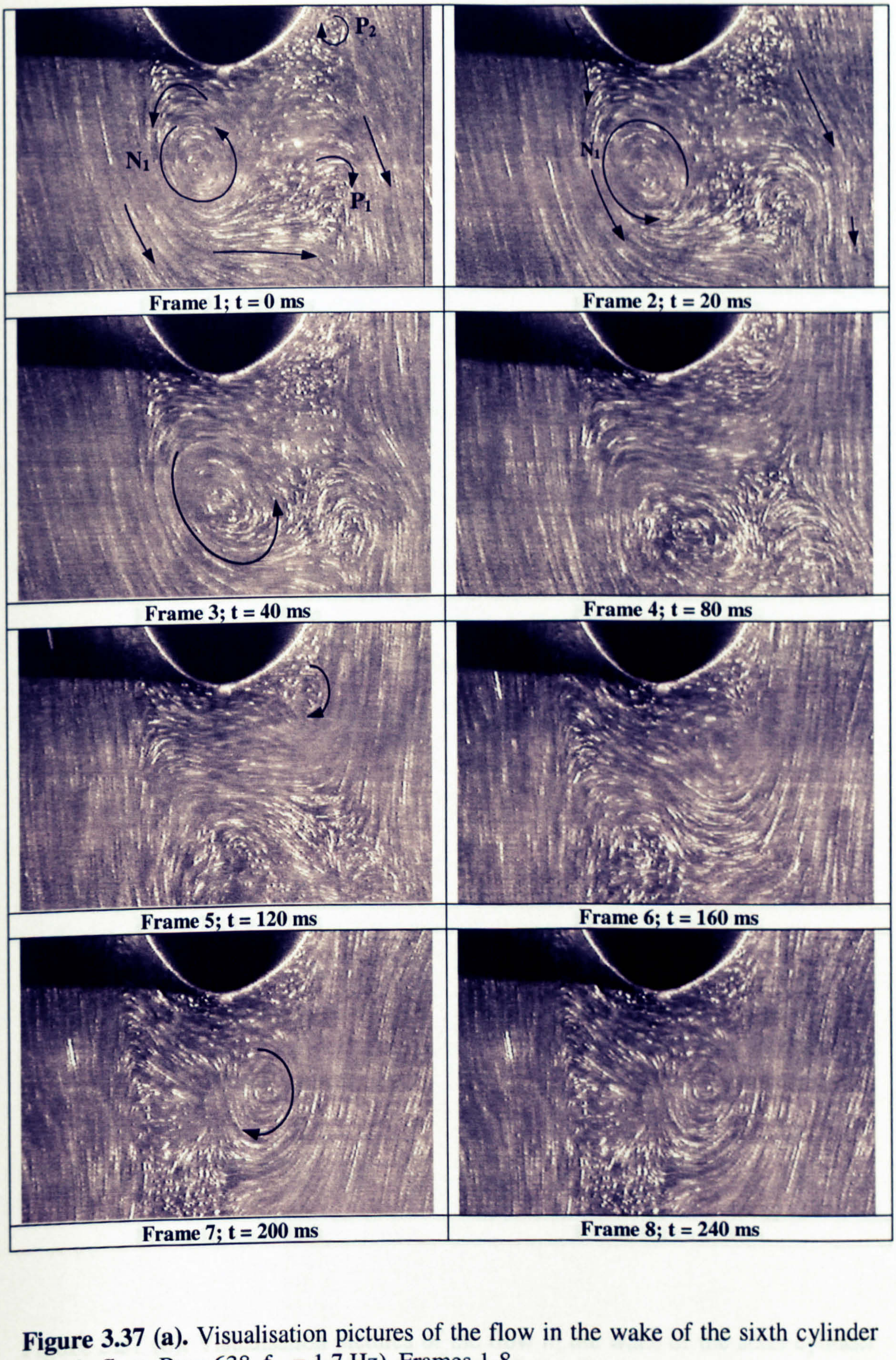

Figure 3.37 (a). Visualisation pictures of the flow in the wake of the sixth cylinder (steady flow, Re = 638, f_{so} = 1.7 Hz). Frames 1-8.

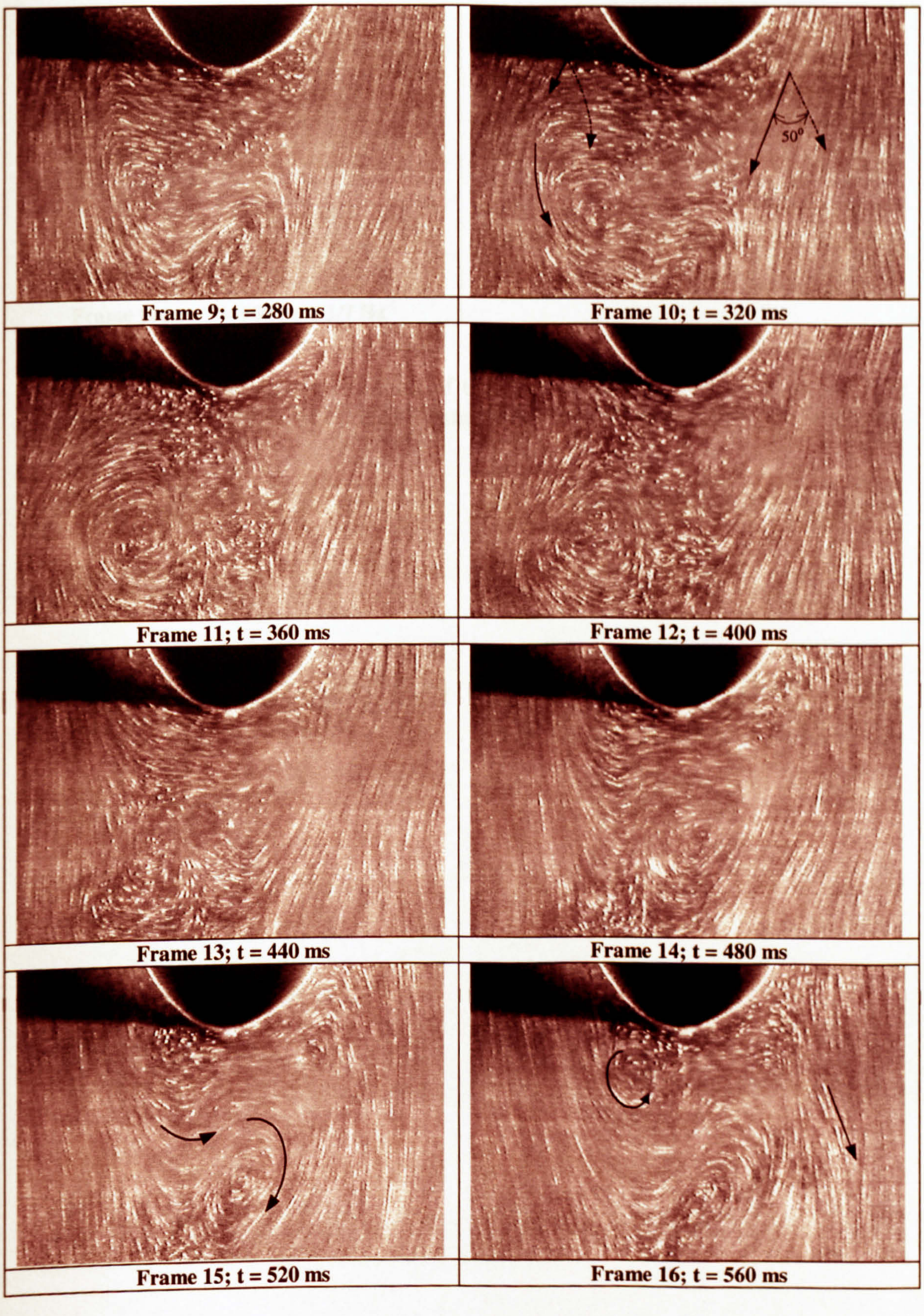

Figure 3.37 (b). Visualisation pictures of the flow in the wake of the sixth cylinder (steady flow, Re = 638, f_{so} = 1.7 Hz). Frames 9-16.

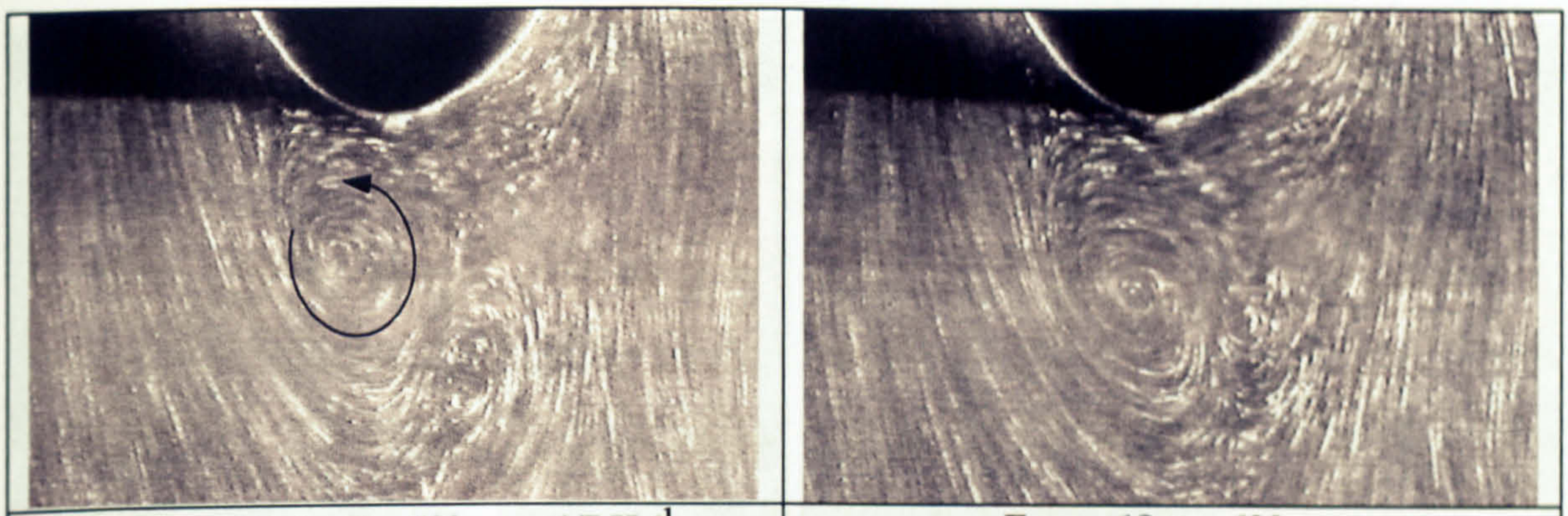

Frame 17; t = T = 600 ms ≅ 1/7 Hz^{-1}	Frame 18; t = 620 sec

Figure 3.37 (c). Visualisation pictures of the flow in the wake of the sixth cylinder (steady flow, Re = 638, f_{so} = 1.7 Hz). Frames 17-18.

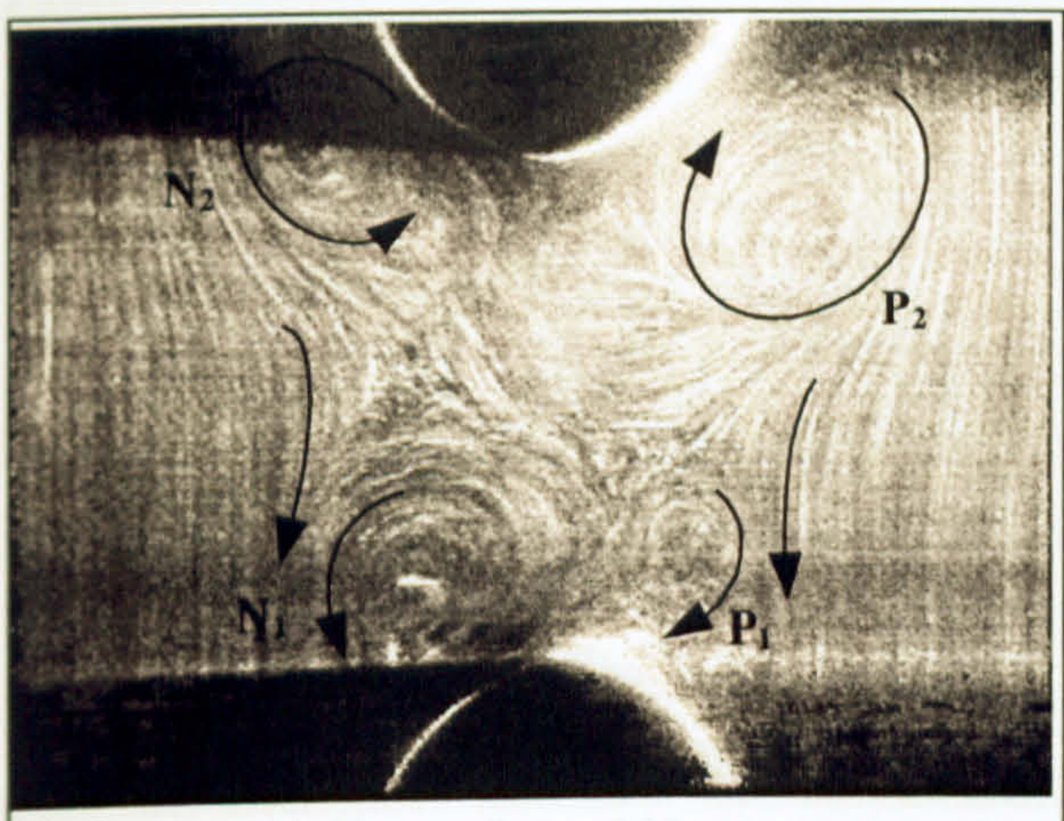

Frame 1; t = 0 ms

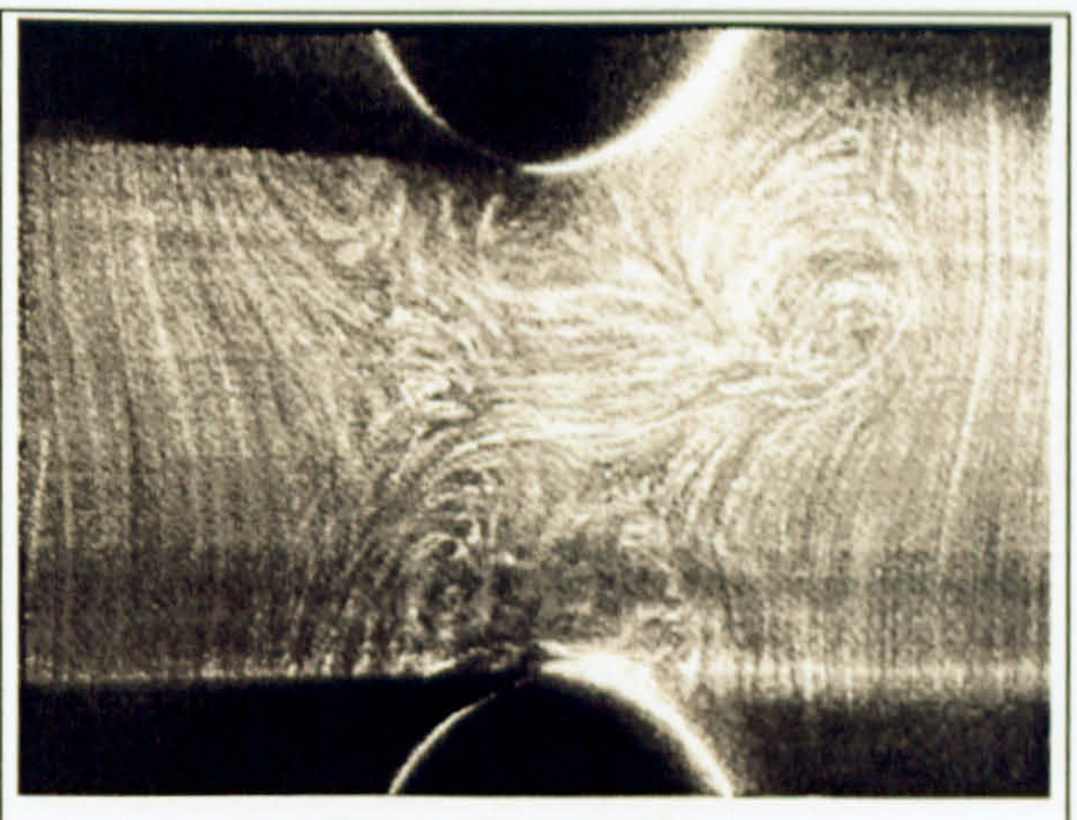

Frame 2; t = 20 ms

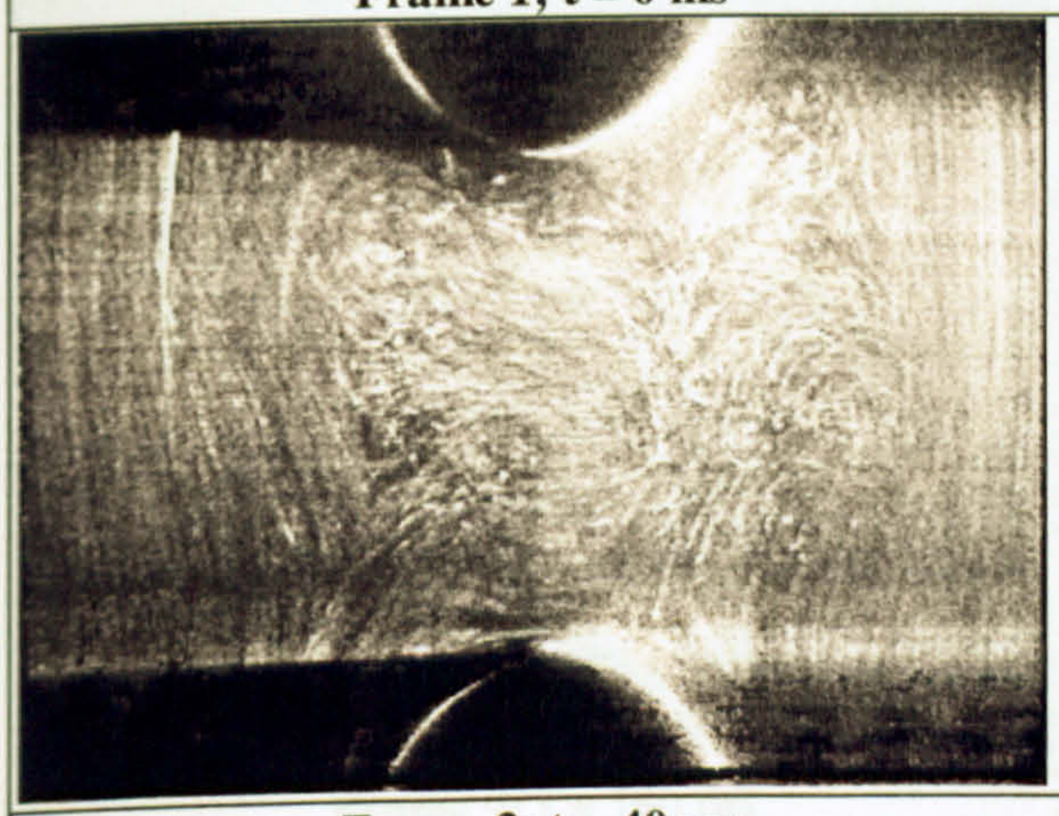

Frame 3; t = 40 ms

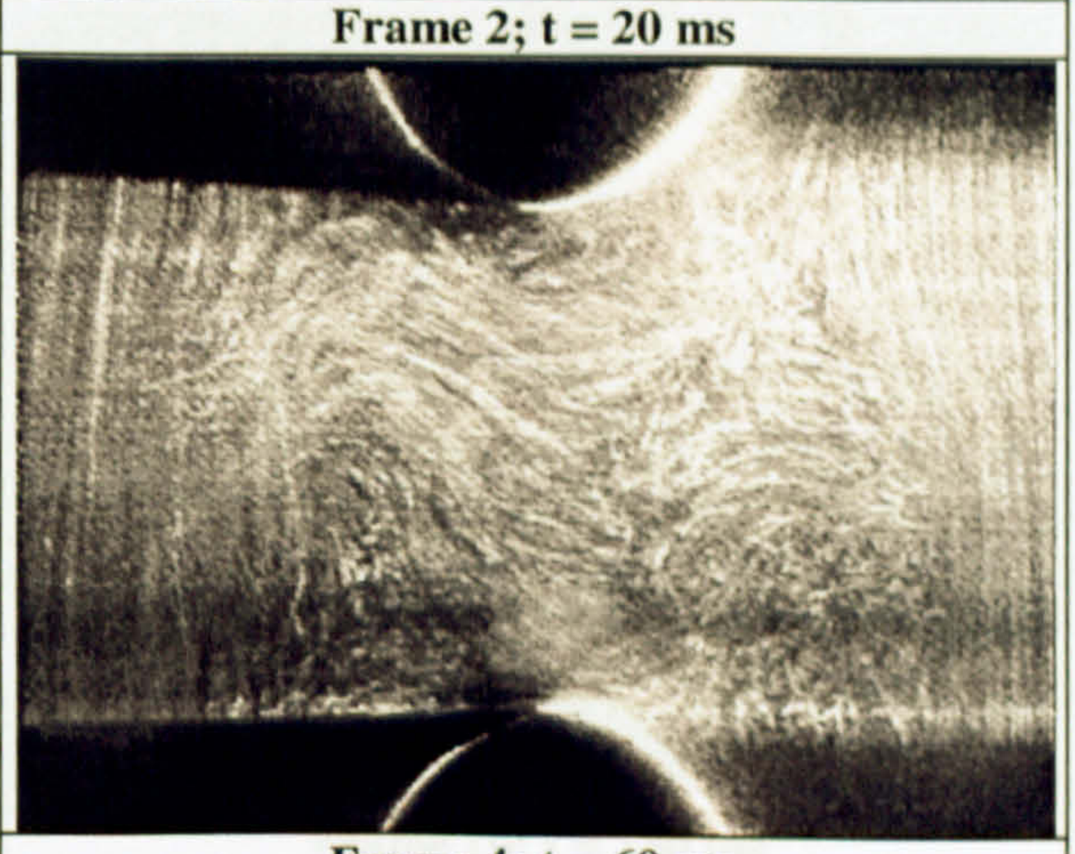

Frame 4; t = 60 ms

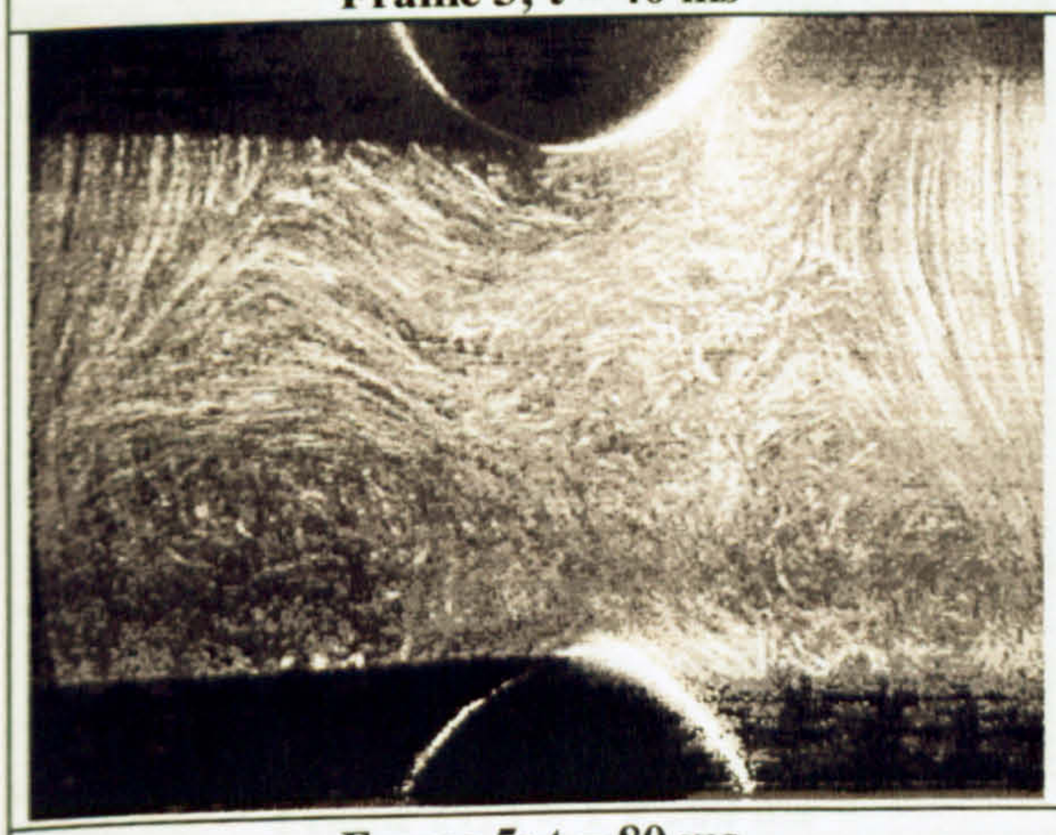

Frame 5; t = 80 ms

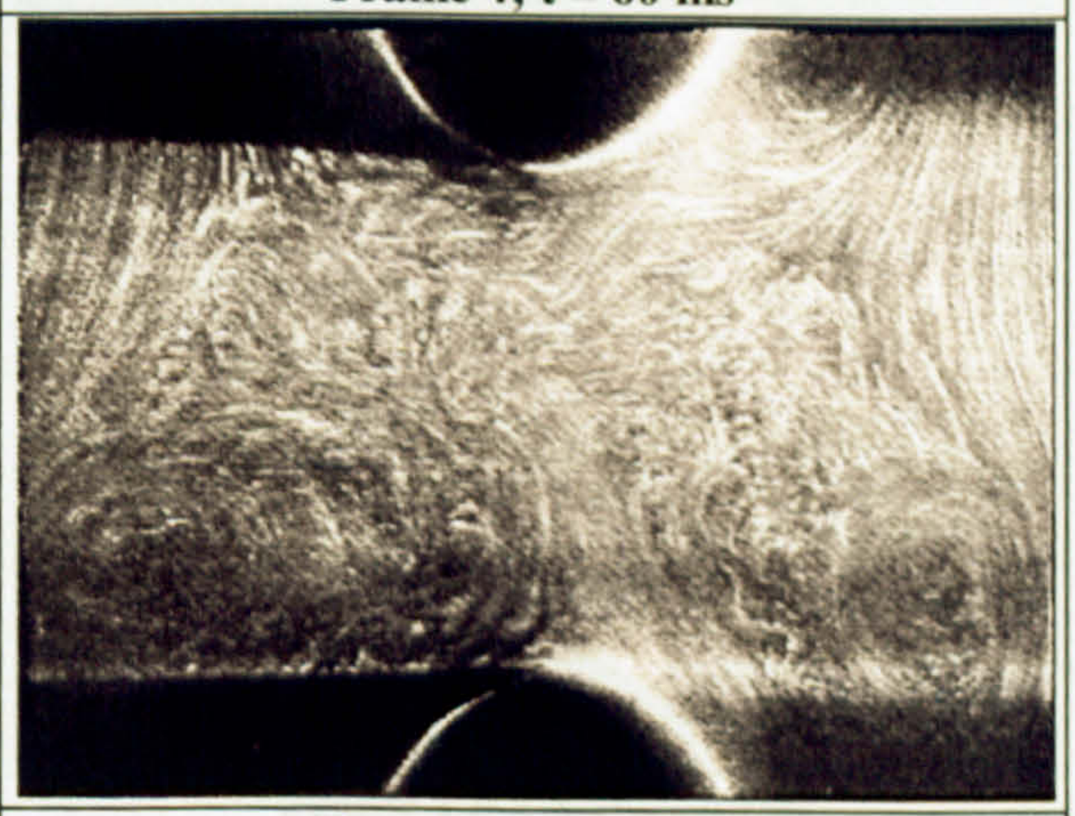

Frame 6; t = 100 ms

Figure 3.38 (a). Visualisation pictures of the flow in the wake of the first row in pulsating flow (Re = 1,560, f_d = 10 Hz). Frames 1-6.

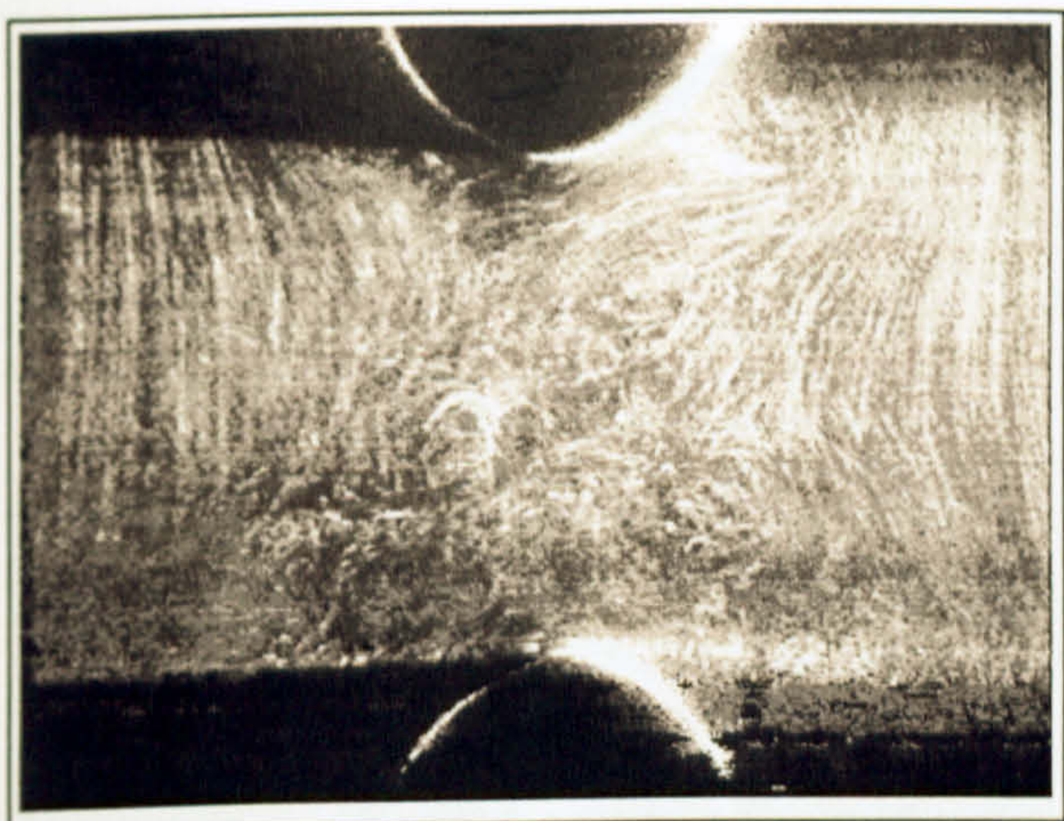

Frame 7; t = 120 ms

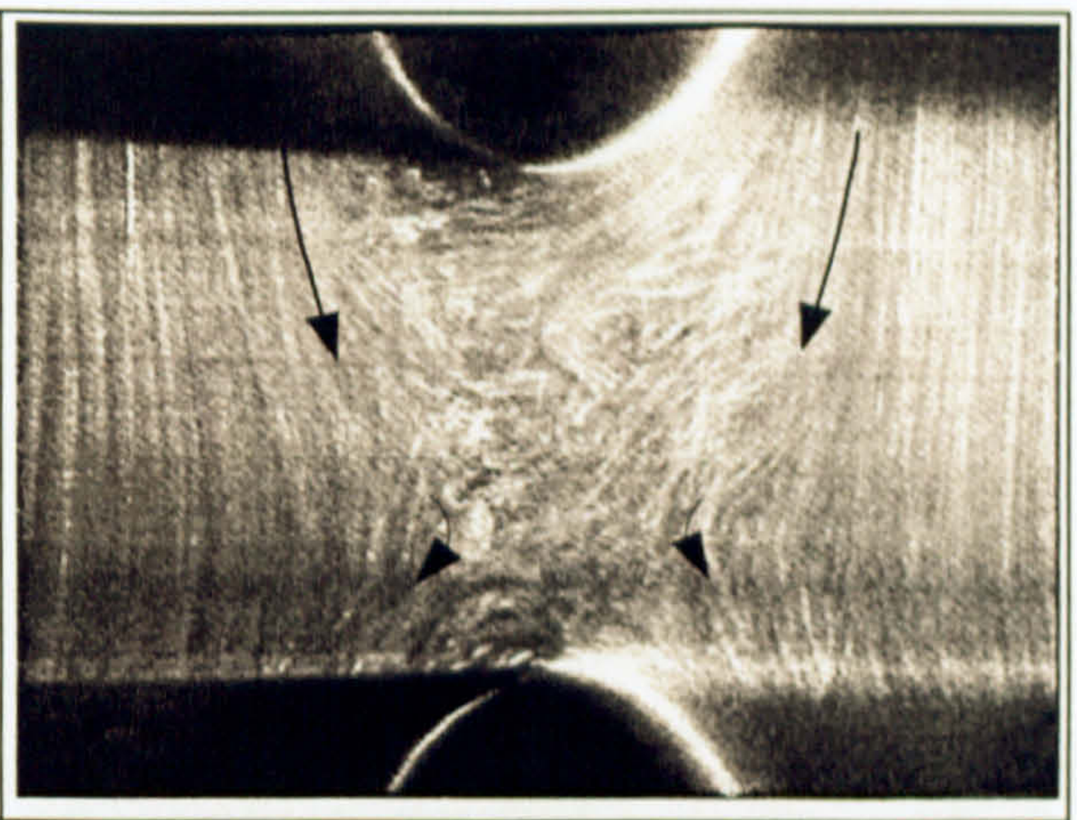

Frame 8; t = 140 ms

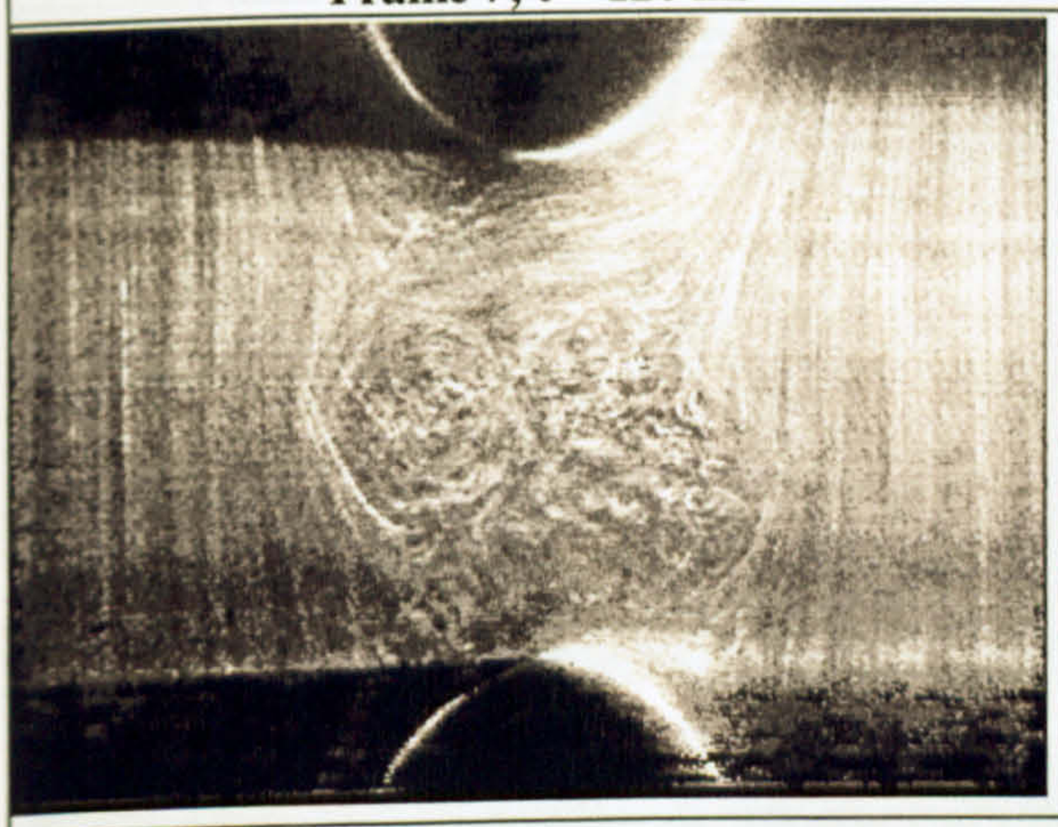

Frame 9; t = 160 ms

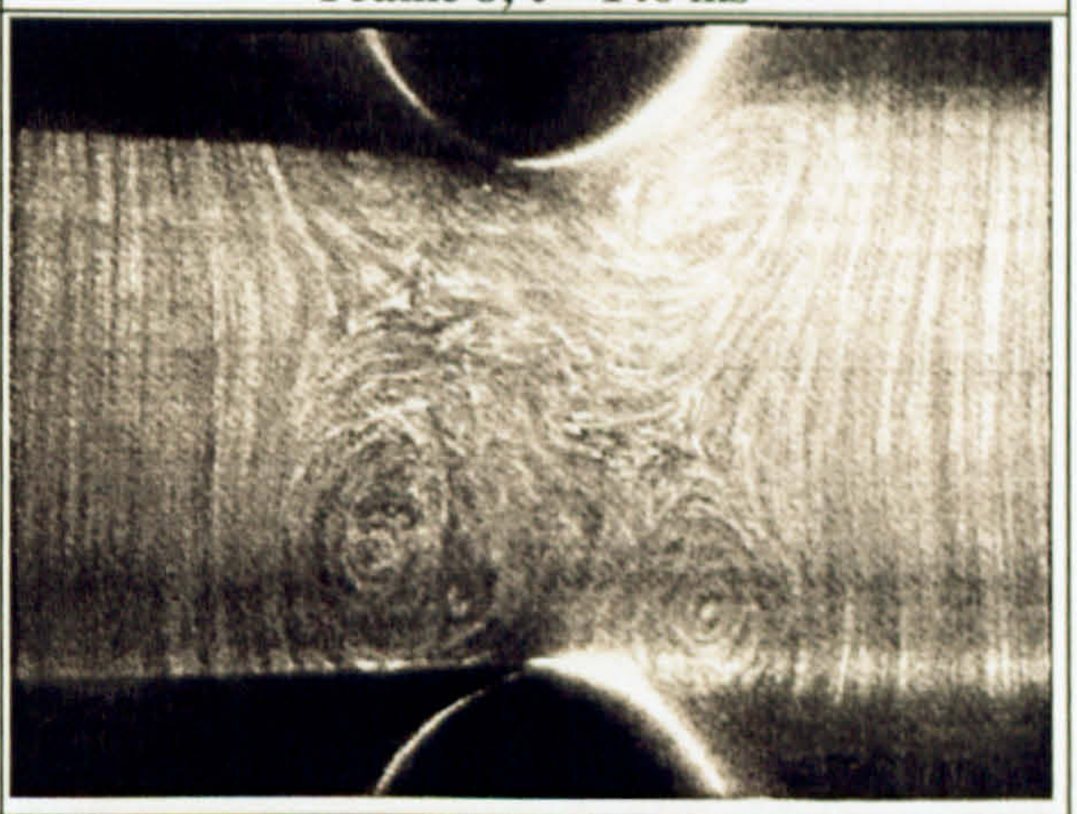

Frame 10; t = 180 ms

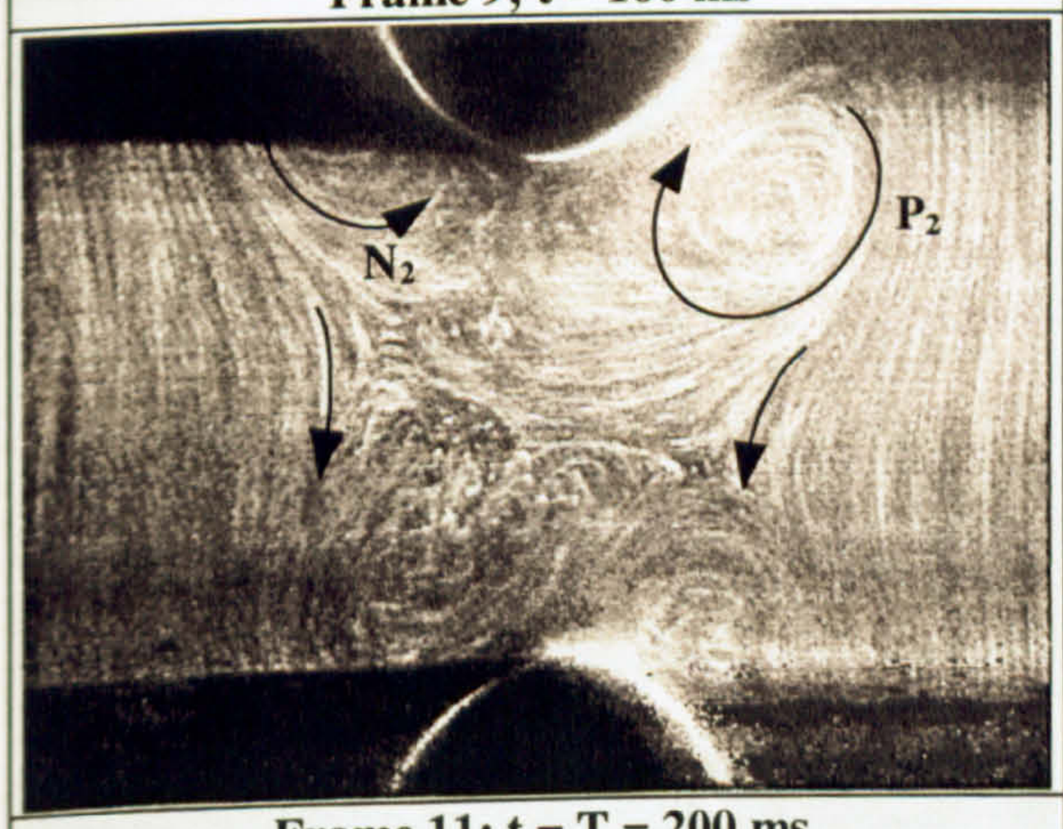

Frame 11; t = T = 200 ms

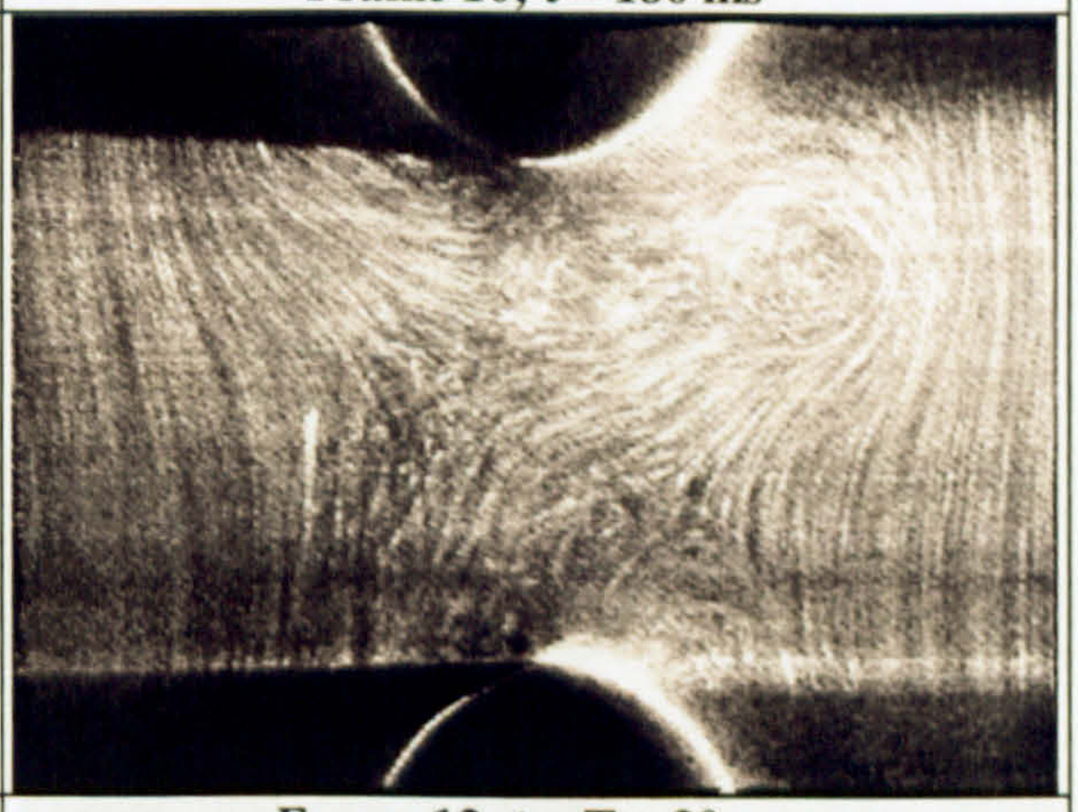

Frame 12; t = T + 20 ms

Figure 3.38 (b). Visualisation pictures of the flow in the wake of the first row in pulsating flow (Re = 1,560, f_d = 10 Hz). Frames 7-12.

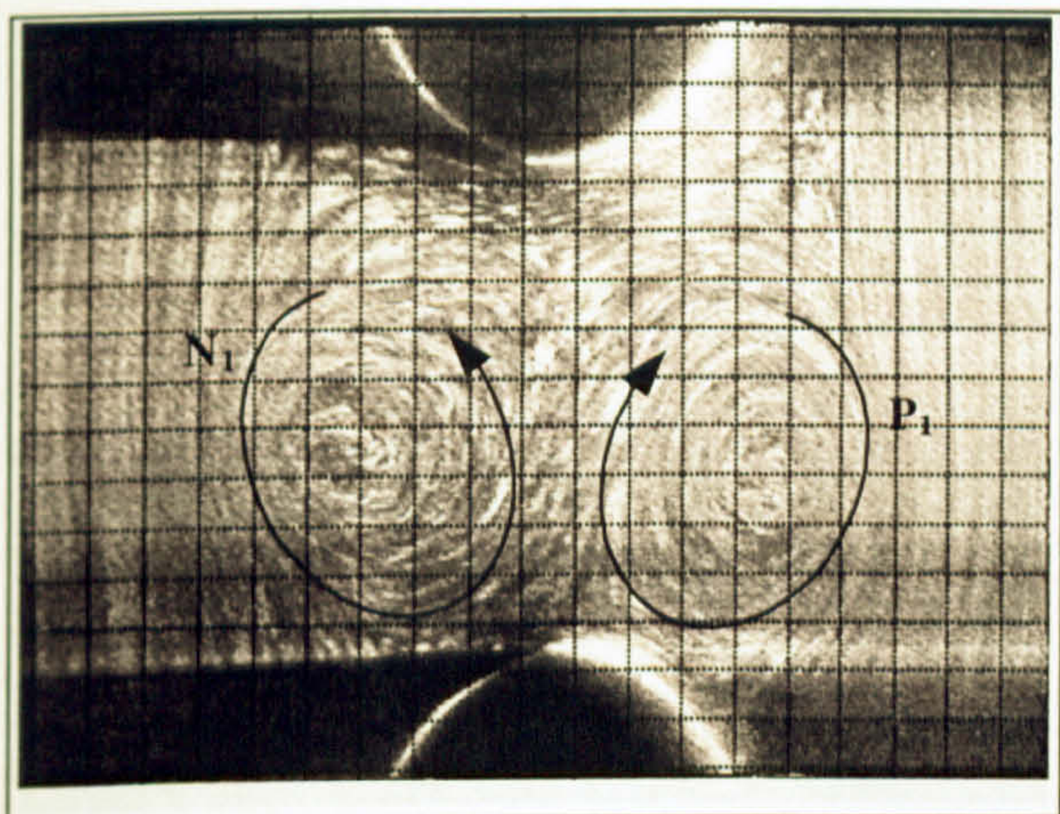

Frame 1; t = 0 ms

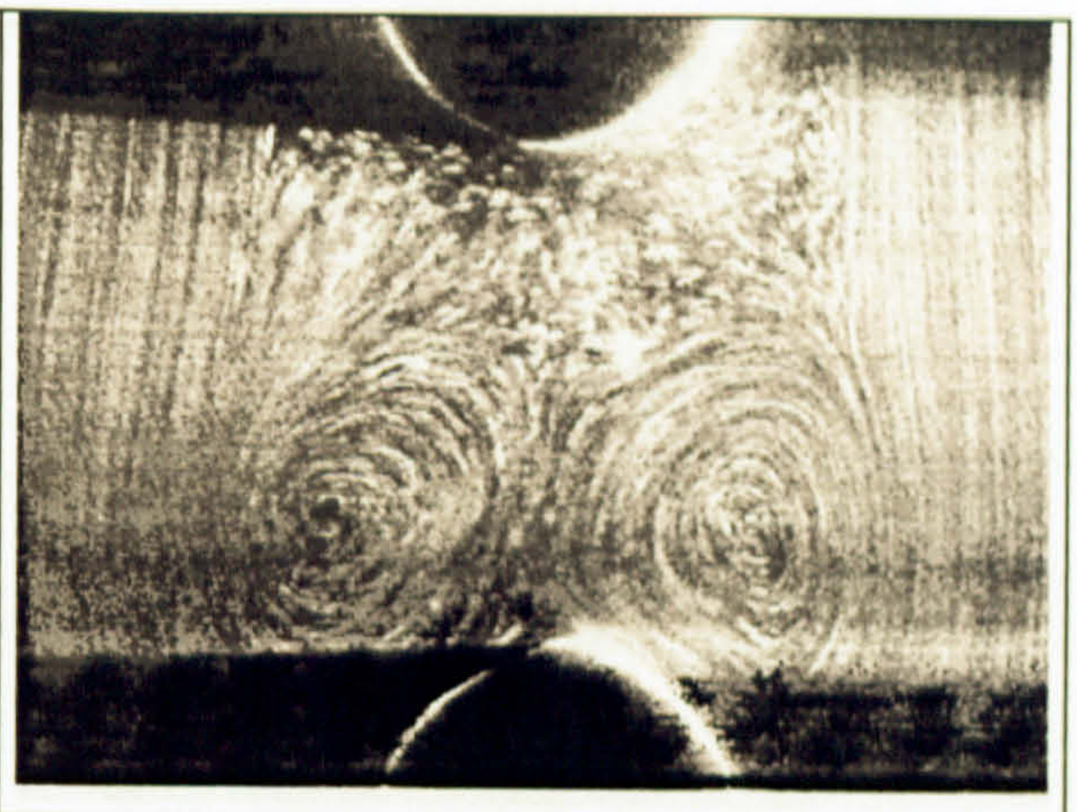

Frame 2; t = 20 ms

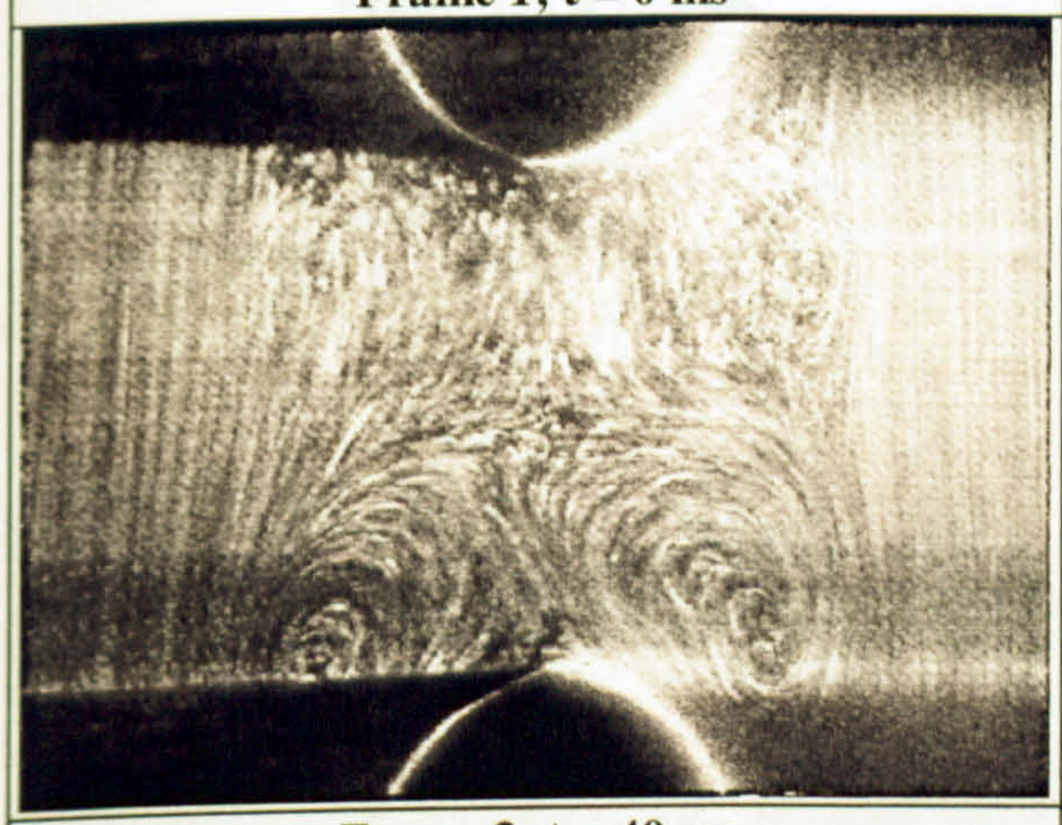

Frame 3; t = 40 ms

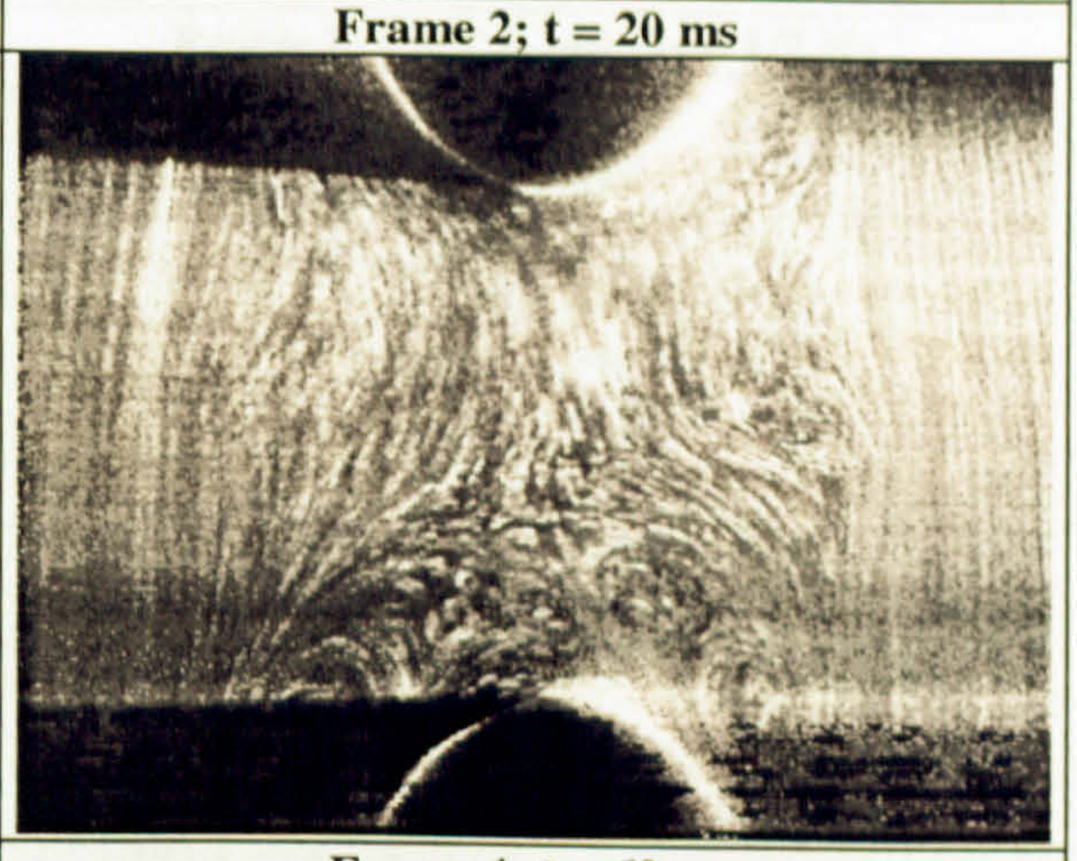

Frame 4; t = 60 ms

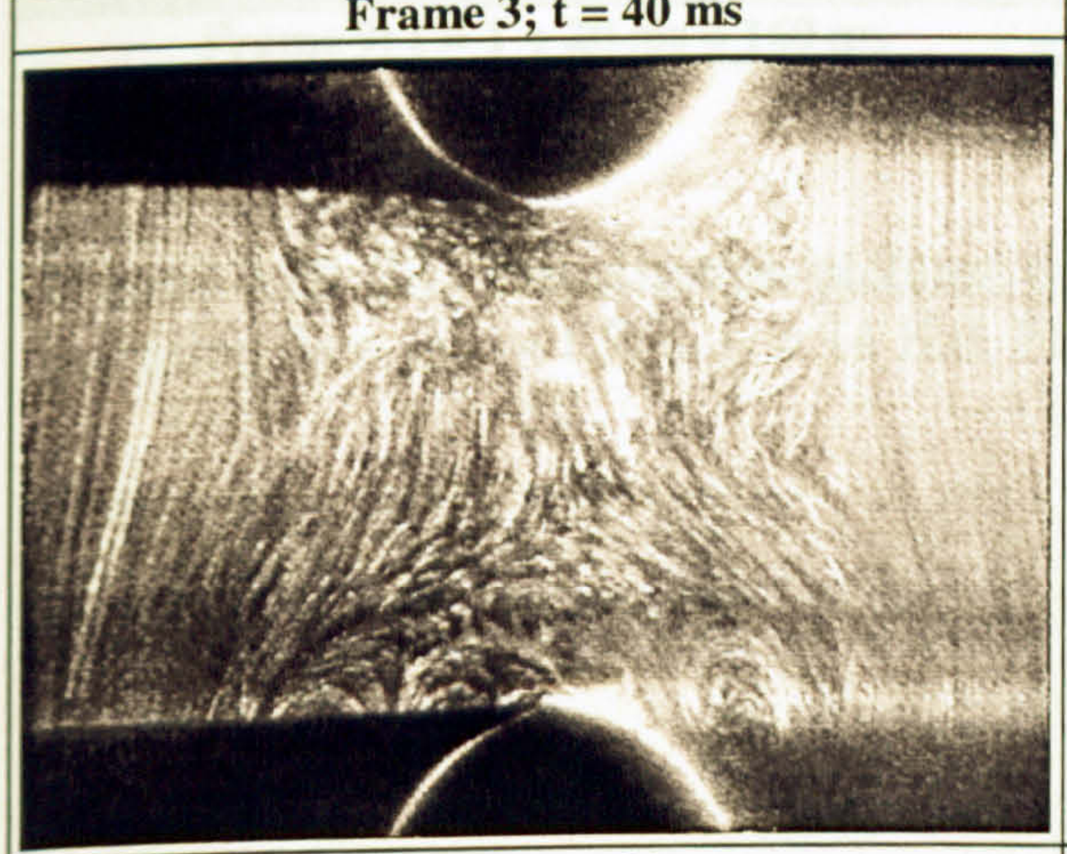

Frame 5; t = 80 ms

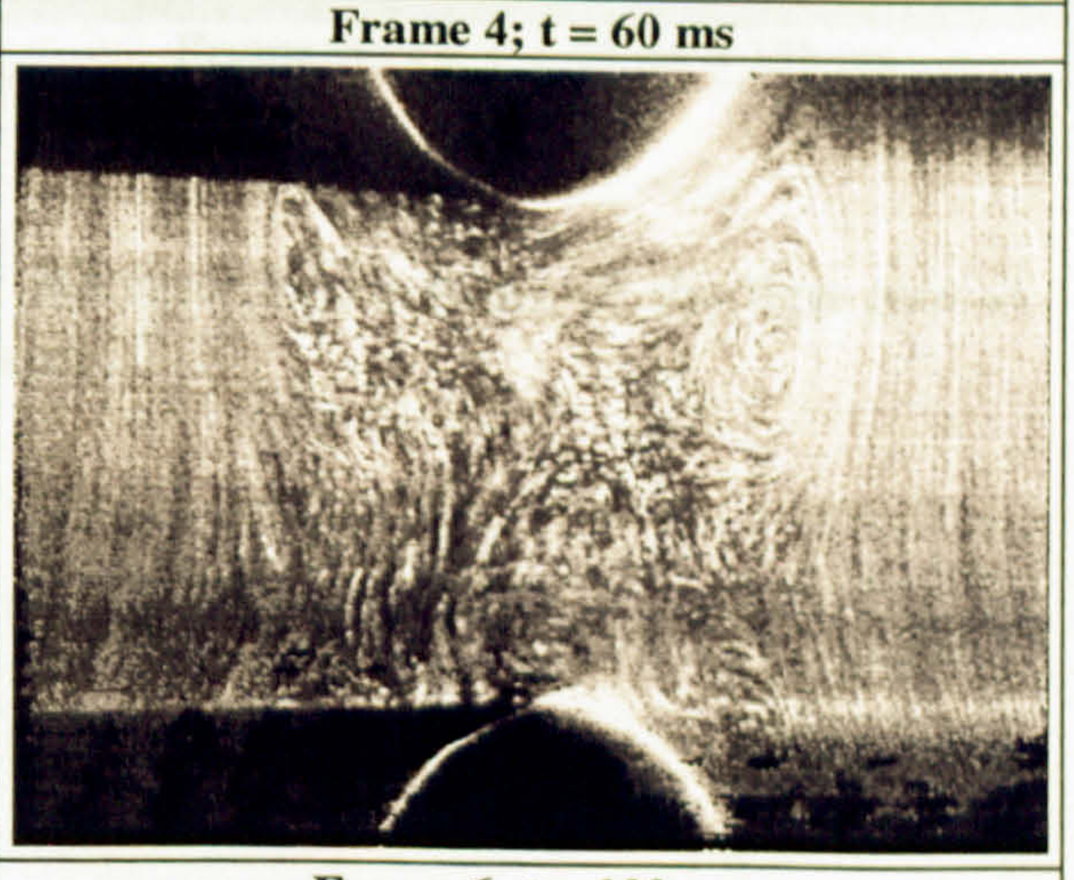

Frame 6; t = 100 ms

Figure 3.39 (a). Visualisation pictures of the flow in the wake of the first row in pulsating flow (Re = 1,950, f_d = 14 Hz). Frames 1-6.

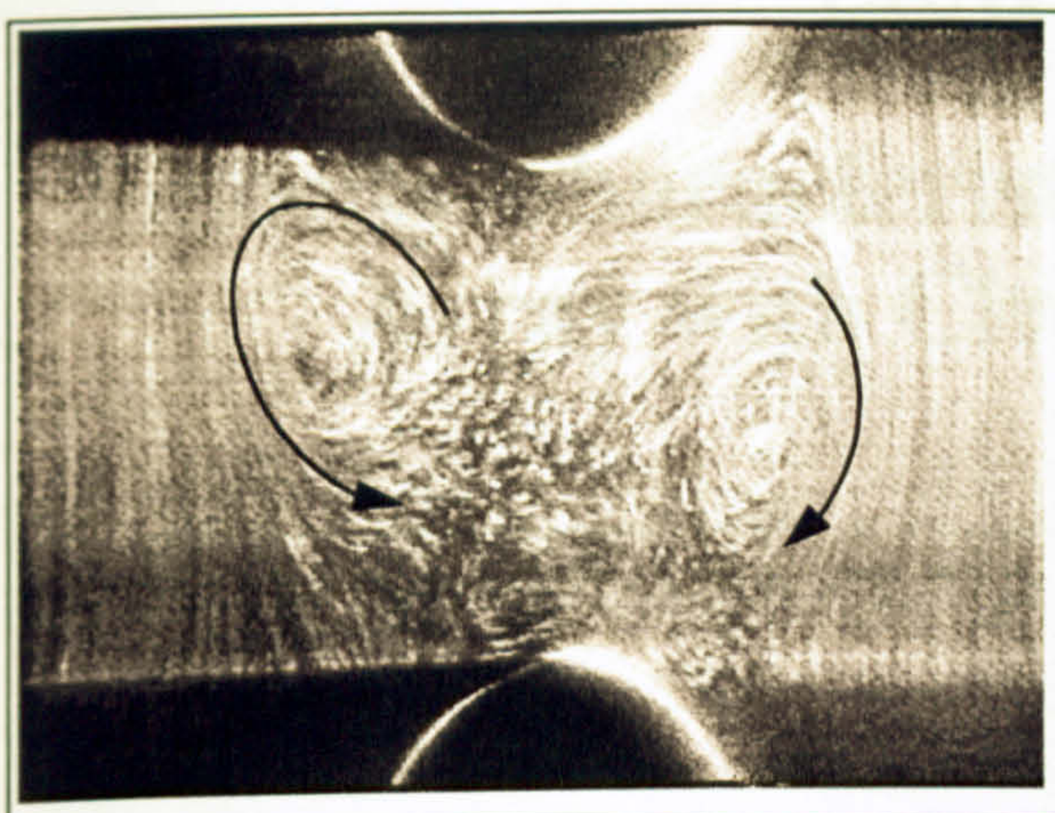

Frame 7; t = 120 ms

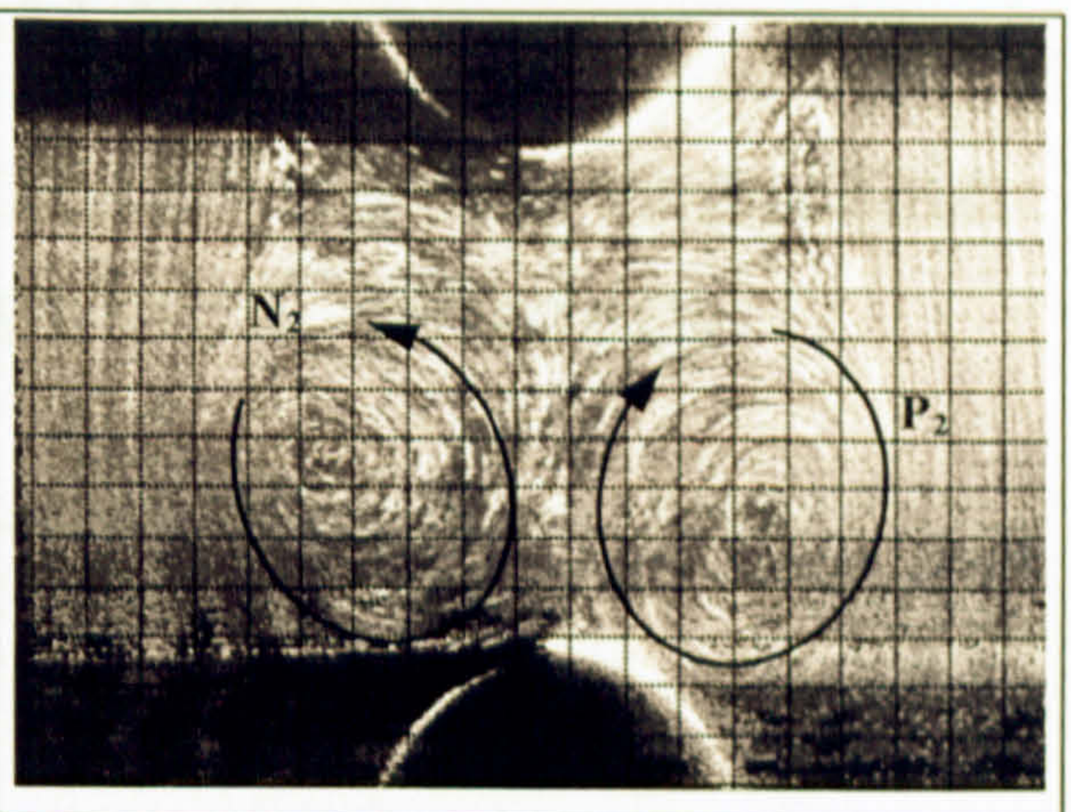

Frame 8; t = T = 140 ms ≅ 1/7 Hz^{-1}

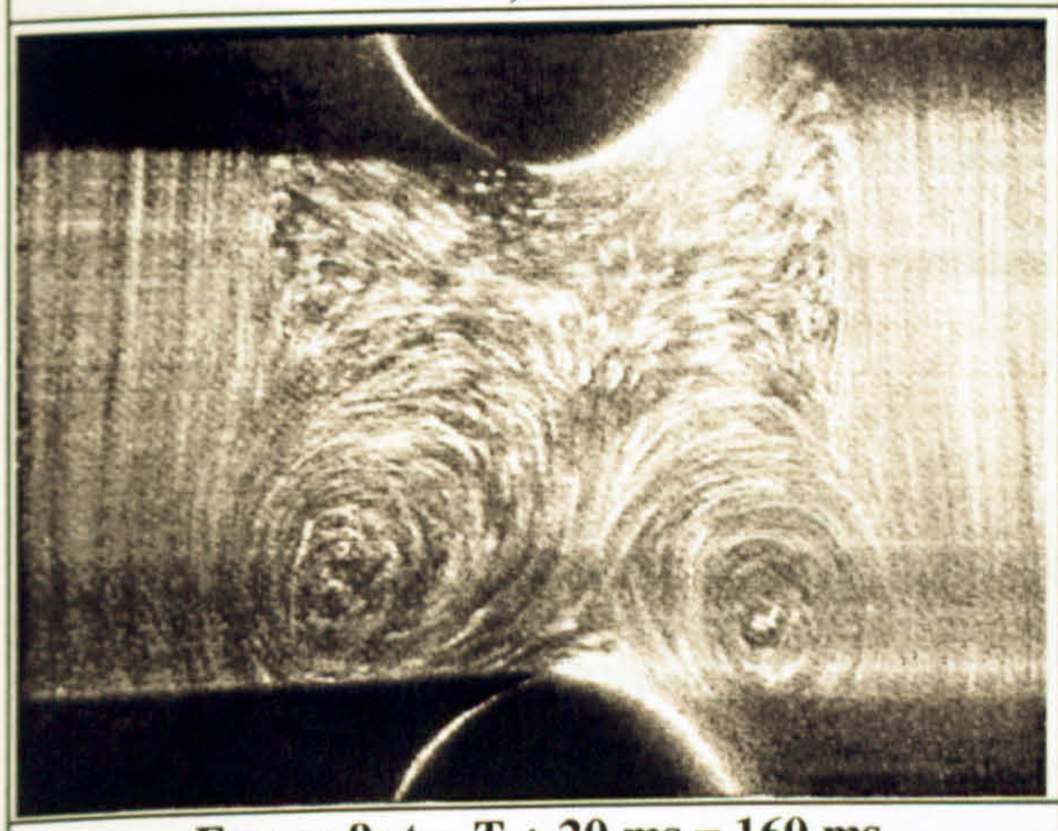

Frame 9; t = T + 20 ms = 160 ms

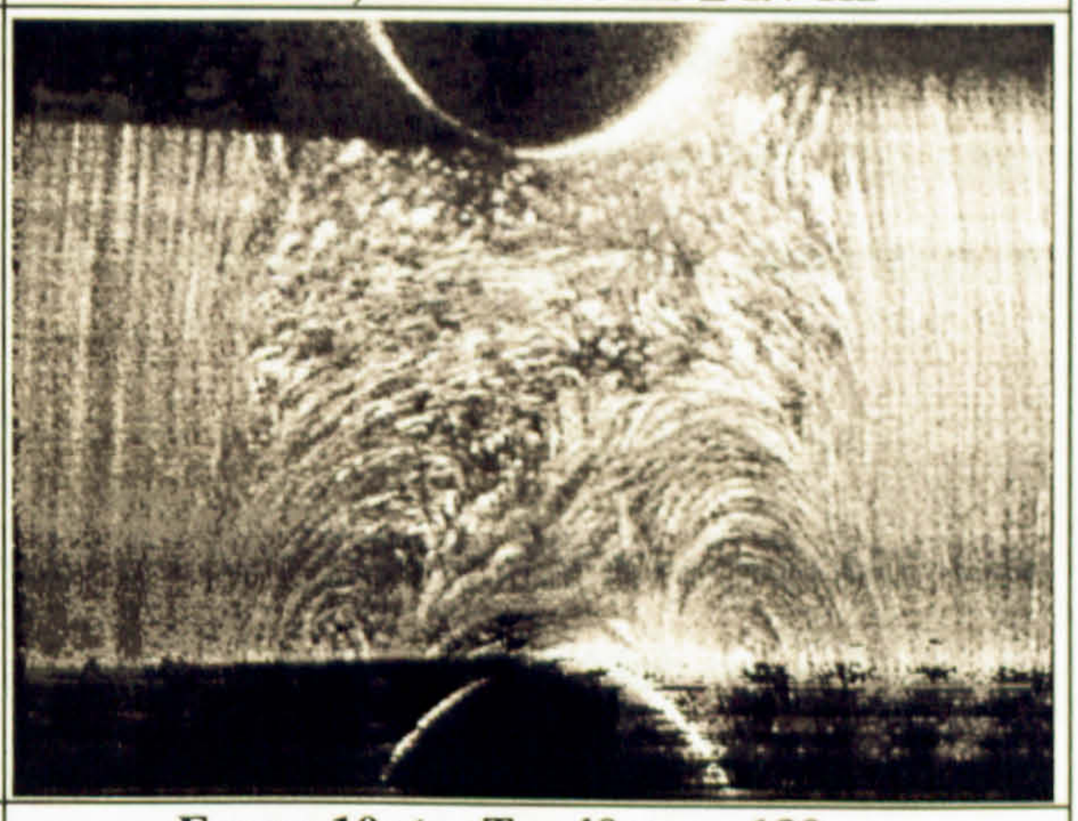

Frame 10; t = T + 40 ms = 180 ms

Figure 3.39 (b). Visualisation pictures of the flow in the wake of the first row in pulsating flow (Re = 1,950, f_d = 14 Hz). Frames 7-10.

CHAPTER 4

Velocity Characteristics of an Asymmetric Array with Circular Cylinders

4.1 Introduction

The present chapter describes the experimental investigation carried out on an asymmetric array with circular cylinders in cross-flow. The water tunnel, the tube bundle arrangement and the LDA system employed have already been described in Chapter 2.

The array was composed by six tube rows in the main flow direction and five columns. Two of the columns comprised half circular cylinders, which were fixed on the side walls to minimise boundary layer effects and simulate an infinite tube bundle. The circular cylinders were manufactured from cast acrylic material. The diameter, d, of the tubes was equal to 10 mm. The longitudinal pitch ratio, S_L/d, was 2.1 and the transverse one, S_T/d, equal to 3.6. These pitch ratios were the same as the ones used in the staggered and in-line arrays studied by Balabani (1996) in order to facilitate comparisons. However, in the asymmetric array the even rows have been displaced by one diameter in relation to the in-line array. Therefore the asymmetric array can be considered as a semi-staggered array. The aim of this investigation was to study the effect of tube displacement on the flow and spectra characteristics of the arrays and eventually on heat transfer.

Measurements were taken at the plane of symmetry ($z/d = 0.0$) in the region $-0.5 \leq y/S_T \leq 0.5$ and $0.0 \leq x/S_L \leq 5.5$ since the flow approaching the bundle was found to be two-dimensional. Ensemble-averaged and time resolved measurements were taken in the above arrangement in both steady and pulsating flow conditions and a flow

visualisation study was carried out for Reynolds number ranging from 1,100 to 12,800 and driving frequencies ranging from 0 Hz (steady flow) to 17 Hz[1].

4.2 Steady flow conditions

4.2.1 Mean velocity distributions (Re = 12,800)

Detailed ensemble-averaged measurements of the axial and radial mean velocities were taken at Re = 12,800. The velocity upstream of the bundle, U_∞, was equal to 0.93 m/s and the working fluid was water. The Reynolds number was defined by the actual diameter of the tubes, d, and the maximum velocity at the gap between adjacent tubes in a row, U_g, which is equal to $1.38U_\infty$ (1.28 m/s) for the arrangement investigated. The equivalent Reynolds number, defined by the upstream velocity and the hydraulic diameter of the duct upstream of the bundle was 66,900. The flow regime at this Re is subcritical, characterised by laminar boundary layer separation as in the investigation on the array with the elliptic tubes.

In order to study the effect of the Reynolds number on the velocity characteristics of the array as well as the effect of flow pulsations, velocity measurements were also taken at Re = 4,900 throughout the flow domain and at Re = 2,700 behind each row. The mean velocity vectors are shown in Figure 4.1. Both the vector length and heads are proportional to the velocity magnitude. Vectors are nearly uniform and vertical in the free stream on the entrance to the tube bank ($x/S_L = 0.0$) and slightly deflect outwards in the neighbourhood (about one diameter away, $y/S_T = 0.28$) of the first row cylinder. Inside the tube bundle the deflection of the flow due to the presence of the cylinders extends up to $y/S_T = \pm 0.5$ in the transverse direction. The vectors are deflected outwards and inwards as the flow passes past the cylinders' shoulders and through the gaps between successive rows respectively. The vector plot also shows the mean recirculation region behind each cylinder, its geometrical characteristics and shape. Due to the fact that the wake flow is deflected by the downstream cylinders, the mean recirculation region is asymmetric around the cylinders' centreline. Flow reversal is evident mainly in the first two rows in Figure 4.1 and

[1] Only selected results are shown for the case of pulsating flow.

consequently the extent of the recirculation region decreases significantly in downstream rows. The distribution of the axial mean velocities, U/U_∞, is shown in Figures 4.2 and 4.3 as profiles and contours, respectively. Figure 4.2 shows that the axial mean velocity profile is uniform within 1% upstream of the tube bundle (x/S_L = - 2.1). It should be noted that positive axial mean velocities indicate velocities in the downward direction and that each profile refers to measurements taken in the y-direction, on the x-plane indicated by the dotted lines. The flow field is characterised by high velocities along the free stream and over the shoulders of the cylinders and flow reversal and low velocities in the wake regions. The asymmetry of the flow, which reflects the asymmetry of the tube arrangement, becomes noticeable from about one diameter downstream of the first row cylinder, and increases further downstream. A relative minimum in the axial mean velocity in the wake of the first cylinder ($x/S_L = 0.4$) is observed at about $x/S_T = 0.03$. In the subsequent profiles the relative minimum shifts further away from the centreline in the positive y-direction. Flow reversal is pronounced only behind the first two cylinders reaching (negative) values up to 0.27 U_∞ ($x/S_L = 1.25$, $y/S_T = 0.59$). A weak flow reversal can be observed behind the downstream rows. A steep velocity gradient can be observed in the shear layer separating from the first and second row cylinders. Velocity gradients become progressively less steeper in the downstream tubes as the recirculation becomes less pronounced.

Axial mean velocity

Figure 4.3 shows the axial mean velocity distribution, U/U_∞, in contour plot form. A comparison with the in-line array with elliptic tubes studied by the author and both the staggered and in-line array with circular tubes studied by Balabani (1996) shows that the flow field of the asymmetric array exhibits intermediate characteristics between the in-line and the staggered arrays. In the in-line arrangements, and in particular the one with elliptic tubes, velocities are uniform along the flow passages, as already observed in Chapter 3, while in the asymmetric arrangement they are approximately equal to 1.75 - 2.00 times the upstream bulk velocity (measured at $x/S_L = -1.0$, $y/S_T = 0$), U_∞, in the positive ($y/S_T > 0$) free stream, indicating a significant interference from the neighbouring tubes in the transverse direction. Flow

reversal is pronounced behind the first and the second rows, but negative velocities are also observed behind the downstream cylinders, as in the staggered arrangement. The magnitude of the negative velocities is lower than that observed in the staggered array. It can be observed that the asymmetry of the wake flow seems also to be more pronounced in the first two rows compared to the third and fourth ones. This might be attributed to the fact that the wakes seem to be more elongated in the first two rows.

Radial mean velocity

The distribution of the radial mean velocities, V/U_∞, is shown in Figures 4.4 and 4.5 as profiles and contours, respectively. Positive values in Figure 4.4 represent velocities in the positive y-direction. Transverse mean velocities reach higher values (higher than $0.5U_\infty$) at the gaps between successive rows and alternate between negative and positive values as the flow passes through successive gaps. Figure 4.5 shows that the mean radial velocity distribution is anti-symmetrical with respect to the centreline at the entrance to the tube bank and up to one diameter downstream of the first row cylinder. In fact, on both side of the centreline the velocities have approximately the same amplitude but opposite direction. The velocities are rather uniform in the most of the flow domain apart from the region where the flow deflects as it encounters the cylinders.

The axial and radial mean velocity profiles (normalised by the upstream bulk velocity U_∞) behind each row cylinder were compared with those of both the staggered and the in-line arrays with circular cylinders[2] studied by Balabani (1996). It should be noted that, although measurements were taken at the same transverse stations, the cylinders are located at different positions along the corresponding planes and their wakes cover different regions along the y-axis in the three arrays.

[2] The three arrays have the same longitudinal and transverse spacings. The diameter, d, is the same for the three arrays.

The comparison of the axial velocities is shown in Figure 4.6. The profiles on the entrance to the tube banks are identical so that any difference between the profiles inside the tube bundle is due to a different arrangement of the cylinders.

Asymmetric and staggered arrays. Behind the first and third cylinders (whose centres lie on the bundle centreline) the two profiles are similar along the shear layers separating from the upstream cylinders but higher recirculation is observed in the wakes of the staggered array. The profiles behind rows 2 and 4 appear obviously dissimilar due to the fact that the centres of the cylinders in the asymmetric array are displaced by 0.8 diameters with respect to the staggered ones in the transverse direction as shown in Figure 4.6. However, if the profiles refer to the cylinders' local co-ordinates they look very similar. The y-co-ordinate of the centres of the even row cylinders of the asymmetric and staggered arrays were $y/S_T = -0.277$ and $y/S_T = \pm 0.5$[3] respectively. Again the negative velocities in the wakes of the staggered array reach higher values. These, in the asymmetric array, are higher behind the even row cylinders than behind the odd ones. The flow around the tube bundle centreline ($y/S_T = 0.0$, $y/S_T = 0.0$) shows similar trends and velocity magnitudes in both arrays.

Asymmetric and in-line arrays. Behind the first cylinder the profiles of the staggered and in-line arrays are similar, but they exhibit higher negative velocities in the wake and higher velocities in the free stream in comparison to the asymmetric array. It can be noticed that behind the second cylinder the velocity gradient along the shear layer of the in-line array is less steep than in the asymmetric array. Negative velocities in the wake have similar magnitude of those in the asymmetric array. It should be observed, however, that while in the in-line array negative velocities can be observed only in the proximity of the centreline, in the asymmetric array negative velocities were recorded in a significantly wider transverse region ($-0.40 < y/S_T < -0.20$). Out of the wake the flow is rather uniform compared to that of the asymmetric array, which is clearly affected by the presence of the upstream cylinder.

In contrast to what observed in both the asymmetric and staggered arrays, no evidence of flow reversal is observed in downstream rows. Correspondingly, the

[3] Only the profiles on the positive y-direction are shown because symmetry of the flow was assumed around the tube bundle centreline.

velocity gradient in the shear layers separating form the upstream cylinders becomes less steep in the downstream direction.

Figure 4.7 shows the comparison of the radial velocities between the three arrays. Again the profiles on the entrance to the tube banks are identical.

Asymmetric and staggered arrays. Lower negative velocities than those in the staggered array (positive values represent velocities in the positive y-direction) were observed in the wake of the first cylinder confirming that the staggered array is characterised by higher recirculation. A profile at $x/S_L = 1.0$ is also shown. Radial mean velocities are higher than in the staggered array throughout the plane, but it can be seen that the magnitude of the negative velocities in the freestream of the asymmetric array is approximately equal to that of the radial velocities in the flow passage of the staggered array. Slightly higher negative radial velocities are observed in the wake of the third row of the staggered array with respect to the first one. The profiles behind the second and fourth row cylinders are similar but the velocity magnitude in the shear layers of the staggered array are significantly higher. Similar velocity magnitude and profile are observed again around the tube bundle centreline.

Asymmetric and in-line arrays. The profiles behind the first cylinder show that the negative radial velocities have similar magnitude in the freestream, while they are lower in the shear layer and in the wake of the in-line array. The profile at $x/S_L = 1.0$ shows that the radial velocity in the in-line array is rather uniform with respect to that in the asymmetric array. The profile of the in-line array is characterised by negative velocities (slightly decreasing from the freestream to the centreline) whose magnitude is lower than that in the asymmetric array. It should be noted that in the in-line array the profiles behind downstream rows show similar trends. The velocity magnitude is similar, but lower than that in the asymmetric array.

4.2.2 Turbulence level distributions (Re = 12,800)

In order to visualise the turbulence characteristics of the tube bundle the measured axial and radial normalised r.m.s. velocities, u'/U_∞, and v'/U_∞, have been plotted, both as profiles and contours in Figures 4.8, 4.9 and 4.10, 4.11 respectively. The

normalised axial r.m.s. velocities are relatively low behind the first cylinder, but start rising downstream of the second row. Behind the first cylinder at $x/S_L = 0.407$ and $x/S_L = 0.595$ the peak velocity fluctuations were recorded at $y/S_T = 0.139$, $y/S_T = -0.152$ and $y/S_T = \pm 0.139$ respectively. The distances between the r.m.s peaks correspond to wake widths of 1.05 ($x/S_L = 0.407$) and 1.0 ($x/S_L = 0.595$) times the cylinder diameter respectively. Behind the second cylinder the wake width is much larger than behind the first one at the same relative axial distance from the centre of the cylinder. This, in conjunction with the U/U_∞ distribution shown in Figure 4.3 suggests a longer mean recirculation region[4] as it will be confirmed later by an estimation of the vortex formation lengths. Although the r.m.s. values increase in downstream rows, the high turbulence mixing compared to the one in the in-line array with elliptic tubes flattens the r.m.s. distribution in the wake of the third and fourth rows (the r.m.s distributions behind the fifth and sixth rows are not shown). The contours in Figure 4.9 show again that the flow is symmetrical around the centreline up to about one diameter downstream of the first cylinder. At the entrance to the tube bank the radial r.m.s velocity is rather uniform. Values lower than $0.1U_\infty$ are recorded in the downstream direction from $x/S_L = 0.0$ up to the third row along the flow passage (positive y-direction) and up to the proximity of the second cylinder on the negative side of the centreline. The r.m.s. increases along the flow passage and reaches its maximum asymptotic value downstream of the third row ($0.3U_\infty$). The highest values of the r.m.s. are recorded in the wakes of the second, third and fourth cylinders (up to $0.5U_\infty$). Figures 4.10 and 4.11 show the distribution of the radial, v'/U_∞, r.m.s. velocity as profiles and contours respectively. In general, the distribution of v'/U_∞ looks very similar to that of the axial r.m.s. one. Both distributions are symmetrical with respect to the centreline on the entrance to the tube bank with magnitudes lower than 10% of the upstream bulk velocity. They are symmetrical up to about 1 diameter downstream of the first cylinder. The magnitude of v'/U_∞ in the wake of the first cylinder increases from the outer shear layer towards the centreline from the upstream value to $0.3U_\infty$. Although both the axial and radial r.m.s. velocity magnitudes increase in the downstream rows, the radial ones are slightly higher particularly as the flow passes over the shoulder of each circular cylinder.

---

[4] It is assumed that the length of the mean recirculation region increases with its width.

Figure 4.12 shows a comparison of the axial r.m.s velocity profiles, $(u'- u'_{ups})/U_\infty$[5], behind the first four row cylinders of the asymmetric array with those measured in the staggered and in-line array by Balabani (1996). u'_{ups} is the upstream axial r.m.s. velocity.

Asymmetric and staggered arrays.

Odd row cylinders. The profiles look similar behind the first row. The r.m.s. velocities have the same magnitude in the freestream, but they differ by up to 80% in the wake, with the asymmetric array exhibiting lower velocities. The r.m.s peak velocity appears at the same position ($y/S_T = \pm 0.14$ for the staggered array and $y/S_T =$ + 0.14 and y/S_T = - 0.15 for the asymmetric one) for both arrays implying that the wake width (at this measurement plane) is the same. Behind the third cylinder the axial r.m.s is significantly lower in the asymmetric array than that of the staggered one. The higher difference in magnitude is not observed in the wake (130%) but along the shear layer (230%). It should be observed that the r.m.s peak in the positive y-direction has shifted towards the centreline (y/S_T = 0.11) with respect to the one behind the first row cylinder and occurs again at the same location for the two arrays. However, the r.m.s. peaks in the asymmetric array are not located symmetrically with respect to the cylinder centreline as in the staggered one; in the negative y-direction, the r.m.s. peak is observed at y/S_T = - 0.18 and not at y/S_T = - 0.11. This suggests that the mean recirculation region is not symmetrical as opposed to that in the staggered arrays. Its width is approximately the same as behind the first row cylinder in contrast to that for the staggered array, which is 24% smaller than the one (measured at the same x-plane) behind the first cylinder.

Even row cylinders. The profiles behind the even row cylinders are similar. The normalised axial r.m.s behind the second and fourth rows is again significantly in the asymmetric lower than in the staggered array. On average, the difference of the r.m.s magnitudes between the two arrays is higher than behind the odd row cylinders. The wake width behind the second row cylinder of the staggered array is the same as behind the first one, while the wake width of the asymmetric array is increased by

[5] The value of the upstream axial r.m.s. velocity was subtracted from the local one in order to take into account the different upstream turbulence levels between the three arrays.

about 12%, in agreement with the observed increase of the vortex formation length discussed later in the chapter. Considering that the contribution of surface friction to the total drag coefficient is small compared to the contribution of the pressure drag any increase of the turbulent wake width and length, that is of the size of the mean recirculation region, has the effect of substantially increasing the drag coefficient. It should be observed that in heat exchangers an increased drag coefficient would require a larger pumping power on the shell-side.

In general the turbulence levels increase in both arrays in downstream rows. The mean of the normalised axial r.m.s values (showed in Figure 4.12) measured along each of the transverse planes ($x_c/S_L = 0.4$) was calculated for both arrays behind each row. The results show that in the staggered array the mean increases steeply (+ 300%) from the first to the third row whereas downstream of the third row there is no significant variation. Although an increase of the mean was also observed in the asymmetric array from the first to the third row, its magnitude was significantly lower than in the staggered array. Furthermore, a slight decrease was observed from the third to the fourth row.

A decrease of the r.m.s velocity gradients, particularly in the asymmetric array, can be observed as indicated by the flatter r.m.s velocity distributions. The wake width behind the fourth row of the asymmetric array is also decreased (the wake width behind the fourth row of the staggered array is approximately the same as behind the second one).

Asymmetric and in-line arrays. Figure 4.12 shows that the axial r.m.s. velocity profiles behind the first four row cylinders of the asymmetric array are very similar to those of the in-line array. The r.m.s. peak velocity on the positive y-direction of the asymmetric array is slightly closer to the centreline ($y/S_T = 0.14$) than that in the in-line array ($y/S_T = \pm 0.17$), while the ones on the negative y-direction appear at the same position ($y/S_T = - 0.17$). This implies that the wake width of the asymmetric array is slightly smaller at the station considered. The magnitude of the corresponding r.m.s. peaks is lower than in the in-line array by about 40% in the positive y-direction and by about 60% in the opposite one. As already mentioned, the axial r.m.s. peak in the asymmetric array does not shift significantly towards the

centreline in the downstream direction as opposite to what observed in the in-line array (compare the profiles behind the first and third rows of the two arrays). The magnitude of the axial r.m.s. peak increases behind downstream rows in both arrays, but that in the in-line one remains slightly higher. In general, the magnitude of the in-line axial r.m.s. velocity, although higher than that recorded in the asymmetric array, is significantly lower than that in the staggered one, particularly behind even row cylinders.

Figure 4.13 shows a comparison of the radial r.m.s velocity profiles, $(v'- v'_{ups})/U_\infty$, behind the first four row cylinders between the three arrays.

Asymmetric and staggered arrays. Firstly, it can be seen that the distributions of the normalised radial r.m.s. velocity are the same for both arrays on the entrance to the tube bank and uniform across the measurement plane. The profiles behind the first row cylinder are similar to the corresponding axial r.m.s. ones shown in Figure 4.12. Slightly lower magnitude values than those in the staggered array are observed along the inner shear layer and in the wake. The r.m.s. peak magnitude in the asymmetric array is 19% lower than the staggered ones. In downstream rows the radial r.m.s velocities of the asymmetric array are significantly lower.

Asymmetric and in-line arrays. Figure 4.13 shows clearly that, although at the entrance to the tube bank the normalised radial r.m.s. velocities of the two arrays are identical, the development in the downstream direction is significantly different. Behind the first row the r.m.s. peak in the asymmetric array is slightly closer to the centreline and its magnitude about 33% lower than that in the in-line array (which is approximately the same as that in the staggered array). The downstream profiles of the in-line array, which are symmetrical with respect to the centreline, show that the radial r.m.s. magnitude increases by up to 190% from the first to the fourth row. Furthermore, the same figure shows a relative steep gradient in the r.m.s. profiles of the in-line array behind all row cylinders. This trend is opposite to that observed in the asymmetric array where the average value of the radial r.m.s. magnitude along the plane investigated behind each row decreases slightly from the second to the fourth row and profiles become flatter downstream.

Degree of isotropy

The distributions of the difference, $|v' - u'|/U_\infty$, and ratio, v'/u', of the r.m.s. velocities, plotted in Figure 4.14 and 4.15 respectively, assess the degree of anisotropy in the turbulence generated by the tube bank. The difference of the two r.m.s. components (Figure 4.14) is near zero over the whole flow domain indicating that the turbulence could be assumed highly isotropic, with the exception of the shoulders of the third and fourth cylinders where the difference between the two components reaches a value of about $0.4U_\infty$. In the staggered array with circular cylinders studied by Balabani (1996) a pronounced difference between the two r.m.s. components could be observed downstream of the second row (50% of U_∞) whereas differences up to 30% of U_∞ occurred downstream of other rows.

More information can be obtained from the distribution of the ratio of the radial and axial r.m.s. velocities shown in Figure 4.15. Although the contour plot confirms that over the outer shoulders of downstream rows (especially the third and fourth rows) the turbulence is highly anisotropic ($v'/u' > 1.8$), it also shows that the turbulence cannot be considered isotropic through the rest of the flow domain particularly in the wakes. It should be noted that the turbulence is isotropic on the entrance to the bank and that the degree of anisotropy, $(1 - v'/u')$, is less than 20% in the wake of the first row. However, in the wakes of the downstream rows the anisotropy raises above 60% with maximum values in the proximity of the downstream cylinders (80%).

Vortex formation length

The vortex formation length, L_F, was estimated at Re = 12,800. Due to the larger longitudinal spacing between cylinders in a longitudinal row than in the in-line array with elliptic cylinders the vortex formation length could be measured behind all row cylinders. As already stated in Chapter 3, the vortex formation length is defined here as the distance downstream of the cylinder axis to a point where the r.m.s. velocity fluctuations are maximised on the wake centre line, u'_{max} (Williamson, 1996). Figure 4.16 shows the variation of the ratio of the axial r.m.s. velocity to u'_{max}, u'/u'_{max} [7], with

[7] See note at page 77 (Chapter 3).

the normalised distance, x_c/d from the centre of each cylinder for the Reynolds number studied. In Table 4.1 the vortex formation length, L_F, behind each row cylinder of the asymmetric array is given.

Table 4.1. Vortex formation length, L_F, in the asymmetric array with circular cylinders.

	ASYMMETRIC ARRAY WITH CIRCULAR CYLINDERS
Row Cylinder	L_F/d (Re = 12,800)
1st	1.65
2nd	$2.2 < L_F/d < 2.5$
3rd	1
4th	1
5th	1.1
6th	1.6

It can be seen that the location of the maximum r.m.s. velocity and consequently the vortex formation length depends on the row cylinder, as expected. The vortex formation length normalised with d, L_F/d, has similar values for the first ($L_F/d = 1.65$) and sixth ($L_F/d = 1.6$) rows, and for the inner rows, that is the third ($L_F/d = 1$), fourth ($L_F/d = 1$) and fifth ($L_F/d = 1.1$) row. The vortex formation length behind the first cylinder ($L_F/d = 1.6$) is expected to be similar to the one of a single cylinder and the same is true for the 6th cylinder. This suggests that the formation length behind the sixth cylinder is hardly effected by the presence of the upstream cylinders. As already stated in Chapter 3, the vortex formation length decreases with increasing the turbulence level. The turbulence levels increase in downstream rows; however, a

continuous decrease of the vortex formation length in downstream rows was not observed. This suggests that in the asymmetric array the effect of the turbulence level on the vortex formation length is negligible compared to the effect that the arrangement of the tubes has on the fluid dynamics of the wake and, consequently, on the vortex formation length itself. The contour plot in Figure 4.3 (which does not show the velocity distribution behind the fifth and sixth cylinder) clearly shows a larger and longer mean recirculating bubble behind the second row and a smaller one behind the third and fourth rows, confirming the results shown in Table 4.1. However, it should be noted that the second row profile is relatively flat around its peak and a small difference between r.m.s. values may lead to large errors in formation length determination. Table 4.1 gives, therefore, a range of values rather than a single figure for the vortex formation length. The size of the mean recirculating bubble behind the first cylinder is intermediate between the third, or fourth, and the second one. The u'/u'_{max} profiles behind the first and second cylinder differ significantly from those of the other cylinders, probably due to the fact that the flow approaching them is only partially obstructed if not at all as for the first one. In fact, the corresponding u'/u'_{max} distribution is rather flat compared to that of the third, fourth and fifth cylinders, which peak around the maximum r.m.s. velocity. The second cylinder distribution is however flatter than that of the first one and presents a long tail characterised by a relatively more gradual r.m.s. velocity gradient.

4.2.3 Flow periodicity

Velocity spectra were estimated in selected locations at Re = 8,870 ($x_c/S_L = 0.5$, $y/S_T = \pm 0.139$ and - 0.417). In order to evaluate the dependence of the vortex shedding frequency on the Reynolds number, additional time resolved measurements were taken at $x_c/S_L = 0.5$ at two transverse locations ($\pm 0.139 S_T$ away from the cylinders' centrelines), in the range $1{,}570 < Re < 8{,}870$.

Figure 4.17 shows typical power spectra behind each row at Re = 8,870 and steady flow conditions (note that the spectra do not have the same scale due to both the significant different amplitude of the peaks and the necessity to highlight the smaller ones).

First and second row cylinders. It can be observed that there is not any distinct periodicity behind the first row of the bundle. A distinct frequency peak appears instead behind the second row at $y/S_T = - 0.417$ with $f_{so} \cong 20$ Hz. The corresponding Strouhal number, defined by the cylinders' diameter and the gap velocity, is 0.22, which agrees with the Strouhal number for a single circular cylinder ($St \cong 0.20$). This peak is not detectable on the position symmetrically located with respect to the cylinder centreline, that is, at $y/S_T = - 0.139$. Similarly, two peaks appear around the 20 Hz frequency behind the third and fourth rows.

Third row cylinder. Behind the third row ($y/S_T = + 0.139$) the amplitude of these two peaks, whose frequencies were 18.2 Hz and 22.1 Hz respectively, was approximately equal to 10 (arbitrary units). It should be noted that the average of this frequencies weighted with their relative amplitudes is equal to 20 Hz, which is also the natural shedding frequency recorded behind the second row. Behind the same row, but on the opposite side of the centreline ($y/S_T = - 0.139$) a peak of lower amplitude (4.29) is observed at 19 Hz. It should be noted that, also in this case, the weighted average of this frequency with with the *secondary ones* observed at 19.2 Hz and 22.3 Hz respectively, is equal to 20 Hz.

Fourth row cylinder. Similarly, behind the fourth row two peaks (at $y/S_T = - 0.417$ and $y/S_T = + 0.13$) are observed around the frequency at 20 Hz. The peaks at $y/S_T = - 0.417$ (18 and 22 Hz respectively) have considerately higher amplitudes than the ones recorded behind the upstream rows. At $y/S_T = - 0.139$, the amplitude of the peak at 20 Hz, a frequency which is expected to be related to vortex shedding, is approximately equal to 2.2[8] (compared to 15 for the opposite location).

Fifth row cylinder. Below the fifth row ($x/S_L = + 0.13$) one dominant peak at 20 Hz is observed at $y/S_T = 0.139$. On the negative side of the centreline ($y/S_T = - 0.139$) minor peaks around the 20 Hz frequency are again observed.

---

[8] It should be observed that as Figure 4.17 show power, and not amplitude, spectra, the term "amplitude" refers here to the arbitrary amplitude of the peaks and not to the actual amplitude of the corresponding oscillations.

Sixth row cylinder. The features of the spectra behind the last row (the sixth) are unique. The amplitude-dominant peaks recorded on both sides of the centreline shift towards lower frequencies. The peaks at $y/S_T = -0.417$ and at $y/S_T = -0.139$ were observed at 15.9 Hz ($St \cong 0.17$) and 11.4 Hz ($St \cong 0.13$) respectively.

It is not possible to infer a unique amplitude for the frequency peaks observed in each row due to their multiplicity, and evaluate its dependency on the row depth. Nevertheless, if we consider the amplitude of the dominant peak in the wake of each cylinder, then it is apparent that its amplitude increases from the second row up the fifth one, and decreases afterwards.

Time resolved measurements were taken downstream of each row ($x_o/d = 0.5$ and $y/S_T = -0.417$, $y/S_T = \pm 0.139$) for Reynolds numbers varying from Re = 1,331 to 8,870 to examine how the spectra characteristics vary with the Reynolds number. For brevity, only the power spectra behind the sixth row for various Reynolds numbers are shown (Figure 4.18)[9]. These show the presence of a distinct peak whose frequency shifts as the Reynolds number increases. Furthermore, as the Reynolds number increases the number and amplitude of peaks increases. It should be noted that at Re = 1,331 (the corresponding spectrum is not shown for brevity) no frequency peak of significant amplitude could be observed behind all rows. Finally, Figure 4.19 shows the variation of the natural shedding frequency, f_{so}, with the Reynolds number, Re, at selected locations behind the third, fourth and fifth cylinders. The variation of the shedding frequency is linear behind all rows. However, it is apparent that the linear dependence f_{so}-Re in the inner rows, as previously stated, is similar but differs from that in the last (the sixth) one, which shows unique features. This is probably due to the fact that the shear layers separating from the sixth cylinder do not impinge onto downstream cylinders. Furthermore, the different shedding frequencies recorded on the two sides of the last cylinder centreline are probably caused by the asymmetry of the flow approaching the cylinder and in particular by its effect on the separation of the boundary layers from the two sides of the cylinder.

---

[9] It should be observed that the features of the flow behind the sixth cylinder are not representative of the array. However, the linear variation of the shedding frequency with Re is similar to that observed behind the upstream rows.

4.3 Pulsating flow conditions

A sinusoidal pulsation, $U_{osc} = \Delta U \sin 2\pi f_d$, was superimposed on the flow entering the test section. The pulsation frequency varied between 7 Hz and 14 Hz. The relative amplitude of the pulsation, A_o, and the Reynolds number, Re, varied between 0.24 and 0.35 and between 2,700 and 4,900 respectively.

Detailed measurements were taken at $f_d = 10$ Hz[10], and the corresponding axial mean and r.m.s. velocity distributions are discussed below.

4.3.1 Mean velocity

Figure 4.20 shows a comparison between the axial mean velocity profiles in steady and pulsating flow ($f_d = 10$ Hz, Re = 4,900). The relative amplitude of the pulsation, $\Delta U/U_\infty$, was kept constant at 0.24 ($\varepsilon = \Delta U/(2\pi f_d d) \approx 0.14$). It should be noted that the integral of the velocity profiles evaluated at each station varies within 1% between steady and pulsating flow. In order to compare the effect of pulsations on both the mean flow and the turbulence level measurements were taken at the same Re. The upstream bulk velocity was in both cases equal to 0.6 m/s. As it can be seen from Figure 4.20 at the entrance to the tube bank the flow is symmetrical in both steady and pulsating flow. Furthermore, the magnitude of the mean velocity is generally not altered by the pulsating flow. As was also observed in the in-line array with elliptic tubes, a more pronounced recirculation (higher negative velocities) and a higher symmetry of the flow around the cylinder centreline is observed behind the first row in pulsating flow. Slightly higher negative velocities are observed in the wake of downstream rows in steady flow (i.e. fifth and sixth rows; the differences in the wakes of the second, third and fourth rows are negligible), in contrast to what was observed behind the first row. In general, however, no significant effect of pulsations can be noticed in agreement with the results for the in-line array with elliptic tubes. The difference in the negative velocities is compensated outside of the wake. This is particularly evident behind the fifth and sixth rows where this compensation occurs in the freestream with higher positive velocities observed in steady flow.

4.3.2 Turbulence level distributions

A comparison of the axial r.m.s. velocities measured in steady and pulsating flow is given in 4.21. The r.m.s values correspond to the velocity records from which the mean velocity profiles shown in Figure 4.20 were calculated. The r.m.s. values are based on the entire signal, and therefore include 'a pseudo-turbulence' contribution by the variation of the mean flow due to pulsations. The latter could be evaluated by the difference of the r.m.s velocity magnitudes between pulsating, u'_p, and steady flow, u'_s, upstream of the tube bank ($x/S_L = -1.0$). The normalised "pseudo" turbulence, $\Delta u'/U_\infty = (u'_p - u'_s)_{upstream}/U_\infty$, was estimated to be equal to 0.20. It can be observed that on the entrance to the tube bank the turbulence difference between pulsating and steady flow has increased with respect to the upstream value ($\Delta u'/U_\infty = 0.20$). This difference is about 0.24 in the freestream and reaches a value of 0.61 in the proximity of the cylinder wall. The increase in the turbulence levels in pulsating flow cannot be attributed to the "pseudo-turbulence" introduced, but to changes in the structure of the flow caused by the pulsations. In agreement with the results for the in-line array with elliptic tubes, the most significant effect of the pulsations on the turbulence of the flow can be observed in the wake of the first cylinder itself. The average turbulence difference between pulsating and steady flow on the entrance plane ($x/S_T = 0.0$) was estimated to be equal to $\Delta u'/U_\infty = 0.53$. It can be seen clearly that even when the contribution of the pulsations to the velocity signal is removed the r.m.s. velocities in pulsating flow are still higher than those in steady flow. The r.m.s. amplitude of the velocity fluctuations rises by about 270% when the flow is pulsed, but only 180% of this increase can be attributed to changes in the structure of the wake caused by the pulsations. The effect of pulsations in the freestream is negligible.

In general, in contrast to what was observed in the in-line array with elliptic tubes, the r.m.s. values for pulsating flow are not higher throughout the flow-field, despite the pseudo-turbulence introduced by the flow pulsation. Outside of the wakes the difference of the normalised r.m.s velocities between pulsating and steady flow is negligible behind downstream rows partly due to the fact that the steady flow turbulence levels increase. In the wake regions the effect of pulsations is still

---

[10] This frequency of 10 Hz was not chosen arbitrarily. In fact, it was the one at which the pulsations waveform best approximated a sinusoid.

noticeable, but it is significantly lower than that behind the first cylinder and slightly higher than the one upstream of the tube bank.

As mentioned earlier, the "pseudo-turbulence" was determined from the difference of the r.m.s velocity magnitudes between pulsating, u'_p, and steady flow, u'_s, upstream of the tube bank. In order to verify the above estimation, the contribution of the pulsations to the turbulence level was "filtered out" from the measured signal in pulsating flow, and the "filtered" or real turbulence so obtained was compared with the corresponding one obtained in steady flow. As expected, no difference in the real turbulence between pulsating and steady flow was observed upstream of the bundle.

Figure 4.22[11] shows a comparison of the time trace and spectrum of the upstream (x/S_L = -1.0, y/S_T = 0.0) axial instantaneous velocity in pulsating (Figures 4.22 (a) and (b)) and steady flow (Figures 4.22 (c) and (d)) at Re = 4,900. The frequency and relative amplitude of the pulsation were f_d = 10 Hz and $A_o \cong 0.24$ respectively. The amplitude spectra clearly shows a well defined peak at 10 Hz whose amplitude, ΔU, is about 0.145 m/s. The frequency spectrum of Figure 4.22 (b) was notch-filtered[12] in order to remove any frequency associated with the variation of the mean flow (in the present case the frequency was the one of the superimposed pulsations, that is 10 Hz) and estimate the effect of the pulsation on the turbulence of the flow. The periodic contribution of the pulsation obtained is shown in Figure 4.23 (b). This was removed from the signal and the "real r.m.s" was estimated (Figure 4.23 (c)). A comparison of the r.m.s velocity magnitudes between steady (Figures 4.22 (c)[13]) and pulsating flow (Figure 4.23 (c)) showed that there is no effect of the pulsations on the turbulence of the flow upstream of the tube bundle. Figure 4.23 (d) shows the superimposition of the filtered pulsating mean flow (blue line) onto the original time-velocity record (in red), which gives a qualitatively assessment of the filtering technique.

---

[11] The graphs in Figure 4.23 were obtained by processing time-velocity records by means of the commercial software package called MATLAB.
[12] The technique was briefly described in Chapter 2.
[13] It should be noted that the time trace shown in Figure 4.23 (b) is not filtered of its steady mean flow.

Vortex formation length

Figure 4.24 shows the centreline development of the axial mean and r.m.s. velocities normalised with u'_{max} and U_{max} respectively for pulsating conditions (Re = 4,900, f_p = 10Hz). It should be noted that, as expected, the position of the r.m.s peaks coincide with the one defined by the point of zero mean velocities (rear stagnation point). The latter indicates how rapidly the axial mean velocity defect in the wake has recovered or the end of the recirculation bubble.

It can be seen from Figure 4.24 that the r.m.s. distribution behind the first cylinder has its peak at 1.4 diameter downstream from the centre of the cylinder, that is x_c = 1.4d. The profile differs from the downstream ones in that the variation of the r.m.s magnitude along the cylinder centreline is more apparent (steeper velocity gradient) then those behind downstream rows. These, in fact, appear flatter and the correspondent r.m.s. peaks are less defined than those behind the first row. This is due, as previously stated, to an increased turbulence mixing in downstream rows favoured by the asymmetrical arrangement of the cylinders. It should be observed that the r.m.s. increases steeply from the proximity of the rear stagnation point up to x_c = 1.4d, which also defines the vortex formation length of the first cylinder. At x_c = 2.1d, x-co-ordinate of the centre of the downstream cylinder (the 2nd one) the r.m.s. magnitude rises again. Behind the second cylinder the r.m.s. peak is observed at x_c = 1.2d. Again the r.m.s. velocity magnitude increases (the increase is characterised by a steep gradient but less steep than the corresponding one observed behind the first row) up to the r.m.s. peak. This is followed by a gradual decrease up to about x_c = 2.1d; at $x_c > 2.1d$ a slight increase is observed. The profiles behind the third, fourth and fifth rows are slightly different; the r.m.s. peak is closer to the rear stagnation point of the upstream cylinder (x_c = 0.9d - 1.0d). The main difference between these profiles is the location and the slope of the r.m.s. velocity gradient downstream of the relative r.m.s peak x-co-ordinate. The velocity gradient increases significantly from the third to the fifth cylinder. Behind the latter the r.m.s. increases up to values higher than that of the r.m.s. peak magnitude in the near wake. The profile behind the last cylinder shows unique features. The peak is observed at x_c = 1.2d as behind the second cylinder, but the increase of the r.m.s. magnitude up to the relative peak and

its successive decrease are very smooth and no further increase is observed in the far wake probably due to the absence of downstream cylinders.

Figure 4.24 shows also the variation of the normalised mean velocity along the cylinders' centrelines. The normalised main velocity profiles show similar features. Three regions can be identified along the profile behind the first row. A first one, which extends from the rear stagnation point up to x_c =1.2d, characterised by a negative uniform value of the mean velocity, a second one, which extends from x_c =1.2d up to about to x_c =2.1d (position corresponding to the centre of the downstream cylinder), identified by a steep uniform increase and, finally, a last one characterised by an approximately uniform positive value of the axial mean velocity.

Three regions can also be identified in the downstream profiles. However, they are not as well defined as behind the first one: in particular as the vortex formation length (position of the maximum r.m.s velocity along the centreline) decreases, the first region shortens. It can be seen that behind the fifth cylinder, whose vortex formation length is about 0.9d, the first region cannot be detected, while behind the sixth one both the first and third regions can be identified only by a very slight variation of the slope of the velocity gradient.

Finally, as already stated, the point along the centreline where the mean velocity magnitude is zero is approximately equal to that of the maximum r.m.s velocity in all profiles. Table 4.2 shows a comparison of the vortex formation length obtained in steady and pulsating flow (f_d = 10 Hz) at Re = 12,800 and 4,900 respectively. It is apparent that despite of the lower Reynolds number, the pulsations have the effect of reducing the vortex formation length behind the first two rows and the sixth one. In inner rows, where the effect of pulsations is weaker, the vortex formation length is unchanged. It should be noted that although the effect of pulsations on the turbulence levels is more pronounced in the wake of the first cylinder, the reduction of the vortex formation is significantly larger behind the second one. This can probably be attributed to the effect of the pulsations on the fluid dynamics characteristics of the flow approaching the cylinder[14], and in particular of the flow in the wake of the

[14] It should be observed that the unique features of the flow around the second cylinder are partly due to the fact that, as already stated, the flow approaching it is only partly obstructed by the first one.

upstream one (the first cylinder). As was also confirmed by the visualisation study (see paragraph 4.9), the most significant effect of the pulsations was observed in the wake of the first cylinder. The changes in the structure of the flow caused by the pulsations have, as stated, an apparent impact on the mean recirculation region and the vortex formation length of the downstream cylinders and particularly of the second one. The larger variation in the vortex formation length behind the second cylinder than behind the first one also implies that any change in the vortex formation cannot be directly or solely related to the variation of the turbulence levels of the cylinders themselves caused by the pulsations.

Table 4.2. Comparison of the vortex formation length obtained in steady and pulsating flow (f_d = 10 Hz) at Re = 12,800 and 4,900 respectively.

	ASYMMETRIC ARRAY WITH CIRCULAR CYLINDERS (steady flow)	ASYMMETRIC ARRAY WITH CIRCULAR CYLINDERS (pulsating flow)
Row Cylinder	L_F/d (Re = 12,800)	L_F/d (Re = 4,900, f_d = 10 Hz)
1st	1.65	1.4
2nd	$2.2 < L_F/d < 2.5$	1.2
3rd	1.0	1.0
4th	1.0	1.0
5th	1.1	1.0
6th	1.6	1.2

It should be observed that if the measurements in pulsating flow had been taken at the same Re as in steady flow (Re = 12,800), the location of the r.m.s peak behind all rows would occur closer to the cylinder rear wall. It is possible that the peak location is too close to the wall to be identified using LDA.

4.3.3 Vortex shedding characteristics and lock-on

Velocity spectra in pulsating flow (Re = 2,700 and 4,900, f_d = 10 Hz) were estimated at one axial location behind each cylinder (x_c/d = 0.5), at different transverse locations and for two different relative amplitudes, A_o, that is $A_o \approx 0.35$ (Case 1) and $A_o \approx 0.24$ (Case 2) respectively. Generally two lock-on modes can be identified in tube arrays in crossflow (Konstantinidis, 2001): the vortex shedding frequency can either lock on the pulsation frequency or half of it. The experimental results showed that in the asymmetric array with circular tubes both modes of lock-on could be identified, depending on both the driving frequency, f_d, and the relative amplitude, A_o.

Case 1. Pulsating flow (Re = 2,700, f_d = 10 Hz and $A_o \approx 0.35$). Figure 4.25 shows amplitude spectra and time traces upstream of the tube bank and behind the first row cylinder in pulsating flow at Re = 2,700 and $A_o \approx 0.35$. A peak is observed at 10 Hz (A = 0.069 m/s), (Figure 4.25a) corresponding to the frequency of the superimposed pulsations. The time trace (Figure 4.25 (b)) clearly shows the time-dependent mean flow (nearly sinusoidal). Figures 4.25 (c) and (d) show clearly that while the steady flow spectra recorded behind the first row were characterised by the absence of a well defined vortex shedding frequency the pulsating flow spectra exhibit two dominant peaks, one at the frequency of pulsation, 10 Hz (A = 0.054 m/s), and the second, of higher amplitude, at half the pulsation frequency, 5 Hz (A = 0.155 m/s). The superimposed pulsations incite vortex shedding from the first cylinder, which was suppressed in steady flow, as was also observed in both the in-line arrays with elliptic (Castiglia et al, 2001) and circular tubes (Konstantinidis et al, 2000) respectively,

Figure 4.26 shows a comparison of selected amplitude spectra[16] and time traces behind the first row at different transverse locations. Although two dominant peaks can be observed in all spectra, one at the pulsation frequency, 10 Hz, and the second at half of it, 5 Hz, the amplitude of the peaks varies along the transverse direction. In

[16] It should be noted that the amplitude of both the pulsations and the natural vortex shedding peak play a key role in the lock-on phenomenon. Therefore, amplitude spectra were here preferred to power spectra which were instead used in steady flow.

particular the amplitude of the peak at 5 Hz increases significantly from $y/S_T = 0.389$ ($A = 0.04$ m/s) to $y/S_T = 0.167$ ($A = 0.155$ m/s) as the cylinder wake is approached.

Figure 4.27 shows amplitude spectra in the wake of the downstream rows. It can be seen that the first mode of lock-on (i.e. at half the pulsation frequency) occurs primarily behind the first row. In general, the corresponding lock-on effect is less strong in inner rows and weakens with row depth (as was also observed in the in-line array with elliptic tubes; the amplitude of the 5 Hz peak generally decreases in the downstream direction while that of the peak at 10 Hz increases).

Case 2. Pulsating flow ($Re = 4{,}900$, $f_d = 10$ Hz and $A_o \approx 0.24$). Velocity spectra were also estimated in pulsating flow at the same driving frequency, $f_d = 10$, and locations as those of the spectra described above, at $Re = 4{,}900$. The relative amplitude, A_o, upstream of the tube bundle was approximately equal to 0.24. Figure 4.28 show amplitude spectra and time traces of the flow upstream of the tube bundle ($x/S_L = -1.0$), behind the first and fifth cylinders in pulsating flow. It is apparent that the amplitude ($A = 0.155$ m/s) of the incoming pulsations (Figure 4.28 (a)) is significantly higher than that ($A = 0.07$ m/s) corresponding to the velocity spectrum shown in Figure 4.25 (a) previously discussed. It should be noted that although the amplitude of the pulsations upstream of the tube bundle is higher, the relative amplitude, A_o, that is, the ratio between the amplitude of pulsations (averaged in time) and the upstream bulk velocity, is considerably lower ($A_o \approx 0.24$ against $A_o \approx 0.35$). It should be observed also that due to the increased Reynolds number (from $Re = 2{,}700$ to $Re = 4{,}900$) the natural vortex shedding frequencies (in the present array, as already stated, multiple shedding frequencies could be identified) in steady flow also increase. Therefore, the natural vortex formation frequency, f_{so}, was, in general, closer to the superimposed driving frequency, f_d. This condition favoured the occurrence of the first mode of lock-on. It should be noted that no peak at 5 Hz, that is at half the pulsation frequency, is observed in Figure 4.28, confirming that the vortex shedding frequency locks-on at the pulsation frequency, that is at 10 Hz. The amplitude of the frequency peak at 10 Hz is also substantially increased in relation to the upstream value ($A = 0.27$ compared with 0.145 upstream). However, the amplitude of the peak behind the fifth row (Figure 4.28 (e)) is significantly lower

than that behind the upstream rows denoting a diminishing effect of pulsations with row depth.

4.4 Skewness and kurtosis in steady and pulsating flow

The skewness and kurtosis of the velocity probability function were also determined in both steady and pulsating flow at one axial station behind each row ($x_o/S_L = 0.5$) at Re = 4900. Figures 4.29 (a) and (b) show the kurtosis and skewness profiles[17] respectively behind the first and second rows in steady flow (Re = 4900). The planes along which measurements were taken are shown in the same figures by dashed lines. It is apparent that both skewness and kurtosis profiles are quite uniform on the entrance to the tube bank. Their magnitudes are approximately equal to those for a normal distribution, that is 3 for the kurtosis and 0 for the skewness. Their profiles and magnitudes behind the first cylinder do not seem to be affected by the presence of the downstream one up to about $x/S_L = 0.59$.

Kurtosis in steady flow. In the wakes of the first and second cylinders the kurtosis (Figure 4.29 (a)) values are similar to the ones in the freestream and comparable to those for a normal distribution, that is Kr ≅ 3. Clearly the downstream profiles show two relative maxima, whose magnitude is increasing in the downstream direction. The profile at $x/S_L = 0.59$ presents two maxima, symmetrically positioned around the first cylinder centreline ($x/S_T = \pm 0.167$). Their magnitudes are 5.6 and 4.6 respectively. In downstream profiles the positive peak (that is the one on the positive y-direction) moves away from the centreline in agreement with the outward shift of the outer shear layer separating from the first cylinder. Furthermore, these peaks broaden in downstream direction, in agreement with the increasing shear layer thickness. The latter indicates also the distance along the transverse direction which separates the freestream, characterised by high flow velocities, and the wake. This implies that in this restricted region very similar velocity scales are recorded.

[17] It should be noted that the skewness and kurtosis values in Figures 4.29 (a) and (b) were multiplied by a factor of 2 and 5 respectively in order to magnify the profiles' gradients.

Skewness in steady flow. Figure 4.29 (b) shows the skewness distribution behind the first two rows in steady flow (Re = 4900). The skewness profiles at $x/S_L = 0$ and 0.19 are quite uniform. The magnitude of the skewnees along these profiles as well as along the freestream is approximately equal to that for a normal distribution, that is 0. The profile at $x/S_L = 0.4$ has two negative maxima at $y/S_T = \pm 0.167$, corresponding to the locations of the maximum kurtosis. Low velocity regions move intermittently into those where the maxima are recorded, where high velocities are mostly present, i.e. on average the flow has large fluctuations below the mean more often than above it. Further downstream the two peaks are observed at the same locations as the maxima kurtosis and accordingly move away from the centreline. The skewness peak recorded on the positive y-direction increases in magnitude while the skewness values along the wake centreline (which differs from the upstream cylinder centreline) do not deviate significantly from that of a normal distribution. Over the shoulder of the second cylinder the value of the peak on the negative y-direction decreases with respect to the one on the opposite direction. This is probably due to the acceleration of the flow, which reduces the effect that the aforementioned incoming low velocity regions have locally on the velocity distribution and therefore on the magnitude of the skewness. In the wake of the second row ($x/S_L \geq 1.59$) the skewness profiles show ($y_c/S_L \leq 0$, where y_c represents the y-axis of the local co-ordinate system of the second cylinder) a negative peak, in a position again corresponding to the shear layer separating from the second cylinder, which moves away from the centreline and decreases in magnitude in the downstream direction. Further downstream ($x/S_L \geq 2.59$) the profiles (not shown) are more uniform and the skewness values tend to those for a normal distribution, that is, Sk = 0. This implies that in the downstream direction the fluctuations are more uniformly distributed around the mean local velocities than behind the first cylinder.

Comparison of skewness and kurtosis profiles between steady and pulsating flow

Figure 4.30 shows a comparison of the kurtosis and skewness profiles between steady and pulsating flow on the entrance to the tube bank and behind the first row. It is apparent from Figure 4.30 (a) that the skewness is not affected by the pulsations

upstream of the tube bundle and the corresponding upstream velocities, as indicated by the zero skewness values, have a normal distribution. However, although both the profiles in steady and pulsating flow exhibit two negative peaks around the centreline, these peaks are higher and broader in pulsating flow. This implies that in pulsating flow large fluctuations below the mean local velocity are much more frequent than in steady flow. This is probably due to the high frequency (10 Hz) at which vortices, which can be considered as carriers of low velocity regions intermittently moving into the accelerated shear layers, were shed. Figure 4.30 (c) shows that upstream of the tube bank (x/S_L = -1.0) the kurtosis values are higher in steady than in the pulsating flow. This means that the velocity distributions upstream of the tube bundle are slightly more peaked than the pulsating ones. Behind the first row, the profiles are identical to the ones recorded upstream of the tube bank in the freestream, while significant differences can be observed along the shear layers and in the wake. Two positive peaks are observed in both profiles, at locations corresponding to the maximum kurtosis values. It is apparent that the peaks in pulsating flow are much higher (Kr = 11.9 and 8.2 on the positive and negative y-directions respectively; the ones in steady flow are not higher than 4.3) and broader. Therefore, in pulsating flow the velocity distributions along the shear layers separating from the upstream cylinder are more peaked around the mean local velocities and have a longer left tail (the distribution is skewed to the right) than the ones in steady flow. The latter, therefore, are flatter and more symmetrical implying that less dissimilar velocity scales are locally recorded. In downstream rows the differences in the skewness and kurtosis profiles between steady and pulsating flow were less significant since the effect of pulsations was less pronounced than in the first row.

4.5 Flow visualisation

In order to investigate the near wake fluid dynamics and the flow periodicities in the asymmetric array with circular tubes and complement the LDA findings visualisation pictures have been taken and extensively examined in both steady and pulsating flow behind the first, second and third cylinders.

Selected visualisation pictures obtained behind the first and second cylinders in steady flow are shown in Figures 4.31-4.43. Selected frames for pulsating flow behind the first cylinder are also shown in Figure 4.44 for a driving frequency of 10 Hz.

The time interval between frames, ΔT_F, was equal to 20 ms. The first frame, Frame 1, was arbitrarily chosen as corresponding to the observation time t = 0. In the sequence of frames time increases from left to right and from top to bottom. The nomenclature adopted does not differ from that used in the description of the visualisation pictures shown in Chapter 3.

Sumner et al (2000) identified nine flow patterns in their visualisation study about the flow around two circular cylinders in cross-flow, arranged in a staggered configuration. The different flow patterns were attributed to the effect of the geometrical parameter, P/d, that is the ratio between the centre-to-centre distance between successive cylinders in a column and the cylinder diameter, and the angle ψ between the axial direction and the direction defined by P[18]. At angles ψ between 10° and 30° and for P/d < 3, a single flow pattern was identified and defined as *synchronised vortex shedding flow pattern.* According to its definition, the separated shear layer from the upstream cylinder does not reattach onto the outer (here "positive") surface of the downstream one. Due to the large angle of incidence, ψ, some of the oncoming mean flow is always permitted to penetrate the gap between cylinders. On the other hand, the given flow pattern was identified also by the geometrical characteristics of the "common" far wake downstream of the second cylinder. The asymmetric array here investigated comprises multiple cylinders in a

[18] In the asymmetric array here investigated the pitch ratio, P/d, and the angle of incidence, ψ, were equal to 2.3° and 25.5° respectively.

row and a direct comparison between the flow patterns identified by Sumner et al (2000) and the ones observed in the present visualisation study cannot be made considering that a "far wake" cannot be identified in inner rows of an array. The comparison was, therefore, limited to the wake of the upper cylinder and the "free" shear layer, that is the one not deflected by the downstream cylinder.

Figures 4.31 (a)-(d) show selected flow visualisation pictures obtained behind the first row at Re = 1,100. Despite of the low Reynolds numbers, clear vortex shedding activity can be observed behind the first row cylinder, which is in sharp contrast with observations in an equivalent in-line array (Konstantinidis et al, 2000). However, it is very difficult to establish from the visualisation pictures if the wake flow is periodical and if a unique vortex shedding frequency exists. Although the flow pattern is nearly symmetrical in the first four frames of the sequence (t = 0-80 ms), at t = 100 ms the wake flow is already asymmetrical. The first frame (t = 0 ms) of Figure 4.31 (a) shows two vortices, P_1 clockwise, and N_1, anticlockwise, shed by the first cylinder and convected downstream. From t = 0 ms to t = 60 ms the two vortices grow in size while convected downstream at approximately the same axial velocity. P_1 is slightly smaller in diameter due to the presence of the downstream cylinder, which has the double effect of deflecting P_1 toward the centreline and limiting its growth in size. P_1, therefore acquires a transverse velocity component which delays its downstream axial convection. Overtaken by N_1 at t = 80 ms, P_1, is again free to grow in size. At t = 120 ms it crosses the centreline and about 20 ms afterwards it finally dissipates into turbulence. Meanwhile a second anticlockwise vortex, N_2, has formed and is convected downstream. It can be seen that at t = 120 ms N_2 (shown in the successive frame, t = 140 ms) draws into the wake irrotational flow. We can assume this time frame as the one at which the flow begins to cross the wake axis (since the formation of N_2) and the corresponding cross point as the end of the formation region, which was graphically estimated to be approximately equal to L_F/d = 1.3. This value is slightly lower than the one determined by the LDA measurements, that is L_F/d = 1.6. A similar discrepancy is also observed behind the following rows and it can probably be attributed to the asymmetric characteristics of the flow as explained later in this paragraph. It can be observed here that the flow visualisation consists of instantaneous images of the wake structure while the wake parameters determined by the LDA are time-averaged. Furthermore, the deviation

between the instantaneous flow patterns and the averaged one is probably more significant when the flow field is not symmetrical. The time-averaged velocity field is therefore less representative then when the flow is symmetrical. It should be noted that the fact that a single vortex shedding could not be ascertained might indicate that the wake flow field varies from cycle to cycle.

A comparison between the frames at t = 0 ms, 20 and 40 ms, for instance, with those at t = 300, 320 and 340 ms shows that the flow pattern repeats (although some asymmetries are evident, particularly in the size of the individual vortices) after T = 300 ms, therefore suggesting a flow periodicity with frequency equal to f_s = 1/300 ms^{-1} = 3.3 Hz. On the other hand if the frames at t = 300 ms (Figure 4.31 (b)) and t = 300 + T = 600 ms (Figure 4.31 (d)) are compared it is clear that the flow pattern as a whole is either not periodical or the corresponding vortex shedding is not well defined. Furthermore it is important to notice that this vortex activity does not involve the whole wake, as a region close to the cylinder wall is almost stagnant, resembling the wake characteristics of the first elliptic cylinder in the in-line array described in Chapter 3. At this Reynolds number, therefore, the flow images show the absence of any significant vorticity in the base region. Furthermore, the observation of the flow patterns shown by the visualisation images suggests that the process of vortex formation occurring further downstream is not related to any vortical activity adjacent to the base of the cylinder. Identical conclusions were drawn by Lin et al (1995) in their investigation about the instantaneous near wake of a circular cylinder.

It becomes interesting at this point to investigate if the individual "clockwise" or "anticlockwise" vortices are shed periodically and eventually to determine the corresponding frequencies. It should be noted that in many of the staggered flow patterns, the vortex shedding frequencies are mostly unique for each individual shear layer rather than for each cylinder (Summer et al, 2000). A comparison between N_1 (t = 0 ms), N_2 (t = 140 ms), N_3 (t = 280 ms), N_4 (t = 420 ms) and N_5 (t = 560 ms) shows that the anticlockwise vortices are shed at a frequency of about 1/140 Hz ≅ 7.0 Hz. A comparison of the individual positive vortices P_1 (t = 0 ms), P_3 (t = 280 ms), P_4 (t = 420) and P_5 (t = 560 ms) and the frame at t = 140 ms indicates that if a clockwise vortex with similar characteristics as P_1, P_3, P_4 and P_5 could be identified at t = 140

ms, then the same shedding frequency of that of the anticlockwise vortices, that is 7 Hz, could be ascertained. However, it can be seen that the positive vortex P_2 that appears[19] in the time frame t = 120 ms is not present in the following one (t = 140 ms). The reason for that can be found observing the frame at t = 120 ms. Three vortices can be distinguished: N_1, anticlockwise, P_1 and P_2, clockwise. P_1 is delayed in his downstream convection by both N_1 and by the deflected positive shear layer, as previously stated. This delay causes P_1 and P_2, which bear vorticity of the same sign, to collide.

This implies probably that the clockwise vortices are formed at the same frequency as the anticlockwise ones, but both the cycle-to-cycle variations and the asymmetric arrangement of the tubes affect only the flow pattern of the convected vortices which, therefore, is not periodical, or again whose periodicity is not well defined.

The presence of the downstream cylinder in fact affects differently the convection pattern of clockwise and anticlockwise vortices but not the frequency at which they are formed and shed. If the geometrical configuration was symmetrical then the downstream cylinders would affect equally the vortices shed from both sides of the upstream cylinders and the flow pattern would be eventually clearly periodical. The LDA measurements showed that no dominant peak could be observed in the frequency spectra obtained behind the first cylinder. This could be partly due to the measurement location (as already stated, in the region within the shear layer that extends in the downstream direction up to about 0.5d away from the rear stagnation point the flow is nearly stagnant) and partly to the described asymmetry of the flow, which affects the periodicity of the flow pattern.

Figures 4.32 (a)-(c) show selected flow visualisation pictures obtained behind the second cylinder at Re = 1,100 in steady flow. Significant differences can be noticed with the wake geometry and flow dynamics of the first cylinder. Firstly, no stagnant region is discernible near the base of the cylinder. The wake is, in fact, characterised by intense vortex activity and intense mass transfer across the centreline, which inhibits symmetrical vortex shedding. The accelerated and deflected flow through

---

[19] The vortex is not clearly shown both because it is dissipating and because the image is not as clear as the video recording corresponding one, but it can be clearly seen in the time frame at t = 40 ms.

the gap between the first and second cylinder causes an early separation of the boundary layer from the left (inner) hand side of the cylinder wall (see Frame 1, t = 0 ms). This was also confirmed by the heat transfer measurements described in Chapter 6. At t = 0, Frame 1, although not clearly shown, an anticlockwise vortex N_1 is formed. In the successive time frames it grows in size and is convected downstream (see t = 80 ms) while moving across the wake. Flow is violently drawn into the wake by both N_1 and by the accelerated shear layer deflected by the downstream cylinder (the third one) across the wake. It is interesting to notice that the particular asymmetric configuration of the array results into different vortex patterns on the two sides of the cylinder. In fact while the negative[20] shear layer is subjected to large transversal oscillation, due to the effect of the growth and convection of N_1, the positive shear layer, at least in the near wake of the upstream cylinder, flows undisturbed in an approximately axial direction. From t = 80 ms to t = 120/130 ms N_1 is convected downstream at a very low velocity (in this time interval therefore N_1 stands close to the cylinder base continuously sweeping its surface).

Vortex convection velocity. The convection velocity of N_1 could be determined by estimating the distance travelled by N_1 between t = 20 ms and t = 200 ms. In order to do so the same grid was superimposed to both frames. The axial and radial convection velocity components of N_1 were estimated to be about 35.1 mm/s and 31.9 mm/s respectively. The absolute convection velocity was therefore 47.4 mm/s. The convection velocity of the clockwise vortex P_1 was also evaluated by measuring the distance travelled between t = 0 ms and t = 240 ms. The axial and radial velocity components of P_1 were estimated to be equal to 48.7 mm/s and 19.8 mm/s respectively. The resulting absolute convection velocity is therefore approximately equal to 52.6 mm/s. The significant difference (even considering the approximation of the evaluation) between the magnitude of the radial velocity components shows the effect of the downstream cylinder on the convection of the vortices and the asymmetry of the flow.

---

[20] As already stated, the negative (also anticlockwise) shear layer is the one on the left-hand side of the frame. Oppositely, the positive (also clockwise) shear layer is the one on the right-hand side of the frame.

Vortex formation length. The frame at t = 40 ms can be assumed as the one at which the flow begins to cross the wake axis (since the formation of N_1) and the corresponding cross point as the end of the formation region. The latter was graphically estimated to be equal to $L_F/d = 1.1$, again much lower than the one determined by the LDA measurements, that is $L_F/d = 2.2$-2.5.

This discrepancy can be probably attributed to the fact that the graphical estimation of the formation length was made by identifying the point at which the irrotational flow was drawn into the wake by the anticlockwise vortices only. The clockwise ones show a different pattern. They are convected downstream at a nearly constant convection velocity, whose radial component is negligible, their size is smaller than the anticlockwise ones and the flow they entrain is not visibly drawn across the wake.

Furthermore, it is possible to identify two vortex shedding frequencies, the one referring to the shedding frequency of anticlockwise vortices and the other to the shedding frequency of the clockwise ones. In fact the flow pattern on the "negative half-wake"[21] in the frame at t = 60 ms of Figure 4.32 repeats at t = 220/240 ms and again at t = 420 ms, with a period of 180 ms corresponding to a shedding frequency, f_s, equal to 5.55 Hz. It is more difficult to identify a well-defined frequency for the positive half-wake vortex activity due to the fact that the vorticity of the shed vortices is much lower than that of the anticlockwise ones and also due to the different phase and therefore different interaction pattern between clockwise and anticlockwise vortices in time. By comparing Frame 1, t = 0 ms, with that at t = 120 ms of Figure 4.32, it can be seen that the flow patterns repeats after t = 120 ms and, therefore, clockwise vortices (the vortex in Frame 1 is not clearly shown, but visible) are shed with a frequency of about 1/120 ms = 8.3 Hz. However, it should be noted that the LDA measurements showed that no dominant peak could be observed in the frequency spectrum (not shown for brevity) obtained behind the second cylinder at such low Re (Re = 1,100).

---

[21] The negative (also anticlockwise) half-wake is the one on the left-hand side of the frame. Conversely, the positive (also clockwise) half-wake is the one on the right-hand side of the frame.

Figure 4.33 (a)-(b) show four zoomed images of the separation points of the steady flow past the first cylinder (a) and the separation point of the flow past the negative (or anticlockwise) side of the second cylinder (b) respectively. Figure 4.33 (a) shows that the separation points of the flow past the first cylinder can be located by direct observation at approximately 90 degree from the front stagnation point. From Figure 4.33 (b) it can be clearly seen that, as previously stated, the separation of the flow past the anticlockwise side of the second cylinder occurs earlier than 90 degree. On the opposite side (clockwise) the separation point (not shown) can be again located at about 90 degree from the front stagnation point.

Figures 4.34 (a)-(b) show a complete cycle of vortex shedding behind the first cylinder under pulsating flow conditions (f_d = 10 Hz, A_o = 0.24, Re = 4,900). The sequence of pictures shows clearly that the superimposed pulsations have significantly altered the flow pattern. The first frame (t = 0 ms) shows two vortices, P_2 clockwise, and N_2 anticlockwise, that are forming, while other two, P_1 and N_1 are shed and convected downstream. It is noticeable that, similarly to what observed in the in-line array with elliptic tubes, the pulsations promote symmetrical vortex shedding (see in particular the frames at t = 120 ms, and the one at t = 140 ms). The downstream cylinder has the effect of limiting the growth of the clockwise vortices (which are, in fact, smaller than the corresponding anticlockwise ones) by deflecting and accelerating the clockwise shear layer into the gap between the cylinders. The deflection of the shear layer can be estimated by the frame at t = 80 ms, which shows a comparison between the direction of the shear layer on opposite sides of the centreline. The direction of the anticlockwise shear layer does not vary significantly in time, it only follows the formation and growth of new vortices. The angle between the direction of the positive shear layer and that of the cylinder centreline is approximately equal to 60°.

The sequence of frames shows that the flow pattern at t = 0 repeats after 100 ms. This corresponds to a flow periodicity (vortex shedding) with a frequency, f_s, of 1/100 kHz = 10 Hz; the pulsations have therefore triggered vortex shedding at the driving frequency in agreement with the LDA findings.

It is also evident by comparing Figures 4.34 and 4.31 that the pulsations "break" the quasi-stagnant "steady" wake that was confined to the proximity of the cylinder wall, increase the turbulence of the flow and decrease the formation length to the proximity of the rear stagnation point of the upstream cylinder.

4.6 Conclusions

An experimental investigation was carried out on the flow around an asymmetric array with circular cylinders. LDA and flow visualisation were used to study the velocity and vortex shedding characteristics in both steady and pulsating flow. The results showed that the tube bundle configuration investigated generates less turbulence than a staggered array (with the same longitudinal and transverse spacing) with circular tubes (Balabani, 1996). In the freestream the streamwise turbulence increases in the downstream direction from its upstream value up to $0.3U_\infty$. Values up to $0.5U_\infty$ are instead recorded in the wake of the first row. In contrast to what was observed in the in-line array with elliptic tubes, therefore, the interference between adjacent columns is not negligible. The turbulence is isotropic on the entrance of the bank (v'/u' = 1), but in the wakes of the downstream rows the anisotropy (1 - v'/u') raises above 60% with maximum values in the proximity of the downstream cylinders (80%), especially the third and fourth ones. This is in agreement with the flow in the wake regions of the staggered array that was found to be highly anisotropic, especially in the wake regions. A vortex shedding activity was detected, but it is not as well defined as in the in-line arrays with elliptic and circular cylinders respectively (Konstantinidis et al, 2000; Castiglia et al, 2001). The Strouhal number, defined by the gap velocity and the diameter of the circular cylinders, d, was found to be approximately equal to 0.22 in inner rows. The only significant effect of the pulsations on the turbulence of the flow was observed in the wake of the first cylinder. Lock-on of the natural vortex shedding at either the superimposed pulsation frequency or at half of it, depending on the relative amplitude of pulsations, was observed in all rows. Behind the first row, where no clear vortex shedding frequency could be determined (although, in contrast to what was observed in the in-line array with elliptic tubes, shed and convected vortices could be clearly distinguished) the

superimposed pulsations triggered the shedding of vortices and its frequency locked at the driving frequency or at half of it.

The flow visualisation study confirmed the findings of the LDA measurements and in particular the lack of a well-defined and unique vortex shedding frequency. Furthermore, it showed a weak vortex activity behind the first row, but also the presence of a region close to the cylinder wall, which is almost stagnant resembling only partially the wake characteristics of the first cylinder of the in-line array with elliptic tubes described in Chapter 3. In that case, the flow in the wake at the first row was entirely stagnant and was characterised by the absence of vortex activity. The chapter that follows examines the flow and vortex shedding characteristics of an in-line array with drop-shaped cylinders.

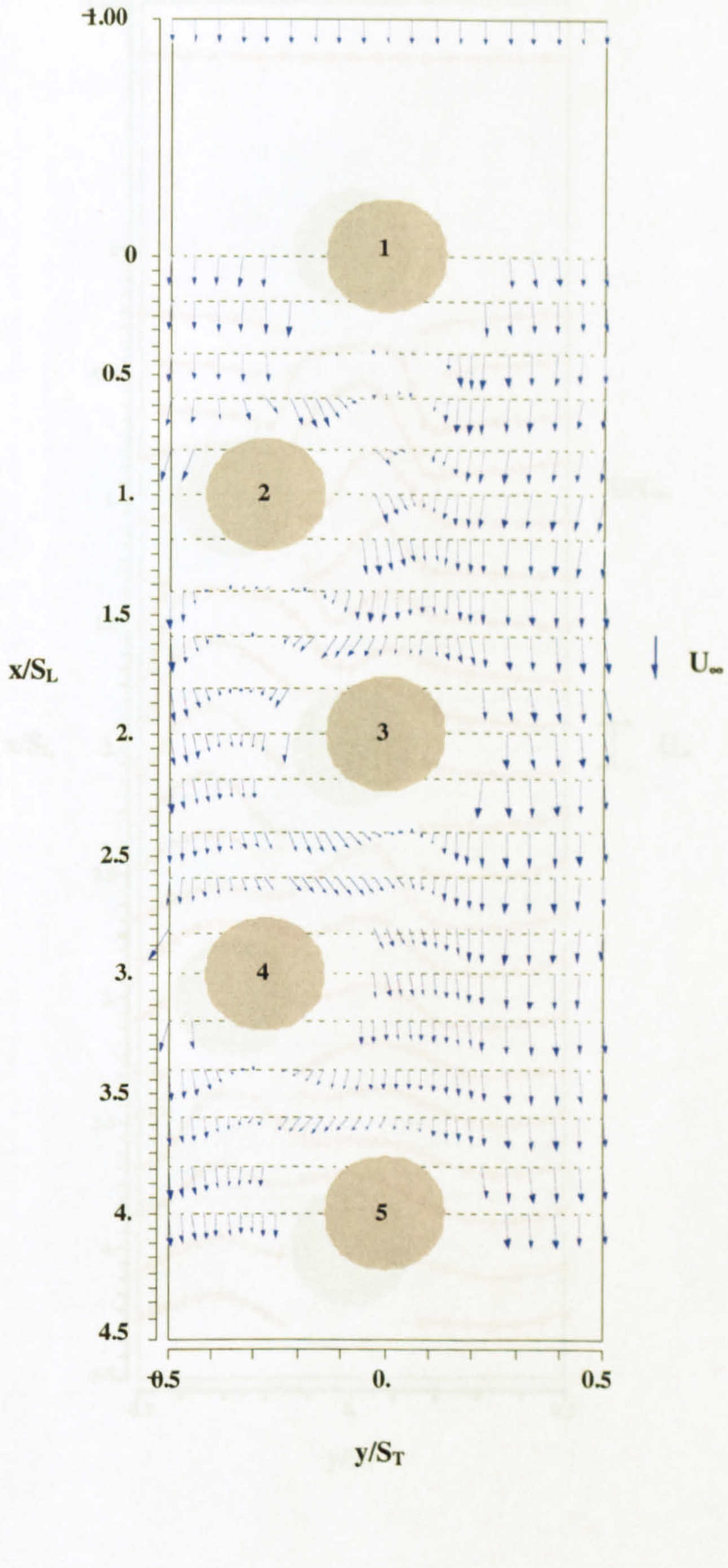

Figure 4.1. Velocity vectors in the 3.6 x 1.6 in the asymmetric tube bundle with circular tubes (steady flow, Re = 12,800).

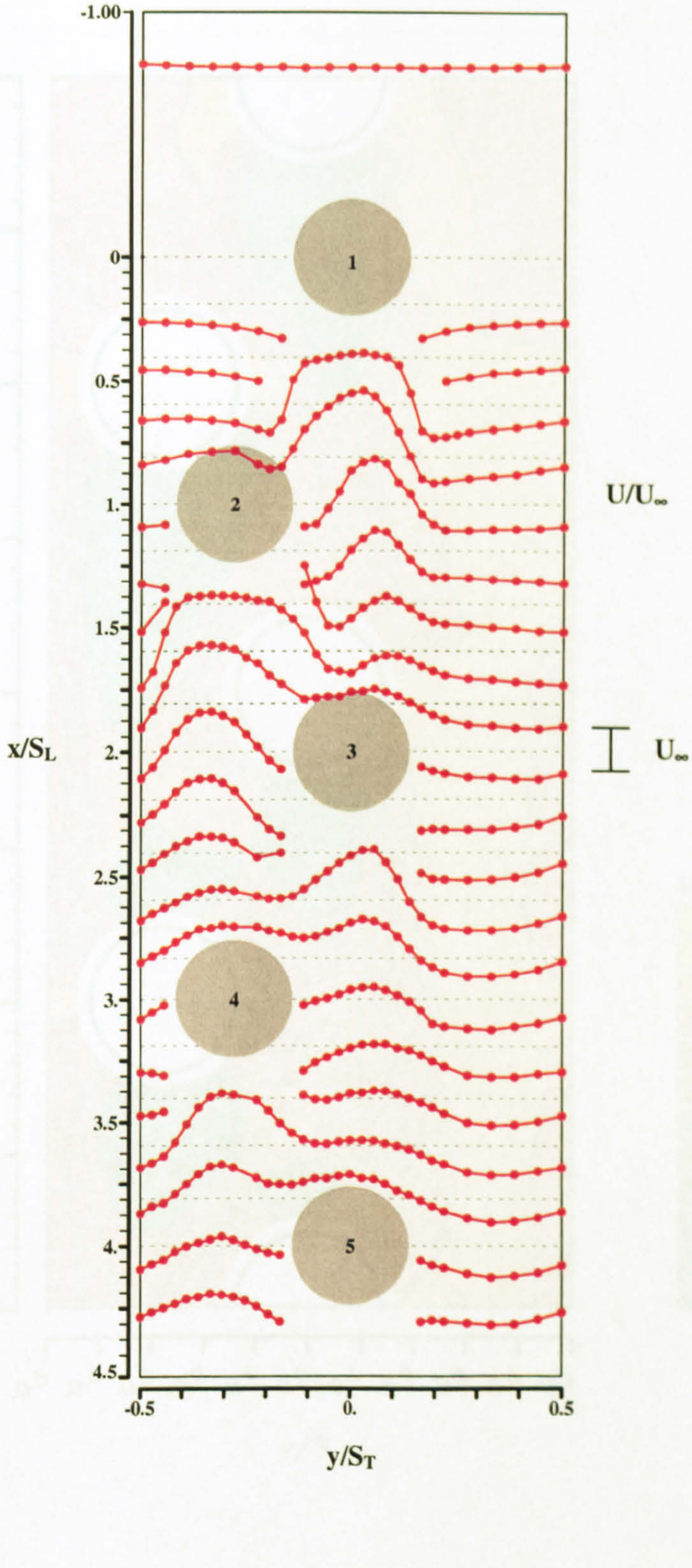

Figure 4.2. Axial mean velocity profiles, U/U_∞, in the asymmetric tube bundle with circular tubes (Re = 12,800).

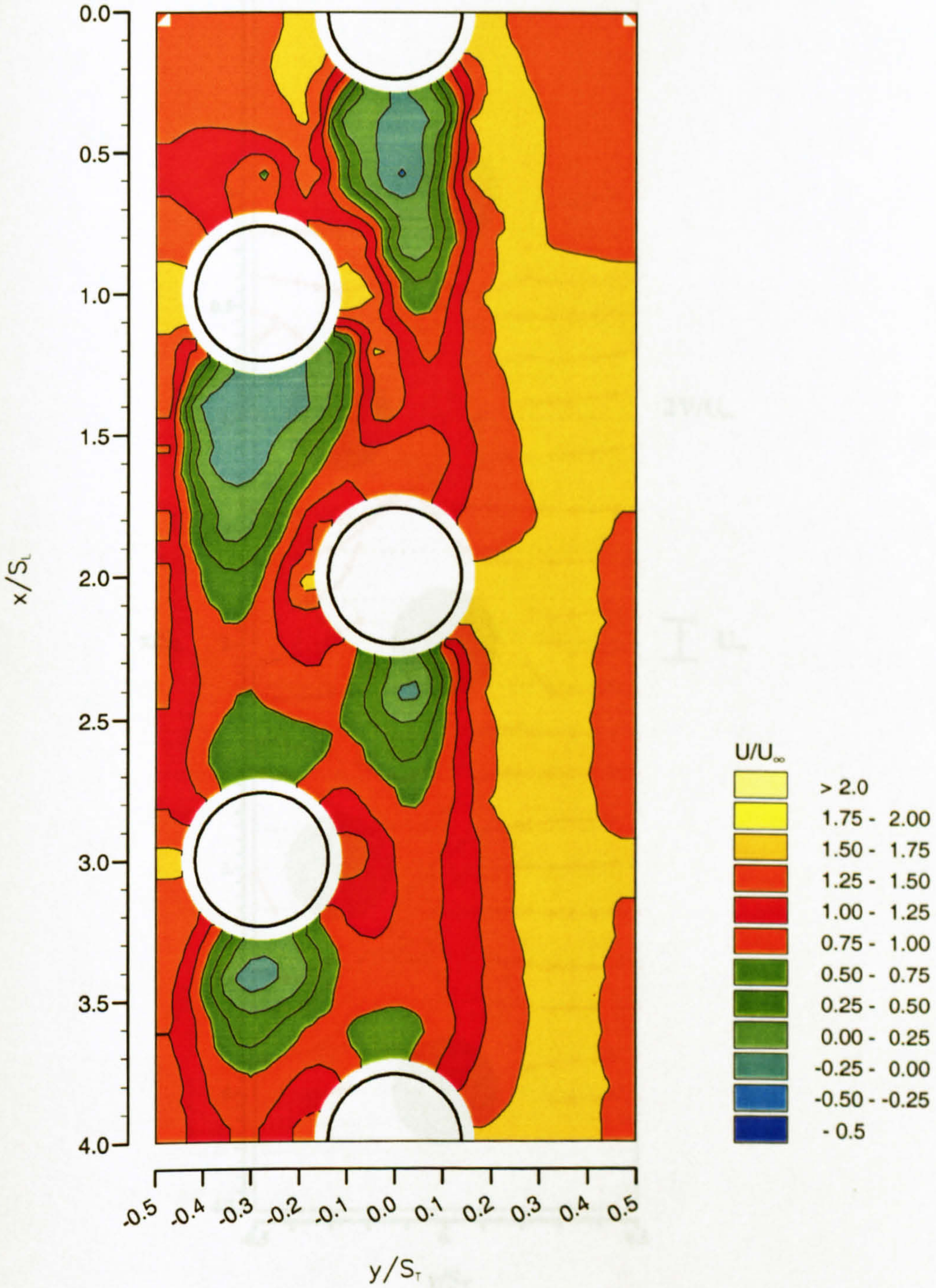

Figure 4.3. Contours of U/U_∞, in the asymmetric tube bundle with circular tubes (steady flow, Re = 12,800).

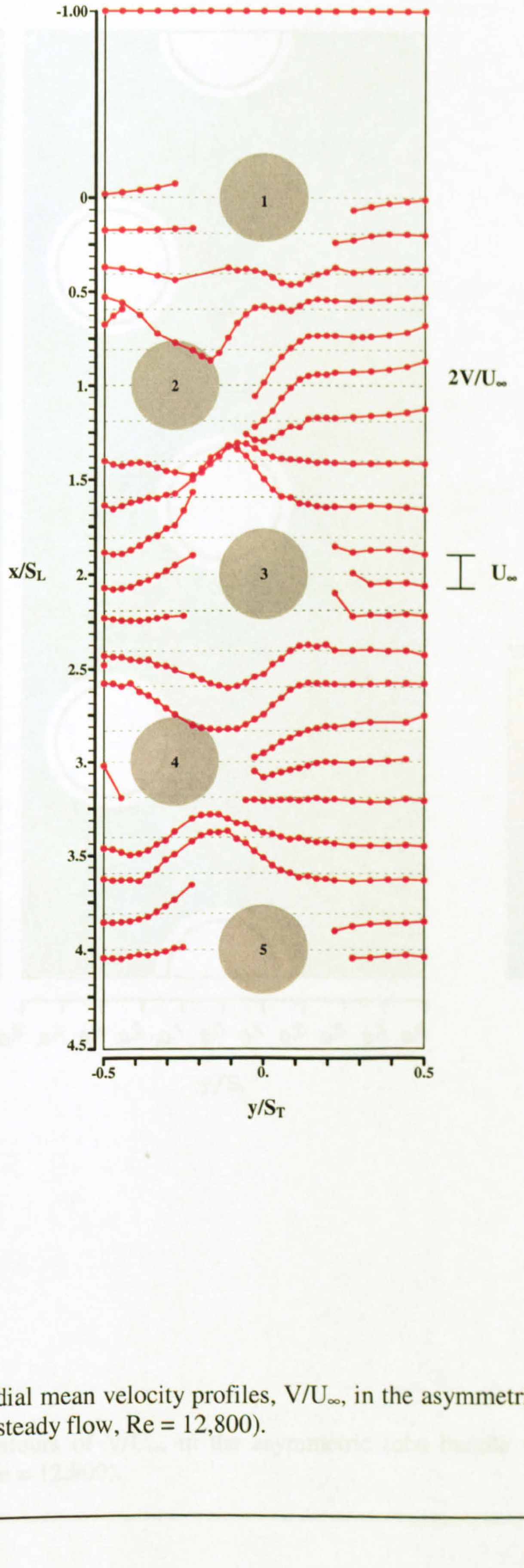

Figure 4.4. Radial mean velocity profiles, V/U_∞, in the asymmetric tube bundle with circular tubes (steady flow, Re = 12,800).

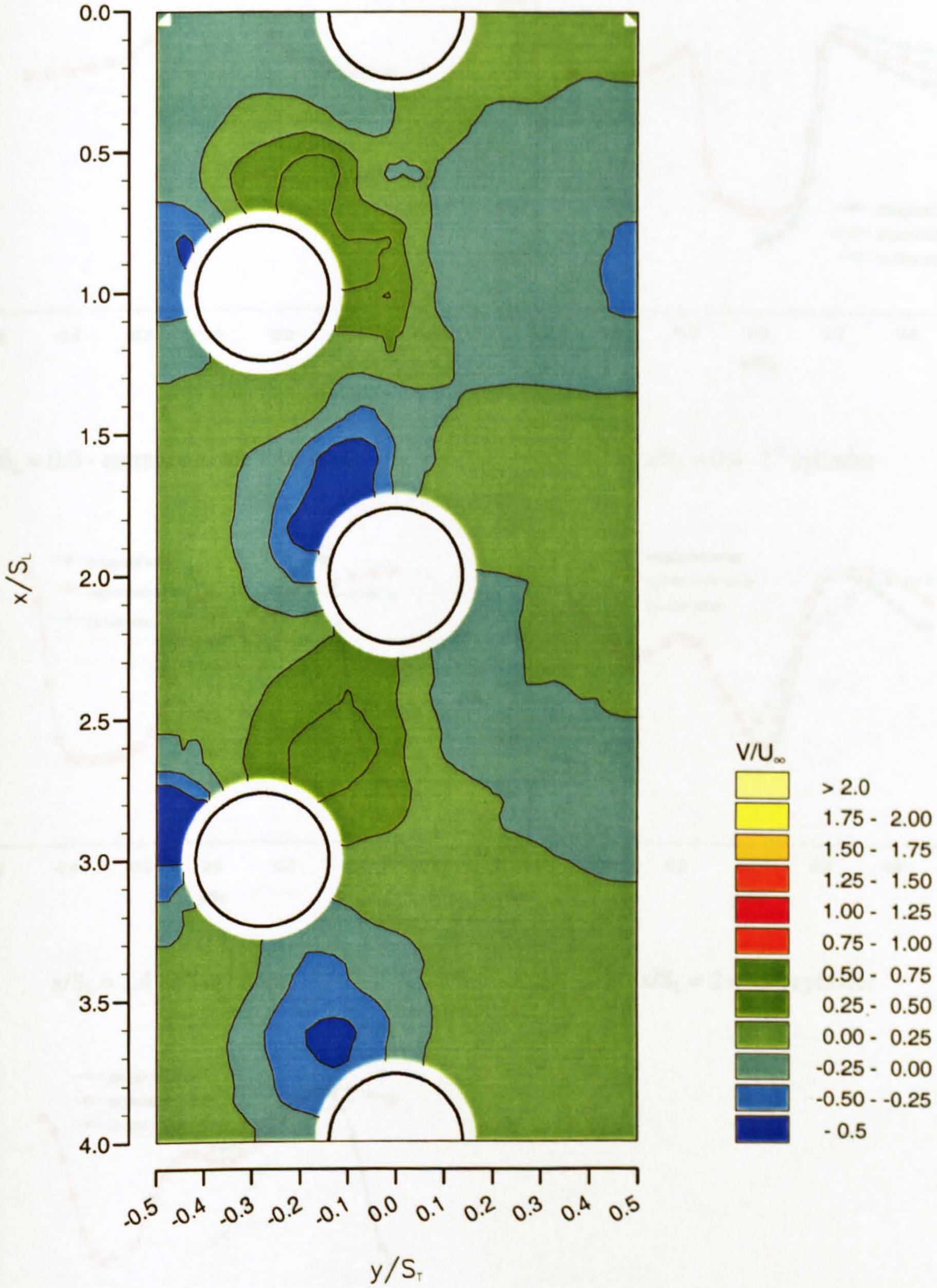

Figure 4.5. Contours of V/U_∞, in the asymmetric tube bundle with circular tubes (steady flow, Re = 12,800).

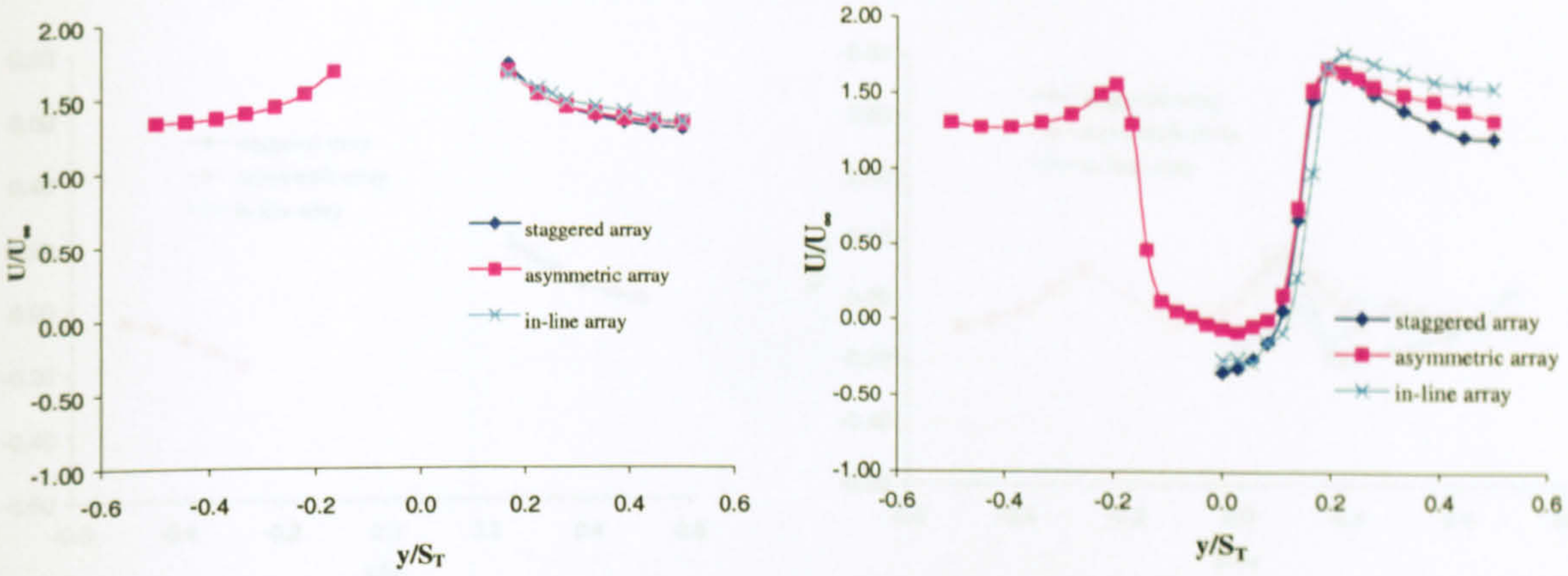

$x/S_L = 0.0$ - entrance to the tube bank

$x/S_L = 0.4$ - 1st cylinder

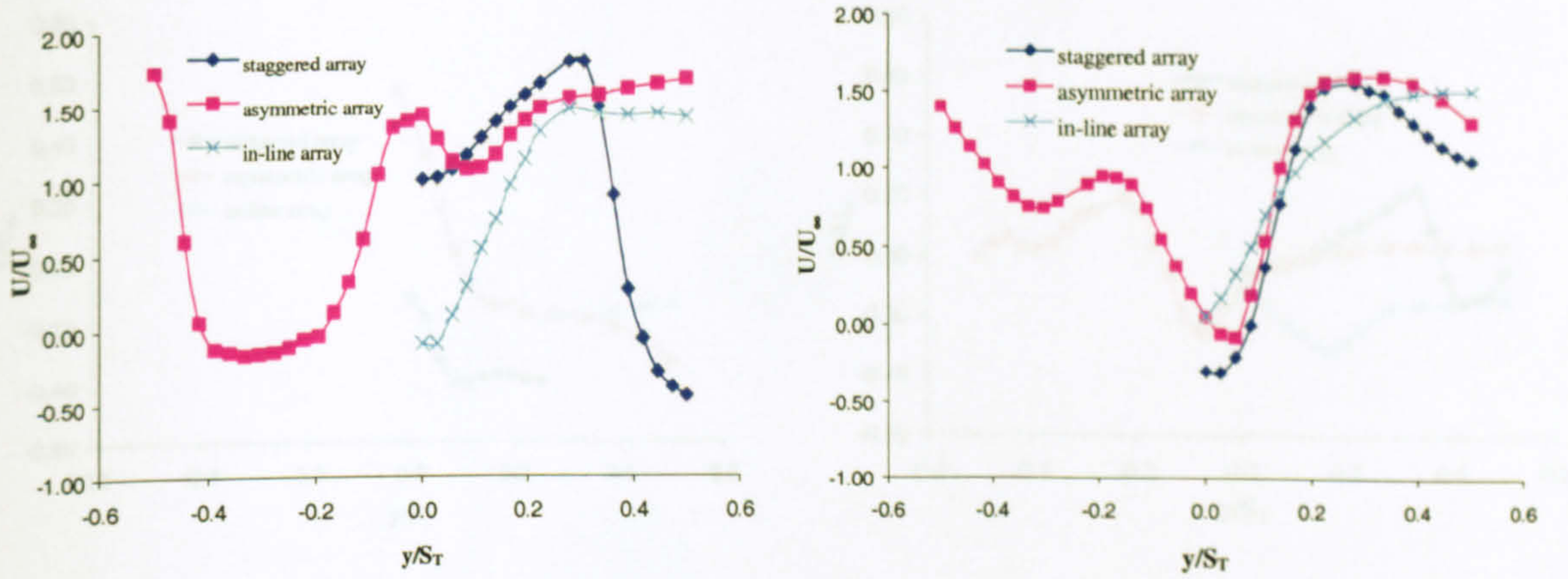

$x/S_L = 1.4$ - 2nd cylinder

$x/S_L = 2.4$ - 3rd cylinder

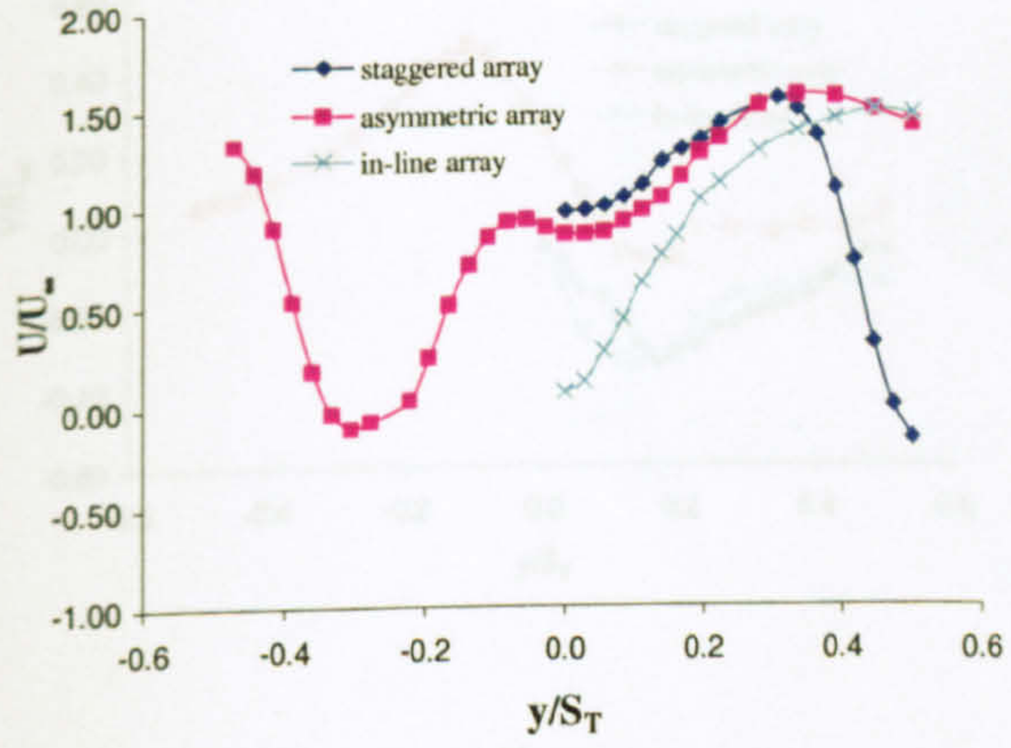

$x/S_L = 3.4$ - 4th cylinder

Figure 4.6. Comparison of the U/U_∞ profiles between the asymmetric bundle and both the staggered and the in-line one (Balabani, 1996).

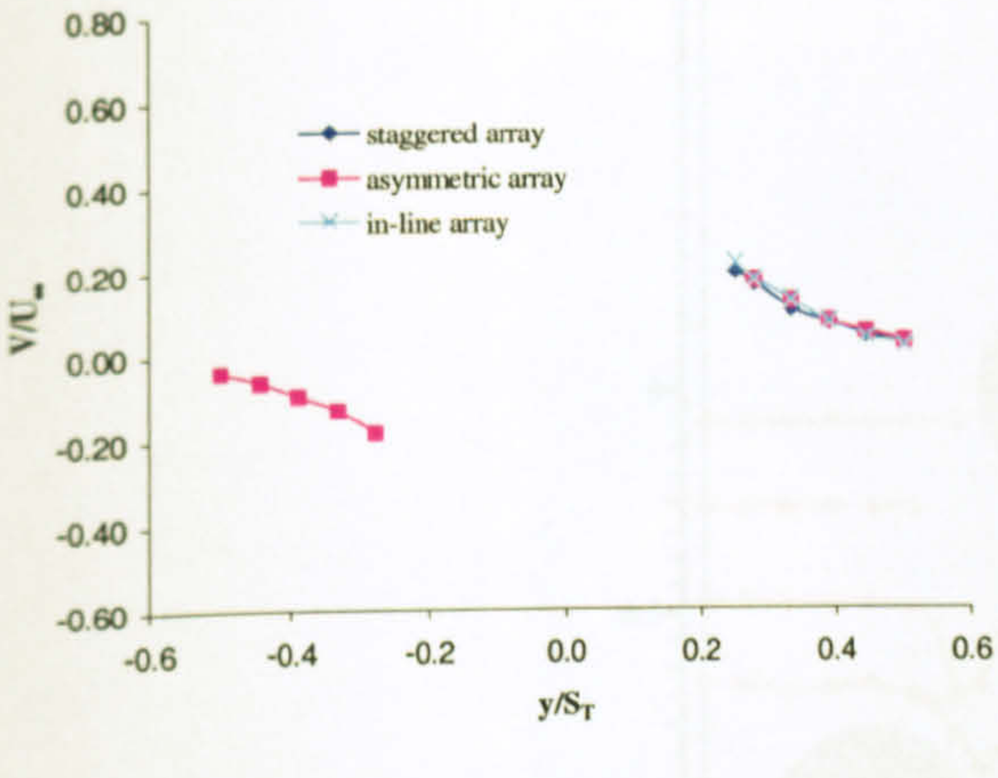

$x/S_L = 0.0$ - entrance of the tube bank

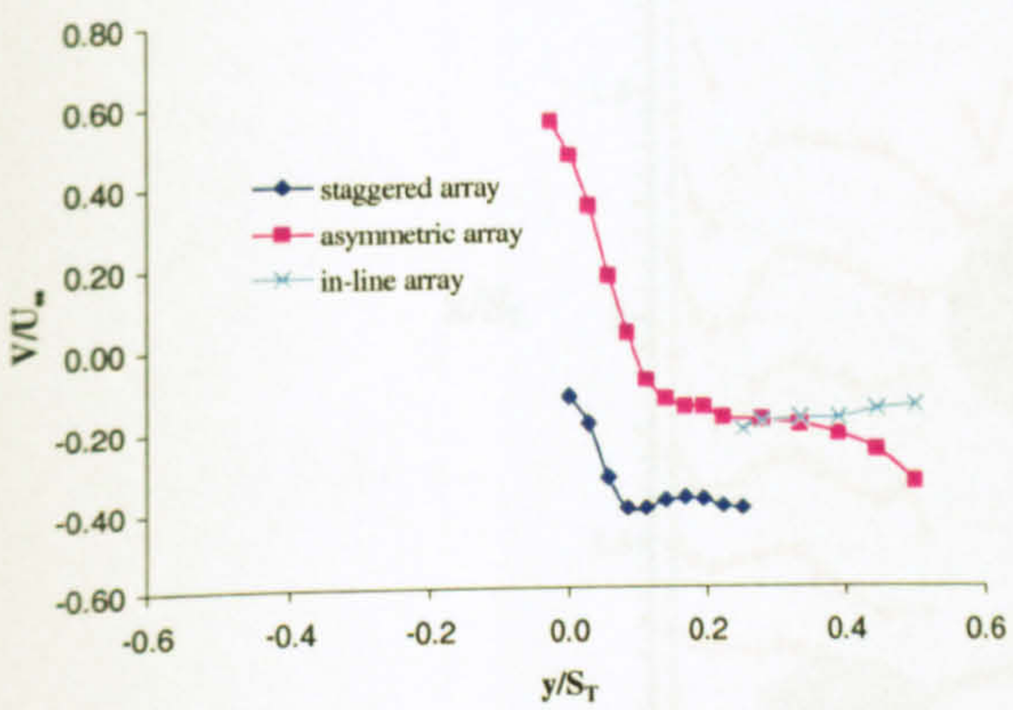

$x/S_L = 0.4$ - 1st cylinder

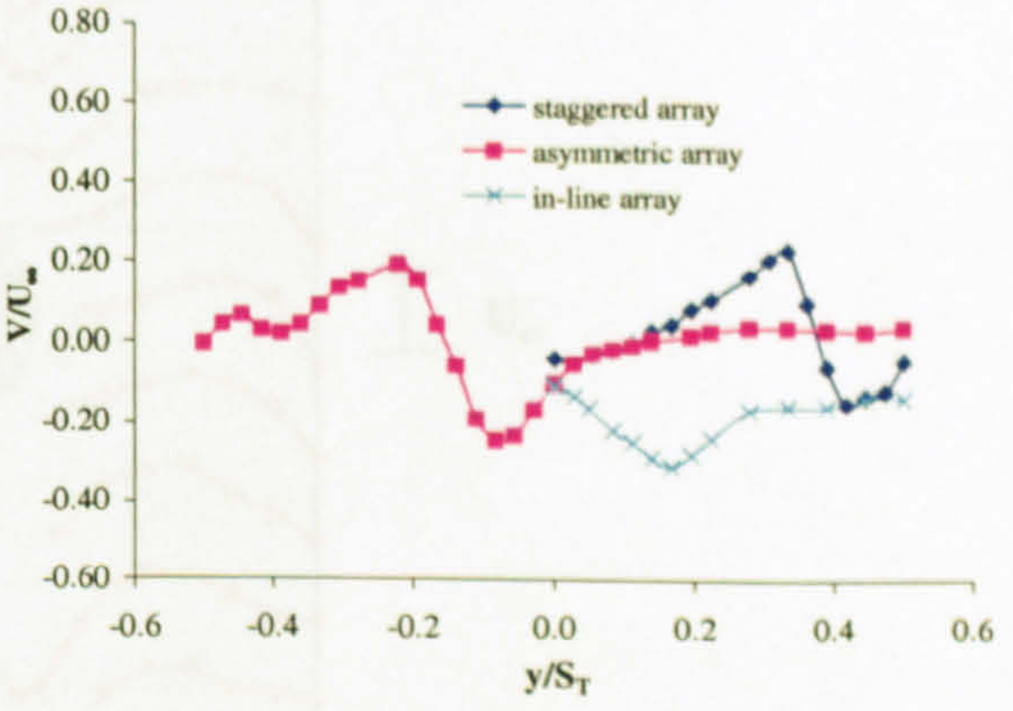

$x/S_L = 1.0$ - 1st cylinder

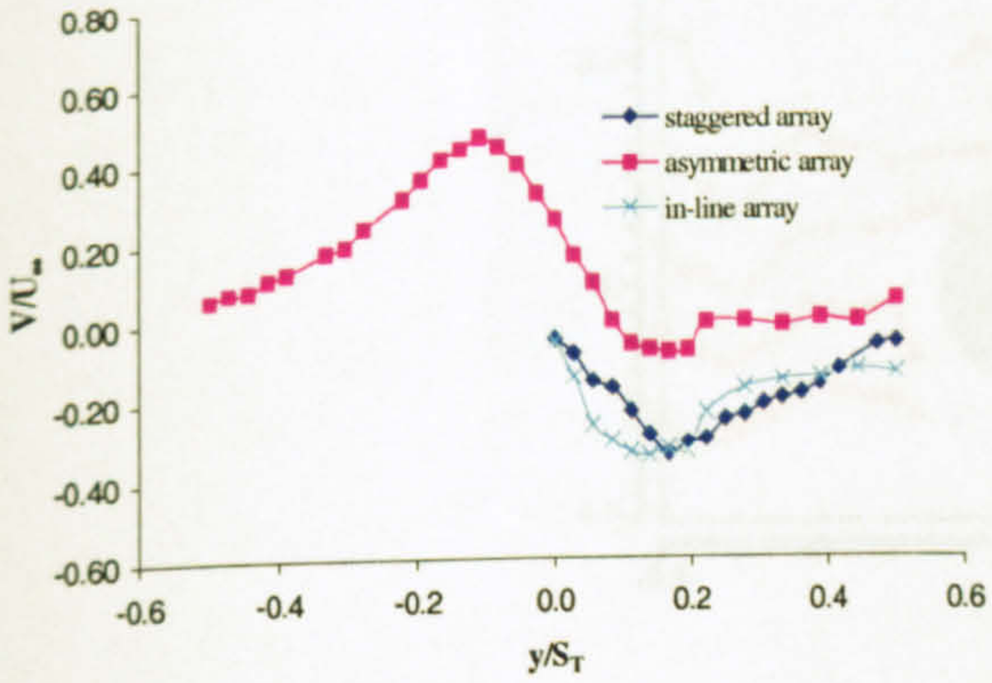

$x/S_L = 1.4$ - 2nd cylinder

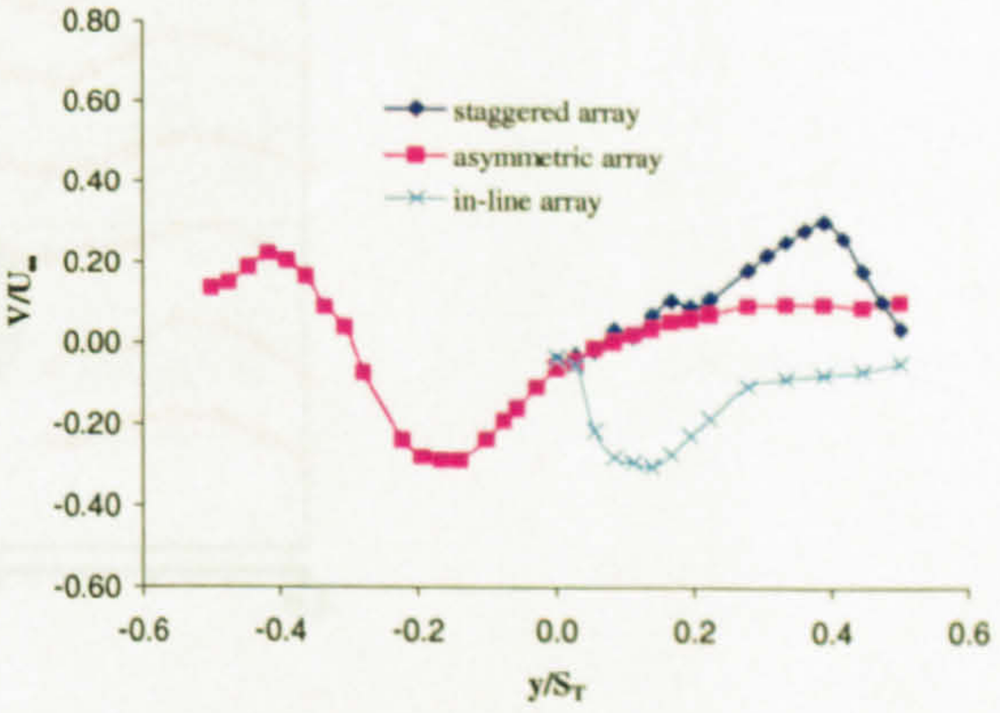

$x/S_L = 2.4$ - 3rd cylinder

$x/S_L = 3.4$ - 4th cylinder

Figure 4.7. Comparison of the V/U_∞ profiles between the asymmetric bundle and both the staggered and the in-line one (Balabani, 1996).

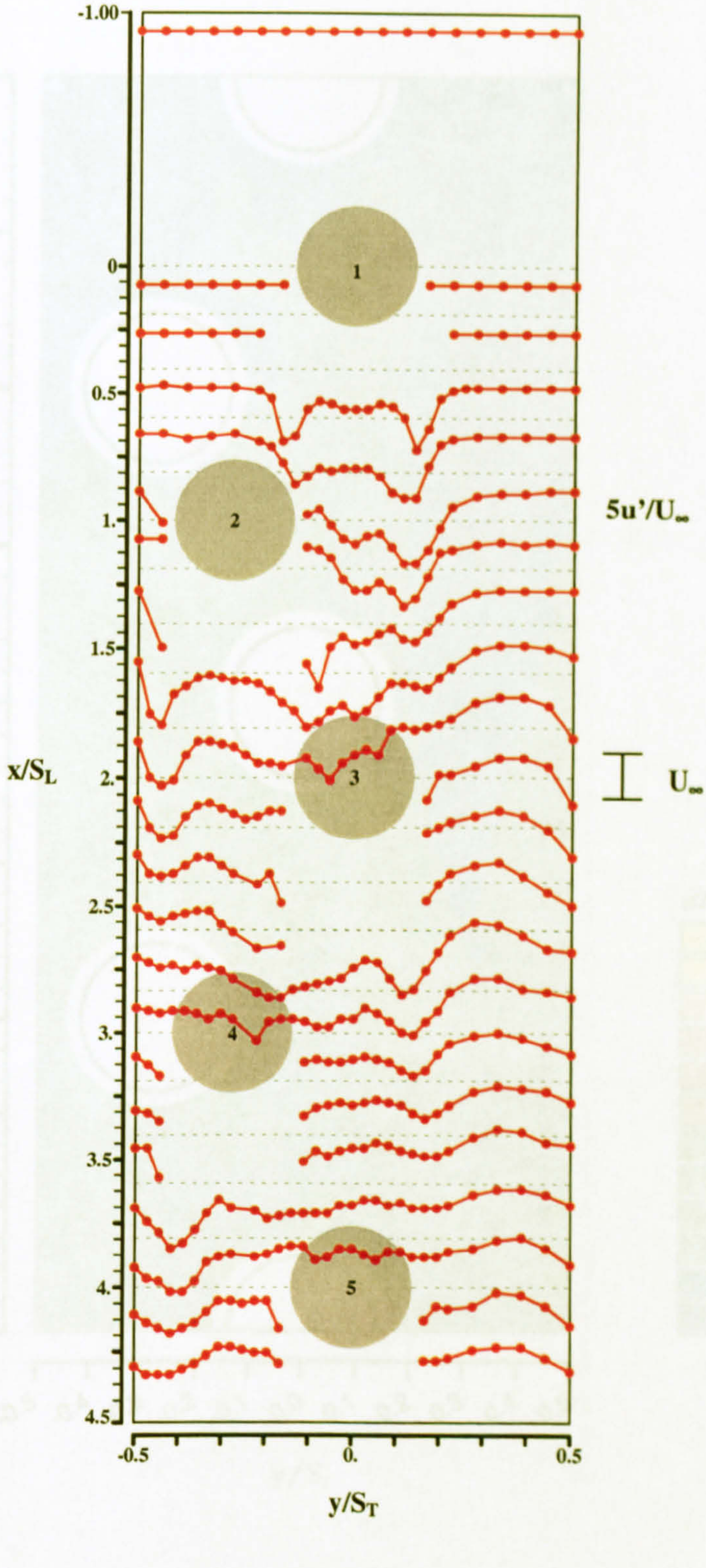

Figure 4.8. Axial r.m.s. velocity profiles, u'/U_∞, in the asymmetric tube bundle with circular tubes (steady flow, Re = 12,800).

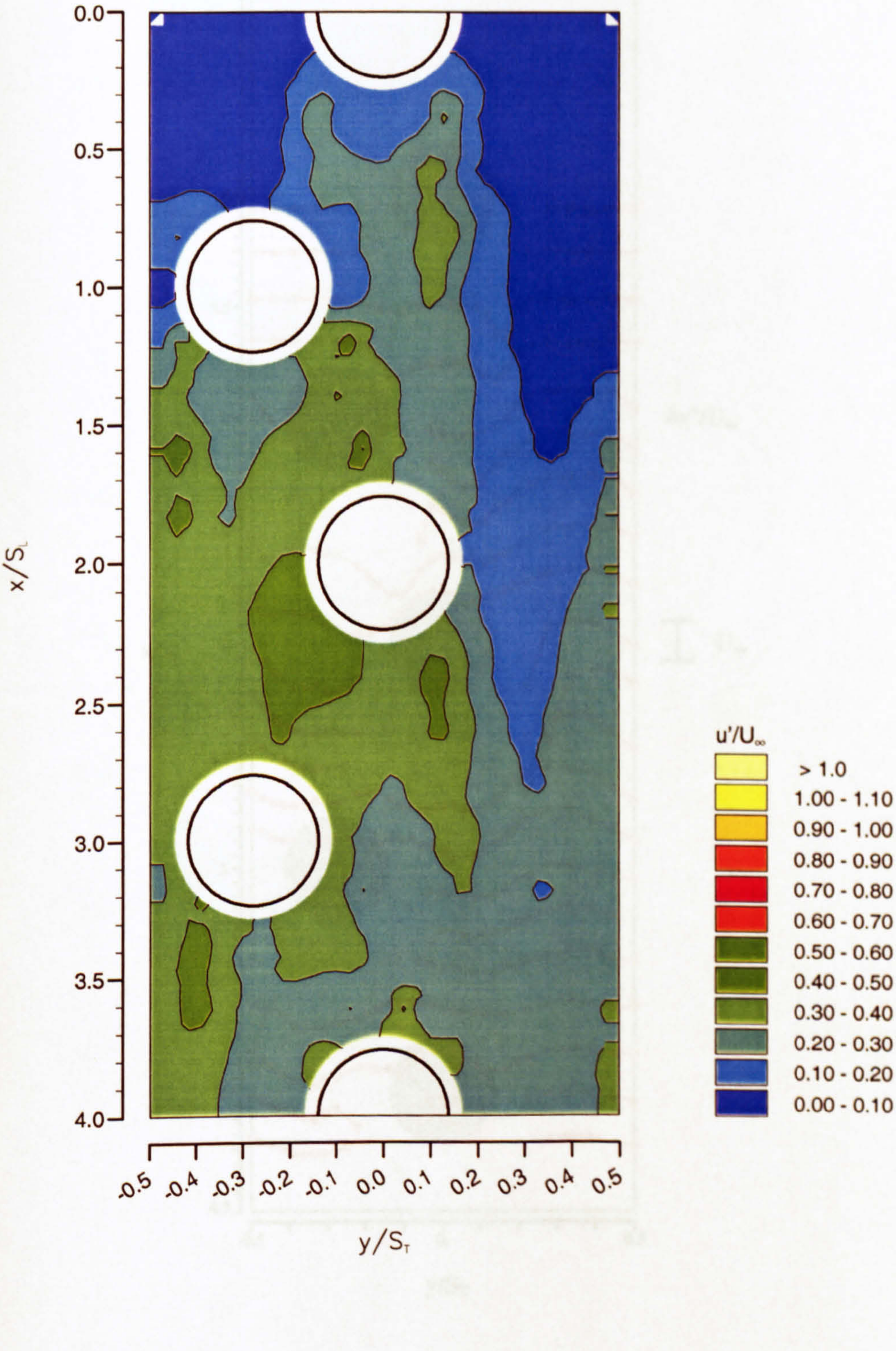

Figure 4.9. Contours of u'/U_∞, in the asymmetric tube bundle with circular tubes (steady flow, Re = 12,800).

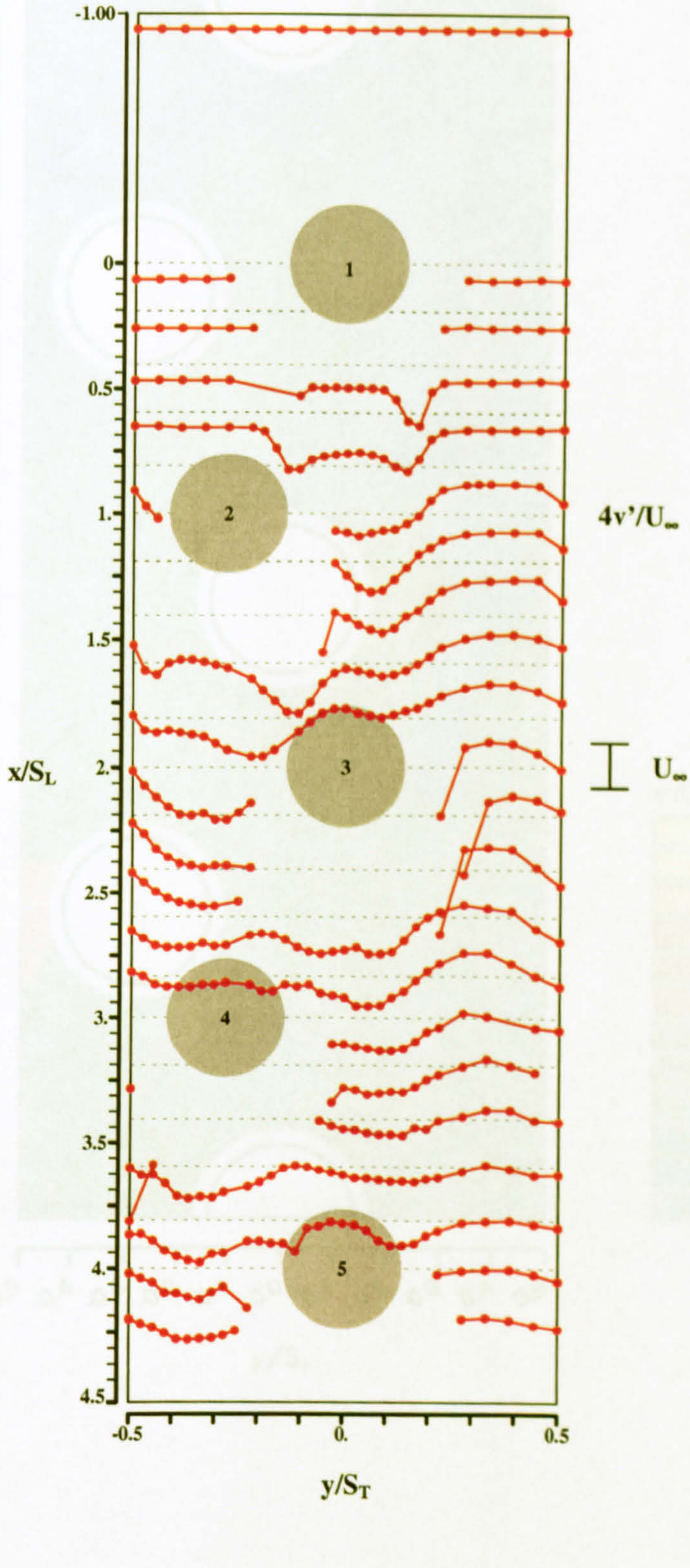

Figure 4.10. Radial r.m.s. velocity, v'/U_∞, in the asymmetric tube bundle with circular tubes (steady flow, Re = 12,800).

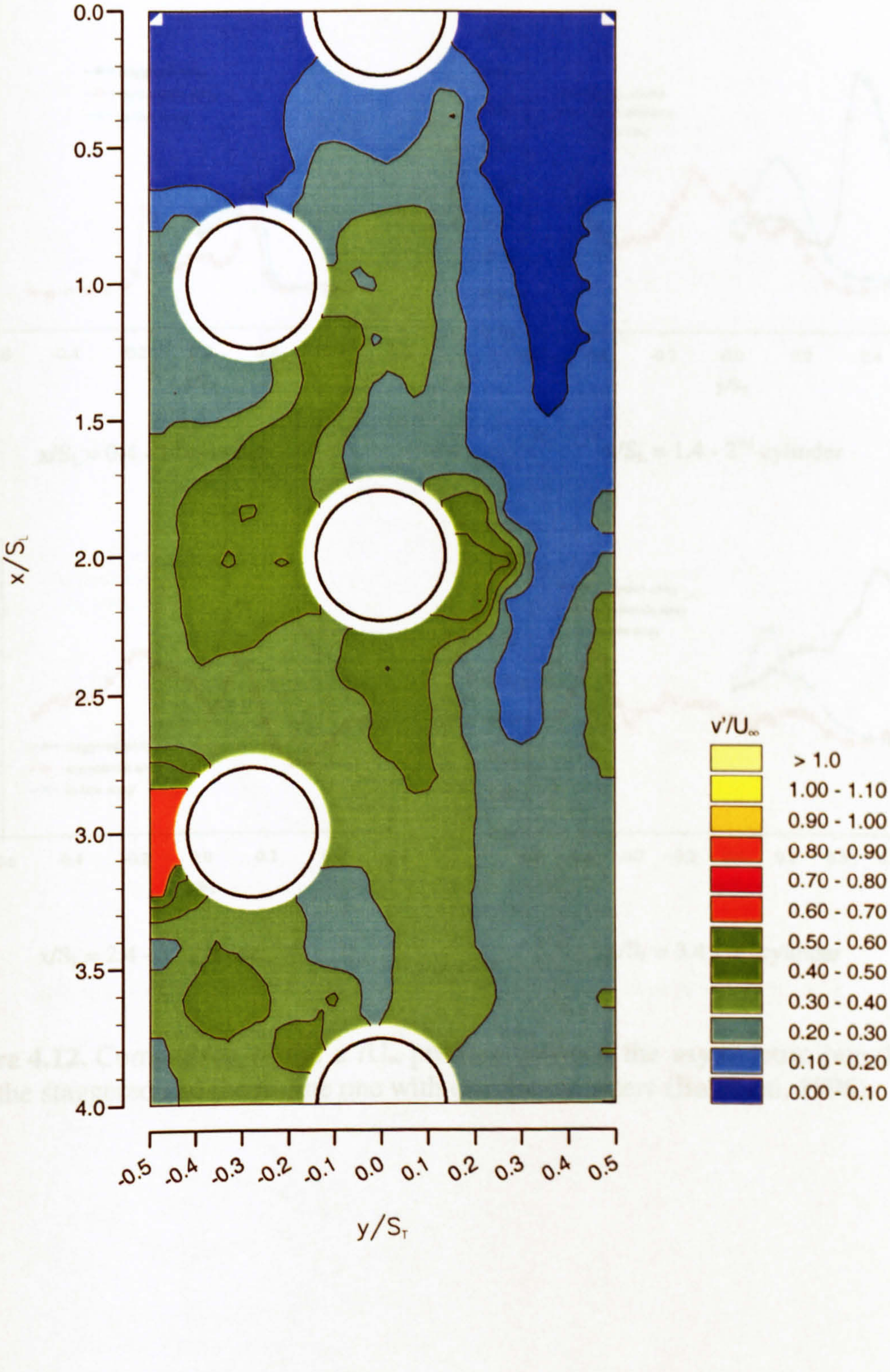

Figure 4.11. Contours of v'/U_∞, in the asymmetric tube bundle with circular tubes (steady flow, Re = 12,800).

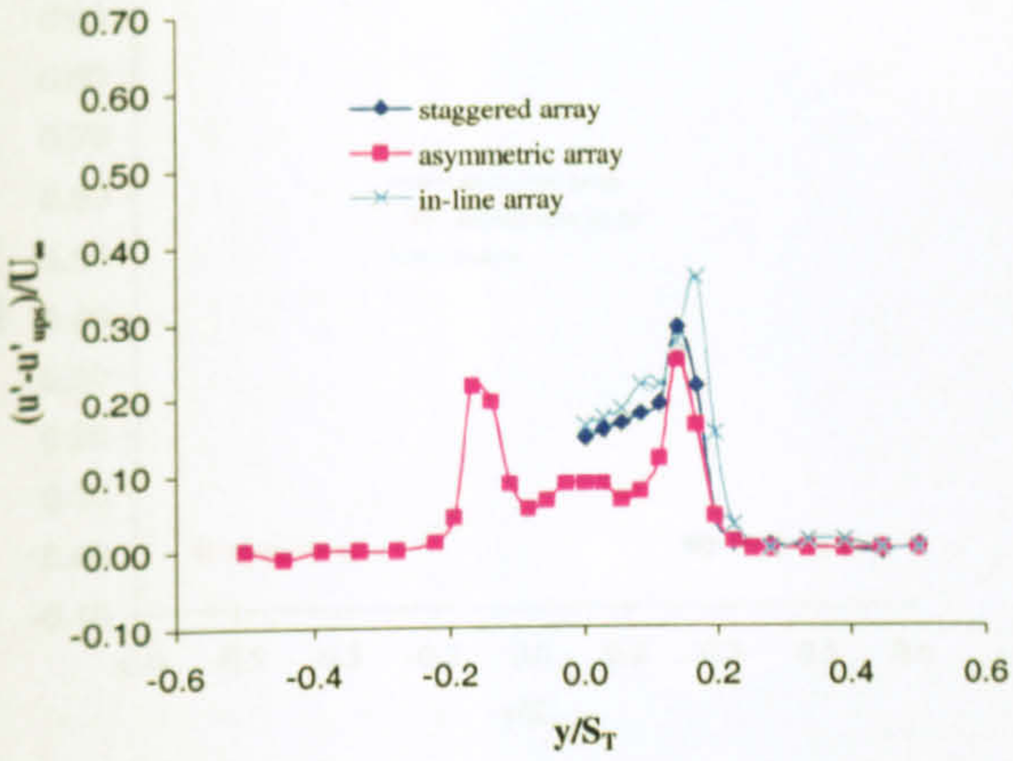

$x/S_L = 0.4$ - 1st cylinder

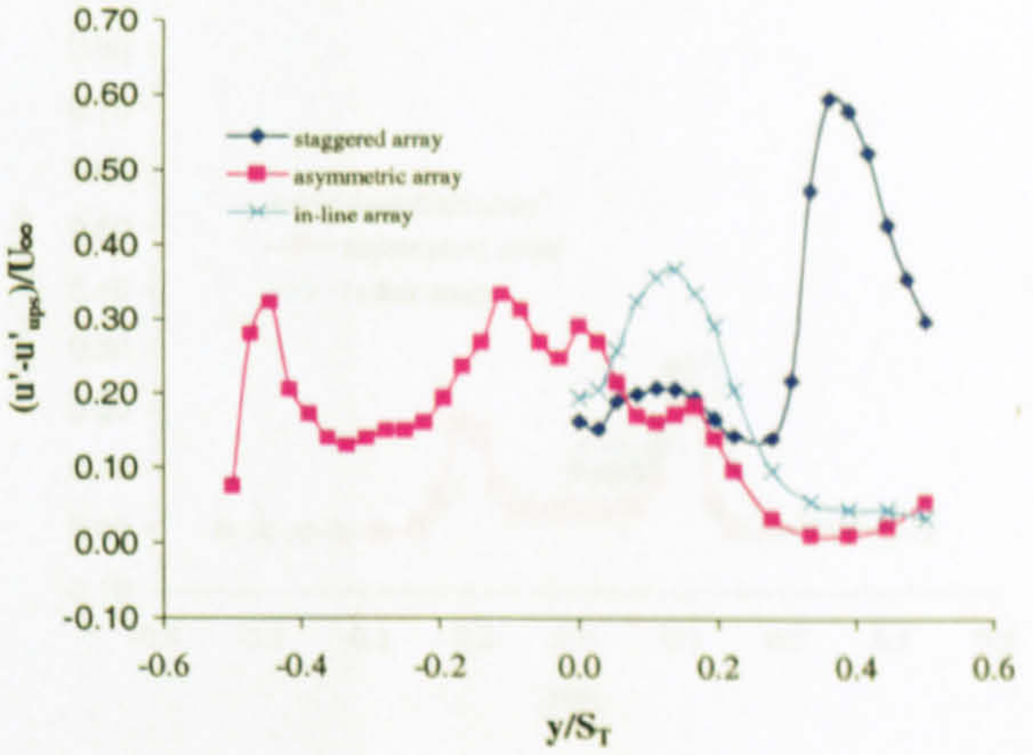

$x/S_L = 1.4$ - 2nd cylinder

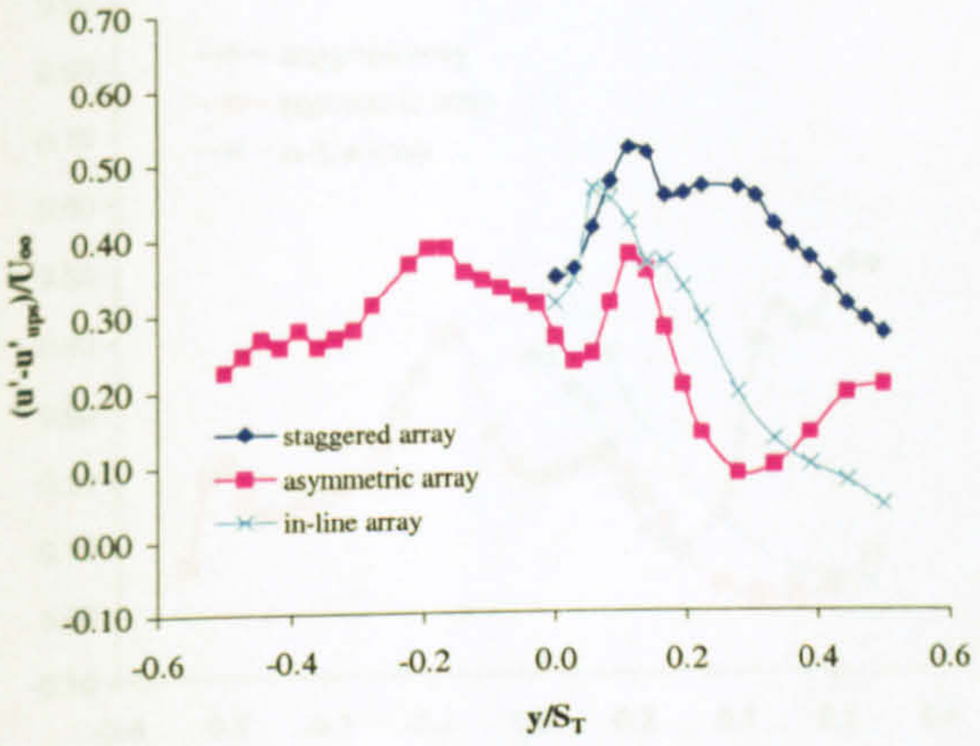

$x/S_L = 2.4$ - 3rd cylinder

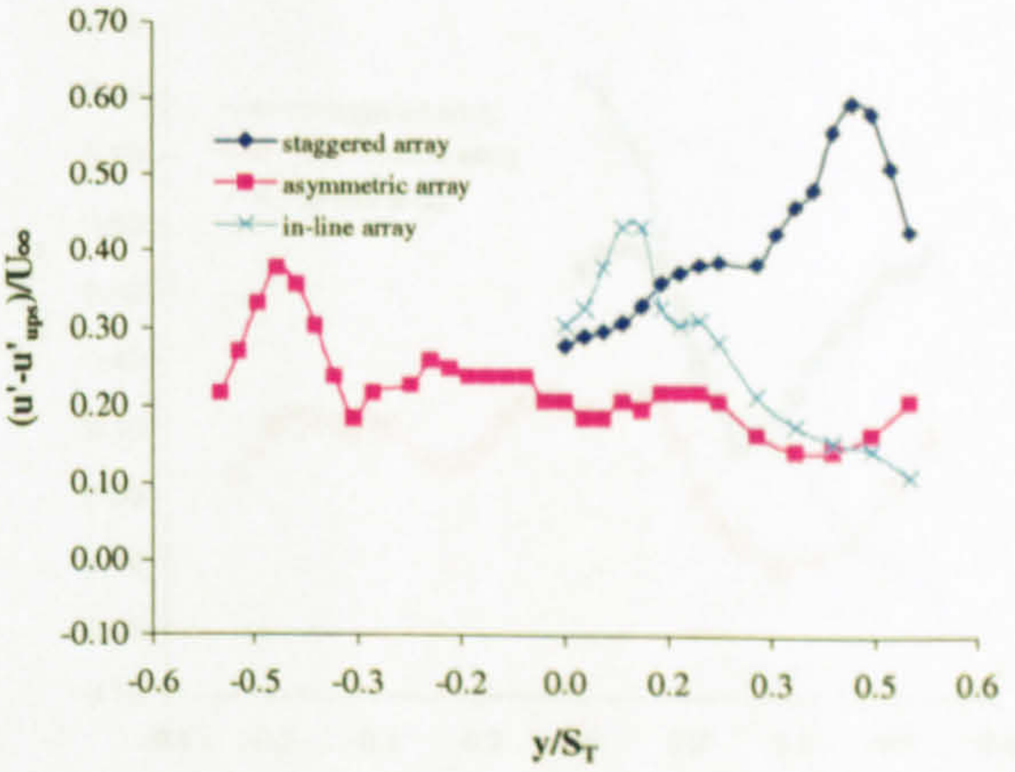

$x/S_L = 3.4$ - 4th cylinder

Figure 4.12. Comparison of the u'/U_∞ profiles between the asymmetric bundle and both the staggered and the in-line one with circular cylinders (Balabani, 1996).

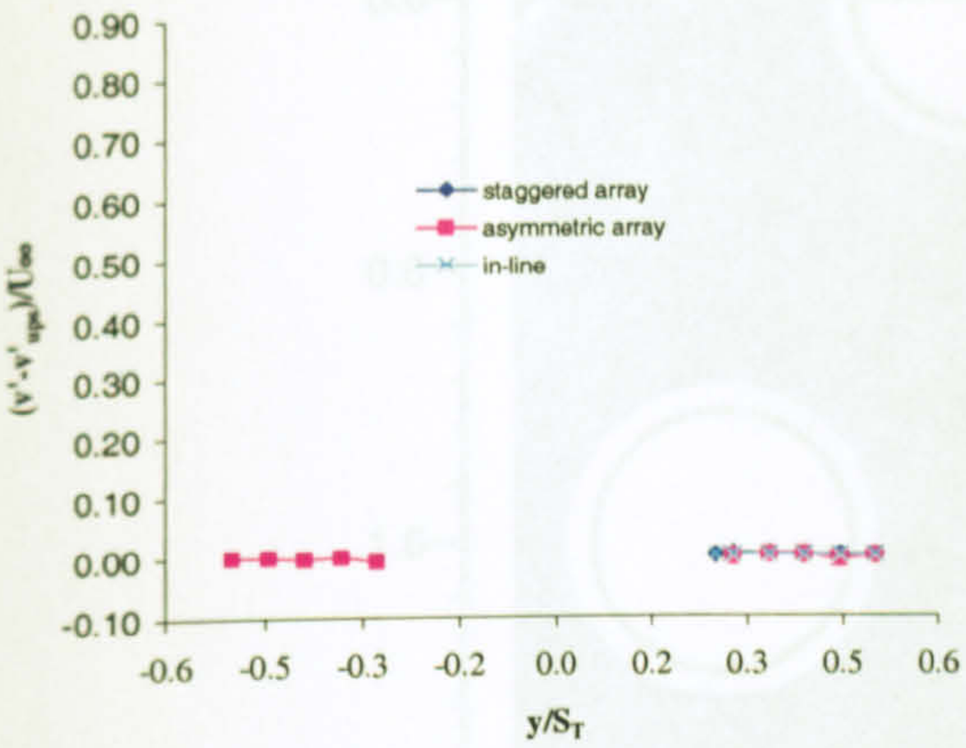

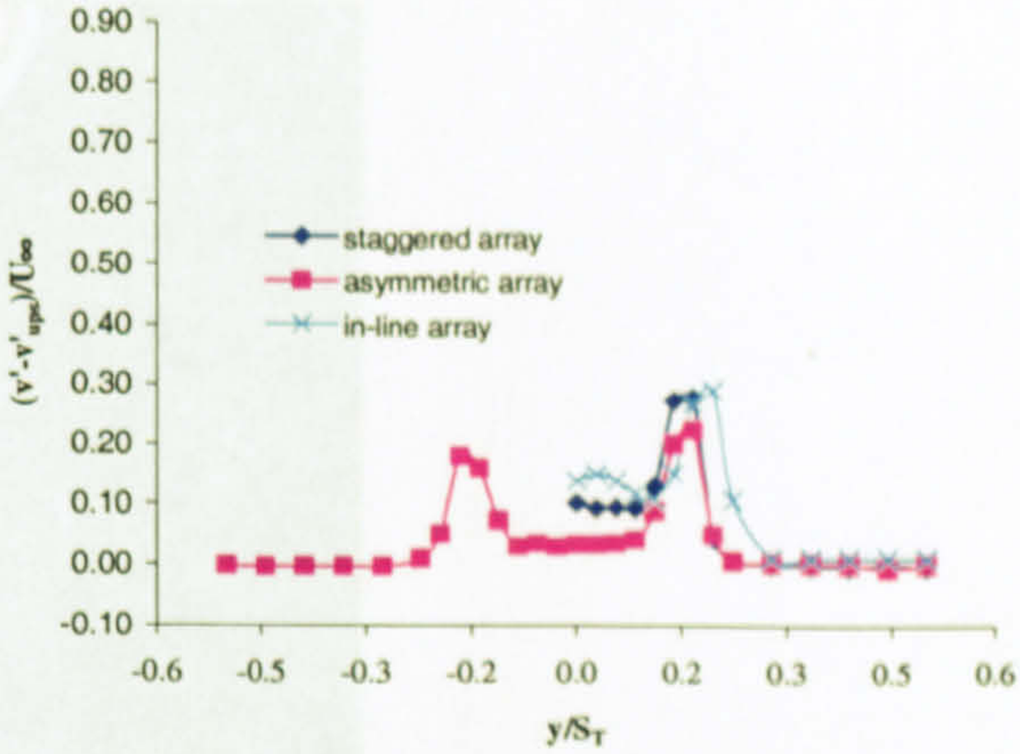

$x/S_L = 0.0$ - entrance of tube bank

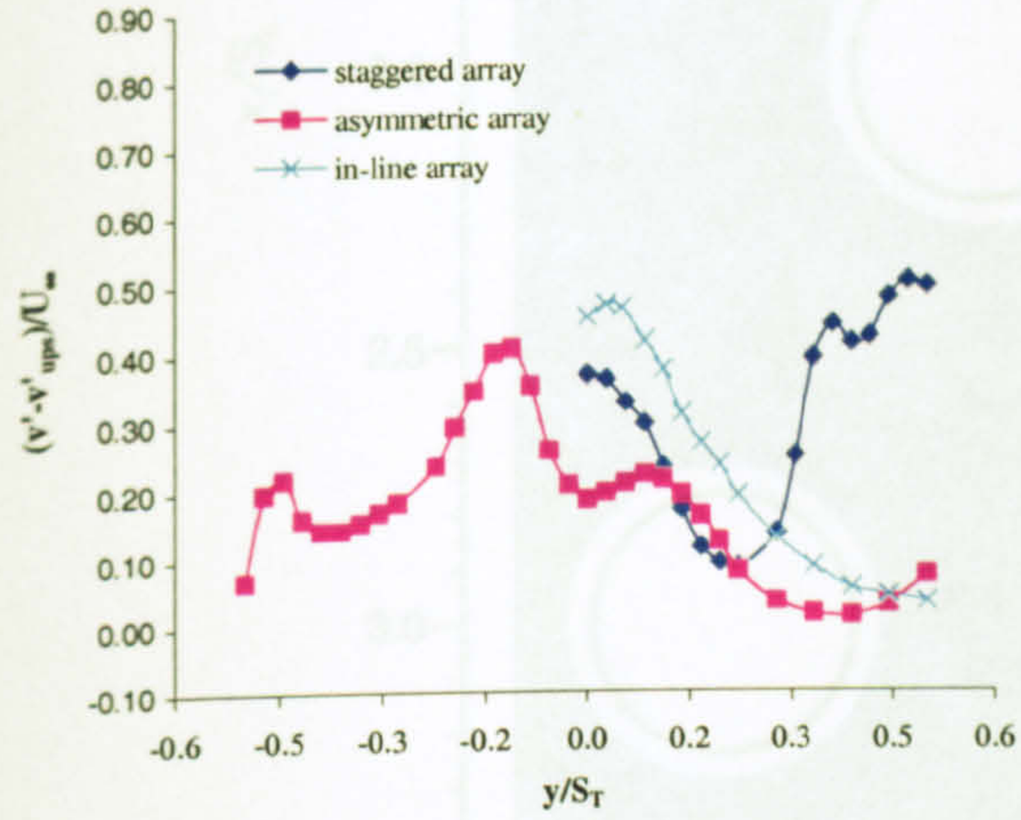

$x/S_L = 0.4$ - 1st cylinder

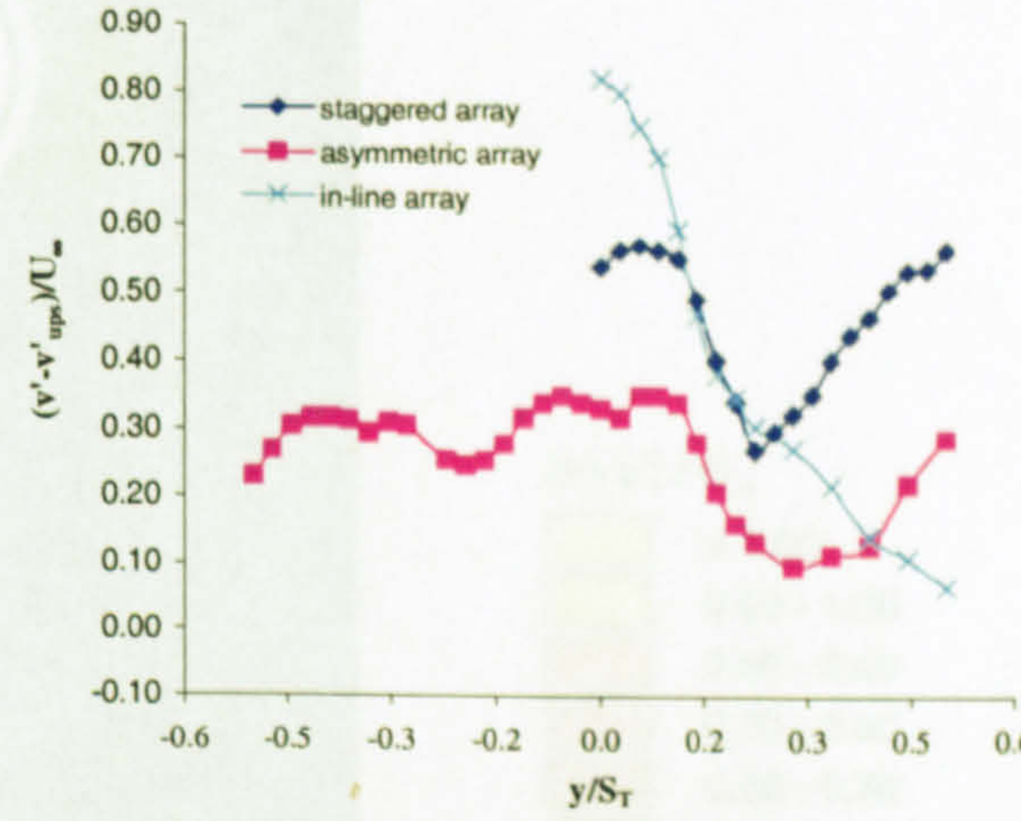

$x/S_L = 1.4$ - 2nd cylinder

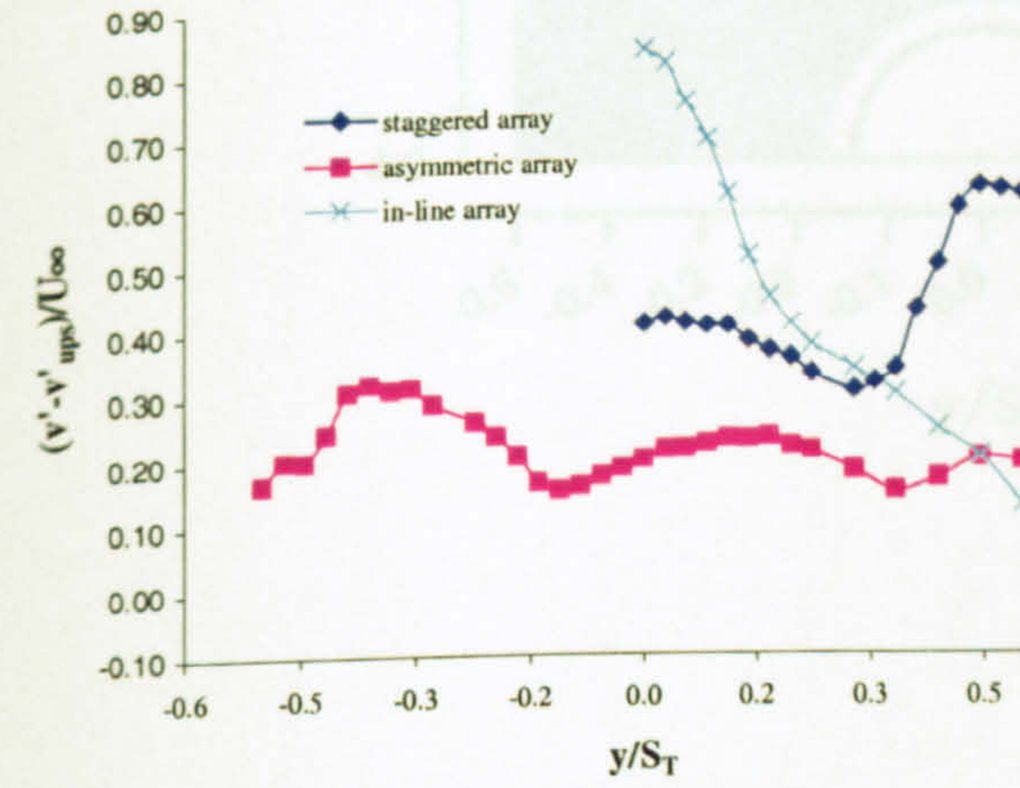

$x/S_L = 2.4$ - 3rd cylinder

$x/S_L = 3.4$ - 4th cylinder

Figure 4.13. Comparison of the v'/U_∞ profiles between the asymmetric bundle and both the staggered and the in-line one with circular cylinders (Balabani, 1996).

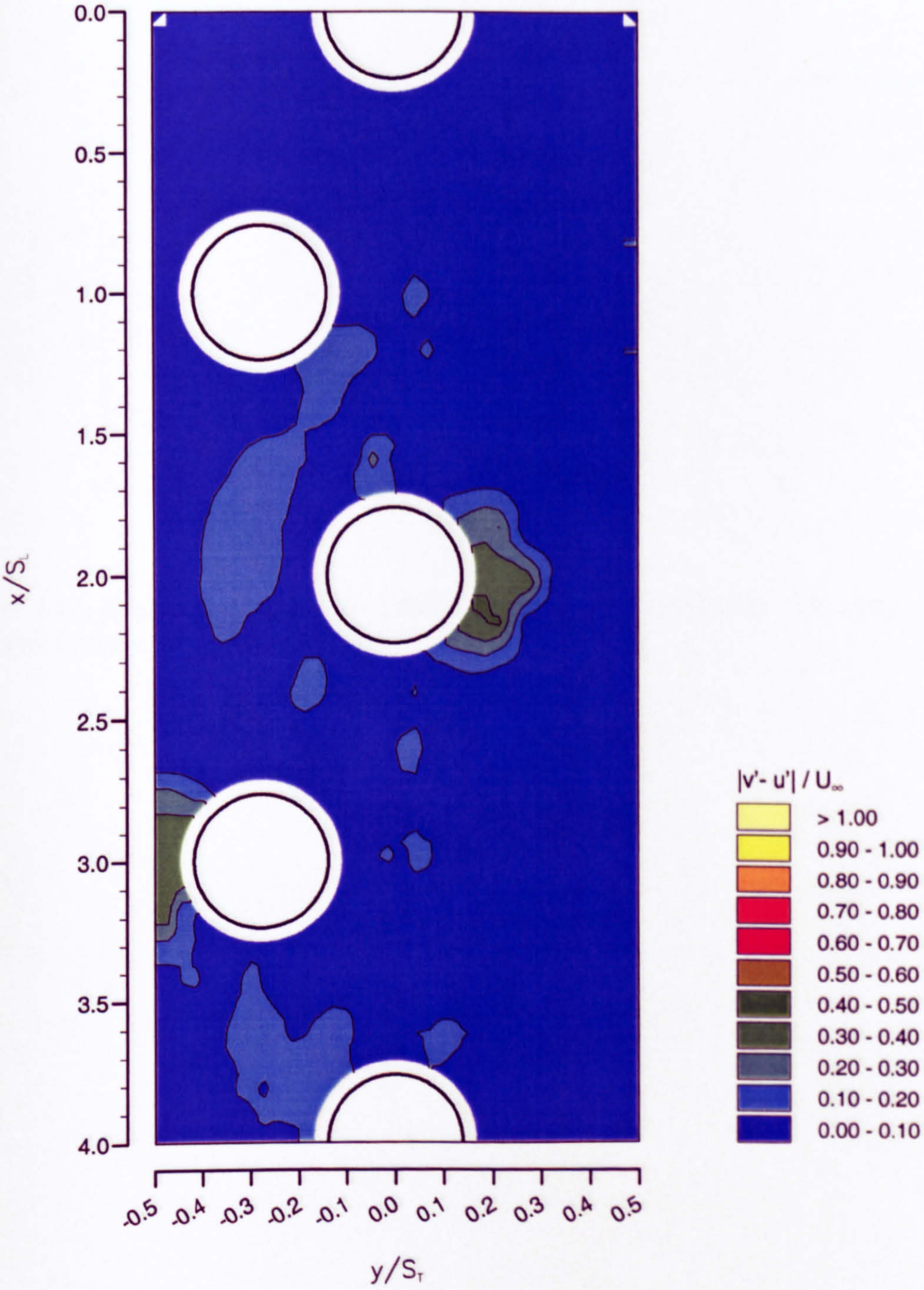

Figure 4.14. Distribution of $|v' - u'|/U_\infty$ in the asymmetric tube bundle with circular tubes (steady flow, Re = 12,800).

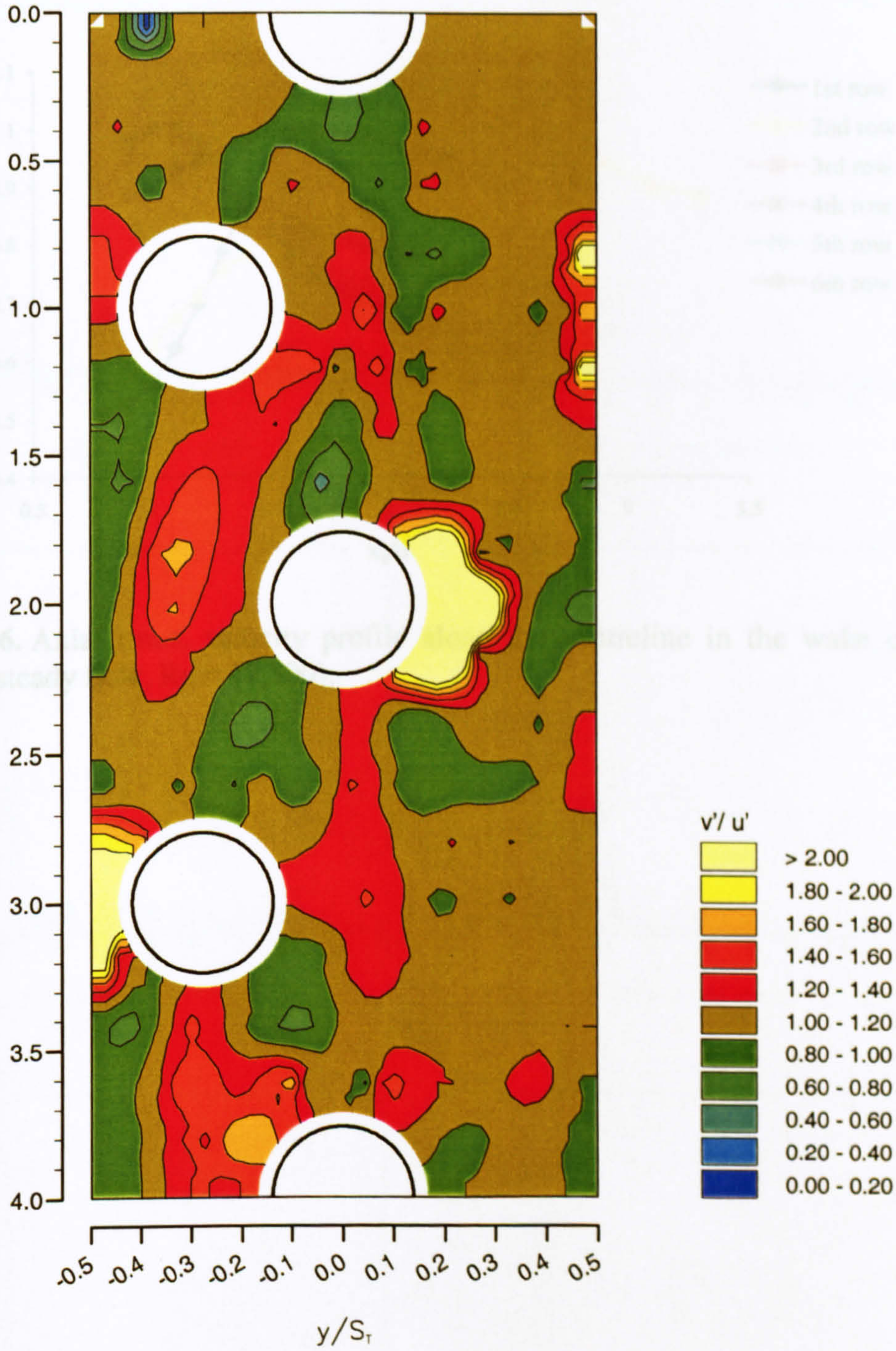

Figure 4.15. Distribution of $(v'/u')/U_\infty$ in the asymmetric tube bundle with circular tubes (steady flow, Re = 12,800).

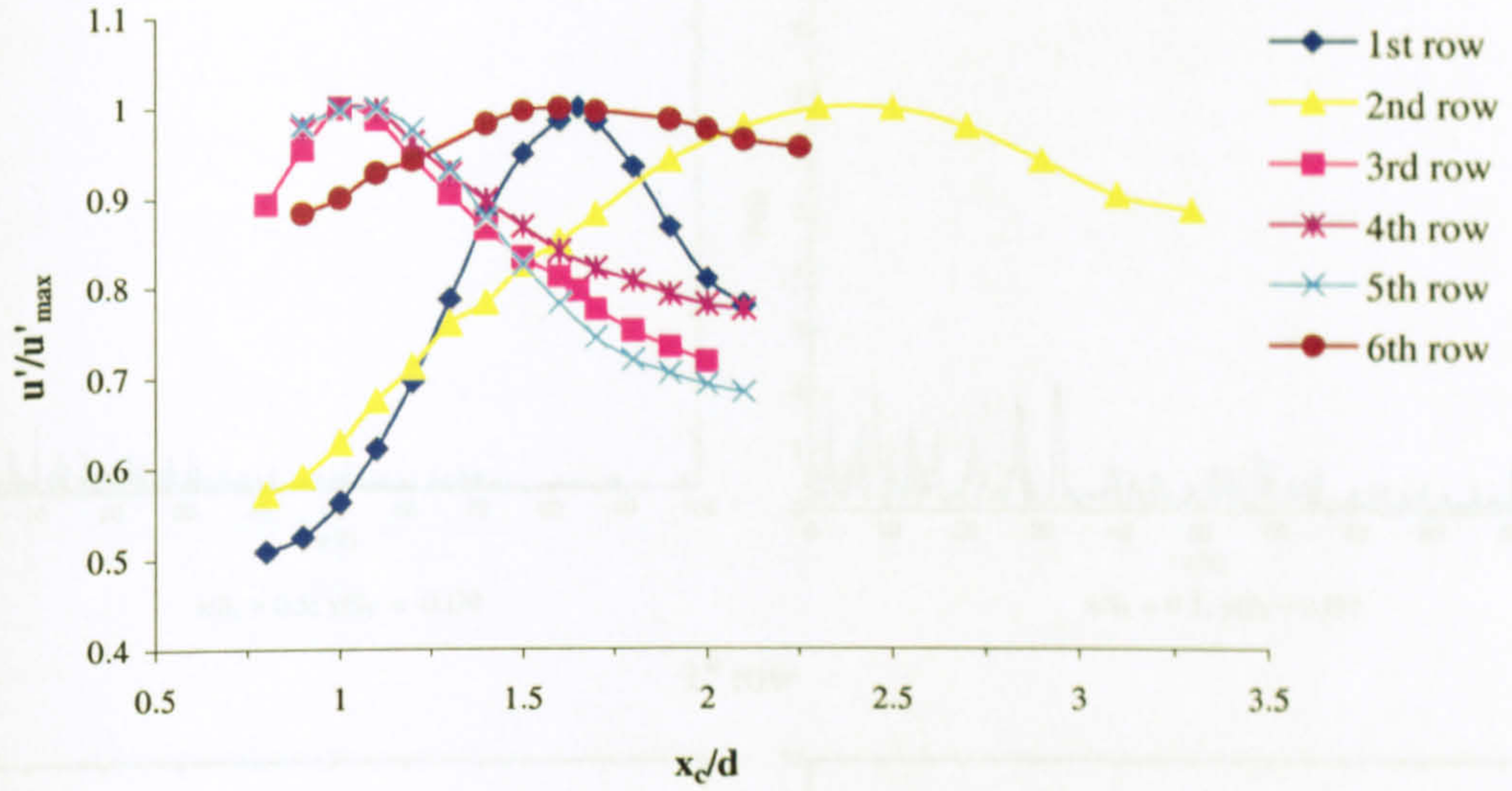

Figure 4.16. Axial r.m.s. velocity profile along the centreline in the wake of the cylinders (steady flow, Re = 12,800).

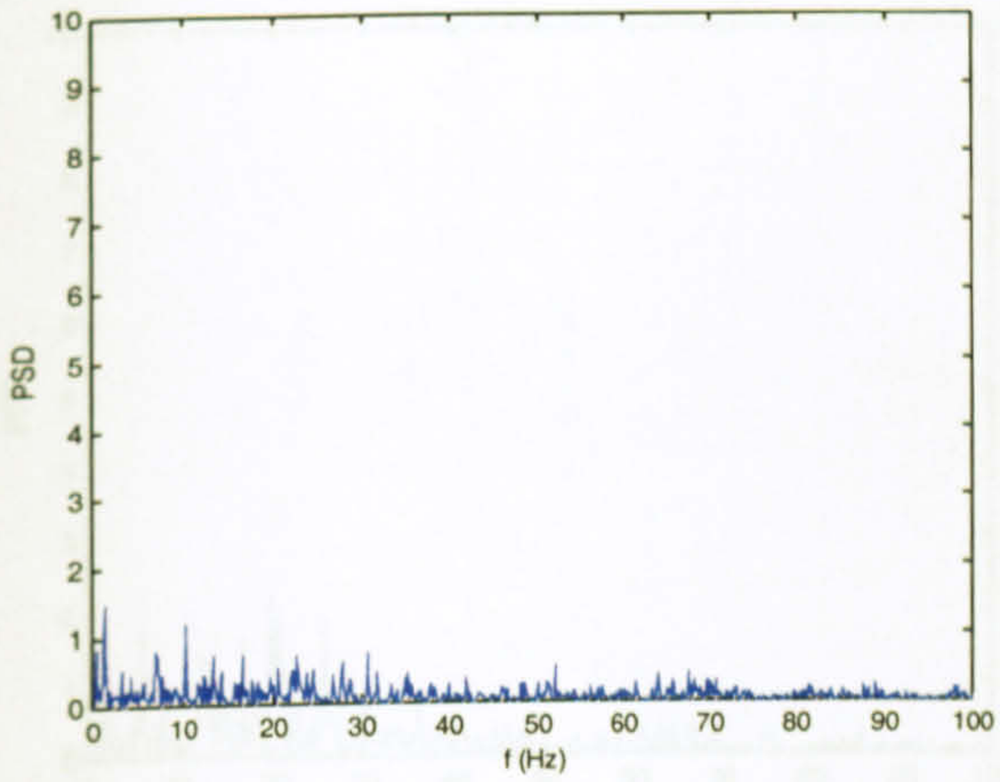

$x/S_L = 0.5$; $y/S_T = -0.139$

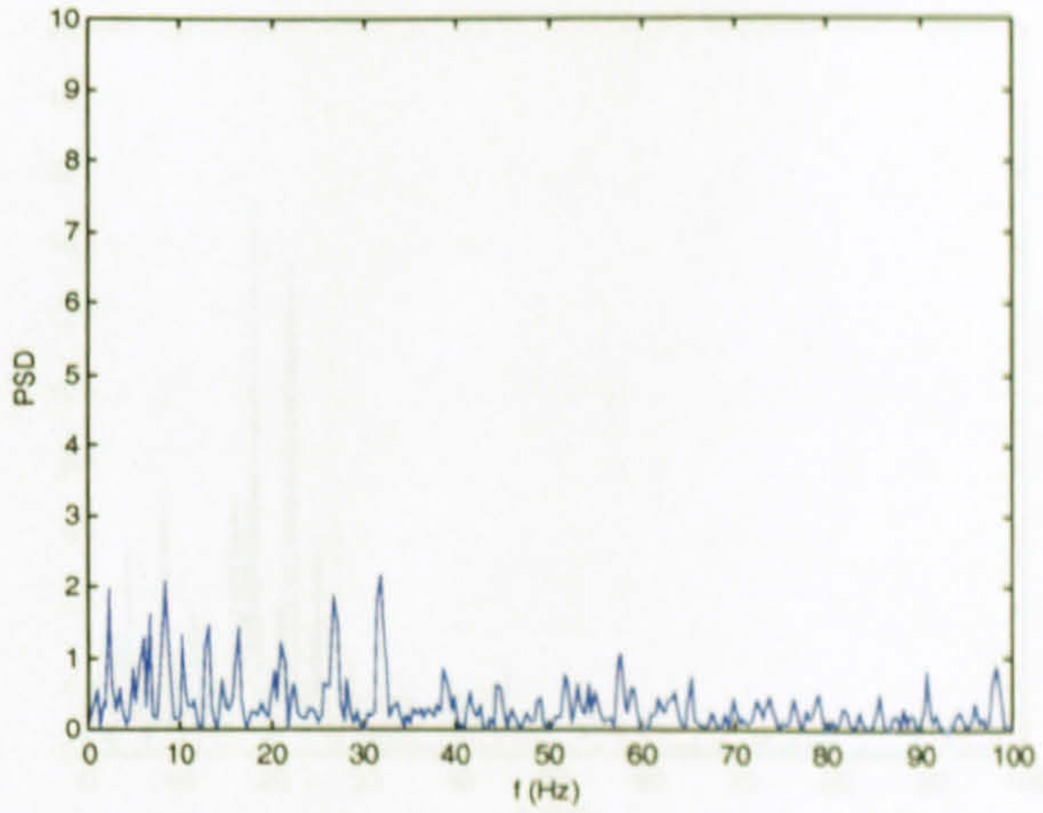

$x/S_L = 0.5$; $y/S_T = 0.139$

1st row

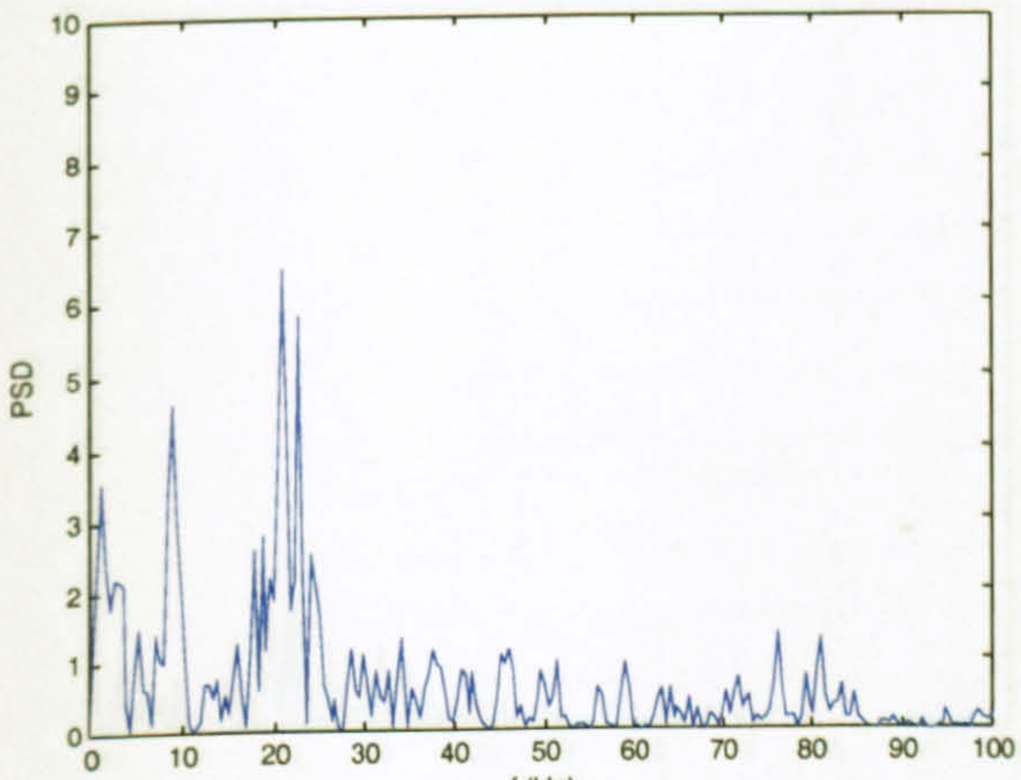

$x/S_L = 1.5$; $y/S_T = -0.417$

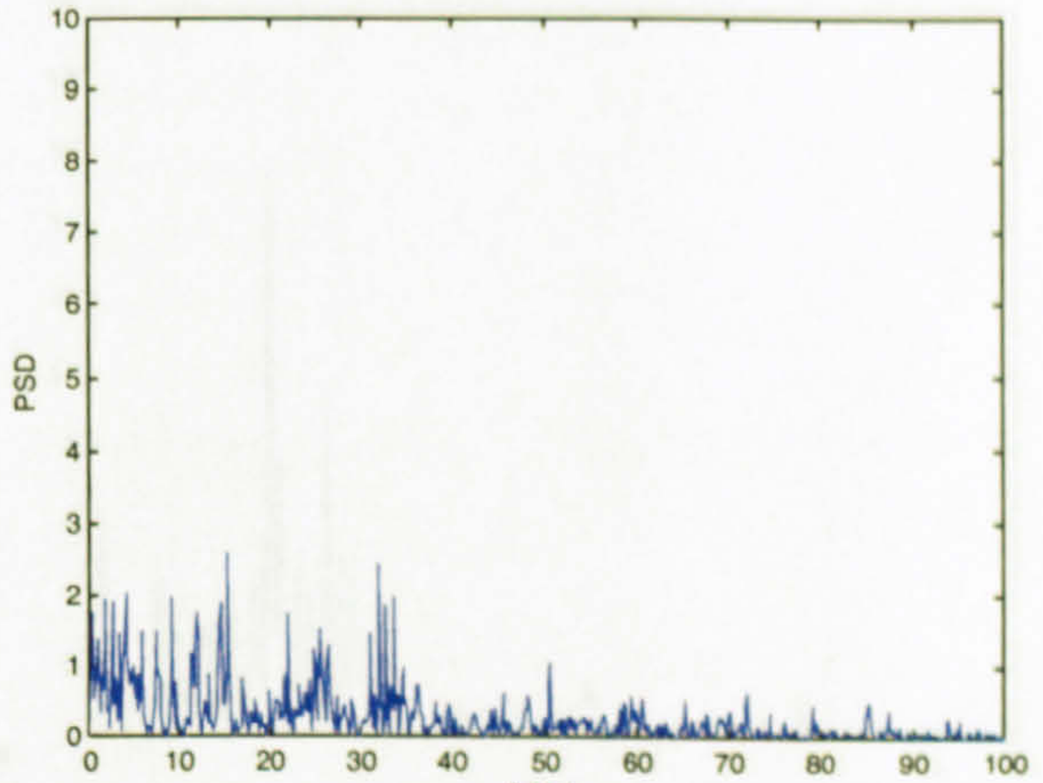

$x/S_L = 1.5$; $y/S_T = -0.139$

2nd row

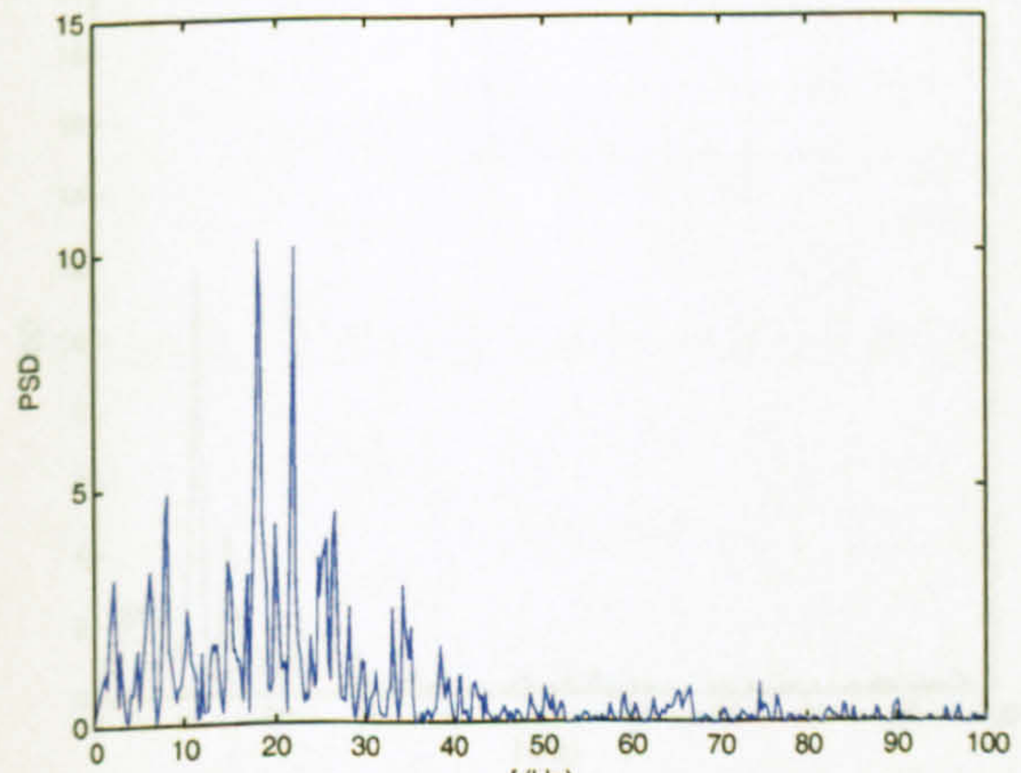

$x/S_L = 2.5$; $y/S_T = 0.139$

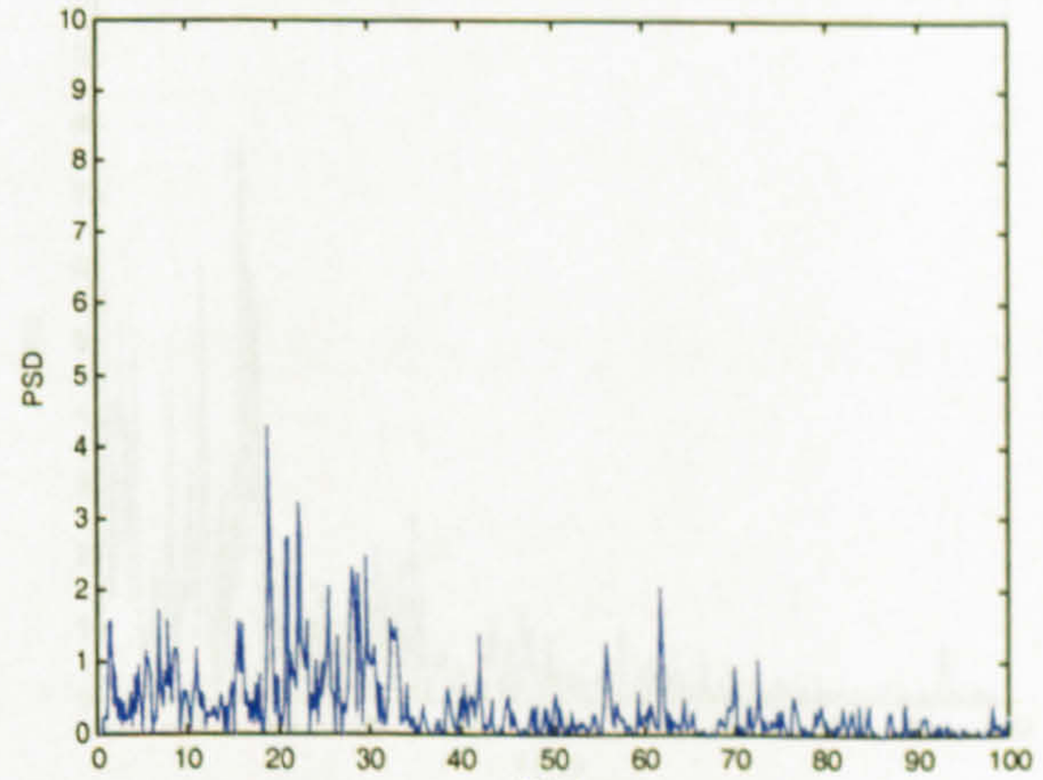

$x/S_L = 2.5$; $y/d = -0.139$

3rd row

Figure 4.17. Power spectra behind each row in the asymmetric array with circular cylinders (steady flow; $Re = 8,870$).

For Caption see next page.

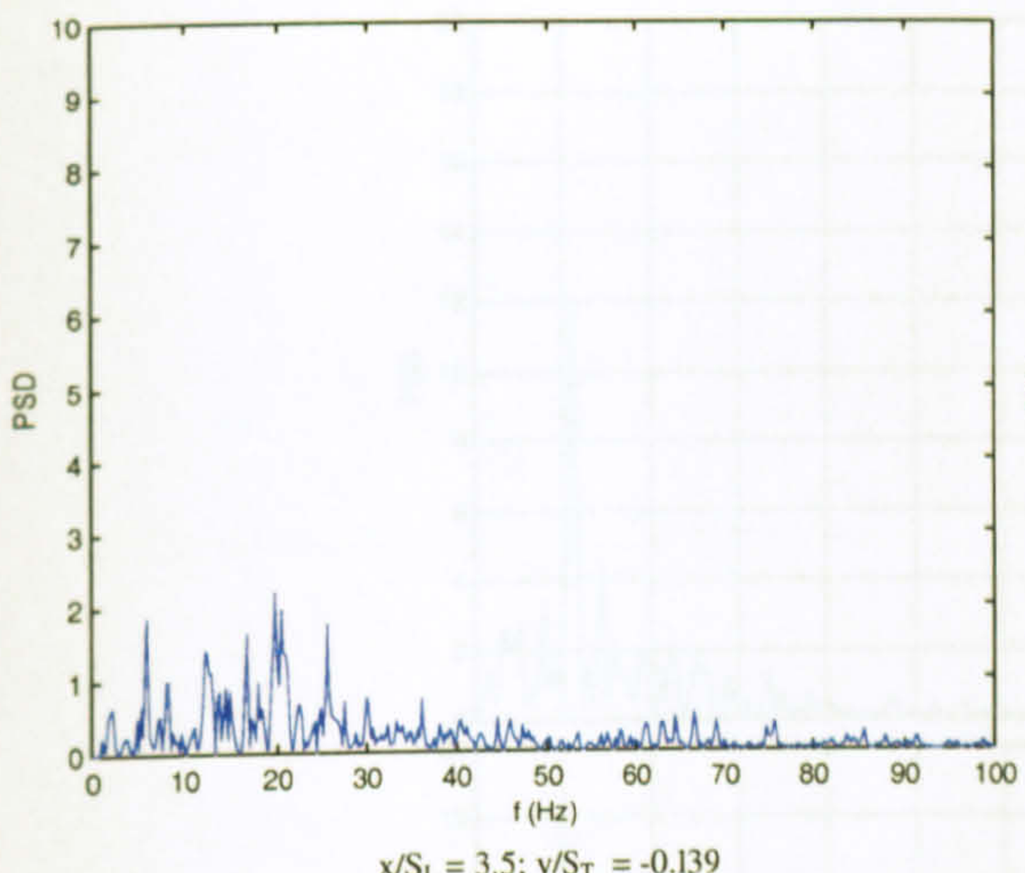

$x/S_L = 3.5$; $y/S_T = -0.139$

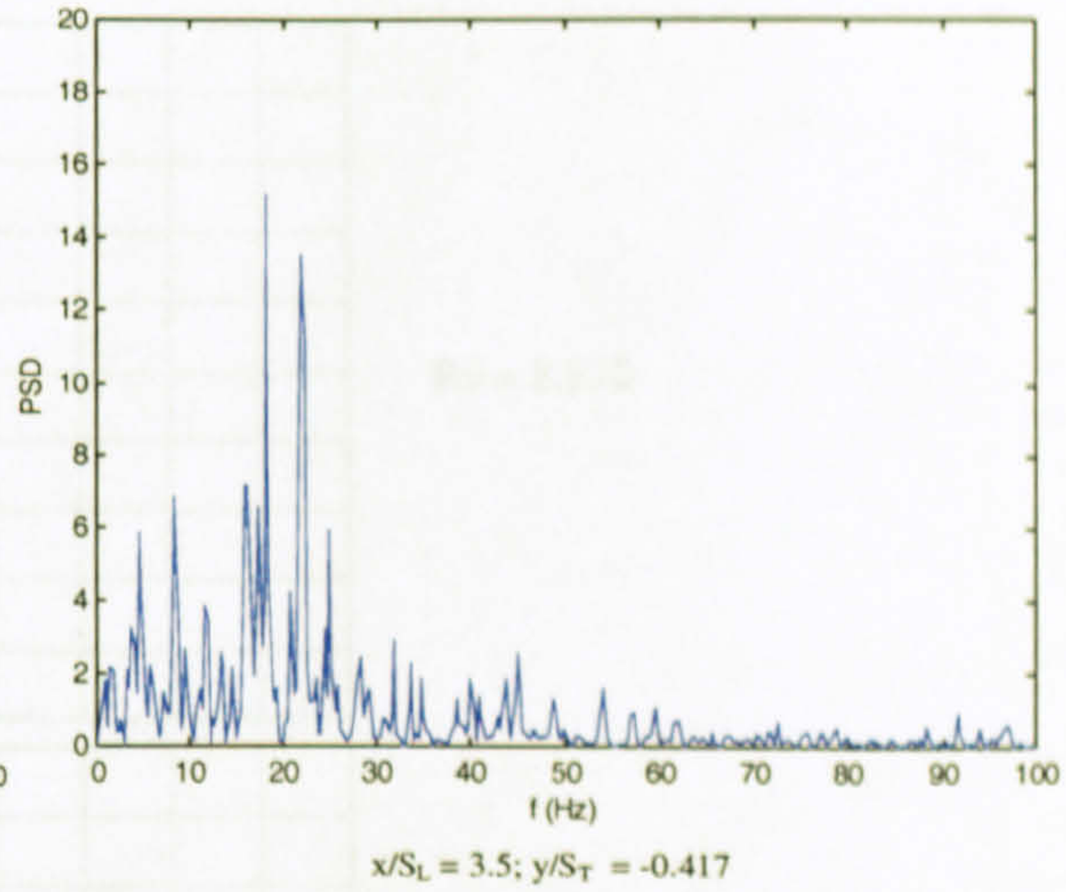

$x/S_L = 3.5$; $y/S_T = -0.417$

4^{th} row

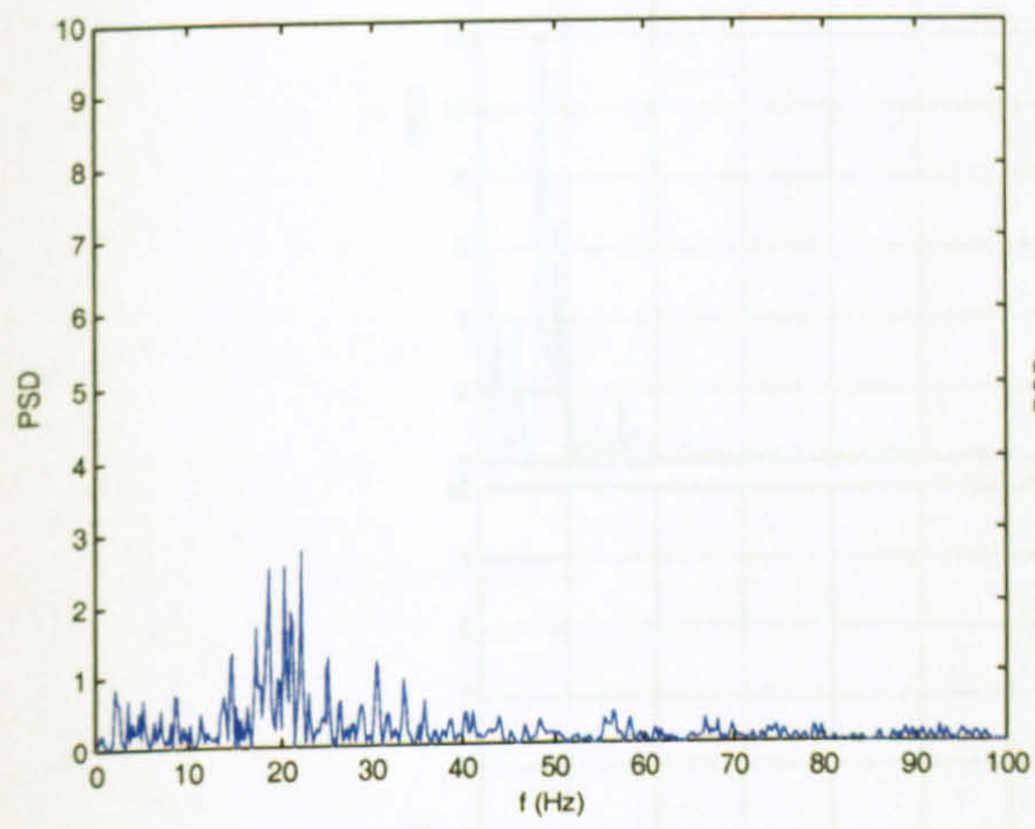

$x/S_L = 4.5$; $y/d = -0.139$

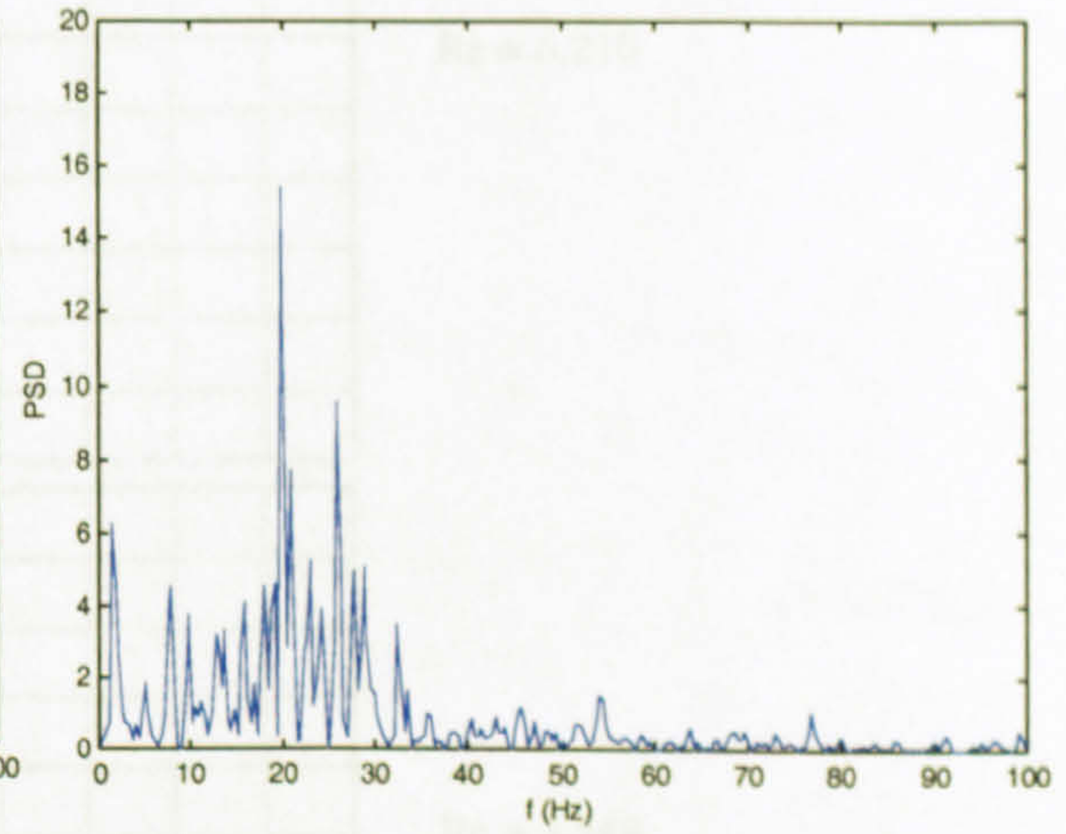

$x/S_L = 4.5$; $y/S_T = 0.139$

5^{th} row

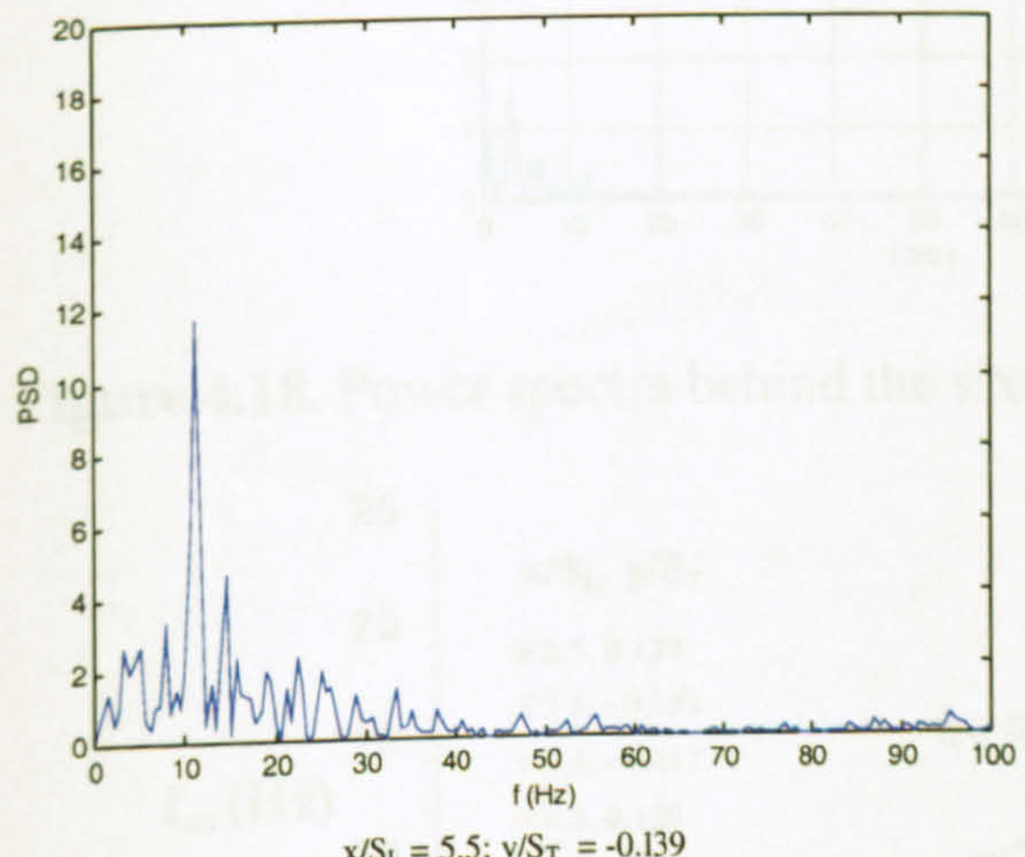

$x/S_L = 5.5$; $y/S_T = -0.139$

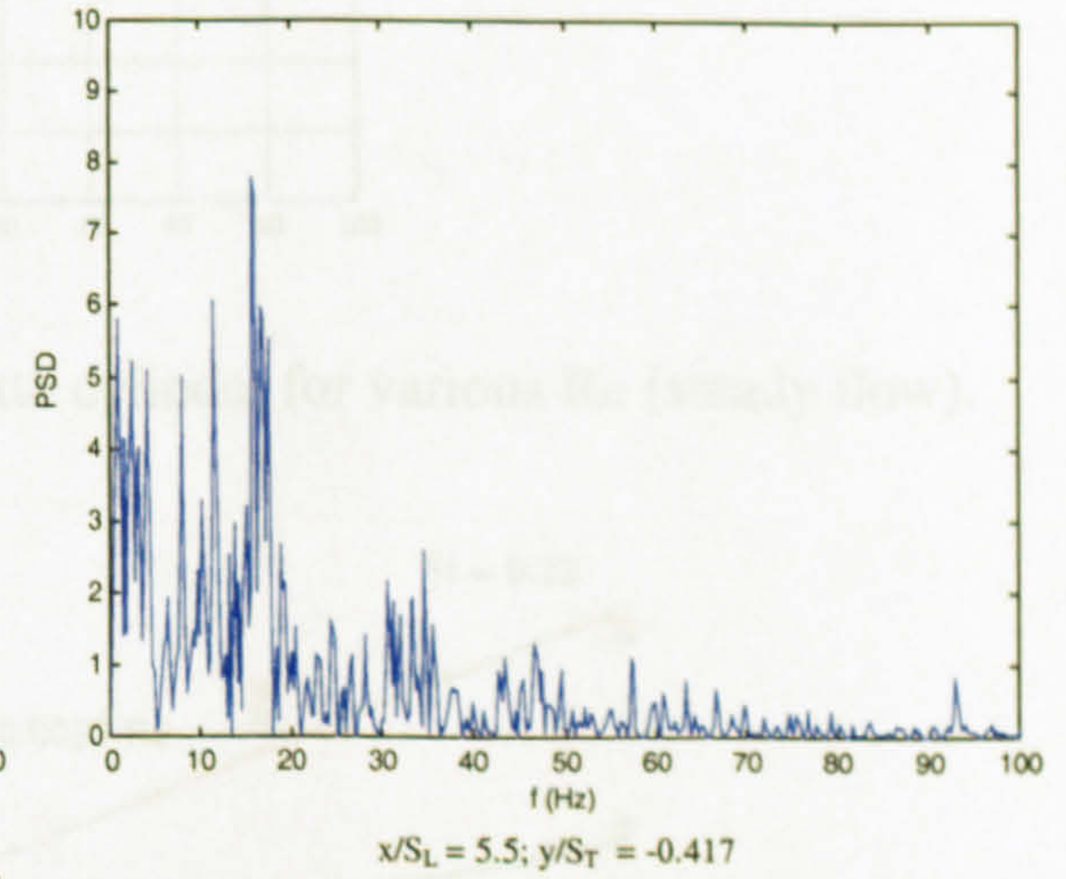

$x/S_L = 5.5$; $y/S_T = -0.417$

6^{th} row

Figure 4.17. Power spectra behind each row in the asymmetric array with circular cylinders (steady flow, Re = 8,870).

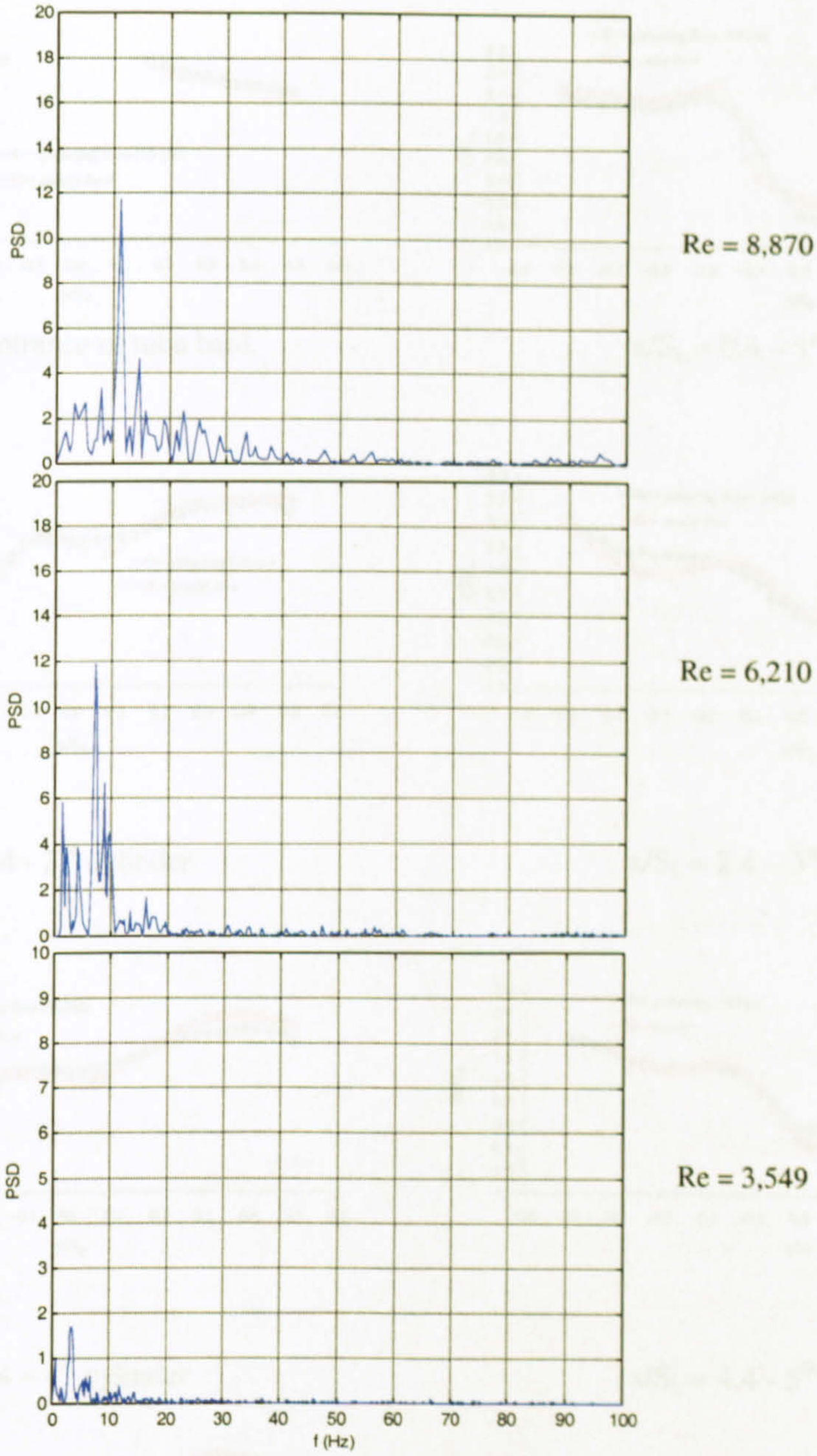

Figure 4.18. Power spectra behind the sixth cylinder for various Re (steady flow).

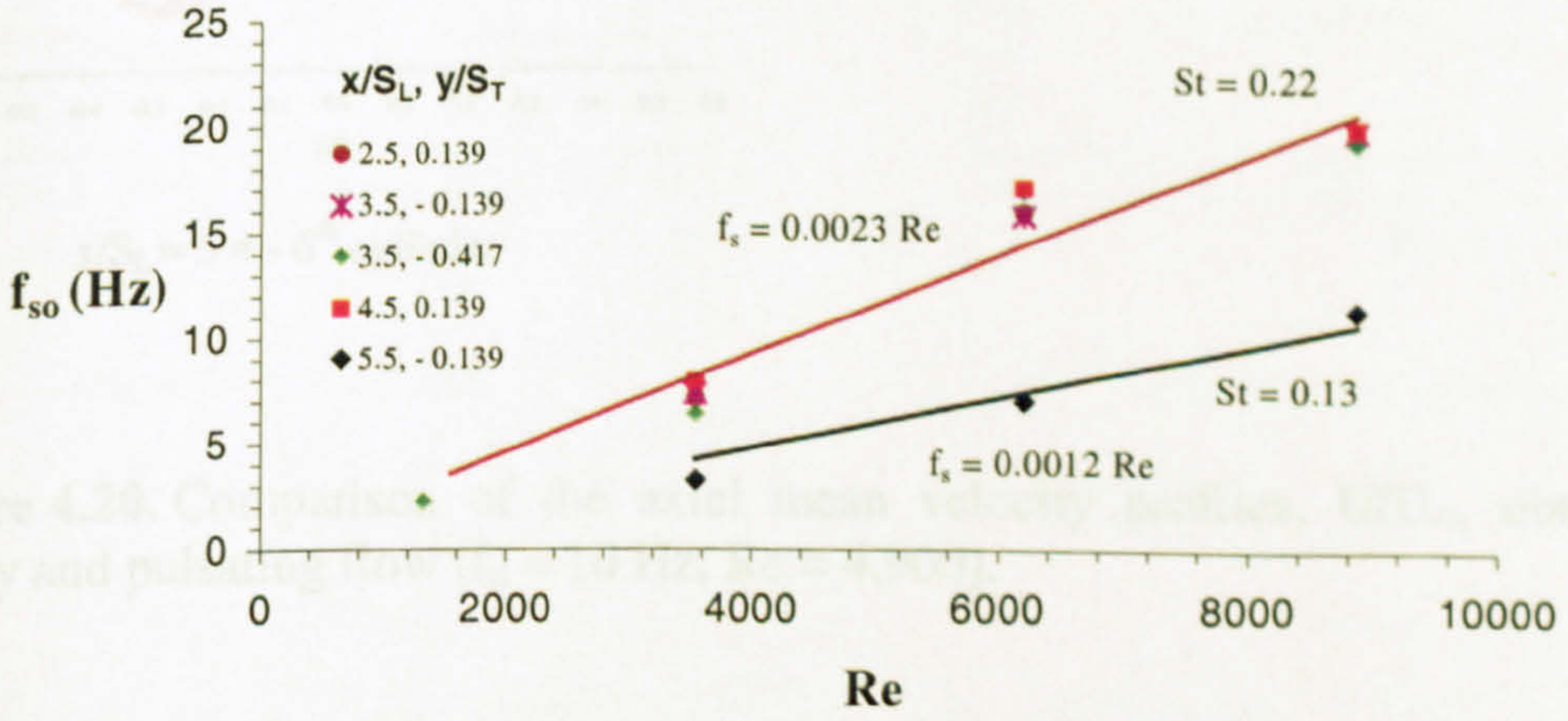

Figure 4.19. Dependency of the shedding frequency, f_{so}, on the Reynolds number, Re, at selected locations.

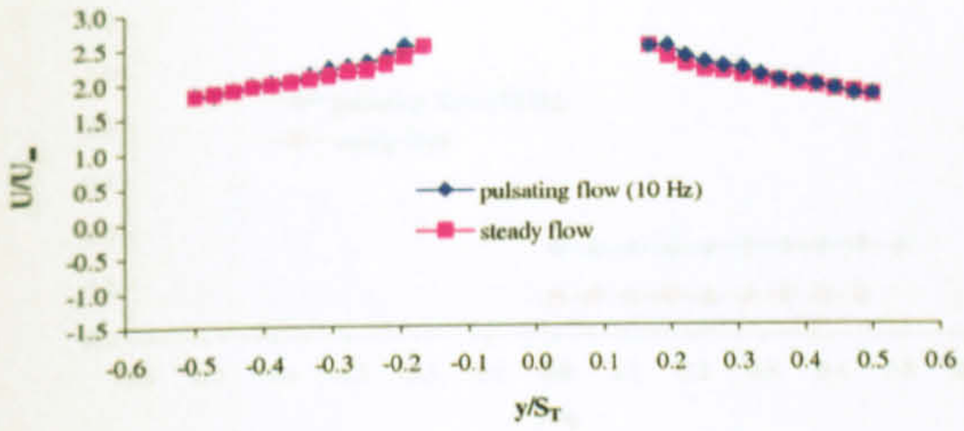

$x/S_L = 0.0$ - entrance of tube bank

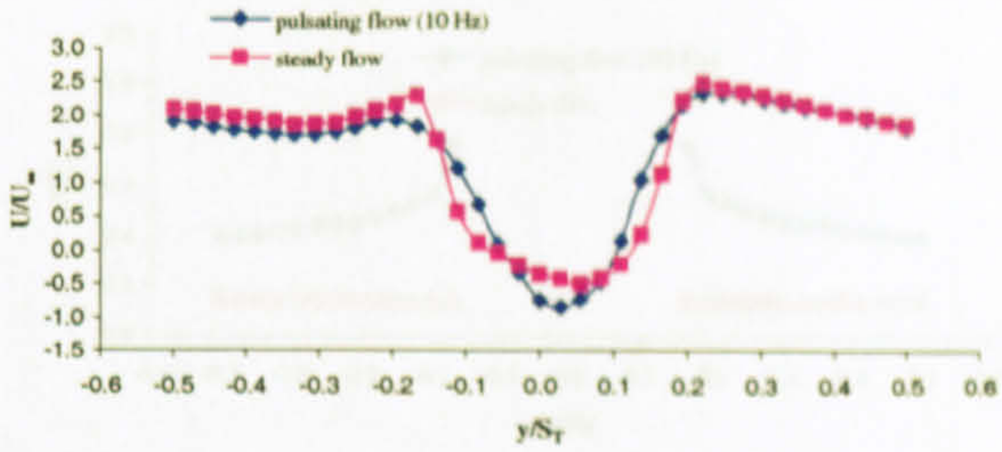

$x/S_L = 0.4$ – 1st cylinder

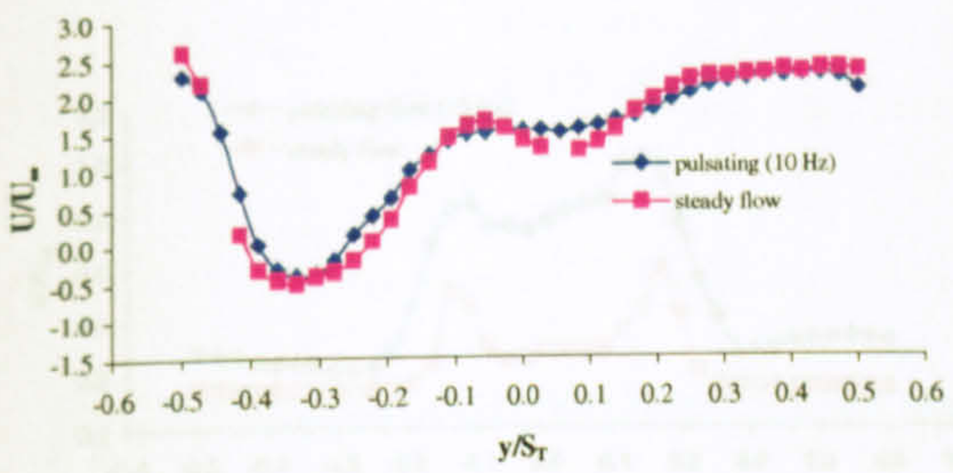

$x/S_L = 1.4$ - 2nd cylinder

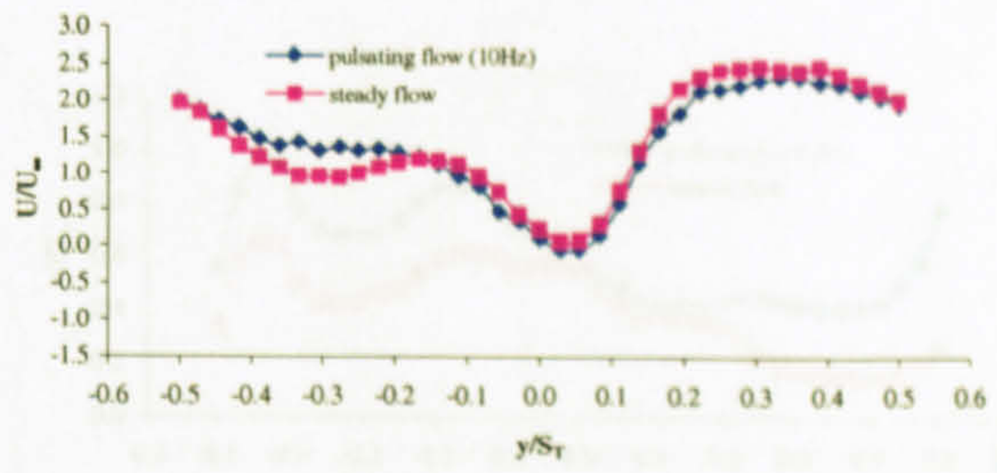

$x/S_L = 2.4$ – 3rd cylinder

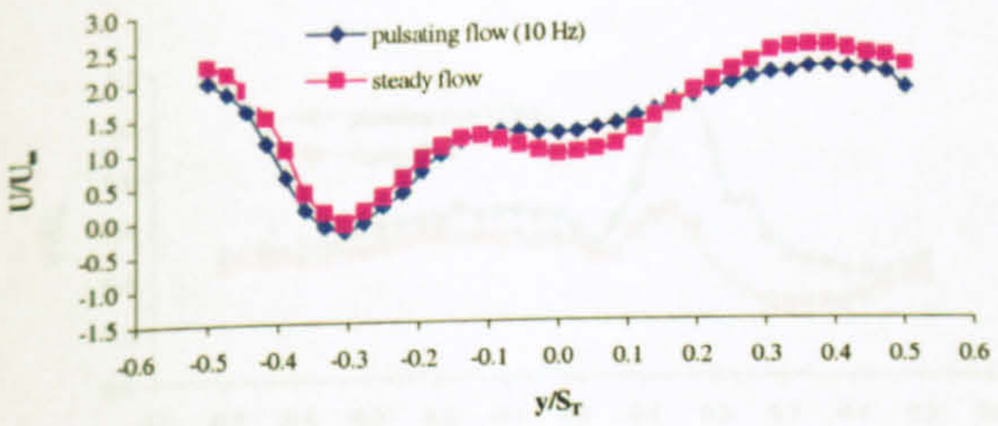

$x/S_L = 3.4$ – 4th cylinder

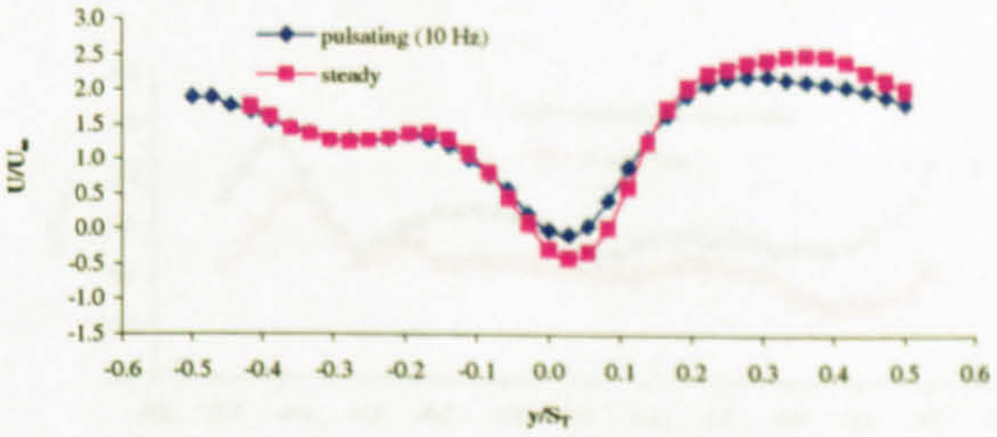

$x/S_L = 4.4$ - 5th cylinder

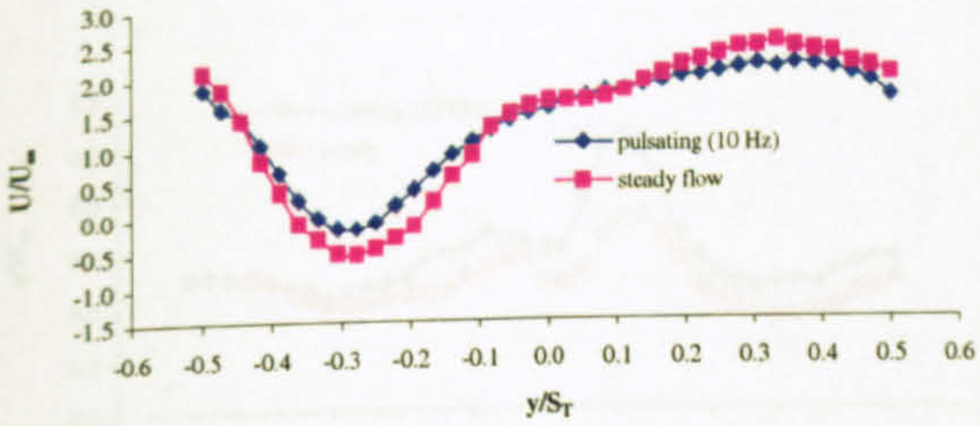

$x/S_L = 5.4$ - 6th cylinder

Figure 4.20. Comparison of the axial mean velocity profiles, U/U_∞, obtained in steady and pulsating flow (f_d = 10 Hz, Re = 4,900).

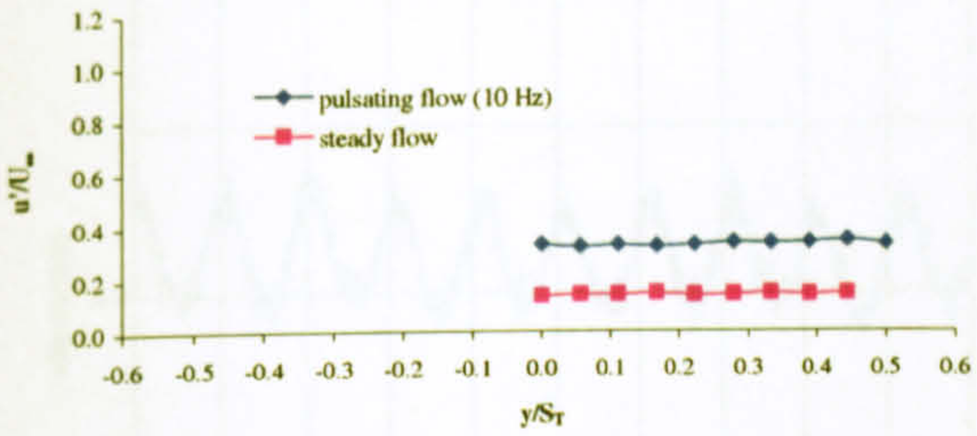

$x/S_L = -1.0$ - upstream of tube bank

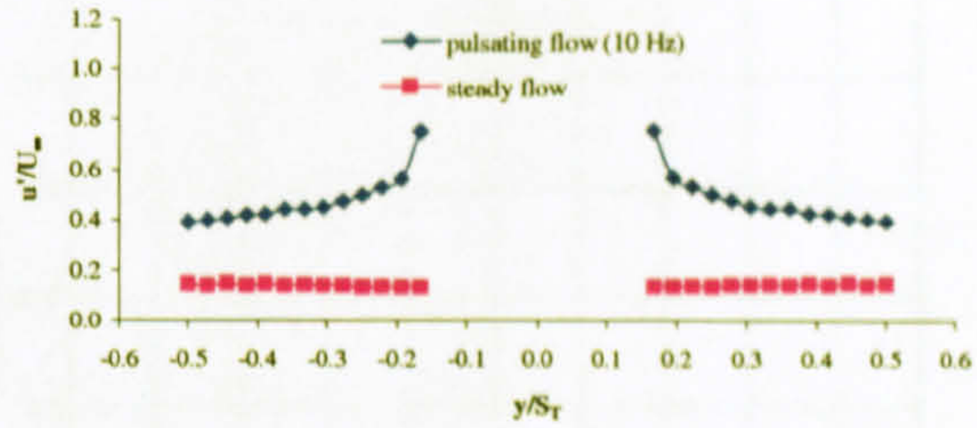

$x/S_L = 0.0$ - entrance of tube bank

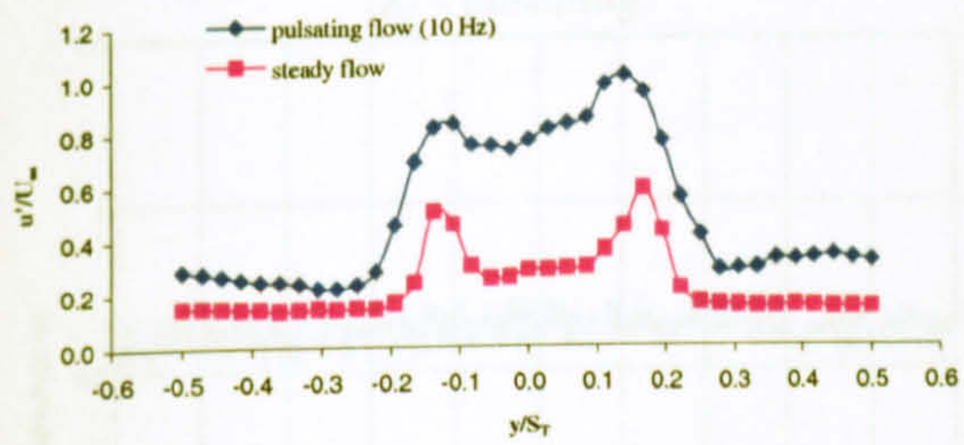

$x/S_L = 0.4 - 1^{nd}$ cylinder

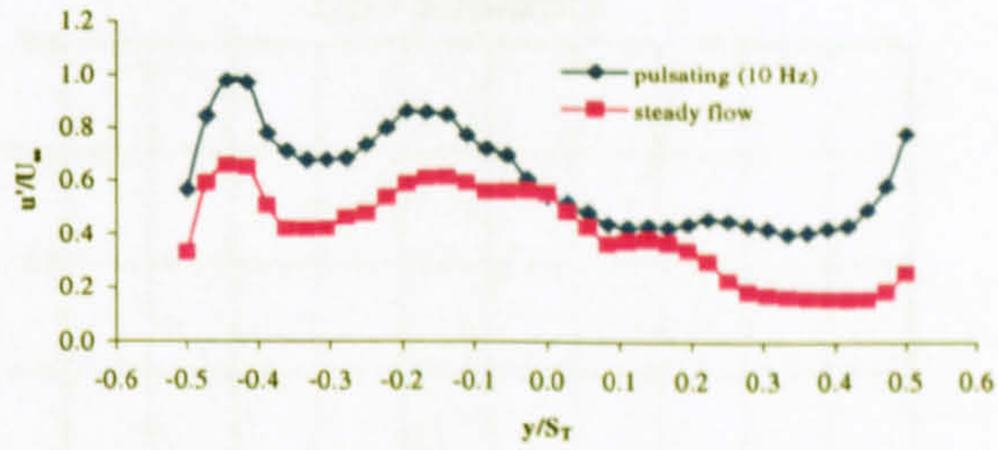

$x/S_L = 1.4 - 2^{nd}$ cylinder

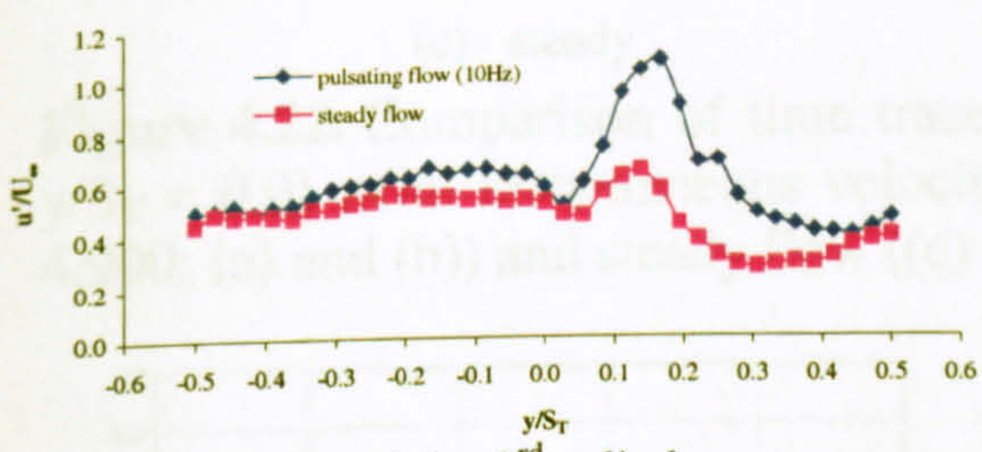

$x/S_L = 4.4 - 3^{rd}$ cylinder

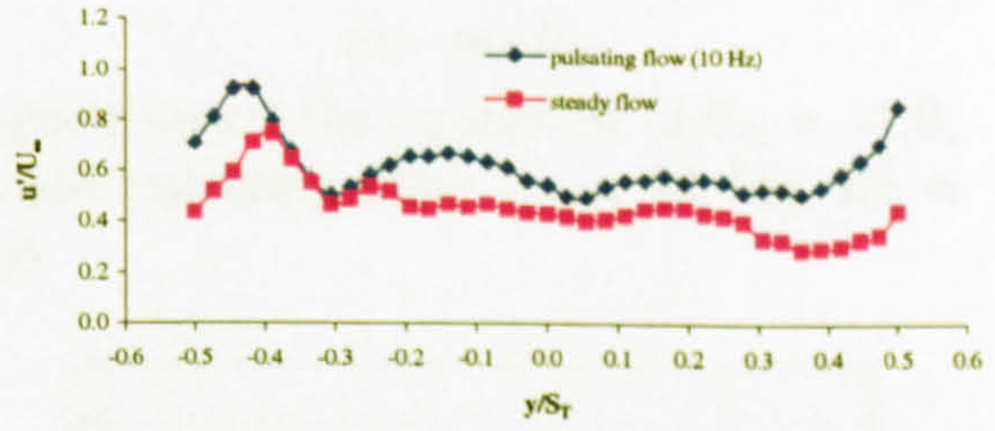

$x/S_L = 5.4 - 4^{th}$ cylinder

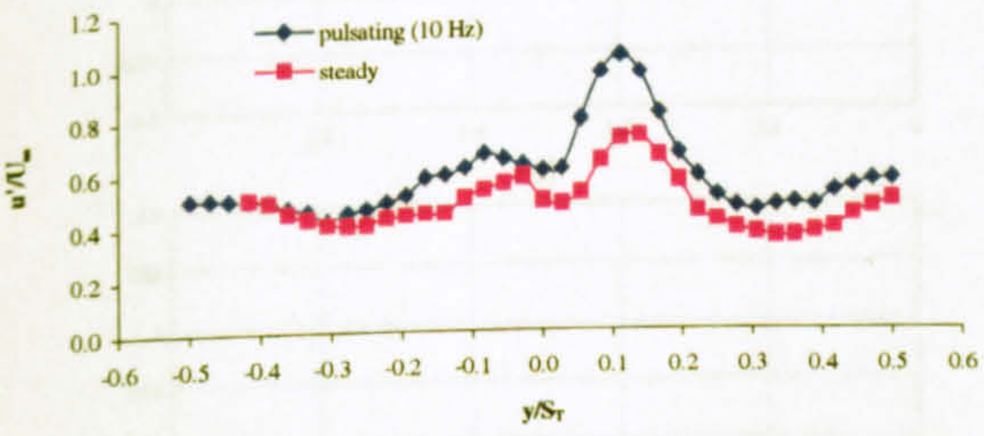

$x/S_L = 4.4 - 5^{th}$ cylinder

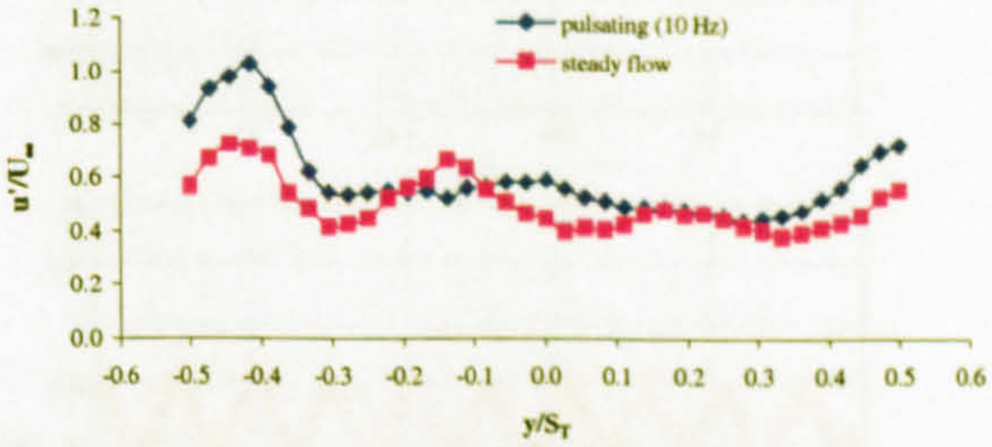

$x/S_L = 5.4 - 6^{th}$ cylinder

Figure 4.21. Comparison of the axial r.m.s. velocity profiles, u'/U_∞, obtained in steady and pulsating flow (f_d = 10 Hz, Re = 4,900).

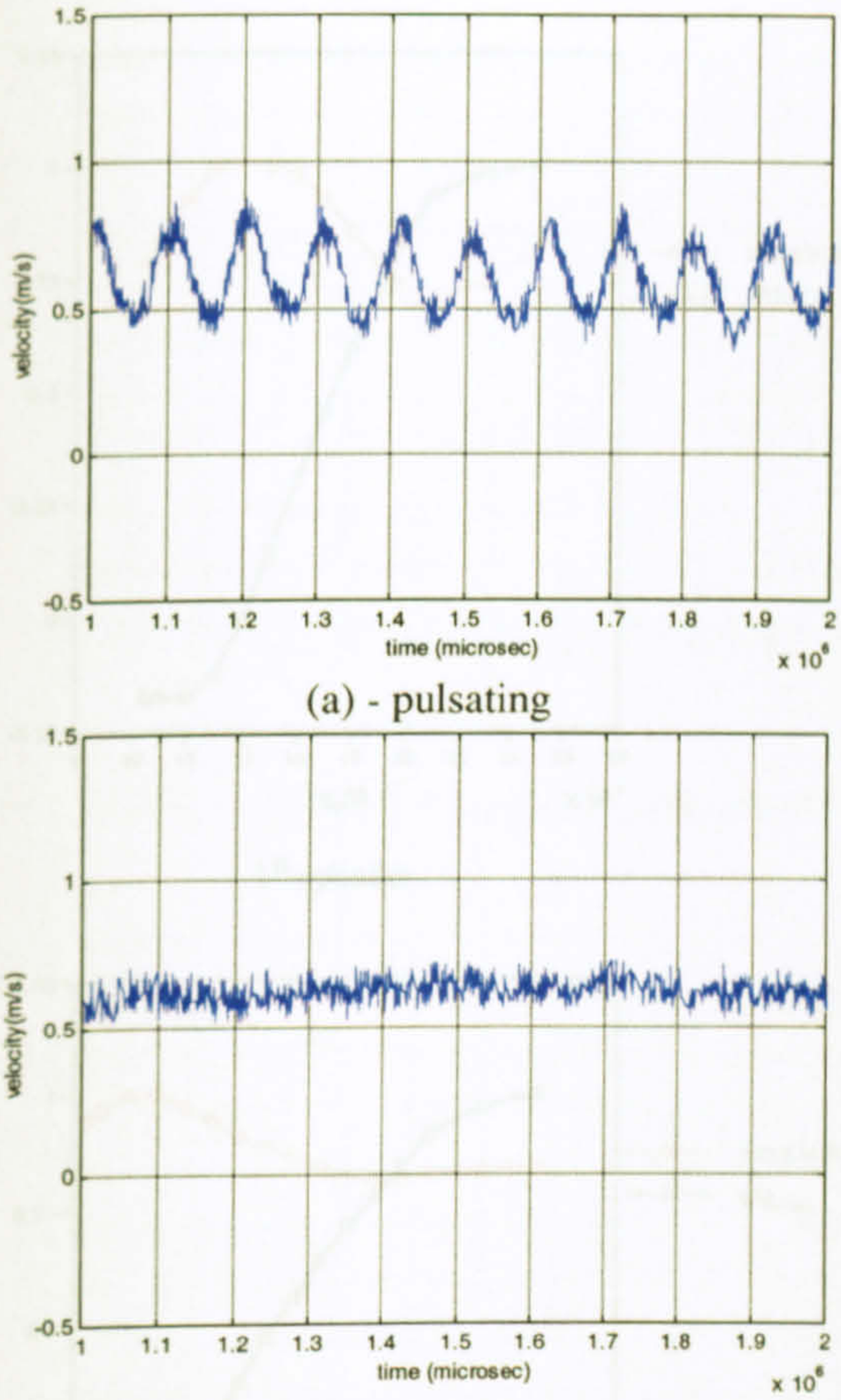

(a) - pulsating (b) - pulsating

(c) - steady (d) - steady

Figure 4.22. Comparison of time trace and spectrum of the upstream (x/S_L = -1.0, y/S_T = 0.0) axial instantaneous velocity between pulsating flow (f_d = 10 Hz, Re = 4,900; (a) and (b)) and steady flow ((c) and (d)).

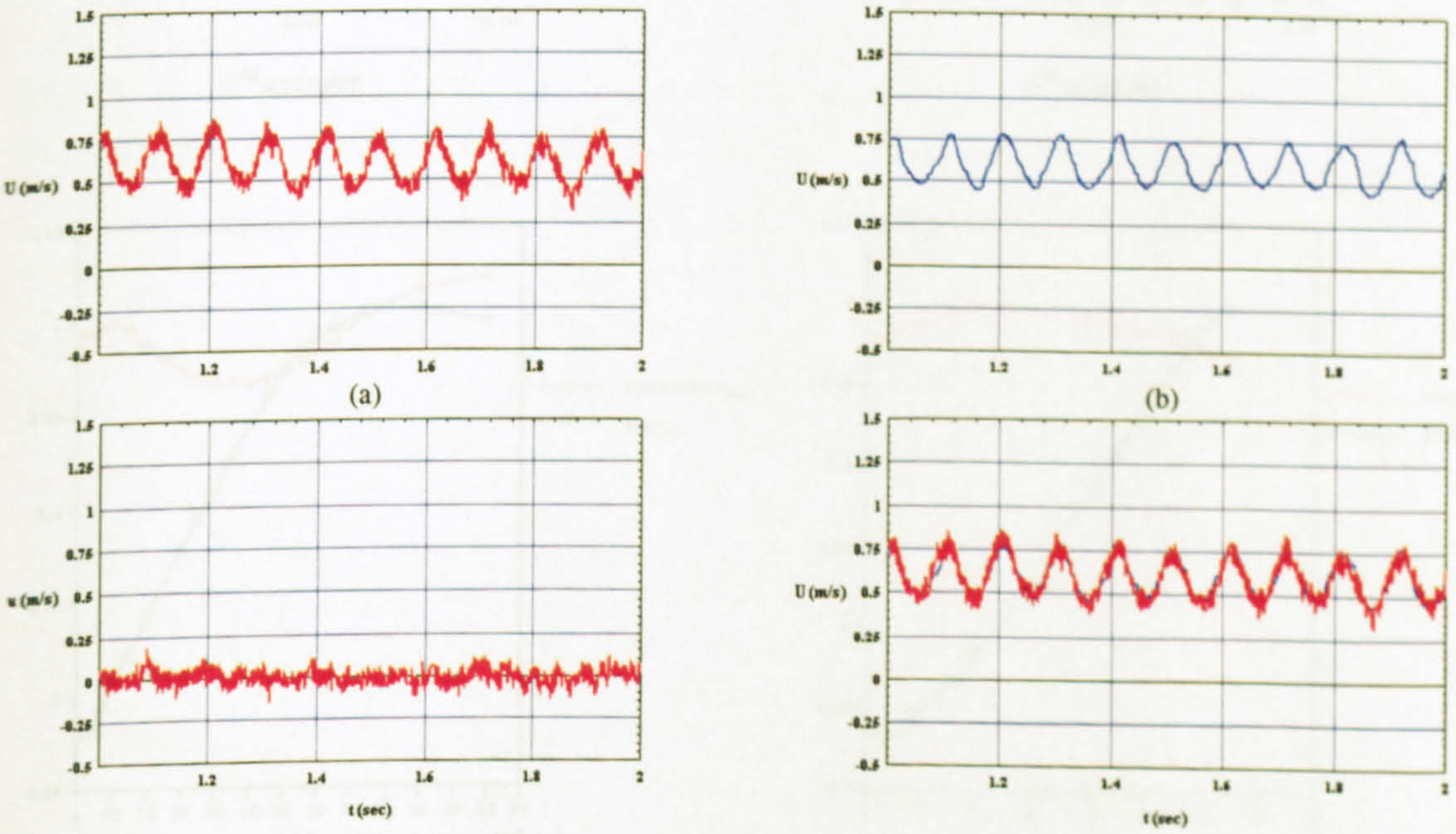

(a) (b)

(c) (d)

Figure 4.23. Velocity time traces showing the sequence of the notch-filtering technique adopted (f_d = 10 Hz, Re = 4,900). (a): unfiltered signal; (b) filtered pulsating mean flow; (c) filtered r.m.s.; (d) superimposition of the filtered pulsating mean flow onto the unfiltered signal.

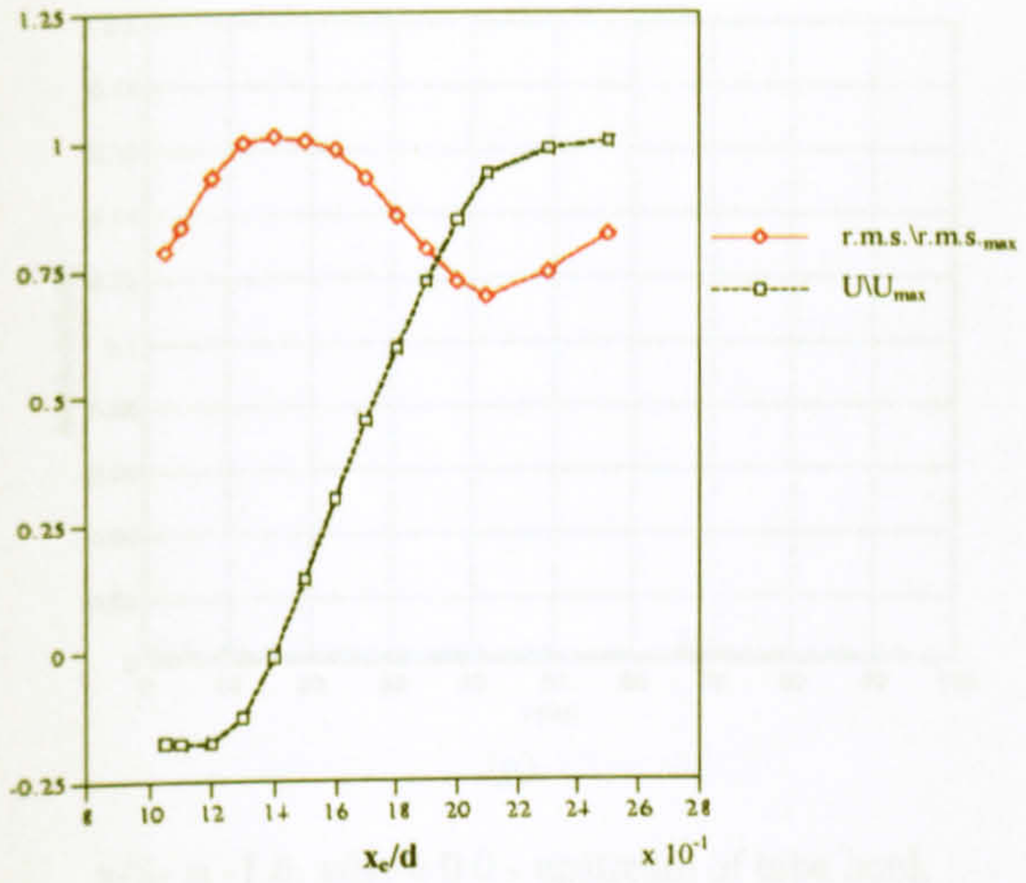

1st cylinder

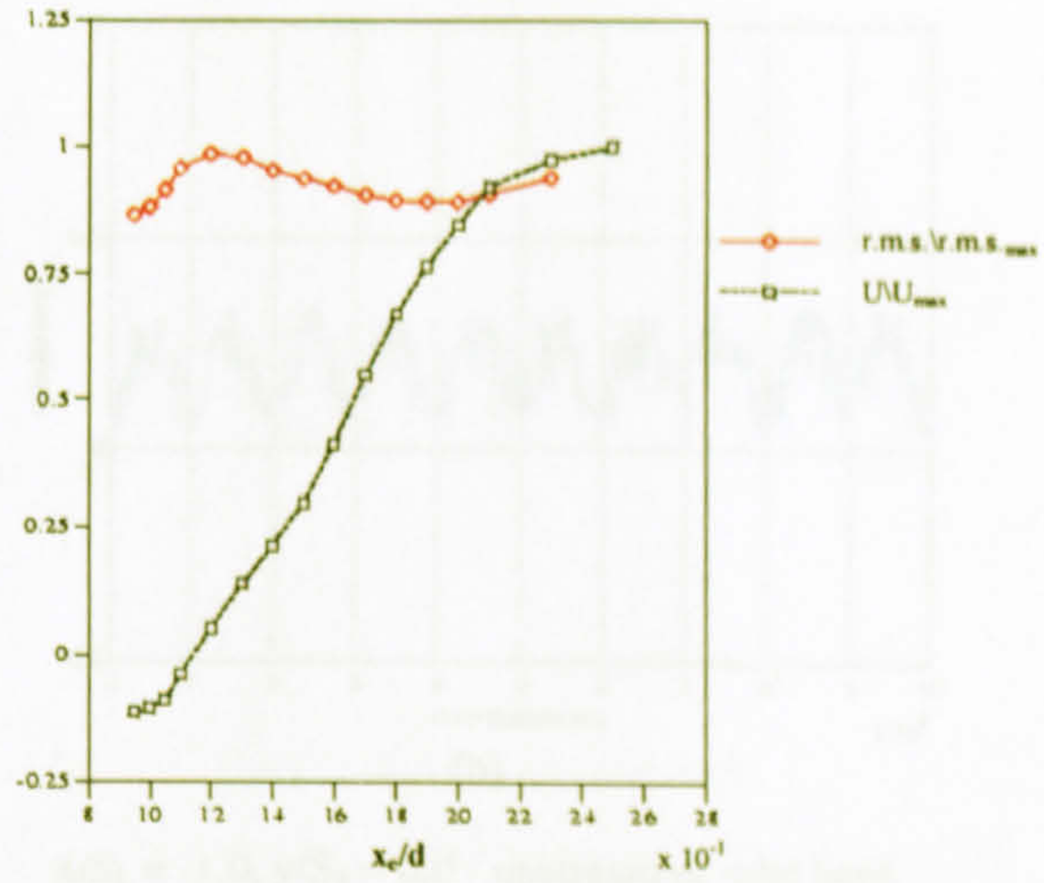

2nd cylinder

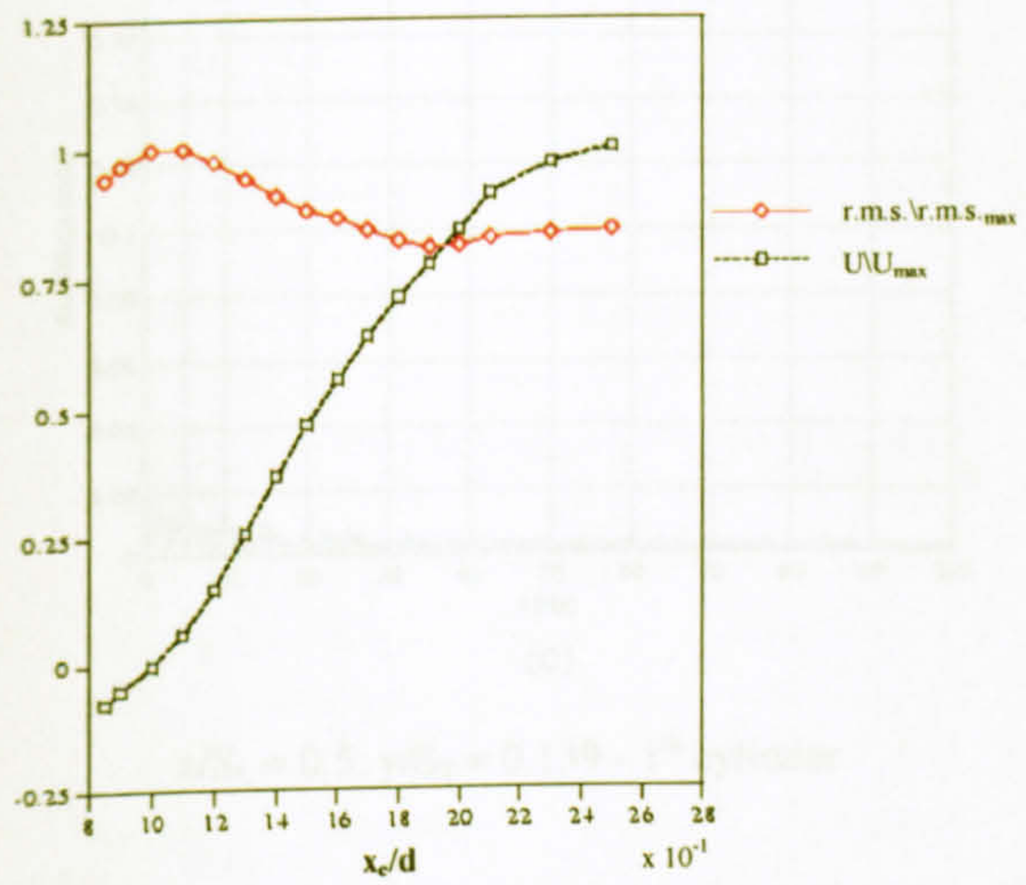

3rd cylinder

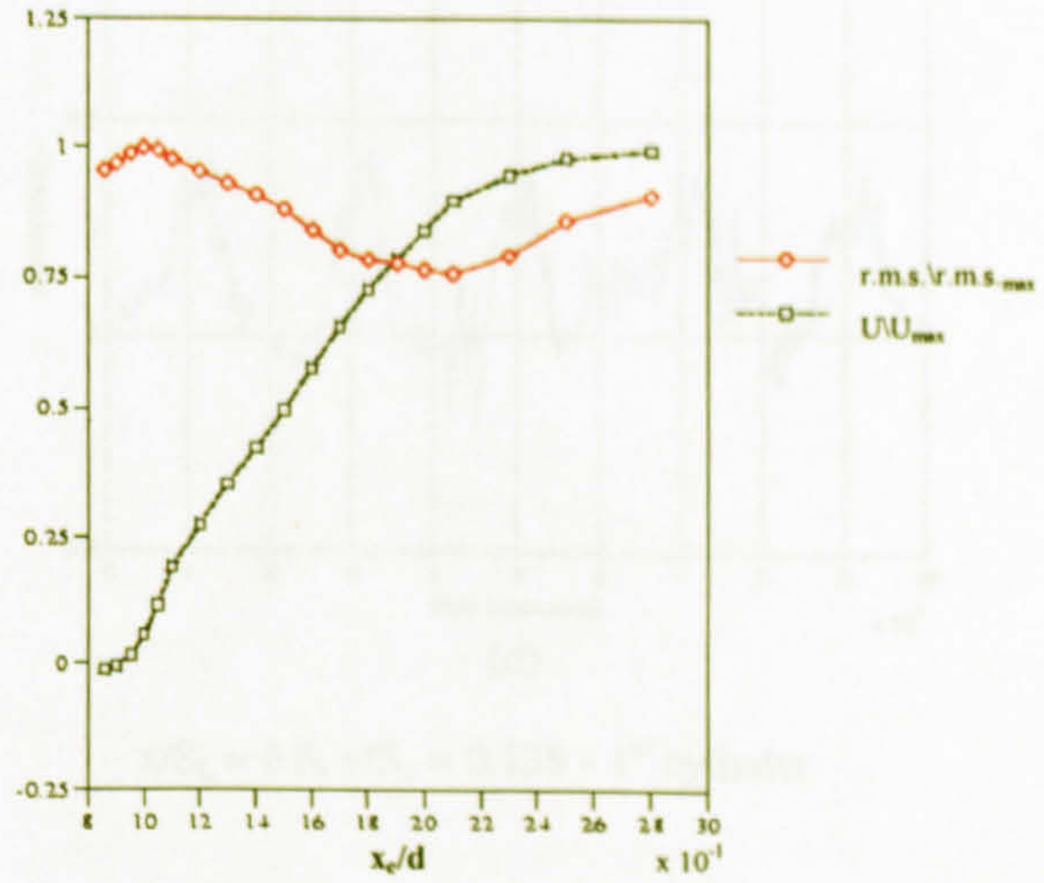

4th cylinder

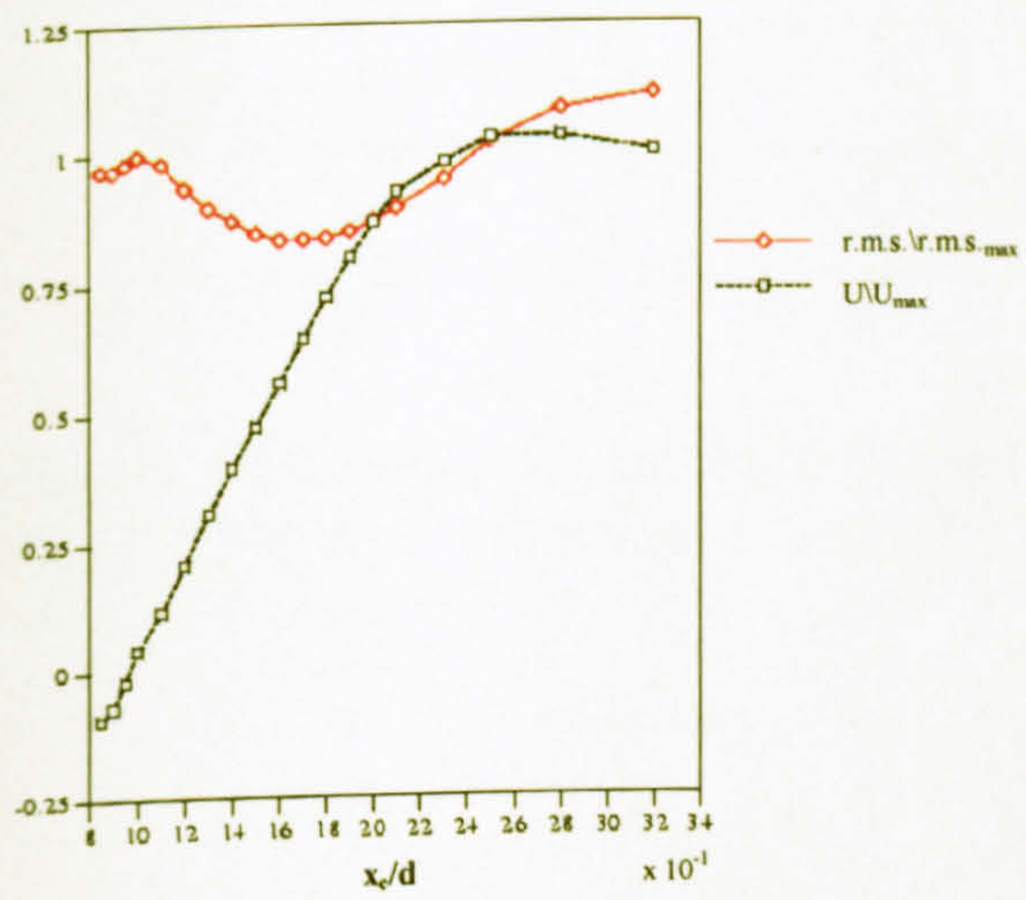

5th cylinder

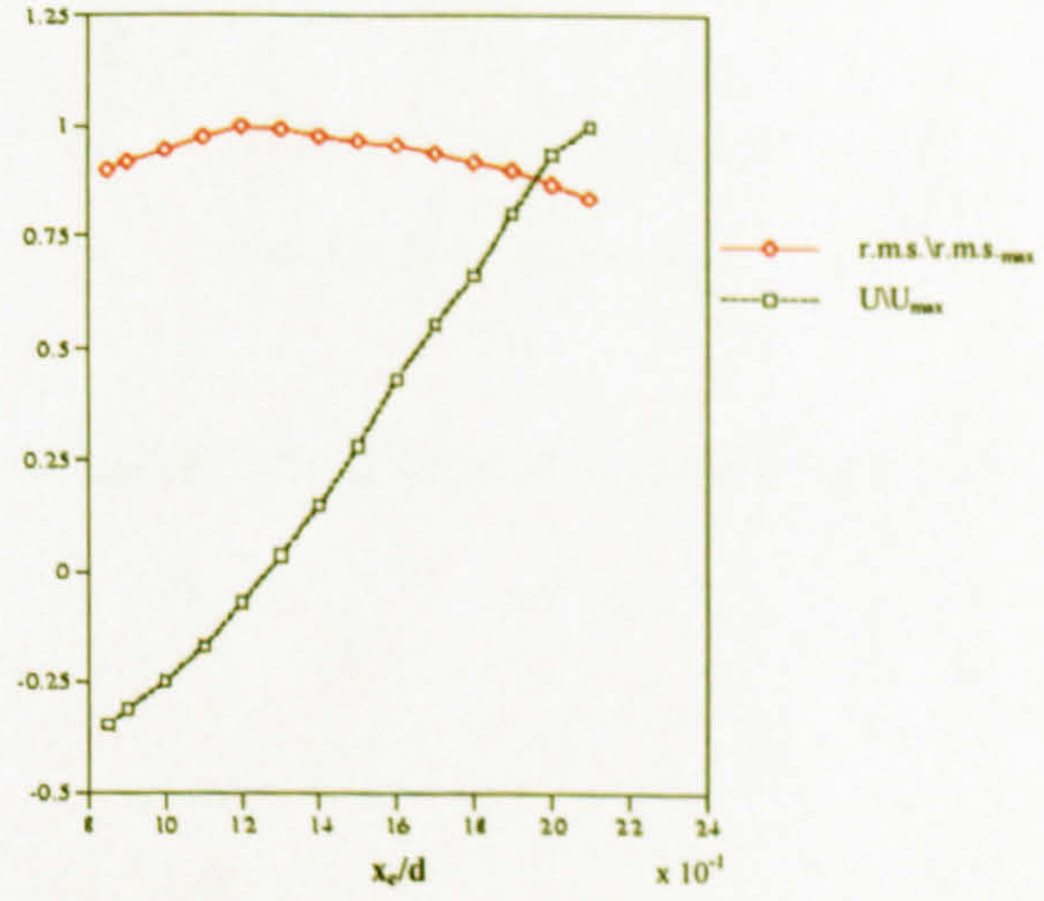

6th cylinder

Figure 4.24. Normalised mean and r.m.s. velocity profiles along the wake centreline of all rows of the asymmetric array in pulsating flow (Re = 4,900, f_p = 10 Hz).

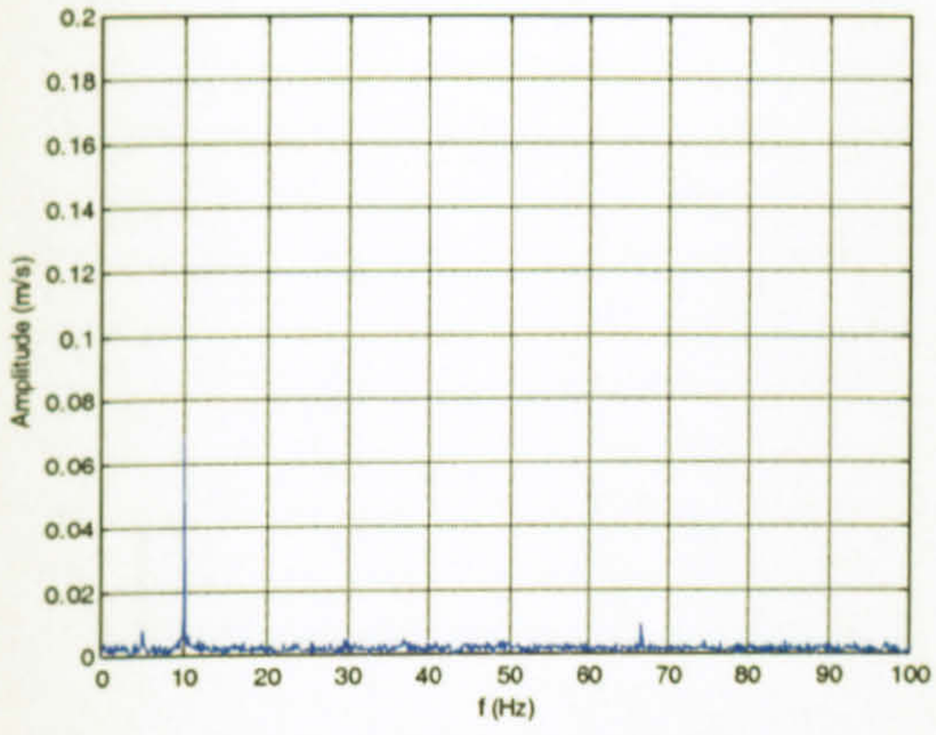

(a)

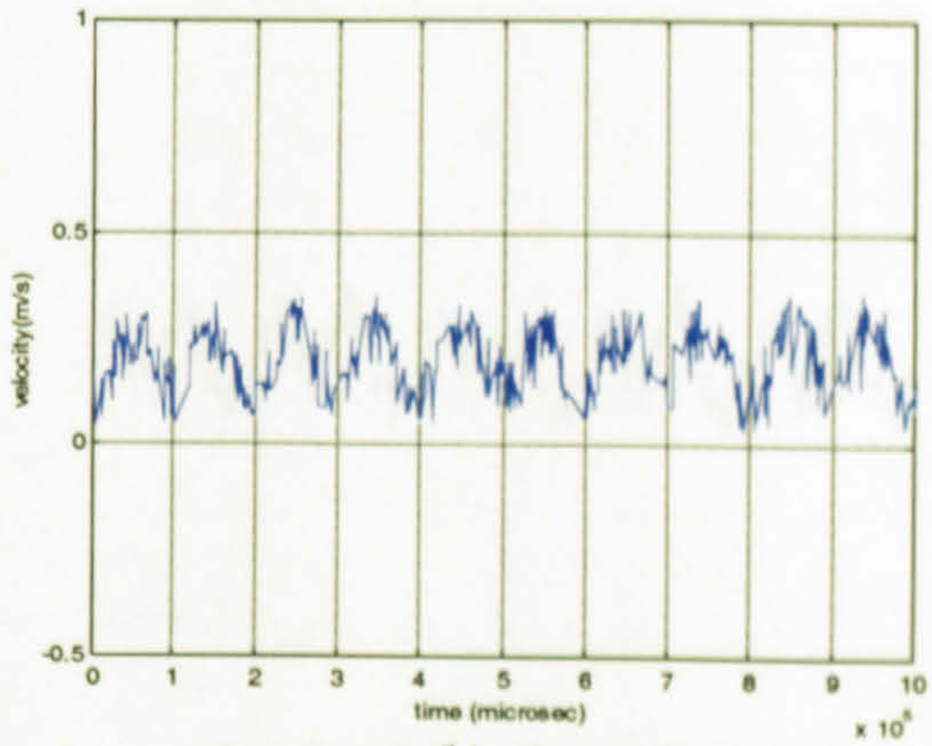

(b)

$x/S_L = -1.0$, $y/S_T = 0.0$ - upstream of tube bank

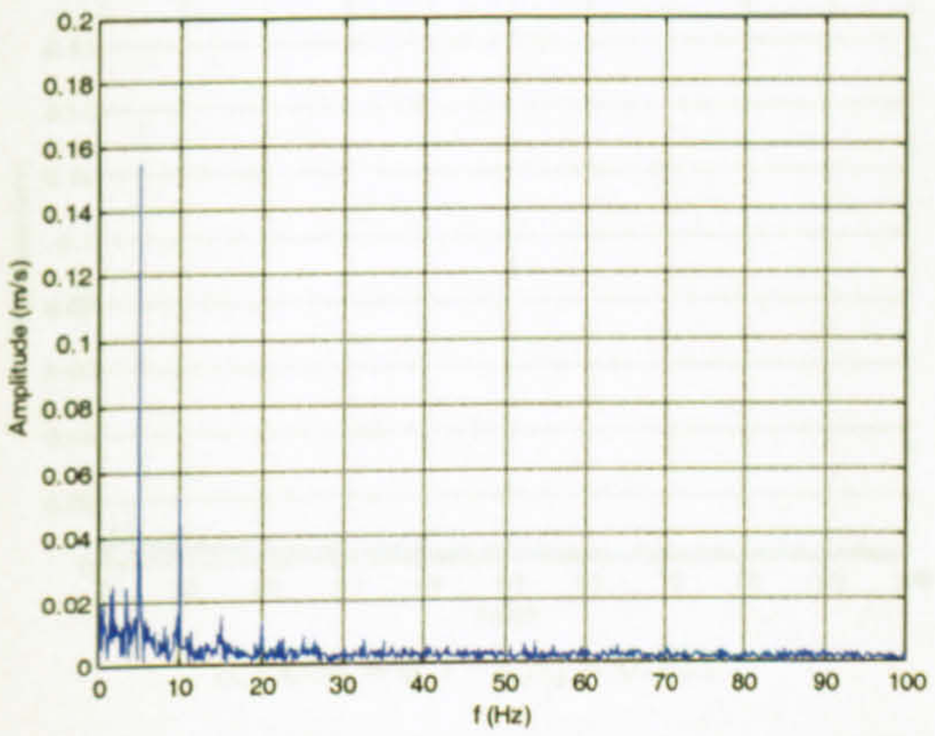

(c)

$x/S_L = -1.0$, $y/S_T = 0.0$ - upstream of tube bank

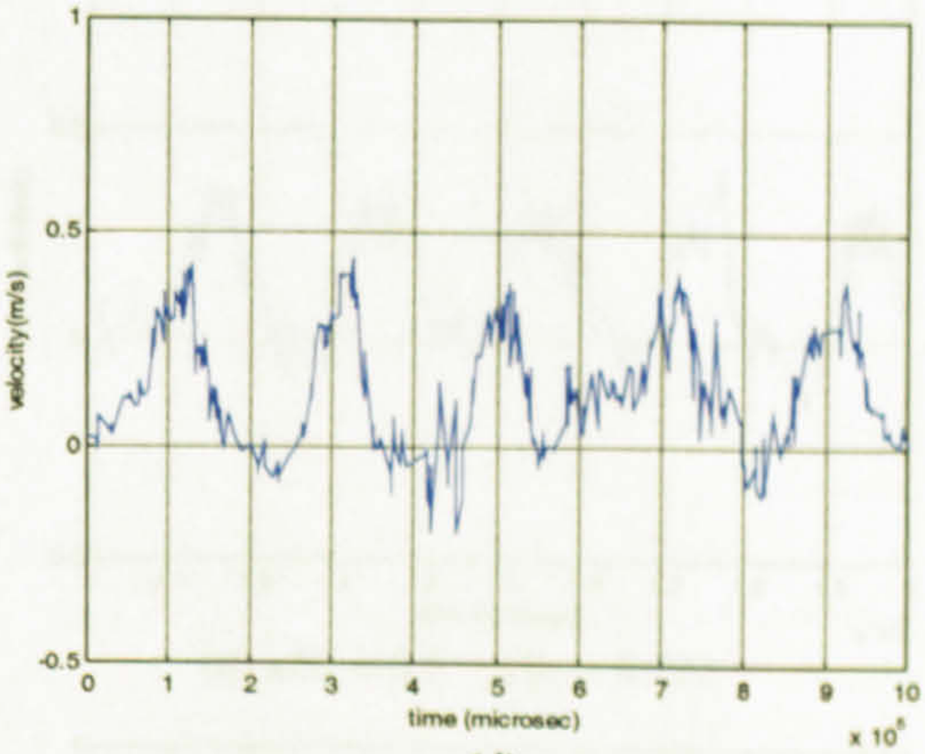

(d)

$x/S_L = 0.5$, $y/S_T = 0.139$ - 1st cylinder

$x/S_L = 0.5$, $y/S_T = 0.139$ - 1st cylinder

Figure 4.25. Amplitude spectra and time traces upstream of the tube bank and behind the first row in pulsating flow (Re = 2,700, f_p = 10 Hz and $A_o \approx 0.35$).

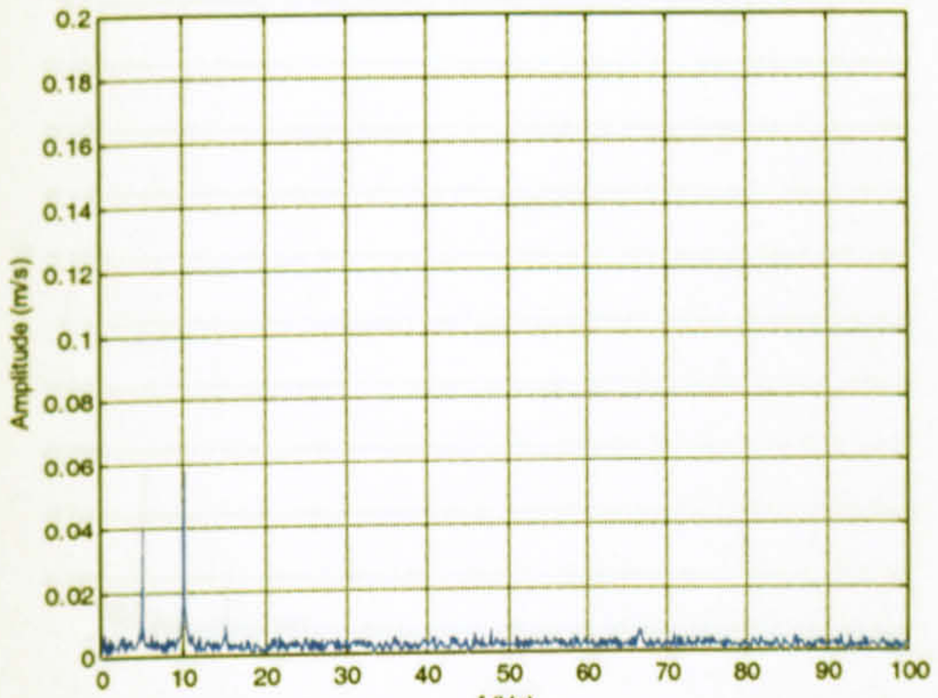

(a) $x/S_L = 0.5$ - $y/S_T = 0.389$

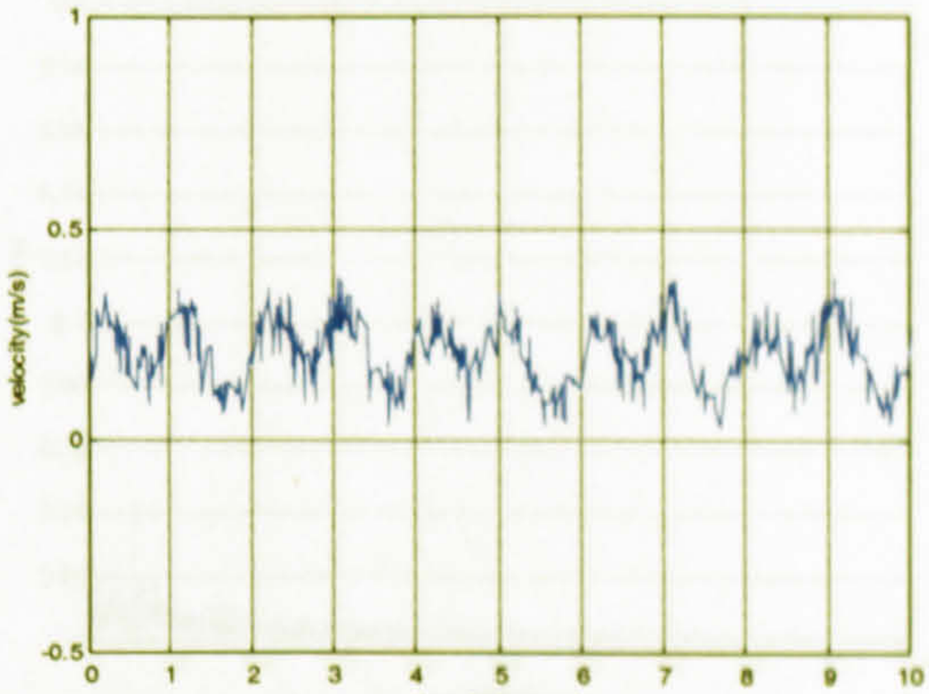

(b) $x/S_L = 0.5$ - $y/S_T = 0.389$

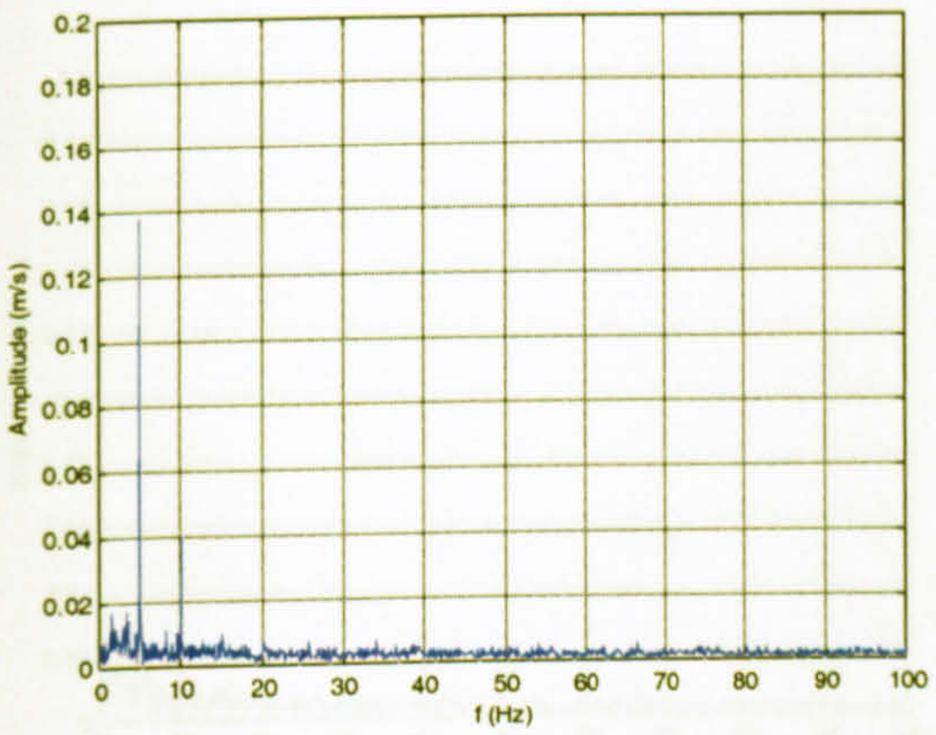

(c) $x/S_L = 0.5$ - $y/S_T = 0.222$

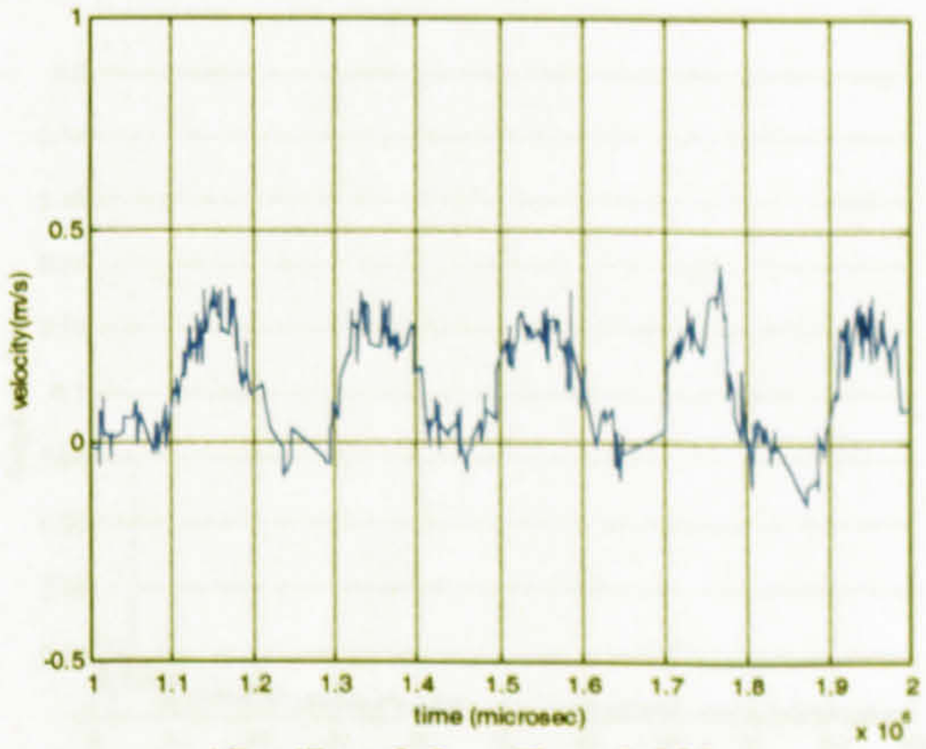

(d) $x/S_L = 0.5$ - $y/S_T = 0.222$

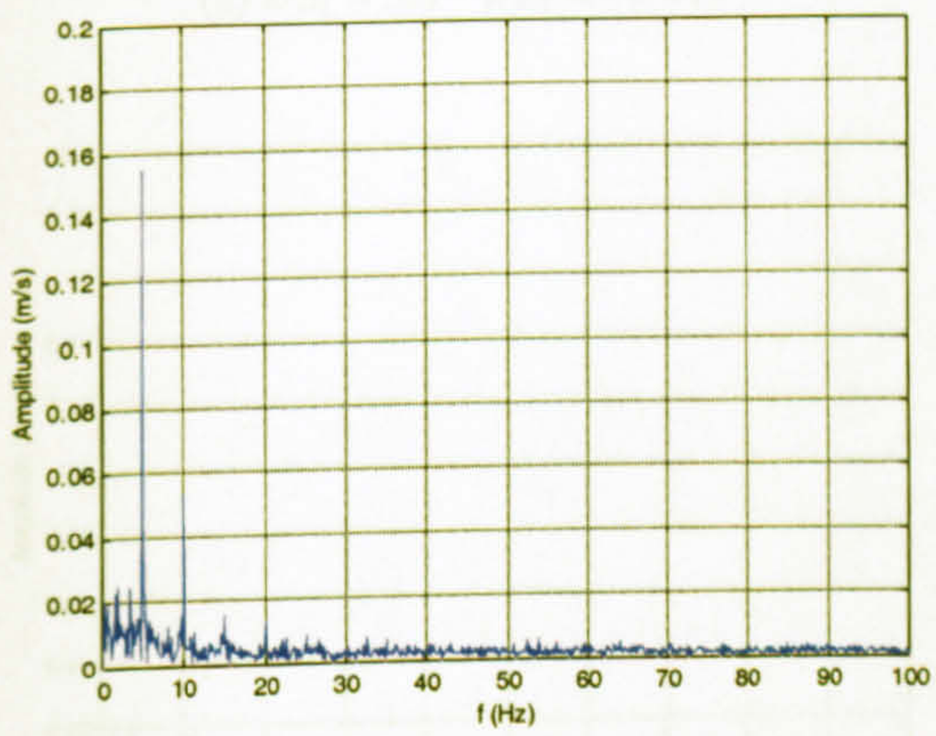

(e) $x/S_L = 0.5$ - $y/S_T = 0.167$

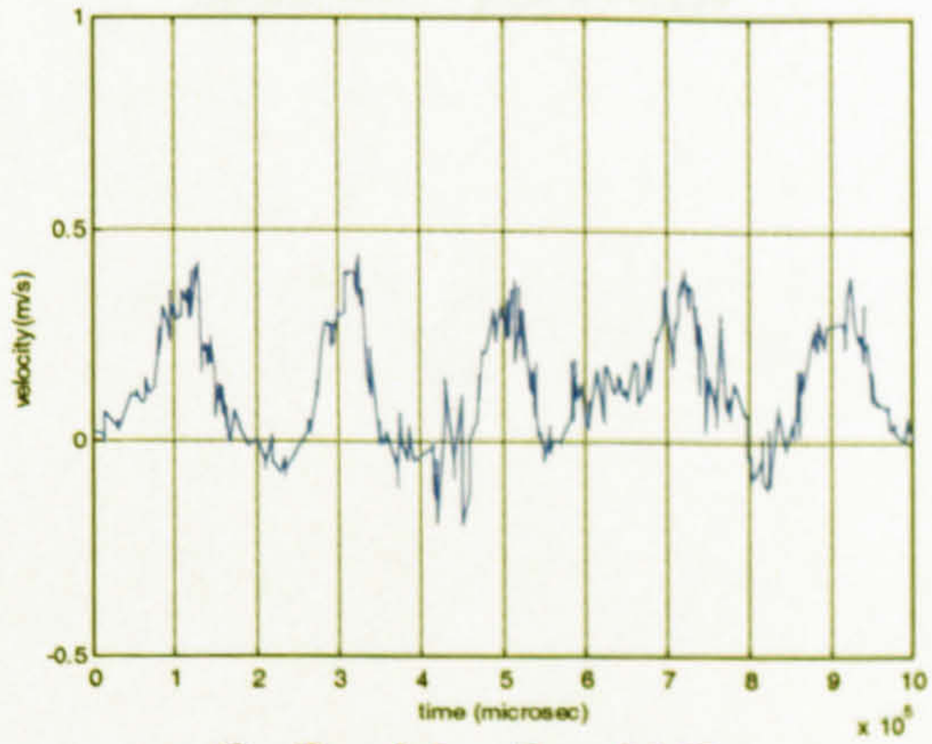

(f) $x/S_L = 0.5$ - $y/S_T = 0.167$

Figure 4.26. Amplitude spectra and time traces behind the first row in pulsating flow (Re = 2,700, f_p = 10 Hz and $A_o \approx 0.35$).

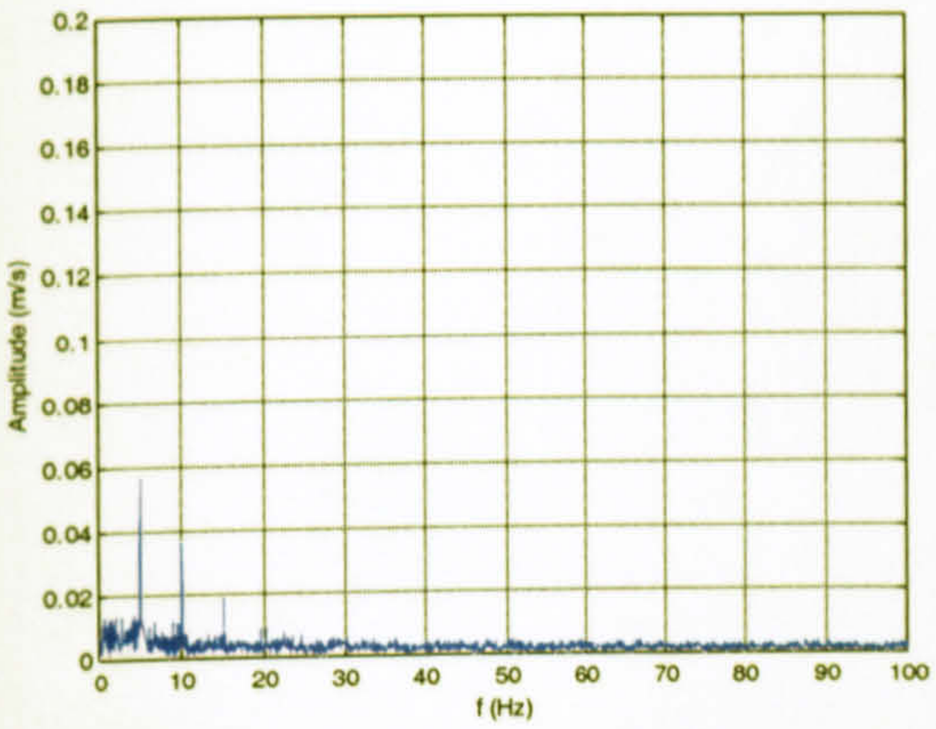

(a) $x/S_L = 1.5$ - $y/S_T = -0.139$

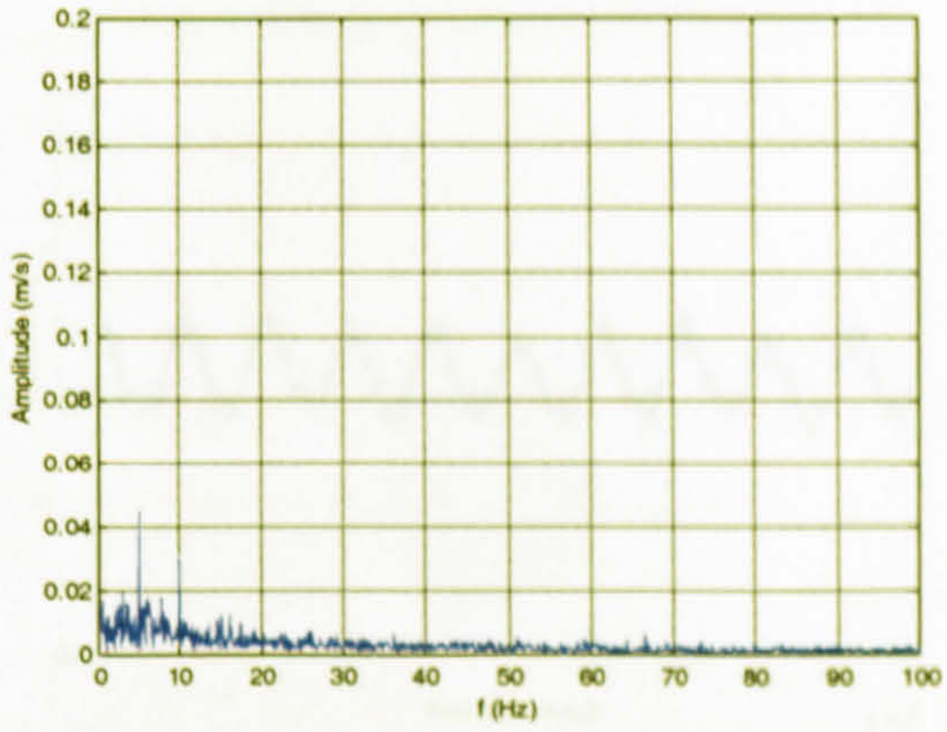

(a) $x/S_L = 2.5$ - $y/S_T = -0.139$

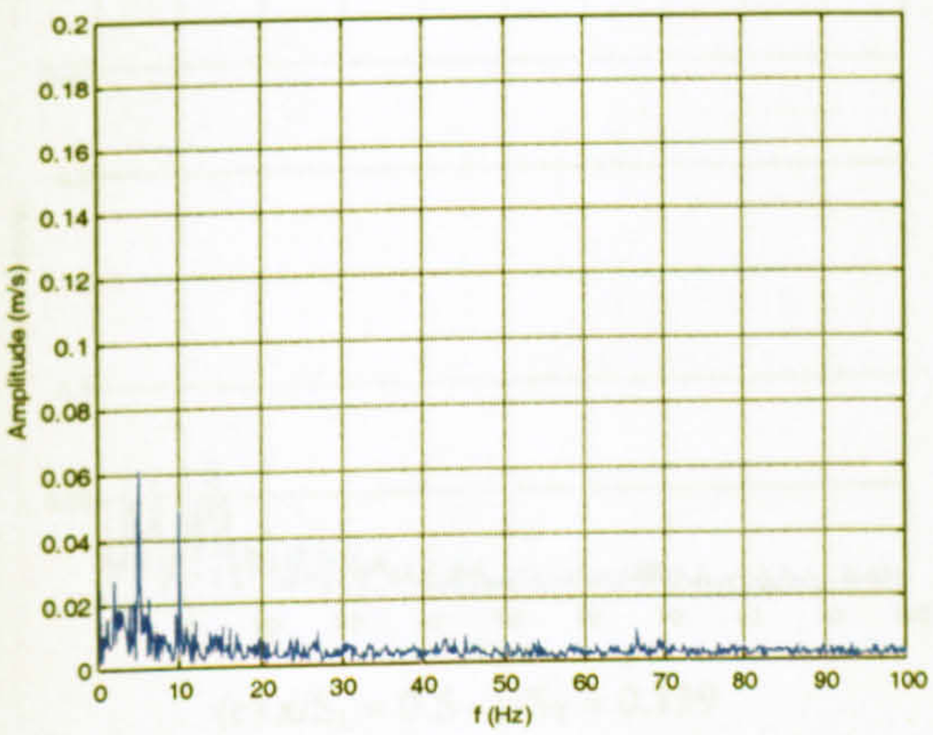

(a) $x/S_L = 3.5$ - $y/S_T = -0.417$

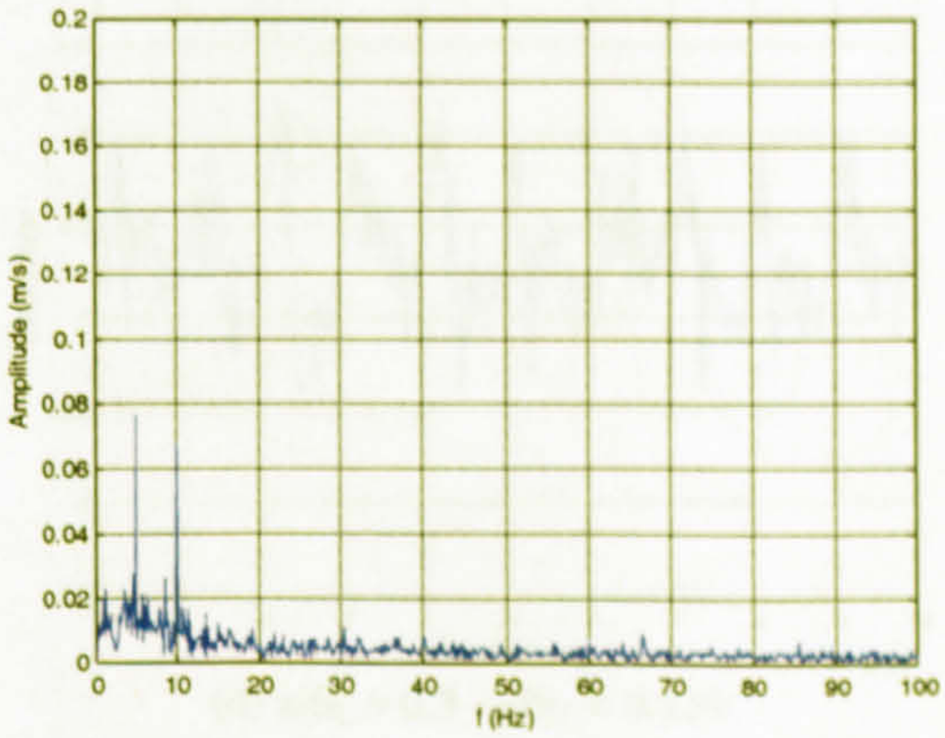

(c) $x/S_L = 4.5$ - $y/S_T = -0.139$

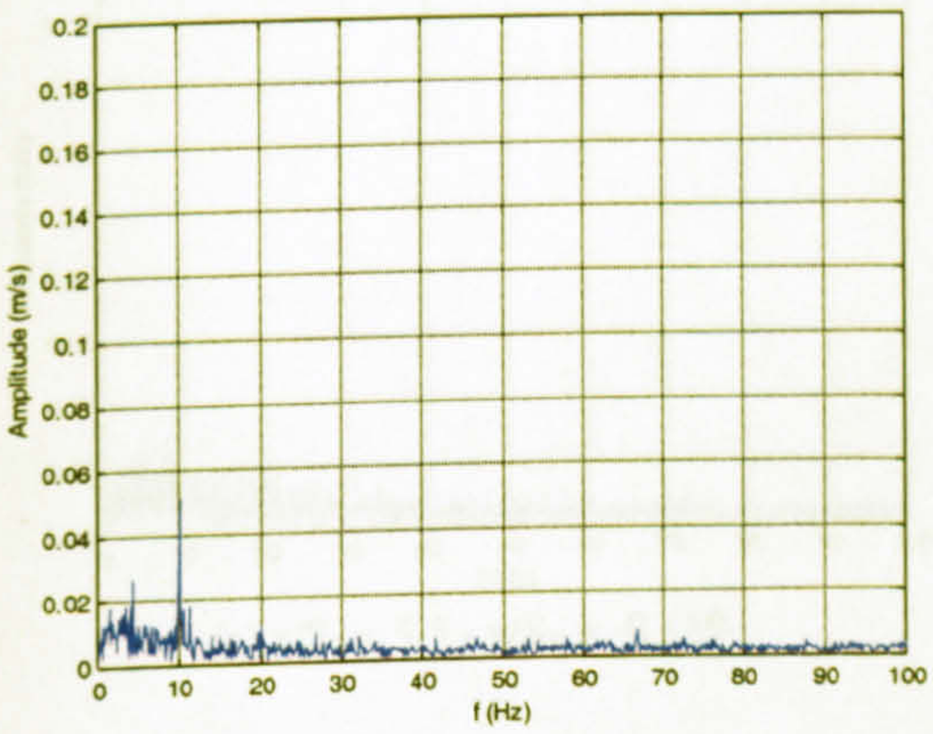

(a) $x/S_L = 5.5$ - $y/S_T = -0.139$

Figure 4.27. Amplitude spectra in pulsating flow (Re = 2,700, f_p = 10 Hz and $A_o \approx$ 0.35).

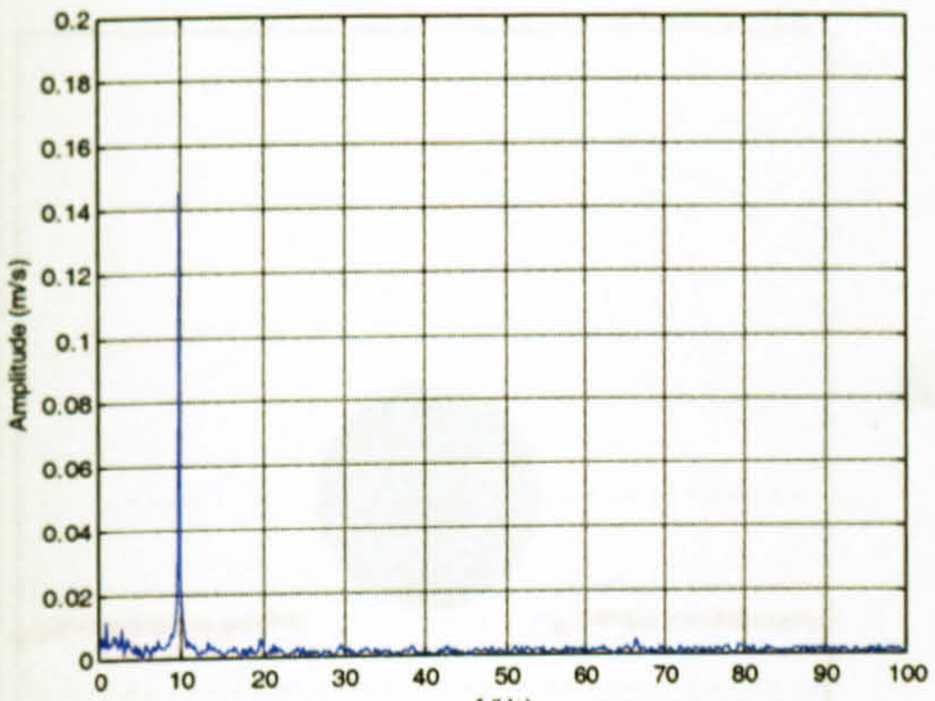

(a) $x/S_L = -1.0$ - $y/S_T = 0.0$

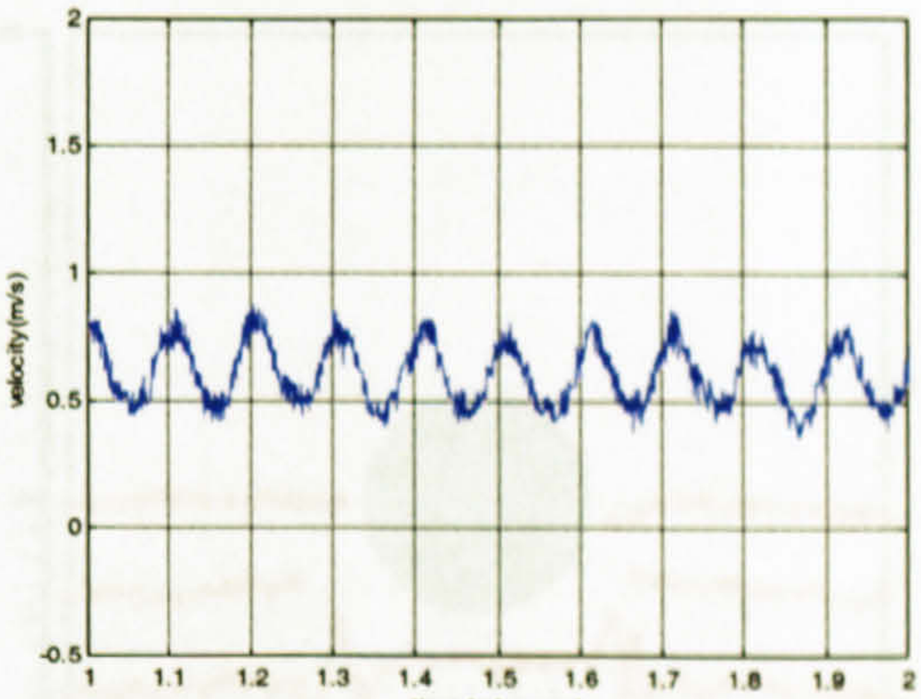

(b) $x/S_L = -1.0$ - $y/S_T = 0.0$

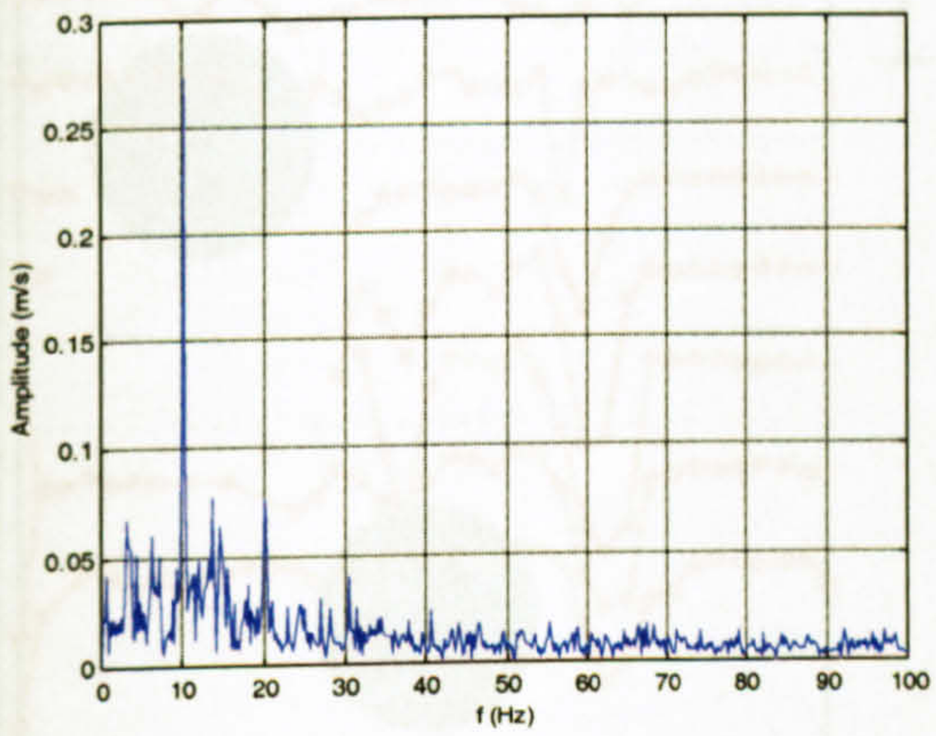

(c) $x/S_L = 0.5$ - $y/S_T = 0.139$

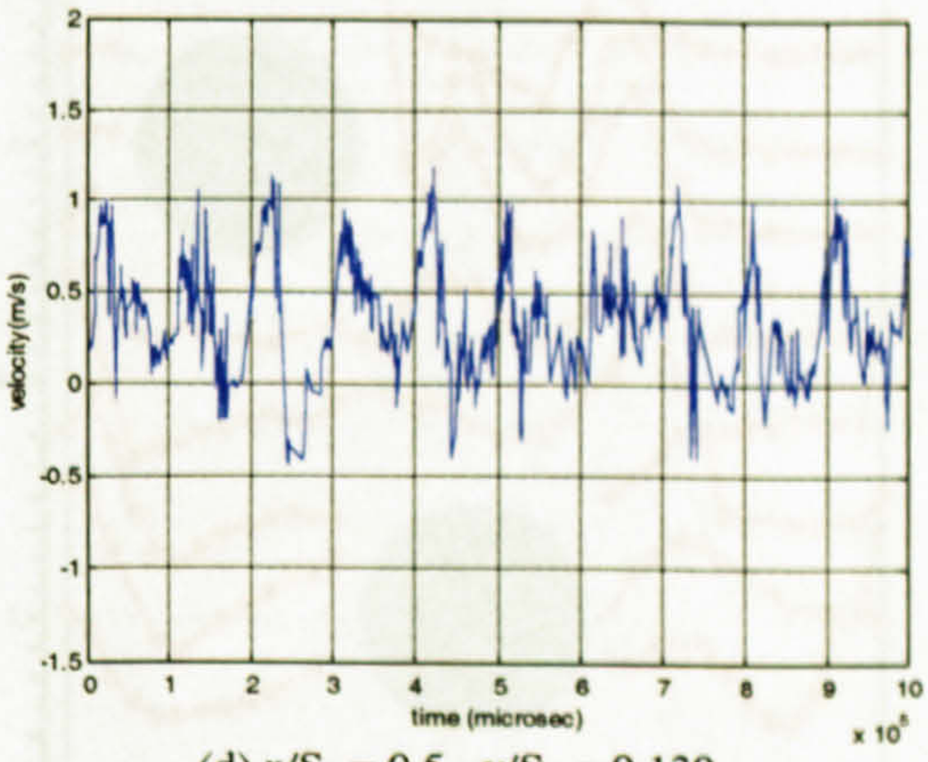

(d) $x/S_L = 0.5$ - $y/S_T = 0.139$

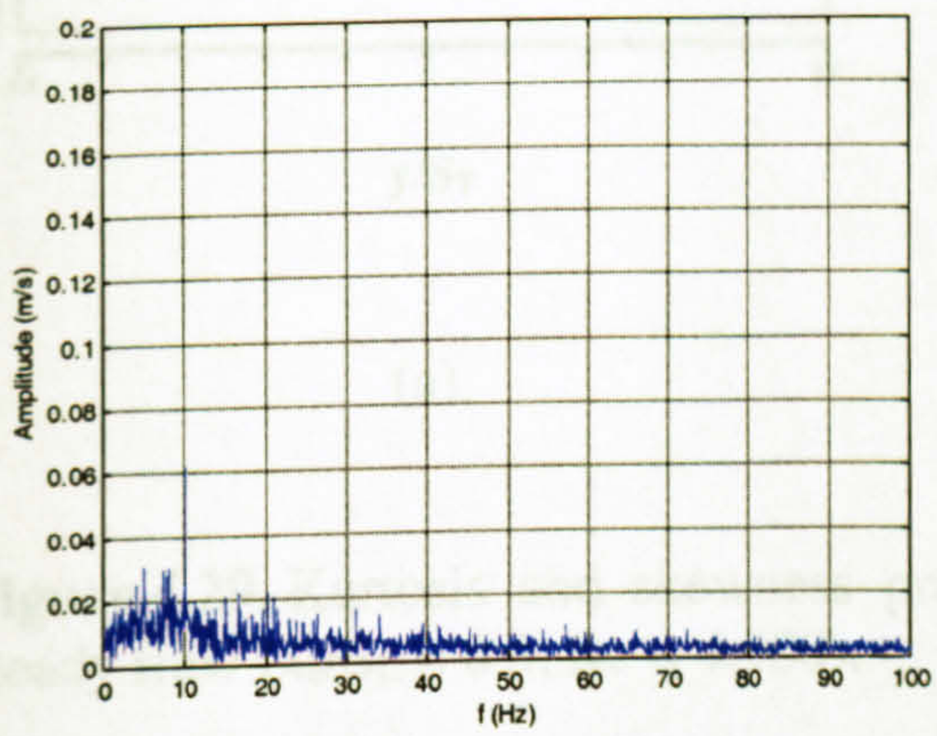

(e) $x/S_L = 5.5$ - $y/S_T = -0.139$

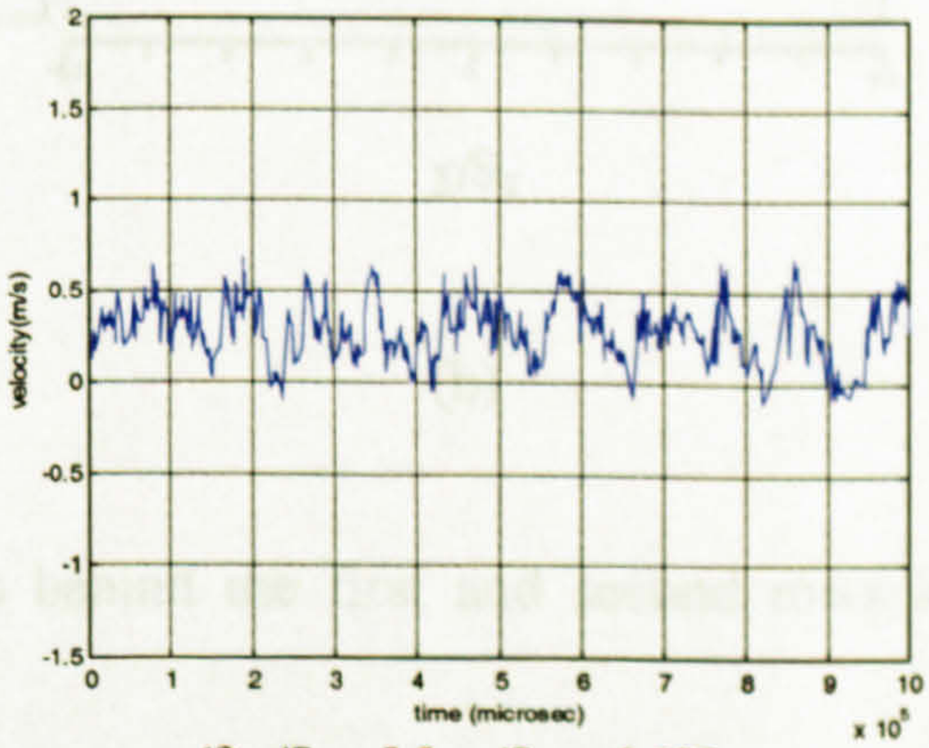

(f) $x/S_L = 5.5$ - $y/S_T = -0.139$

Figure 4.28. Amplitude spectra and time traces in pulsating flow (Re = 4,900, f_p = 10 Hz and $A_o \approx 0.24$).

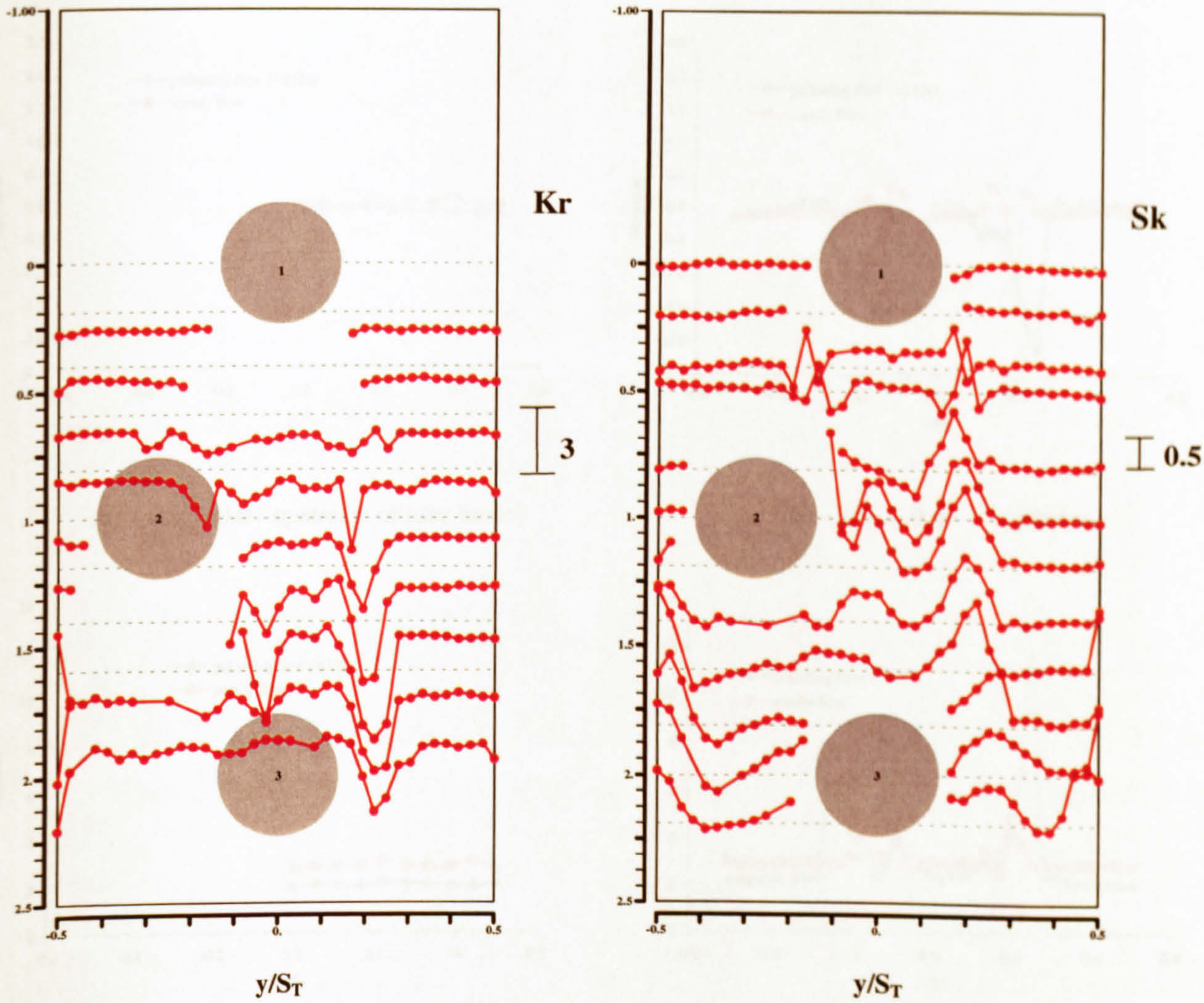

(a) (b)

Figure 4.29. Kurtosis and skewness profiles behind the first and second rows in steady flow ($x_c/S_L = 0.5$, Re = 4,900).

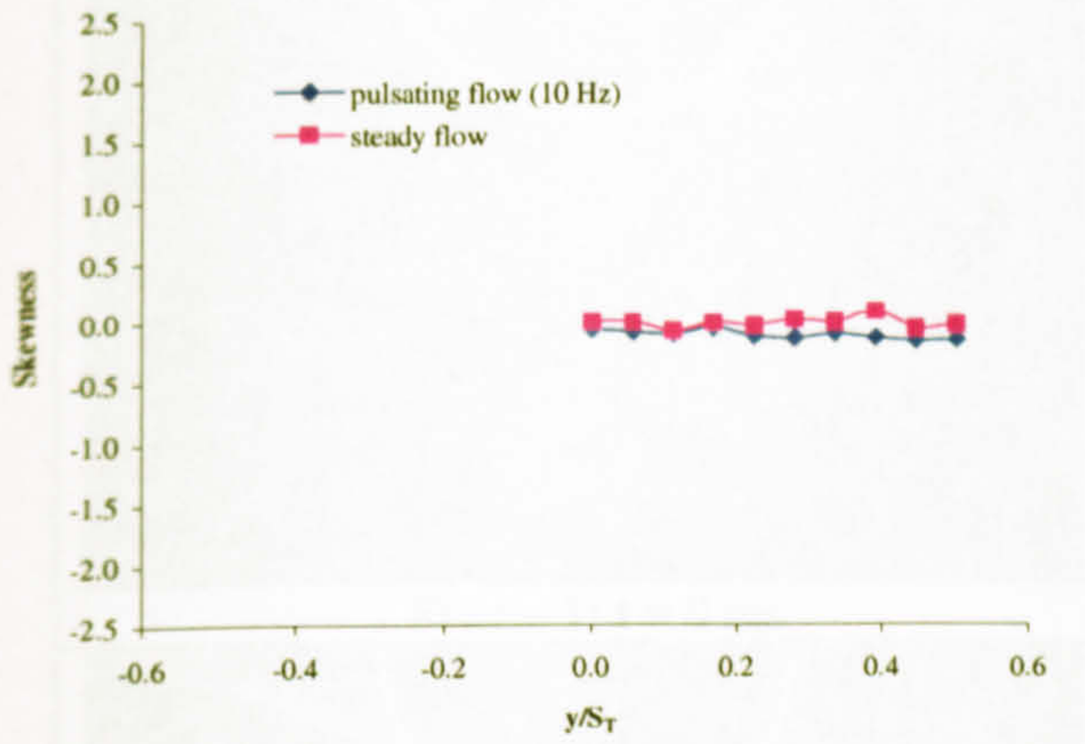

(a) - $x/S_L = 0.0$ - upstream of tube bank

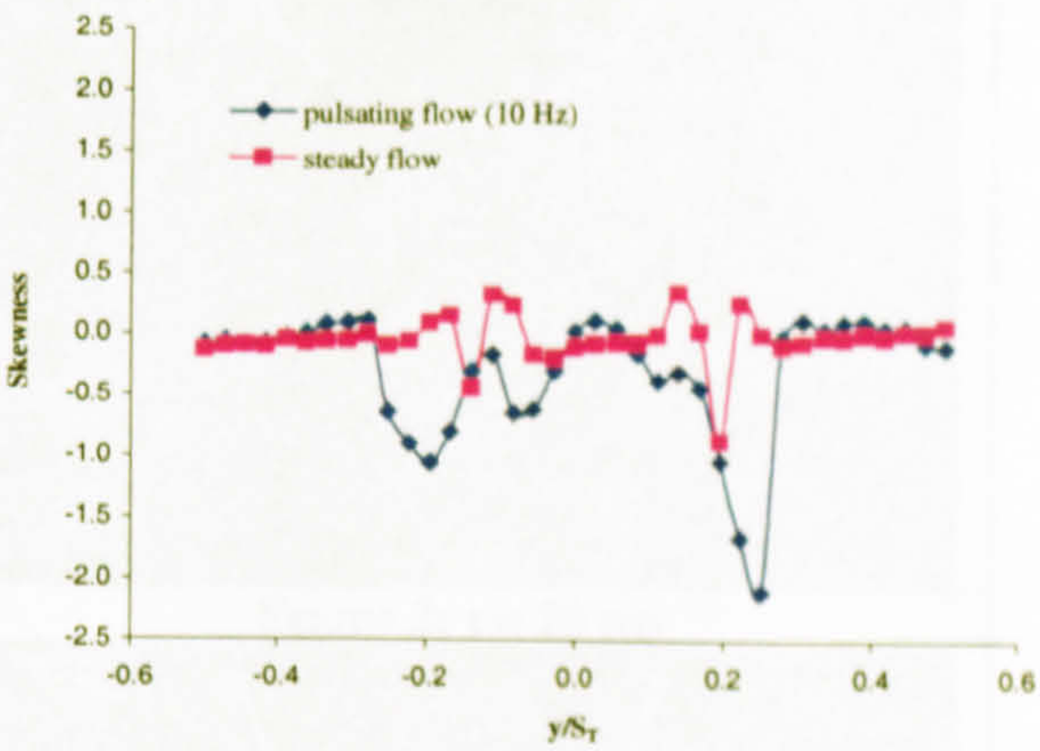

(b) - $x/S_L = 0.4$ - 1st cylinder

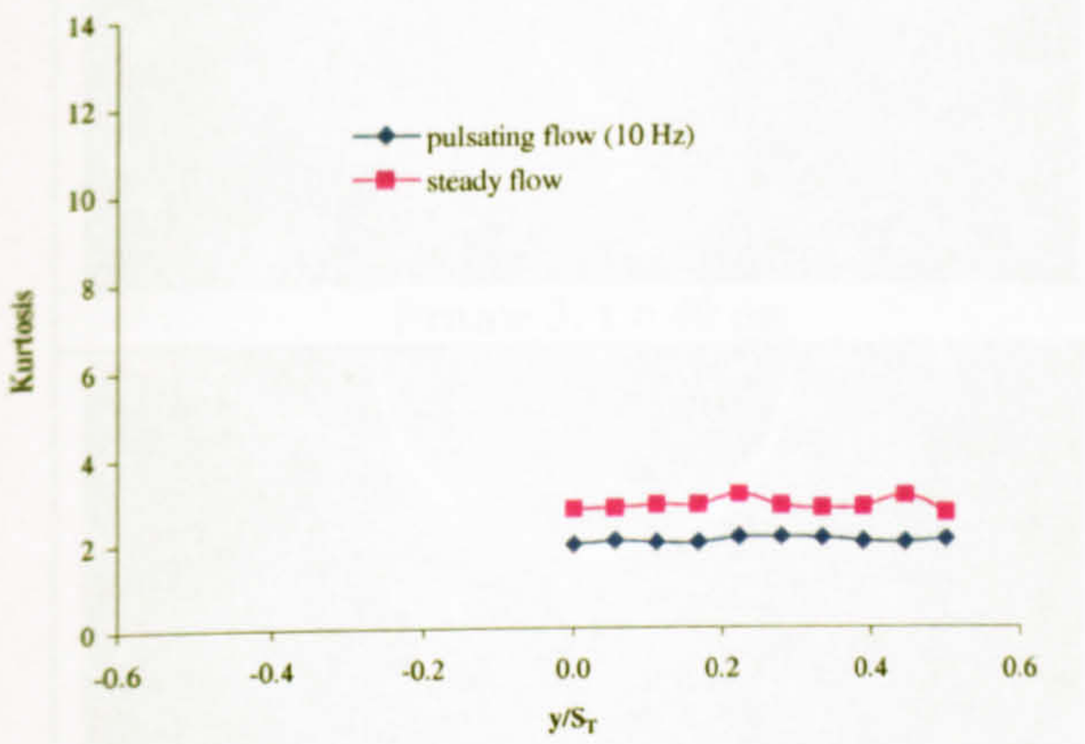

(c) - $x/S_L = 0.0$ - upstream of tube bank

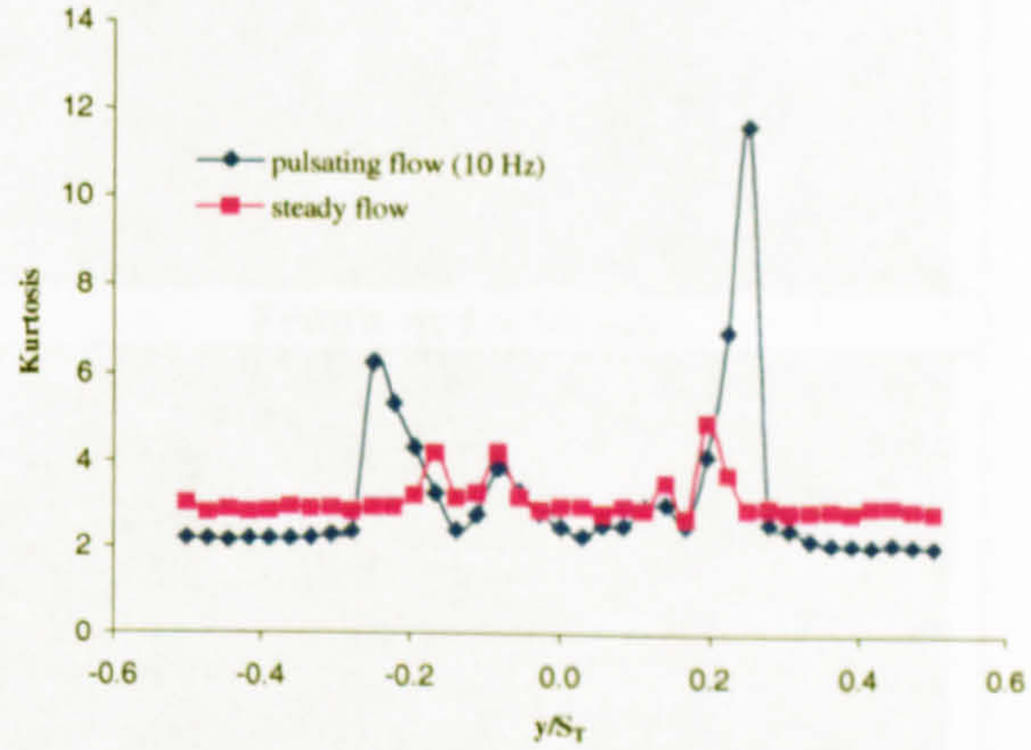

(d) - $x/S_L = 0.4$ - 1st cylinder

Figure 4.30. Skewness and kurtosis profiles behind at the entrance to the tube bank and behind the first row ($x/S_L = 0.5$, Re = 2,700) in both steady and pulsating flow.

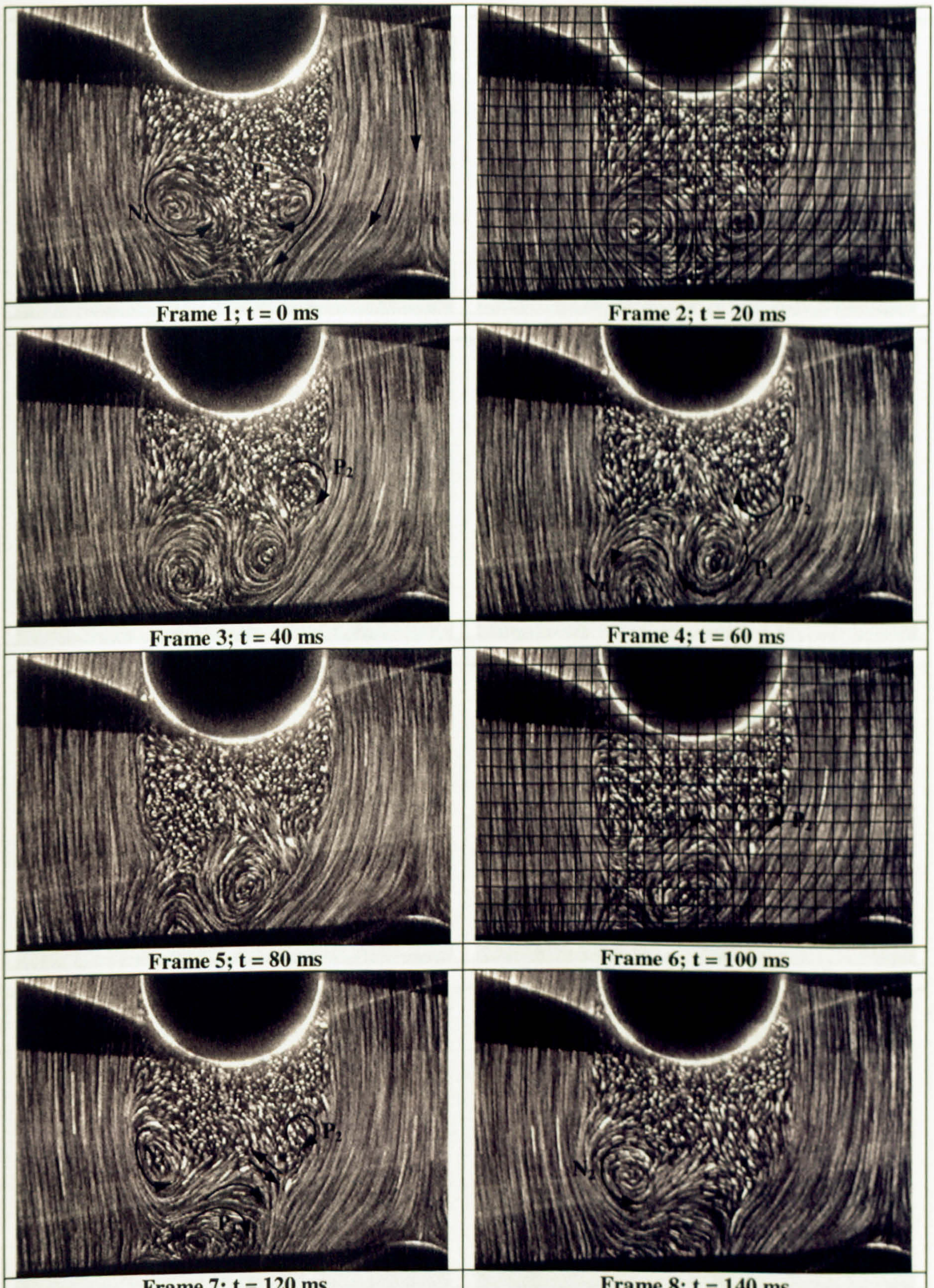

Frame 1; t = 0 ms | Frame 2; t = 20 ms

Frame 3; t = 40 ms | Frame 4; t = 60 ms

Frame 5; t = 80 ms | Frame 6; t = 100 ms

Frame 7; t = 120 ms | Frame 8; t = 140 ms

Figure 4.31 (a). Visualisation pictures of the flow in the wake of the first cylinder (Re = 1,100). Frames 1-8.

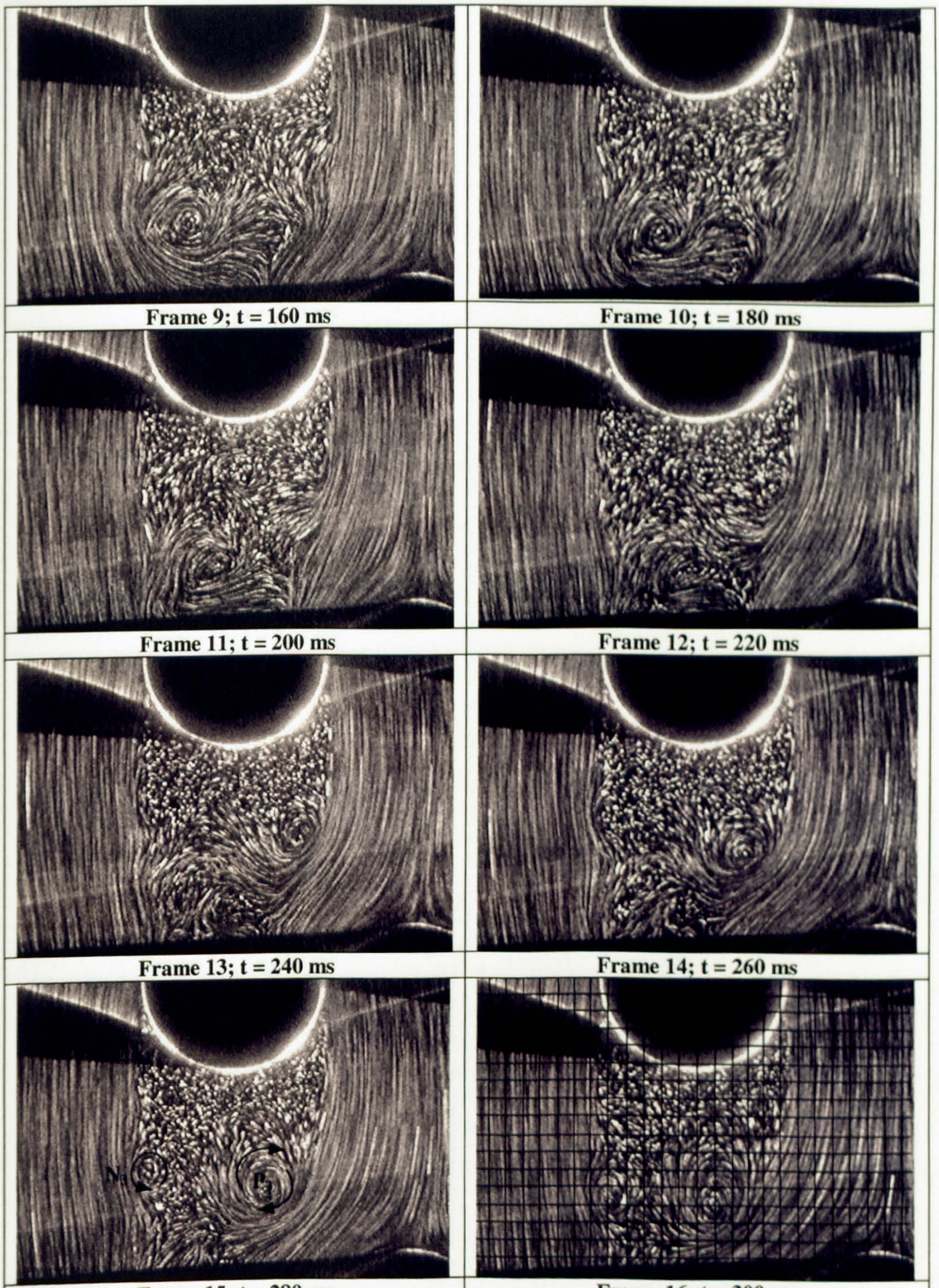

Figure 4.31 (b). Visualisation pictures of the flow in the wake of the first cylinder (Re = 1,100). Frames 9-16.

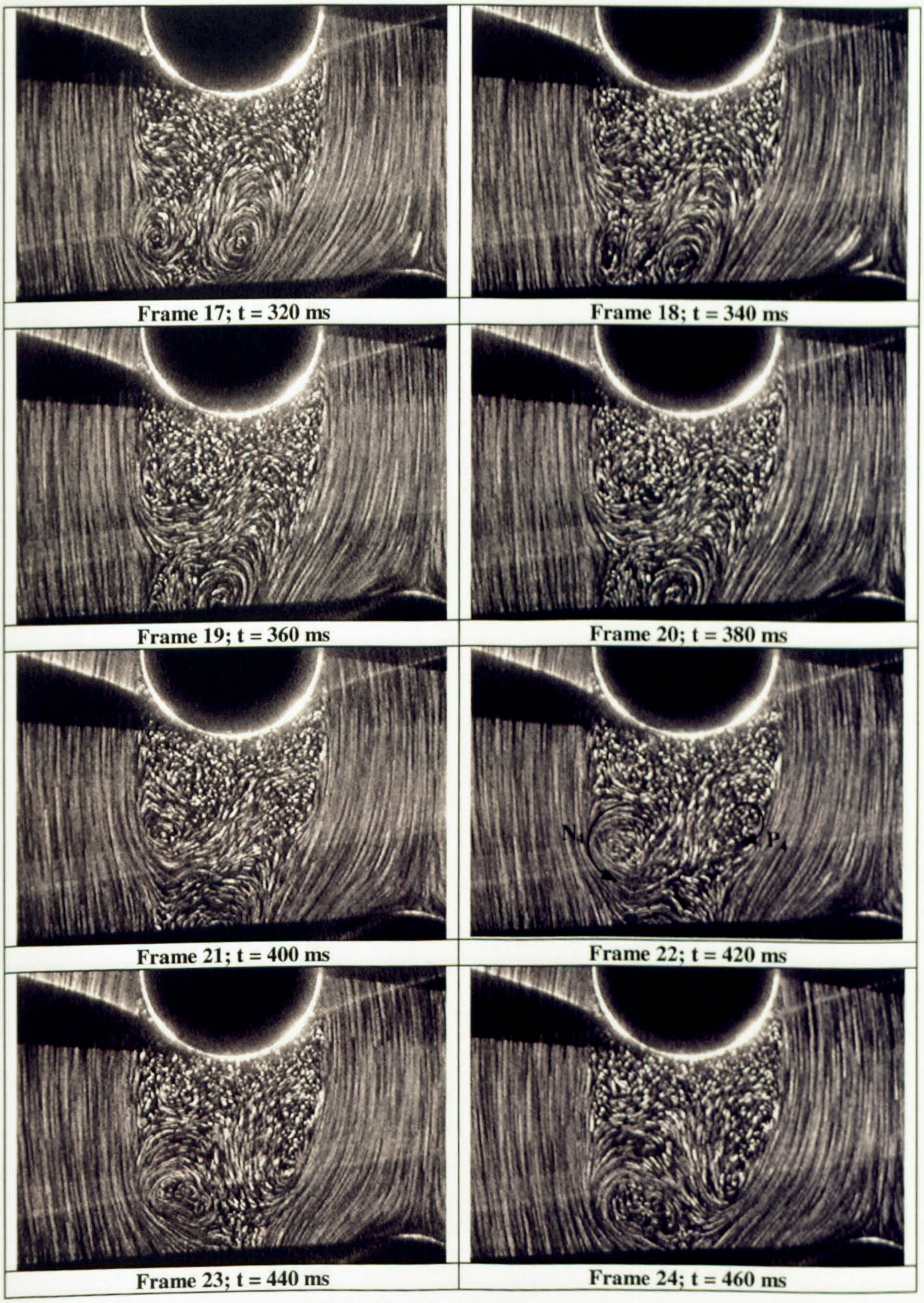

Frame 17; t = 320 ms | Frame 18; t = 340 ms

Frame 19; t = 360 ms | Frame 20; t = 380 ms

Frame 21; t = 400 ms | Frame 22; t = 420 ms

Frame 23; t = 440 ms | Frame 24; t = 460 ms

Figure 4.31 (c). Visualisation pictures of the flow in the wake of the first cylinder (Re = 1,100). Frames 17-24.

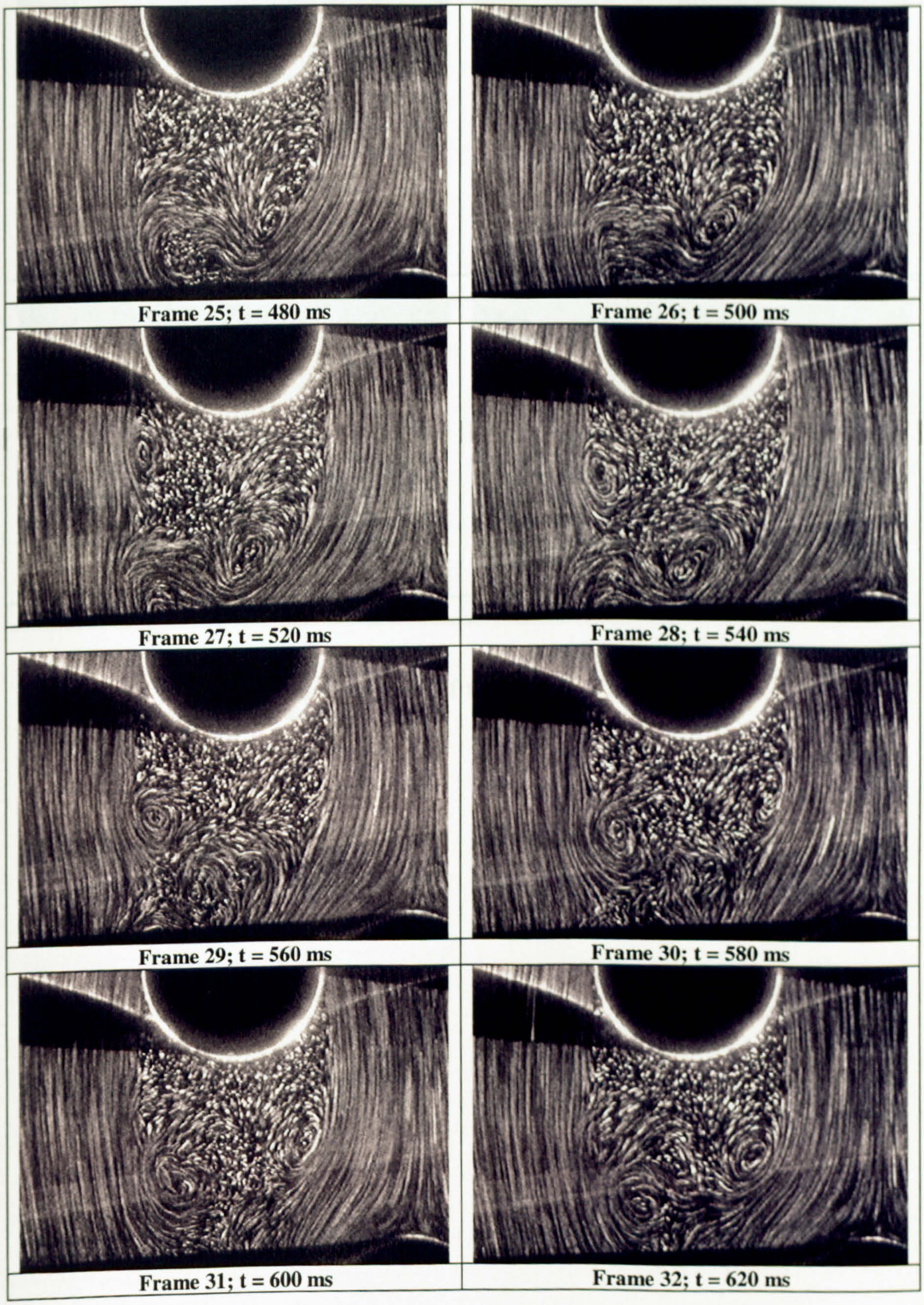

Figure 4.31 (d). Visualisation pictures of the flow in the wake of the first cylinder (Re = 1,100). Frames 25-32.

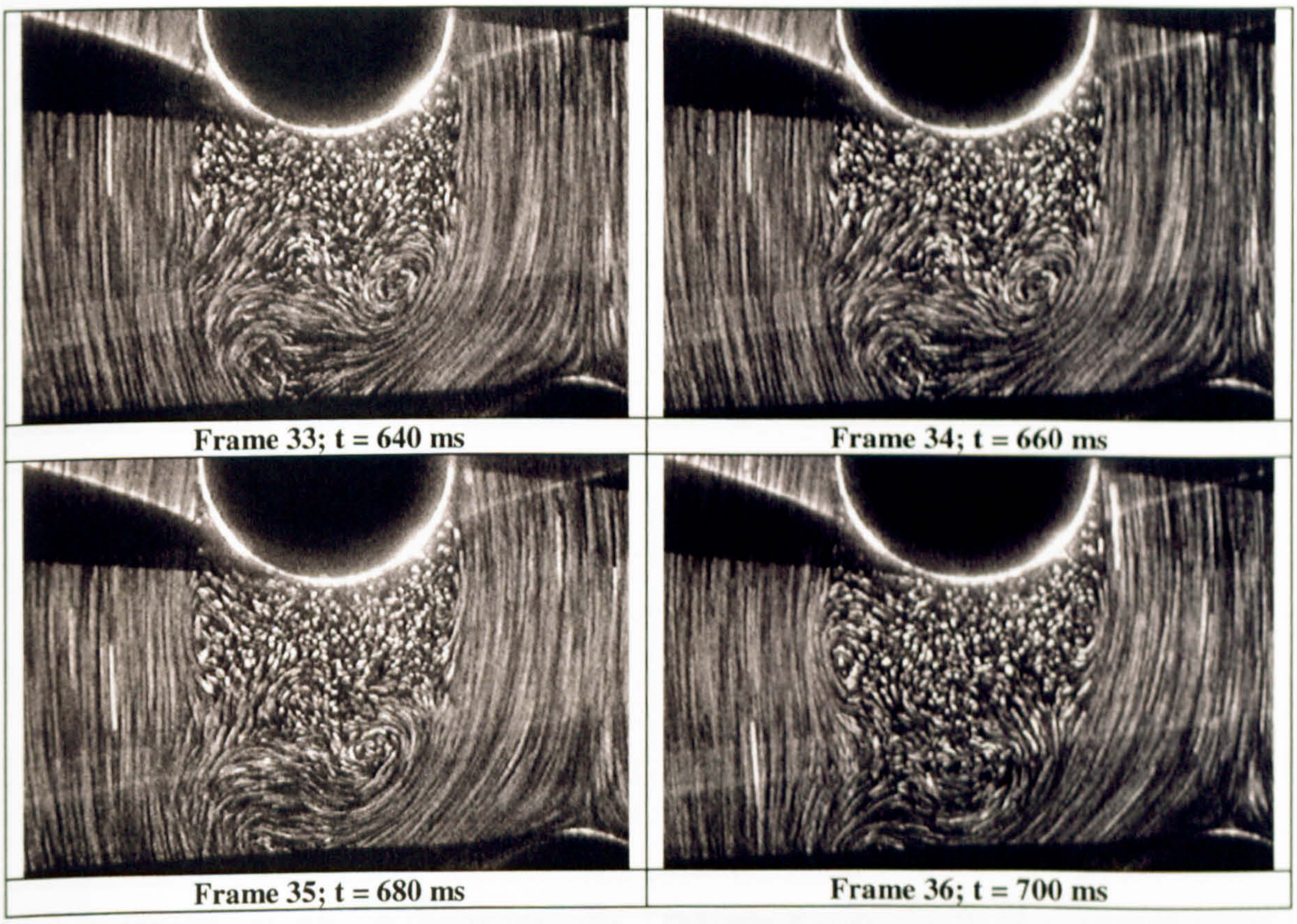

Figure 4.31 (e). Visualisation pictures of the flow in the wake of the first cylinder (Re = 1,100). Frames 33-36.

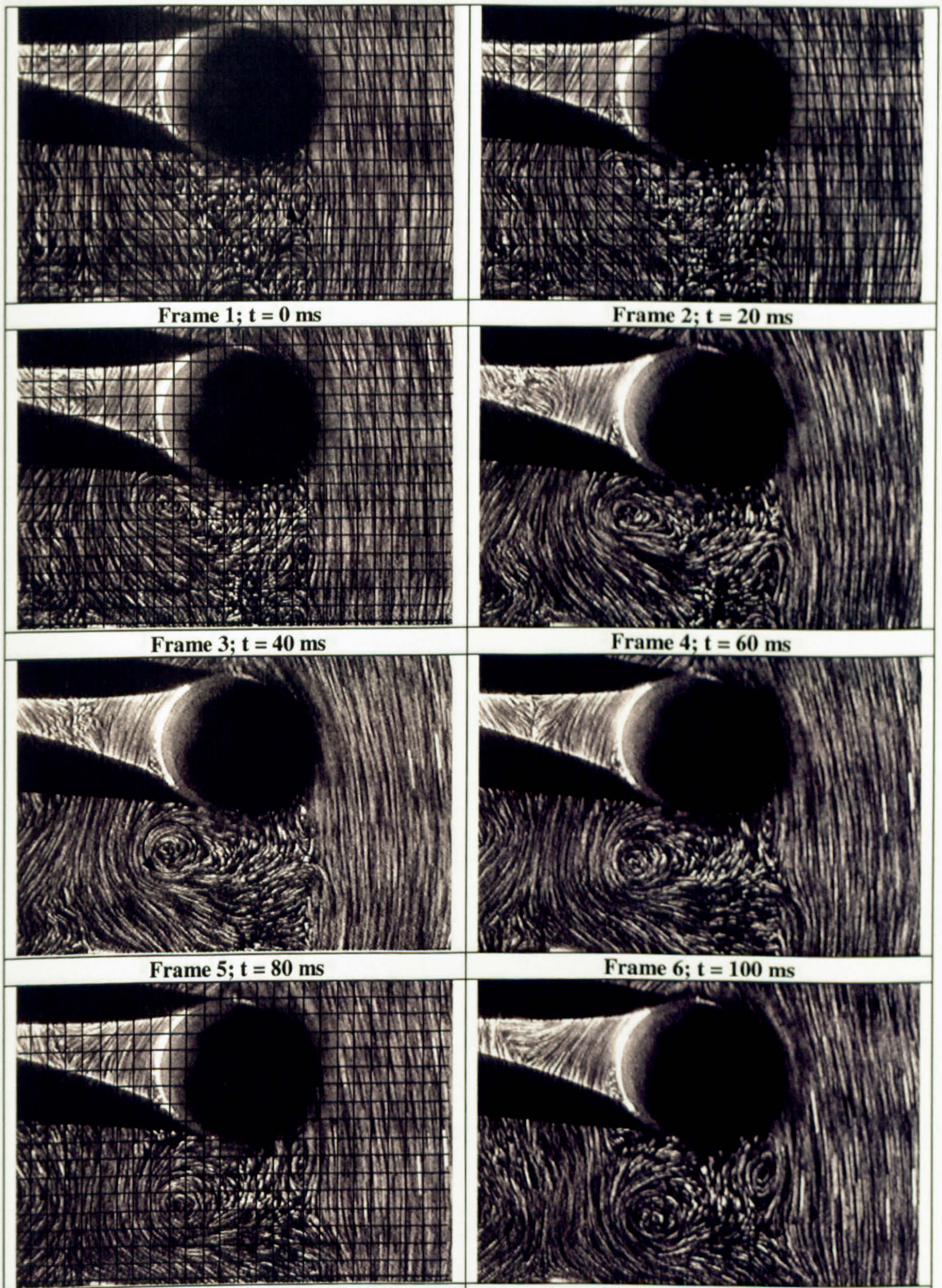

Figure 4.32 (a). Visualisation pictures of the flow in the wake of the second cylinder (Re = 1,100). Frames 1-8.

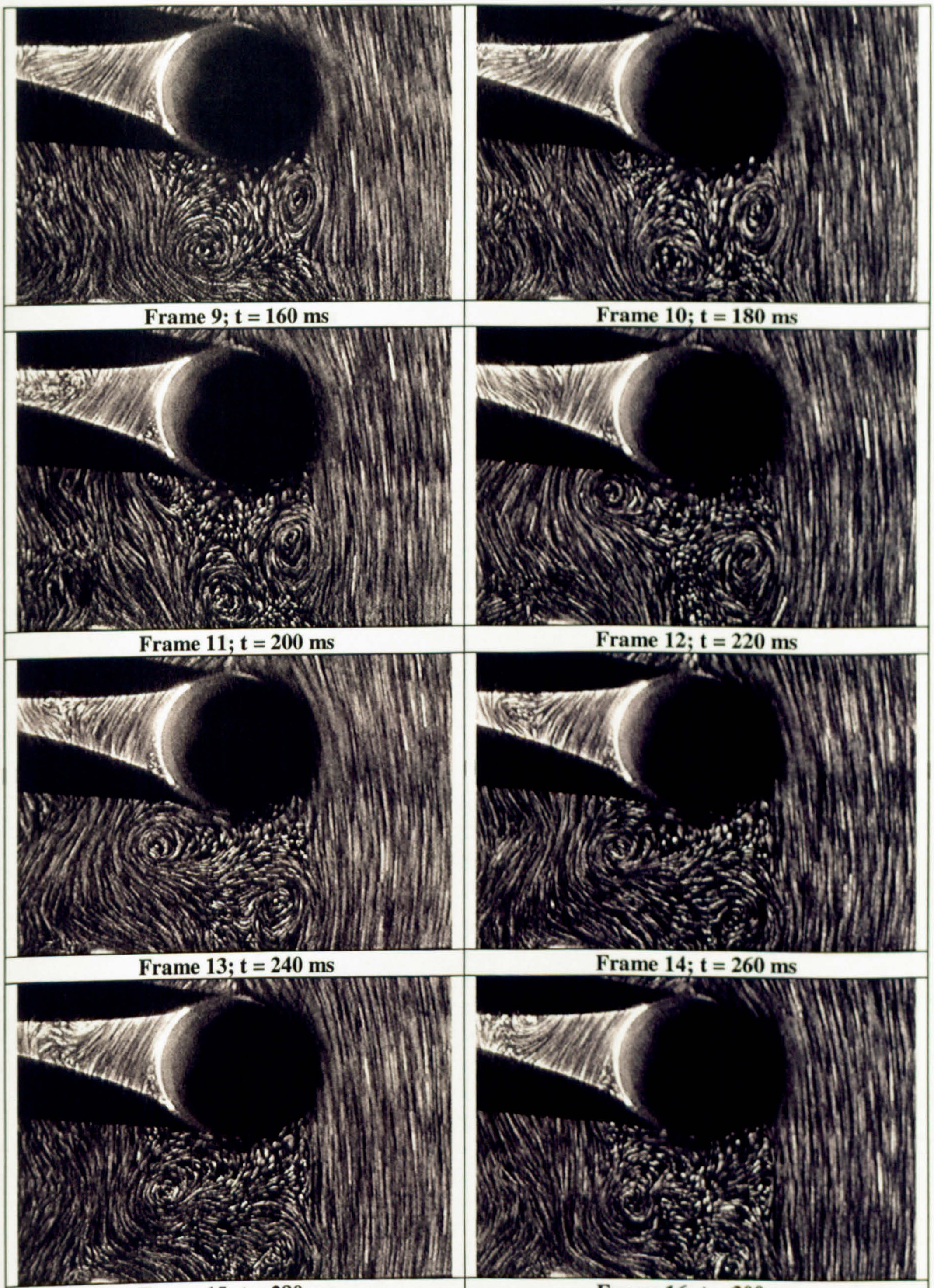

Figure 4.32 (b). Visualisation pictures of the flow in the wake of the second cylinder (Re = 1,100). Frames 9-16.

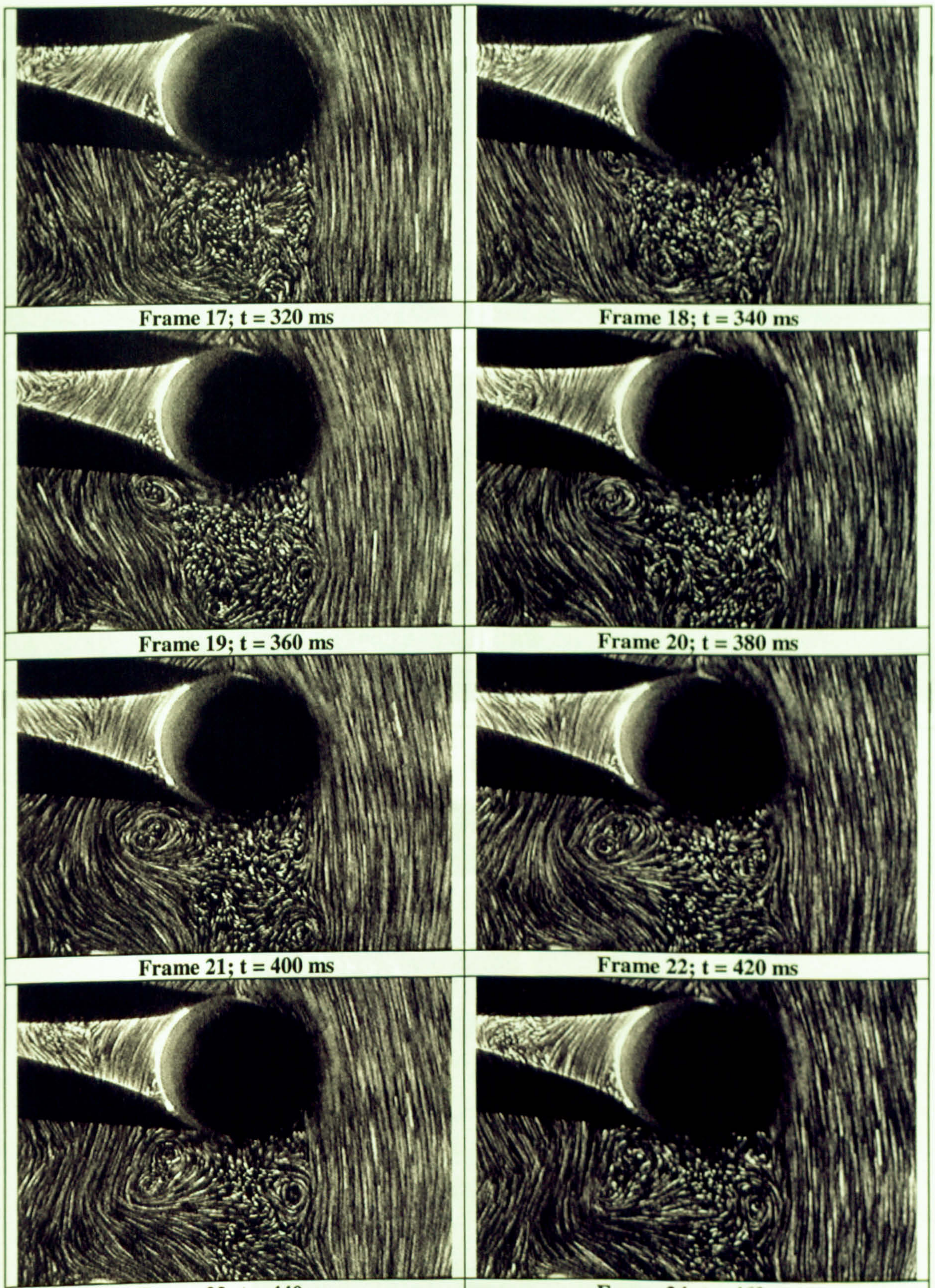

Figure 4.32 (c). Visualisation pictures of the flow in the wake of the second cylinder (Re = 1,100). Frames 17-24.

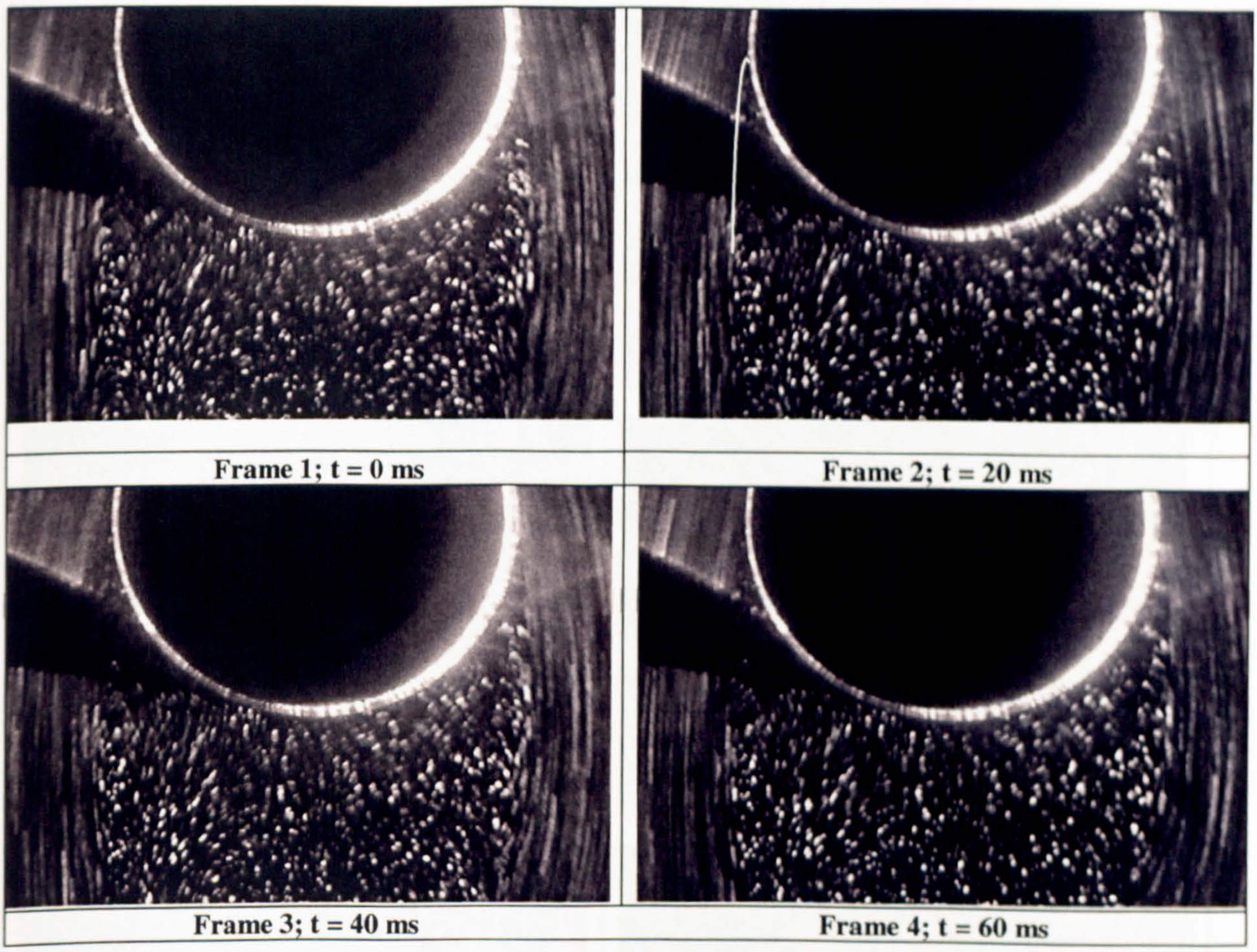

(a)

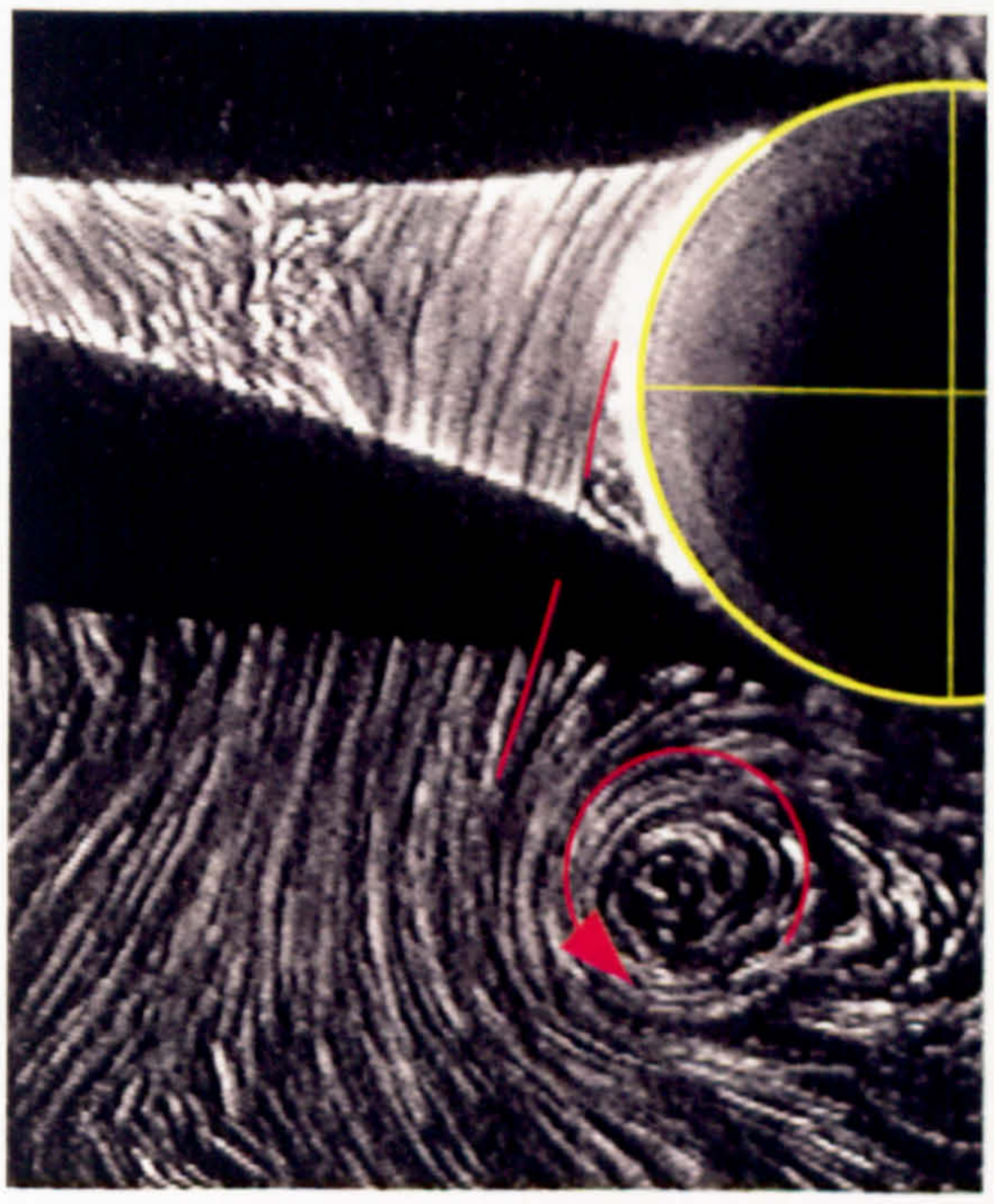

(b)

Figure 4.33. Visualisation pictures focusing on the separation points of the steady flow past the first row cylinder ((a), frames 1-4) and on the anticlockwise separation point of the flow past the second one (b) respectively (Re = 1,100).

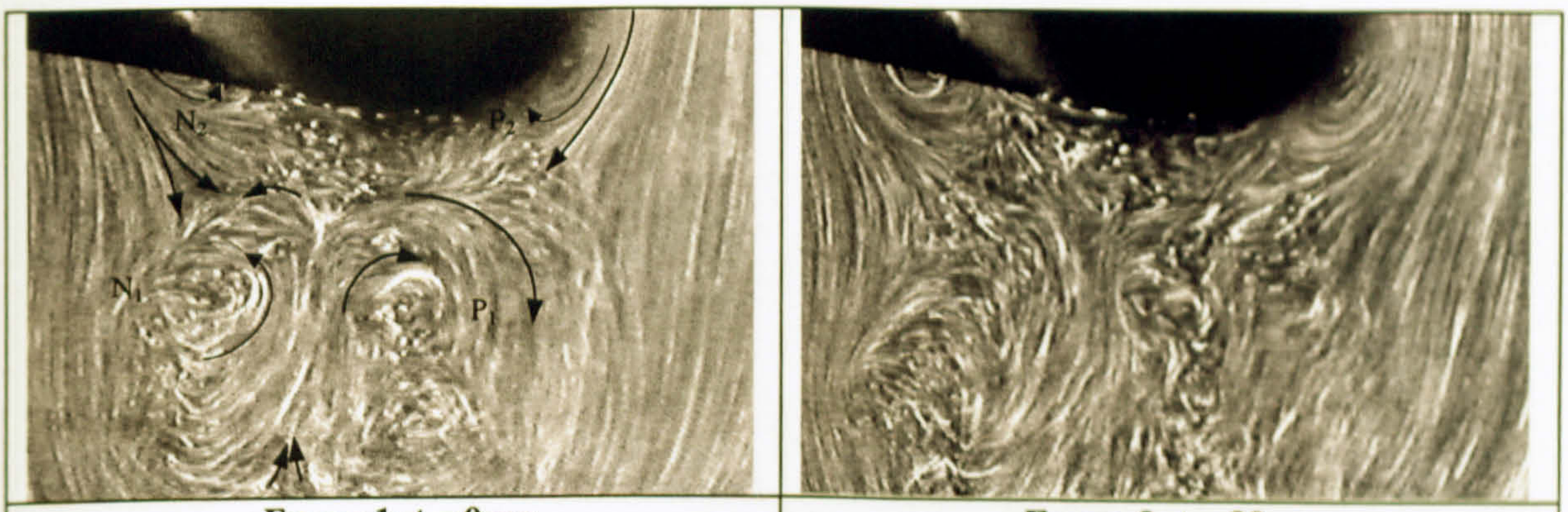

Frame 1; t = 0 ms | Frame 2; t = 20 ms

Frame 3; t = 40 ms | Frame 4; t = 60 ms

Frame 5; t = 80 ms | Frame 6; t = 100 ms

Frame 7; t = 120 ms | Frame 8; t = 140 ms

Figure 4.34 (a). Visualisation pictures of the flow behind the first row. Pulsating flow (Re = 1,100; f_d = 10 Hz). Frames 1-8.

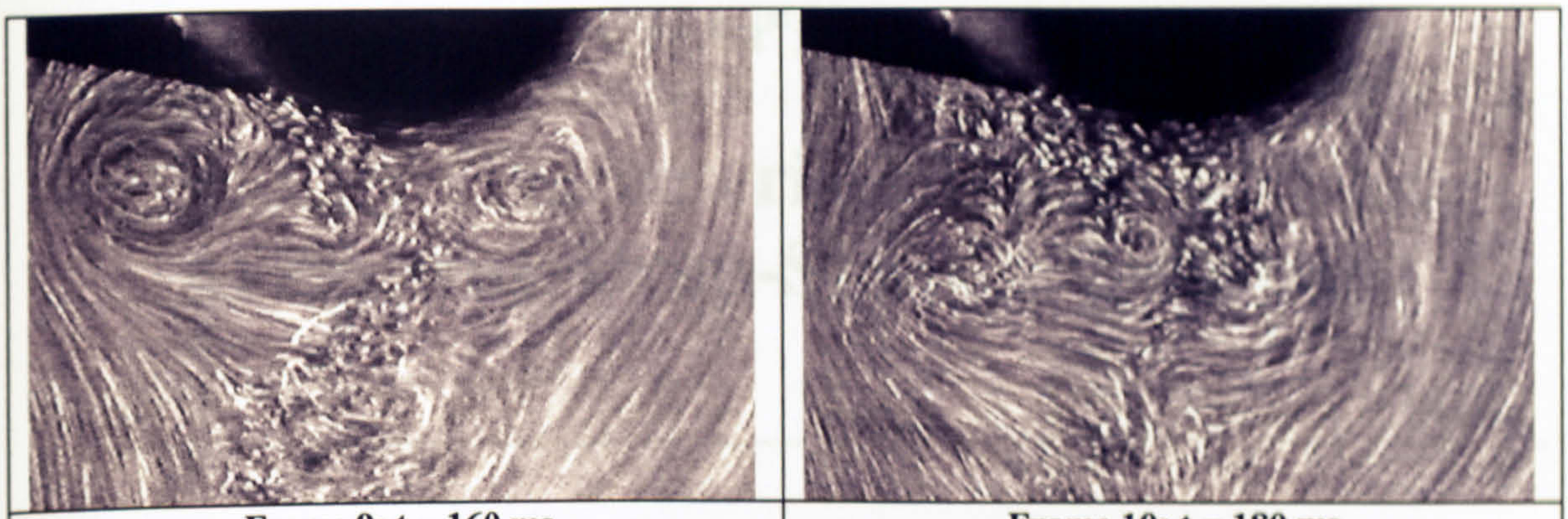

Figure 4.34 (b). Visualisation pictures of the flow behind the first row. Pulsating flow (Re = 1,100; f_d = 10 Hz). Frames 9-10.

CHAPTER 5

Velocity Characteristics of an In-Line Array with Drop-Shaped Cylinders

5.1 Introduction

The present chapter describes the experimental investigation carried out on an in-line array with drop-shaped cylinders in cross-flow. The water tunnel, the tube bundle arrangement and the LDA system employed have already been described in Chapter 2.

The array was composed of six tube rows in the main flow direction and three columns. As in both the in-line and the asymmetric test section with elliptic and circular cylinders respectively, two of the columns comprised half drop-shaped cylinders, which were fixed on the side walls to minimise boundary layer effects and simulate an infinite tube bundle. The drop-shaped cylinders were designed in such a way that the heat transfer area is kept the same as those of the elliptic and circular cylinders respectively and were manufactured from cast acrylic material. The total cross-sectional longitudinal, d_x, and transversal lengths, d_y, of the cylinders were 13.08 mm and 6.16 mm respectively. The longitudinal pitch ratio, S_L/d_x, was 1.6 and the transverse one, S_T/d_y, approximately equal to 5.8.

Measurements were taken at the plane of symmetry ($z/d = 0.0$) in the region $-0.5 \leq y/S_T \leq 0.5$ and $0.0 \leq x/S_L \leq 5.5$ as for the in-line and asymmetric arrays studied in the previous chapters. Ensemble-averaged and time resolved measurements were taken in the above arrangement in both steady and pulsating flow conditions and a flow visualisation study was carried out for Reynolds number ranging from 842 to 6,300 and driving frequencies ranging from 0 Hz (steady flow) to 17 Hz[1].

[1] For economy of presentation, only selected results are shown.

To the knowledge of the author no such extensive investigation has been carried out on either arrays with drop-shaped cylinders or single drop-shaped cylinders. This novel shape of the cylinders was selected with fouling minimisation in mind.

5.2 Steady flow conditions

5.2.1 Mean velocity distributions (Re = 6,300)

Detailed ensemble-averaged measurements of the axial and radial mean velocities were taken at Re = 6,300. The velocity upstream of the bundle, U_∞, was equal to 0.85 m/s. The Reynolds number was defined by the transversal length, d_y, of the cylinders, and the maximum velocity at the gap between adjacent tubes in a row, U_g, which is equal to $1.20U_\infty$ (1.025 m/s) for the arrangement investigated. The equivalent Reynolds number, defined by the upstream velocity and the hydraulic diameter of the duct upstream of the bundle was 61,200. The flow regime at this Re is subcritical.

In order to study the effect of the Reynolds number on the velocity characteristics of the array, velocity measurements were also taken at Re = 1,660 behind each row and velocity spectra were estimated in selected locations in the range $1,188 < Re < 6,300$.

The mean velocity vectors are shown in Figure 5.1. It should be mentioned that due to optical access restrictions, the axial mean and r.m.s. velocity components, U and u' respectively, were measured at only two transverse planes behind each row and halfway between adjacent rows ($x_c/S_L = 0.5$). Accordingly, the vector plots show the velocity vectors in those locations where both the mean (U, u') and radial (V, v') velocities were measured.

The vector plot features are very similar to those of the in-line array with elliptic tubes (Figure 3.1). Due to the relatively large transverse spacing between adjacent columns, the flow field is characterised, as in the elliptic array, by areas of high and relatively uniform velocities at the flow passages between tube columns. Low velocities are observed only in the wake regions. The only significant difference between the vector plots of the two arrays is that in the present one flow reversal is

observed not only behind the first row (the vectors in the wake of the first cylinder are not clearly visible due to both their low magnitude and the scale adopted for the plot[2]), but also behind the downstream ones.

Axial mean velocity

The axial mean velocity, U/U_∞, profiles measured across the array are shown in Figure 5.2. It should be noted that positive axial mean velocities indicate velocities in the downward direction and that each profile refers to measurements taken along the y-direction on the x-plane indicated by the dotted lines. The velocity profiles along the flow passages between columns are approximately uniform. The velocity magnitude slightly decreases towards the centreline (this decrease is less apparent in the proximity of the upper part of the cylinders than in the proximity of the circular rear one[3]). A steep velocity gradient can be observed across the shear layer separating from the first cylinder. The velocity gradient becomes progressively less steep in the downstream direction and the recirculation becomes less pronounced than that observed behind the first row cylinder. As was observed in the elliptic array, the velocities in the flow passages have approximately the same magnitude as that of the upstream velocity (measured at $x/S_L = -1.0$, $x/S_T = 0.0$), U_∞. This indicates very little interference from the neighbouring tubes in the transverse direction (the flow is, therefore, similar to that over a single column of drop-shaped cylinders). Flow reversal is evident only behind the first three rows as shown by the profiles at $x/S_L = 0.29$ and $x/S_L = 0.34$ behind the first row, those at $x/S_L = 1.27$ and $x/S_L = 1.33$ and those at $x/S_L = 2.28$ and $x/S_L = 2.35$ behind the second and third rows respectively. It should be noted that the velocity profile in the wake of the first row (which, at $x/S_L = 0.29$, extends from about $y/S_T = 0.11$ to about $y/S_T = -0.11$ and defines the lowest negative velocity region of the measuring station) is quite uniform compared to that in the elliptic array. On the contrary, in the wake of the downstream cylinders (see

---

[2] The flow reversal behind the first row is clearly shown in Figure 5.2 described later on.

[3] A comparison with Figure 3.2 shows also that the profiles in the elliptic array (*elliptic array* stands here for *in-line array with elliptic cylinders*), particularly in downstream rows, slightly increase towards the cylinders' shoulders with a gradient that is less steep than in the drop-shaped one (*drop-shaped array* stands for *in-line array with drop-shaped cylinders*). It should be noted, in fact, that the profiles in the drop-shaped array, particularly over the shoulders of the first four rows are uniform up to about $x/S_T = 0.2$ where an abrupt decrease occurs.

particularly behind the third, fourth and fifth rows) the negative velocity peak, occurring at $x/S_T = 0.0$, is significantly narrower than that in the elliptic array.

Figures 5.3 and 5.4[4] show the comparison of the axial mean velocities between the in-line array with drop-shaped cylinders and that with elliptic ones described in Chapter 3[5] (see also Castiglia et al, 2001). The Reynolds numbers were Re = 6,300 and Re = 6,760 for the present array and the one with elliptic cylinders respectively. It should be noted that for brevity the comparison is made only with the elliptic array. An indirect comparison with the in-line one with circular cylinders (Balabani, 1996) can be made by considering the comparison between the latter and the in-line array with elliptic cylinders described in Chapter 3.

The contours in Figures 5.3 (a)-(b) show that the velocity magnitude varies within the same range for the two arrays, that is $U/U_\infty > -0.25$. The velocities are uniform along the flow passage with values varying between 1.25 and 1.50 times the upstream velocity, U_∞. The flow accelerates as it approaches the first cylinder as evidenced by the high velocities (1.5 - 1.75 U_∞) in that region in both arrays. This high velocity region extends to the proximity of the tip of the second cylinder in the drop-shaped array whereas in the elliptic one it ends over the shoulder of the first cylinder. The most significant difference between the two arrays is that the shear layer separating from the first cylinder as well as the low velocity regions behind the cylinders of the drop-shaped array do not extend or spread into the freestream as much as in the elliptic array. The flow separating from the first elliptic cylinder (red contours) was found to reattach onto the second one. On the contrary, no such reattachment could be observed in the in-line array with drop-shaped cylinders. Due to the different shape of the cylinders and the actual spacing between successive cylinders, the wake geometry exhibits different geometrical characteristics: it is longer and narrower behind the drop-shaped cylinders (as indicated by the green contours, corresponding to the low speed regions). Its width normalised with the transverse spacing, W/S_T, increases in the downstream direction with values up to about 0.24 and 0.36 behind the last drop-shaped and elliptic cylinders respectively.

---

[4] Figure 5.3 (b) was already shown as Figure 3.2 (b) in Chapter 3, but it is shown here again to facilitate the comparison.

Figure 5.4 shows a comparison of the axial mean velocity profiles, U/U_∞, between the two arrays at one axial station behind each of the first four cylinders[6]. The profiles were plotted against y/d*, where d* corresponds either to the minor axis of the elliptic (2b = 6.5 mm) or the transversal length of drop-shaped (d_y = 6.16 mm) cylinders respectively. The normalised profiles look very similar, particularly behind the downstream cylinders. A slightly higher recirculation is observed behind the drop-shaped cylinders with the exception of the first one. The recirculation is higher behind the first elliptic cylinder whose corresponding profile exhibits a steeper mean velocity gradient across the shear layer.

Radial mean velocity

The distribution of the radial mean velocities, V/U_∞, is shown in Figure 5.5 as profiles and in Figure 5.6 (a) as contours. Contours of V/U_∞ in the in-line array with elliptic cylinders (Figure 3.5 (b)) are also shown in Figure 5.6 (b) for comparison.

Positive values in Figure 5.5 represent velocities in the positive y-direction. As was also observed in the in-line array with elliptic cylinders, the first two profiles (x/S_L = 0.0 and x/S_L = 0.11) of the figure show a significant variation of the radial mean velocity magnitude along the transverse direction from the flow passages, ($V/U_\infty \cong$ 0.0) up to the proximity of the cylinder ($V/U_\infty \cong - 0.2U_\infty$)[7]. The V/U_∞ profiles become more uniform along the flow passages in the downstream direction. The radial mean velocity has slight positive values (outward velocities) in the proximity of the upper parabolic edge of all cylinders. Small negative values (inward velocities) are recorded as the flow approaches the rear circular part of the first four cylinders and positive ones near the rear part of the last two cylinders. The radial mean velocity profiles behind the first row exhibit a negative relative maximum at $x/S_L = 0.1$ and a positive one at x/S_L = 0.125. These maxima increase in magnitude and occur closer to the centreline behind the second row. The only positive maximum is observed in

---

[5] Note that the two in-line arrays have the same longitudinal and transverse spacings.
[6] It should be noted that the two stations are not exactly the same as different measuring planes were chosen for the two arrays.
[7] The description of the radial mean velocity profiles refers only to the positive y-direction as the profiles are clearly anti-symmetrical. The same description can be extended to the negative y-direction if the sign of the velocities is changed ($\pm \rightarrow \mp$).

downstream rows. It increases significantly in magnitude and broadens along the transverse direction in the downstream direction.

Figure 5.6 (b) show the comparison of the radial r.m.s velocity contours between the in-line array with drop-shaped cylinders and those with elliptic ones studied in Chapter 3. It should be noted that at the entrance to the tube bank the mean radial velocities have similar magnitudes in both arrays for $y/S_T > 0.38$ (values vary between 0 and $-0.25U_\infty$). The transverse mean velocities have near zero values along the flow passages and low negative values over the shoulders of the upstream cylinders. For $y/S_T < 0.38$ the radial mean velocities are slightly lower ($0 < V/U_\infty < -0.25$) in the array with drop-shaped cylinders. This is generally reversed through the remaining domain where slightly higher (and positive) values are observed.

The radial velocity distribution appears slightly more uniform than in the configuration with circular cylinders studied by Balabani (1996). In both cases low positive velocities were recorded on the shoulder of the penultimate row cylinder, but in the arrangement with circular cylinders low positive values were also observed over the shoulder of the last row cylinder.

5.2.2 Turbulence level distributions (Re = 6,300)

The turbulence levels are described by comparing them with those observed in the in-line array with elliptic cylinders. The aim is to determine the effect of the cylinder shape on both the axial, u'/U_∞, and the radial, v'/U_∞, velocities. The axial r.m.s velocities are plotted as profiles and contours form in Figures 5.7 and 5.8 and 5.9 (a) respectively. The radial ones are shown in contour form in Figure 5.9 (b).

Figure 5.7 shows a comparison of the u'/U_∞ profile along the flow passages ($y/S_T = 0.5$) between the in-line array with elliptic cylinders and that with drop-shaped ones. For comparison the same figure shows the r.m.s profile in the in-line array with circular cylinders studied by Balabani (1996).

The upstream axial r.m.s. velocity magnitude is subtracted from the measured r.m.s. velocities and their difference is normalised with the upstream bulk velocity, U_∞. This results in the turbulence levels at the entrance to the tube bank having the same values in the two arrays. The difference between the r.m.s. levels in the elliptic and drop-shaped arrays is very small at the entrance to the tube bank and decreases further downstream (the turbulence levels are slightly higher in the drop-shaped array). It can be seen that the turbulence levels of both arrays are significantly lower than those in the array with circular cylinders from the second row onwards. The turbulence levels increase sharply in the array with circular cylinders whereas in the other two arrays they remain approximately uniform from the entrance to the tube bank up to the exit.

Figure 5.8 shows the r.m.s profiles of the two arrays (with elliptic and drop-shaped cylinders) behind the first four rows. The comparison is made between the profile at $x_c/S_L = 0.5$ behind the elliptic cylinders and those at $x_c/S_L = 0.293$ and $x_c/S_L = 0.343$ behind the drop-shaped ones. Differences can be observed only in the cylinder wakes. Behind the first row (Figure 5.8 (a)) no difference can be noted between the profiles for $y/S_L > 1.0$. A steep gradient is observed between $y/d^* = 1$ and $y/d^* = 0.75$. Although the r.m.s peaks are observed at approximately the same position along the y axis, that is at $y/d^* = 0.61$, the magnitude of the peak behind the elliptic cylinder is about 40% and 75% higher than those observed behind the drop-shaped one at $x_c/S_L = 0.293$ and $x_c/S_L = 0.343$ respectively. Behind the second row cylinder the magnitude of the peak behind the elliptic cylinder is lower then that observed in the two profiles behind the drop-shaped cylinder, despite the fact that both the axial turbulence levels in the freestream and the r.m.s. velocity gradients along the shear layers are approximately the same for the three profiles examined. In downstream rows slightly higher r.m.s. values are observed along the flow passages (this is not clear from the figure due to the large y-range adopted; see also Figure 5.7, plotted in a larger scale for clarity) of the array with drop-shaped cylinders. Furthermore, although the position of the r.m.s. peaks shifts towards the centreline in both arrays, the shift is more evident behind the one with drop-shaped cylinders. In fact, a comparison between Figure 5.8 (a) and (d) shows that the peak has shifted from $y/d^* = 0.61$ to $y/d^* = 0.32$ and $y/d^* = 0.16$ along the profiles at $x_c/S_L = 0.343$ and $x_c/S_L = 0.293$ respectively.

Figures 5.9 (a) and (b) show the axial and radial r.m.s. velocities in contour form in the in-line array with drop-shaped cylinders. At the entrance to the tube bank both the r.m.s. velocity components have values between 0 and $0.1U_\infty$. Slightly higher values, up to $0.2U_\infty$, were recorded for both components along the shear layer separating from the first cylinder. However, differences can be observed in the wakes and along the shoulders of the cylinders, where higher values of the axial r.m.s. velocity component were recorded. The axial r.m.s velocity in the wakes increases in the downstream direction reaching values up to $0.4U_\infty$ behind the fifth and sixth rows. These regions, characterised by higher values of u', spread further inside the freestream in the downstream direction (e.g. up to $y/S_T = 0.2$ behind the sixth row). On the contrary, radial velocities higher than $0.2U_\infty$ and $0.3U_\infty$ can be observed only behind the fourth cylinder and further downstream.

Degree of isotropy

The distributions of the difference, $|v'- u'|/U_\infty$, and ratio, v'/u', of the r.m.s. velocities, are plotted in Figures 5.10 (a) and (b). The difference of the two r.m.s. components (Figure 5.10 (a)) is near zero over the whole flow domain, indicating that the turbulence could be assumed highly isotropic, with the exception of the shoulders of the third cylinder and in the proximity of the separation points of the fifth and sixth rows where the difference reaches values in the range $0.1U_\infty < |v'- u'| < 0.2U_\infty$. The distribution of the ratio of the radial and axial r.m.s. v'/u' is shown in Figure 5.10 (b). It can be observed that at the entrance (x/S_L) to the tube bank, for $y/S_T > 0.20$, the ratio attains values between 0.8 and 1, i.e. the flow can be assumed isotropic. In general the axial r.m.s. component throughout the flow field is higher than the radial one, particularly over the shoulder of the drop-shaped halves of the cylinders. The opposite trend is observed in the wakes of the cylinders, especially along the shear layer separating from the first one and in the wake of the last two. In these regions the magnitude of v' is up to 1.4 times higher than the axial r.m.s. velocity component.

5.2.3 Flow periodicity

Spectra were obtained behind each cylinder for Re ranging from 1,188 to 4,753 in steady flow. For brevity only the spectra obtained behind the fourth and sixth cylinders are shown (Figures 5.11 and 5.12 respectively).

It should be noted that, as in both the in-line and the asymmetric array with elliptic and circular cylinders respectively, no distinct periodicity could be detected behind the first two rows of the bundle. On the contrary, a prominent peak associated with the shedding of vortices could be observed behind all downstream rows.

Figures 5.11 and 5.12 show that all the spectra obtained behind the fourth and sixth rows (in the Reynolds number range investigated) exhibit a distinct peak at the natural vortex shedding frequency[8]. Its amplitude depends on both the Reynolds number and the row depth. For clarity, the variation of the vortex shedding peak amplitude versus Re in the wakes of the fourth and sixth cylinders is shown in Figure 5.13. Figure 5.11 shows the amplitude spectra behind the fourth row. In general there is an increase of the peak amplitude with Re, but this is not consistent throughout the whole Re range investigated. In fact, although the variation of the peak amplitude is not significant (as if a saturation phenomenon occurred) for $Re \geq 3{,}565$ the amplitude at Re = 3,565 is slightly higher than those at Re = 4,040 and Re = 4,753. Furthermore, the natural vortex shedding frequency clearly shifts towards higher values with Re. A comparison of the spectra in Figure 5.11 with those in Figure 5.12 (see also Figure 5.13) shows that up to Re = 1,664 (low Re) no significant difference in the peak amplitude can be found between the fourth and the sixth rows. This implies that the row depth affects the shedding frequency peak amplitude only at moderate Re. At Re = 2,614 the difference in amplitude becomes already substantial (A = 0.0125 m/s and A = 0.0265 m/s behind the fourth and sixth row respectively). At Re = 3,090 an abrupt increase of the peak amplitude behind the sixth row (up to A = 0.047 m/s at Re = 4,753) occurs. However, for $Re \geq 3{,}090$ the amplitude does not vary substantially with Re. As already observed behind the fourth row it saturates at values ranging between A = 0.042 m/s and A = 0.047 m/s. It should be noted that the

[8] The scale of the spectra was chosen in order to magnify the frequency peaks. Due to their relative low amplitude the backround turbulence levels are also high.

ratio of the vortex shedding peak amplitude behind the two rows varies between 1 at Re = 1,188 and 2.14 at Re = 4,753. This confirms that amplitude differences between the two rows occur only at higher Re. However, the variation of the vortex shedding frequency with the Reynolds number is the same (within the experimental error) behind the two rows.

It should be noted that an increase of the number and amplitude of secondary peaks can be observed (e.g. compare the spectrum at Re = 4,753 with that at Re = 3,090 in Figure 5.12) particularly behind the last row, as a result of the increase of Re

Figure 5.14 shows the natural vortex shedding frequency detected behind each row as a function of the normalised gap velocity, U_g/d_y. It is clear that the shedding frequency of the vortices varies linearly with the gap velocity behind all rows but the first two, where prominent peaks could not be detected as in the case of the in-line array with elliptic cylinders. The equation of a linear fit (black line in Figure 5.14) to the data is the following:

$$f_s = -0.24 + 0.16\ U_g/d_y \qquad (5.1)$$

The Strouhal number, defined by the transversal lenght of the drop-shaped cylinders, d_y, and the gap velocity, U_g, is given by the slope of the equation, that is St = 0.16.

Table 5.1 compares the St number values measured in the drop-shaped, elliptic and circular cylinders (Konstantinidis et al, 2000) arrays. Both St based on the gap, U_g, and bulk velocity, U_∞, are considered.

It should be noted that the Strouhal number is similar (slightly higher) or equal to that for the array with circular cylinders depending on the characteristic velocity adopted (U_g or U_∞, and equal to either St = 0.16 or St = 0.19). The Strouhal number value observed in the present array is instead higher than that of an equivalent array with elliptic cylinders. This may be attributed to the circular profile of the drop-shaped cylinders after the separation point, which therefore seems to play a key role in the vortex shedding phenomenon.

Table 5.1. Strouhal number definitions and relative values for Re ranging between Re = 1,188 and 4,753 in the in-line array with drop-shaped cylinders

	IN-LINE ARRAY WITH DROP-SHAPED CYLINDERS	IN-LINE ARRAY WITH ELLIPTIC CYLINDERS	IN-LINE ARRAY WITH CIRCULAR CYLINDERS
Definition	St (1,188 < Re < 4,753) (present investigation)	St (Re = 6,760 and Re = 1,755) (present investigation)	St (Re^{**} = 2,800) (Konstantinidis et al, 2000)
$St = \frac{f_{so} h^*}{U_g}$	0.16	0.11	0.14
$St = \frac{f_{so} h}{U_\infty}$	0.19	0.14	0.19

* $h = d_y$ for the drop-shaped cylinders, $h = 2b$ and $h = d$ for the elliptic and the circular ones respectively.

Figures 5.15-5.17 show a comparison between radial and axial velocity spectra behind the first, third and sixth rows respectively.

Figure 5.15 shows the radial and axial amplitude spectra obtained behind the first row. It is clear that a dominant peak referring to the shedding of vortices cannot be identified. The only noticeable difference between the radial and axial velocity spectra is the generally higher axial turbulence level.

Both the radial and axial velocity spectra behind the third and sixth rows (Figures 5.16-5.17) exhibit a dominant peak of significant amplitude at the frequency corresponding to that of the vortex shedding. It should be noted that the shedding frequencies have similar values for the two velocity components since the radial and axial spectra were obtained at approximately the same Reynolds number. Although there is an effect of Re on the peak amplitude, the Re difference in the estimated axial and radial spectra is so small that this effect can be neglected. As a consequence, the higher amplitude of the axial peaks observed in the downstream rows can only be attributed to the fact that the convection axial velocity component

of the shed vortices is significantly higher than the radial one (see paragraph 5.5). It should be noted that both the radial and axial peaks decrease as the measuring location moves from the shear layer region ($y/S_T = 0.19$) to the freestream ($y/S_T = 0.36$). Only the axial amplitude peak can still be observed at the latter location behind the third row, as shown in Figure 5.16. Finally, it can clearly be noticed (Figure 5.17) that the peak amplitude of both the radial and axial spectra behind the last row has considerably increased compared to that behind the third one. However, the difference between the radial and axial peaks is the same as that observed behind upstream rows. In general, in all the radial velocity spectra the background turbulence level is lower and the amplitude of the secondary peaks is negligible compared to that of the axial ones.

5.3 Pulsating flow conditions

The frequency of the superimposed sinusoidal pulsation varied between 7 Hz and 14 Hz. The relative amplitude of the pulsation, A_o, and the Reynolds number, Re, varied between 0.04 and 0.31 and between 1,443 and 5,237 respectively. Detailed measurements were taken at $f_d = 10$ Hz and Re = 1,901, and the corresponding axial mean and r.m.s. velocity distributions are discussed below.

5.3.1 Mean velocity

Figure 5.18 shows a comparison between the axial mean velocity profiles in steady and pulsating flow ($f_d = 10$ Hz, $A_o = 0.16$) at Re = 1,900. Figure 5.18 (a) shows that there is no difference in the magnitude of the axial mean velocities between steady and pulsating flow at the entrance to the tube bank. This observation, together with the fact that along the flow passages no difference can be observed between the two flows, indicates that the pulsations affect the mean flow only in the wake regions behind the cylinders and mainly behind the first one (see Figure 5.18 (a)). The most significant differences can be found behind the first cylinder, as was also observed in the in-line array with elliptic cylinders and that with circular ones. Higher recirculation is observed in pulsating flow. The profiles are similar for $y/S_T > 0.17$ (the velocity magnitudes are almost identical). At $y/S_T \cong 0.17$ the velocity magnitude

of the pulsating profile starts decreasing, quite smoothly, in the negative y-direction, up to the centreline, where the mean velocity magnitude reaches its minimum ($U/U_\infty \cong -0.3$). The steady flow profile grows slightly as we move from the flow passage to the centreline up to $y/S_T \cong 0.13$ ($U/U_\infty \cong 1.7$) and decreases afterwards with a steep gradient up to about $y/S_T \cong 0.85$ ($U/U_\infty = 0.22$). As was already observed in the in-line array with elliptic cylinders, in downstream rows the mean velocity magnitude in steady flow decreases in the transverse direction as the wake is approached. It varies from the freestream value up to $-0.2U_\infty$ at the centreline ($y/S_T \cong 0.0$).

5.3.2 Turbulence level distributions

Figure 5.19 shows the comparison of the turbulence levels between steady and pulsating flow (the r.m.s values correspond to the velocity records from which the mean velocity profiles, shown in Figure 5.18, were calculated). The profiles show similar characteristics to those observed behind the elliptic cylinders. Figure 5.19 (a) shows the comparison of the axial r.m.s. velocities at the entrance to the tube bank ($x/S_L = 0.0$). As already stated, the difference between the turbulence levels in the freestream ($y/S_T = 0.5$) is equal to that observed at the reference point ($x/S_L = -2.1$, $y/S_T = 0.0$) upstream of the bundle, which can be attributed, as demonstrated in Chapter 4, to the pseudo-turbulence introduced by the pulsations. Nevertheless, in the proximity of the cylinder the pulsations seem to promote or generate more turbulence. In fact, while the steady profile is uniform along the transverse direction up to the closest measuring point to the cylinder wall, that is $y/S_T = 0.11$, the pulsating one is approximately uniform up to $y/S_T = 0.27$, and then increases in the negative y-direction up to 277% of the steady r.m.s value at $x/S_L = 0.11$ (compared to the 170% difference between pulsating and steady turbulence levels in the freestream, which are due to pseudo-turbulence). As for the mean velocity, the region of the flow most affected by the pulsations is the wake of the first cylinder. The difference in the turbulence levels between the two flows is apparently higher than the one upstream of the bundle and, therefore, it can only partly be attributed to the pseudo turbulence. In fact about 80% of the observed (Figure 5.19 (b)) increase of the normalised r.m.s. velocity is caused by the production of turbulence by the pulsations which modify the structure of the wake flow. Downstream of the first row,

this turbulence increase can be still observed in the wakes of the cylinders, but its magnitude is significantly reduced. Here the normalised r.m.s magnitude reaches a maximum of approximately $0.7U_\infty$ at $y/S_T = 0.08$, value to be compared with the peak magnitude behind the first cylinder, about $0.9U_\infty$, recorded at the same transverse position. In downstream rows no significant differences can be observed between the steady and pulsating profiles. This is due to the fact that while the r.m.s. magnitudes in pulsating flow decrease, from $0.9U_\infty$ behind the first row to values varying between $0.7U_\infty$ (second row) and $0.6U_\infty$, the r.m.s. magnitudes in steady flow increase, slightly, from a value of $0.25U_\infty$ behind the first row to values varying between $0.34U_\infty$ (second row) and $0.3U_\infty$ in downstream rows.

Mizushina et al (1974) carried out an experimental investigation to study the structure of turbulence in pulsating flow. Their results showed that turbulence is generated during the "break-up" of low-speed/stagnant regions near the wall. Although the experiments were conducted in a fully developed pipe flow, the author of the present investigation believes that their results can be extended to the cross-flow past a single cylinder or arrays with multiple cylinders, and in particular to the low-speed/stagnant region of the cylinder wakes. The generation of turbulence occurs when superimposed pulsations break up the steady flow low-speed/stagnant region in the proximity of the cylinder rear wall while its propagation is considered to be associated with the large-scale vortices. It should be noted that the spatial extension of these low-speed regions depends on both the cylinder shape and arrangement and on the Reynolds number which affects the turbulence levels.

As previously mentioned, the region of the flow most affected by the pulsations is the wake of the first cylinder. Both the LDA and the visualisation study (see paragraph 5.5), in fact, showed that the wake behind the first row cylinder is quasi-stagnant in all the arrays so far investigated. Therefore, the generation of turbulence is more pronounced behind the first row than behind the downstream ones (the steady flow turbulence levels increase in the downstream direction) where the low-speed region is generally confined to the proximity of the cylinder rear wall. It should be noted that the effect of the pulsations decreases with Re. The steady flow turbulence levels

increase with the Reynolds number and correspondingly the low speed-region gets smaller and closer to the cylinder wall.

Vortex formation length

Due to optical restrictions the vortex formation length could be evaluated only behind the last cylinder. Figures 5.20 and 5.21 show the normalised r.m.s. (u'/u'_{max}) and mean (U/U_{max})[9] velocity profiles along the centreline for Re = 4,753 in steady flow and for Re = 1,901 in both steady and pulsating flow.

From Figure 5.20 it can be seen that only the r.m.s. velocity profile at Re = 1,901 in steady flow shows a relative peak. This is observed at approximately $x_c = 0.76 \times d_x$ downstream of the centre of the cylinder and defines the corresponding vortex formation length, as already discussed in both Chapter 3 and Chapter 4. It is interesting to note that both at the higher Reynolds number, that is Re = 4,753, in steady flow, and at the same Reynolds number, that is Re = 1,901, in pulsating flow, no r.m.s. peak, and therefore no *vortex formation length*, could be determined, at least in the locations where measurements could be taken, due to the optical access limitations of the LDA technique. Therefore, it might be assumed that a relative peak in the r.m.s. profiles could exist closer to the rear stagnation point of the cylinder. The comparison between the profile at Re = 4,753 in steady flow with that at Re = 1,901 in pulsating flow, confirms similarities between the pulsating low-Re flow (green symbols) characteristics and the steady high-Re ones (blue symbols). Increasing the Reynolds number has, therefore, the same effect on the vortex formation length as pulsating the flow: in both cases the vortex formation length decreases significantly. It should be noted that the r.m.s velocity in both the high-Re profile and the pulsating one decreases sharply in the downstream direction in contrast to what can be observed in the low-Re profile (brown symbols), where the decrease of the r.m.s. velocity is relatively smaller.

---

[9] The r.m.s. and mean velocities are normalised with the peak r.m.s. and mean velocity respectively and the distance x_c is measured from the cylinder axis and is normalised with the longitudinal length, d_x, of the cylinder. See also note at page 77 (Chapter 3).

Figure 5.21 compares the corresponding normalised axial mean velocity profiles (at the same flow conditions as for Figure 5.20). Again there is no significant difference between the mean velocity profile for steady flow and Re = 4,753, and pulsating flow at Re = 1,901. The high and low Reynolds number profiles in steady and pulsating flow respectively are very similar. In both profiles the mean velocity increases until it reaches a rather uniform value at approximately $x_c = 1.37 \times d_x$ downstream of the centre of the upstream cylinder. The low Re profile in steady flow shows a steeper velocity gradient and is characterised by a significant lower velocity in the proximity of the cylinder than the corresponding profile at high Re. Nevertheless, the normalised velocity reaches the same uniform value of 1 at $x_c/d_x \cong 1.45$. It is expected that downstream of the axial co-ordinate of this asymptotic value the mean velocity is not affected by either the Reynolds number or the flow pulsations. Finally it should be noted that, as expected, the mean zero crossing at low steady Reynolds number is observed at approximately the same axial co-ordinate as the corresponding r.m.s. peak (Figure 5.20).

5.3.3 Vortex shedding characteristics and lock-on

Velocity spectra in pulsating flow were estimated upstream of the tube bundle (x/S_L = -1.0, y/S_T = 0.0) and at one axial location behind each cylinder (x_c/S_L = 0.29). The Reynolds number and the driving frequency, f_d, were varied between Re = 1,443 and Re = 5,237, and between 7 Hz and 17 Hz respectively. Although measurements were taken upstream of the tube bundle and behind all rows, only selected spectra and time-traces obtained behind the first, third and sixth rows are shown (for brevity).

Figure 5.22 shows axial velocity amplitude spectra and selected time-traces recorded at a given location (x/S_L = 0.29, y/S_T = 0.11) behind the first row for various Reynolds numbers in pulsating flow (f_d = 10 Hz). It should be noted that the reduced amplitude $\varepsilon = \Delta U/(2\pi f_d d_y)$ of the upstream pulsations varied between ε = 0.09 at Re = 5,237 and ε = 0.32 at Re = 1,443. The spectra obtained for Re varying between 1,823 and 5,237 show a dominant peak at the driving frequency (10 Hz). The difference

between the amplitude of the peaks observed upstream of the tube bundle[10] (not shown) and those in the wake of the first row is negligible in the same Reynolds number range (4,100 < Re < 5,237). It becomes progressively more significant at lower Reynolds numbers, in which the reduced amplitude of the pulsation is higher. This means that at the high Re there is no increase of the peak amplitude from the value recorded upstream of the bundle to the one behind the first row. It is possible that at the high Re, and consequently at the lower reduced amplitude, ε, the pulsations introduced into the flow do not promote periodical vortex shedding in the wake of the first row.

However, at the lower Re, the increase of the peak amplitude is substantial. It should be noted that the time trace at Re = 2,959 (shown next to the corresponding spectrum) clearly indicates that the sinusoidal waveform of the mean velocity pulsations has a dominant fundamental frequency of 10 Hz. This suggests that at higher values of the reduced amplitude, ε, the pulsations promote periodical vortex shedding, whose frequency locks on the pulsation frequency, that is 10 Hz.

In the spectrum obtained at Re = 1,823 secondary peaks appear around the 5 Hz frequency, that is half the pulsation frequency, in contrast to what was observed in the corresponding one upstream of the bundle. Finally at Re = 1,443 two peaks can clearly be distinguished, one at the driving frequency and the other at half of it. It should be noted that the latter was not present in the corresponding upstream spectrum. This, in conjunction with the characteristics of the corresponding time trace (shown next to the spectrum) obtained from the same velocity record, implies that vortex shedding is promoted at half the pulsation frequency. Although the amplitude of the peak at 10 Hz is higher than that at 5 Hz the corresponding time trace shows clearly that the shedding of vortices occurs at half the pulsation frequency[11]. It shows the superimposition of 5 (corresponding to the 5 Hz peak) shedding cycles of large amplitude onto 10 cycles of significantly lower amplitude. Furthermore, it can be observed that the driving frequency is well defined (it only depends on the pre-selected motor angular speed) and the corresponding peak is

---

[10] These spectra presented the only peak at the superimposed driving frequency, that is 10 Hz. It should be noted that the peak amplitude, A, and reduced amplitude, ε, decreased with the Reynolds number.

[11] See the time trace at Re = 1,443 shown next to the corresponding spectrum.

narrow. On the contrary, the vortex shedding peak is broad as a consequence of cycle-to-cycle variations.

These findings suggest that two different modes of lock-on can be identified depending on the Reynolds number and the relative amplitude of the upstream pulsations. For Re ranging between 1,823 and 2,959 ($0.83 < f_d/f_{so} < 1.37$) the shedding frequency locks on the pulsation frequency (first mode) and for Re lower than 1,823 it locks on half the pulsation frequency (second mode). A transition between the two modes occurs at Re = 1,823.

Figure 5.23 shows axial velocity amplitude spectra and selected time-traces obtained behind the third row ($x/S_L = 2.29$, $y/S_T = 0.11$) for various Reynolds numbers in pulsating flow conditions (10 Hz). The first spectrum obtained at Re = 5,237 clearly shows two peaks, one at the pulsation frequency, that is 10 Hz, and the second at approximately 22 Hz. The latter is related to the natural vortex shedding frequency. The same frequency value is predicted using the expression (5.1) describing the linear variation of the vortex shedding frequency with Reynolds number[12] in steady flow. In the following spectra a shift of this amplitude peak towards lower frequencies can be observed as a result of the decreasing Reynolds number. Furthermore, the amplitude of the vortex shedding peak decreases with Re while that of the driving frequency increases. In the Reynolds number range 2,579 to 3,339 only the peak at 10 Hz can be observed; its amplitude remains approximately constant. It is difficult to ascertain whether the vortex shedding peak, whose amplitude decreases with Re, is submerged in background turbulence, or has locked on the driving frequency, although the abrupt and significant increase of the peak at 10 Hz suggests that lock on might have occurred. However, in the spectrum obtained at the lower Re (Re = 1,823) two peaks can again be distinguished, one at the driving frequency, 10 Hz, and the other at about 5 Hz. Although this peak is related to the shedding vortex frequency, it does not correspond to the natural vortex shedding, f_{so}, whose value (from expression (5.1)) is expected to be approximately equal to 7.4 Hz. Instead it seems that the shedding frequency has locked at half the pulsation frequency, i.e. 5 Hz. This is also confirmed by the spectrum obtained at Re = 1,443,

[12] The time trace at Re = 5,237 (Figure 5.22) shows that both the superimposed and vortex shedding-related pulsations are hidden by the high turbulence levels.

which clearly shows the presence of two peaks, one at $f_d = 9.4$ Hz[13] and the other at half the pulsation frequency, that is 4.7 Hz.

It may be concluded that behind the third row, as behind the first one, two different modes of lock-on can be identified. The first mode occurs at intermediate Re (1,823 < Re < 2,959) and the second one at low Re (Re ≤ 1,823).

Figure 5.24 shows axial velocity amplitude spectra and selected time-traces recorded at a given location ($x/S_L = 5.29$, $y/S_T = 0.11$) behind the sixth row. The Re was kept constant and equal to 2,200 while the driving frequency was varied between 7 Hz and 17 Hz. Note that at Re = 2,200 a natural vortex shedding frequency of approximately 9 Hz is expected according to equation (5.1). The first spectrum of the sequence shows two main peaks, one at 17 Hz (2ε[14] = 0.11) and the other at 8.5 Hz. At $f_d = 17$ Hz, therefore, we have $f_d/f_{so} \cong 2$. It should be noted that upstream of the bundle ($x/S_L = 5.28$, $y/S_T = 0.0$), the amplitude of the pulsation peak (the corresponding spectrum is not shown for brevity), at 17 Hz, is dominant over the subharmonic at 8.5 Hz that has a comparatively negligible amplitude, while downstream of the sixth row, the dominant peak is the one at half the driving frequency (at 8.5 Hz). This suggests that the 8.5 Hz peak behind the sixth row is not a subharmonic but the peak of the shedding frequency that has locked on half the driving one. At $f_d = 15.2$ Hz ($2\varepsilon = 0.12$) again one peak is detectable at the driving frequency and a second one of higher amplitude at $f_s = 7.6$ Hz. For lower values of the driving frequency lock-on was not observed, despite of the increased reduced amplitude of the upstream pulsation, ε. This might suggest that for $2\varepsilon \leq 0.12$ lock-on occurs only for $f_d/f_{so} \geq 1.7$.

Figure 5.25 shows the variation of 2ε with f_d/f_{so} and the lock-on limits in the in-line tube bundle with drop-shaped cylinders under pulsating flow conditions. The lock-on region is the one within the curve (black line); this is the same curve as that described in Chapter 3, paragraph 3.3.3, which was originally obtained by interpolating the data published by Barbi et al (1986) and Griffin and Ramberg (1976) for a single circular cylinder. The blue diamonds represent the same data as in Figure 5.23 and confirm that lock-on does not occur for $f_d = 10$ Hz and Re ranging between Re = 2,959 and Re

---

[13] Note that the driving frequency had shifted from 10 Hz to 9.4 Hz at the lowest Re, but this does not affect the conclusions.

[14] ε is the reduced amplitude of the upstream pulsations and not of the local ones.

= 5,237. The data are not sufficient to extend the lock-on limits to higher values of 2ε, which correspond to the Re = 1,823 and Re = 1,443 cases. For these low Reynolds number cases it is not possible to confirm the spectra findings shown in Figure 5.23.

The data points represented in Figure 5.25 with pink squares and red circles correspond to the same data as the ones obtained behind the sixth row for various driving frequencies ($f_d \leq 17$) and Re = 2,200, shown in Figure 5.24. It can be seen that the two data points (red circles) representing the two cases for $f_d = 17$ Hz and $f_d = 15$ Hz (Re = 2,200) mentioned above fall within the lock-on region in agreement with the findings of the corresponding spectra. All the other data points, with the exception of those very close to the lock-on right limit (black line) corresponding to $f_d = 13$ and 12 Hz, fall outside of the lock-on region, in agreement with the spectra findings showing that for these cases the driving and shedding frequencies are de-coupled. It should be noted that despite the uncertainty of points lying very close to the lock-on boundary (due to both the fact that this was constructed by interpolating experimental data of the flow past a single circular cylinder and to the inherent experimental error associated with the present data), the LDA findings suggest that the probability for lock-on to occur at the flow conditions corresponding to these data points is very low.

5.4 Skewness and kurtosis in steady and pulsating flow

The skewness and the kurtosis of both the axial and radial velocity probability distributions were also determined in steady flow throughout the flow field at Re = 6,300. Figure 5.26 shows the kurtosis contours of the axial (a) and radial (b) mean velocity components. The axial profiles show that the lowest values of the kurtosis (2.2 ÷ 2.8) are recorded in the wake and over the shoulders of the cylinders, particularly the downstream ones. The highest values (> 4) are instead recorded along the shear layers, whose thickness increases in the downstream direction. In the remaining regions of the bundle, values between 3 and 3.2 can generally be observed. Therefore, at the entrance of the tube bank and in the freestream the axial velocity

distributions resemble the normal one (Kr = 3). The kurtosis contours exhibit similar characteristics to those observed in the in-line array with elliptic cylinders.

Figure 5.26 (b) shows the radial velocity kurtosis contours. It can be seen that generally the values are higher than the corresponding axial ones. In particular, values varying between 3 and 4 are recorded behind the first three rows. Values as high as those observed along the shear layers are recorded over the shoulder of the cylinders, in particular over their parabolic half. Again values corresponding to a normal distribution (Kr =3) are recorded in the freestream.

It is therefore apparent that the radial velocities have little fluctuations, and less than the axial ones, around the mean velocity component over large part of the flow field, while high fluctuations are recorded in the proximity of the rear stagnation point of the cylinders.

Figures 5.27 (a)-(b) show the axial and radial skewness profiles in steady flow for Re = 6,300. The skewness was calculated from the same time-velocity records from which the kurtosis was determined. Slightly higher values of the radial velocity skewness are observed along the shear layers and in the flow passages. In both distributions the skewness is not higher than 0.4 behind the first two rows and decreases behind the downstream ones. It should be noted that slightly higher values than those corresponding to the normal distribution (Sk = 0) are observed in the cylinder wakes and lower values in the rest of the flow domain. This implies that high velocity regions move into the wakes and, vice versa, low radial velocity flow lumps move from the high turbulence wake into the shear layer, across which the skewness varies between 0.4 and - 0.4.

5.5 Flow visualisation

Selected visualisation pictures obtained behind the first and third cylinders in both steady and pulsating flow are shown in Figures 5.28-5.31 and Figures 5.32-5.33 respectively.

The time interval between frames, ΔT_F, was equal to 20 ms. The first frame, Frame 1, was arbitrarily chosen to correspond to the observation time t = 0. In the sequence of frames, time increases from left to right and from top to bottom. The nomenclature adopted does not differ from that used in the description of the visualisation pictures shown in Chapter 3 and 4.

Figures 5.28 (a)-(f) show flow visualisation pictures obtained behind the first row at Re = 842. In Figures 5.28 (b) to 5.28 (f) the flow images (column (a)) are compared with those obtained at Re = 1,426 (column (b)) in order to study the effect of Re on the fluid dynamics and periodicities of the flow in the wake of the first drop-shaped cylinder.

The first four frames (t_a = 0 ms - t_a = 60 ms) of Figure 5.28 (a) show the shedding of the clockwise vortex P_{1a}[15] (see frame at t_a[16] = 60 ms) and its downstream convection. P_{1a} grows in size during this time interval and at t_a = 80 ms (Figures 5.29 (b)) its diameter reaches the maximum value in the entire shedding period. It can clearly be seen that P_{1a} draws irrotational flow into the wake. This is entrained in between the downstream cylinder tip and the vortex itself. The entrained fluid slows down the downstream convection of P_{1a} and causes the vortex to move towards the wake centreline (see t_a = 100 ms). The entrained irrotational flow, deflected by the tip of the downstream cylinder, crosses the wake centreline and flows downward along the cylinder wall on the negative side of the wake (see frame at t_a = 120 ms). At t_a = 120 ms the amount of entrained fluid is significantly reduced and the reduced passage area between the tip and the vortex causes it to accelerate. Furthermore, the direction of the entrained flow streamlines is almost parallel to that of the near tip wall (compare the angles between these two directions, indicated by dashed lines, in frames t_a = 40 ms and t_a = 120 ms). As a consequence the entrained flow moves along the cylinder wall and separates at the tip forming the vortex N_{1a}*[17] which grows in the proximity of the front stagnation point (see again frame at t_a = 120 ms).

---

[15] P_{ia} (N_{ia}) and P_{ib} (N_{ib}) indicate anti clockwise (clockwise) vortices referring to the lower (Re = 842) or higher (Re = 1,426) Reynolds number respectively.
[16] t_a and t_b indicate the observation time relative to the lower (Re = 842) and higher (Re = 1,426) Reynolds number respectively.
[17] The star indicates that the vortex is not shed by the upstream cylinder but formed by the separation of the flow over the tip of the downstream one.

It is interesting to note that the distance between the rear stagnation point of the first cylinder and the front stagnation point of the second cylinder is approximately the same as that between the elliptic cylinders in the in-line array described in Chapter 3. A main difference between the two arrays is that the wider wake observed in the present array, due to the circular shape of the bottom part of the cylinders, causes the shear layers not to impinge on the upper part (of parabolic shape) of the downstream cylinder and consequently to be relatively free to oscillate and roll up as opposed to the first elliptic cylinder whose vortex activity in the wake was found to be negligible.

The visualisation pictures obtained at low Re are compared with those at high Re starting from frames at t_a = 140 ms (Re = 842) and t_b = 0 ms (Re = 1,426) in Figure 5.28 (b)[18]. Two clockwise vortices, P_{1a} (t_a = 140 ms) and P_{1b} (t_b = 0 ms), shed from the first cylinder are convected downstream up to the tip of the second one and two anticlockwise ones, N_{1a}^* (t_a = 140 ms) and N_{1b}^* (t_b = 0 ms), are forming by separation of the flow over the tip of the downstream cylinder, in the low and high Re sequences respectively. At t_b = 0 ms, P_{1b}, lies over the parabolic shoulder of the second cylinder and its axis is oriented accordingly. The flow that is drawn into the wake by P_{1b} moves upward along the cylinder upper wall and separates over the tip forming the anticlockwise vortex N_{1b}. The formation sequence of N_{1b} is similar to that of N_{1a} for the low Re sequence, although the latter is more apparent.

Apart from the slight differences in the size and orientation of the vortices P_{1b} and P_{1a} and in the position of their cores, no significant differences can be observed in the vortex pattern. However, it can be seen in this and in the subsequent frames, that the wake referring to the lower Reynolds number is more stagnant and asymmetric than the one at higher Re, and its width, W, larger.

Differences between the vortex patterns of the two Re sequences arise in the successive time frames. At t_a = 140 ms P_{1a} has impinged on the tip of the second cylinder and its axis is inclined by 55° with respect to the cylinder axis. N_{1a}^* is formed and grows in size up to t_a = 220 ms. Meanwhile, it has moved transversely

towards the negative shear layer[19] (see again frame at t_a = 220 ms). As a consequence N_{1a}^* is partly fed by the flow entrained by P_{1a} into the wake (P_{1a} and N_{1a}^* bear vorticity of opposite sign) and partly by the negative shear layer. It should be noted that from t_a = 160 ms to t_a = 220 ms P_{1a} and N_{1a}^*, which constitute a pair of vortices whose relative position, shape and size does not vary, are convected towards the negative shear layer along a direction that is approximately given by the slope of the second cylinder near tip, or otherwise by the direction of the separating flow forming N_{1a}^* (see Frame at t_a = 180 ms). Meanwhile an anticlockwise vortex, N_{1a}, is shed and convected downstream. The frames do not clearly show the shedding time, but the vortex can be more clearly noticed in Frame t_a = 220. In the successive times frames the interaction of the three vortices, P_{1a}, N_{1a}^* and N_{1a} occurs (see frames t_a = 260 ms $\rightarrow$ 300 ms). It should be noted that while P_{1a} is clockwise, N_{1a}^* and N_{1a} are anticlockwise and therefore the interaction between them is disruptive. N_{1a} is dissipated (see frame at t_a = 320 ms) while N_{1a}^* firstly grows in size (see Frame t_a = 340 ms) and then is finally convected downstream.

The frame at t_b = 0 ms shows three vortices, P_{1b}, N_{1b}^* and N_{1b}. N_{1b} shed by the upstream cylinder and convected downstream is dissipating. At t_b = 40 ms a second anticlockwise vortex, N_{2b}, is approaching the downstream cylinder. In contrast to what was observed at the lower Re, (N_{1b}^*, as opposed to N_{1a}^*, does not have the possibility to grow in size before interacting with the incoming vortex N_{1b}) N_{1b}^* interacts with N_{1b} already at t_b = 20 ms. At t_b = 80 ms the three vortices, N_{1b}^*, N_{1b} and N_{2b} are dissipated. Meanwhile P_{1b} grows in size and is convected downstream along the second cylinder side wall. A second clockwise vortex, P_{2b}, is observed at t_b = 200 ms. The latter, delayed in its downstream convection by P_{1b}, is reached by a third clockwise vortex P_{3b} (see frame at t_b = 320 ms) bearing vorticity of the same sign. Due to their interaction, the two vortices first decrease in strength then, after the impingement of P_{2b} on the downstream cylinder wall, merge into one (see frames t_b = 300 $\rightarrow$ 320).

---

[18] The comparison starts with two different time frames (t_a = 140 ms and t_b = 0 ms) as the Frame 1, t = 0 ms, of the two sequences was recorded at different times of the shedding period. The two frames, t_a = 140 ms and t_b = 0 ms, were chosen as they show a similar vortex pattern.

[19] The irrotational flow on the left-hand side of the cylinder.

The comparison between frames at t_a = 140 ms and t_b = 0 ms and between subsequent ones (t_a = 0 ms → 160 ms and t_b = 0 ms → 160 ms) shows that the higher the Re the larger is the amount of irrotational flow drawn into the wake, but the less the amount of fluid which crosses it. The close examination of the frames suggests that a low Re favours the asymmetry of the flow in the wake, although the flow pattern is never perfectly symmetrical.

Although the vortex activity, at both Re, is apparently stronger than that behind the first elliptic cylinder (see Chapter 3) it is not possible to identify clearly a periodicity in the flow pattern of the two sequences. This is particularly true in the low Re sequence where the flow is clearly asymmetrical due to the transversal convection of the clockwise vortex P_{1a} and its consequent interaction with the anticlockwise vortices shed from the opposite side of the wake.

Figures 5.29 (a)-(c) shows three complete cycles of vortex shedding behind the first cylinder under pulsating flow conditions (f_d = 14 Hz, 2ε = 0.2, Re = 1,443). The LDA findings suggest that the flow conditions for the pulsating flow experiment in this case are such that vortex shedding locks at half the pulsation frequency (see Figure 5.25). The effect of pulsations is apparent. The first frame (t = 0 ms) shows the shear layer separating from the left-hand side of the cylinder violently drawn, as indicated by the arrow, towards the centreline of the high turbulence wake (which is consequently slightly skewed on the right) as a result of the rapid dissipation of an anticlockwise vortex[20]. The frame at t = 20 ms shows a clockwise vortex, P_1, shed by the first cylinder which rapidly grows in size. At = 40 ms it occupies the whole wake. It should be noted that this vortex does not appear to be convected downstream but moves along the cylinder wall towards the rear stagnation point (see t = 0 ms → 60 ms). The positive irrotational flow violently drawn into the wake by P_1 crosses the centreline and reaches the shear layer separating from the opposite side of the upstream cylinder. P_1 rapidly dissipates as soon as it interacts with the irrotational shear layer (see frame at t = 60 ms). It should be noted that it is the outer edge of the

[20] The vortex is not shown because its dissipation occurs at a time which precedes that chosen as corresponding to the observation time t = 0 ms. However, its formation and dissipation can be inferred by the observation (see t = 140 ms) of the successive frames. The dissipation time can be evaluated to be approximately equal to 40 ms.

vortex that crosses the wake while its core remains on the right-hand side of the wake (the same is observed for the anticlockwise vortices).

The wake has therefore undergone significant modifications in its structure: no stagnant areas can be identified even along the cylinder wall in the proximity of the rear stagnation point (see t = 40 ms). The flow is essentially transversal to the wake axis. Due to the substantial mass transfer across the wake the vortex shedding is necessarily anti-symmetrical (see also Ziada and Oengören, 1991). Therefore, at the flow conditions adopted for the present flow visualisation study, pulsations do not promote symmetry, although the flow periodicity is well defined and the flow pattern appears well organised. It is clear from the sequence that the flow is periodical with a period of T = 140 ms (compare frame at t = 40 ms with that at t = 180 ms), which corresponds to a frequency of 7 Hz, that is half the pulsation frequency. It should be noted that the corresponding natural vortex shedding frequency in steady flow (Re = 1,443) is approximately equal to 5.8 Hz (see Figure 5.25; $f_d/f_{so} = 2.41$ and $2\varepsilon = 0.2$). As expected, therefore, the vortex shedding locks on half the pulsation frequency.

For comparison visualisation pictures obtained behind the first cylinder under pulsating flow conditions at the same Re as that of the previous case examined, but at a lower driving frequency, f_d, are shown in Figure 5.30 (f_d = 10 Hz, $2\varepsilon = 0.2$, Re = 1,443). The effect of pulsations is also apparent in the present sequence of frames. The first frame (t = 0 ms) shows the wake of the first cylinder after the dissipation of a pair of vortices, of quasi-symmetrical pattern. It can be inferred by the slight asymmetry of the wake, and particularly by the angle of the separating streamlines, that the clockwise vortex was slightly larger. The larger the vortex, the more violently the irrotational flow is drawn into the wake at its dissipation. The sudden dissipation of the vortex causes the irrotational flow on the positive y-direction to be more violently drawn into the wake than that on the opposite side. In the successive frame (t = 20 ms) two new large quasi-symmetrical vortices, the clockwise vortex P_1 and the anticlockwise one N_1, are shed. At t = 20 ms their size and the position of their cores are clearly different as shown in the corresponding frame. During the *formation phase* (t = 0 → 40 ms) (in the single cycle/time period) the downstream convection of N_1 and its growth rate are larger than that of P_1. As a consequence at the start of the *dissipation phase* (t = 60 ms) the differences in the size and the core

location of the two vortices have become negligible. At t = 60 they have reached their maximum size in the entire shedding period. The successive time frame (t = 80 ms) shows their sudden dissipation.

It should be noted that the frames from t = 60 ms to t = 160 ms show a complete cycle of vortex shedding of period T = 100 ms, which corresponds to a frequency of 10 Hz, that is the pulsation driving frequency. The first half-period of the cycle (*dissipation phase*) is represented by the frames t = 60 ms → 100 ms. Frames from t = 120 ms to t = 160 ms represent instead the second half-period, which corresponds to the *formation phase* during this time interval. Two quasi-symmetrical vortices are shed, P_2 and N_2. They again grow in size and reach their maximum at t = 140 ms. It is important to note that the two half cycles are not perfectly symmetrical. As it can be seen, in the first half cycle the clockwise vortex is smaller than the anticlockwise one and the opposite occurs in the second half. The most significant and evident difference between the two pulsating cases examined (f_d = 14 Hz and f_d = 10 Hz) lies in the fact that in the former the vortex shedding is alternate while in the latter it is symmetrical. This difference can only be attributed to the different pulsation frequencies, as the amplitude of the pulsations is the same for the two cases.

Figure 5.31 shows visualisation pictures for pulsating flow with the same driving frequency as in the previous case but at higher Re (Re = 2,139, f_d = 10 Hz, 2ε = 0.2). This in order to determine the effect of the Reynolds number on the fluid dynamics and periodicities of the flow in the wake of the first cylinder. It should be noted that the amplitude of the pulsations upstream of the tube bundle is slightly different than in the previous case. Furthermore, it is clear that, although the experimental set up was the same for the two cases, the resolution of the pictures at higher Re is significantly lower.

The sequence of frames shows (see Frame at t = 40 ms) two vortices, P_1 and N_1, symmetrically shed and convected downstream. The frame at t = 100 ms shows a new vortex pair (P_2, N_2). It is not possible from the pictures to determine their shedding time due to the high turbulence of the flow and the low resolution of the pictures. However, it is possible to infer from the flow patterns that the vortices were

shed at a time t ranging between t = 60 and t = 80 ms[21]. At t = 80 ms, in fact, the wake width has a minimum as a consequence of the dissipation of the two symmetrical vortices, P_1 and N_1. This is then followed by the formation of P_2 and N_2 (compare the pulsating sequence in Figure 5.30). The comparison between the frame at t = 40 with that at t = 140 suggests that the flow pattern is periodical with period T = 100 ms, which corresponds to a frequency of 10 Hz, i.e. the pulsation driving frequency; therefore lock-on occurs at the driving frequency. However, it should be noted that the natural vortex shedding frequency in steady flow for Re = 2,139 is approximately equal to 8.8 Hz (f_d/f_{so} = 1.14), a value not very different from that of the driving frequency. Therefore, due the low resolution of the pictures, which can be partly attributed to the high turbulence levels in the wake, and to the aforementioned time uncertainty it is not possible to draw any relevant conclusion about the frequency of the vortex shedding.

Figures 5.32 (a)-(d) show selected flow visualisation pictures obtained behind the third row at Re = 842 in steady flow. A comparison with the sequence of frames obtained at the same Reynolds number behind the first row (Figure 5.28) allows assessing the effect of the row depth on the fluid dynamics and periodicities of the flow in the wake. It should be noted that the scale of the pictures is not the same as that used for those in Figure 5.31; the width of the frames in Figures 5.32 and 5.32 corresponds to about 17.3 mm and 10.2 mm respectively. Furthermore, in order to provide spatial information two dashed lines are superimposed to the first picture (t = 0 ms) whose distance is equal to the minor axis of the cylinders (d_y = 6.16 mm). The wake region is not as well defined as that behind the first row, due to the higher turbulence of the flow, but the shedding of vortices is clearly shown. It is interesting to note that the formation and shedding of the vortices is accompanied by a transversal and oscillatory[22] motion of a layer of laminar flow along the lower surface of the cylinder (see frame at t = 40 ms). The sweeping of the rear part of the cylinder occurs with a frequency that is related to that of the vortex shedding, and therefore increases with the Reynolds number until the layer breaks up into turbulence. It should also be noted that the flow patterns shown in the sequence resemble those

[21] Consider that there is a time uncertainty of ± 20 ms.
[22] The paths of the particles within the layer show that these move from left to right when clockwise vortices are shed and from right to left when anticlockwise vortices are shed.

observed in Figure 5.30 (pulsating flow), confirming again that similar characteristics to those of the mean flow under pulsating conditions can be obtained in steady flow by simply increasing the corresponding Reynolds number. The comparison of the frame at t = 80 ms (it is chosen as reference as the shedding vortex is clearly shown) with that at t = 380 ms shows that the flow pattern is periodical with period T = 300 ms, which corresponds to a shedding frequency, f_s, of 3.3 Hz. This value is in agreement with that calculated at the same Re by means of equation (5.1).

The clockwise vortex P_1 slowly moves towards the centreline while it is convected downstream (see t = 20 ms). The distance travelled along the radial and axial direction by P_1 from t = 20 ms to 140 ms is indicated in the frame at t = 140 ms where the triangle shows the axial (Δx), radial (Δy) and actual displacement of the vortex core in this time interval. The spatial reference given in Frame 1, t = 0 ms, allows the evaluation of both the vortex core displacements and the mean convection velocity components. The axial and radial displacements are approximately equal to 4.24 mm and 2.28 mm respectively, that is 0.32 and 0.37 times the long and short axis respectively. The actual displacement is therefore approximately equal to 4.81 mm. Hence, the convection axial and radial velocity components (the time interval between the frames is equal to Δt = 120 ms) are approximately equal to 0.036 m/s and 0.019 m/s, that is 0.4 and 0.20 times the upstream bulk velocity, U_∞, respectively.

Finally Figures 5.33 (a)-(d) show a comparison of selected flow visualisation pictures obtained at Re = 1,443 (that is at higher Re then the previous case) behind the third row between steady (column (a) of Figure 5.33) and pulsating flow (A_o = 0.2, f_d = 10 Hz, column (b) of Figure 5.33). The differences between the steady and pulsating flow patterns are apparent. In steady flow the wake is clearly better defined than in pulsating flow, that is the velocity gradients across the shear layer are steeper and as a result the low velocity region can be more easily identified. The two frames at t_a = 0 ms and t_b = 0 ms were chosen as first frames of the time sequences as they both show a clockwise vortex being shed by the third cylinder which is located at a similar position. The frame at t_a = 0 ms shows three vortices. P_{1a} (clockwise) and N_{1a} (anticlockwise) which are convected downstream, and P_{2a} (clockwise) (although not clearly shown) that has been shed. Similarly at t_b = 0 ms, a clockwise vortex, P_{1b}, is

shed under pulsating flow conditions. However, the wake flow pattern is completely different from the corresponding one in steady flow.

P_{2a} is slowly convected downstream although delayed by both N_{1a} and P_{1a} in its radial and axial convection respectively. The frame at t_a = 60 ms shows that a second anticlockwise vortex, N_{2a}, was formed and convected downstream (its shedding and convection is not clear in the preceding frames). Its growth and convection is hindered by N_{1a} until the latter diffuses. From t_a = 60 ms to t = 120 ms N_{2a} can be clearly distinguished as it convects downstrem. It is possible that N_{2a} was formed at the same time as P_{2a} and therefore that the vortex formation is symmetrical despite the asymmetry observed in the downstream convection. In the time interval that goes from t_a = 0 ms to t_a = 80 ms N_{2a} reaches P_{2a}, which is probably delayed by the preceding vortices, and the flow pattern appears symmetrical. The newly shed vortices, P_{3a} and N_{3a}, shown in the frames at t_a = 180 ms and 200 ms are similarly affected in their downstream convection by N_{2a} and P_{2a} whose size and location are also similar, and, as expected, their convection is approximately symmetrical. Note in particular the flow pattern in the frames corresponding to the time interval t_a = 200 ms $\rightarrow$ t_a = 240 ms. This seems to confirm that the vortices are shed symmetrically and asymmetries in the flow pattern develop during their convection phase. This is probably due to flow instabilities promoted by the downstream cylinder which may affect the growth and movement of the incoming vortices differently.

It is interesting to compare the values of the vortex convection velocity components evaluated (by direct observation of the pictures) behind the third row for low (Figure 5.32) and high (present case) Re. The evaluation was made by measuring the axial and radial distance travelled by P_{2a} in the time interval t_b = 20 ms $\rightarrow$ t_b = 80 ms. The axial and radial displacements are approximately equal to 3.66 mm and 1.58 mm respectively, that is 0.28 and 0.26 times the long and short axis respectively, and the actual displacement approximately equal to 3.99 mm. The convection axial and radial velocity components (the time interval between the frames is equal to Δt = 60 ms) are approximately equal to 0.061 m/s and 0.026 m/s, that is 0.38 and 0.16 times the upstream bulk velocity, U_∞, respectively. These values are similar to those found at low Re suggesting that the convection velocity scales with the bulk velocity and consequently with the Reynolds number.

It is clear that the downstream convection of vortices in pulsating flow can be neglected with respect to the steady flow case. P_{lb} sweeps the cylinder rear wall, but in contrast to what was observed in the pulsating case shown in Figure 5.30 (see frames $t_b = 20 \rightarrow t_b = 60$ ms), the convection of the vortex in the radial direction along the negative y-direction is not apparent. The vortex grows, although slightly, from $t_b = 0$ ms to $t_b = 20$ and at $t_b = 40$ ms it dissipates. Its rapid and sudden dissipation causes the positive shear layer to be violently drawn into the wake ($t_b =$ 60 ms). This is a characteristic of the flow under pulsating conditions. In the steady case the slow growth and downstream convection of the vortices prevent the shear layer from being so abruptly and strongly deflected towards the wake centreline. It should be noted, therefore, that the irrotational flow is entrained into the wake as a consequence of both the dissipation (see $t_b = 60$ ms) and formation/shedding (see $t_b =$ 100 ms) of a vortex.

Although not clearly shown by the sequence of frames due to the low resolution of the pictures, the flow pattern of the pulsating flow is periodical with a period of T = 100 ms, which corresponds to a shedding frequency of $f_d = 10$ Hz.

5.6 Conclusions

An experimental investigation was carried out on the flow around an in-line array with drop-shaped cylinders.

The results showed that the difference of turbulence levels along the flow passages ($y/S_T = 0.5$) between the arrays with elliptic and drop-shaped cylinders is very small at the entrance to the tube bank and decreases further downstream (the turbulence levels are slightly higher in the drop-shaped array). Already behind the second row the turbulence levels of both arrays are significantly lower than those in the array with circular cylinders. Differences between the in-line arrays with elliptic and drop-shaped cylinders respectively can be observed only in the cylinder wakes, particularly behind the first one. The magnitude of the r.m.s peak behind the first elliptic cylinder is up to 75% higher than that observed behind the drop-shaped one.

The difference of the two r.m.s. components is near zero over the whole flow domain indicating that the turbulence could be assumed highly isotropic, with the exception of the shoulders of the third cylinder and in the proximity of the separation points of the fifth and sixth rows where the difference reaches values in the range $0.1U_\infty < |v'-u'| < 0.2U_\infty$. A vortex shedding activity could be observed behind all rows, but a well defined vortex shedding frequency was detected only downstream of the second one. The Strouhal number, defined by the minor axis of the drop-shaped cylinders, d_y, and the gap velocity, U_g, was found to be equal to 0.16 in inner rows. The only significant effect of the pulsations on the turbulence of the flow was observed behind the first cylinder as in the in-line array with elliptic cylinders. Lock-on of the natural vortex shedding at either the superimposed pulsation frequency or at half of it depending on the reduced amplitude of pulsations upstream of the tube bundle was observed.

The flow visualisation study confirmed the findings of the LDA measurements. In particular it indicated the presence of an intense vortex activity even behind the first row, in contrast to what was observed in the in-line array with elliptic cylinders, which showed lack of any significant vortex activity behind the first cylinder.

The following chapter examines the heat transfer characteristics of both the in-line and the asymmetric array with elliptic and circular cylinders respectively. All measurements were taken in both steady and pulsating flow. The study was carried out in order to evaluate the effect of the mean flow and turbulence characteristics on the heat transfer and to identify tube bundle configurations as well as flow conditions, which maximise the heat transfer of the outer surface of the tubes.

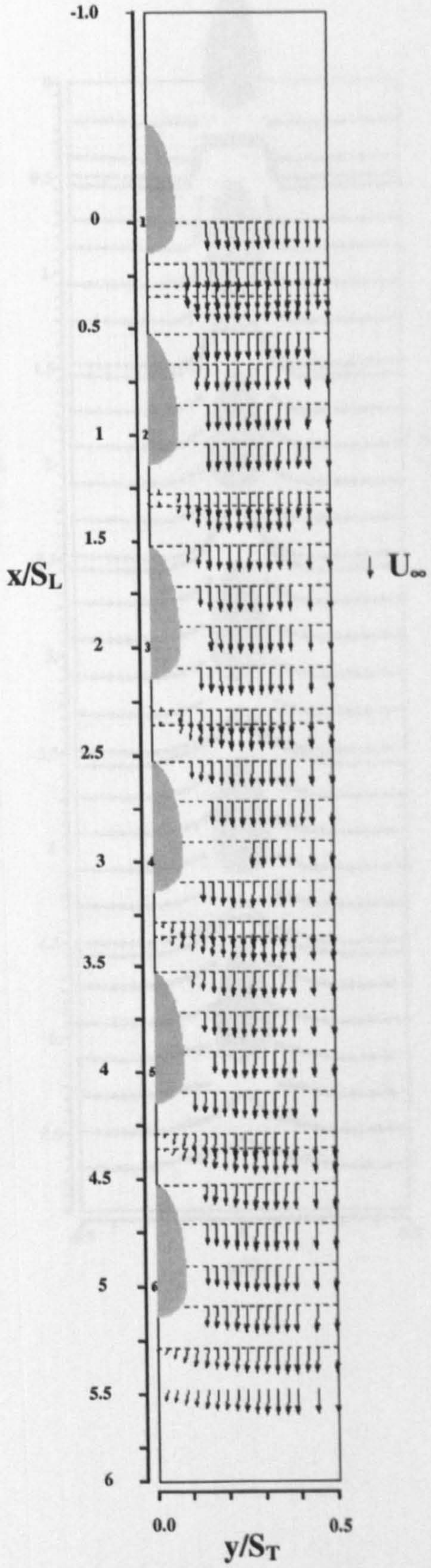

Figure 5.1. Velocity vectors in the in-line bundle with drop-shaped cylinders (steady flow, Re 6,300).

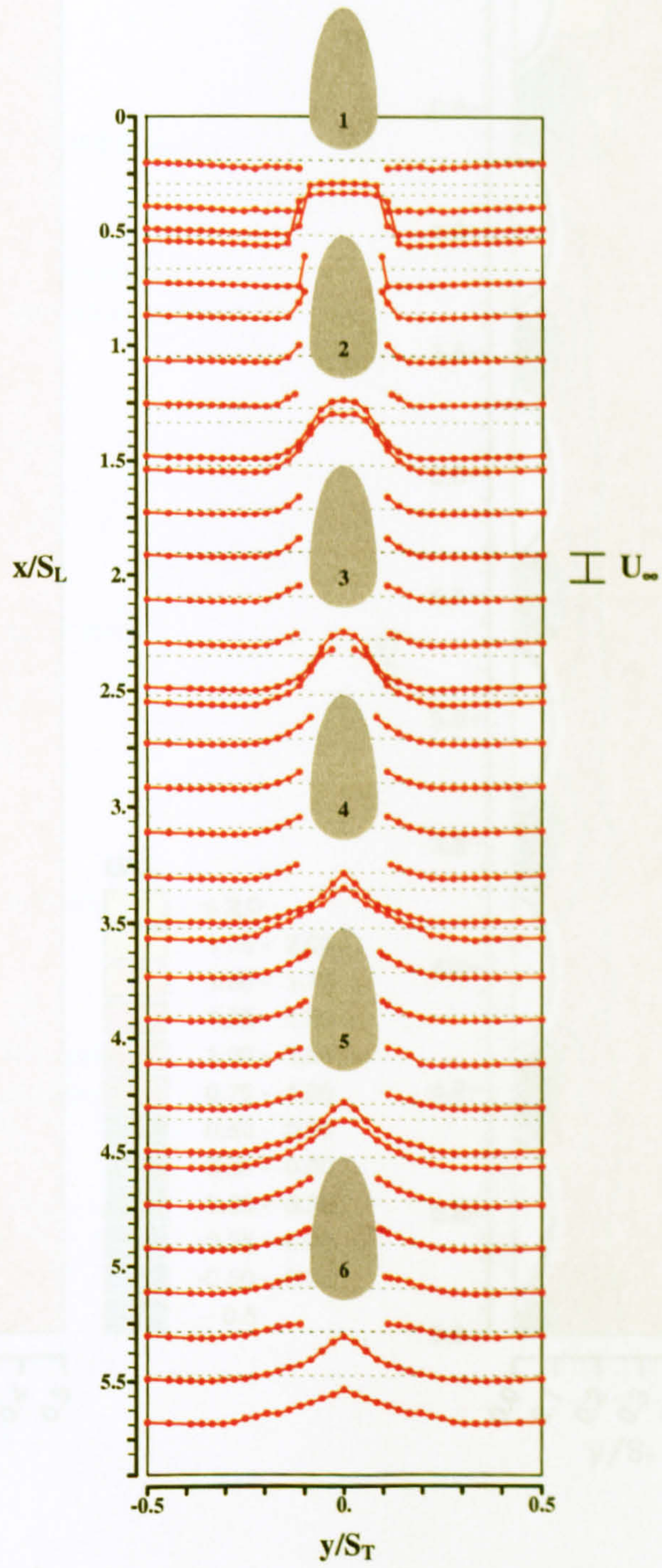

Figure 5.2. Distribution of the axial mean velocity, U/U_∞ in the in-line bundle with drop-shaped cylinders (steady flow, Re = 6,300).

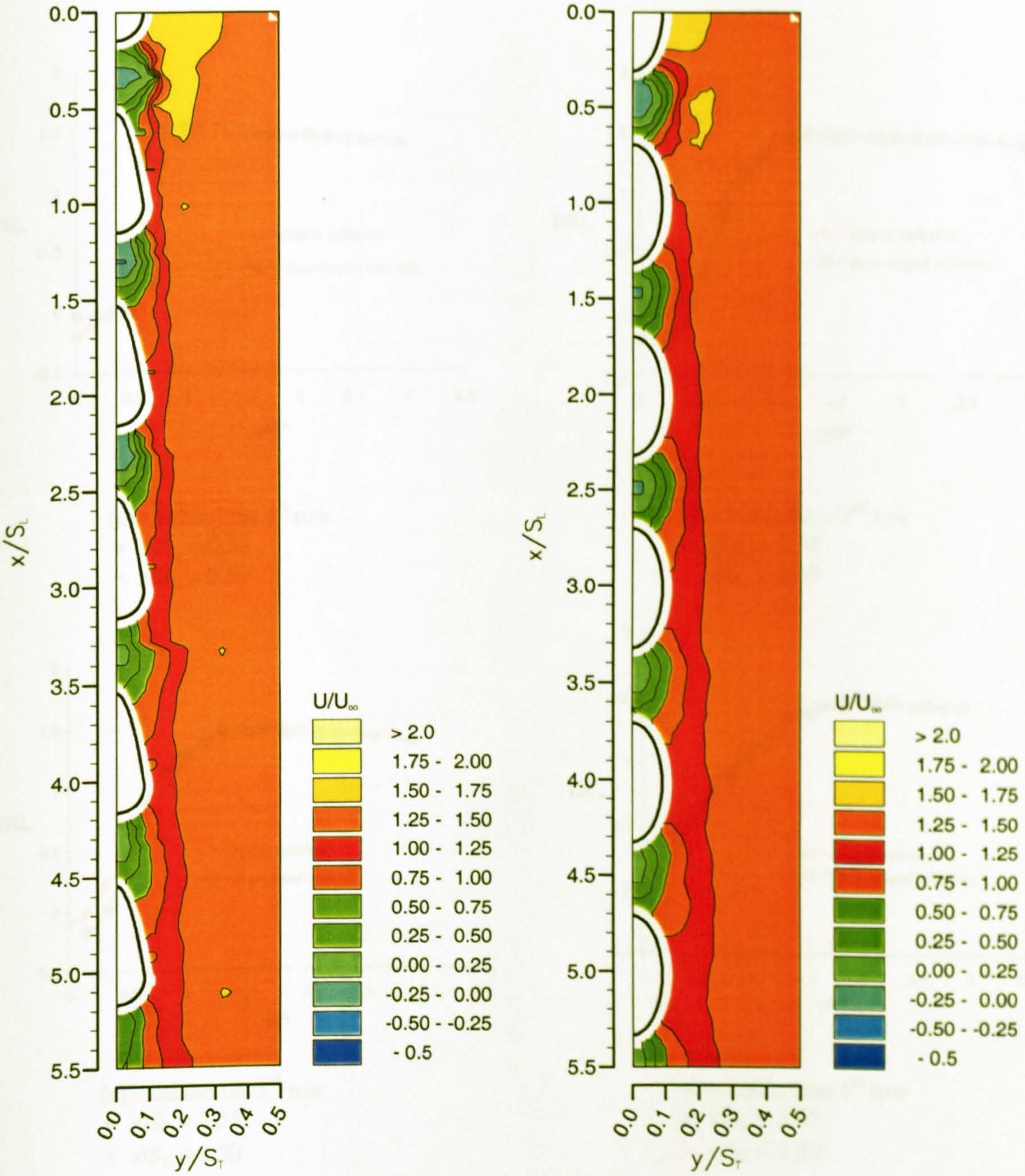

Figure 5.3. Comparison of the axial mean velocity profiles, U/U_∞, between the in-line array with drop-shaped cylinders and the one with elliptic ones (steady flow).

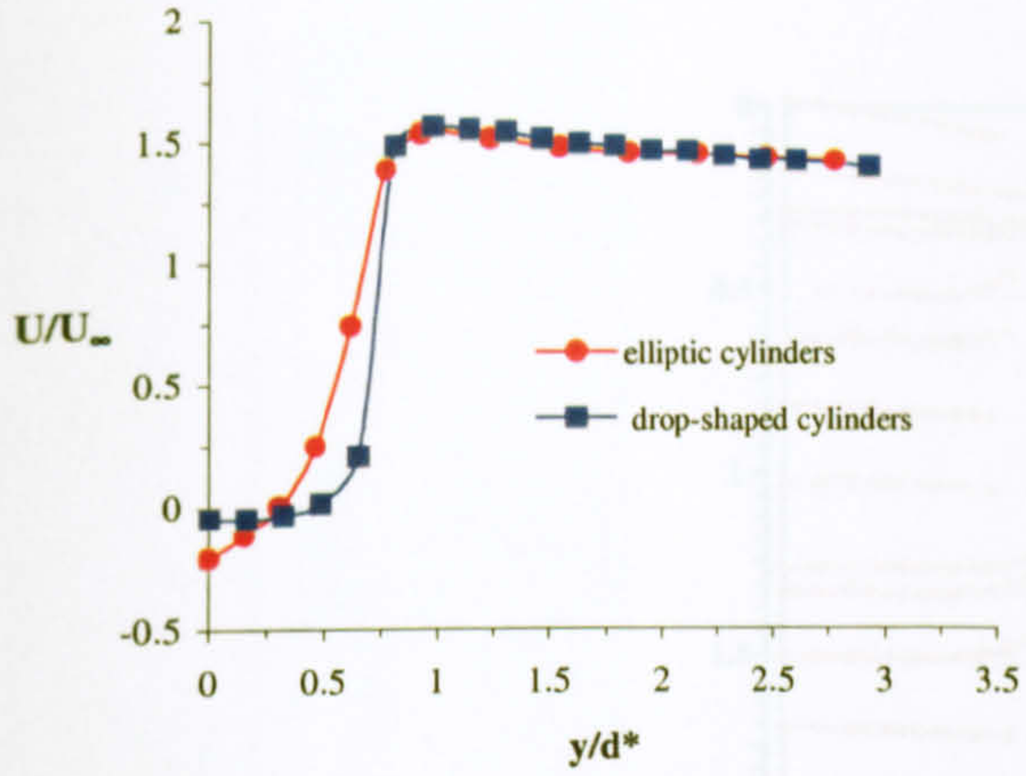

(a) - behind the 1st row
- $x\backslash S_L = 0.35$
- $x\backslash S_L = 0.50$

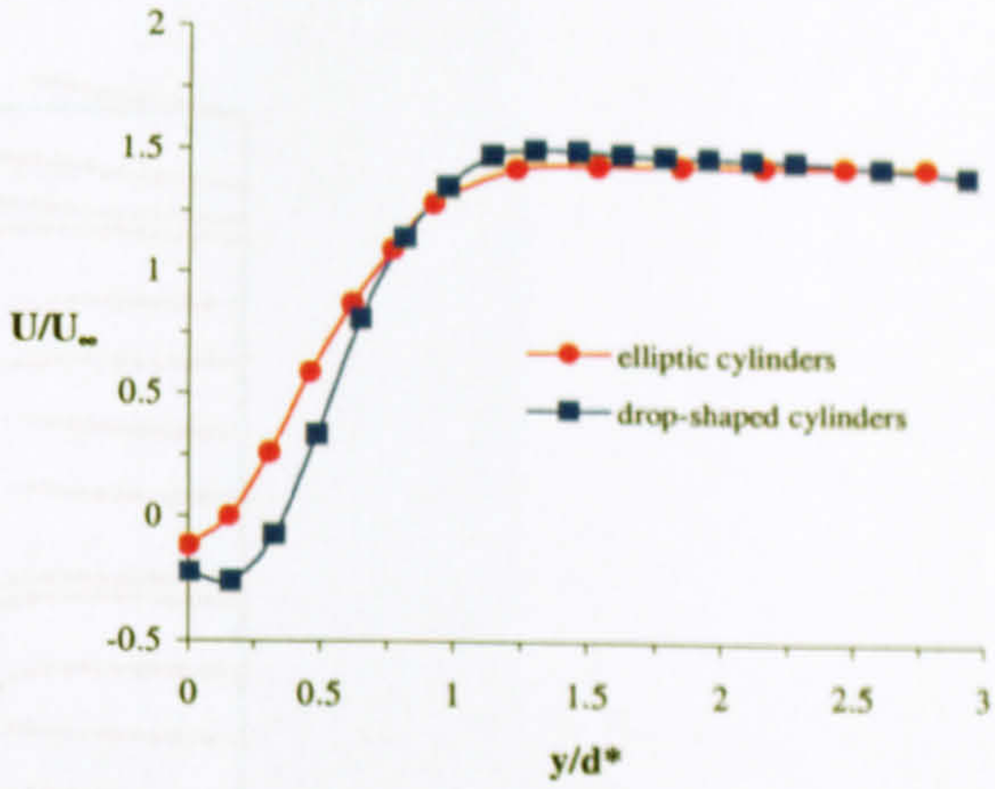

(b) - behind the 2nd row
- $x\backslash S_L = 1.35$
- $x\backslash S_L = 1.50$

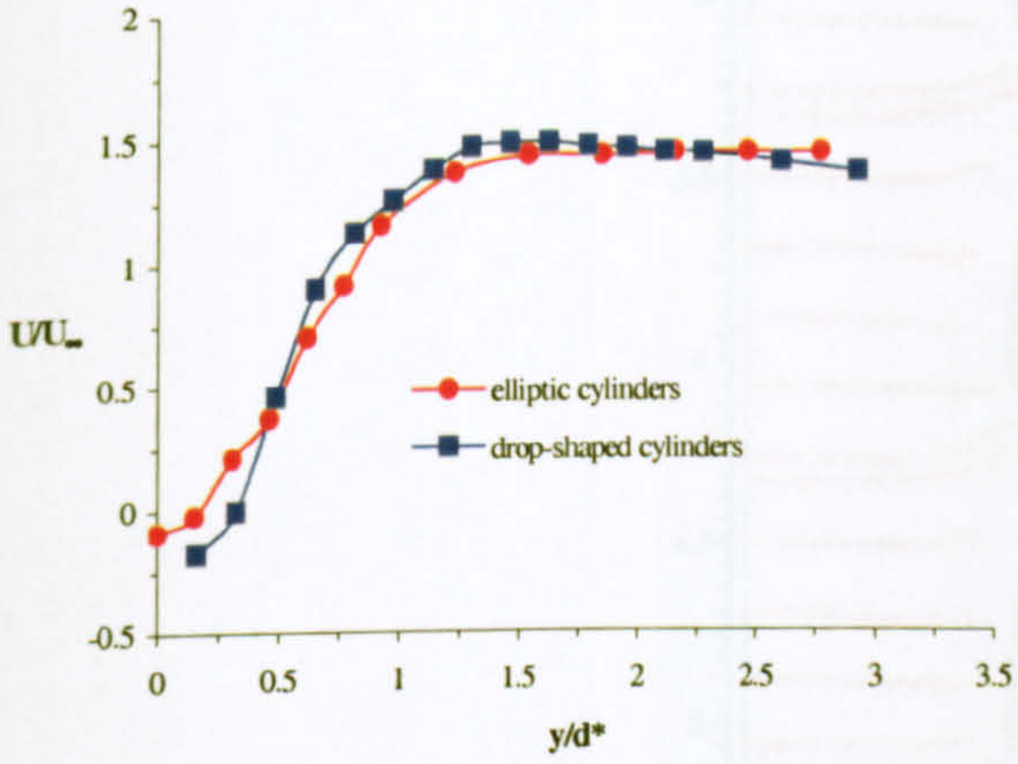

(c) - behind the 3rd row
- $x\backslash S_L = 2.35$
- $x\backslash S_L = 2.50$

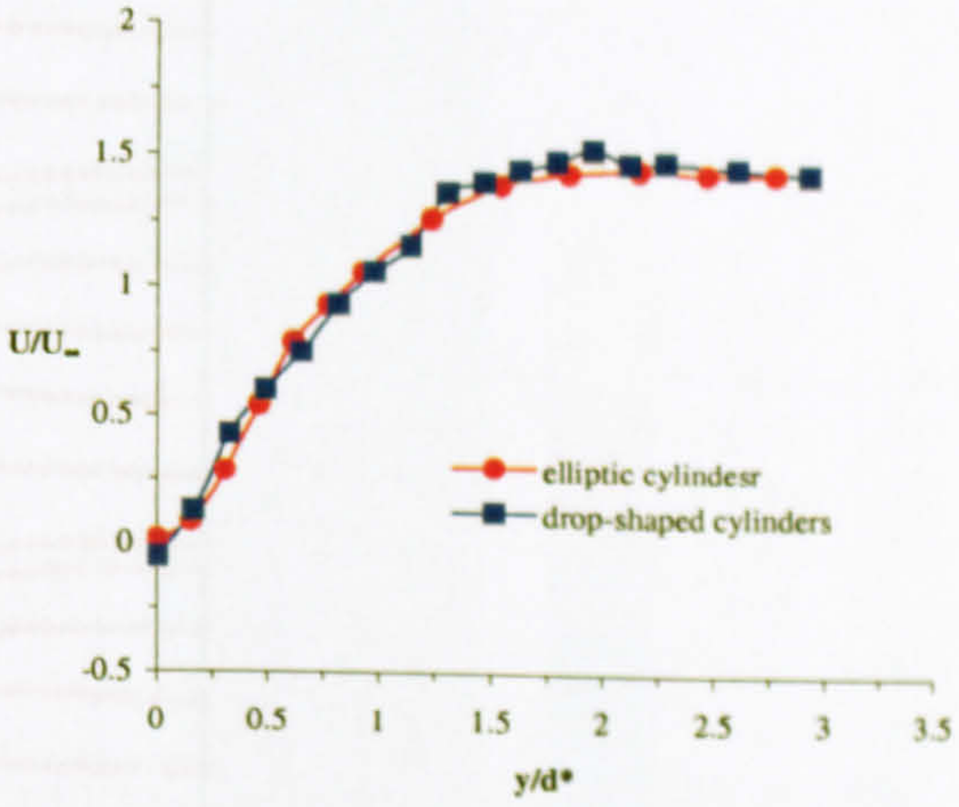

(d) - behind the 4th row
- $x\backslash S_L = 3.35$
- $x\backslash S_L = 3.50$

Figure 5.4. Comparison of the U/U_∞ profiles between the in-line array with drop-shaped cylinders and the one with elliptic ones (steady flow).

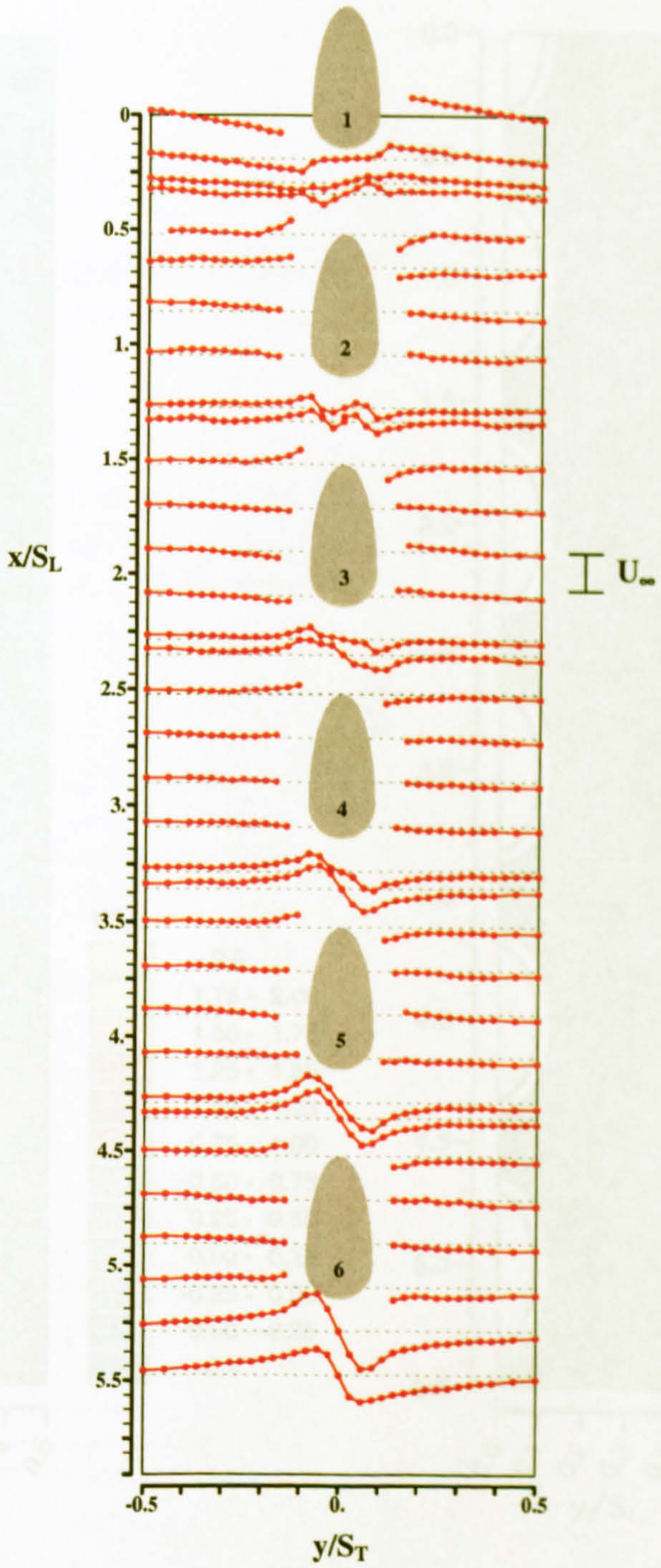

Figure 5.5. Distribution of the radial mean velocity, V/U_∞ in the in-line bundle with drop-shaped cylinders (steady flow, Re = 6,300).

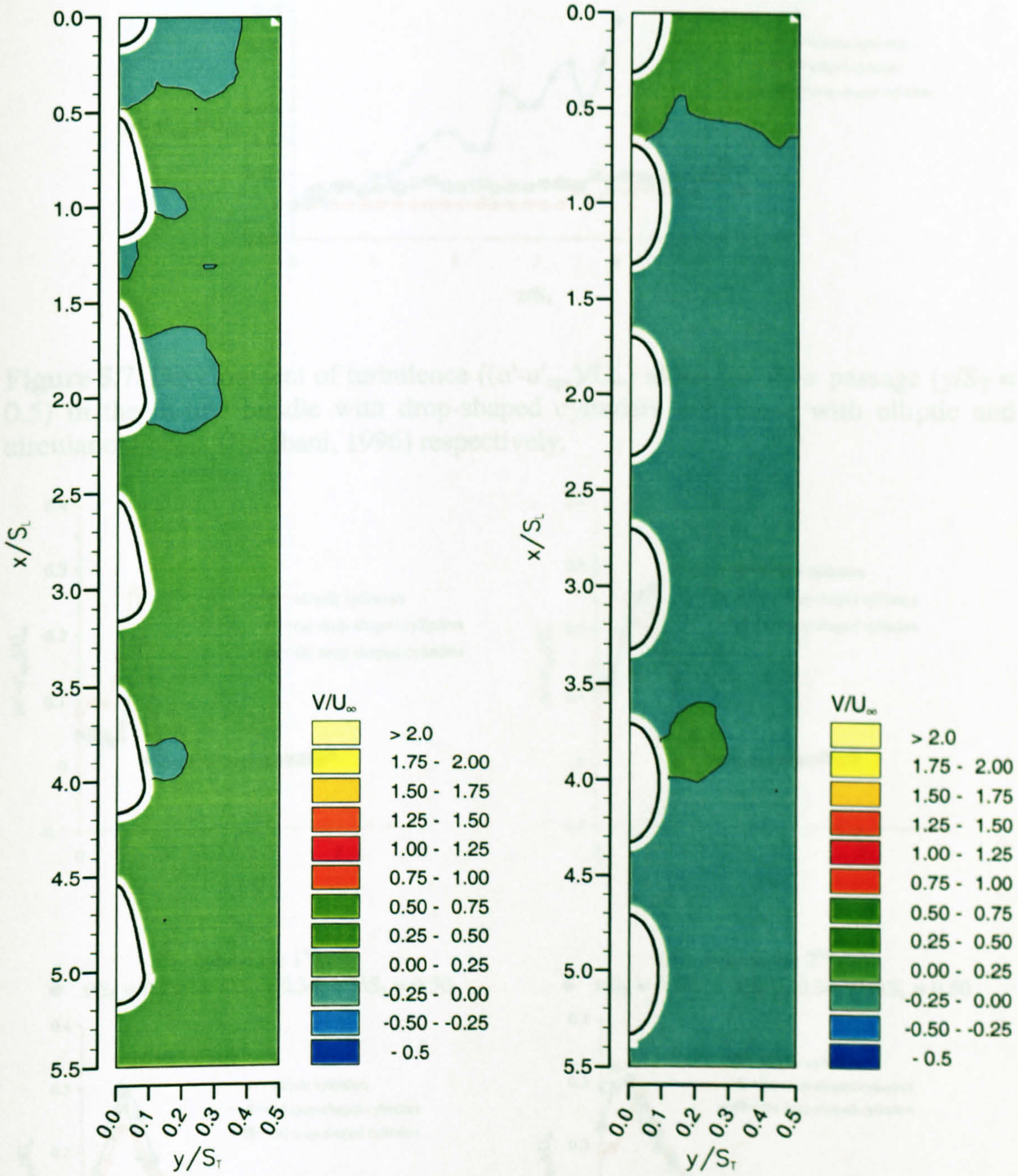

Figure 5.6. Comparison of the radial mean velocity profiles, V/U_∞, between the in-line array with drop-shaped cylinders and the one with elliptic ones (steady flow).

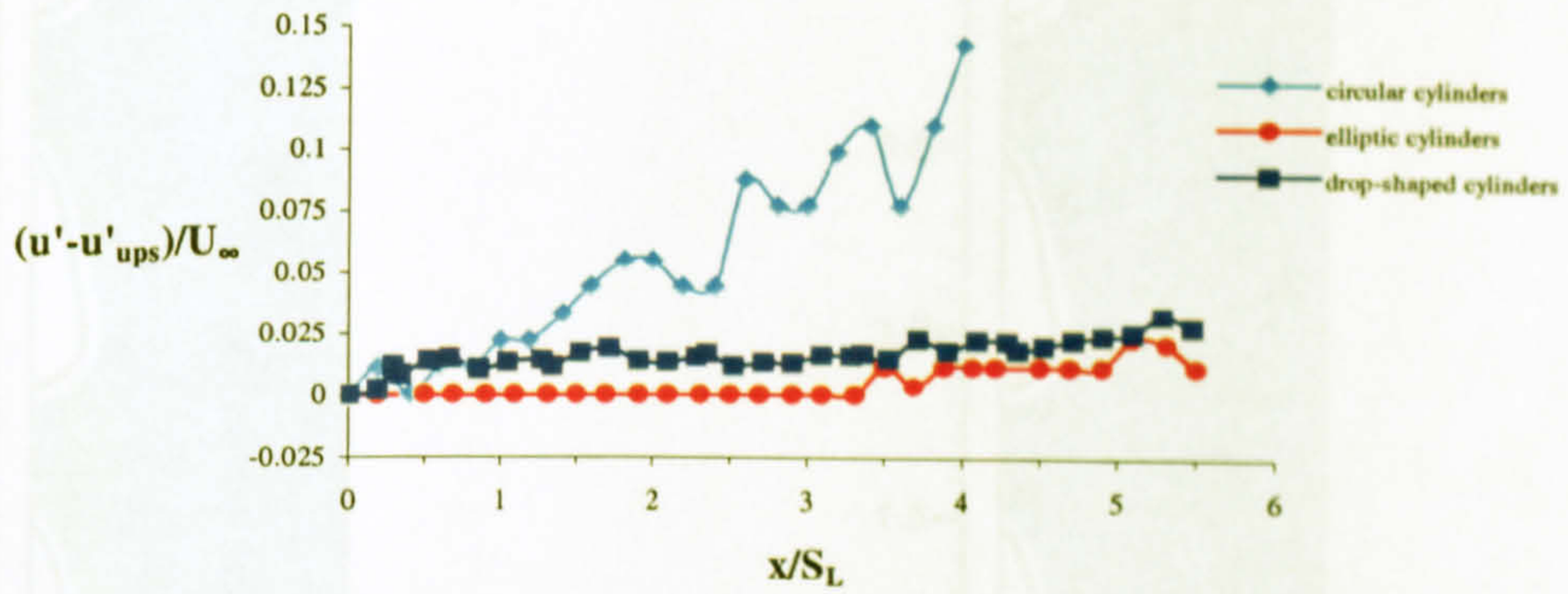

Figure 5.7. Development of turbulence ($(u'-u'_{ups})/U_\infty$) along the flow passage (y/S_T = 0.5) in the in-line bundle with drop-shaped cylinders and those with elliptic and circular cylinders (Balabani, 1996) respectively.

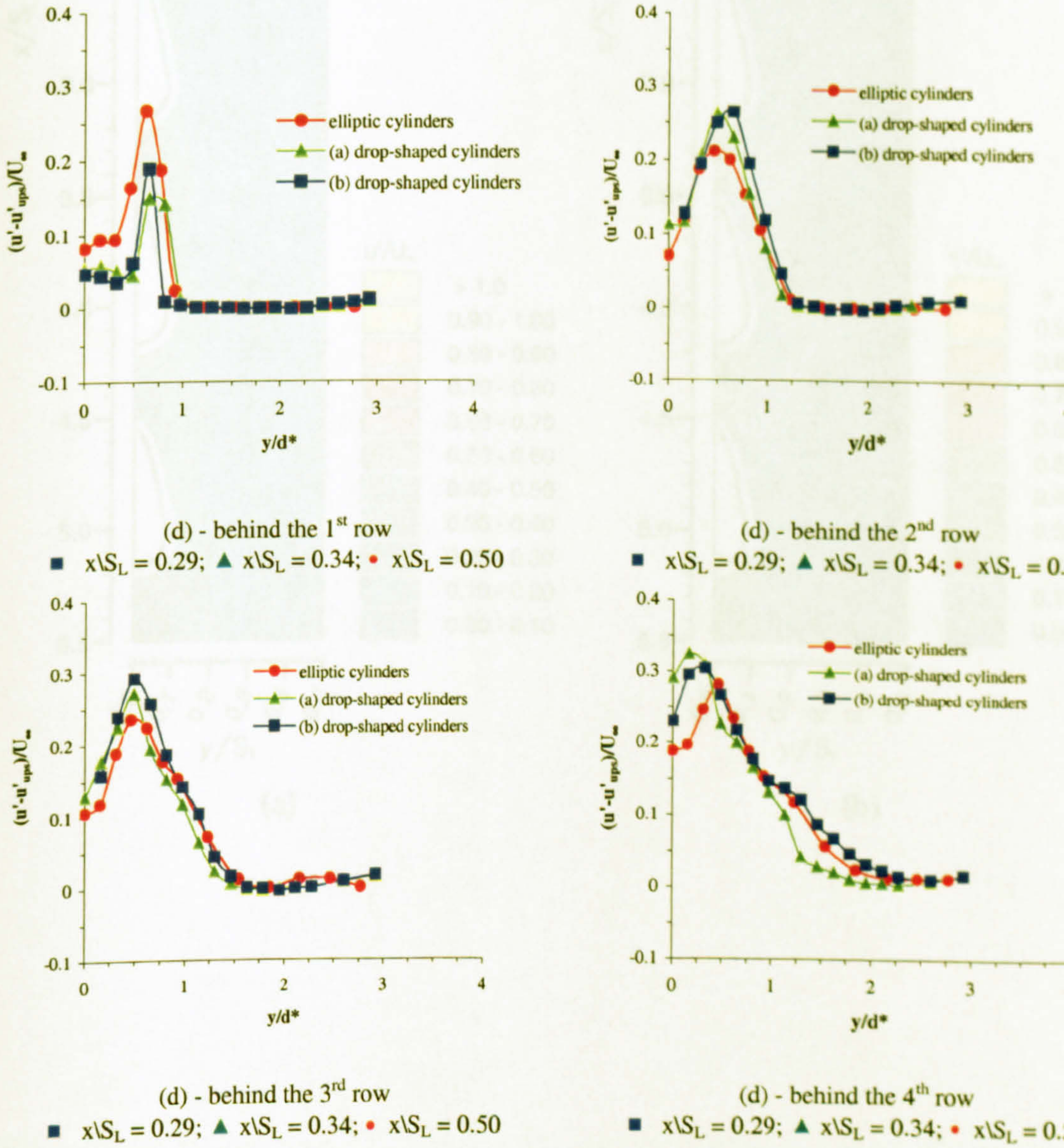

Figure 5.8. Comparison of the axial r.m.s. velocity profiles ($(u'-u'_{ups})/U_\infty$) between the in-line bundle with drop-shaped cylinders and the one with elliptic cylinders (Balabani, 1996).

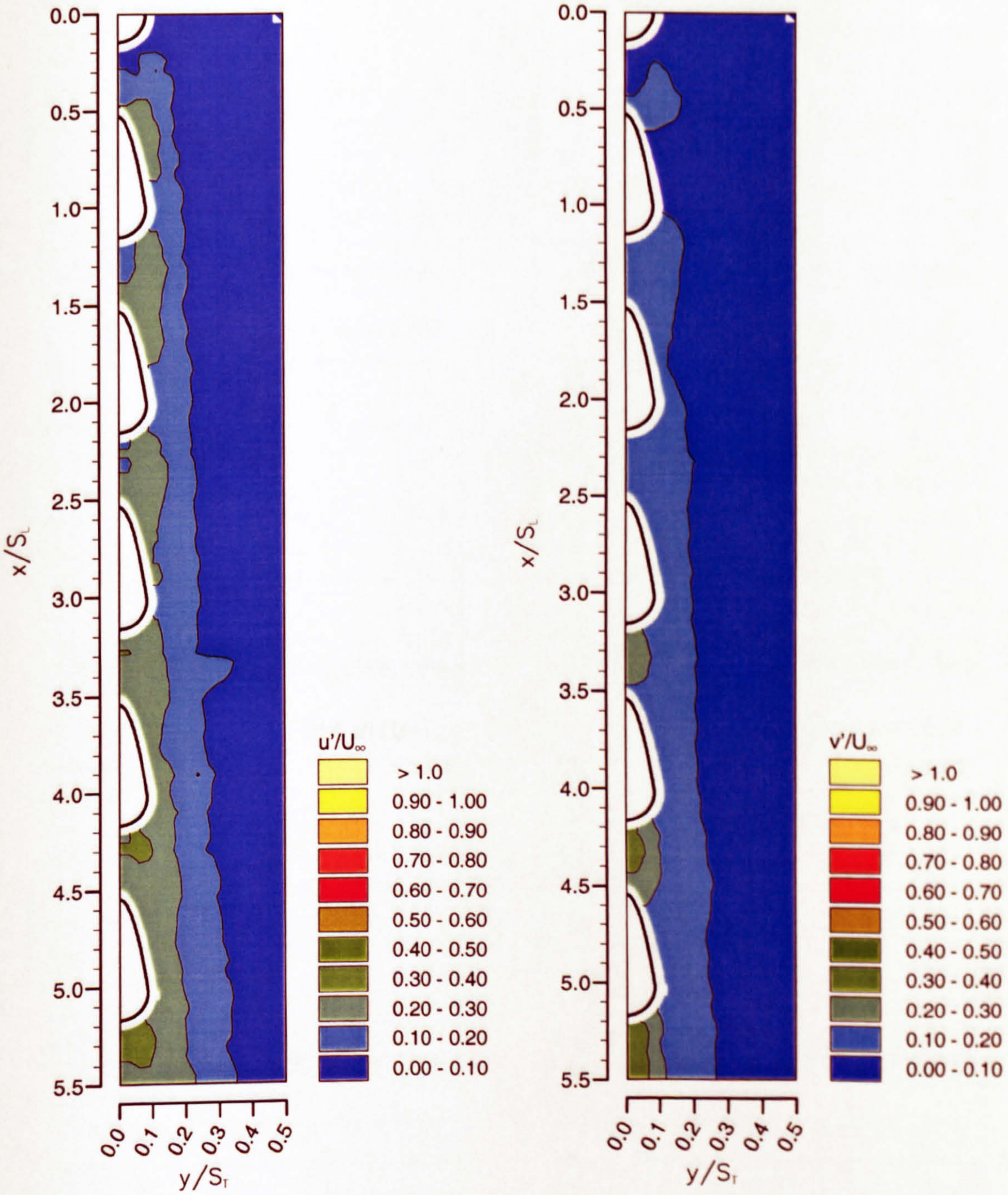

Figure 5.9. Distribution of u'/U_∞, (a), and v'/U_∞, (b), in the in-line bundle with drop-shaped cylinders (steady flow, Re = 6,300).

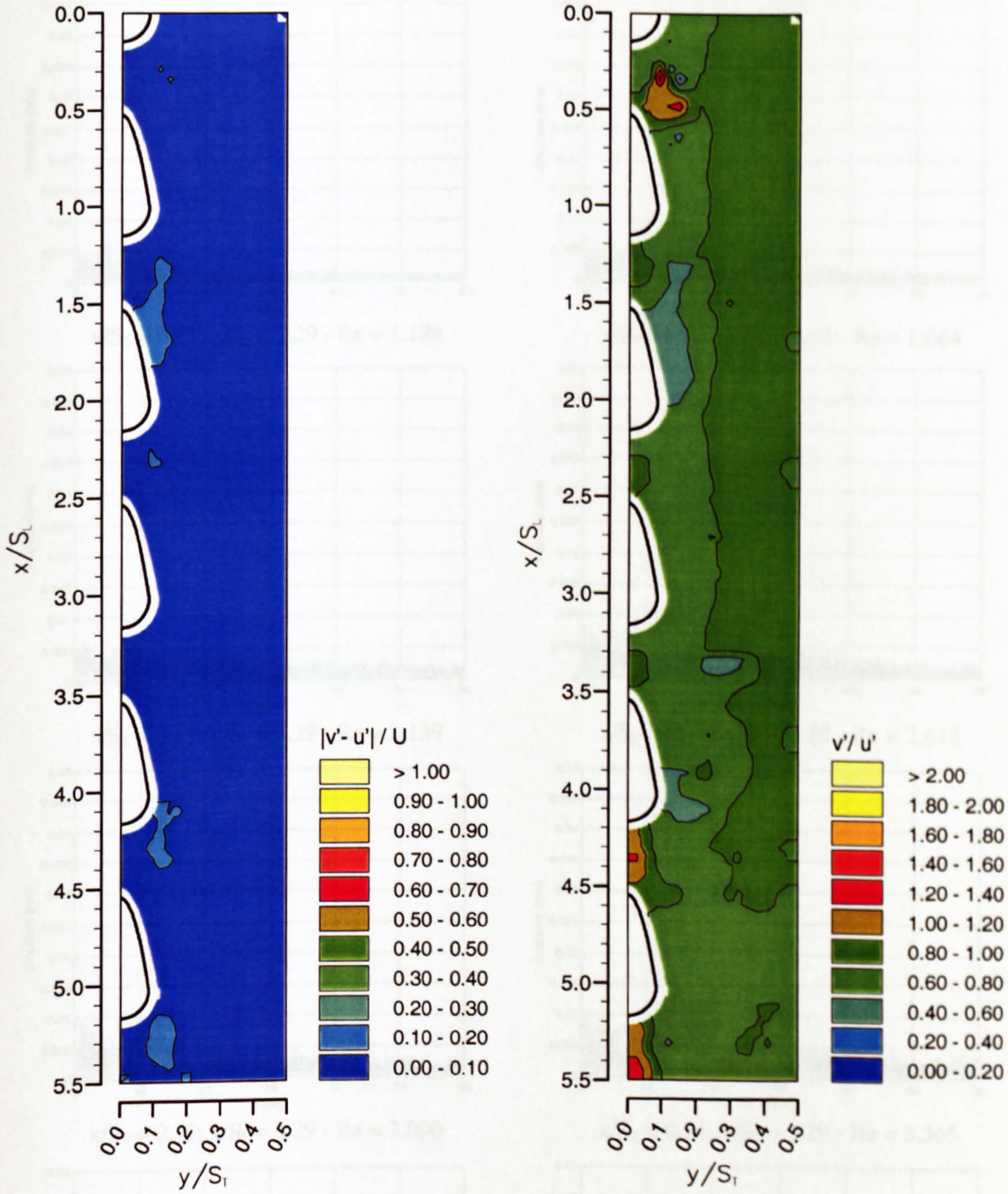

Figure 5.10. Distribution of $| v' - u' | /U_\infty$ and $(v'/u')/U_\infty$ in the in-line bundle with drop-shaped cylinders (steady flow, Re = 6,300).

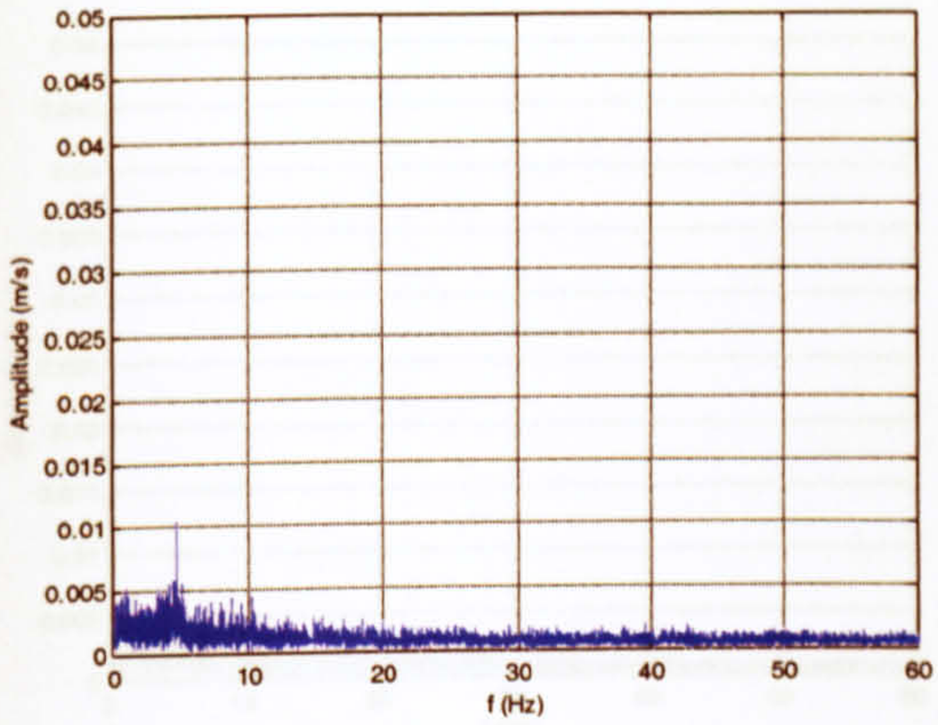

$x/S_T = 0.11$; $x/S_L = 3.29$ - Re = 1,188

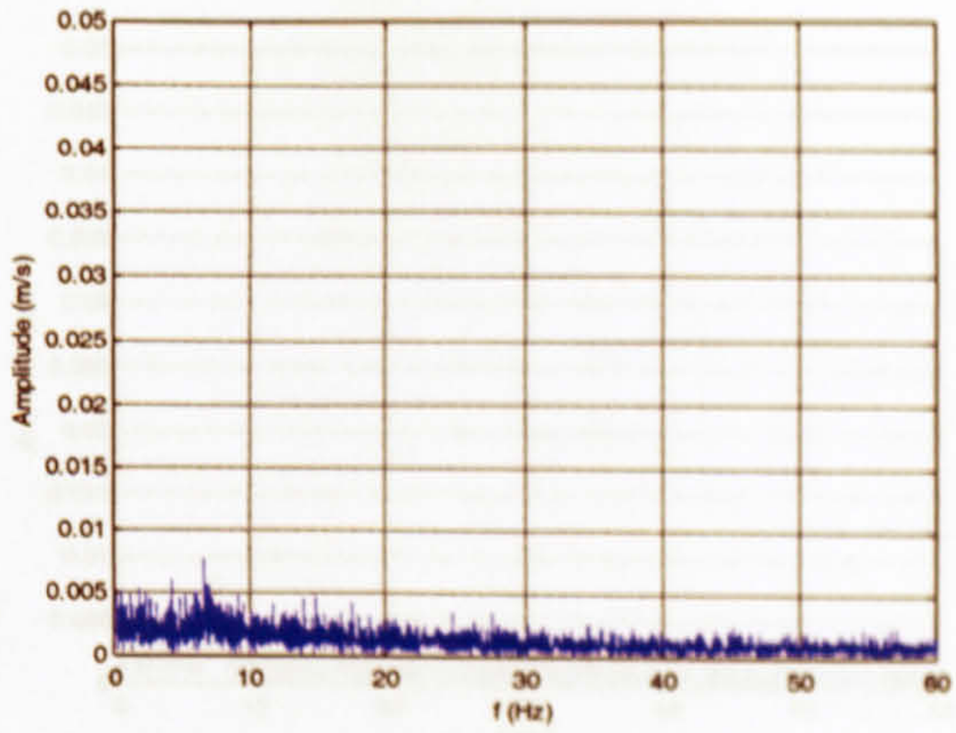

$x/S_T = 0.11$; $x/S_L = 3.29$ - Re = 1,664

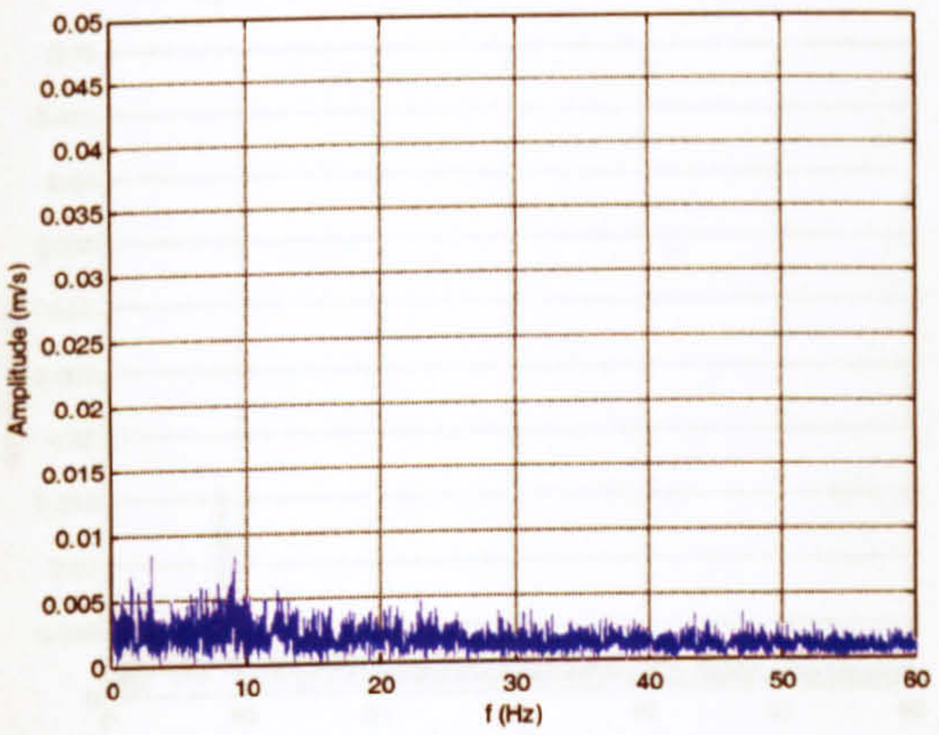

$x/S_T = 0.11$; $x/S_L = 3.29$ - Re = 2,139

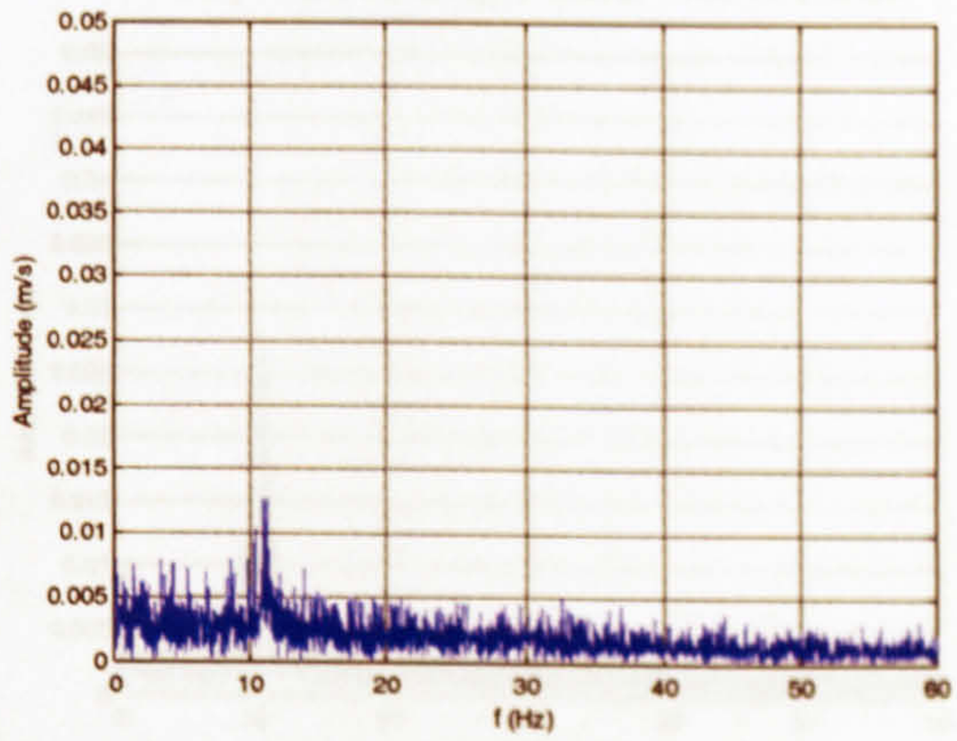

$x/S_T = 0.11$; $x/S_L = 3.29$ - Re = 2,614

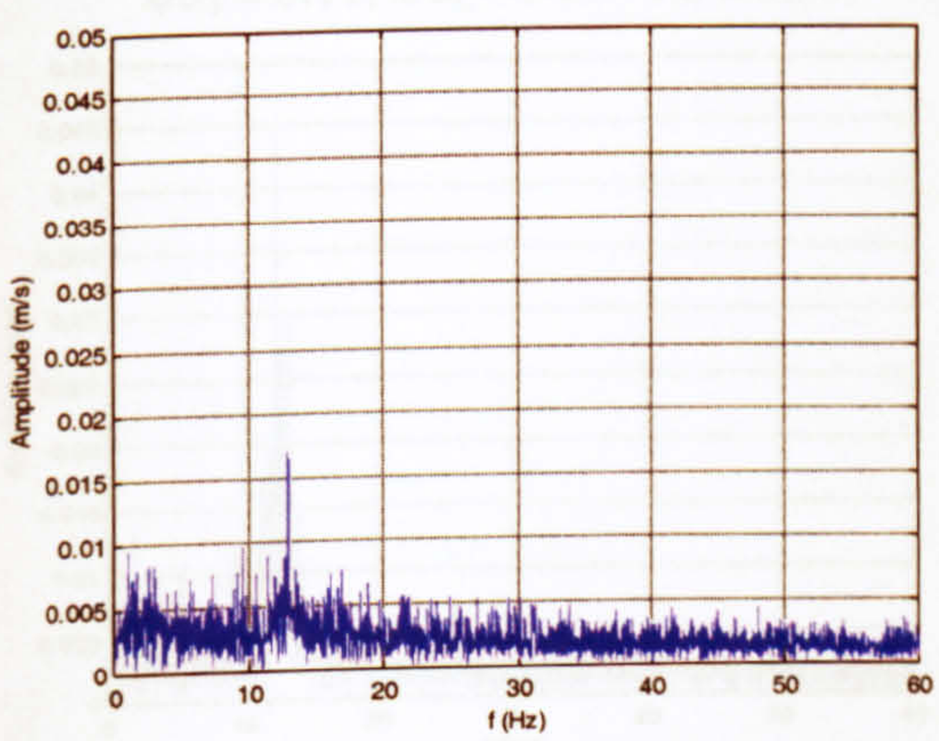

$x/S_T = 0.11$; $x/S_L = 3.29$ - Re = 3,090

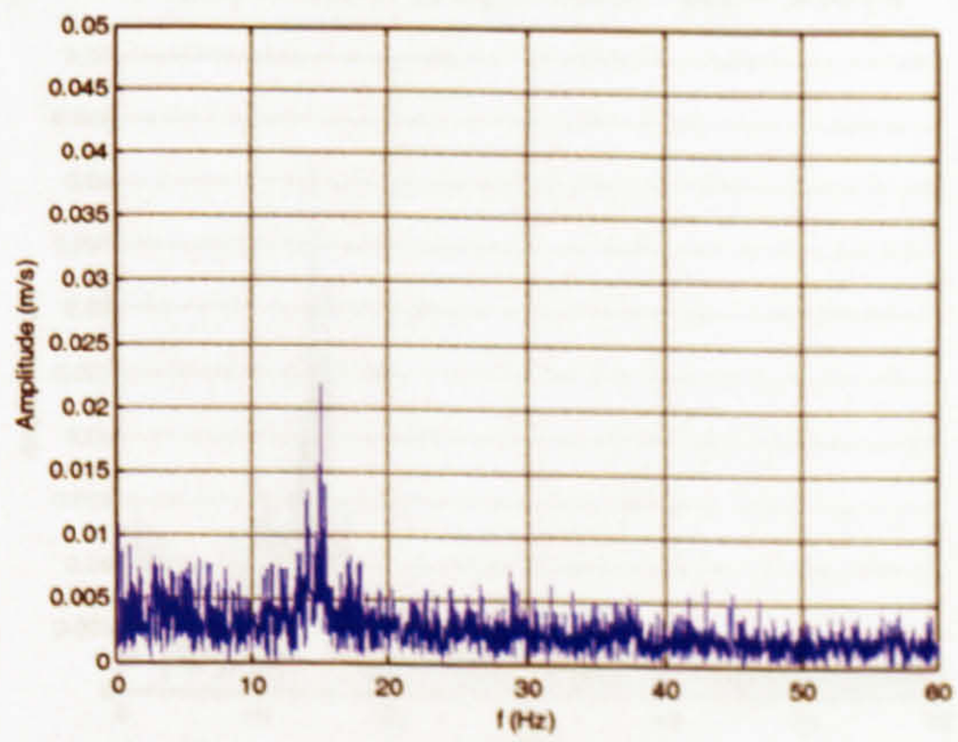

$x/S_T = 0.11$; $x/S_L = 3.29$ - Re = 3,565

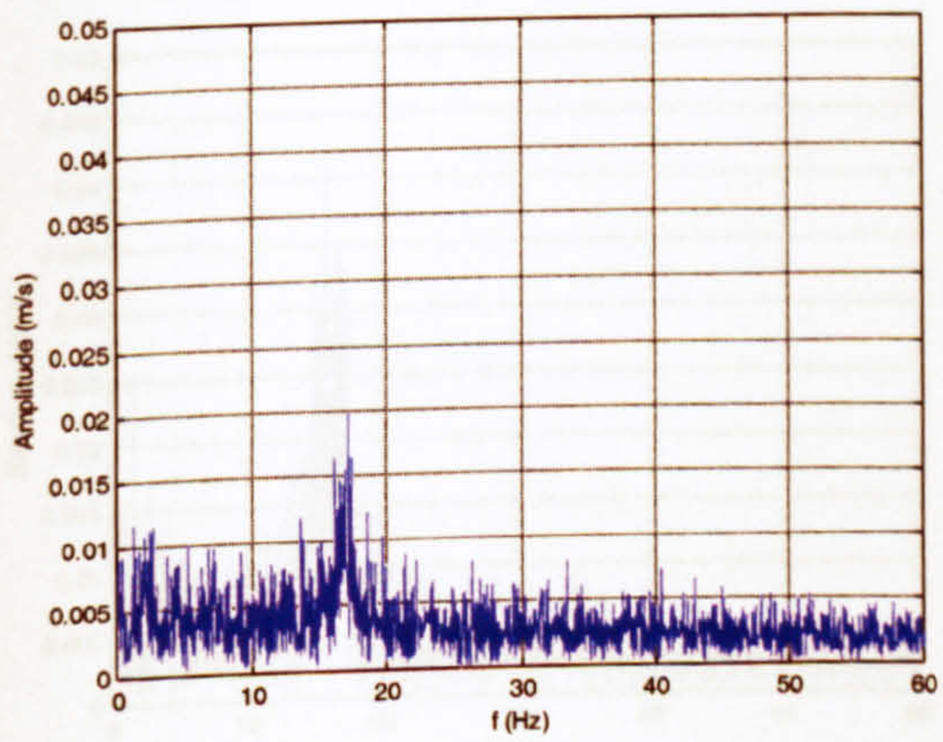

$x/S_T = 0.11$; $x/S_L = 3.29$ - Re = 4,040

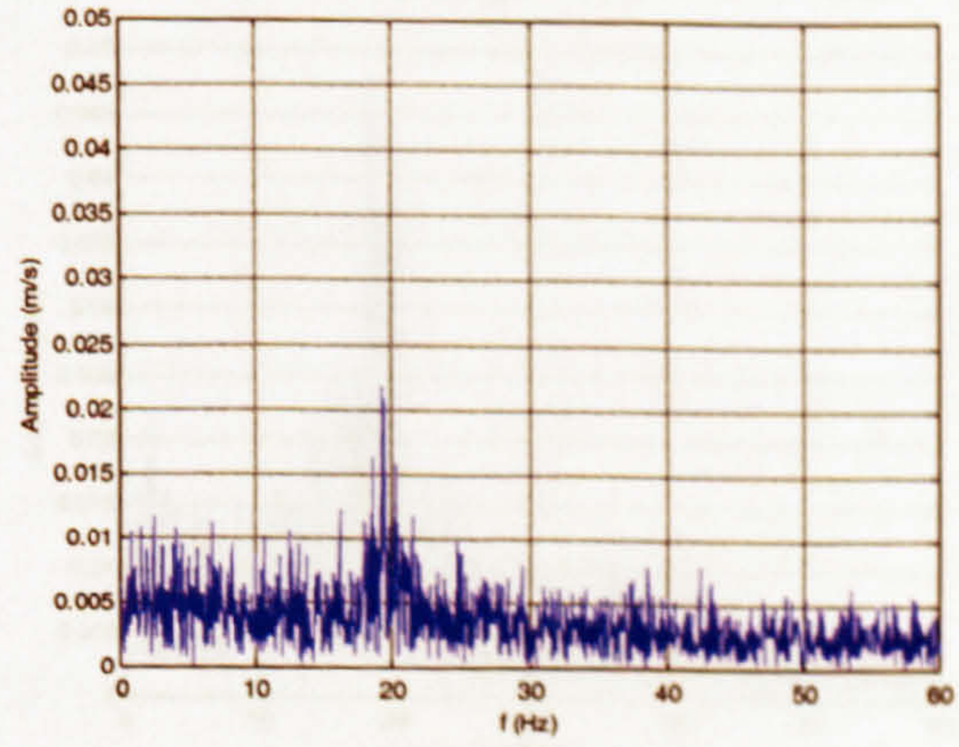

$x/S_T = 0.11$; $x/S_L = 3.29$ - Re = 4,753

Figure 5.11. Amplitude spectra behind the fourth row in the in-line bundle with drop-shaped cylinders for various Re (steady flow).

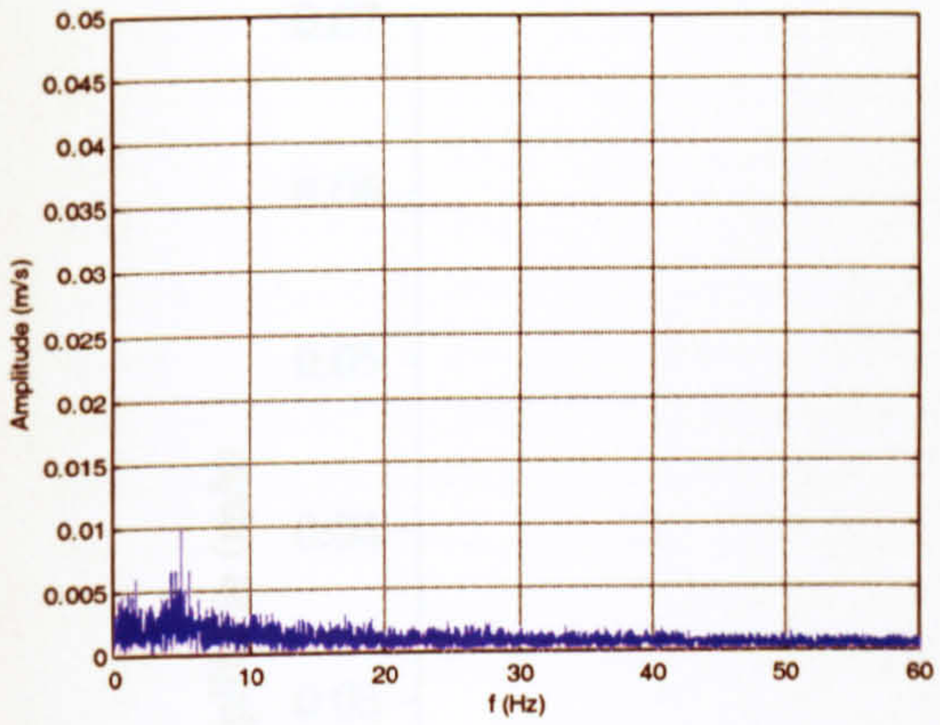

$x/S_T = 0.11$; $x/S_L = 5.28$ - Re = 1,188

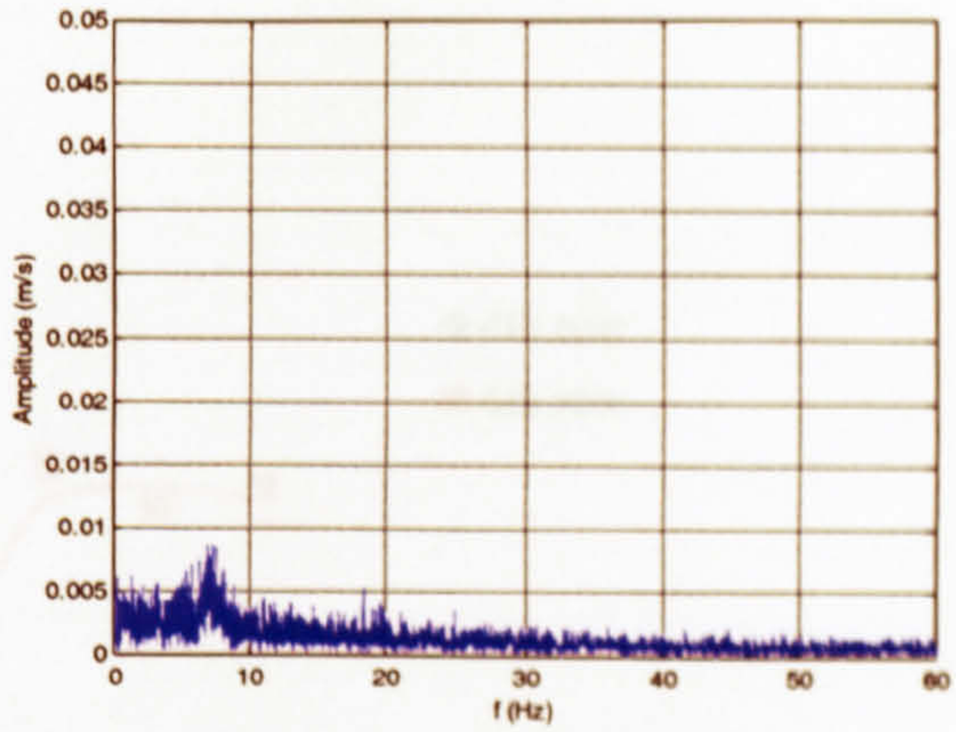

$x/S_T = 0.11$; $x/S_L = 5.28$ - Re = 1,664

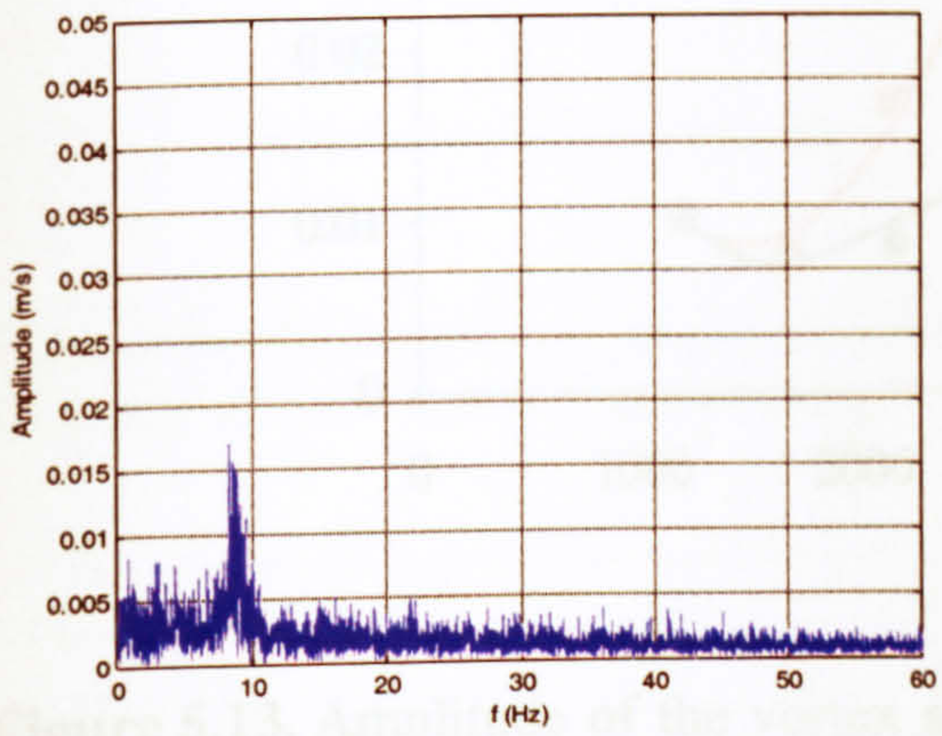

$x/S_T = 0.11$; $x/S_L = 5.28$ - Re = 2,139

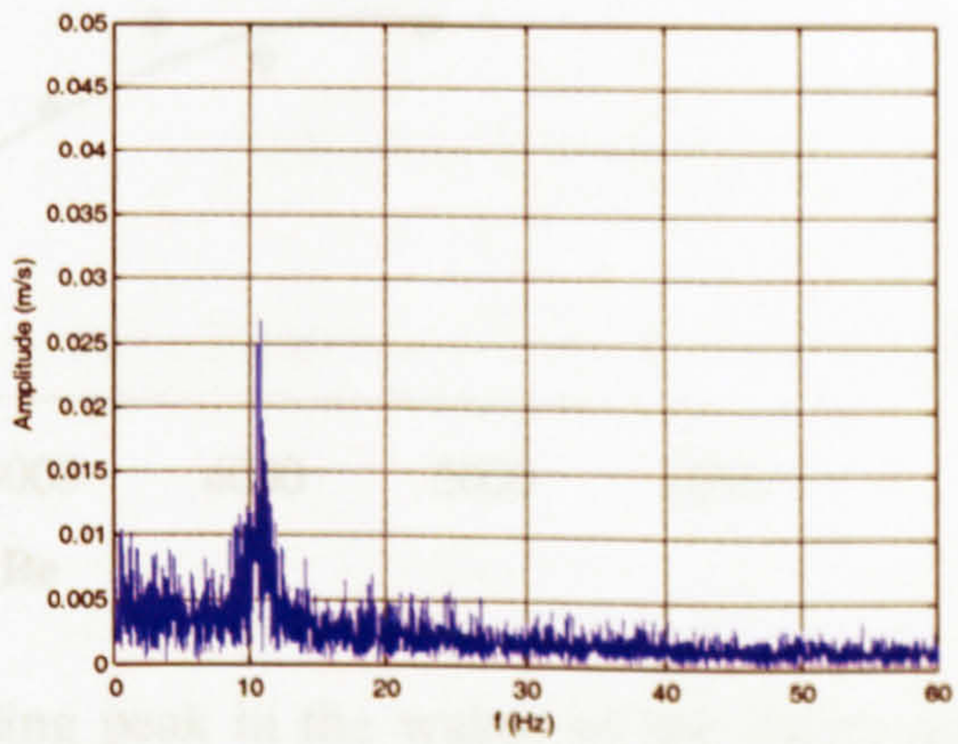

$x/S_T = 0.11$; $x/S_L = 5.28$ - Re = 2,614

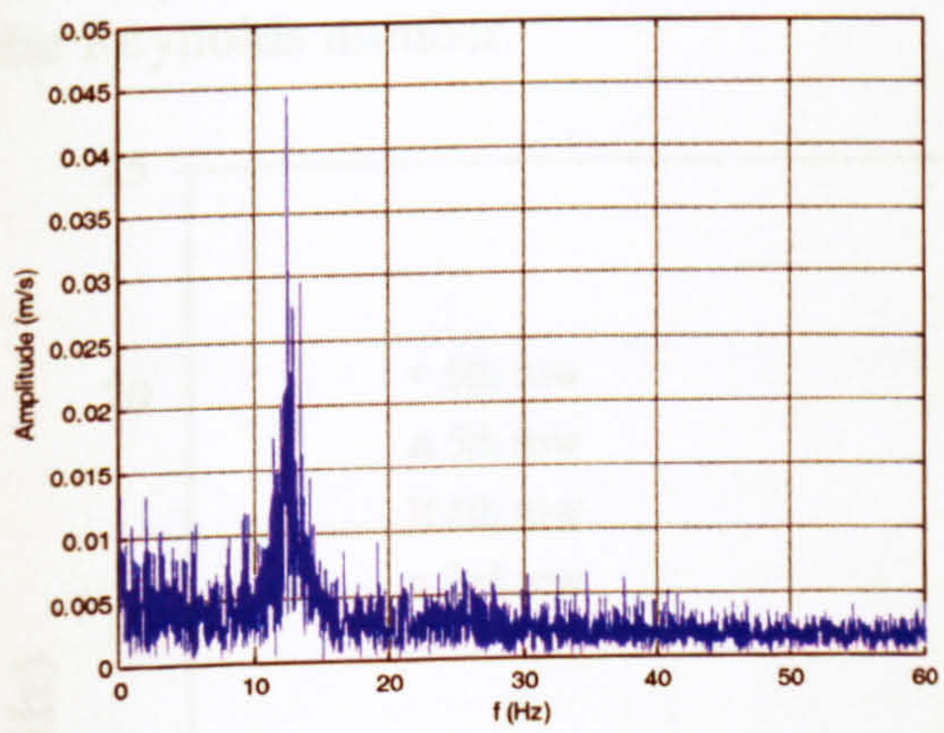

$x/S_T = 0.11$; $x/S_L = 5.28$ - Re = 3,090

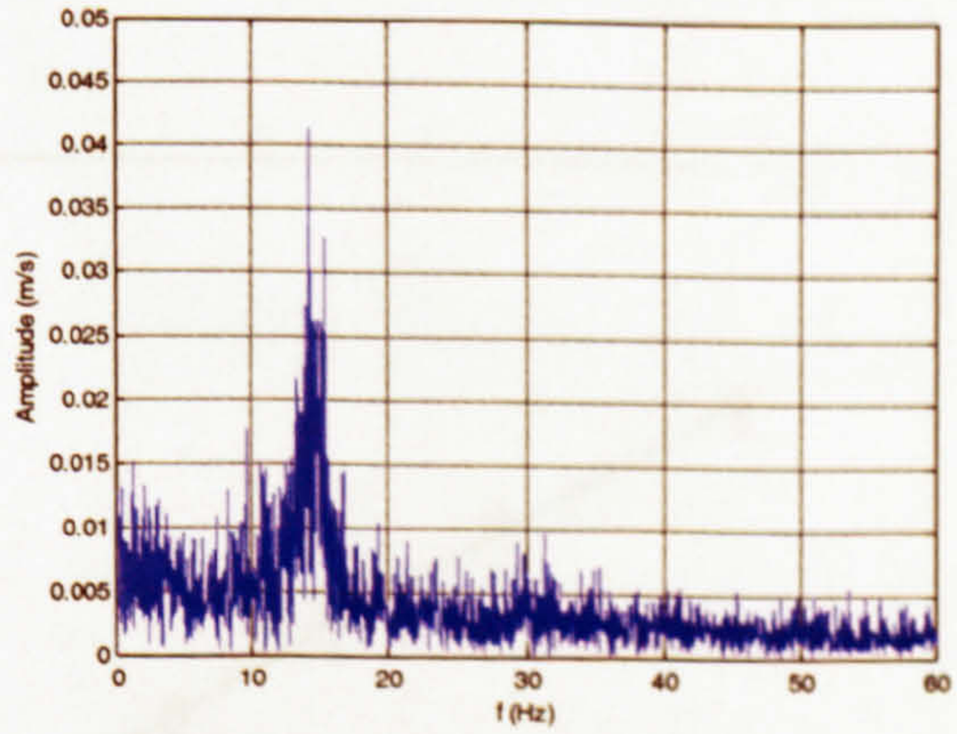

$x/S_T = 0.11$; $x/S_L = 5.28$ - Re = 3,565

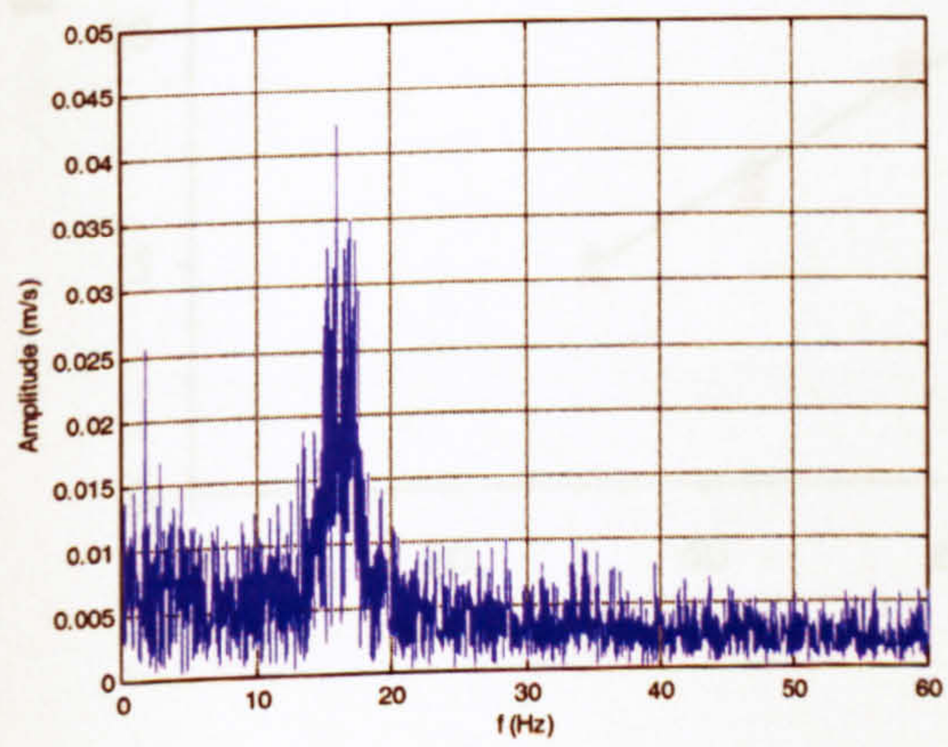

$x/S_T = 0.11$; $x/S_L = 5.28$ - Re = 4,040

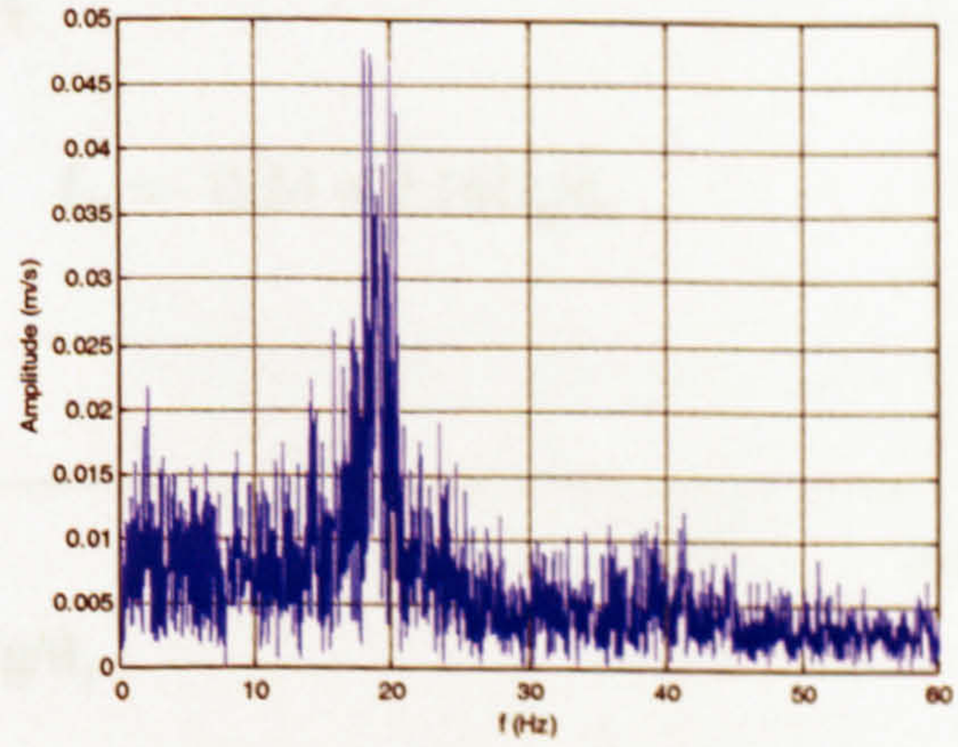

$x/S_T = 0.11$; $x/S_L = 5.28$ - Re = 4,753

Figure 5.12. Amplitude spectra behind the sixth row in the in-line bundle with drop-shaped cylinders for various Re (steady flow).

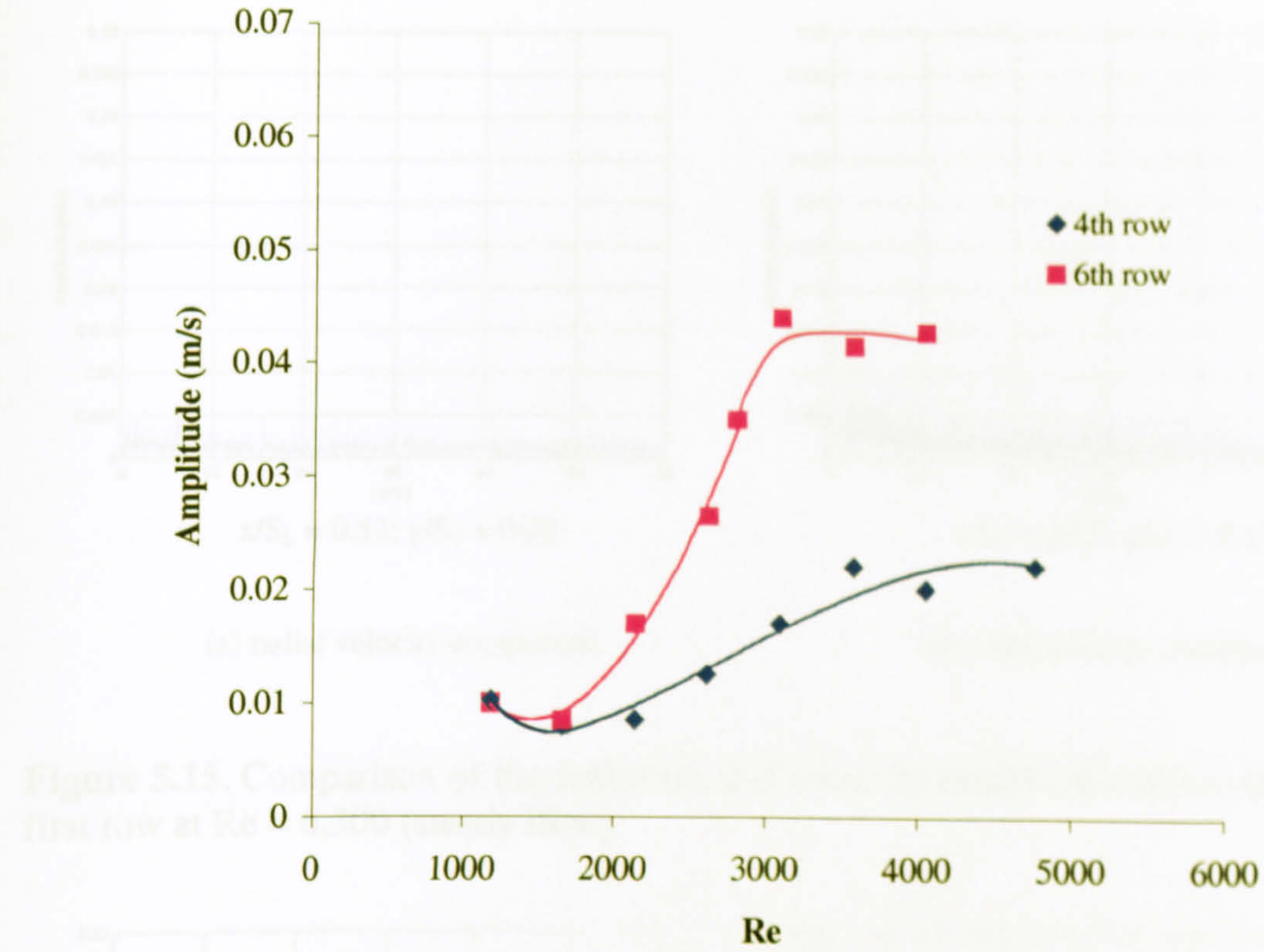

Figure 5.13. Amplitude of the vortex shedding peak in the wakes of the fourth and sixth cylinders ($x/S_L = 3.5$, $x/S_L = 4.5$ and $x/S_L = 5.5$, $y/S_T = 0.11$) as a function of the Reynolds number.

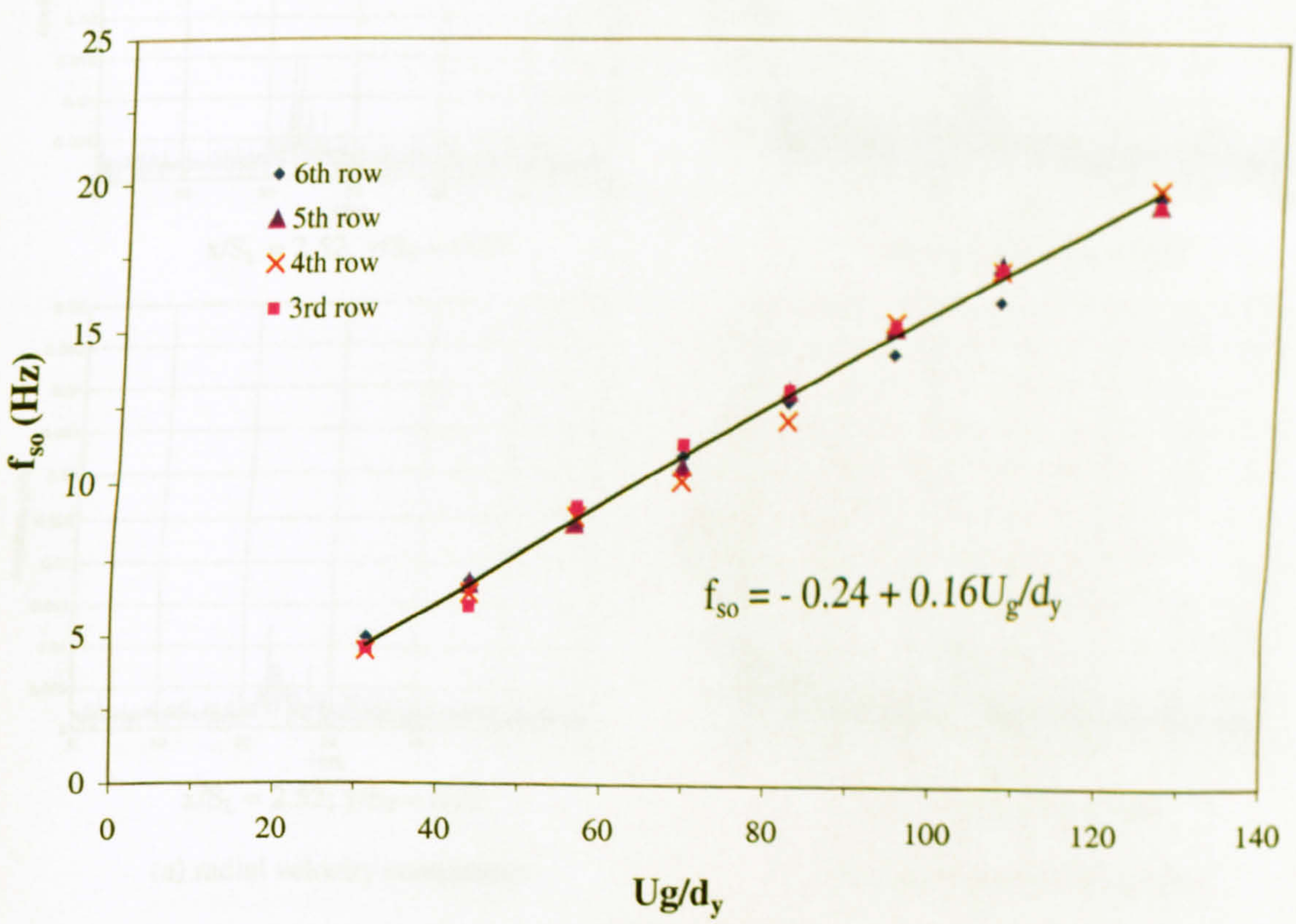

Figure 5.14. Natural vortex shedding frequency, f_{so}, as a function of U_g behind the third, fourth, fifth and sixth cylinders ($x/S_L = 2.5$, $x/S_L = 3.5$, $x/S_L = 4.5$ and $x/S_L = 3.5$, $y/S_T = 0.125$).

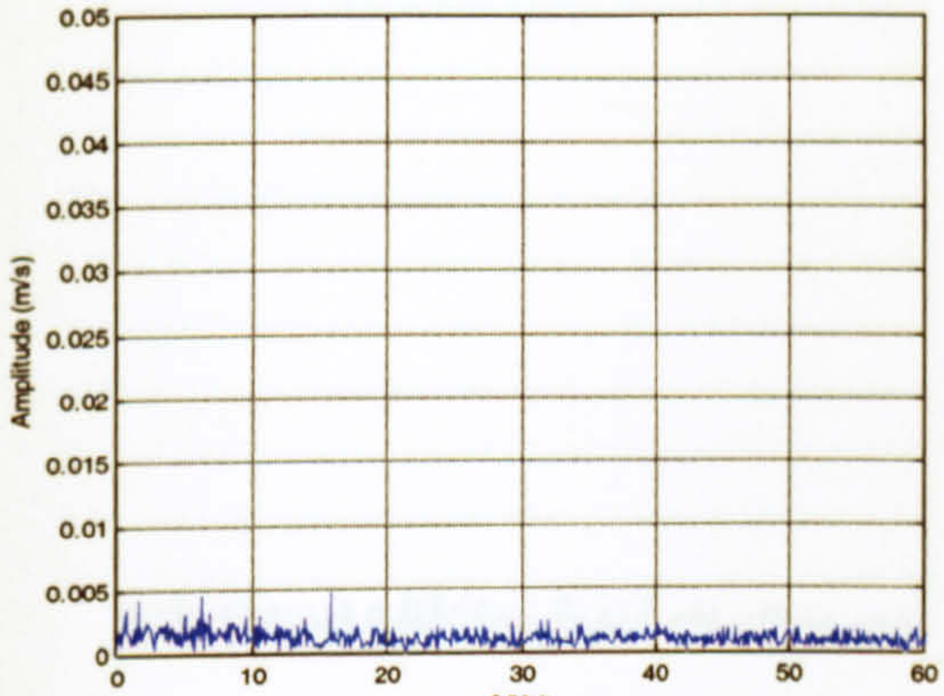

$x/S_L = 0.52$; $y/S_T = 0.22$

(a) radial velocity component

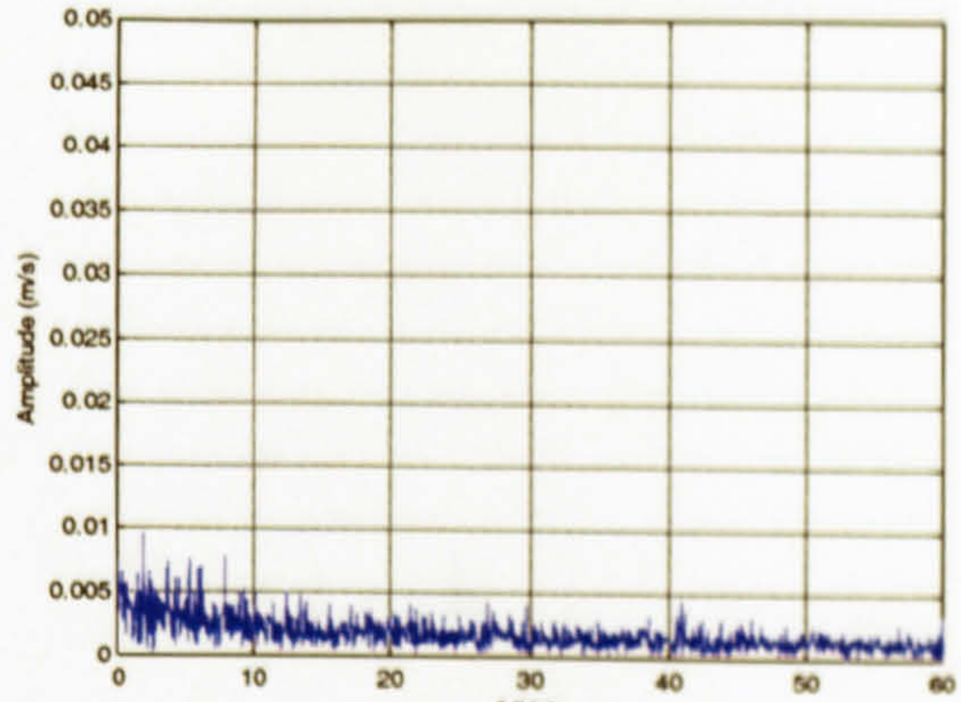

$x/S_L = 0.52$; $y/S_T = 0.22$

(b) axial velocity component

Figure 5.15. Comparison of the radial (a) and axial (b) amplitude spectra behind the first row at Re = 6,300 (steady flow).

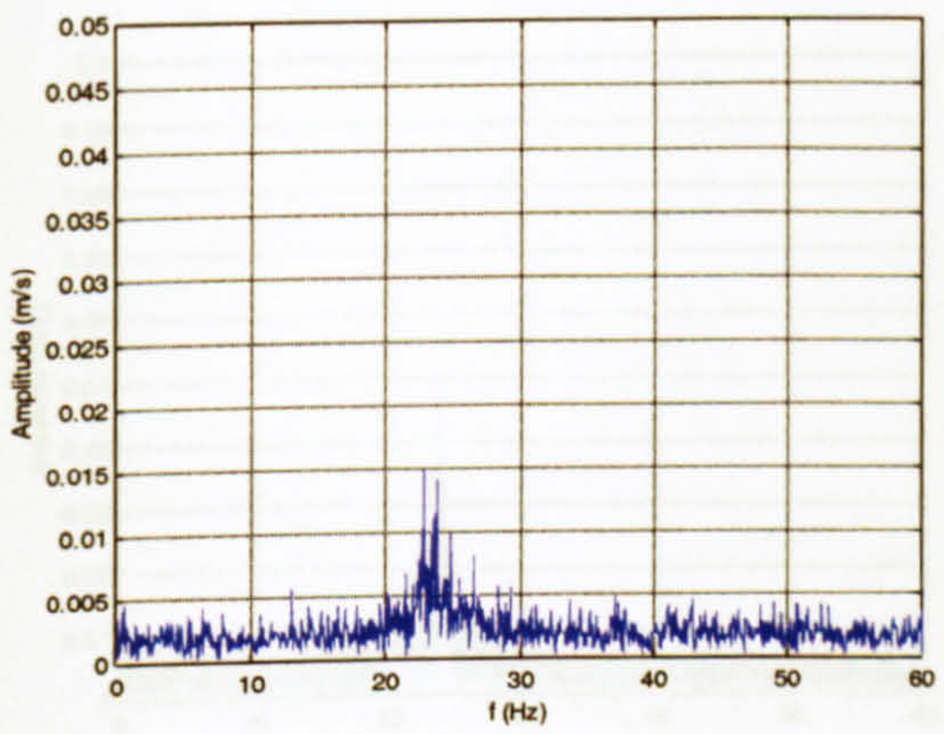

$x/S_L = 2.52$; $y/S_T = 0.19$

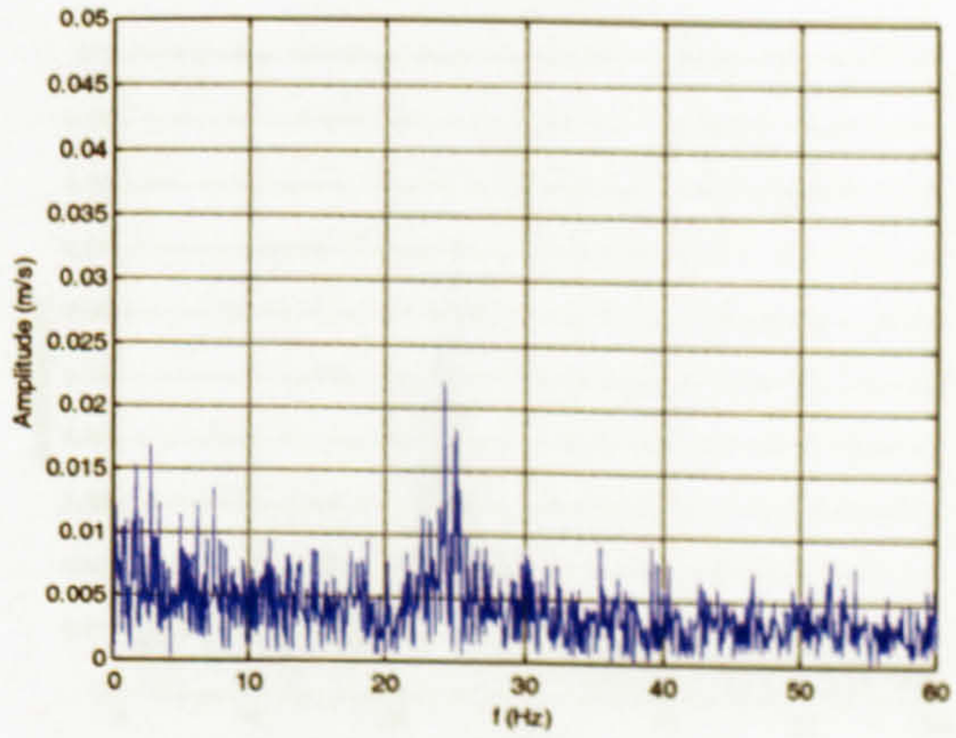

$x/S_L = 2.52$; $y/S_T = 0.19$

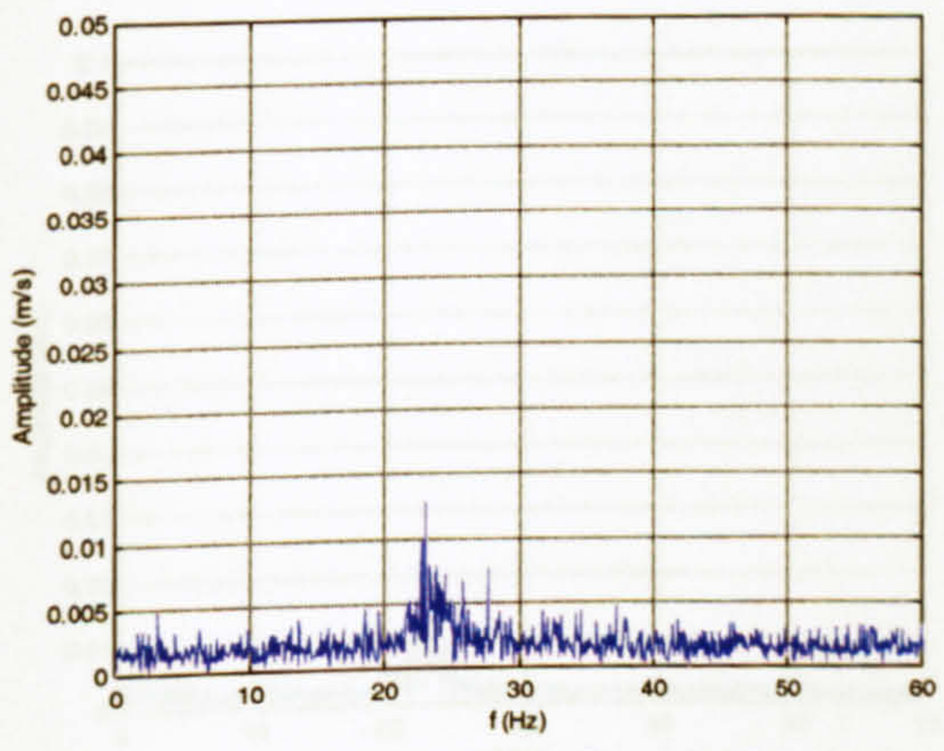

$x/S_L = 2.52$; $y/S_T = 0.22$

(a) radial velocity component

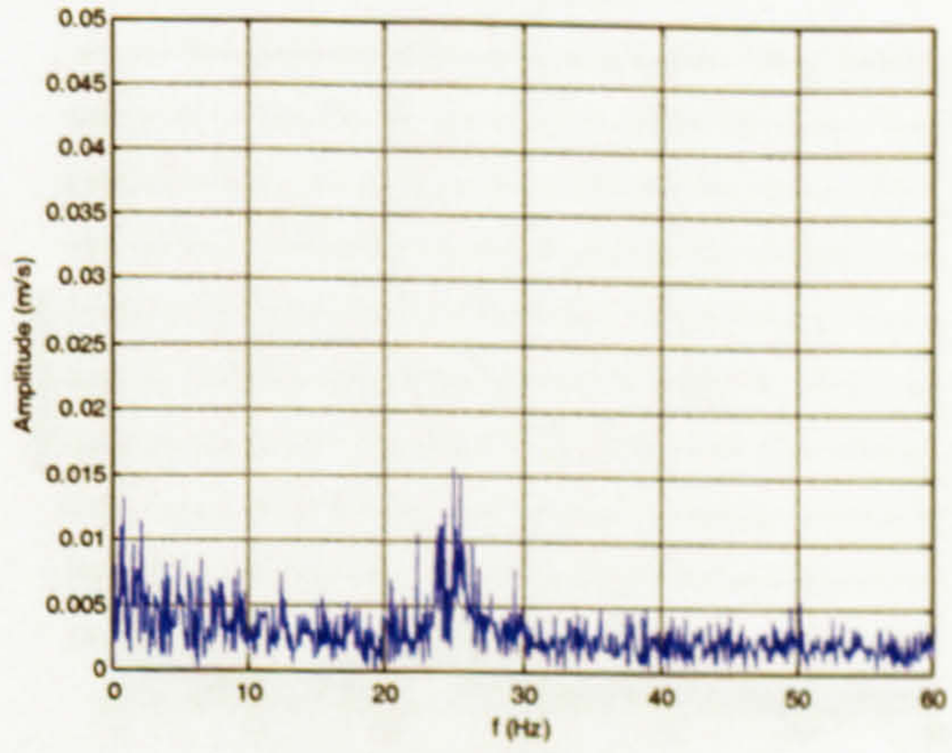

$x/S_L = 2.52$; $y/S_T = 0.22$

(b) axial velocity component

For caption see next page

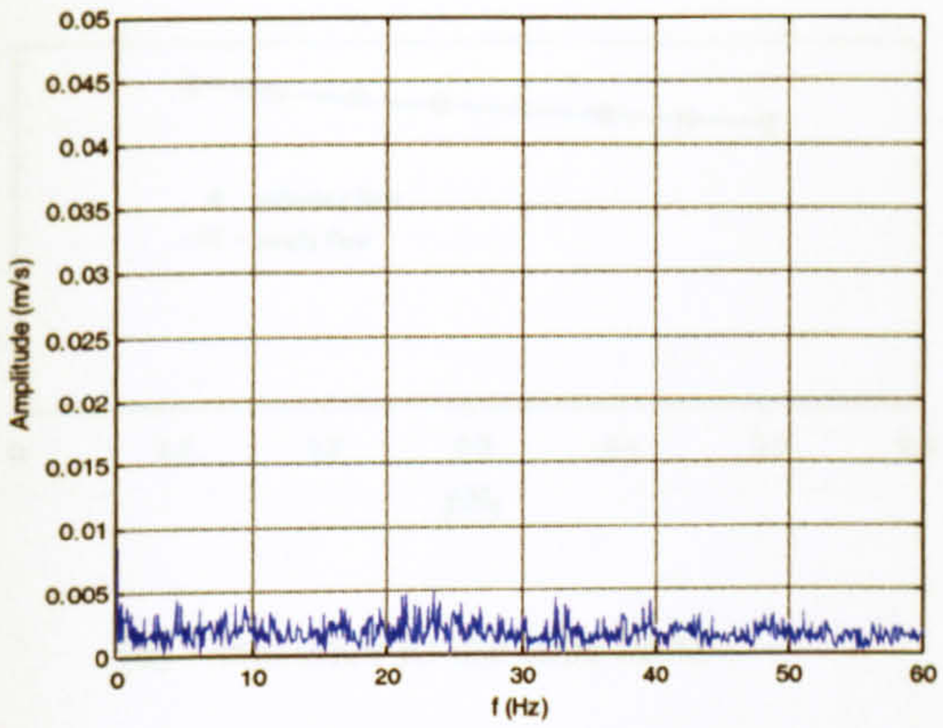

$x/S_L = 2.52$; $y/S_T = 0.36$

(a) radial velocity component

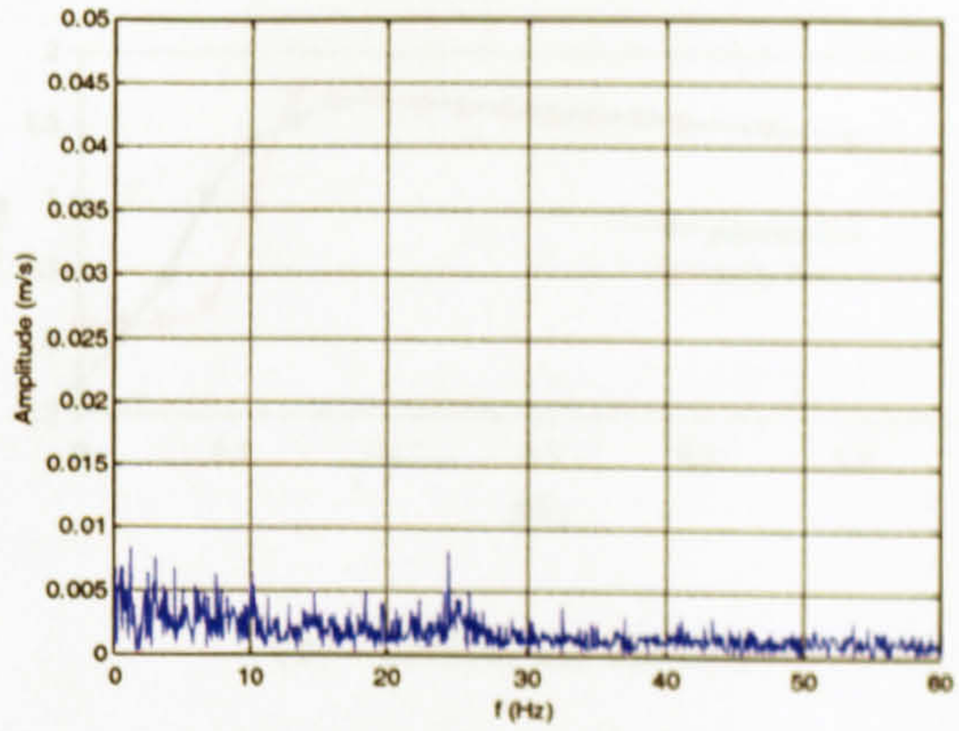

$x/S_L = 2.52$; $y/S_T = 0.36$

(b) axial velocity component

Figure 5.16. Comparison of the radial (a) and axial (b) amplitude spectra behind the third row at Re = 6,300 (steady flow).

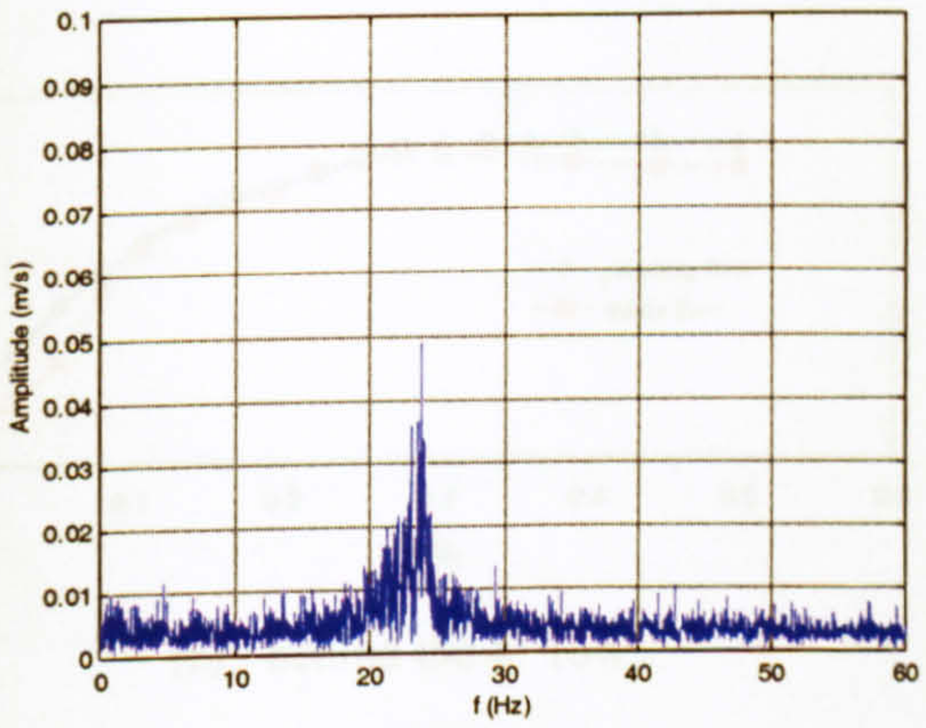

$x/S_L = 5.48$; $y/S_T = 0.11$

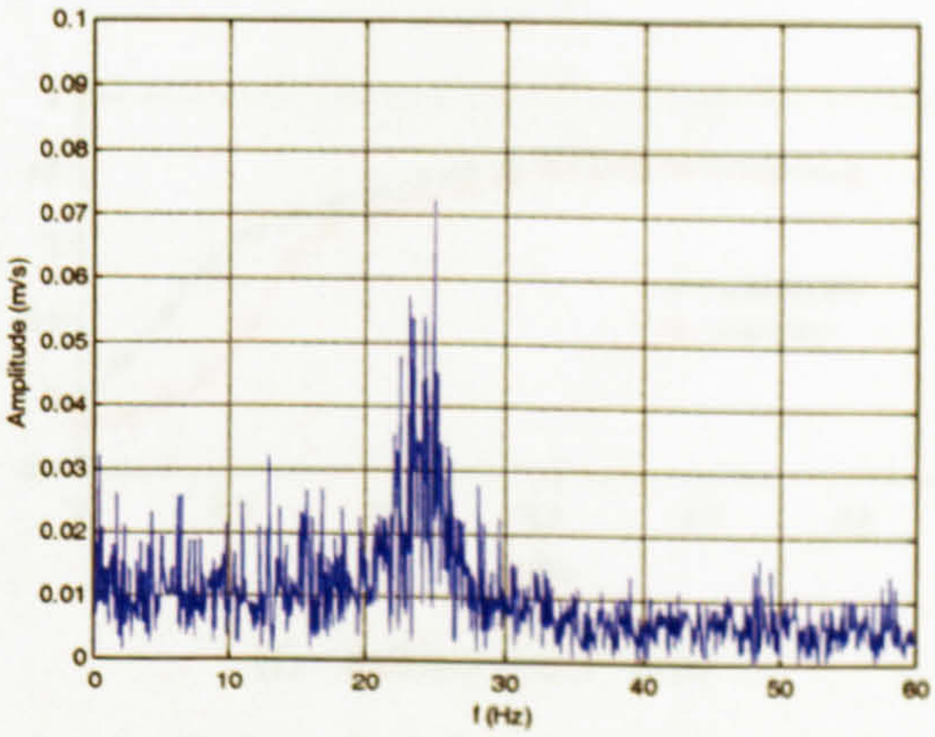

$x/S_L = 5.48$; $y/S_T = 0.11$

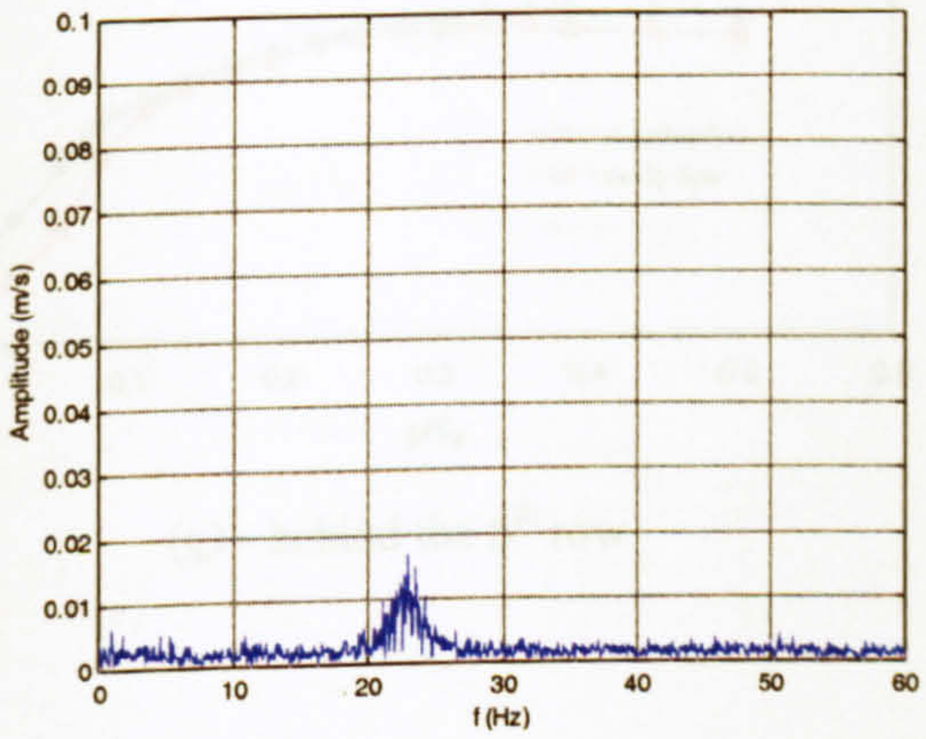

$x/S_L = 5.48$; $y/S_T = 0.33$

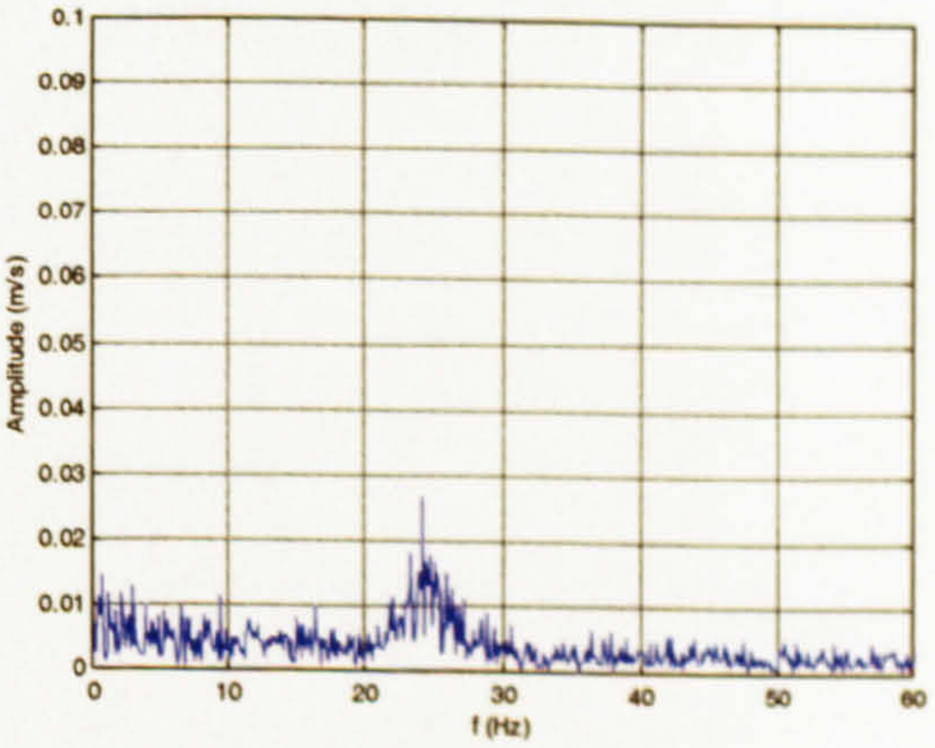

$x/S_L = 5.48$; $y/S_T = 0.33$

(a) radial velocity component

(b) axial velocity component

Figure 5.17. Comparison of the radial (a) and axial (b) amplitude spectra behind the sixth row at Re = 6,300 (steady flow).

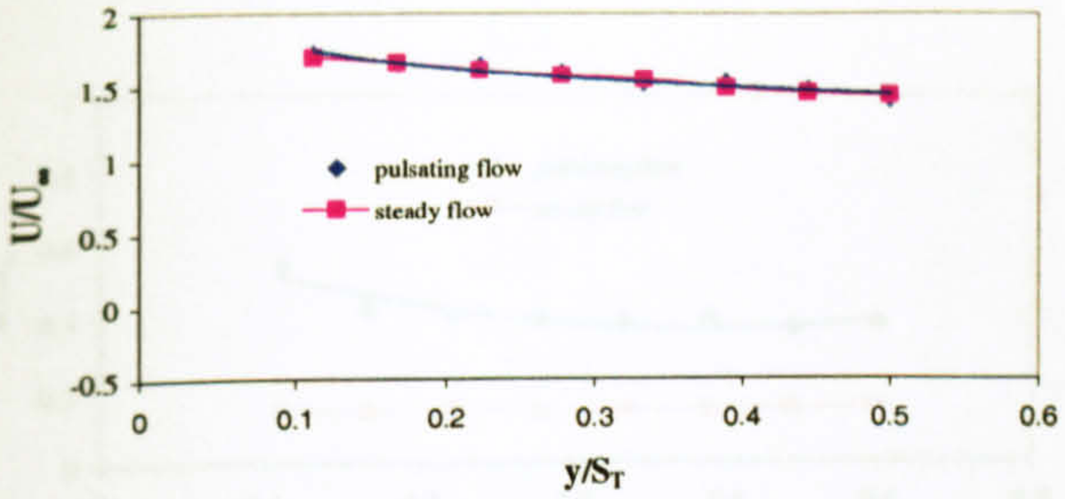

(a) - entrance to the tube bank

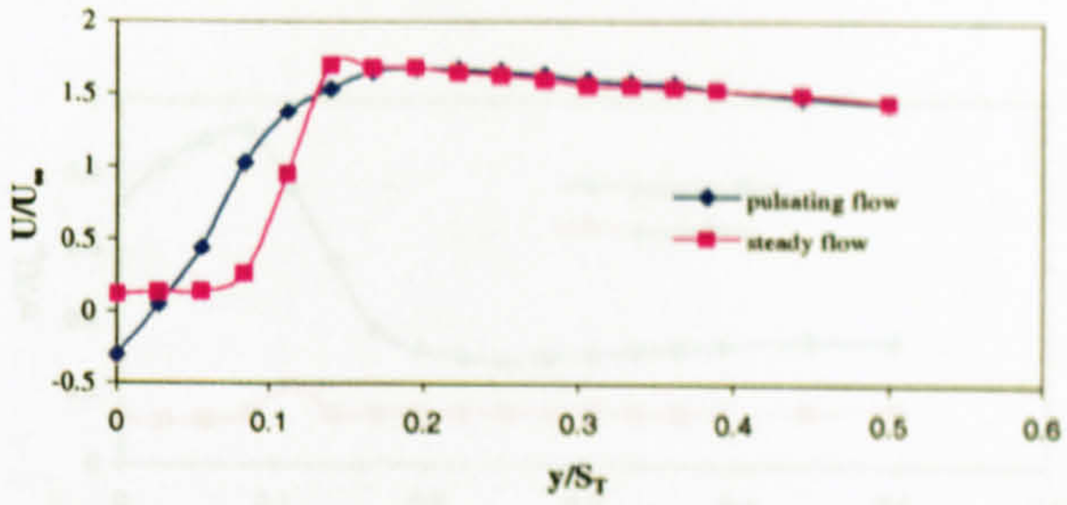

(b) - behind the 1st row

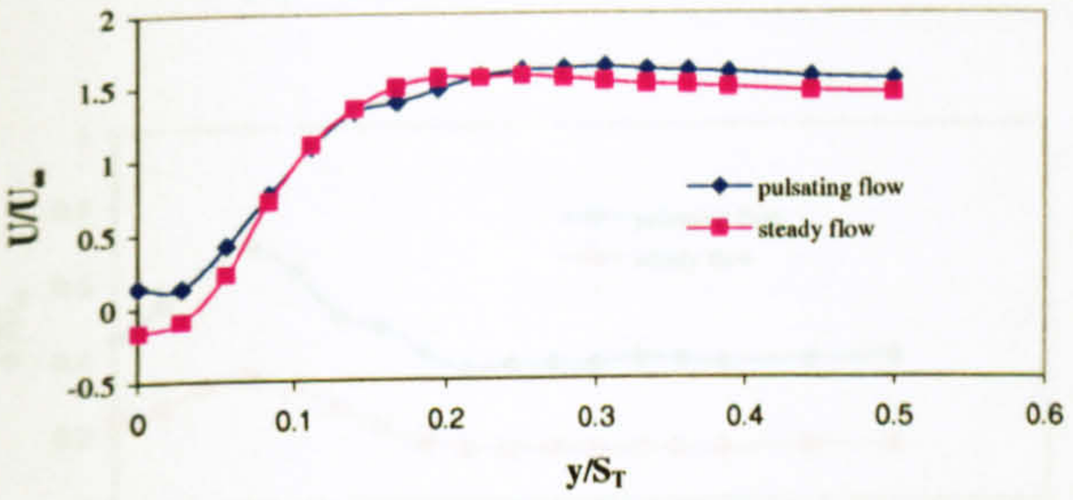

(c) - behind the 2nd row

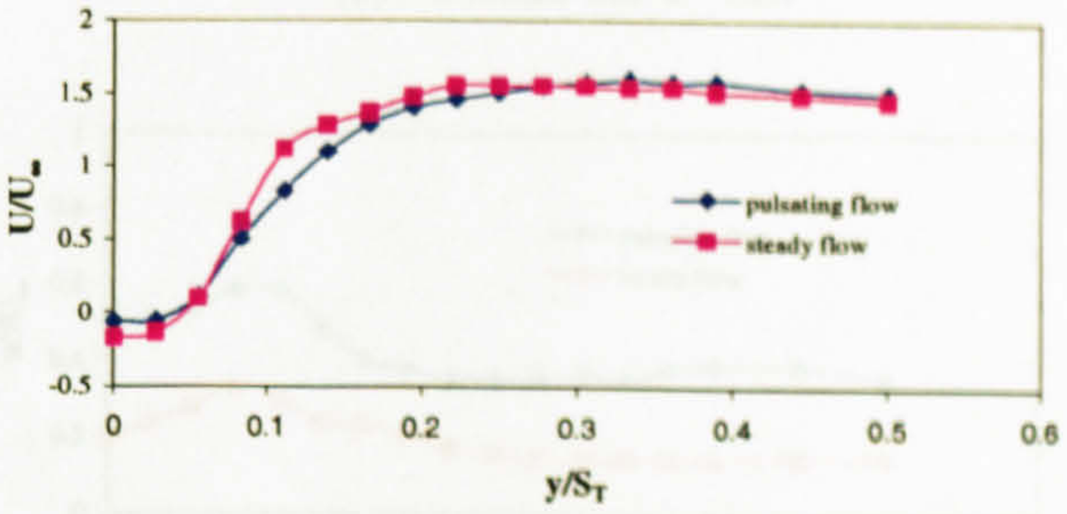

(d) - behind the 3th row

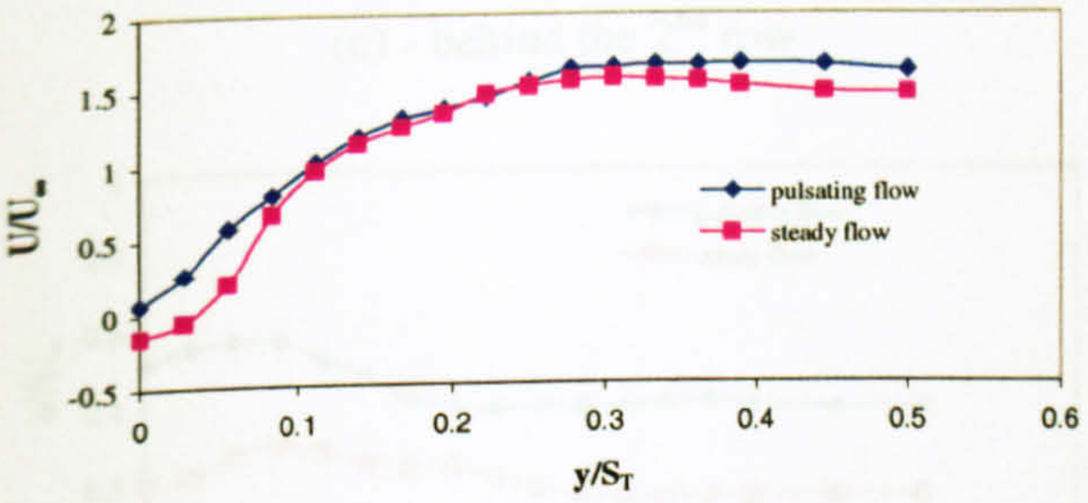

(e) - behind the 4rd row

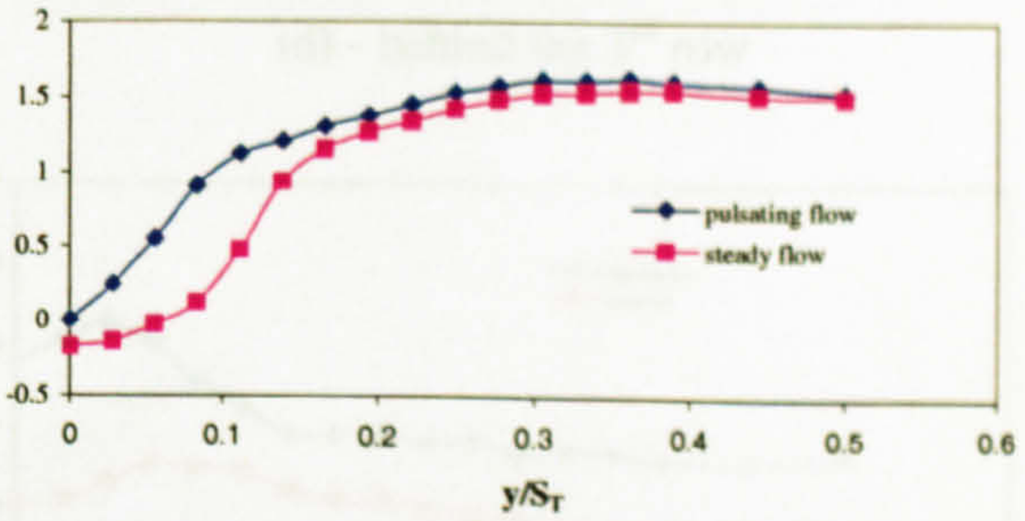

(f) - behind the 5th row

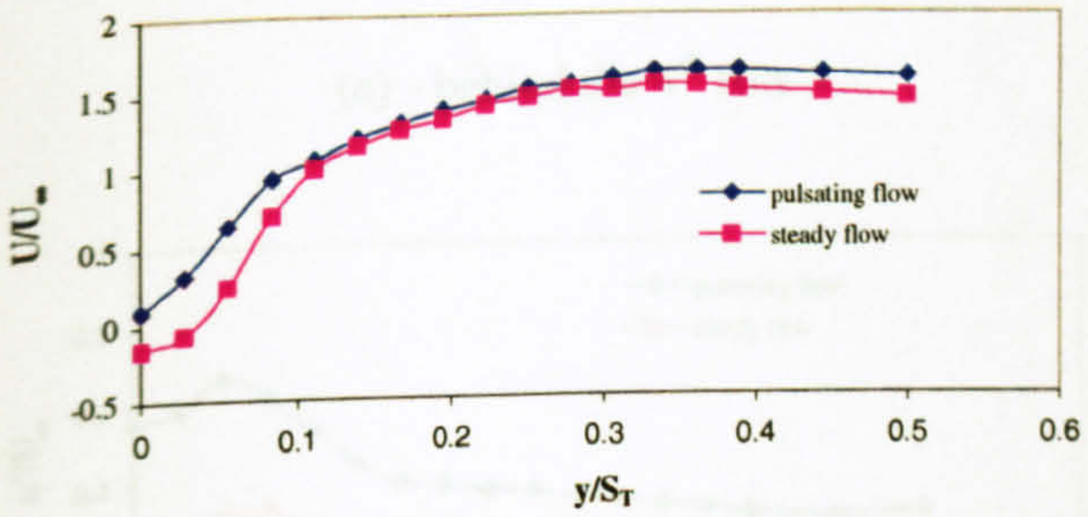

(g) - behind the 6th row

Figure 5.18. Comparison of the axial mean velocity profiles, U/U_∞, obtained in steady and pulsating flow (f_d = 10 Hz, Re = 1,901).

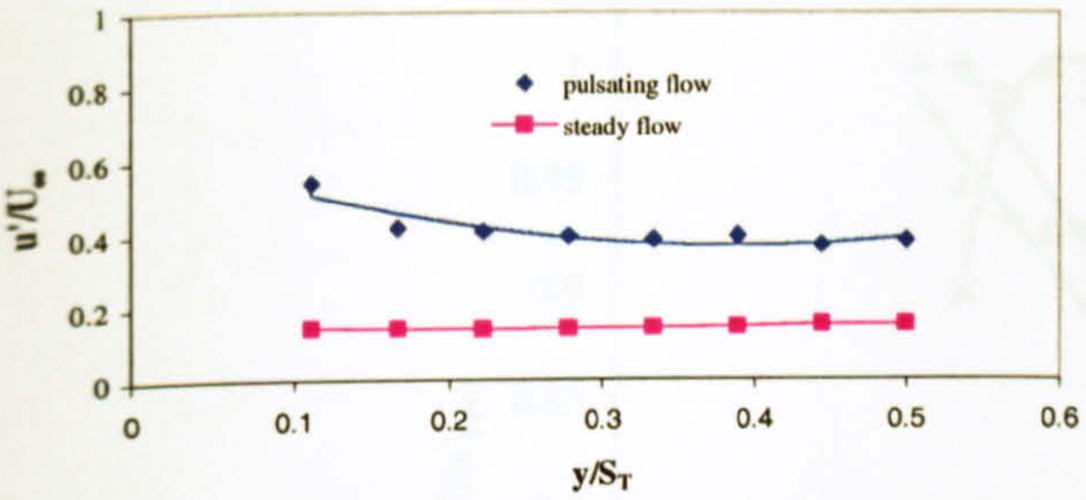

(a) - entrance to the tube bank

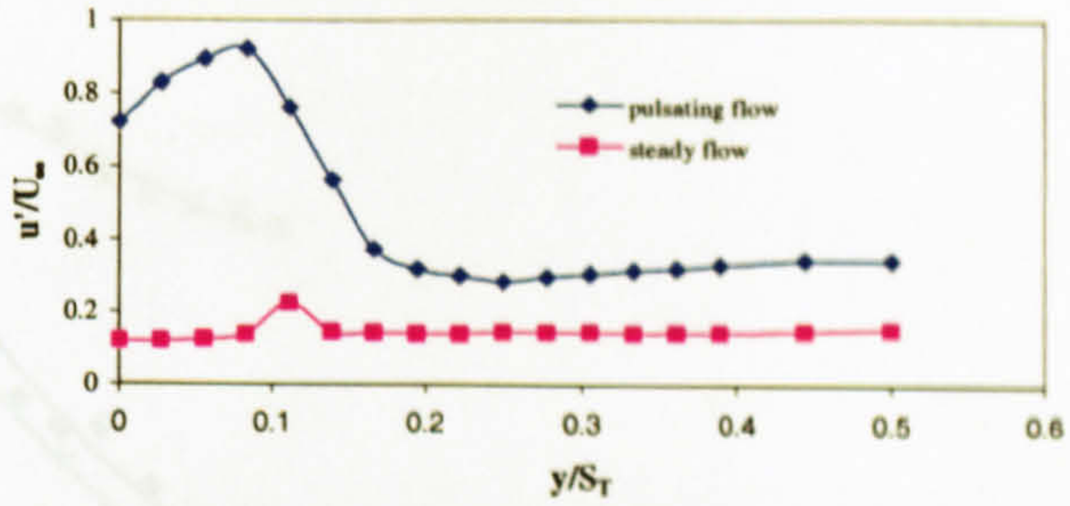

(b) - behind the 1st row

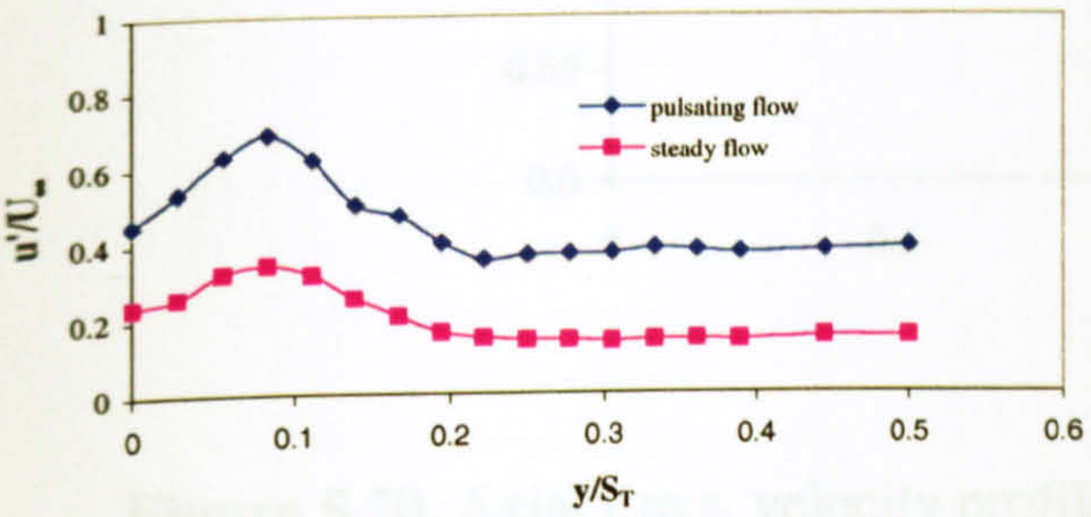

(c) - behind the 2nd row

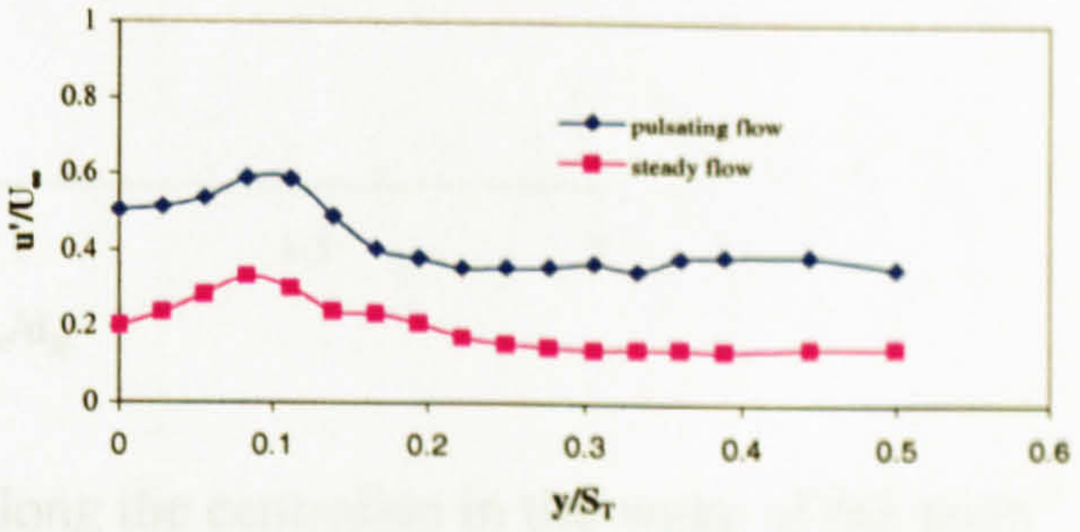

(d) - behind the 3rd row

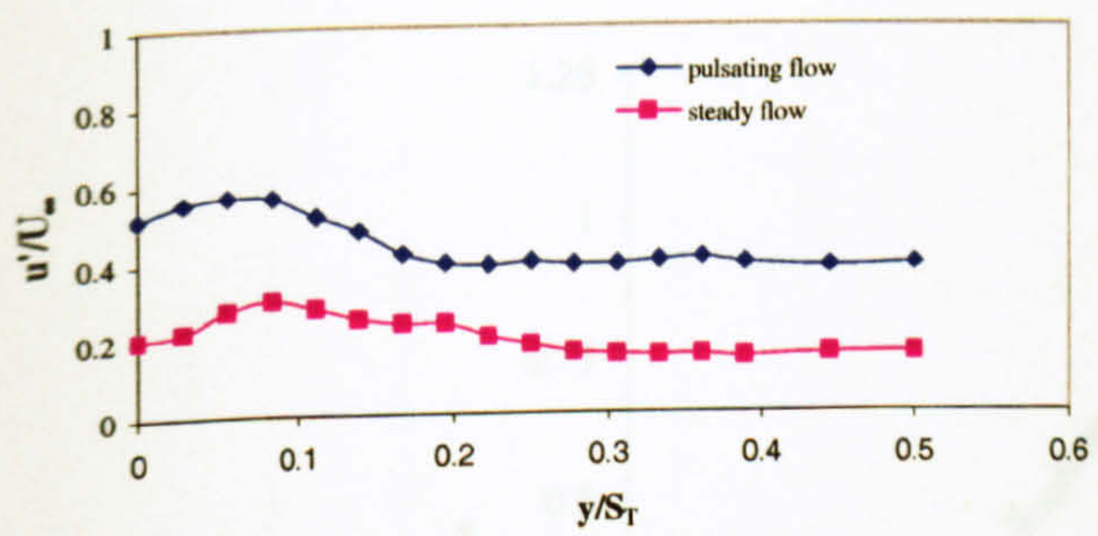

(e) - behind the 4th row

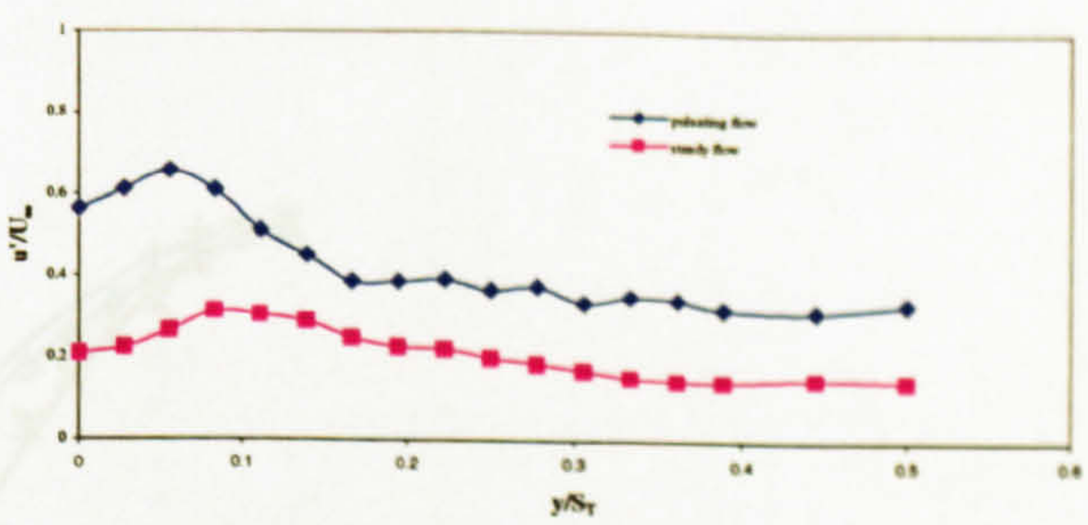

(f) - behind the 5th row

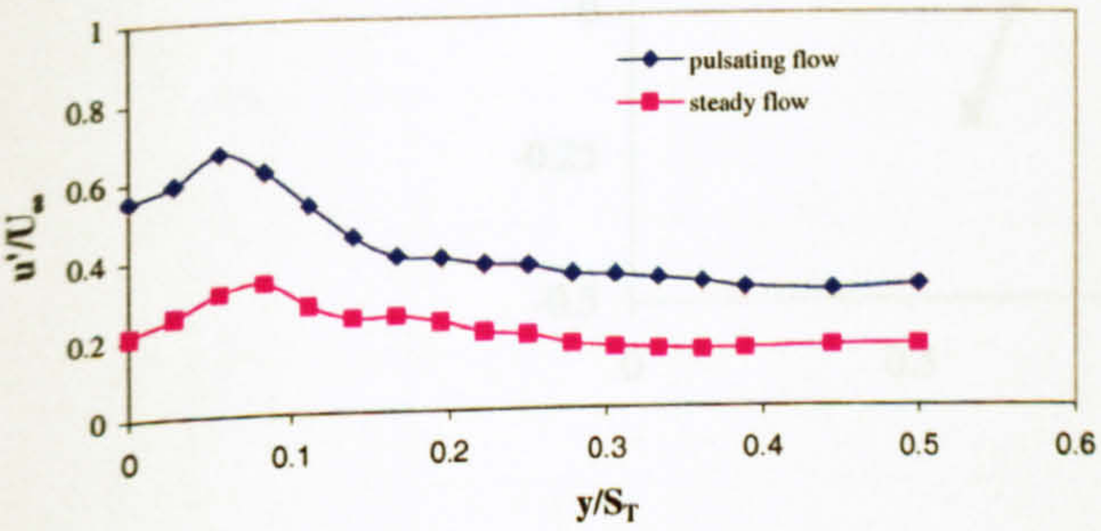

(g) - behind the 6th row

Figure 5.19. Comparison of the axial r.m.s. velocity profiles, U/U_∞, obtained in steady and pulsating flow (f_d = 10 Hz, Re = 1,901).

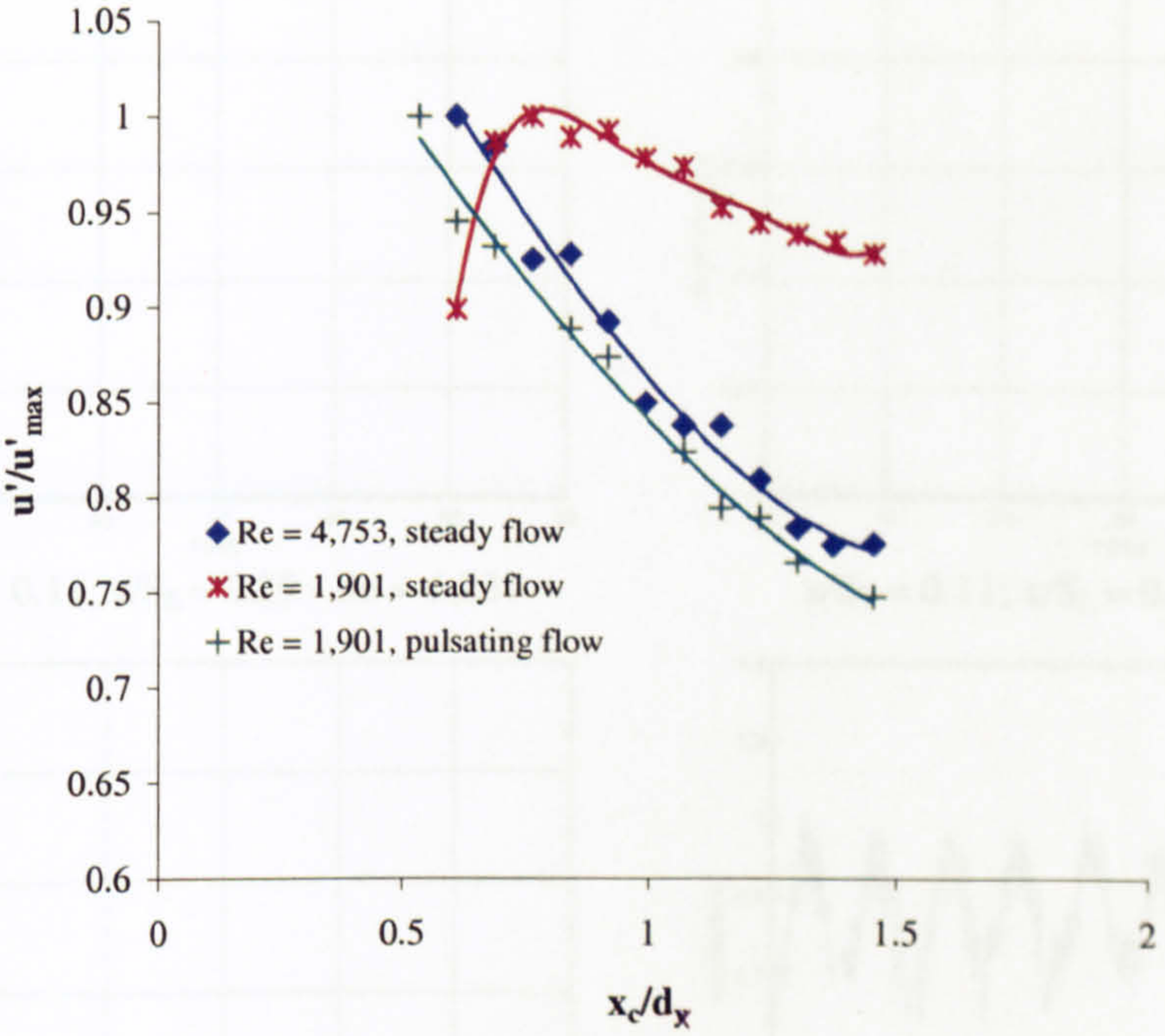

Figure 5.20. Axial r.m.s. velocity profile along the centreline in the wake of the sixth cylinder in steady (Re = 4,753 and Re = 1,901) and pulsating flow (Re = 1,901).

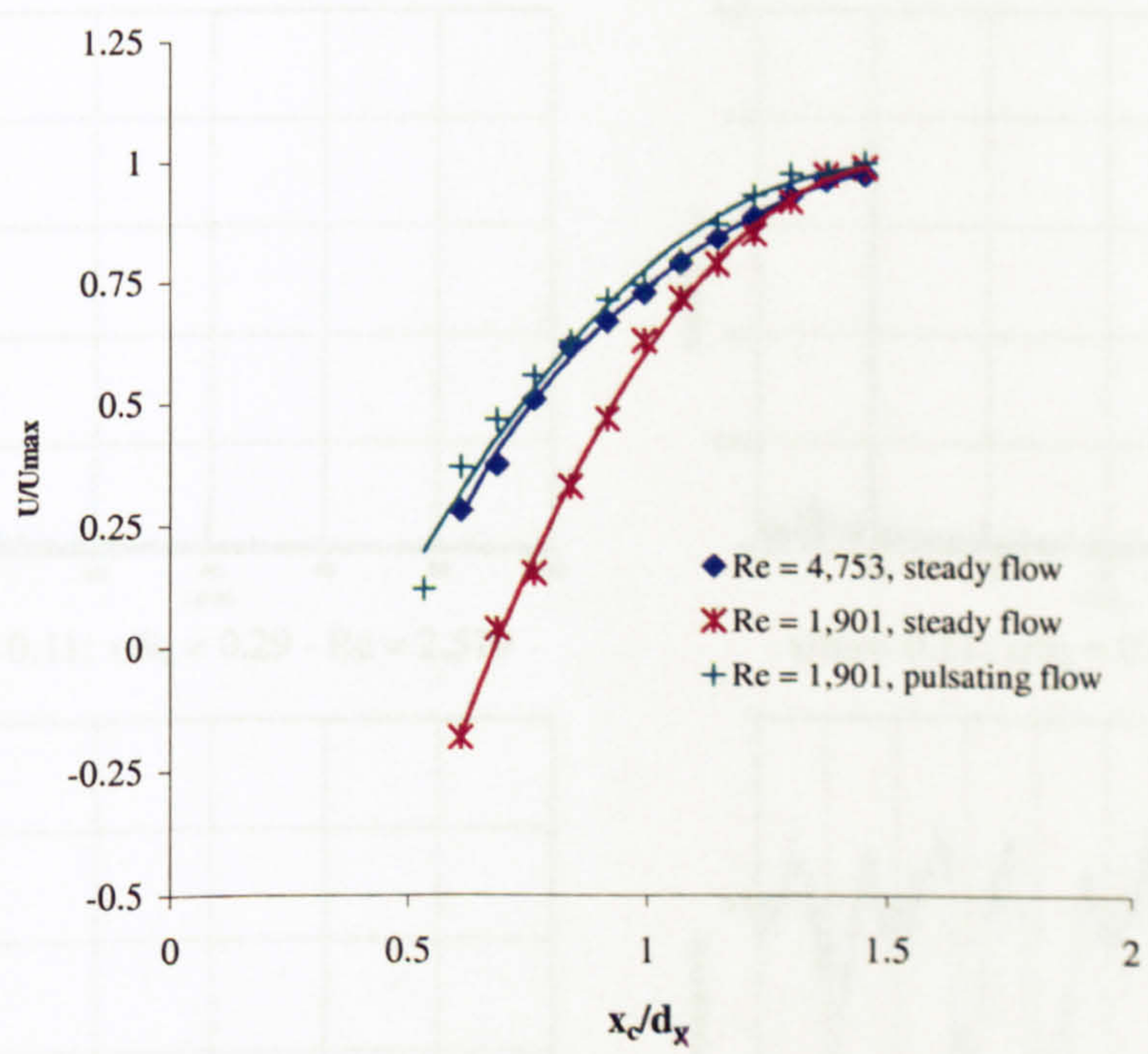

Figure 5.21. Axial mean velocity profile along the centreline in the wake of the sixth cylinder in steady (Re = 4,753 and Re = 1,901) and pulsating flow (Re = 1,901).

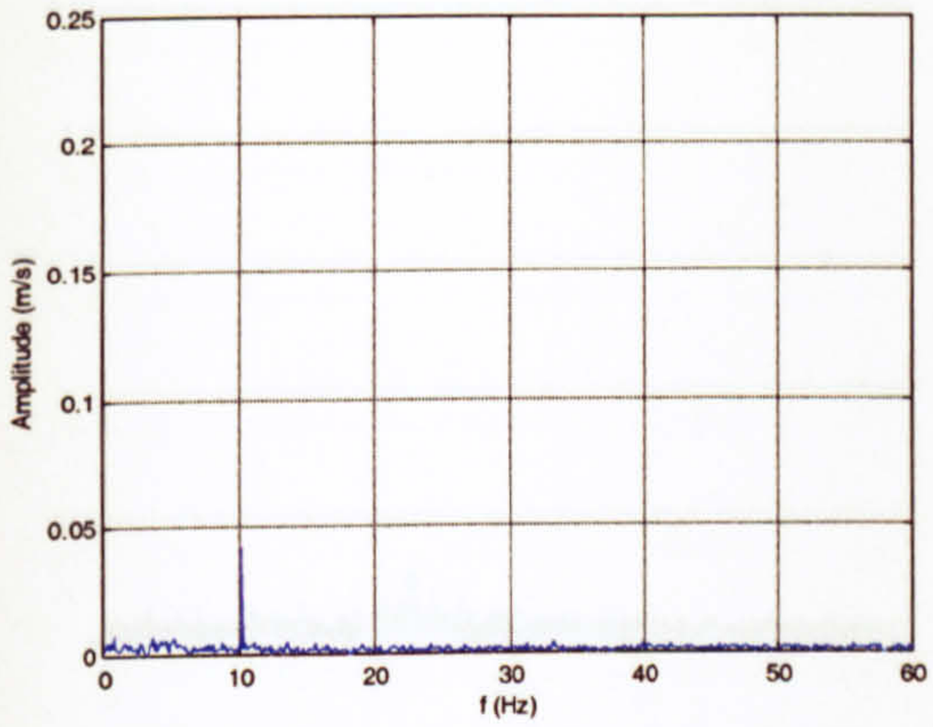

$x/S_T = 0.11$; $x/S_L = 0.29$ - Re = 5,237

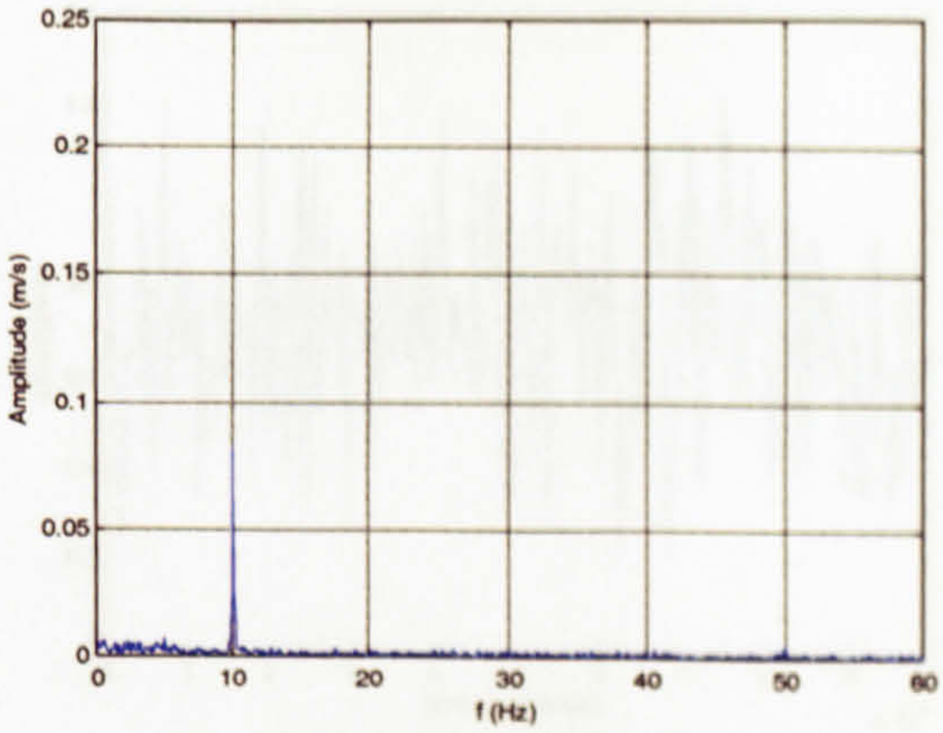

$x/S_T = 0.11$; $x/S_L = 0.29$ - Re = 4,100

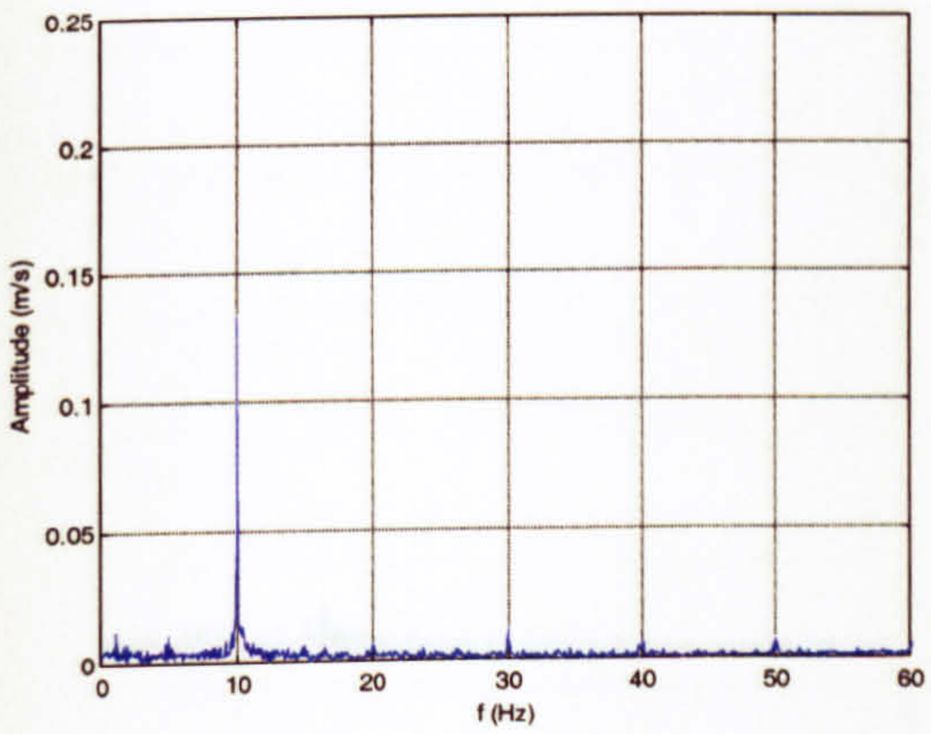

$x/S_T = 0.11$; $x/S_L = 0.29$ - Re = 2,959

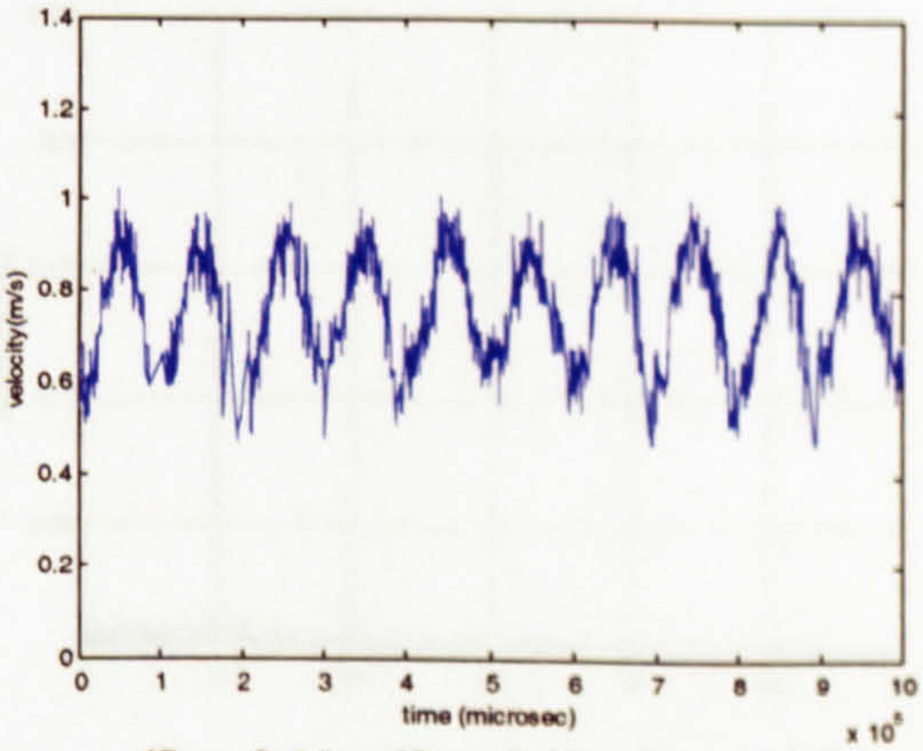

$x/S_T = 0.11$; $x/S_L = 0.29$ - Re = 2,959

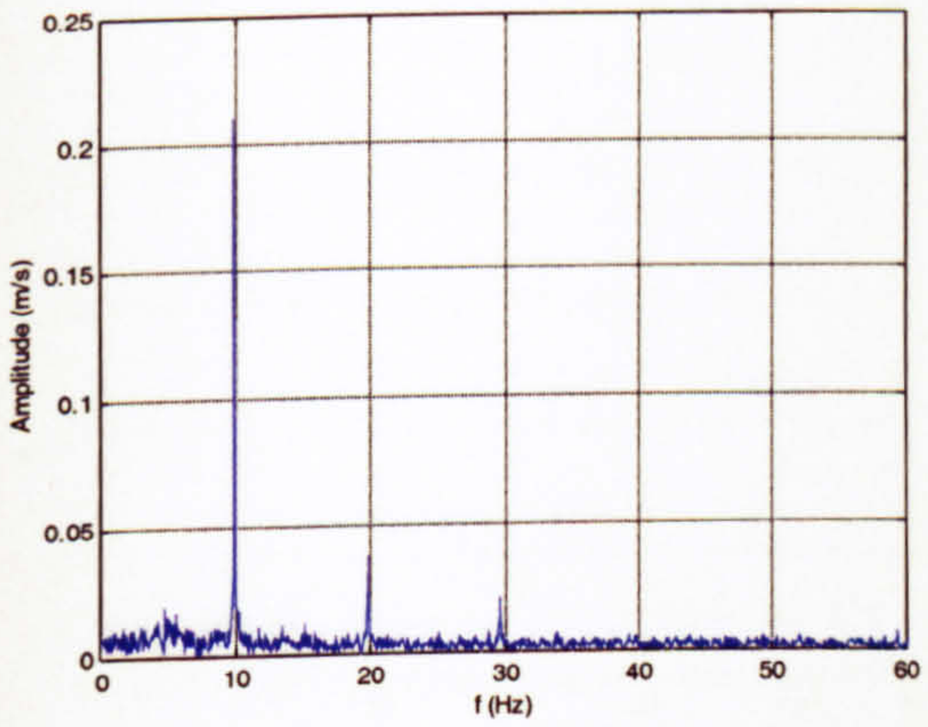

$x/S_T = 0.11$; $x/S_L = 0.29$ - Re = 2,579

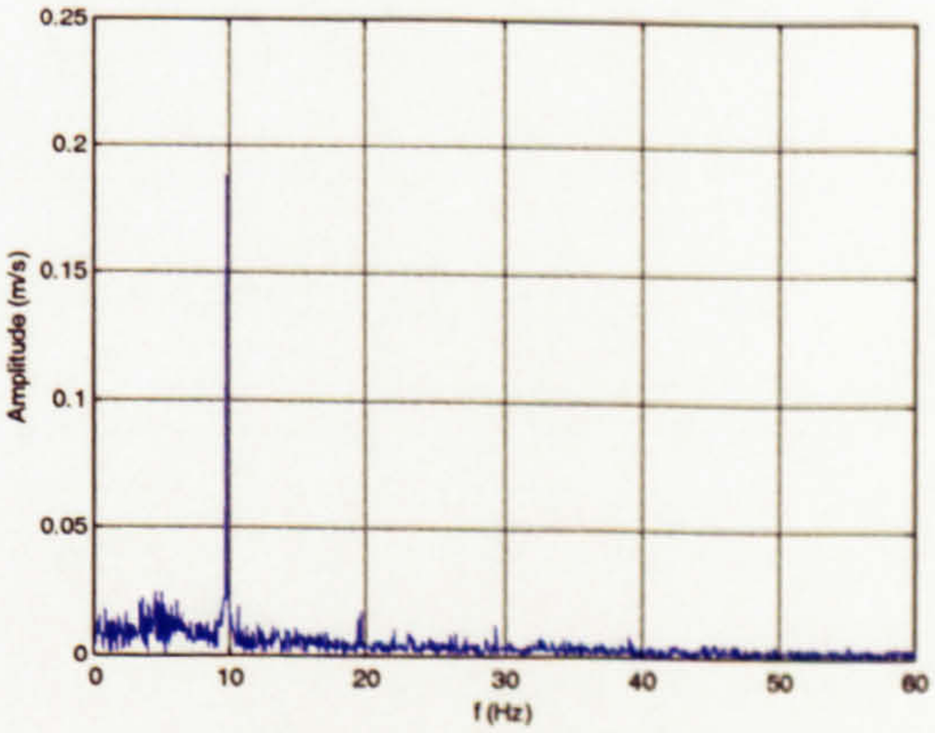

$x/S_T = 0.11$; $x/S_L = 0.29$ - Re = 1,823

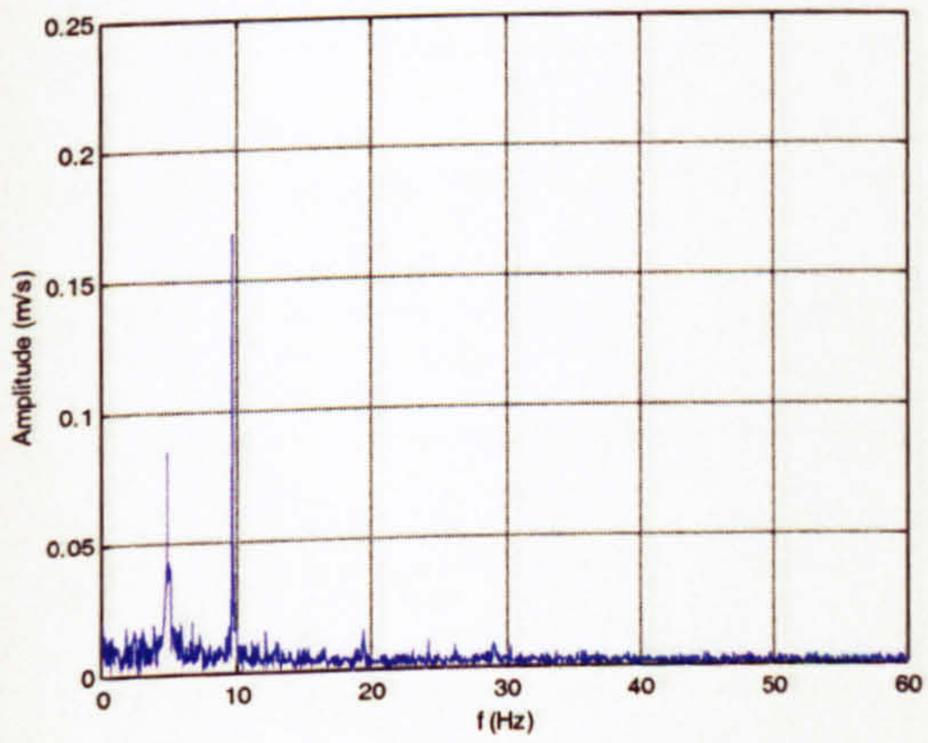

$x/S_T = 0.11$; $x/S_L = 0.29$ - Re = 1,443

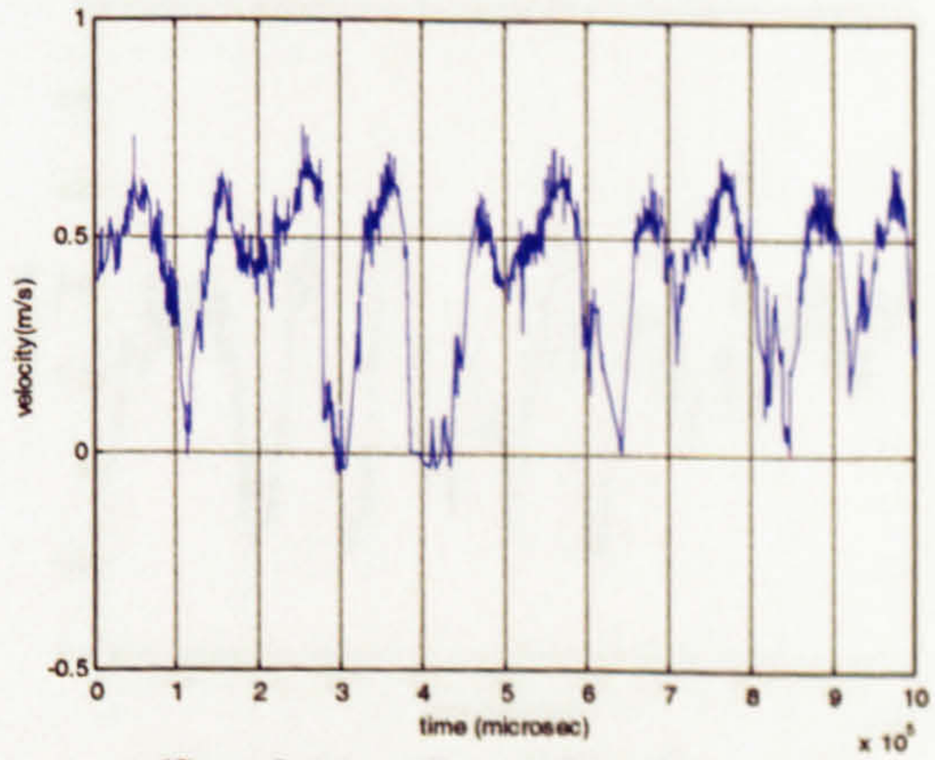

$x/S_T = 0.11$; $x/S_L = 0.29$ - Re = 1,443

Figure 5.22. Amplitude spectra and selected time traces obtained behind the first row in pulsating flow (10 Hz) at various Re.

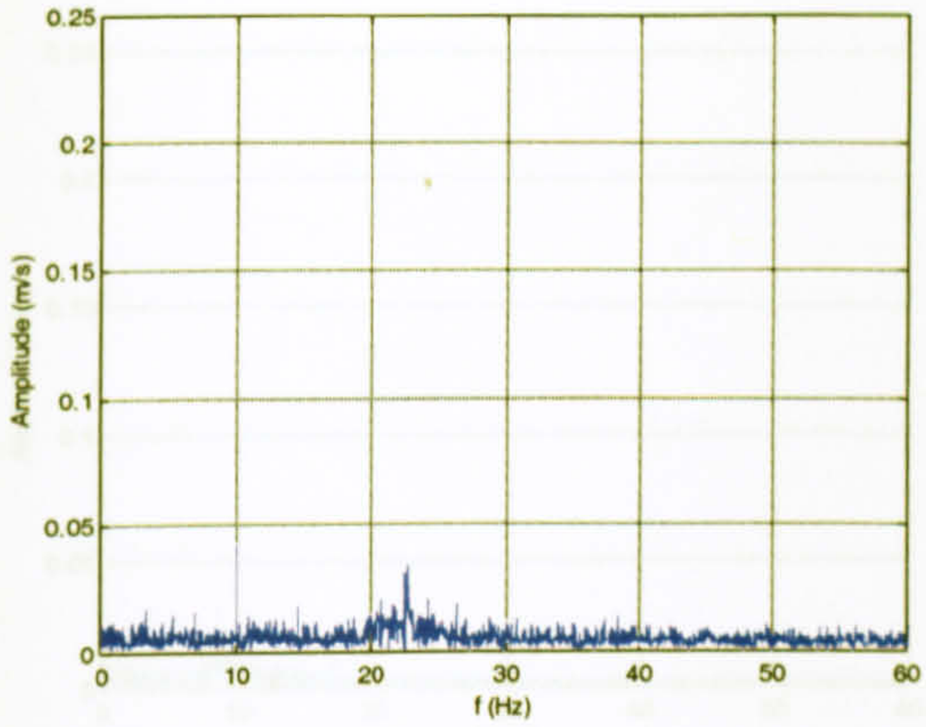

$x/S_T = 0.11$; $x/S_L = 2.29$ - Re = 5,237

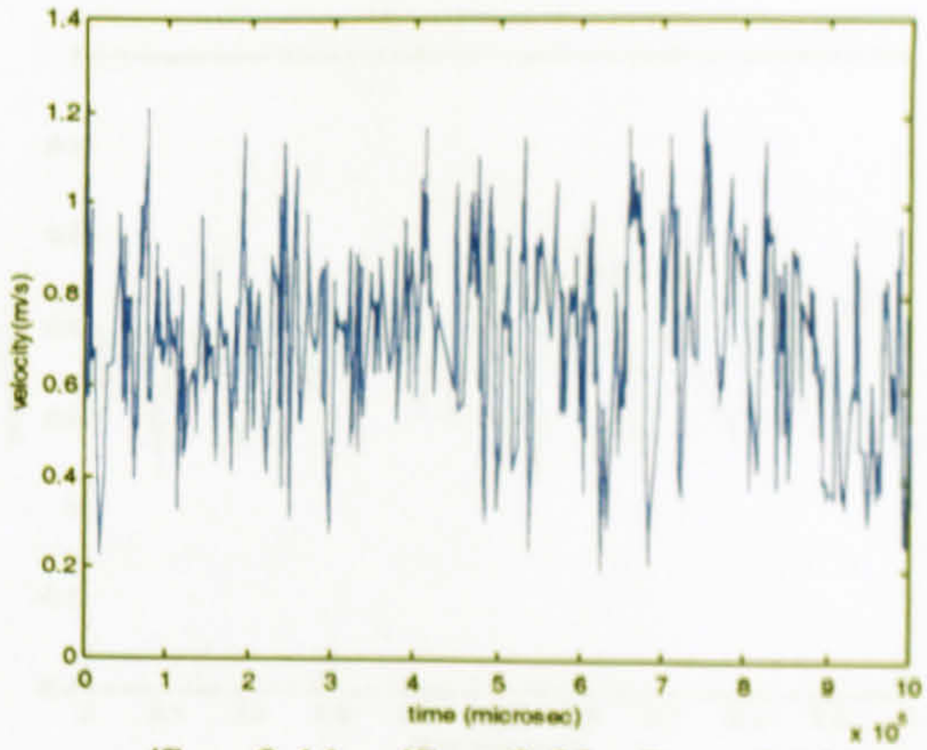

$x/S_T = 0.11$; $x/S_L = 2.29$ - Re = 5,237

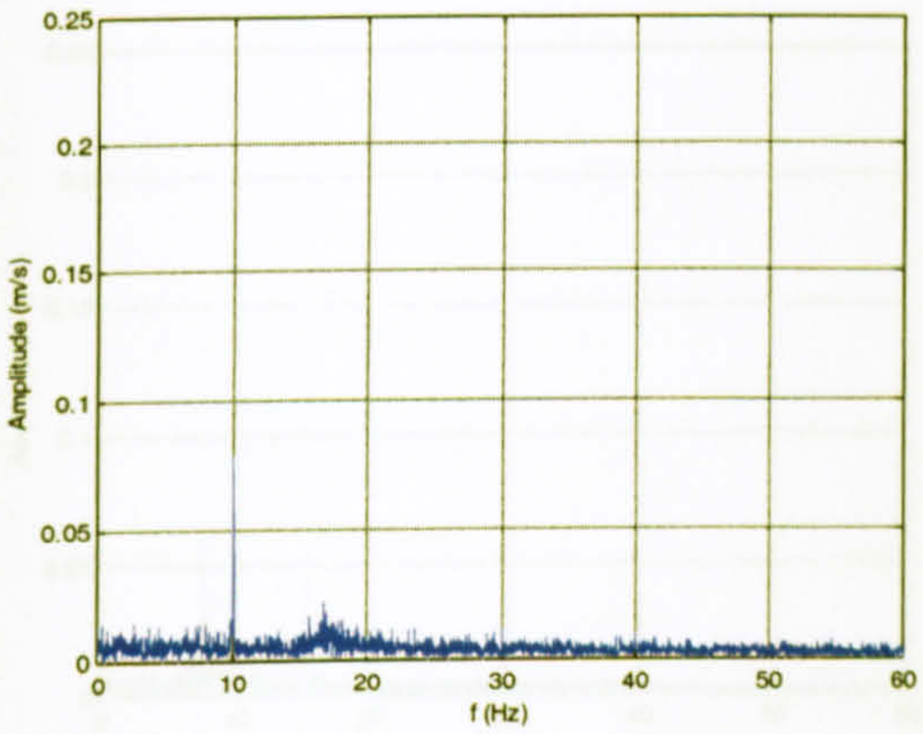

$x/S_T = 0.11$; $x/S_L = 2.29$ - Re = 4,100

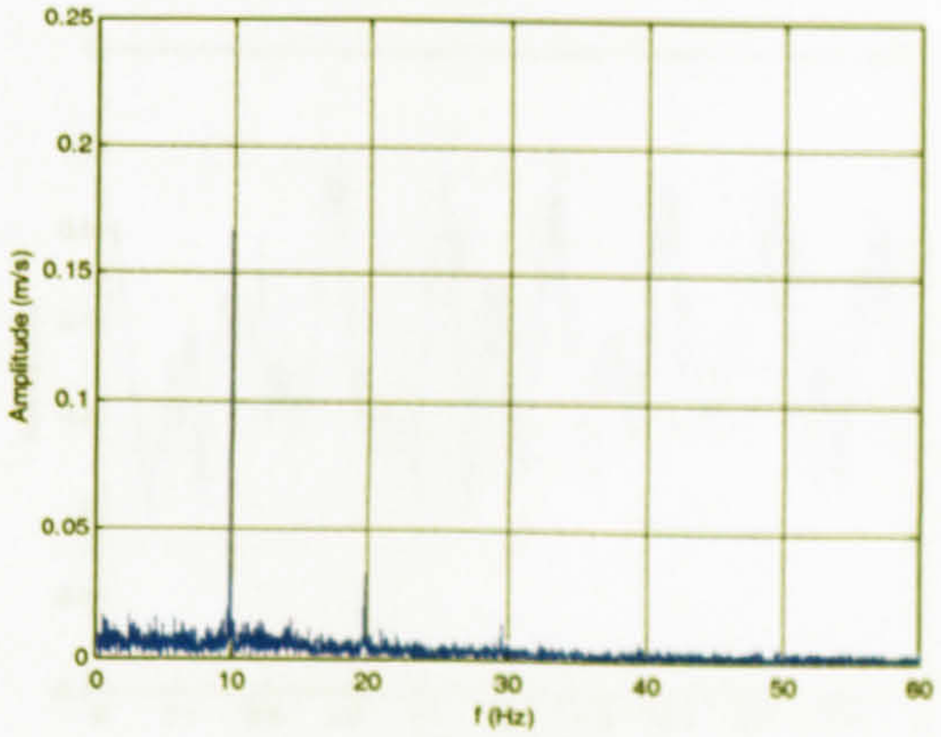

$x/S_T = 0.11$; $x/S_L = 2.29$ - Re = 2,959

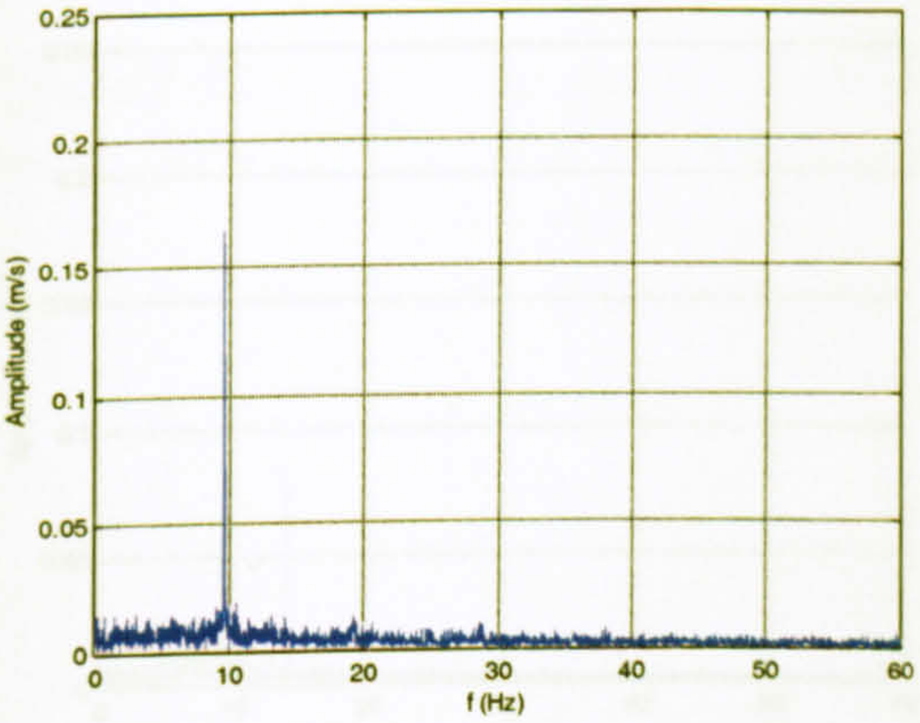

$x/S_T = 0.11$; $x/S_L = 2.29$ - Re = 2,579

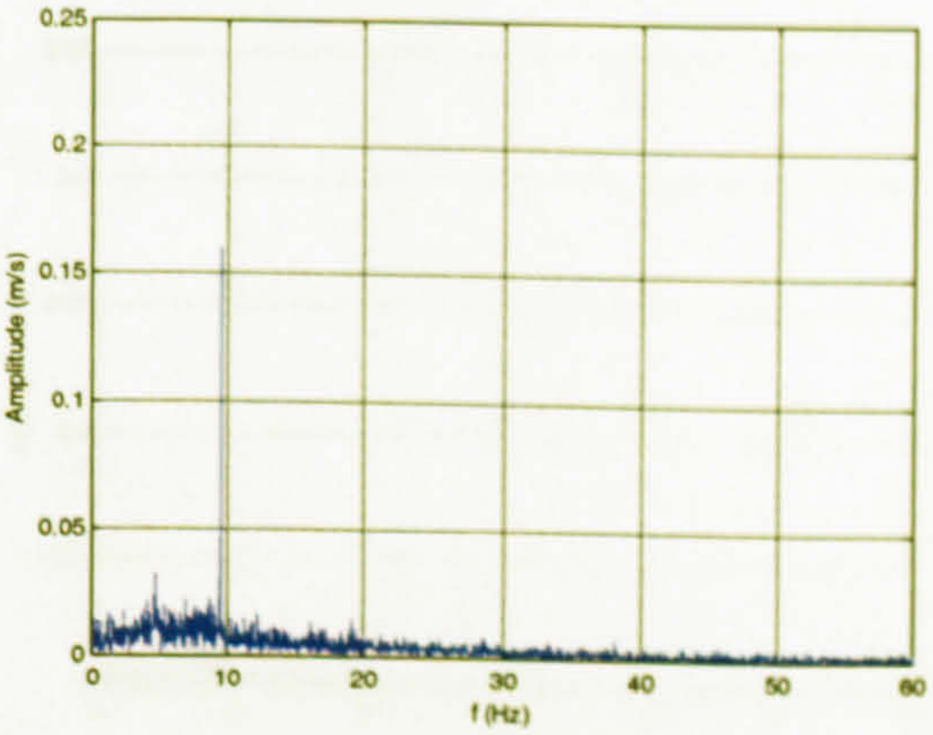

$x/S_T = 0.11$; $x/S_L = 2.29$ - Re = 1,823

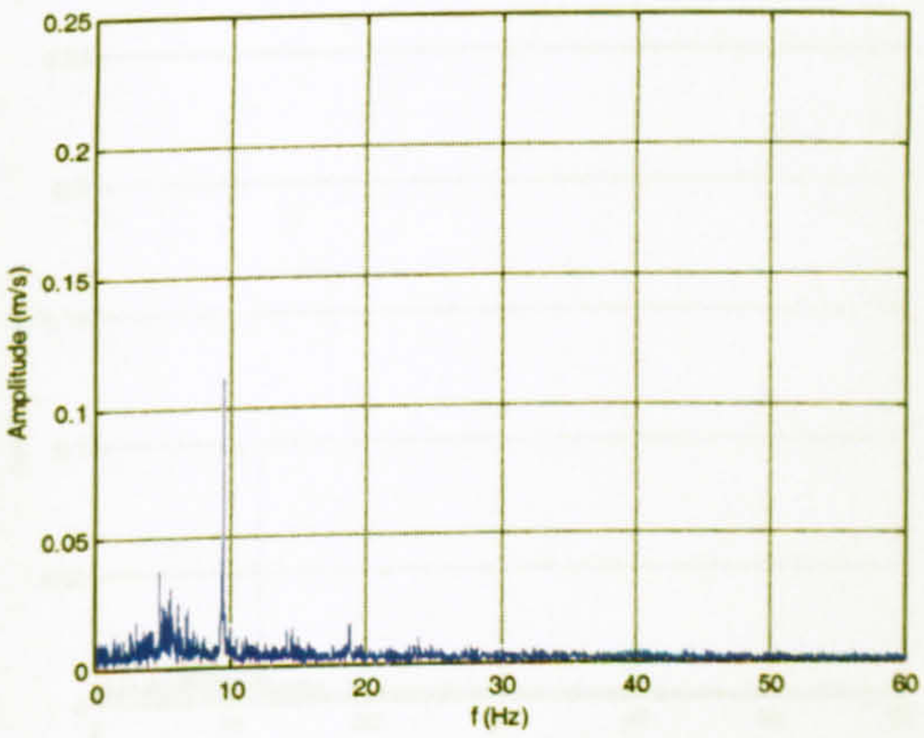

$x/S_T = 0.11$; $x/S_L = 2.29$ - Re = 1,443

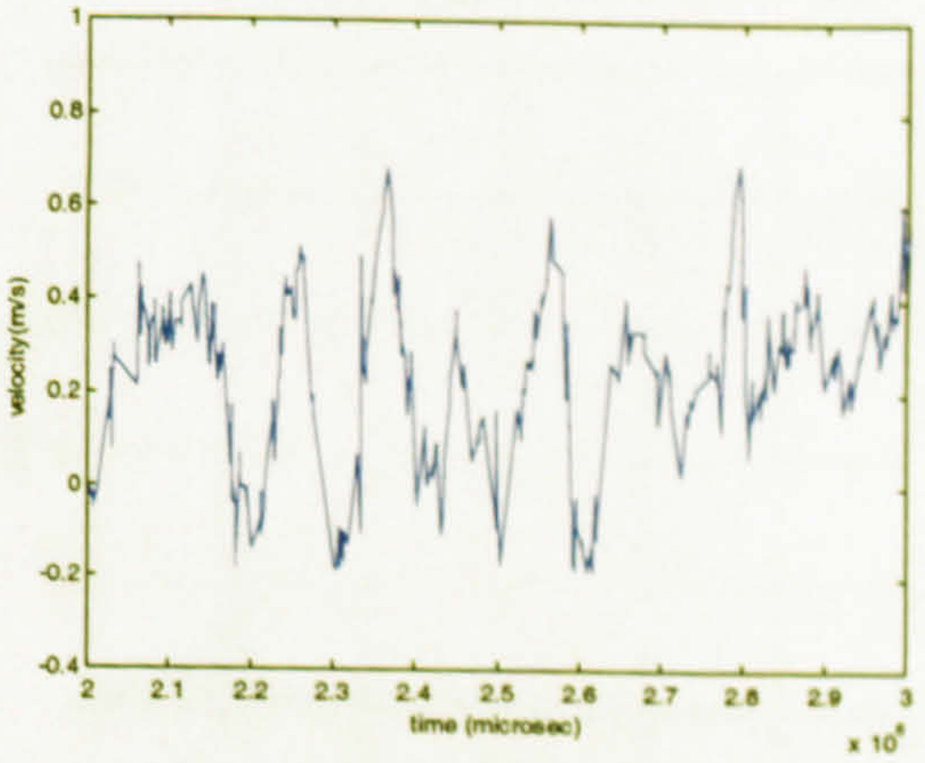

$x/S_T = 0.11$; $x/S_L = 2.29$ - Re = 1,443

Figure 5.23. Amplitude spectra and selected time traces obtained behind the third row in pulsating flow (10 Hz) at various Re.

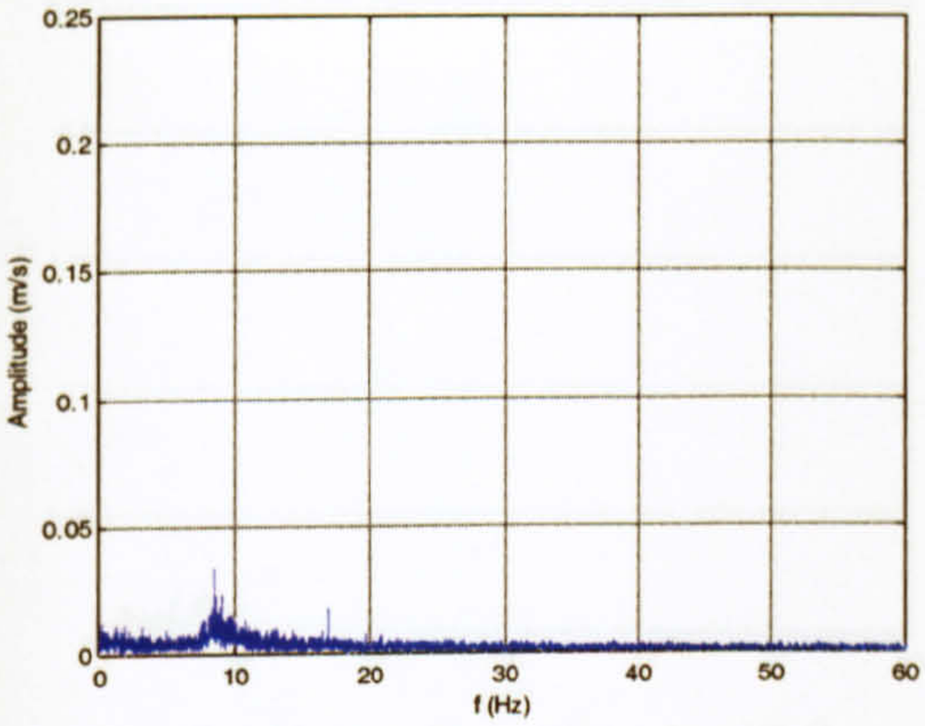

$x/S_T = 0.11$; $x/S_L = 5.29$ - $f_d = 17$ Hz

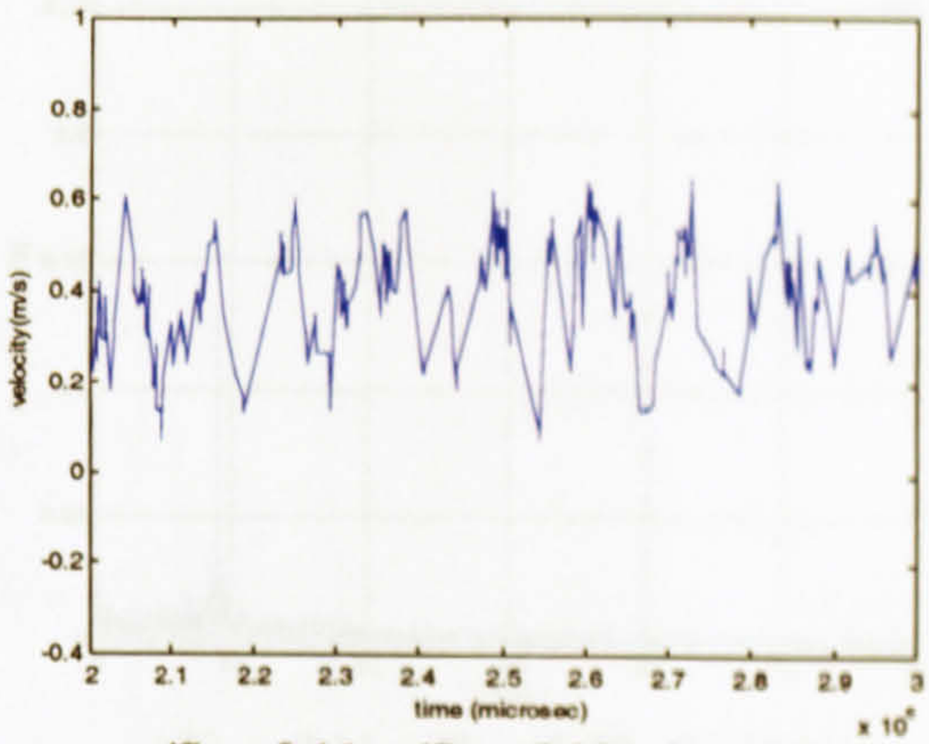

$x/S_T = 0.11$; $x/S_L = 5.29$ - $f_d = 17$ Hz

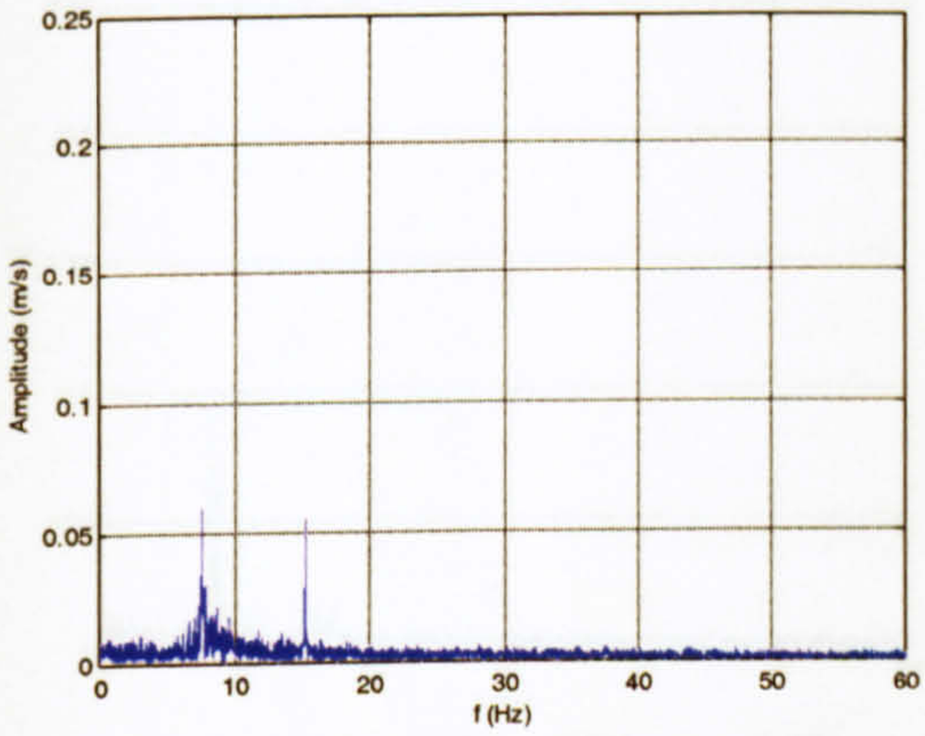

$x/S_T = 0.11$; $x/S_L = 5.29$ - $f_d = 15$ Hz

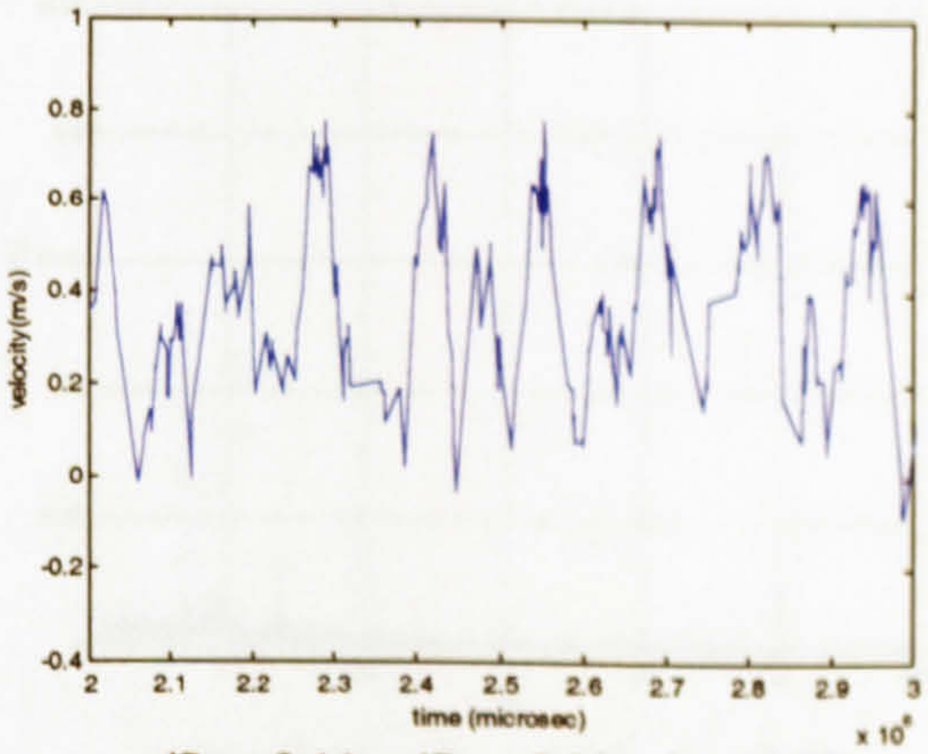

$x/S_T = 0.11$; $x/S_L = 5.29$ - $f_d = 15$ Hz

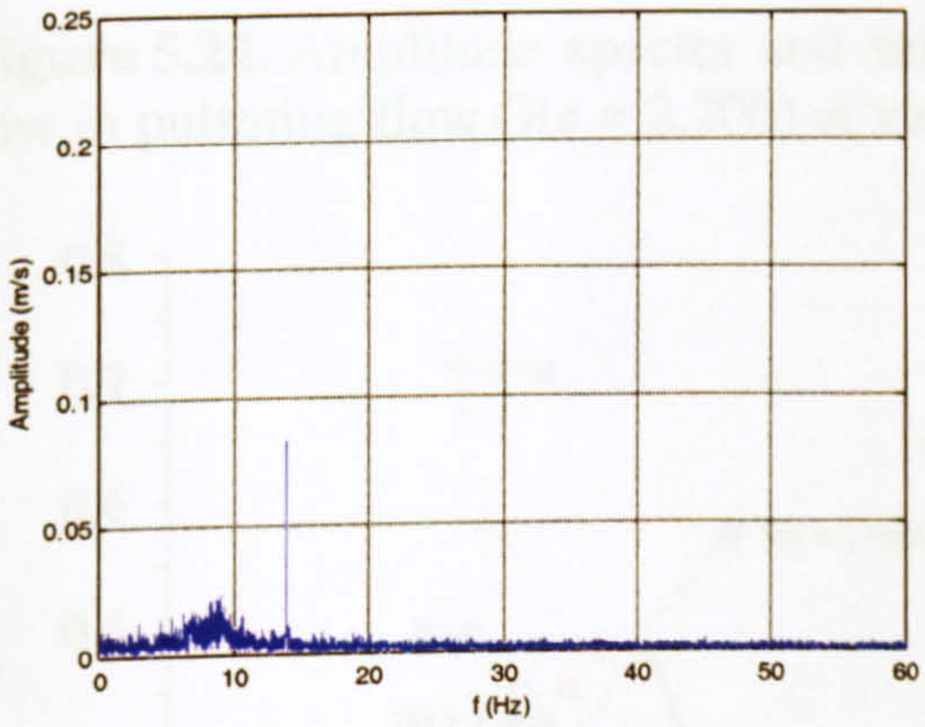

$x/S_T = 0.11$; $x/S_L = 5.29$ - $f_d = 14$ Hz

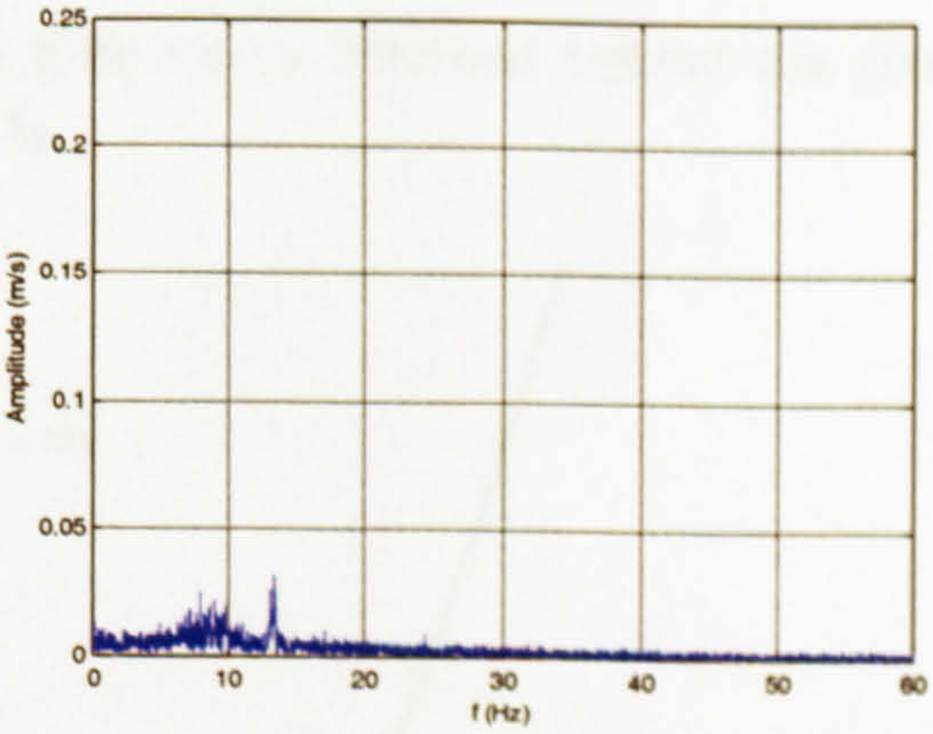

$x/S_T = 0.11$; $x/S_L = 5.29$ - $f_d = 13$ Hz

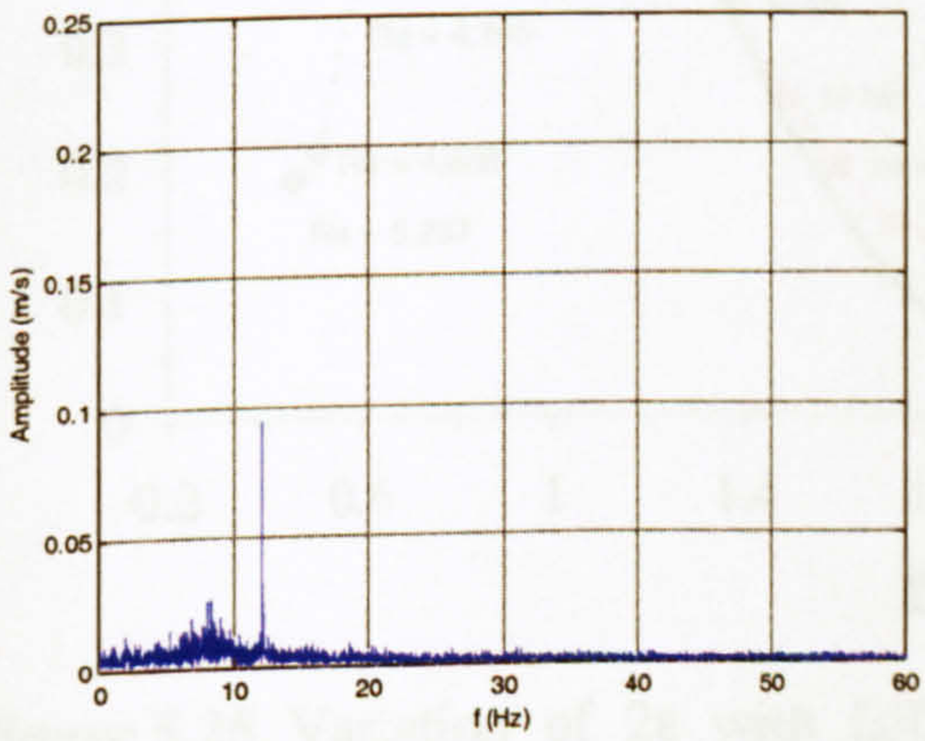

$x/S_T = 0.11$; $x/S_L = 5.29$ - $f_d = 12$ Hz

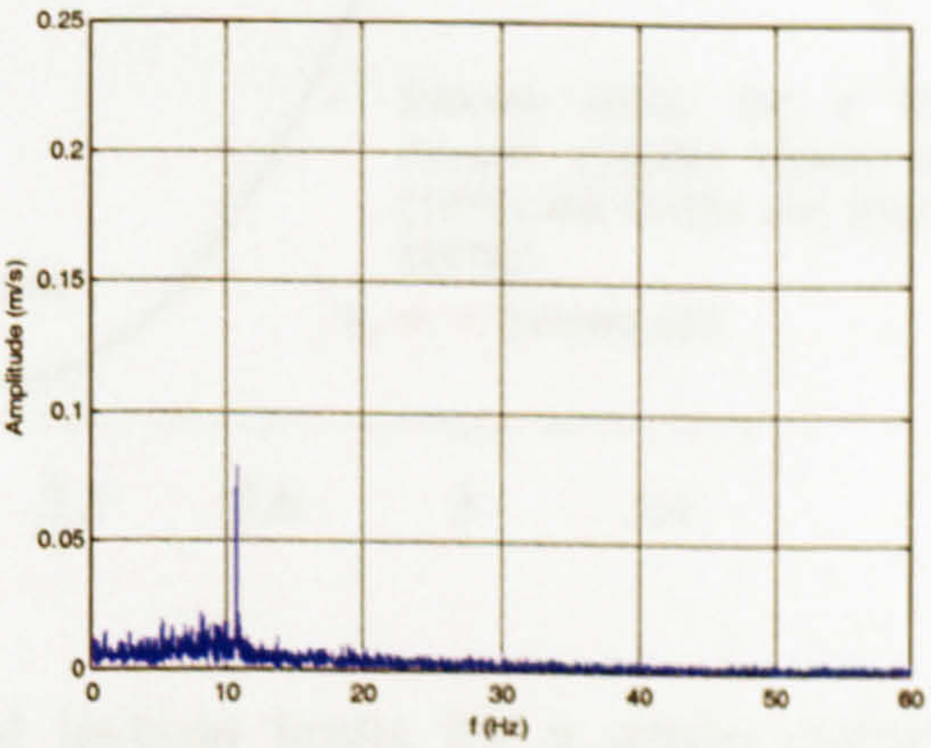

$x/S_T = 0.11$; $x/S_L = 5.29$ - $f_d = 11$ Hz

For Caption see next page.

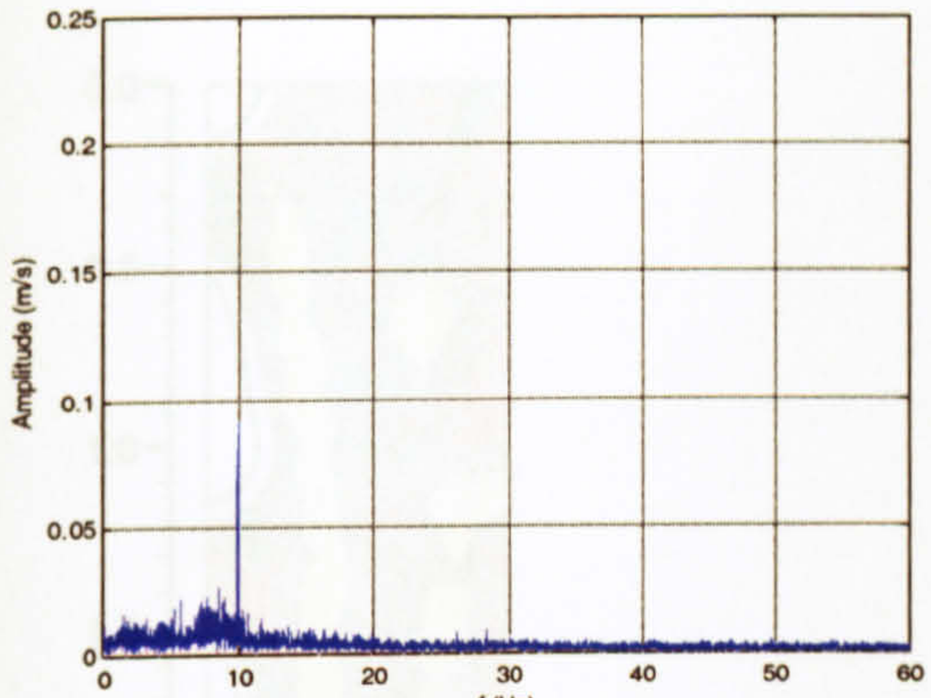

$x/S_T = 0.11$; $x/S_L = 5.29$ - $f_d = 10$ Hz

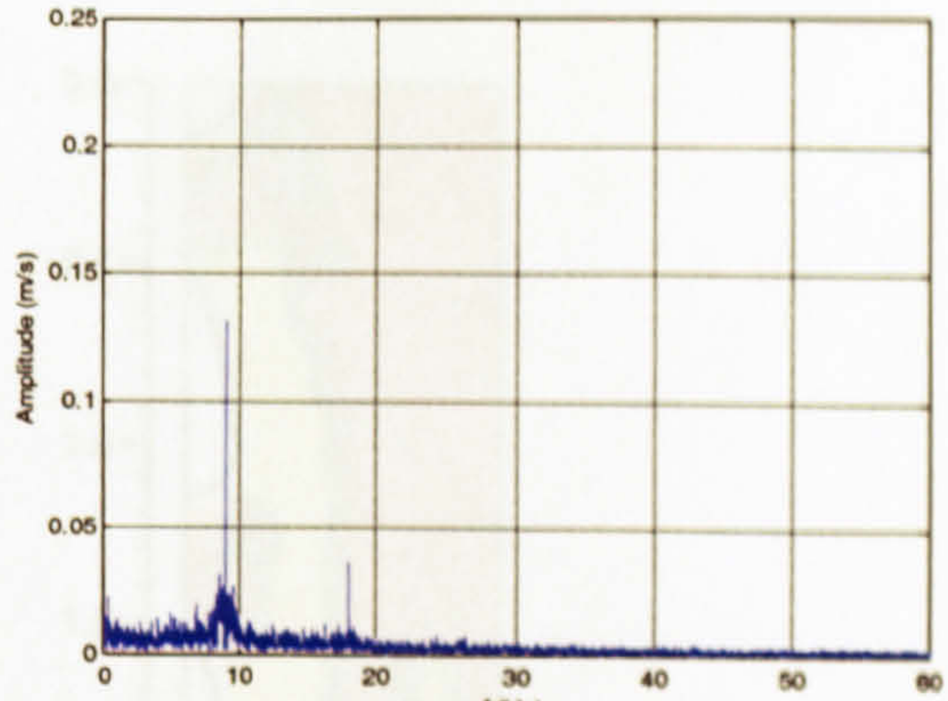

$x/S_T = 0.11$; $x/S_L = 5.29$ - $f_d = 9$ Hz

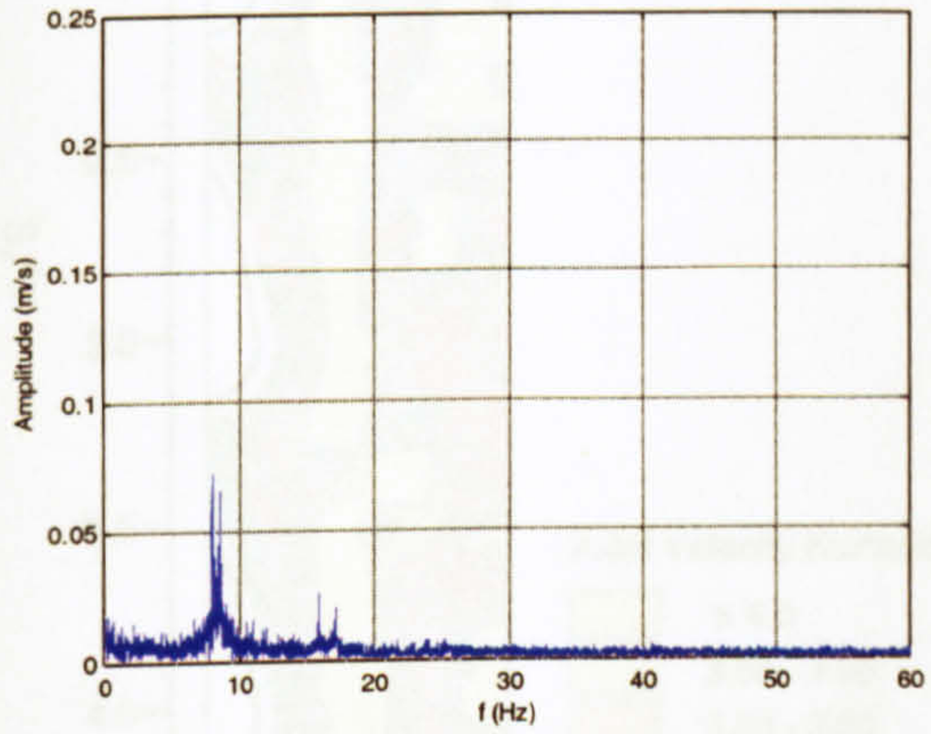

$x/S_T = 0.11$; $x/S_L = 5.29$ - $f_d = 8$ Hz

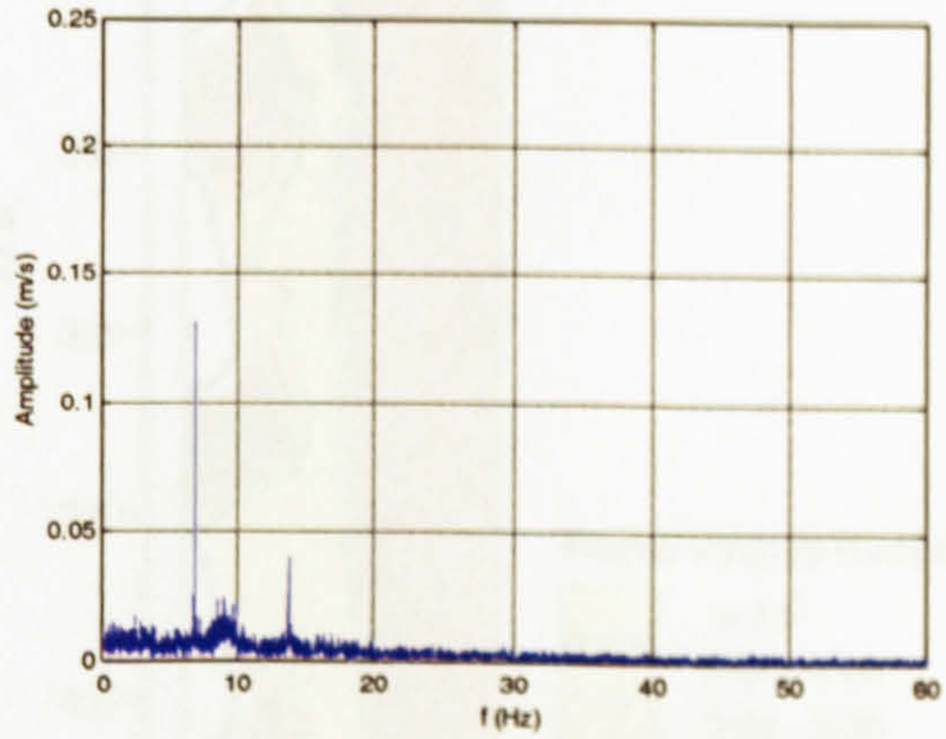

$x/S_T = 0.11$; $x/S_L = 5.29$ - $f_d = 7$ Hz

Figure 5.24. Amplitude spectra and selected time traces obtained behind the sixth row in pulsating flow (Re = 2,200) at various f_d.

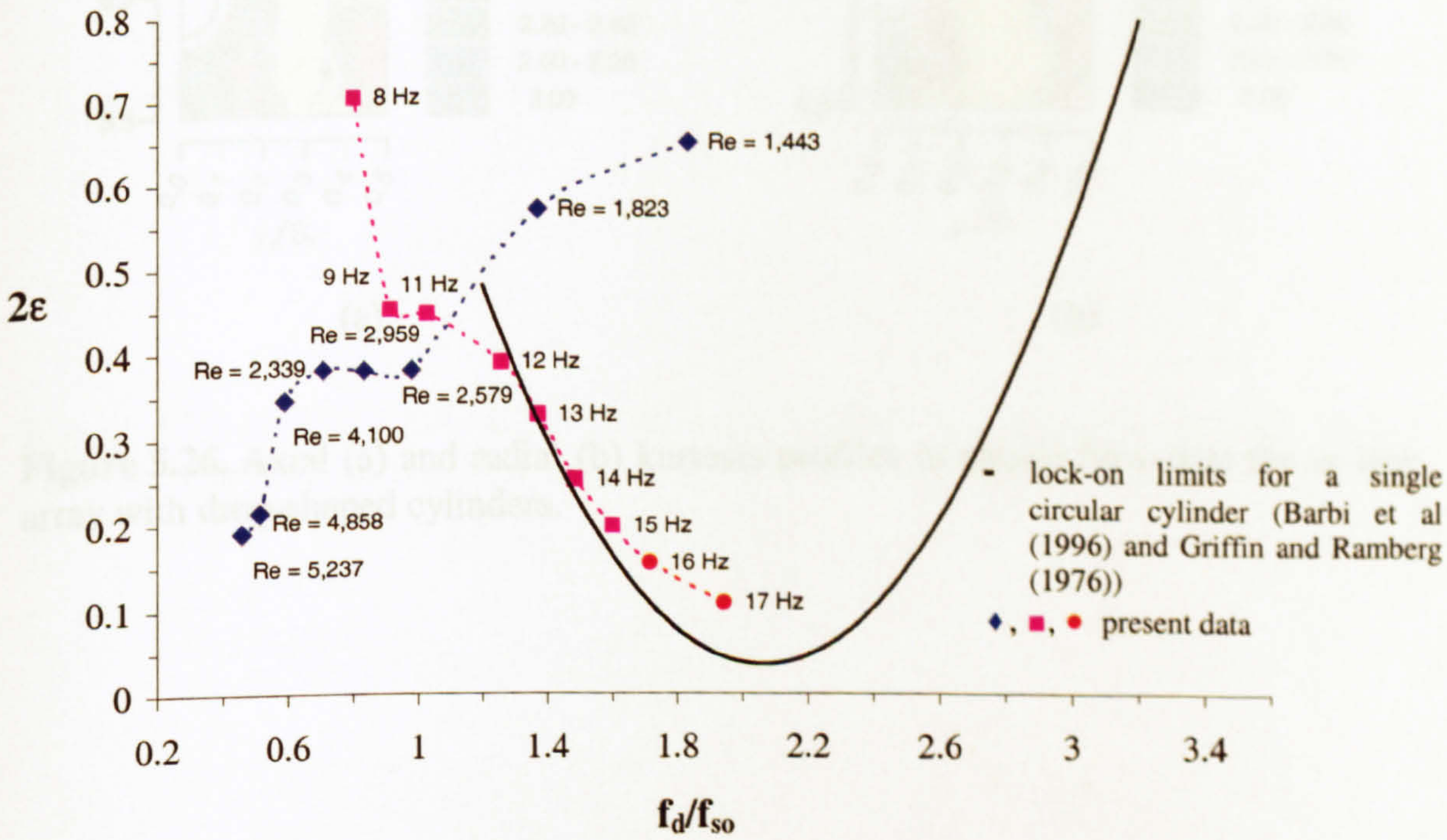

Figure 5.25. Variation of 2ε with f_d/f_{so} and lock-on limits for a single circular cylinder in the in-line tube bundle with drop-shaped tubes under pulsating flow conditions.

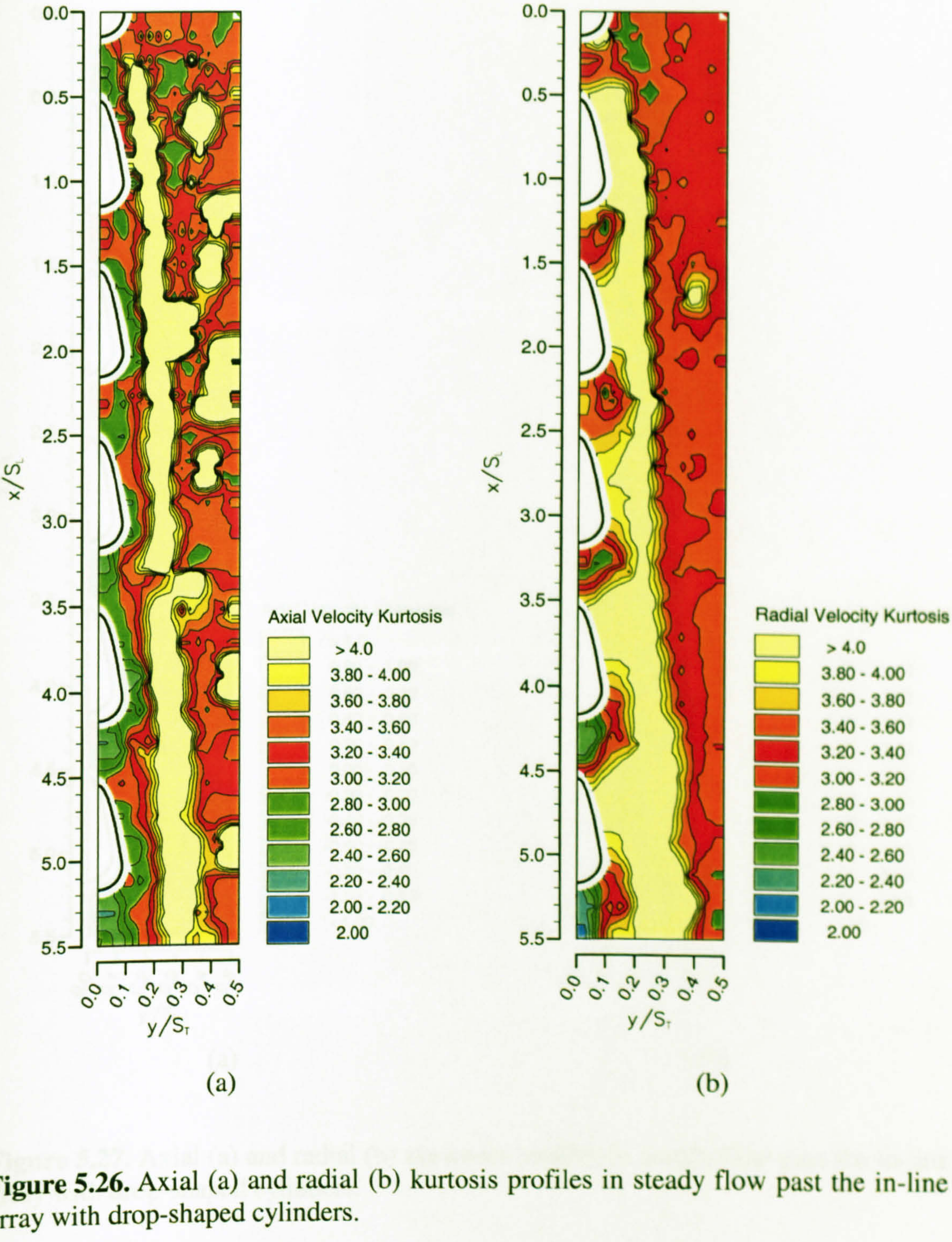

(a) (b)

Figure 5.26. Axial (a) and radial (b) kurtosis profiles in steady flow past the in-line array with drop-shaped cylinders.

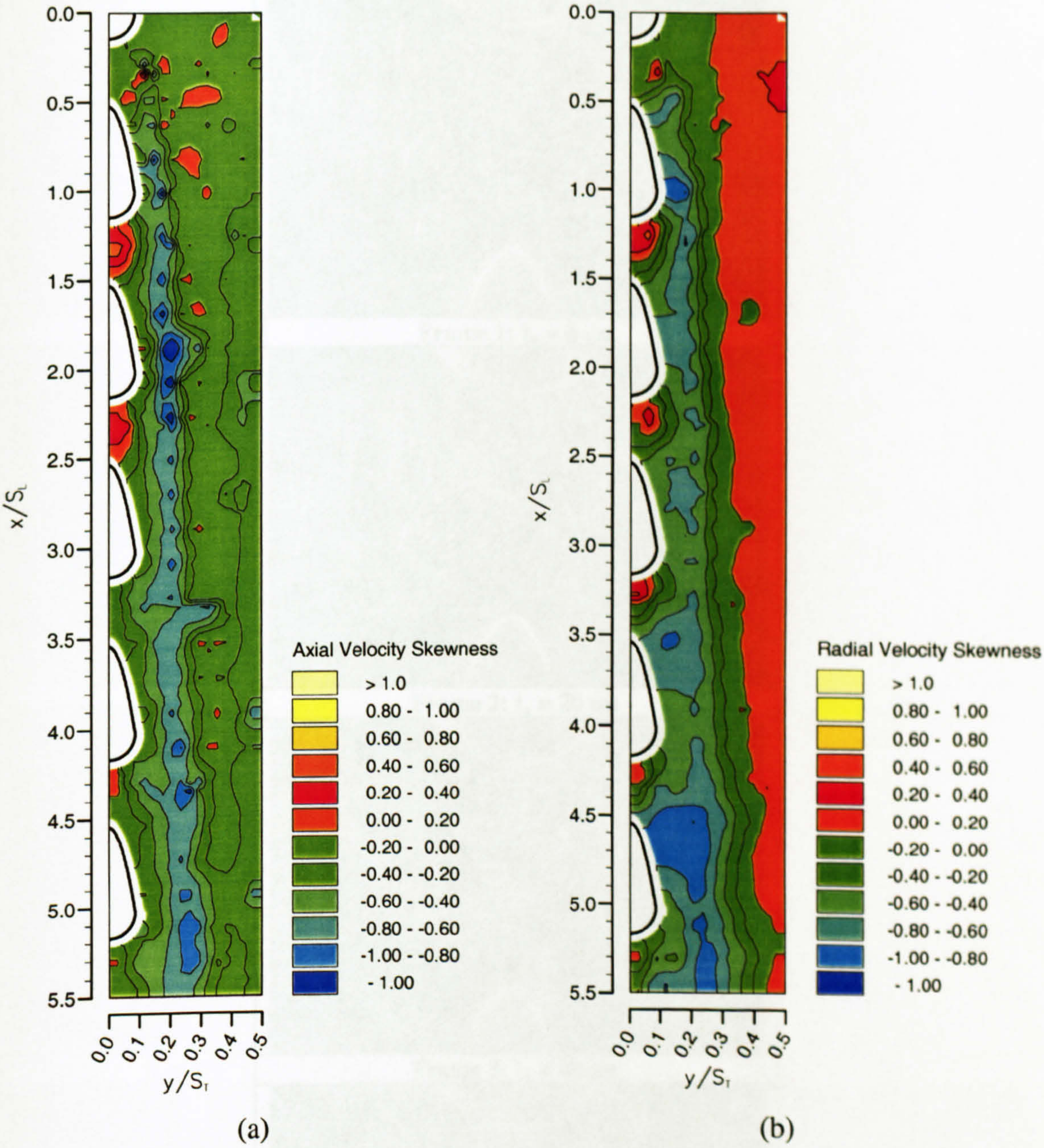

(a) (b)

Figure 5.27. Axial (a) and radial (b) skewness profiles in steady flow past the in-line array with drop-shaped cylinders.

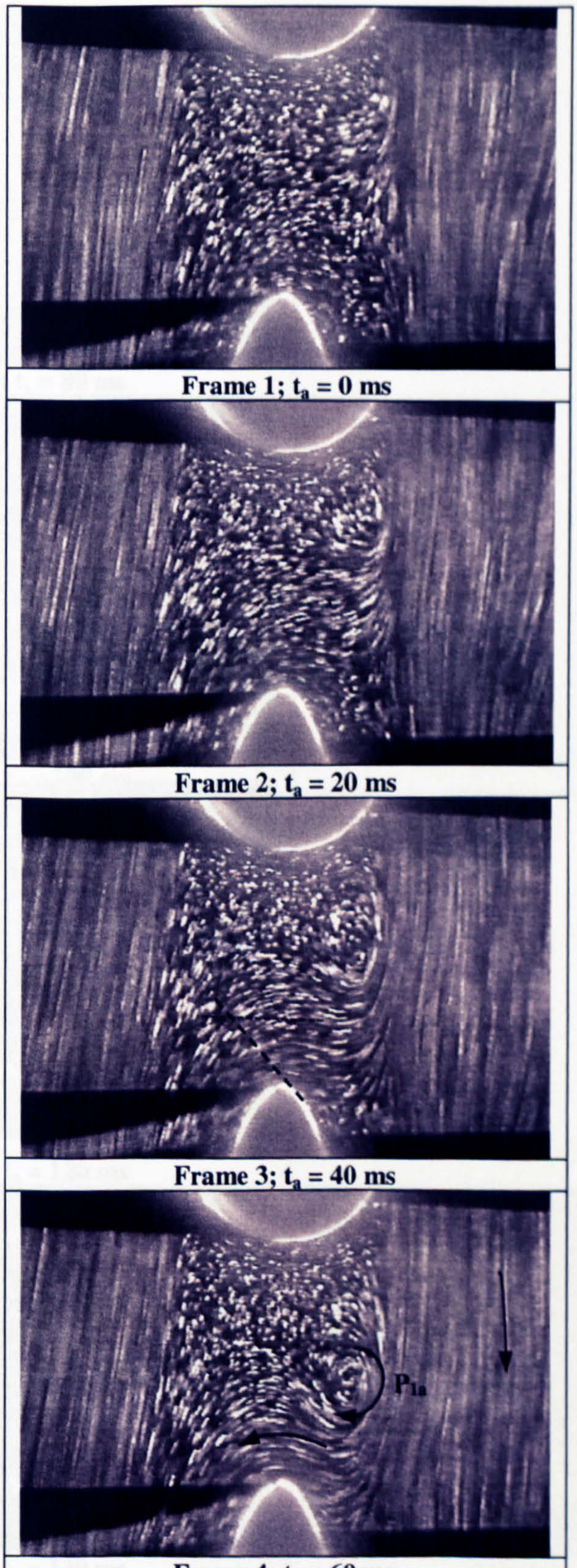

Figure 5.28 (a). Visualisation pictures of the flow in the wake of the first cylinder. (a): Re = 842, frames 1-4.

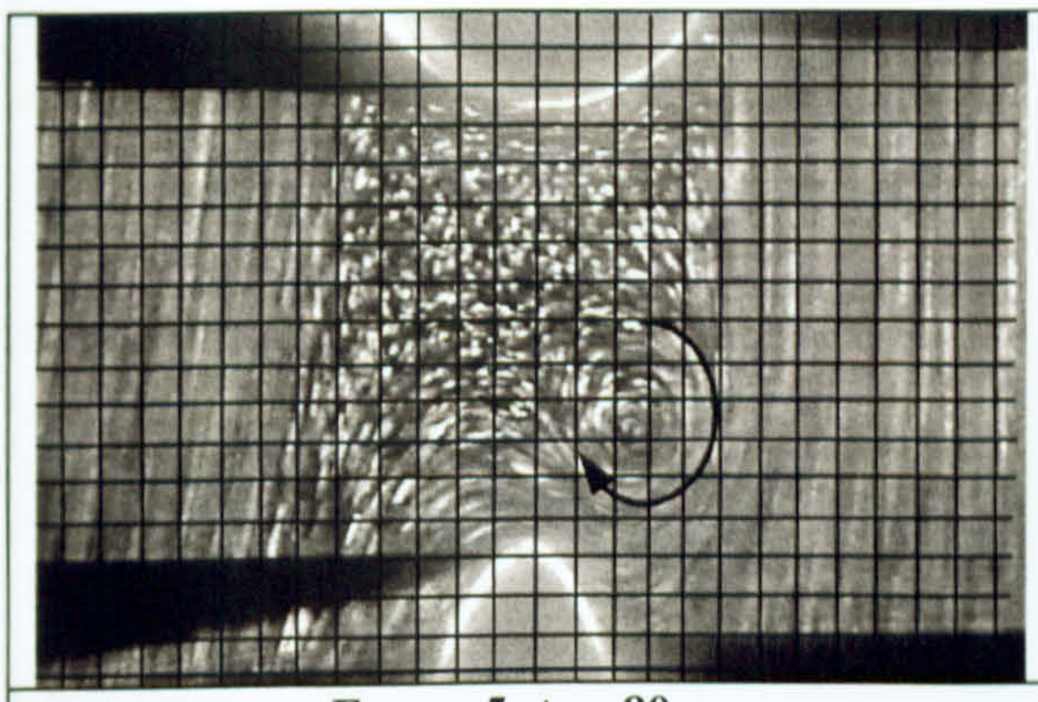

Frame 5; t_a = 80 ms

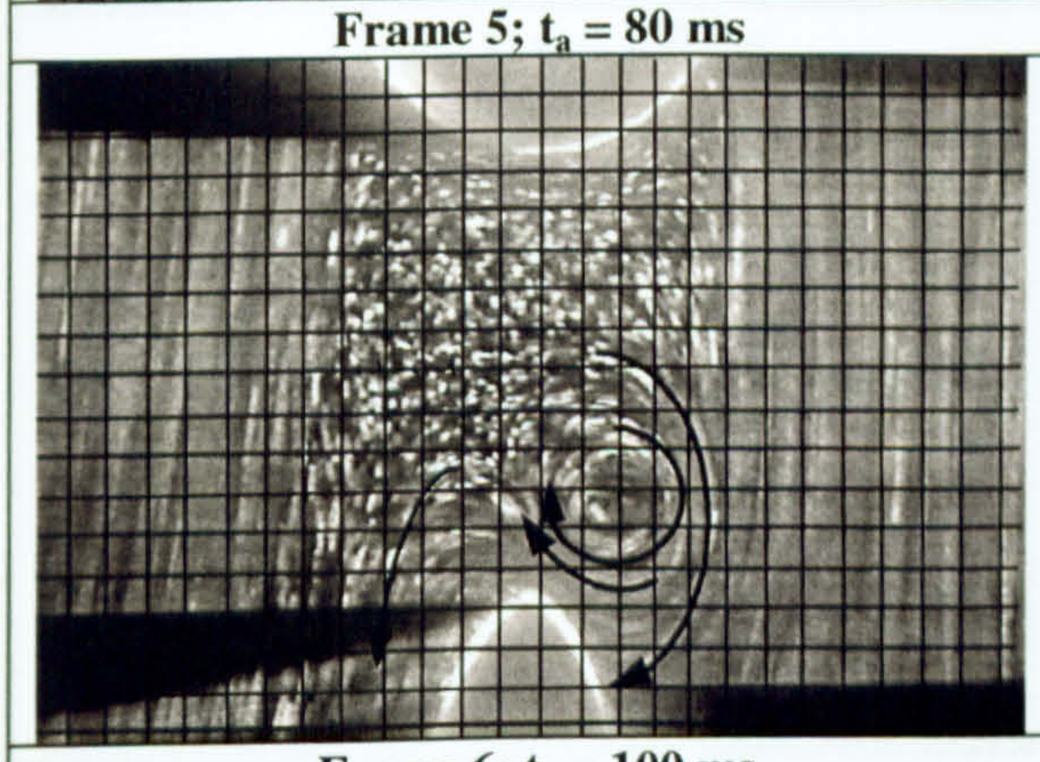

Frame 6; t_a = 100 ms

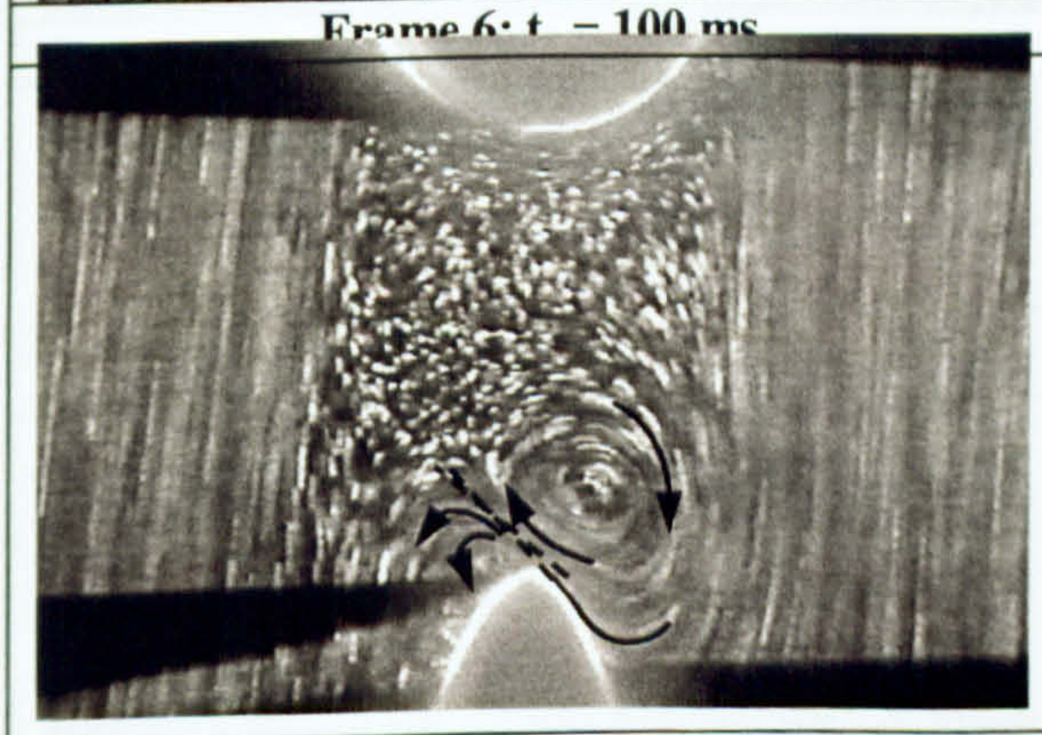

Frame 7; t_a = 120 ms

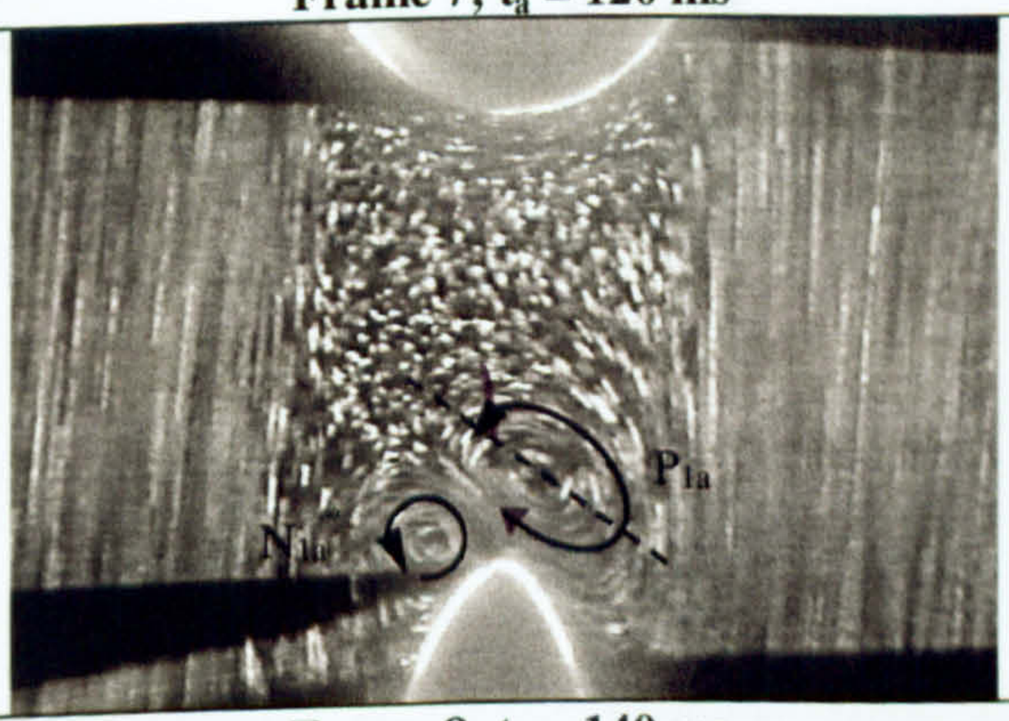

Frame 8; t_a = 140 ms

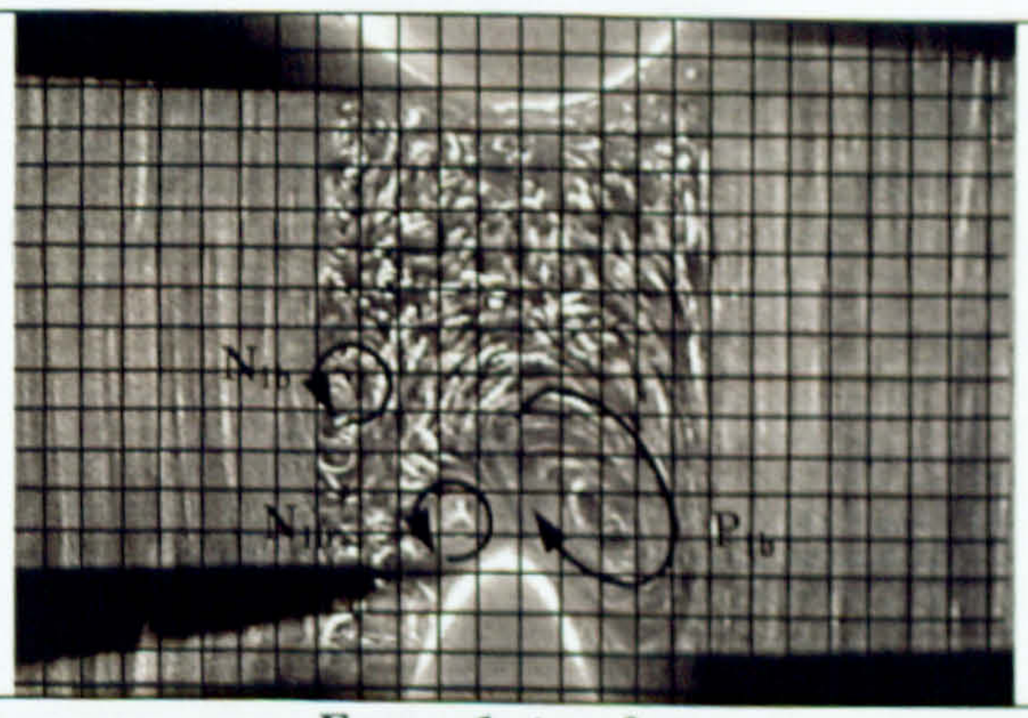

Frame 1; t_b = 0 ms

(a) (b)

Figure 5.28 (b). Visualisation pictures of the flow in the wake of the first cylinder.
(a): Re = 842. Frames 5-8.
(b): Re = 1,426. Frame 1.

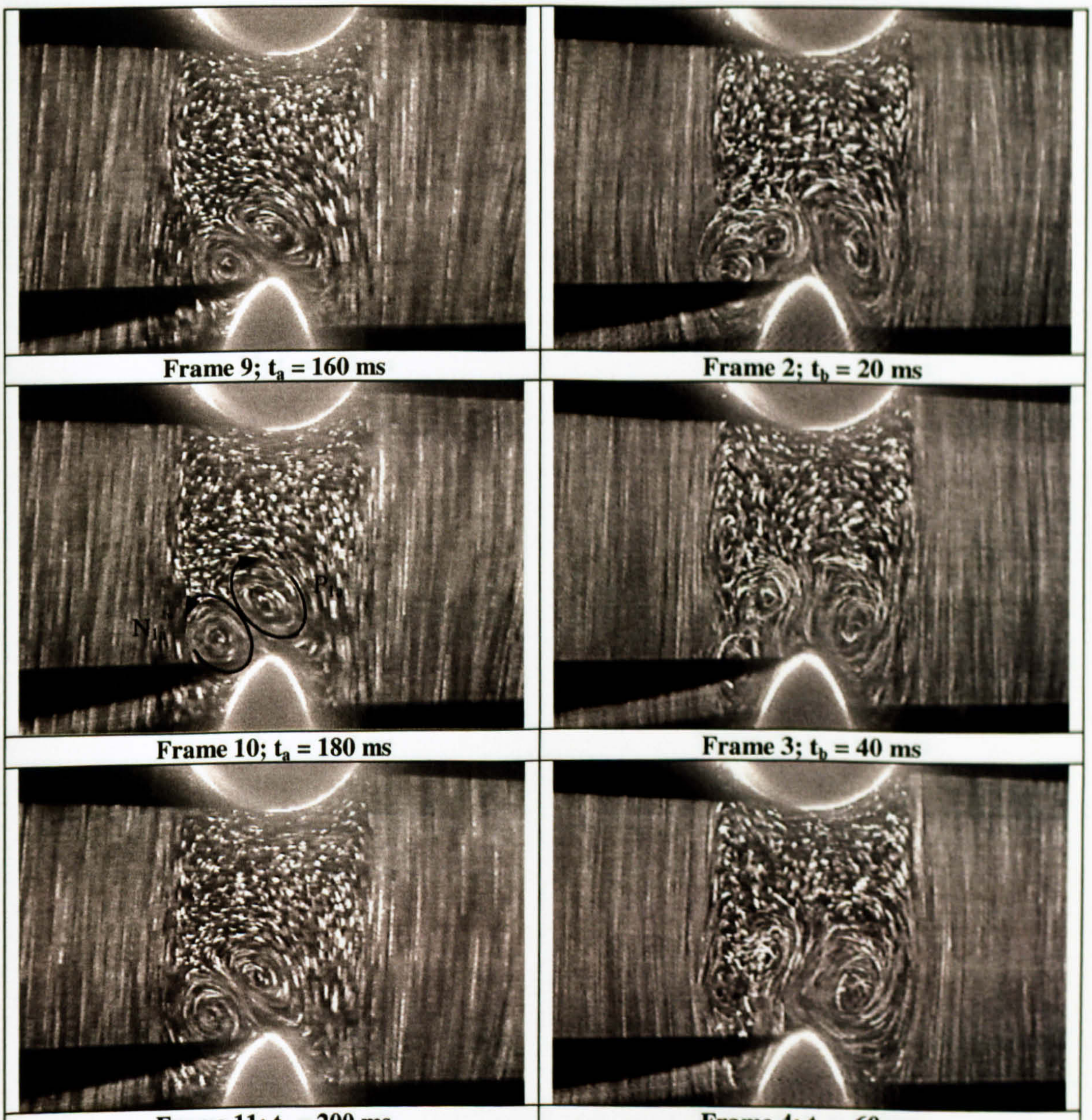

Frame 9; t_a = 160 ms	Frame 2; t_b = 20 ms
Frame 10; t_a = 180 ms	Frame 3; t_b = 40 ms
Frame 11; t_a = 200 ms	Frame 4; t_b = 60 ms
Frame 12; t_a = 220 ms	Frame 5; t_b = 80 ms
(a)	(b)

Figure 5.28 (c). Visualisation pictures of the flow in the wake of the first cylinder.
(a): Re = 842. Frames 9-12.
(b): Re = 1,426. Frames 2-5.

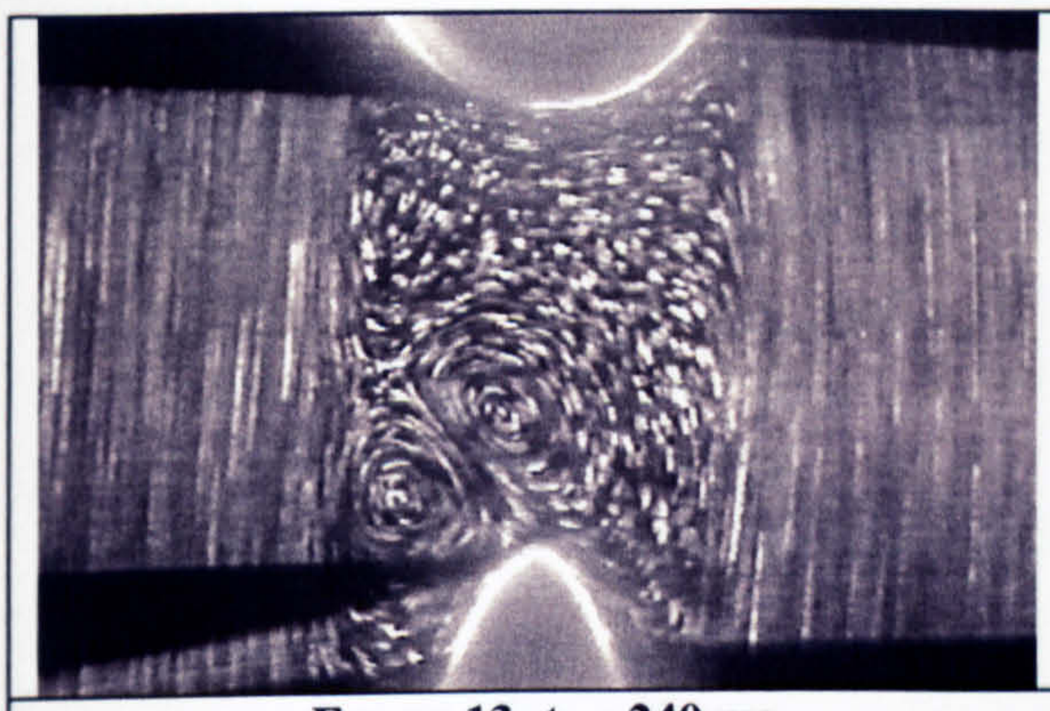	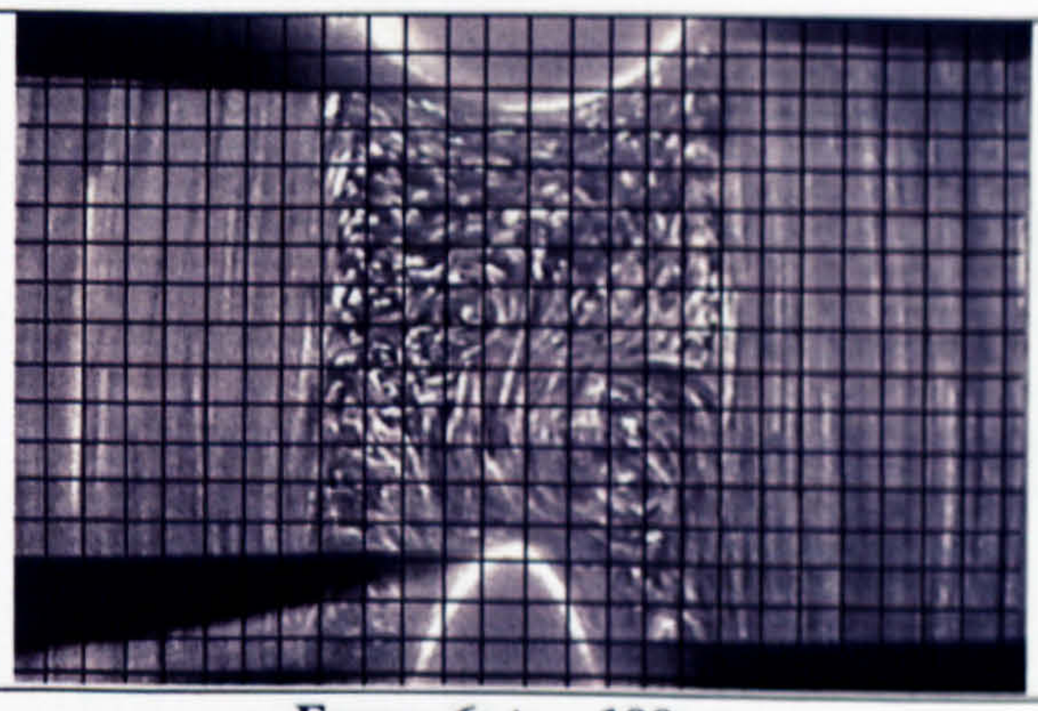
Frame 13; t_a = 240 ms	**Frame 6; t_b = 100 ms**
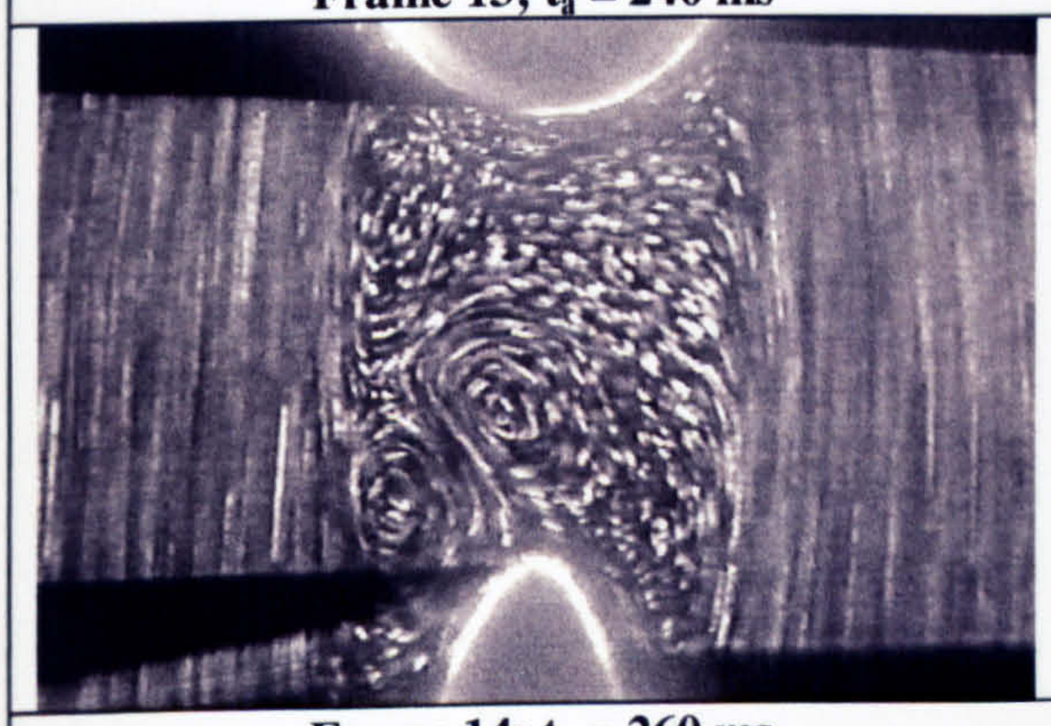	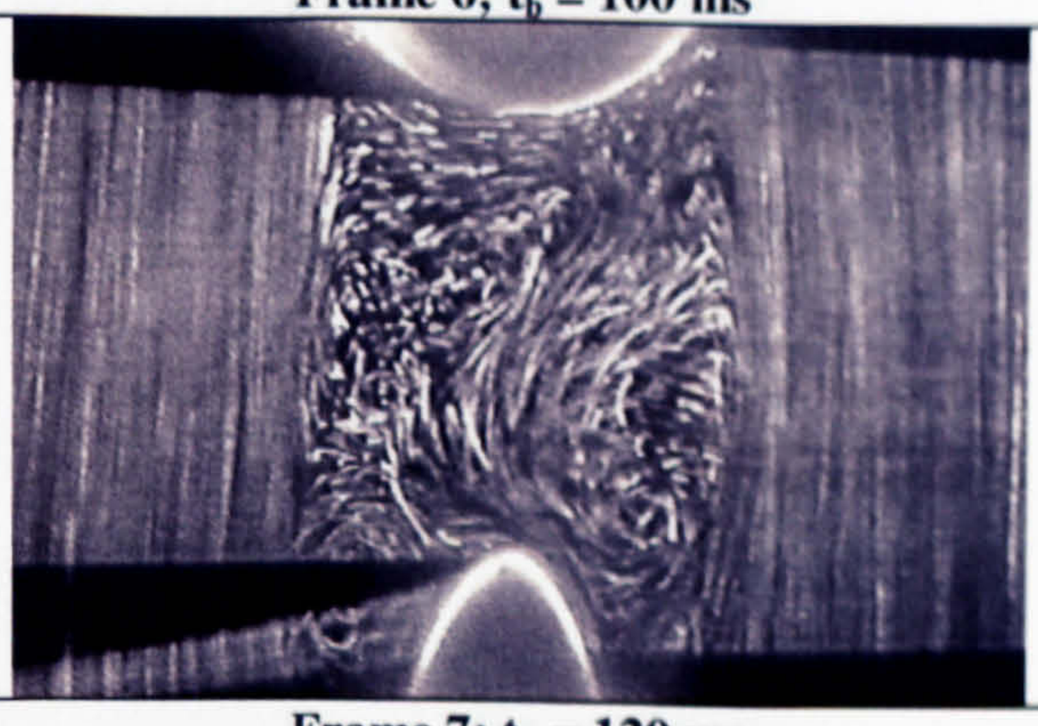
Frame 14; t_a = 260 ms	**Frame 7; t_b = 120 ms**
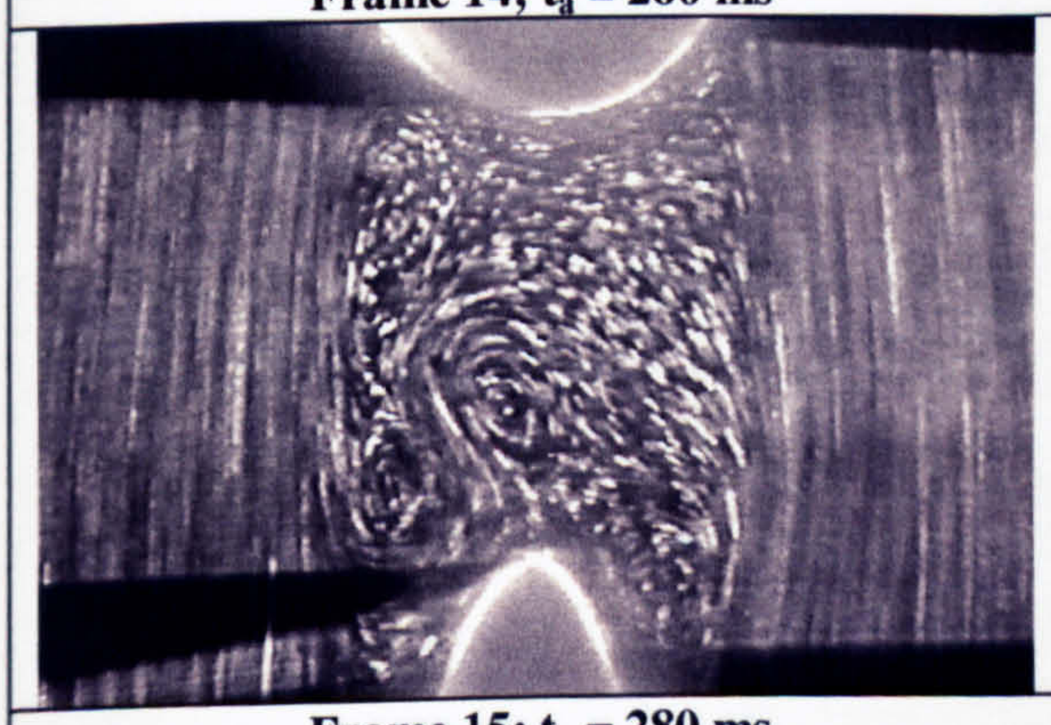	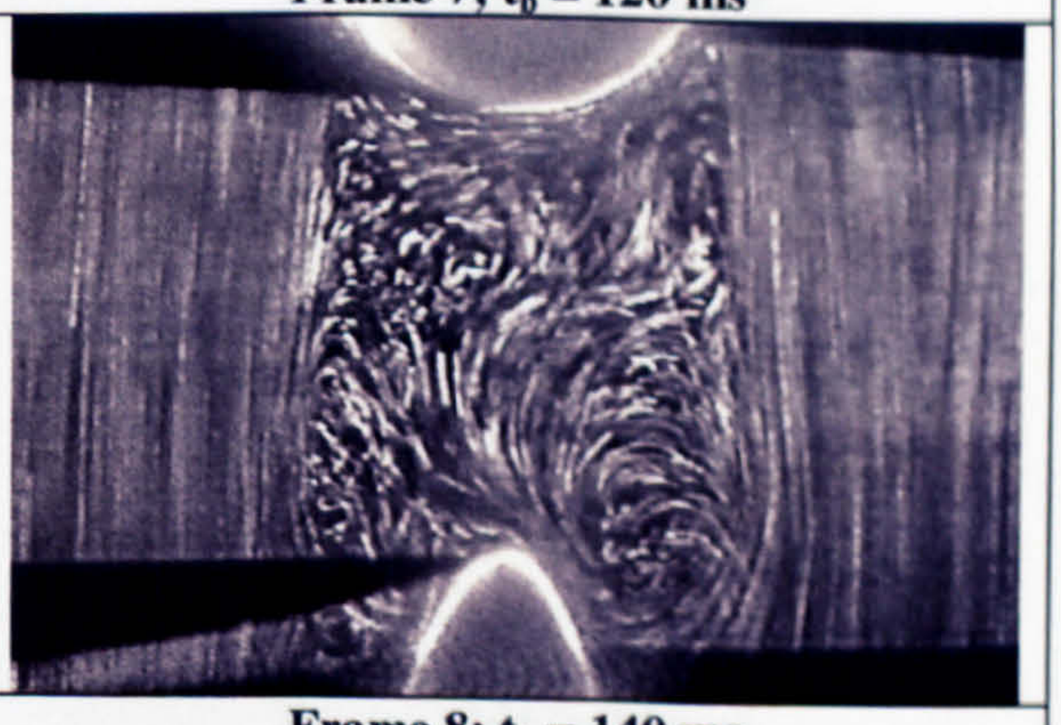
Frame 15; t_a = 280 ms	**Frame 8; t_b = 140 ms**
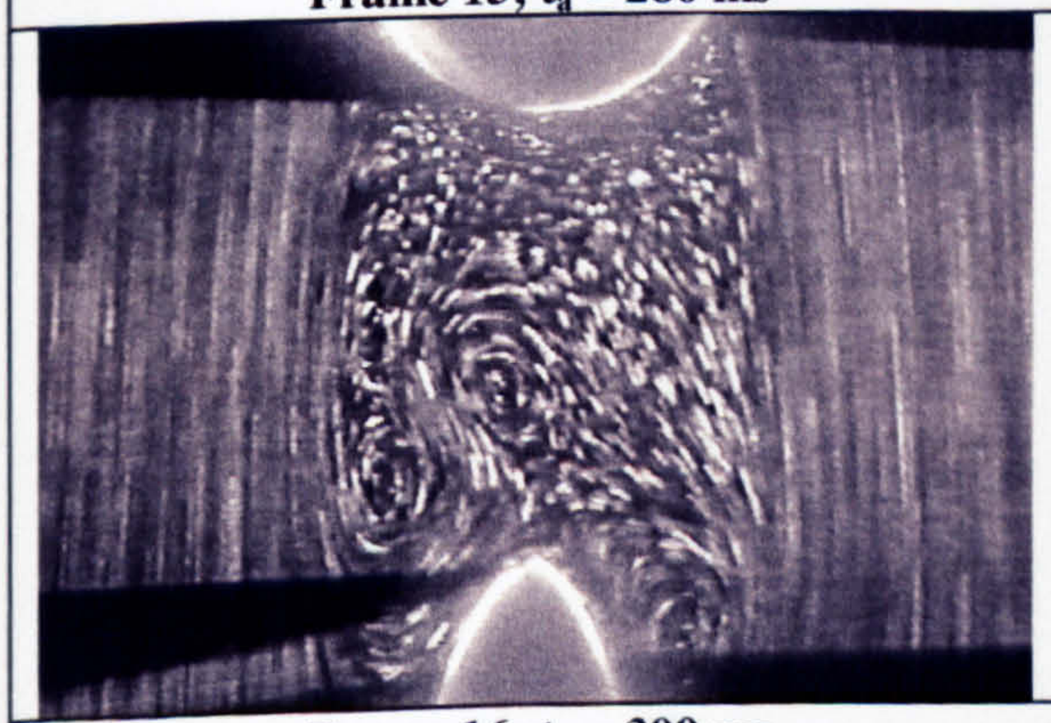	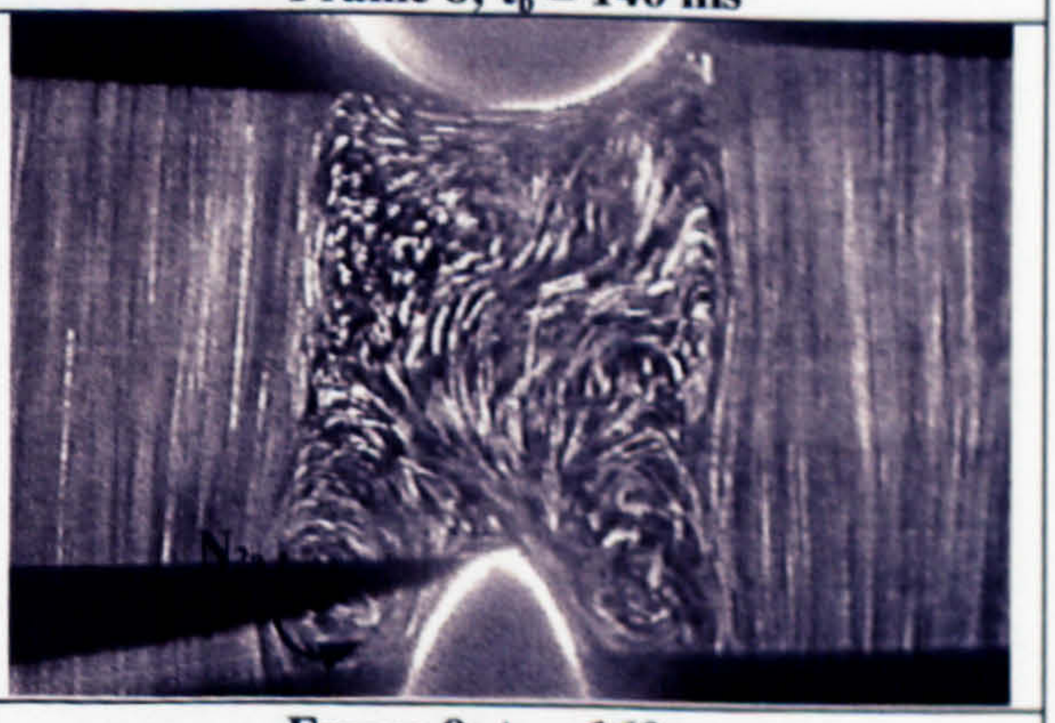
Frame 16; t_a = 300 ms	**Frame 9; t_b = 160 ms**
(a)	**(b)**

Figure 5.28 (d). Visualisation pictures of the flow in the wake of the first cylinder.
(a): Re = 842. Frames 13-16.
(b): Re = 1,426. Frames 6-9.

Frame 17; t_a = 320 ms	Frame 10; t_b = 180 ms
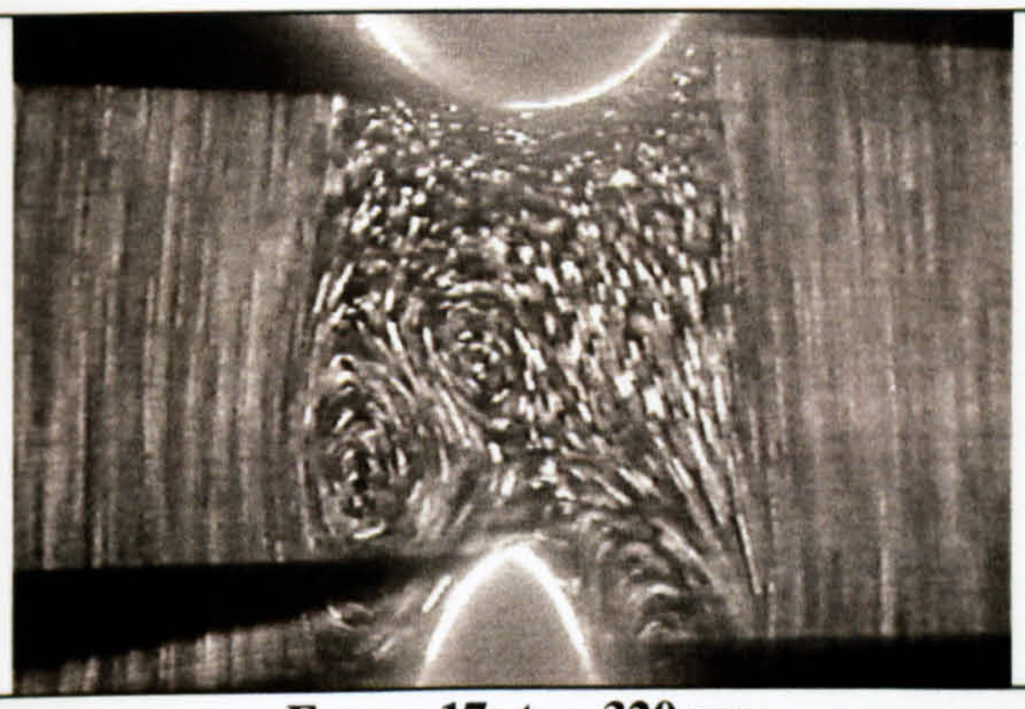	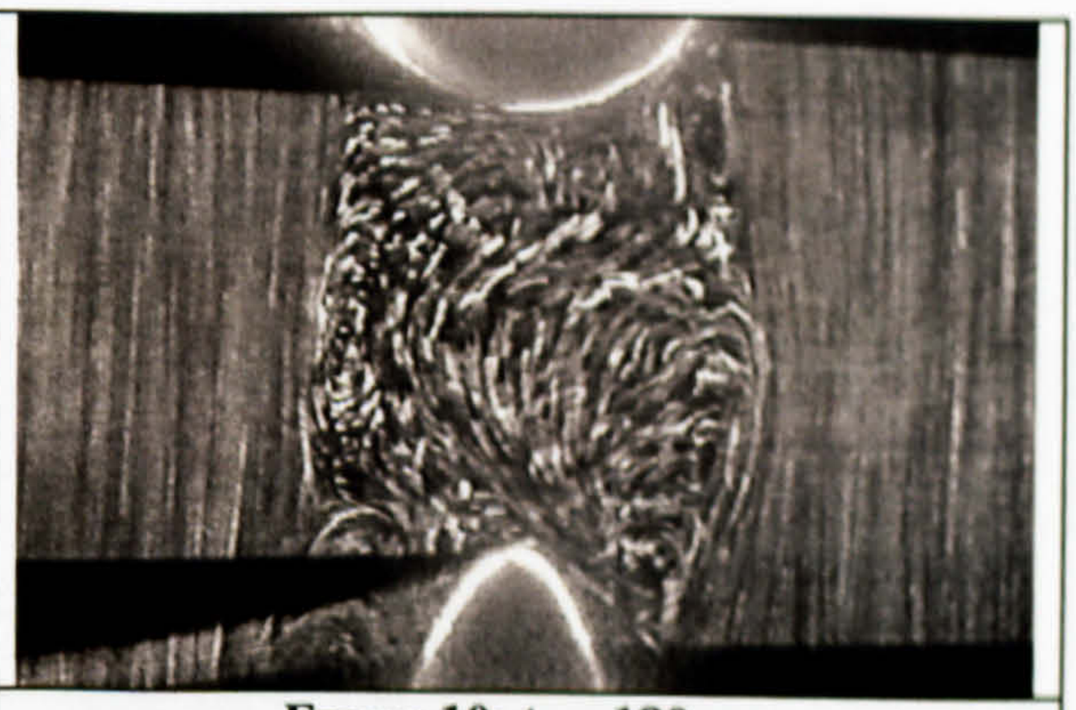
Frame 18; t_a = 340 ms	**Frame 11; t_b = 200 ms**
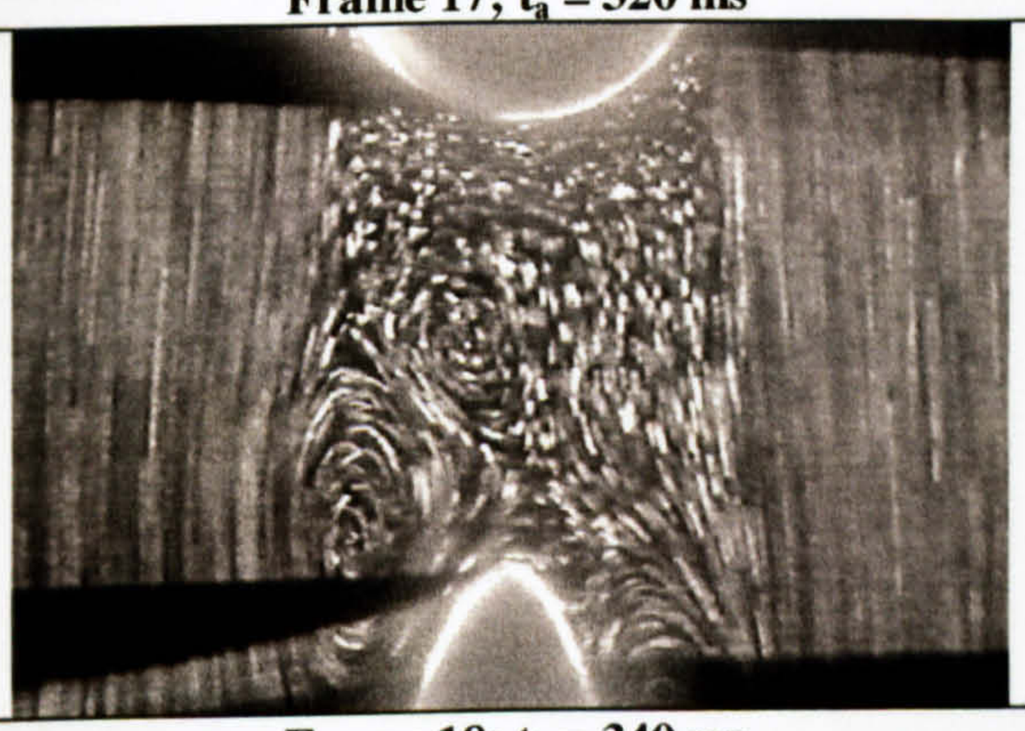	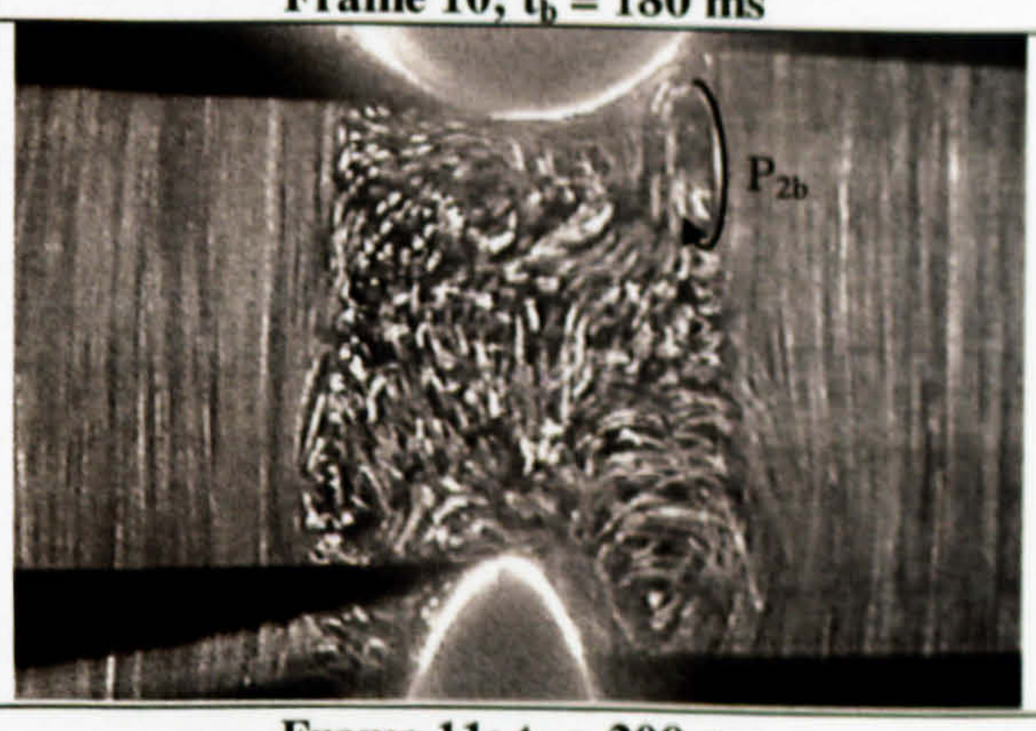
Frame 19; t_a = 360 ms	**Frame 12; t_b = 220 ms**
	
Frame 20; t_a = 380 ms	**Frame 13; t_b = 240 ms**
(a)	**(b)**

Figure 5.28 (e). Visualisation pictures of the flow in the wake of the first cylinder.
(a): Re = 842. Frames 17-20.
(b): Re = 1,426. Frames 10-13.

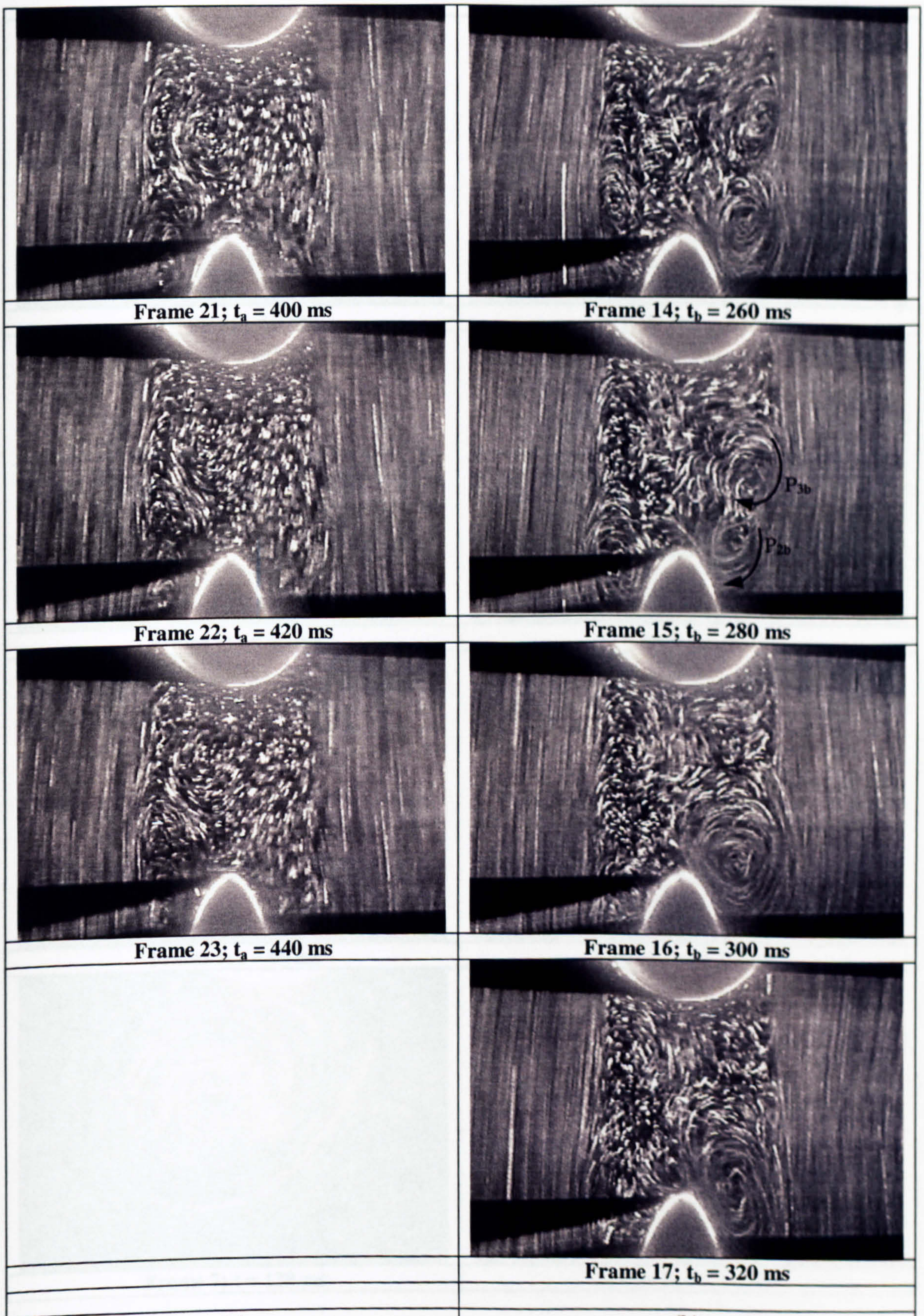

Figure 5.28 (f). Visualisation pictures of the flow in the wake of the first cylinder.
(a): Re = 842. Frames 21-23.
(b): Re = 1,426. Frames 14-17.

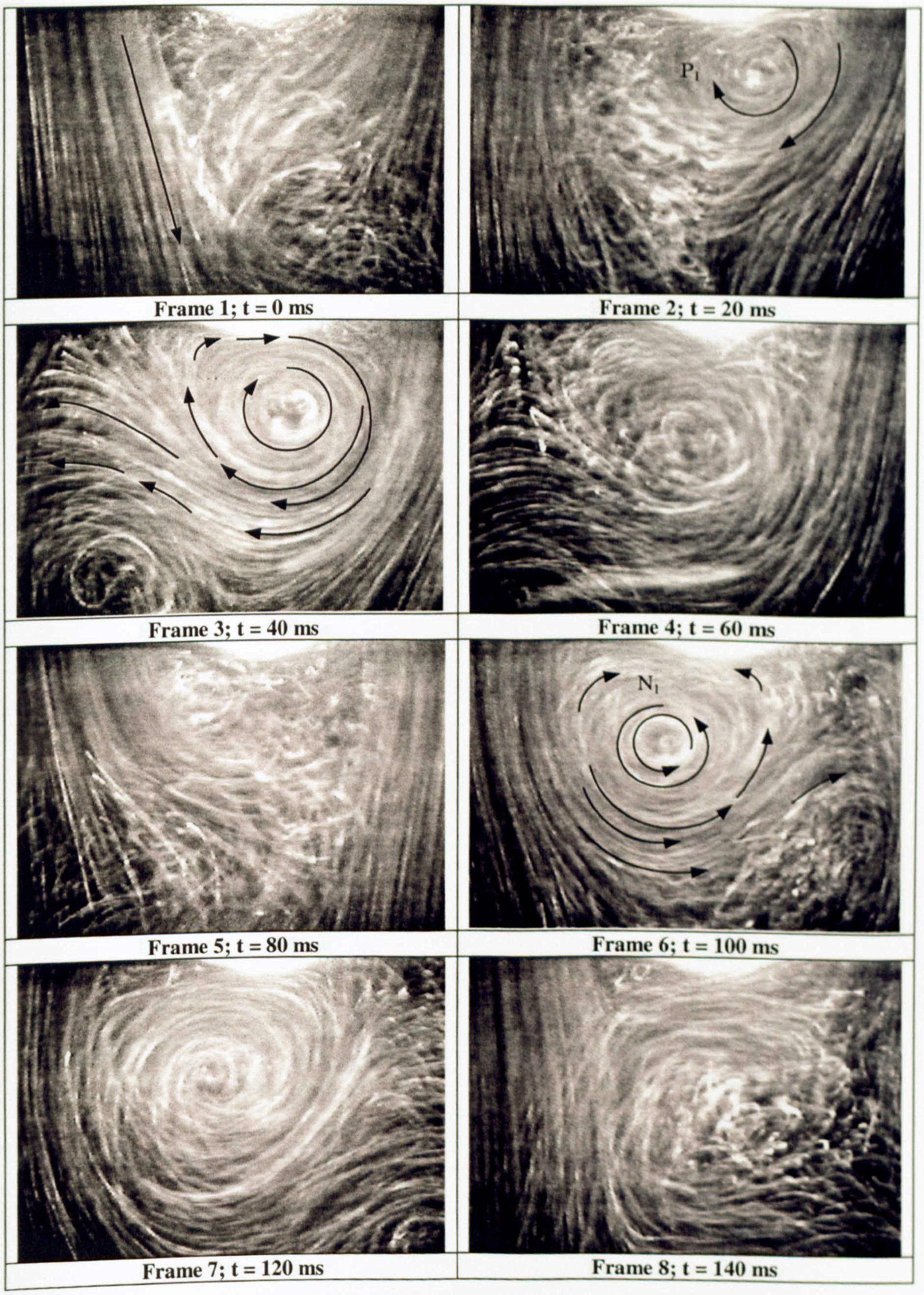

Frame 1; t = 0 ms | Frame 2; t = 20 ms

Frame 3; t = 40 ms | Frame 4; t = 60 ms

Frame 5; t = 80 ms | Frame 6; t = 100 ms

Frame 7; t = 120 ms | Frame 8; t = 140 ms

Figure 5.29 (a). Visualisation pictures of the flow in the wake of the first row in pulsating flow (Re = 1,443, 14 Hz). Frames 1-8.

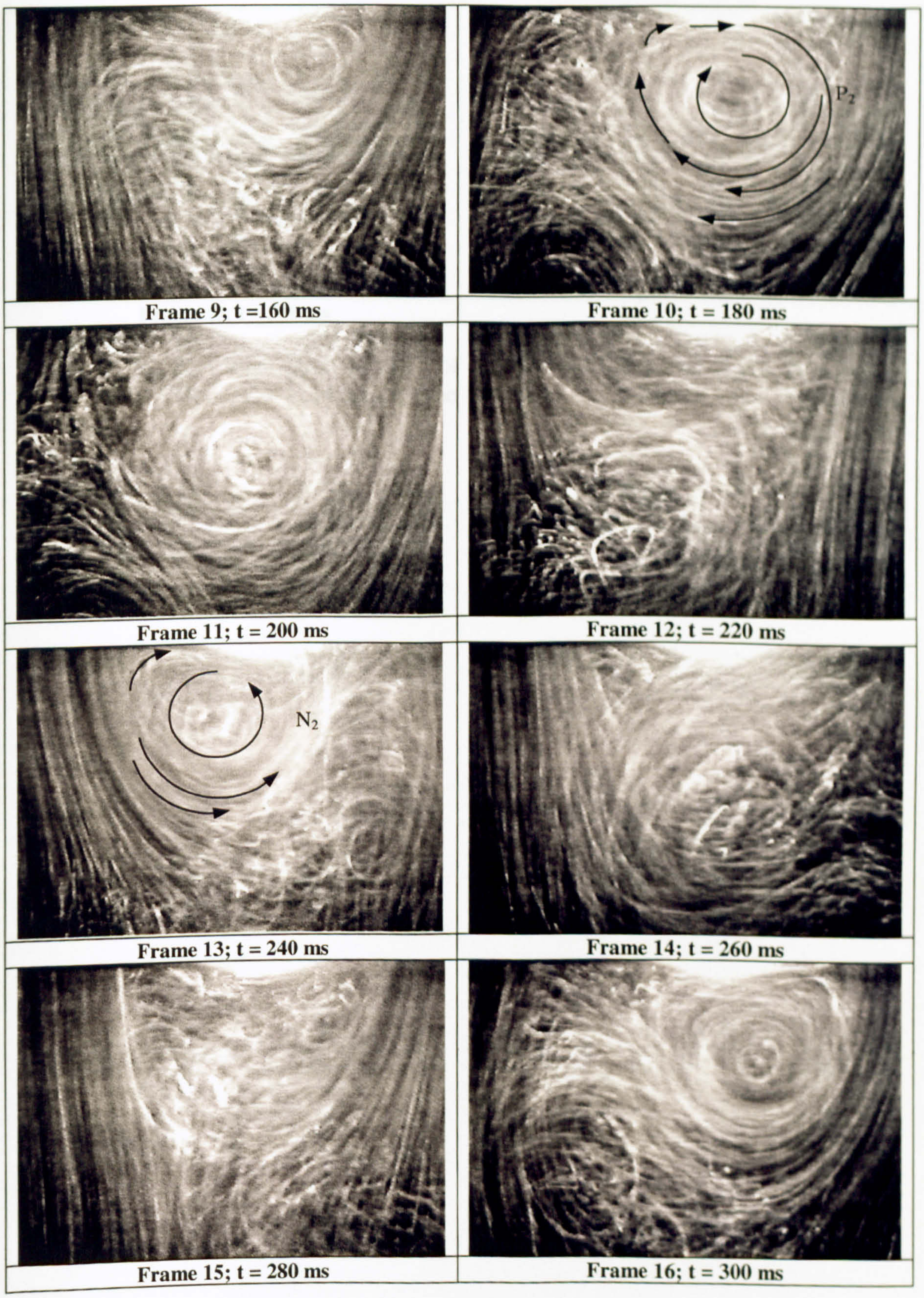

Frame 9; t =160 ms | Frame 10; t = 180 ms

Frame 11; t = 200 ms | Frame 12; t = 220 ms

Frame 13; t = 240 ms | Frame 14; t = 260 ms

Frame 15; t = 280 ms | Frame 16; t = 300 ms

Figure 5.29 (b). Visualisation pictures of the flow in the wake of the first row in pulsating flow (Re = 1,443, 14 Hz). Frames 9-16.

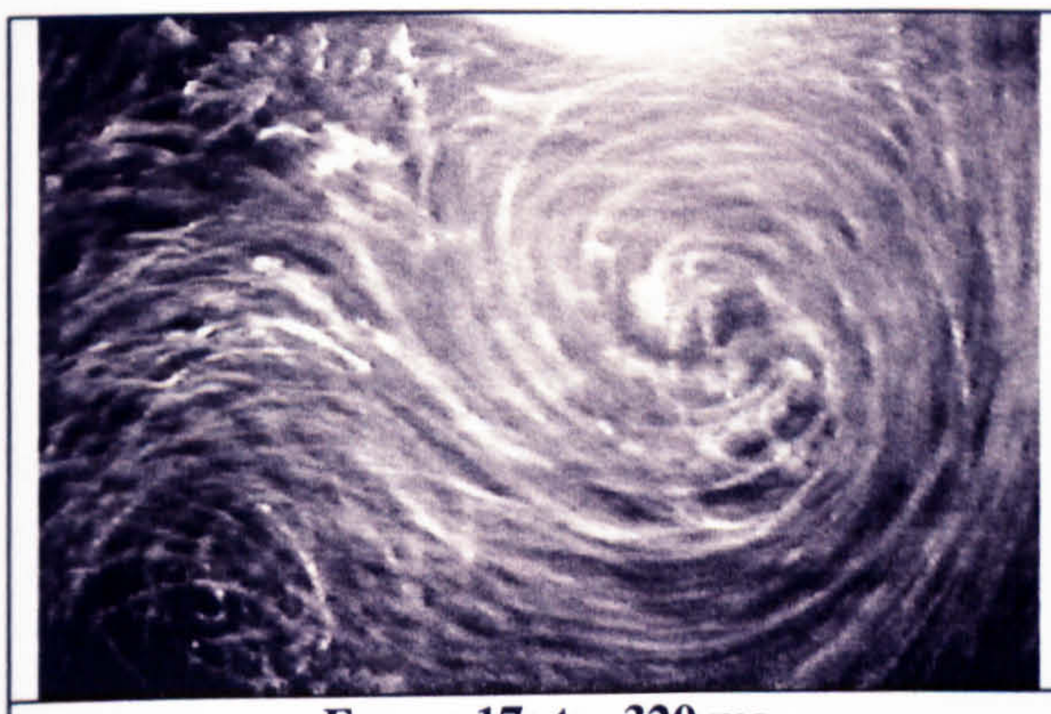

Frame 17; t = 320 ms

Figure 5.29 (c). Visualisation pictures of the flow in the wake of the first row in pulsating flow (Re = 1,443, 14 Hz). Frame 17.

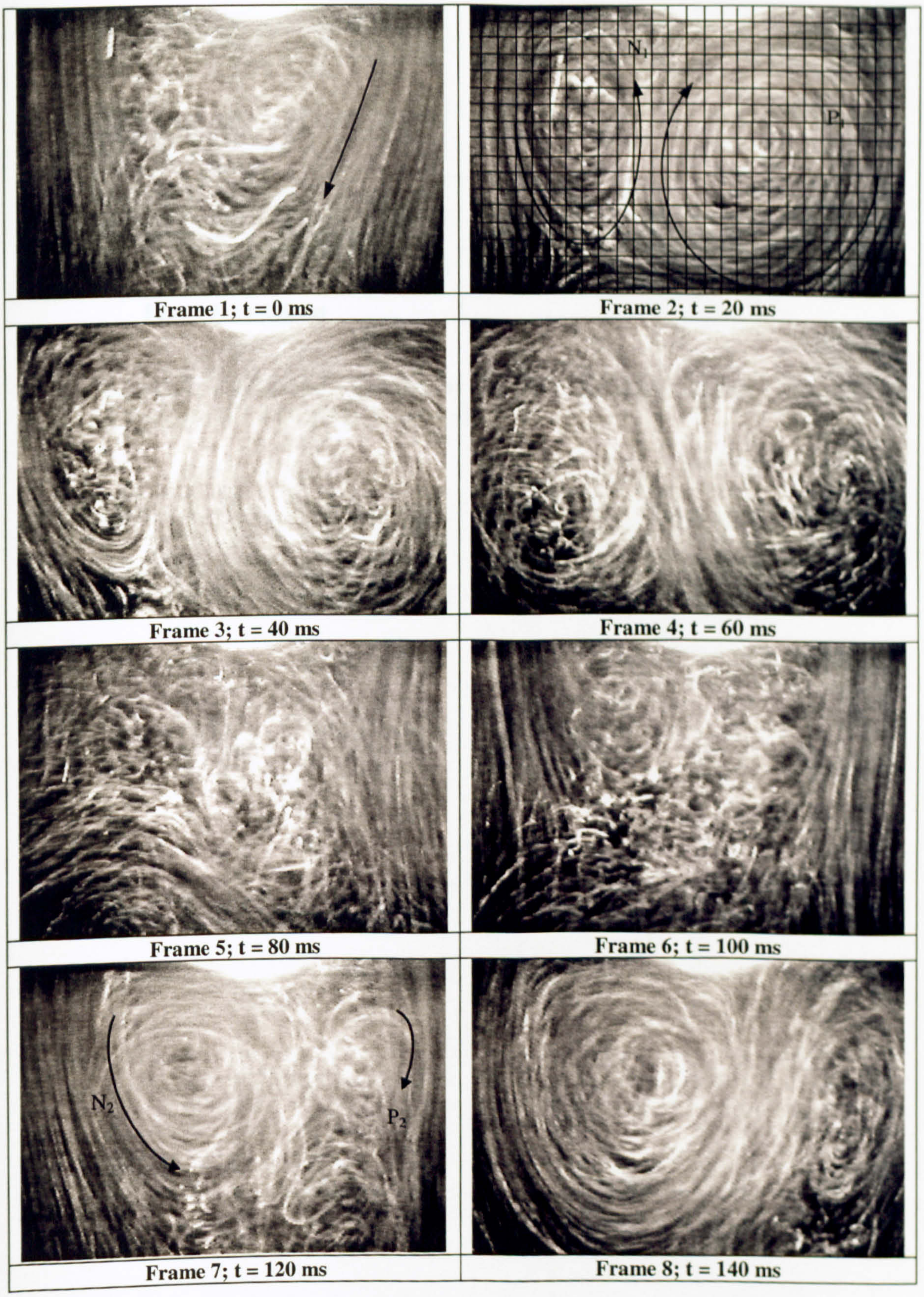

Frame 1; t = 0 ms | Frame 2; t = 20 ms

Frame 3; t = 40 ms | Frame 4; t = 60 ms

Frame 5; t = 80 ms | Frame 6; t = 100 ms

Frame 7; t = 120 ms | Frame 8; t = 140 ms

Figure 5.30 (a). Visualisation pictures of the flow in the wake of the first row in pulsating flow (Re = 1,443, 10 Hz). Frames 1-8.

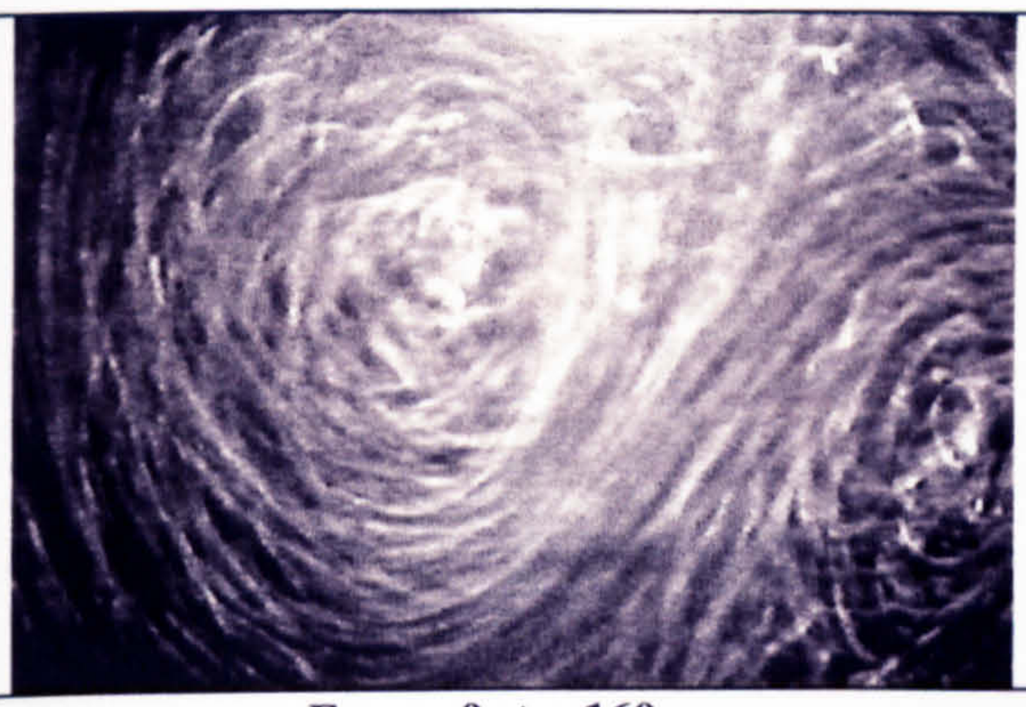

Frame 9; t = 160 ms

Figure 5.30 (b). Visualisation pictures of the flow in the wake of the first row in pulsating flow (Re = 1,443, 10 Hz). Frame 9.

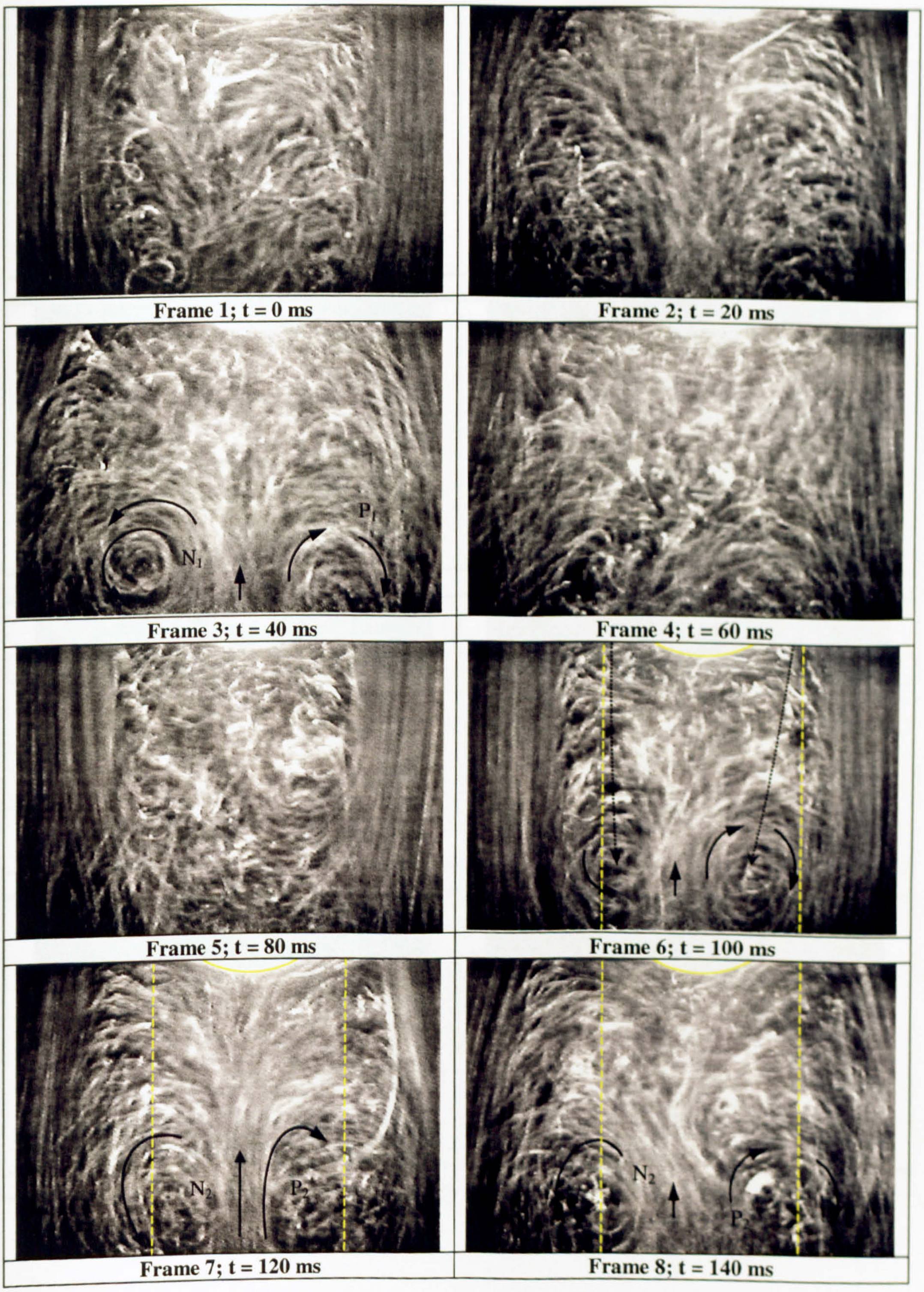

Figure 5.31. Visualisation pictures of the flow in the wake of the first row in pulsating flow (Re = 2,139, 10 Hz). Frames 1-8.

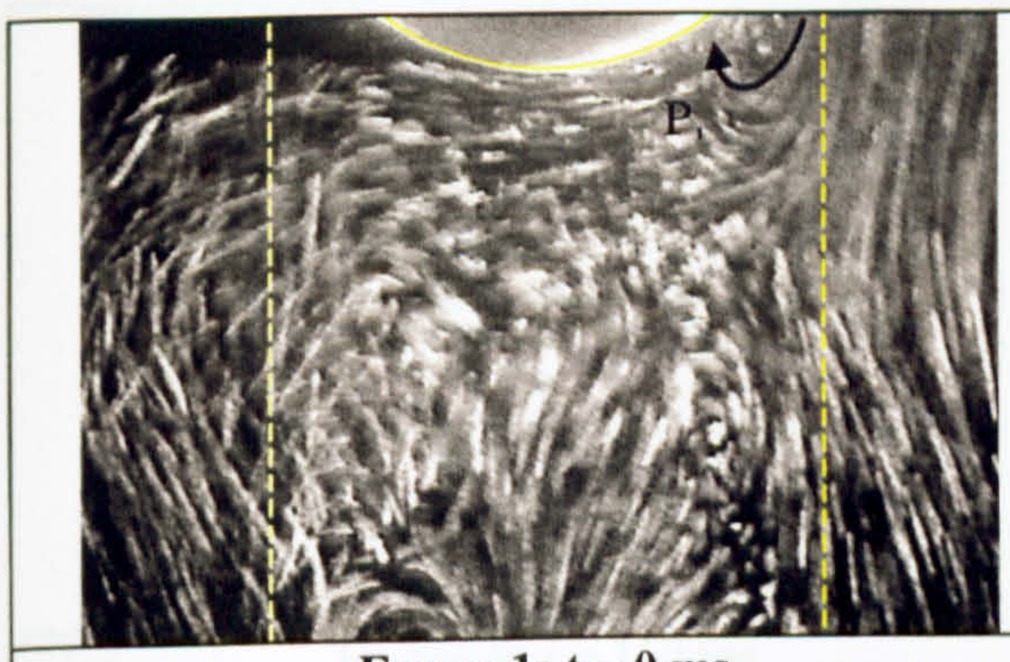

Frame 1; t = 0 ms

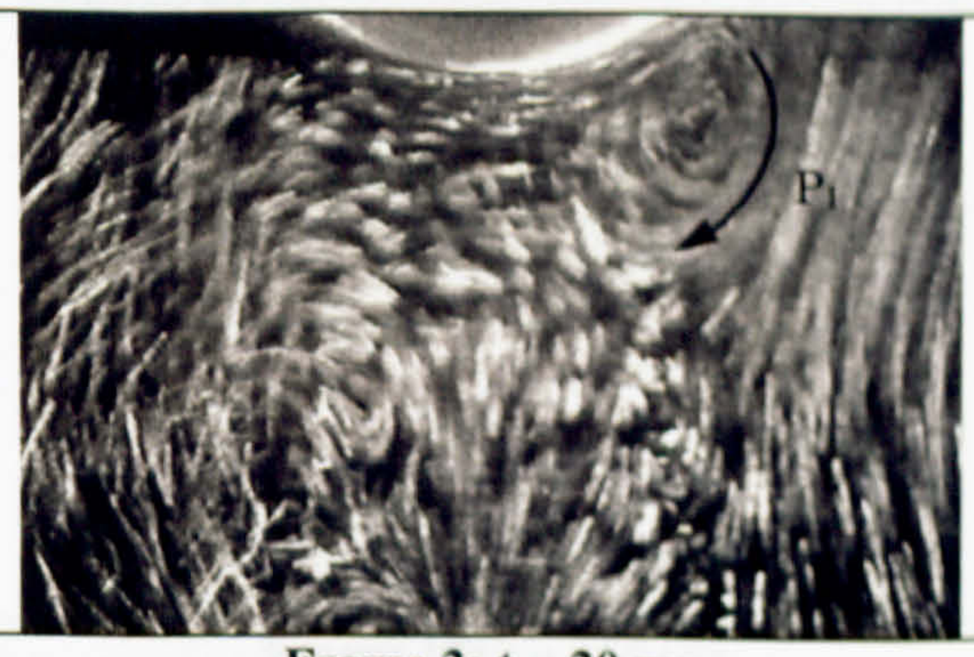

Frame 2; t = 20 ms

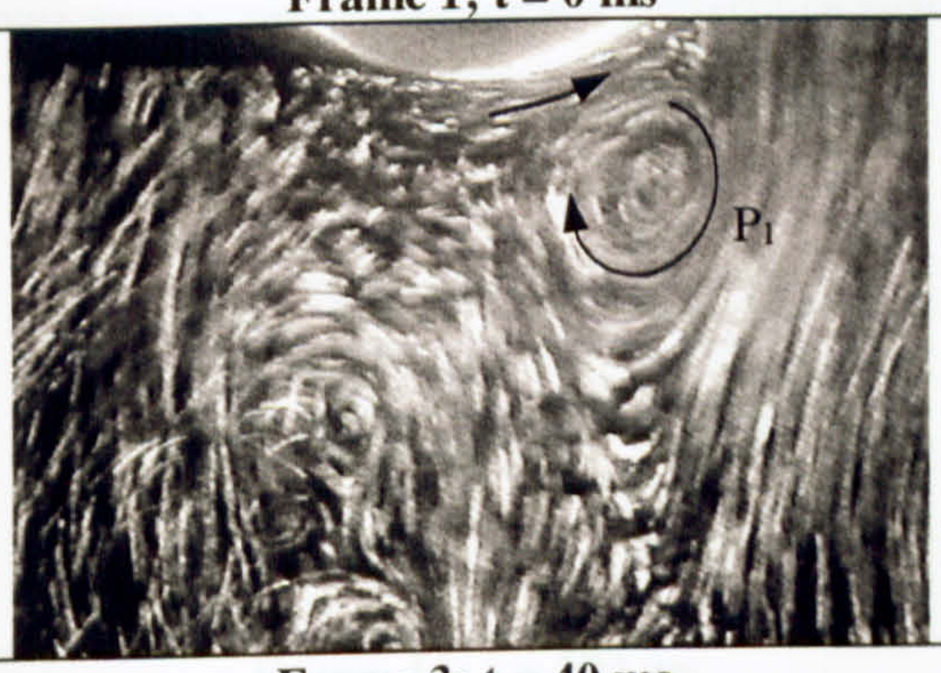

Frame 3; t = 40 ms

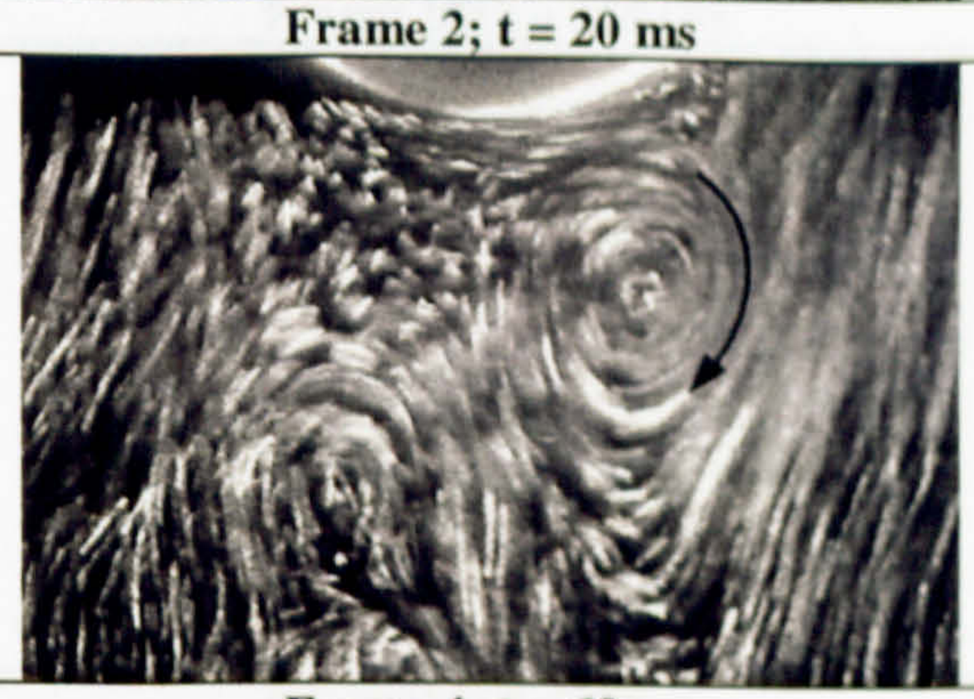

Frame 4; t = 60 ms

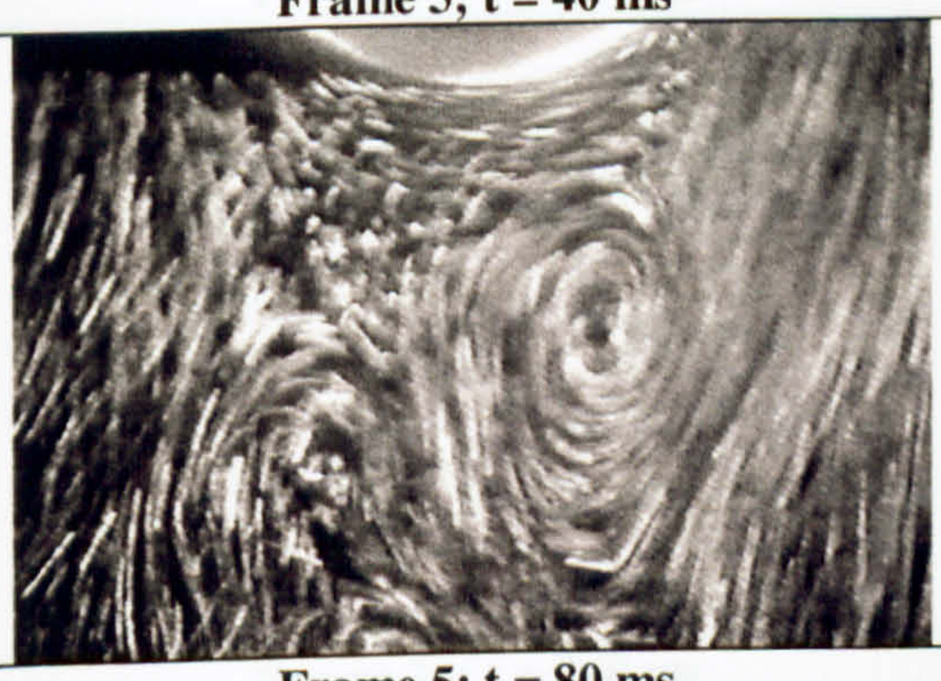

Frame 5; t = 80 ms

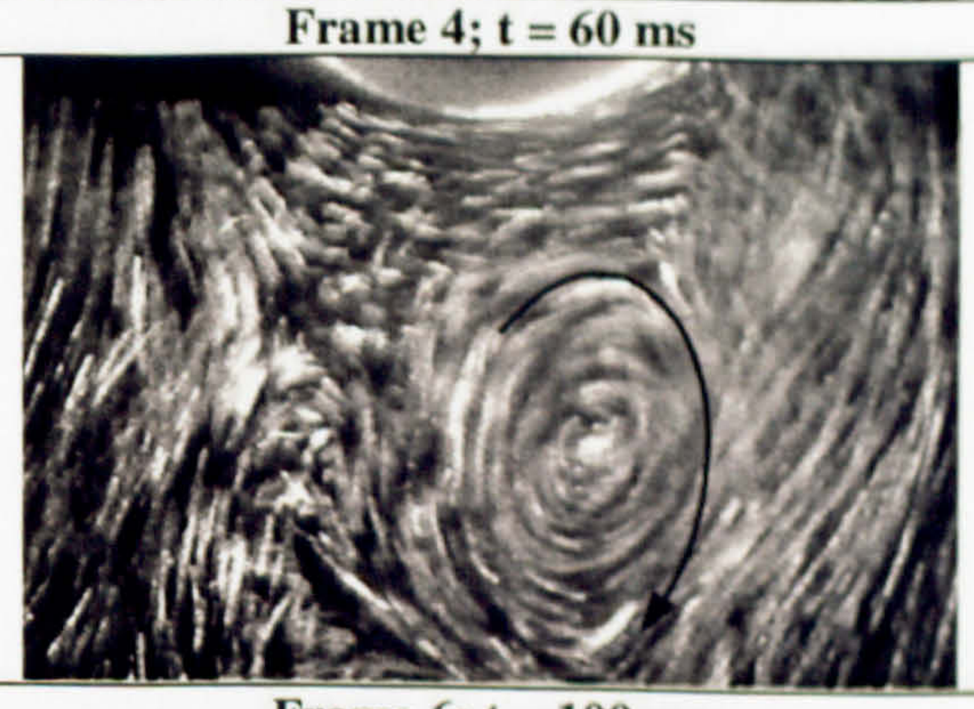

Frame 6; t = 100 ms

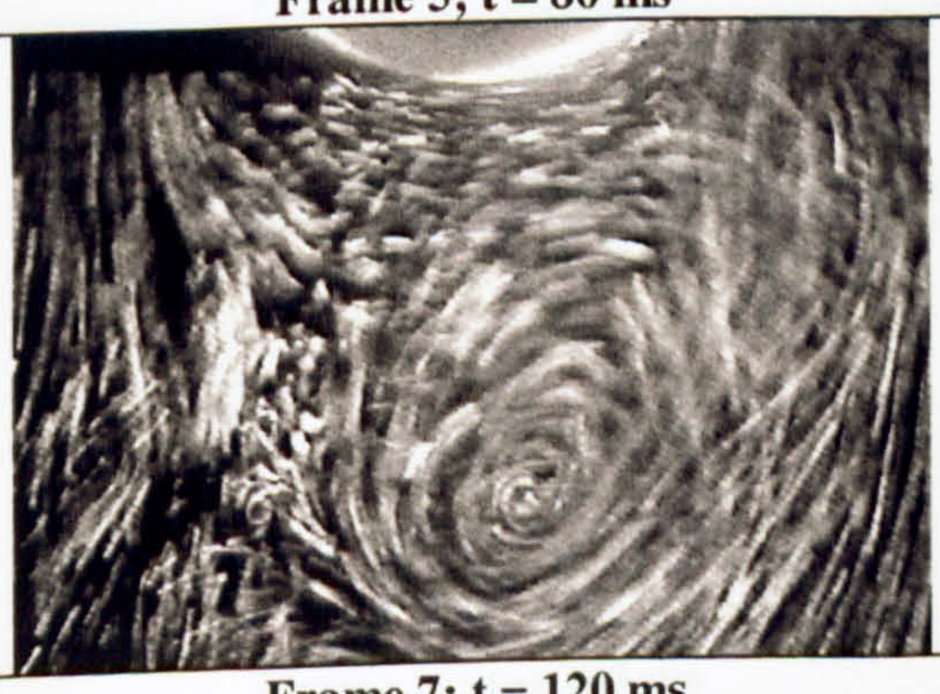

Frame 7; t = 120 ms

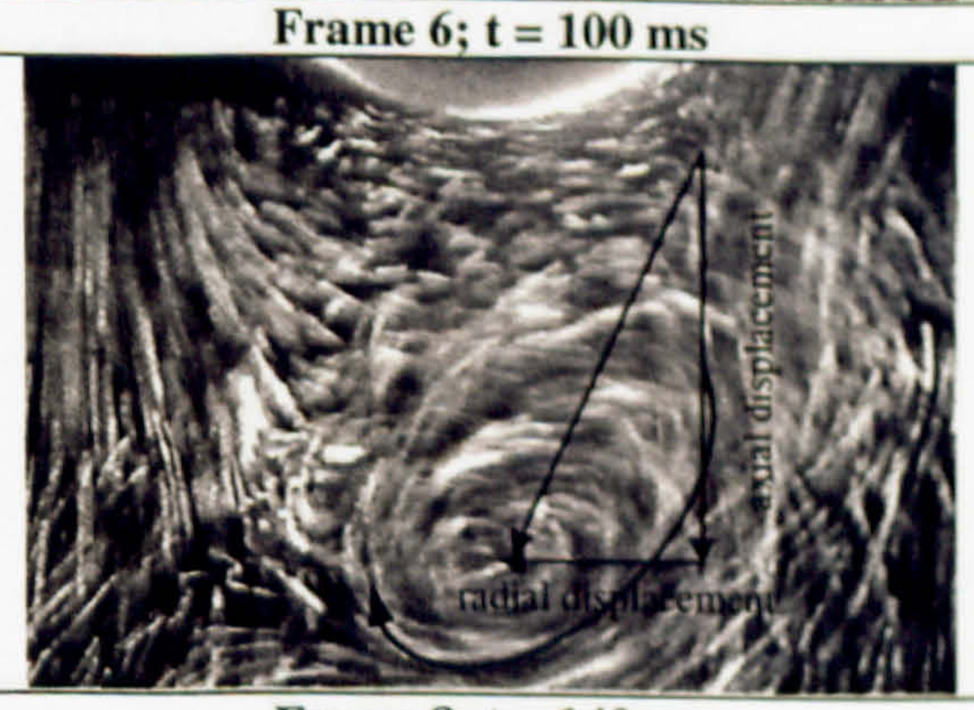

Frame 8; t = 140 ms

Figure 5.32 (a). Visualisation pictures of the flow in the wake of the third cylinder (Re = 842). Frames 1-8.

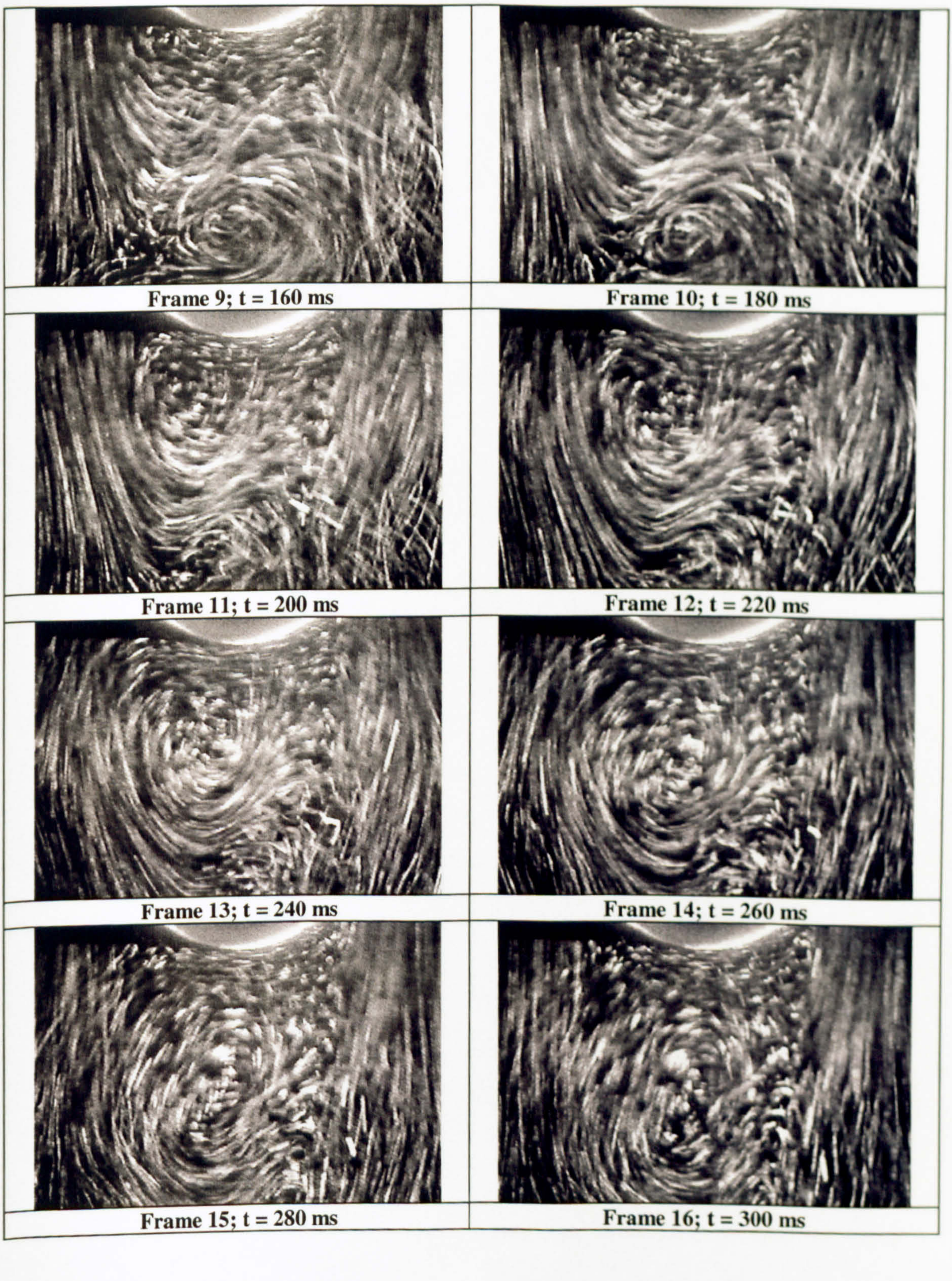

Figure 5.32 (b). Visualisation pictures of the flow in the wake of the third cylinder (Re = 842). Frames 9-16.

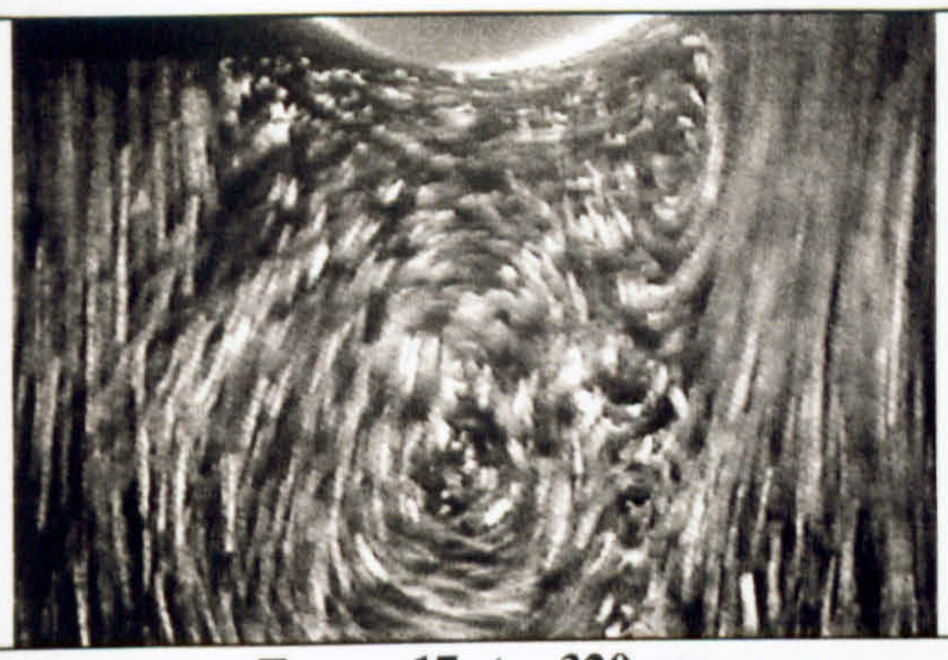

Frame 17; t = 320 ms

Frame 18; t = 340 ms

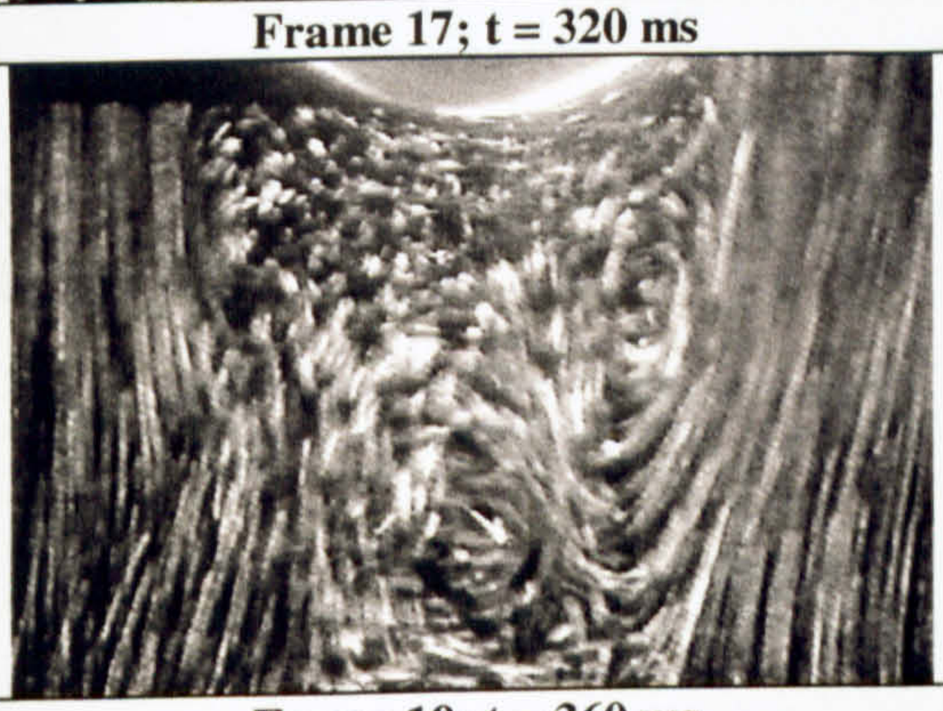

Frame 19; t = 360 ms

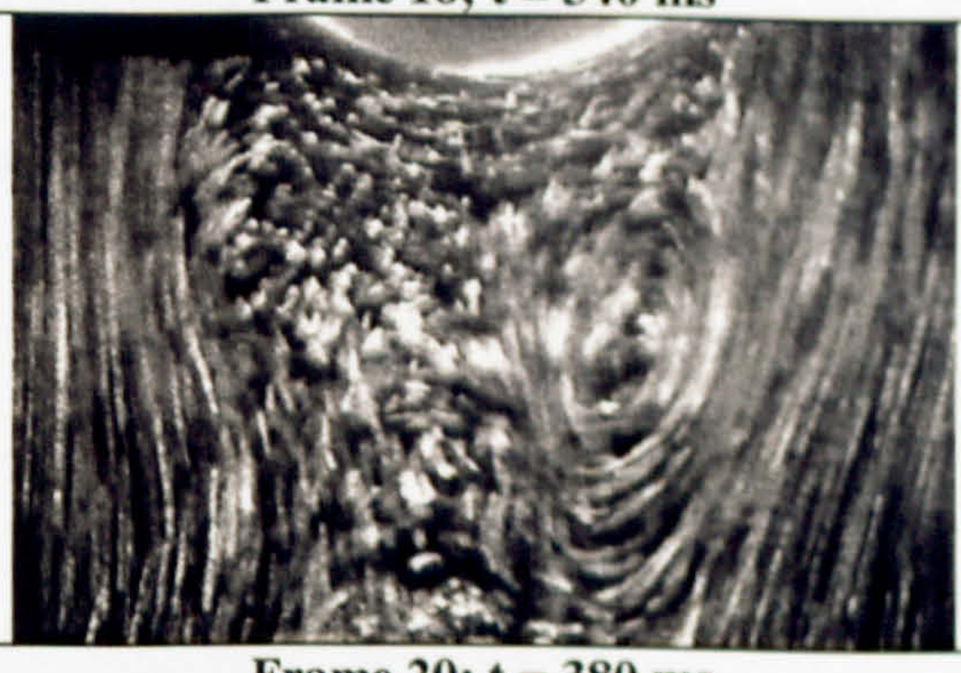

Frame 20; t = 380 ms

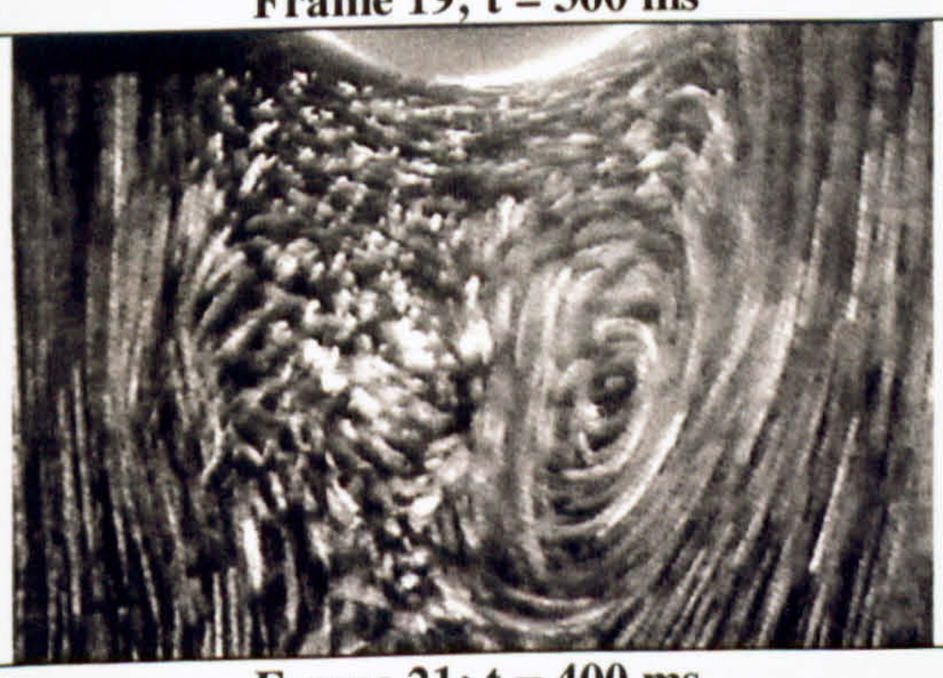

Frame 21; t = 400 ms

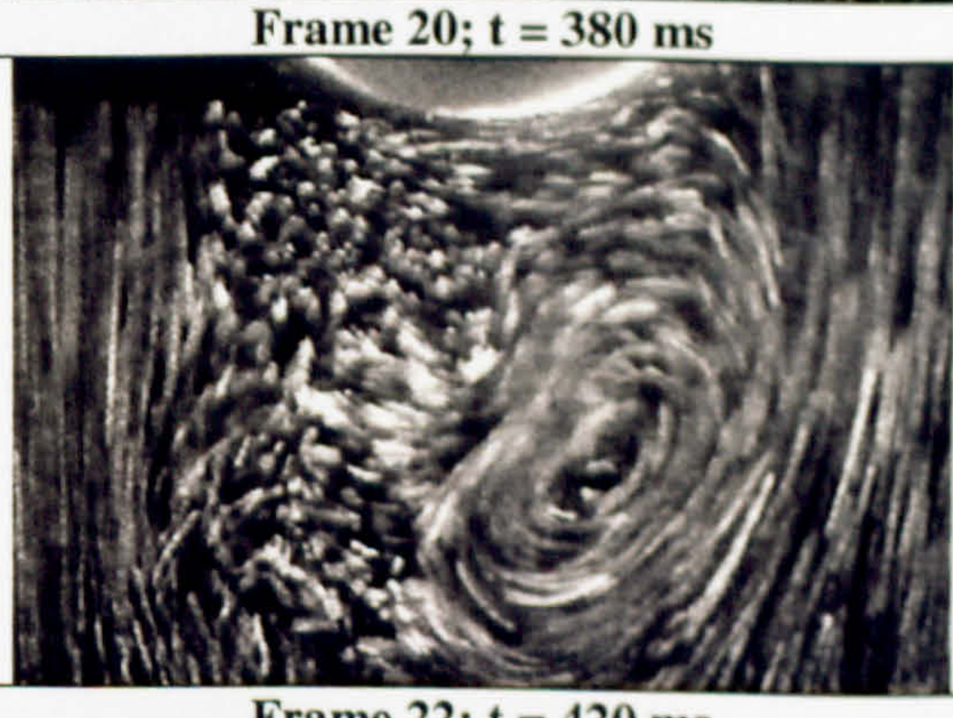

Frame 22; t = 420 ms

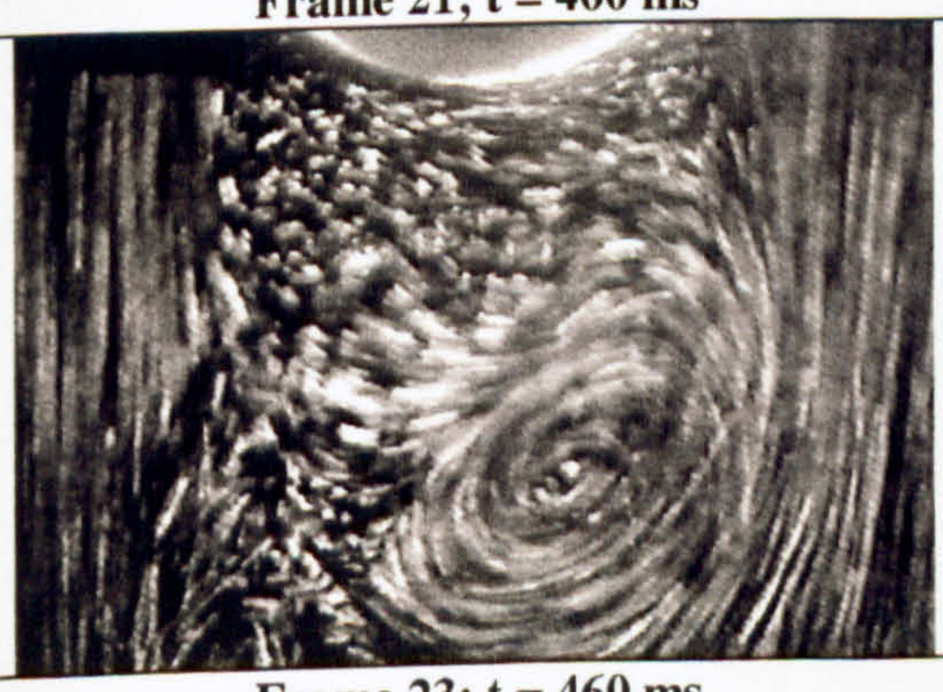

Frame 23; t = 460 ms

Frame 24; t = 480 ms

Figure 5.32 (c). Visualisation pictures of the flow in the wake of the third cylinder (Re = 842). Frames 17-24.

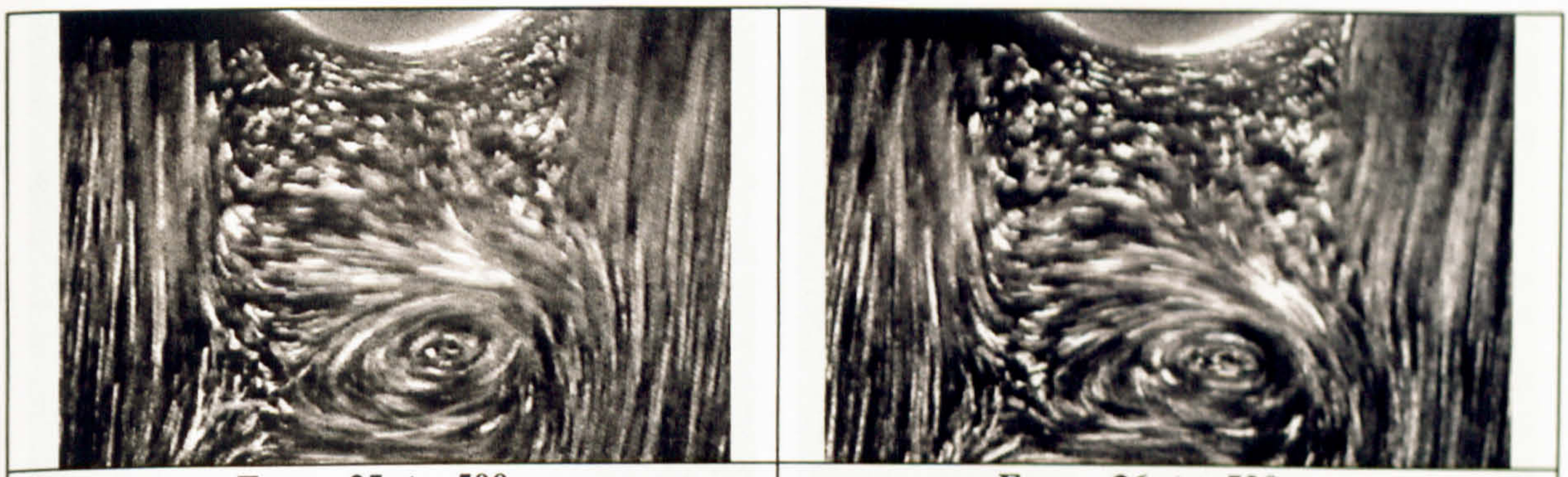

Frame 25; t = 500 ms	Frame 26; t = 520 ms

Figure 5.32 (d). Visualisation pictures of the flow in the wake of the third cylinder (Re = 842). Frames 25-26.

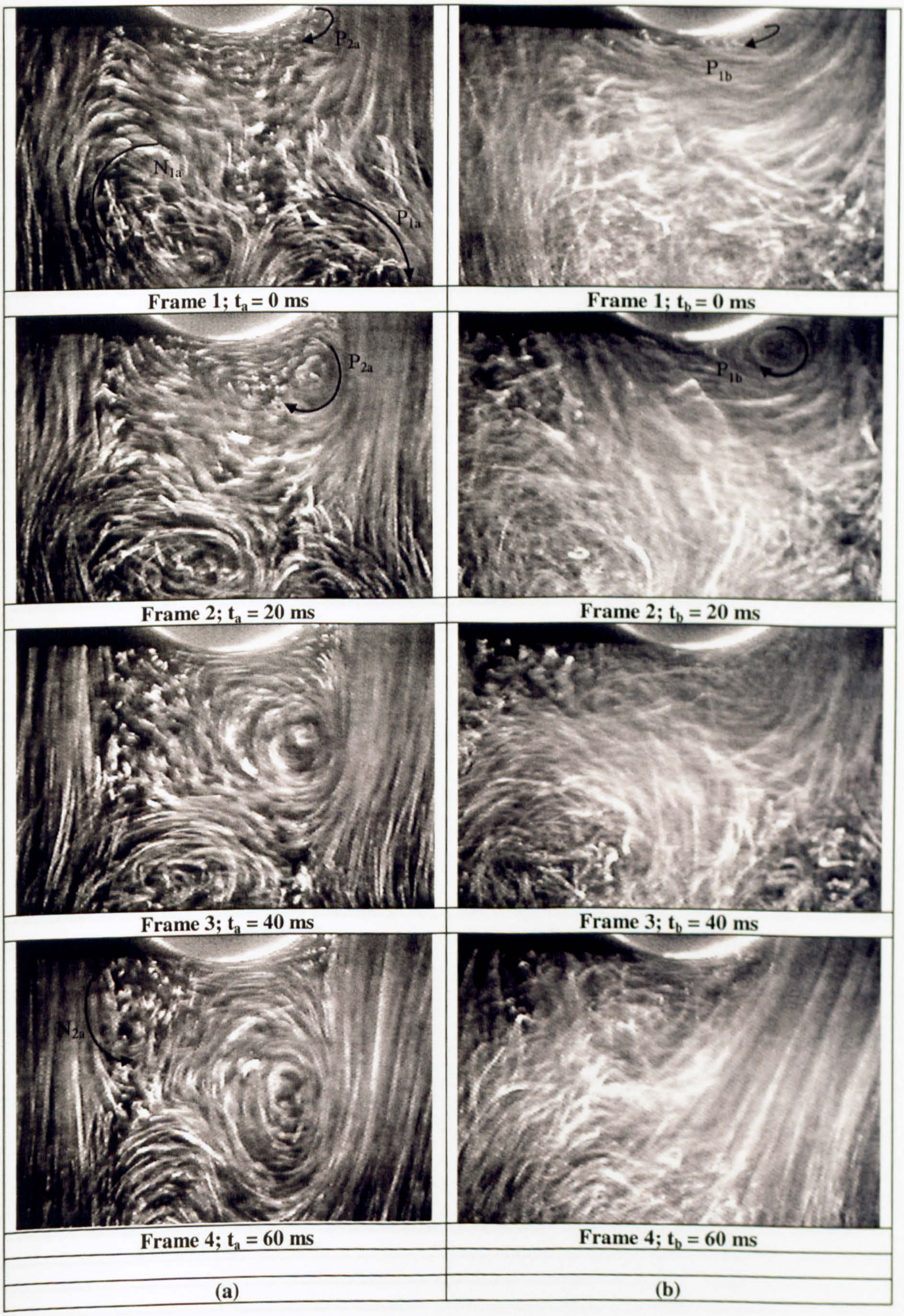

Frame 1; t_a = 0 ms	Frame 1; t_b = 0 ms
Frame 2; t_a = 20 ms	Frame 2; t_b = 20 ms
Frame 3; t_a = 40 ms	Frame 3; t_b = 40 ms
Frame 4; t_a = 60 ms	Frame 4; t_b = 60 ms
(a)	(b)

Figure 5.33 (a). Visualisation pictures of the flow in the wake of the first cylinder in steady ((a), Re = 1,443) and pulsating flow ((b), Re = 1,443, f_p = 10 Hz). Frames 1-4.

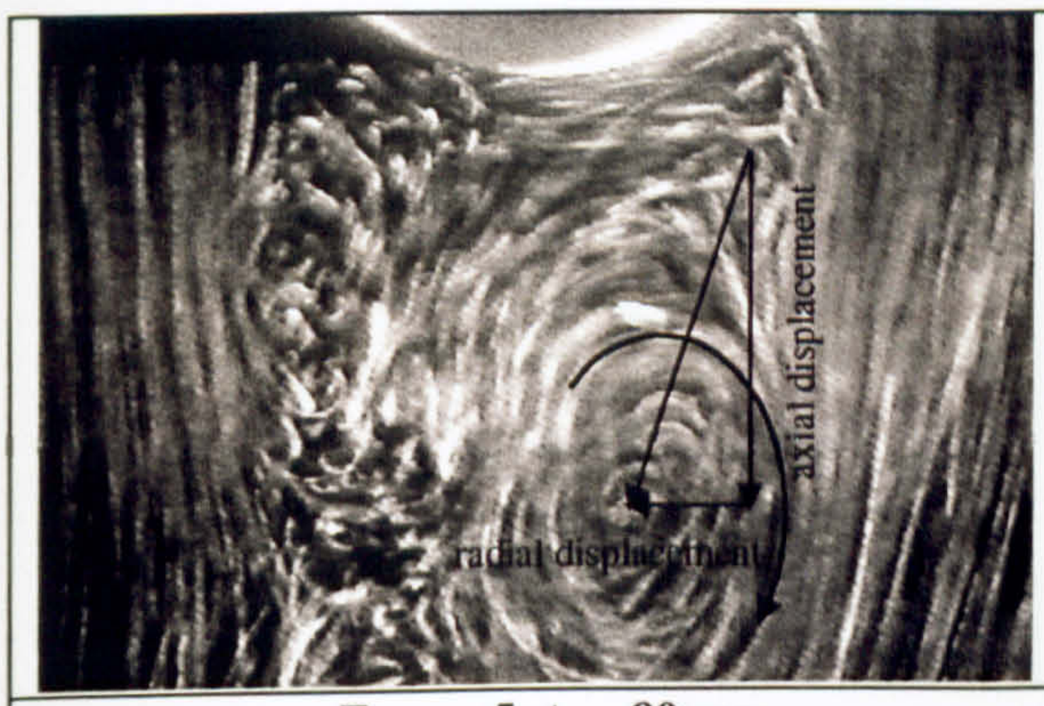

Frame 5; t_a = 80 ms

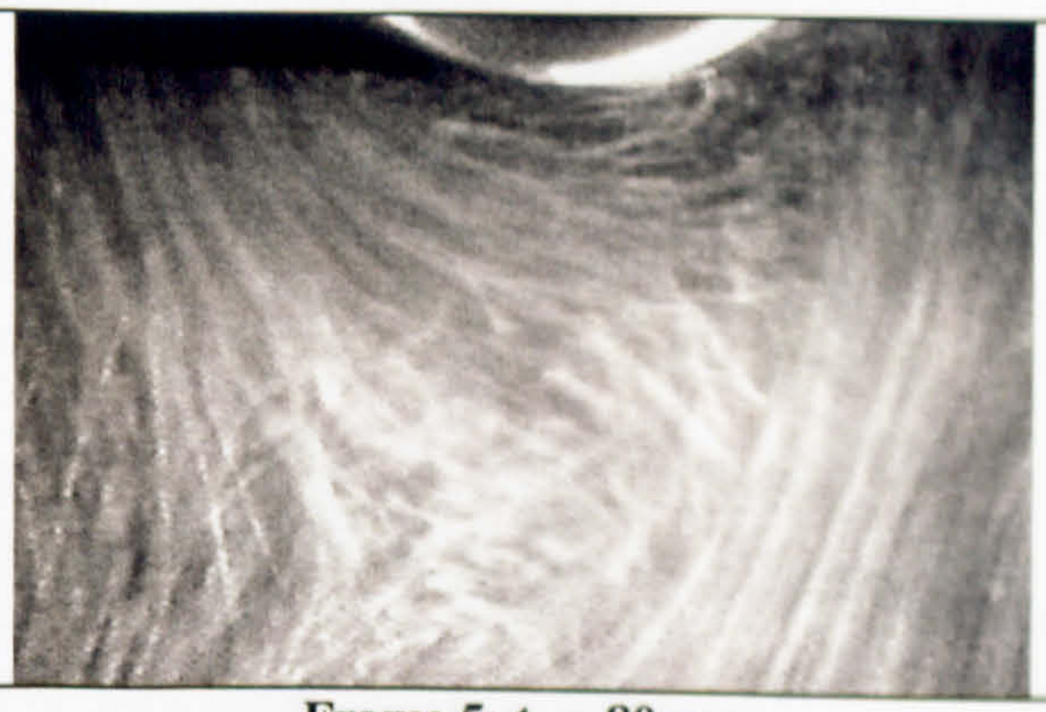

Frame 5; t_b = 80 ms

Frame 6; t_a = 100 ms

Frame 6; t_b = 100 ms

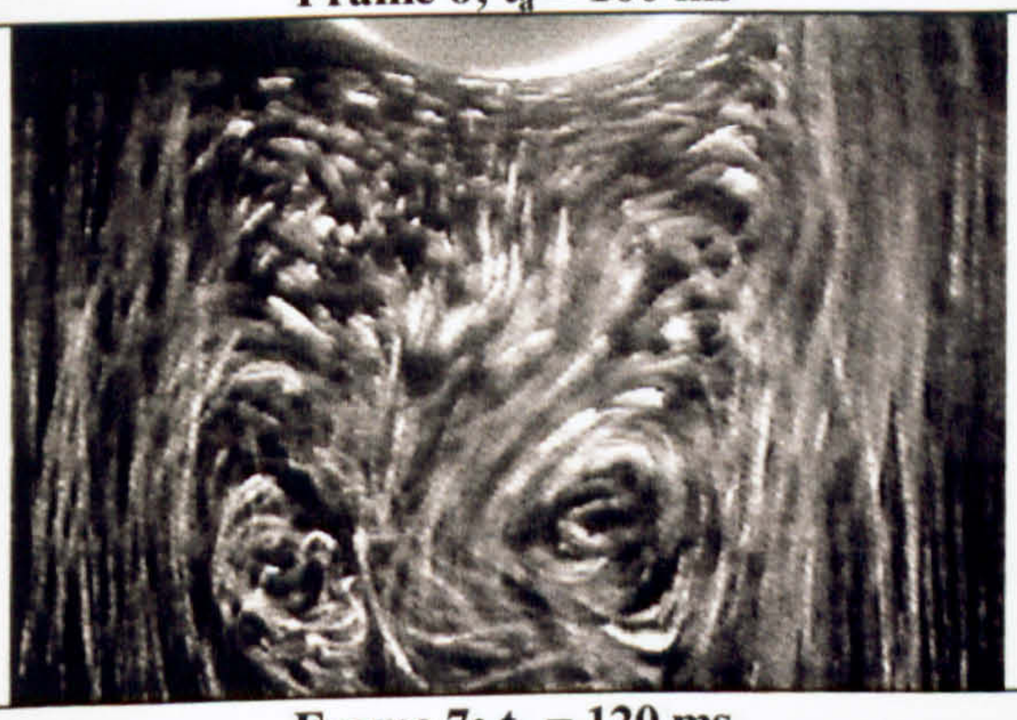

Frame 7; t_a = 120 ms

Frame 7; t_b = 120 ms

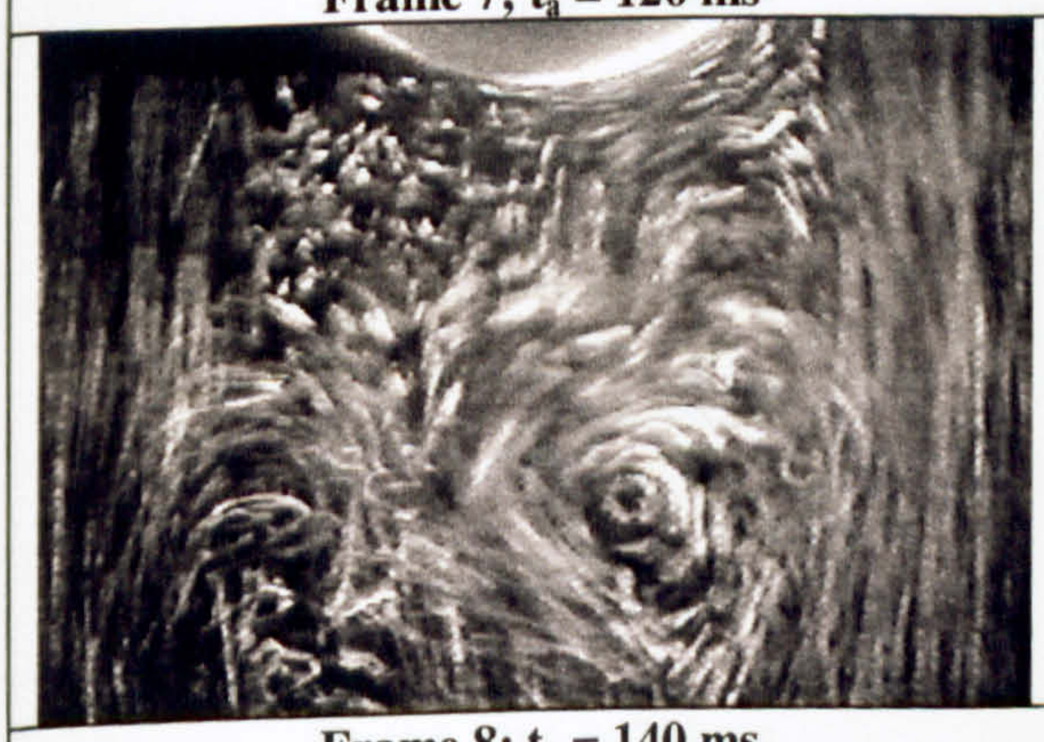

Frame 8; t_a = 140 ms

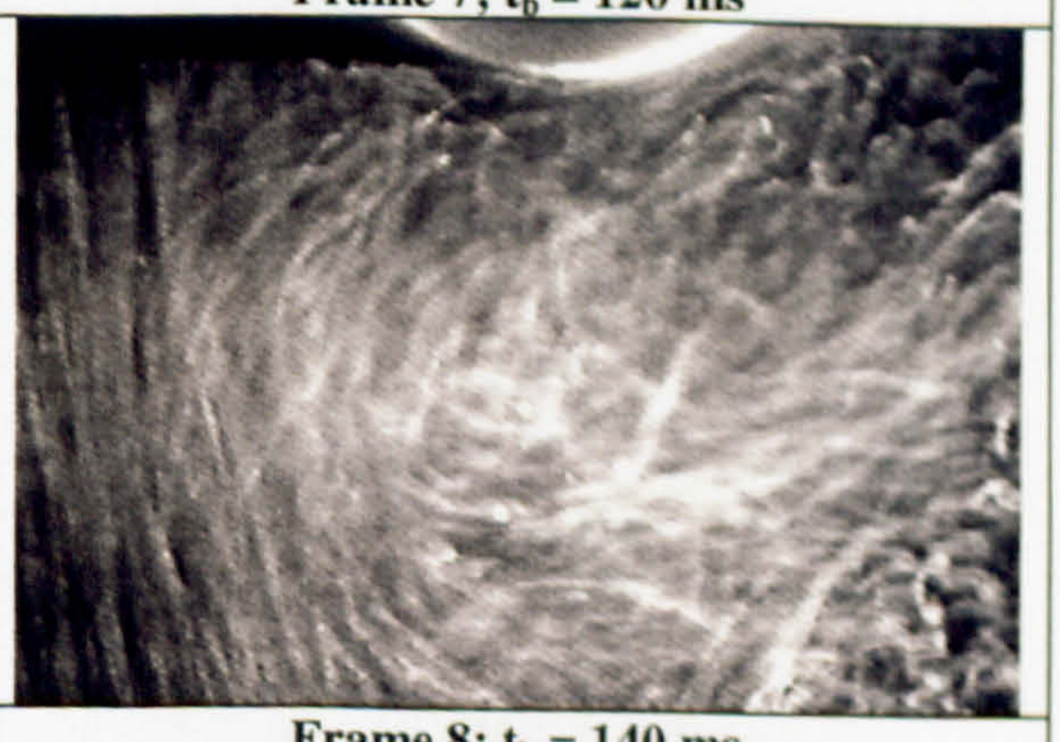

Frame 8; t_b = 140 ms

(a) (b)

Figure 5.33 (b). Visualisation pictures of the flow in the wake of the first cylinder in steady ((a), Re = 1,443) and pulsating flow ((b), Re = 1,443, f_p = 10 Hz). Frames 5-8.

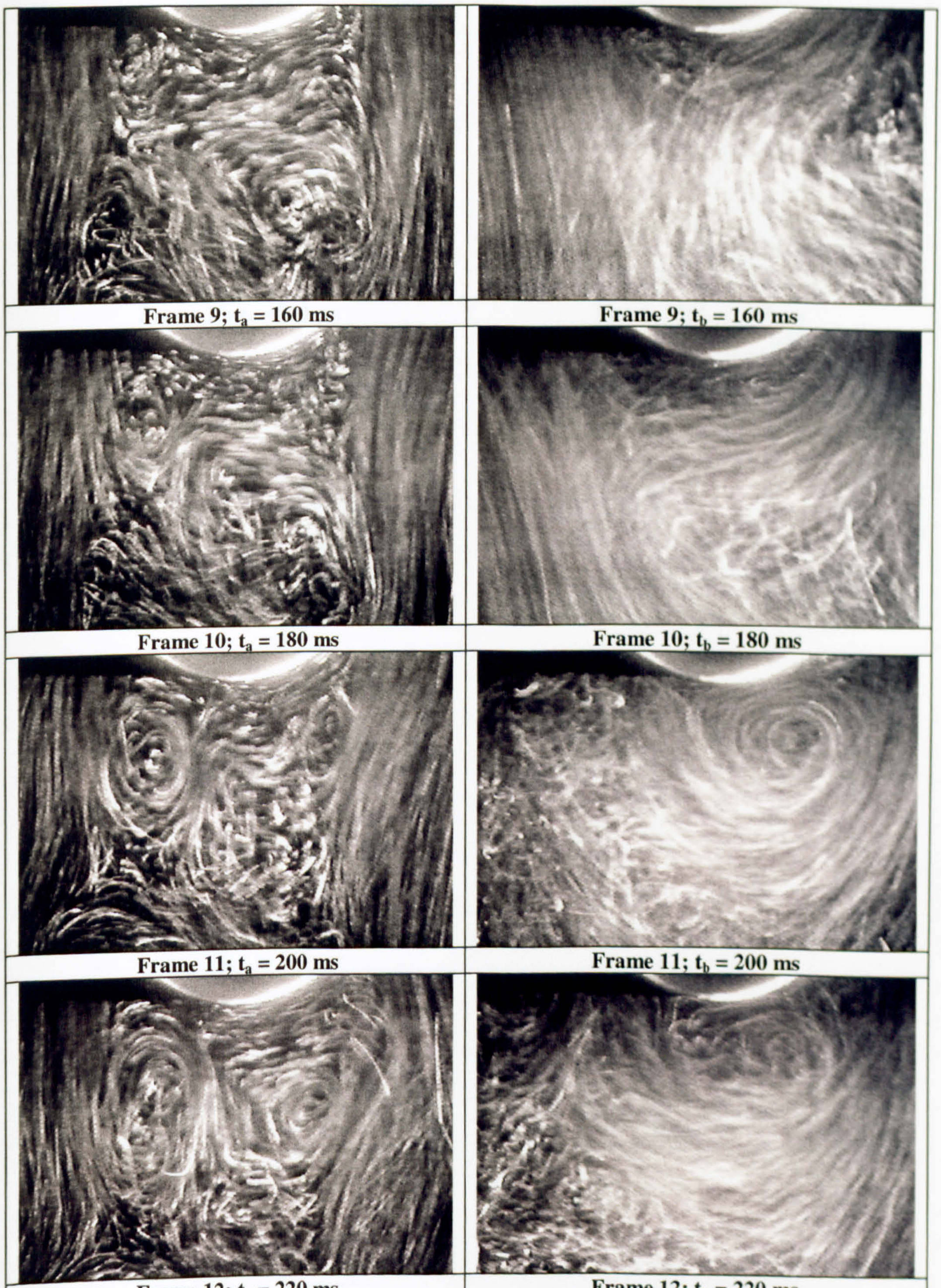

Figure 5.33 (c). Visualisation pictures of the flow in the wake of the first cylinder in steady ((a), Re = 1,443) and pulsating flow ((b), Re = 1,443, f_p = 10 Hz). Frames 9-12.

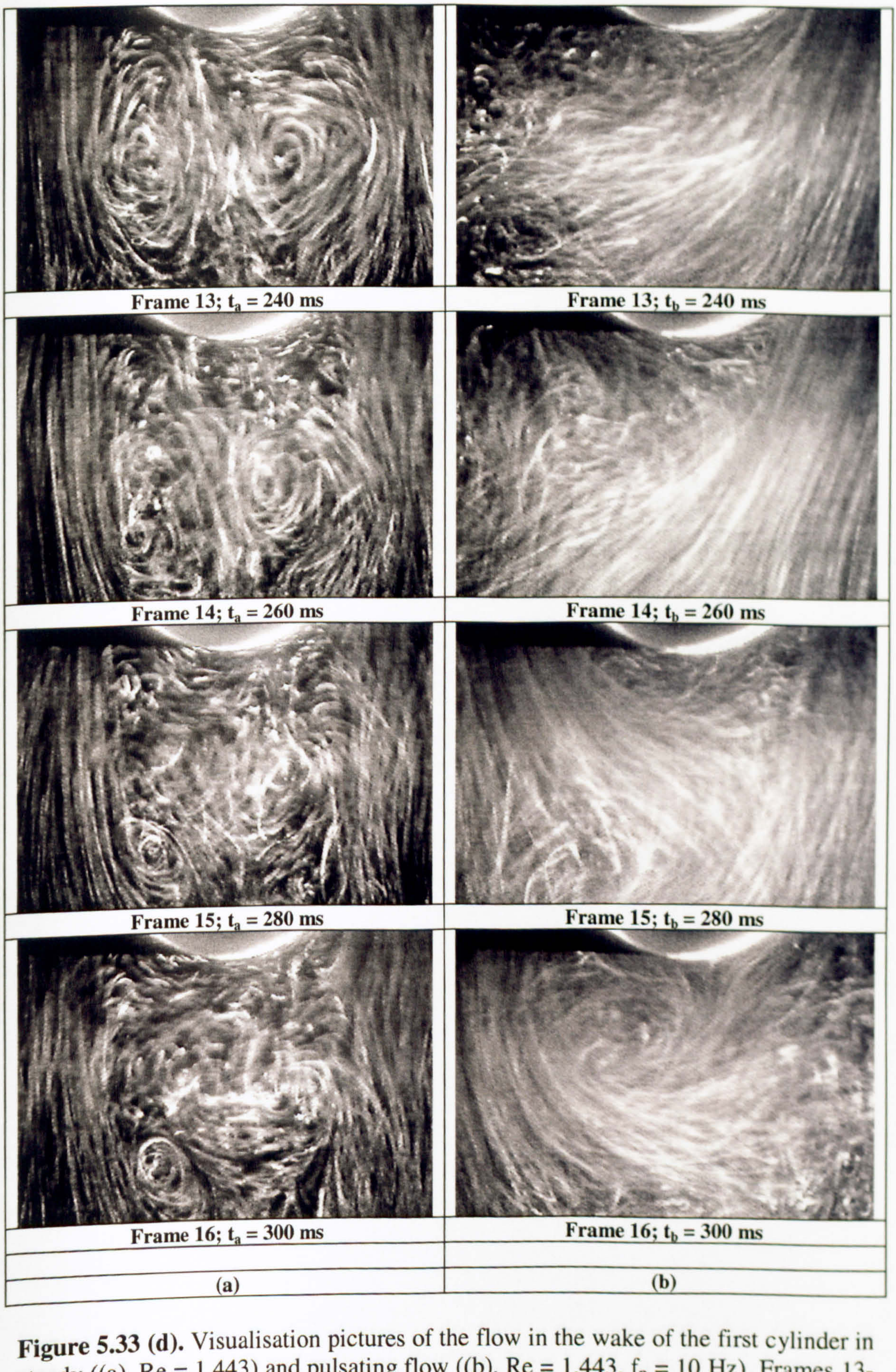

Figure 5.33 (d). Visualisation pictures of the flow in the wake of the first cylinder in steady ((a), Re = 1,443) and pulsating flow ((b), Re = 1,443, f_p = 10 Hz). Frames 13-16.

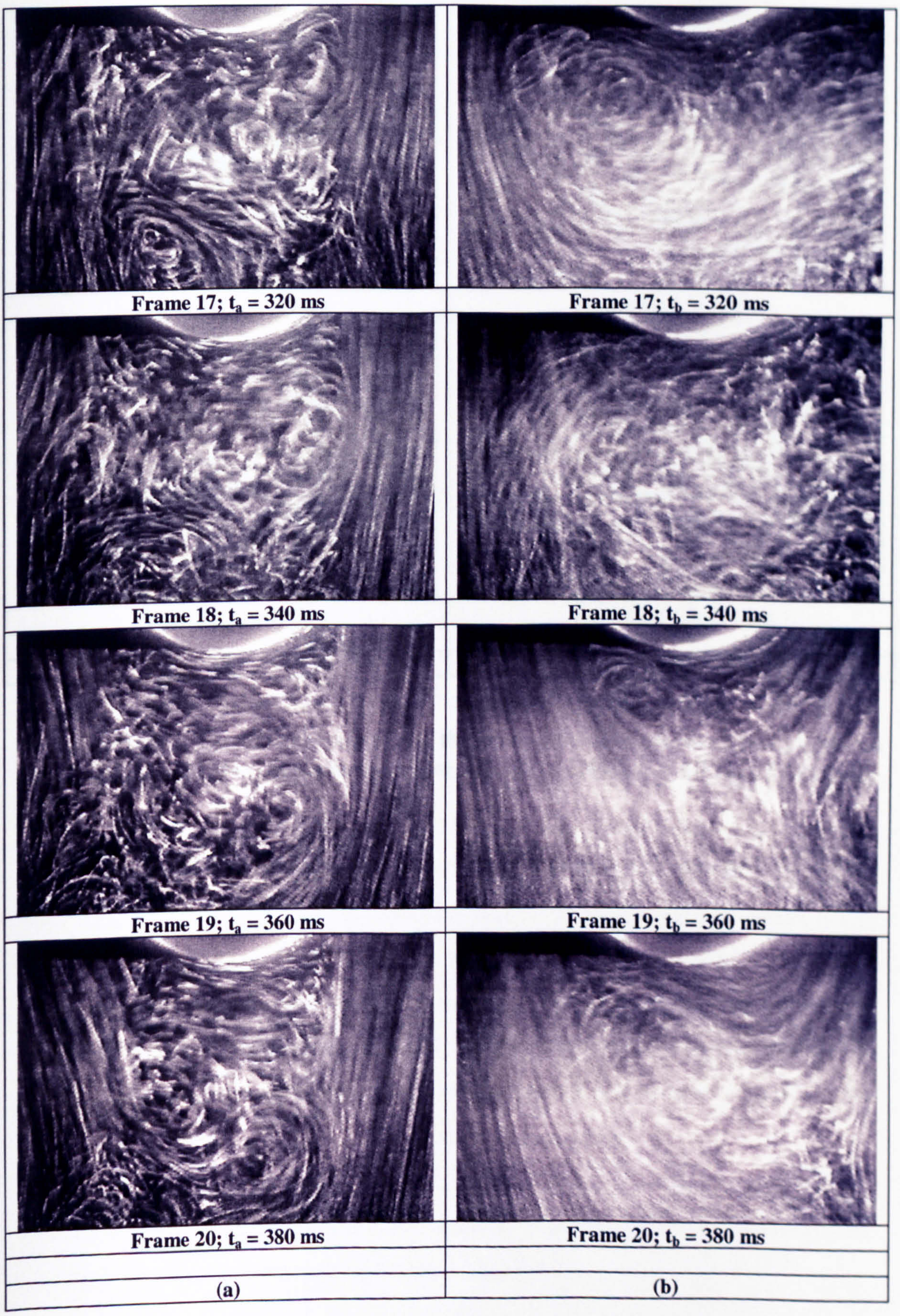

Figure 5.33 (e). Visualisation pictures of the flow in the wake of the first cylinder in steady ((a), Re = 1,443) and pulsating flow ((b), Re = 1,443, f_p = 10 Hz). Frames 17-20.

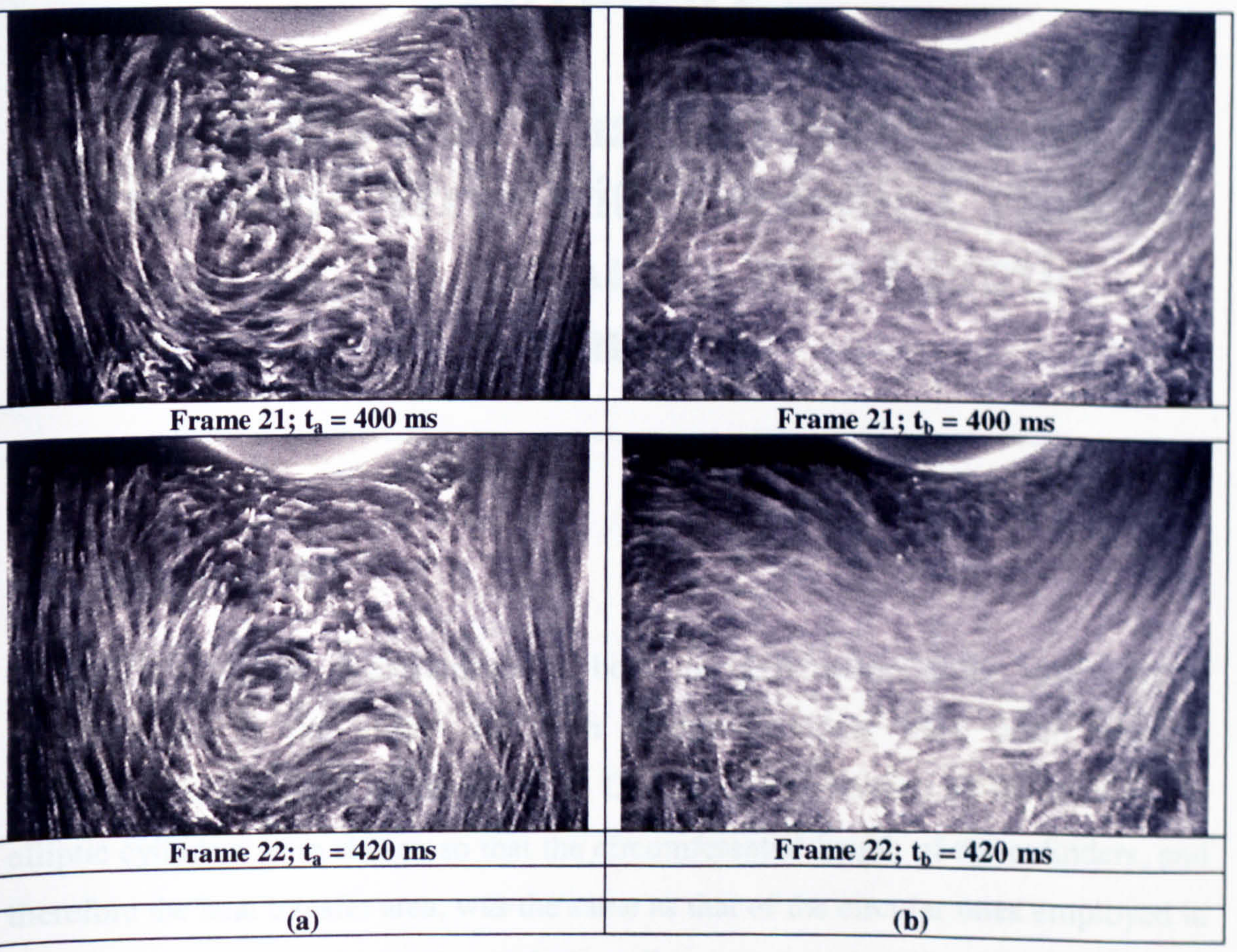

Figure 5.33 (f). Visualisation pictures of the flow in the wake of the first cylinder in steady ((a), Re = 1,443) and pulsating flow ((b), Re = 1,443, f_p = 10 Hz). Frames 21-22.

CHAPTER 6

Heat Transfer Characteristics of an Asymmetric Array with Circular Cylinders and an In-Line Array with Elliptic Cylinders

6.1 Introduction

Surface temperature measurements in both the asymmetric array with circular cylinders and in the in-line one with elliptic cylinders were taken using a thermocouple technique as mentioned in Chapter 2. The lengths of the axes of the elliptic cylinders were chosen so that the circumferential length of the cylinders, and therefore the heat transfer area, was the same as that of the circular ones employed in the asymmetric arrangement. An equivalent diameter, d_e, was defined for the elliptic cylinders (see Table 3.1 in Chapter 3) as the diameter of an equivalent circular cylinder, whose circumferential length was equal to that of the present elliptic cylinder. The Reynolds number was defined using the cylinder diameter, d, and the equivalent one, $d_e = d = 10$ mm, for the circular and elliptic cylinders respectively, as the characteristic length, and the upstream bulk velocity, U_∞, as the characteristic velocity. As detailed measurements were taken in both arrays at the same upstream bulk velocity, this was selected in preference to the gap velocity as characteristic velocity for the definition of the Reynolds number. However, the Re based on the gap velocity, U_g, can be easily calculated considering that U_g is equal to $1.22U_\infty$ and $1.38U_\infty$ for the in-line and the asymmetric array respectively.

Surface temperature measurements were taken in both steady and pulsating flow (10 Hz) for Reynolds numbers ranging from 1,608 to 6,430.

6.2 Asymmetric array with circular cylinders

Figure 6.1 shows a comparison between Nu[1] number distributions at different rows in steady flow. The Reynolds number defined using the upstream bulk velocity, U_∞, as characteristic velocity, was equal to Re = 6,430[2]. The results of Figure 6.1 indicate that the heat transfer rates are low around the first row cylinder and they increase in subsequent rows. Inner rows, i.e. rows 3 to 5, have similar Nu number distributions which implies that the entrance effects in the asymmetric arrangement are restricted to the first three rows only. The heat transfer rates at the exit of the bundle, row 6, are similar to the rates measured in row 2 for angles of 90 - 270°.

The same profiles as those in Figure 6.1 are shown for each row in Figure 6.2. The profiles are plotted with different ordinate scales in order to highlight the variation of the Nusselt number with the circumferential angle, φ. The heat transfer coefficient around the first row cylinder decreases with increasing φ, from its maximum value (Nu ≅ 135) recorded at the front stagnation point, $\varphi = 0°$, to a local minimum (Nu ≅ 95) at approximately $\varphi = 90°$ and 270°, where separation of the flow occurs (as shown in Figure 4.33 (a)). It should be noted that the distribution is nearly symmetrical around the cylinder axis. The heat transfer rates decrease along the cylinder surface as the boundary layer thickness increases from the front stagnation point up to the separation point where a relative minimum of the Nusselt number is recorded. Downstream of the separation point the Nusselt number first increases, as expected, up to approximately $\varphi = 100° - 110°$, then decreases up to a second local minimum (Nu ≅ 90) at $\varphi = 135°$. This minimum in the heat transfer distribution is attributed to the presence of a stagnant region downstream of the separation point. The boundaries of this region must be fluctuating but apparently the position φ = 135° remains always inside the stagnant region. The occurrence of this stagnant region was also revealed by the spectral analysis carried out by Telionis et al (1992) on the flow in the near wake of a circular cylinder in steady flow. For $\varphi > 135°$ the Nusselt number increases again up to a local maximum at the rear stagnation point,

---

[1] Local instantaneous values of the Nusselt number were calculated from the surface temperature data, as mentioned in Chapter 2, by means of Equation 2.26. The Nu used in the present chapter is defined as the time-average of the instantaneous values recorded over the measuring period.
[2] Note that the corresponding Reynolds number based on the gap velocity is 8,873.

i.e. φ = 180°. The Nu number profile around the second cylinder is clearly asymmetrical around the centreline, as expected, due to the asymmetry of the arrangement. In particular the separation of the flow occurs at about 60° and 270° from the front stagnation point. This confirms the finding of the visualisation study described in Chapter 4 (see Figure 4.33 (b)) of an anticipated separation of the flow along the second cylinder due to the presence of the upstream cylinder which deflects the incoming flow. The profiles around downstream cylinders show a similar trend although the distributions are flatter and the location of the separation points and/or the relative maxima and minima might vary.

Figure 6.3 shows a comparison between the $Nu/Re^{1/2}$ distribution in steady and pulsating flow around the first row. The frequency, f_d, and relative amplitude, A_o, of pulsations were 10 Hz and 0.14 respectively. The comparison shows clearly that the heat transfer is enhanced when the flow is pulsed. Although a marked heat transfer enhancement by flow pulsations is observed along the whole circumferential length, the most significant effect, as expected (Žukauskas, 1972; Kikuchi et al, 2000), is observed on the back surface of the cylinder. The flow conditions for the pulsating flow experiment in this case were such that vortex shedding was promoted and locked at the pulsation frequency. The augmentation of the heat transfer due to the pulsations can be partly attributed to the increased turbulence levels (see Chapter 4) and partly to the forced convection in the boundary layer, particularly under lock-on conditions (Karamercan and Gainer, 1979). In steady flow, convection plays no role in the heat transfer through the laminar film of the water side of the tube, which instead occurs by means of conduction. When the flow is pulsed the periodic pressure variation produces forced circulations in the fluid and increases the heat transfer by promoting the formation of vortices, thus introducing convection in the boundary layer (Karamercan and Gainer, 1979). The flow visualisation study had shown that the effect of pulsations on the mean flow structure is not confined to the separation region and the wake, but extends up to the neighbourhood of the front stagnation point. In downstream rows, the Nu number in pulsating flow remains significantly higher than that in steady flow, although, as described in Chapter 4, in the wake region of downstream rows, the effect of pulsations on the turbulence levels is still noticeable, it is significantly lower than that behind the first cylinder, and outside the wakes the difference of the normalised r.m.s velocities between pulsating and steady

flow is negligible. This implies that the enhancement of the heat transfer is dominated by the forced convection in the boundary layer caused by the high amplitude pulsations rather than the increase in the turbulence levels.

A comparison between the local Nusselt number at the front stagnation point between steady and pulsating flow at different amplitudes of oscillations is shown in Figure 6.4. It should be noted that the relative amplitude of pulsations, resulting from the experimental set up, decreases with Re according to the following table:

Table 6.1. Variation of the relative amplitude of pulsations upstream of the tube bundle with the Reynolds number.

Re	A_o
6,430	0.0268
5,466	0.0363
4,823	0.0419
4,180	0.0765
3,537	0.1149

It is clear that from Re = 6,430 (A_o = 0.0268) to Re = 5,466 (A_o = 0.0363), due to the low relative amplitude of pulsations, A_o, the Nusselt number obtained in steady flow has the same value as that obtained in pulsating flow. The pulsations superimposed to the mean flow have, therefore, no effect on the heat transfer rates at low A_0. At Re = 4,823 (A_0 = 0.0419) the Nu in pulsating flow is slightly higher than that in steady flow. As the Reynolds number decreases and correspondingly the relative amplitude, A_o, increases, the Nusselt number in pulsating flow becomes progressively higher, up to 40 % at Re = 2,251, than that in steady flow. It should be noted that the smaller effect of pulsations on the front stagnation point at high Re might be related to both the reduced amplitude of pulsations and to the increased turbulence levels in steady flow. It should be observed that the experimental results shown in Figure 6.4 for the steady flow case are in agreement with the existing data (see Cheng et al (1997) and

Žukauskas (1972)). Based on the present data for steady flow a correlation expressing the relationship between the Nusselt number and Re is obtained as:

$$Nu = 0.88\ Re^{0.55} \tag{6.1}$$

Cheng and al (1997) observed that the Nusselt number increases appreciably under lock-on conditions and concluded that the lock-on effect is the dominant mechanism enhancing the heat transfer. In general, however, the heat transfer augmentation may be attributed to two mechanisms, the lock-on phenomenon and the increase of turbulence with pulsations.

6.3 In-line array with elliptic cylinders

The surface temperatures in this arrangement were measured using the same technique as for the asymmetric array. However, instead of one, four thermocouples were embedded on the surface of the instrumented elliptic cylinder, placed at 0°, 25°, 155° and 180° from the front stagnation point, φ = 0°. Surface temperature measurements at these angular positions were obtained in all rows in steady and pulsating flow. The Reynolds number, based on upstream velocity and equivalent cylinder diameter, ranged from Re = 1,608 to Re = 6, 430[3]. The frequency of the pulsations was 10 Hz and the relative amplitude ranged from A_o = 0.0268 to A_o = 0.1524.

The local Nusselt number distribution in all rows of the in-line array with elliptic cylinders under steady conditions is shown in Figure 6.5. The Reynolds number based on the upstream bulk velocity was chosen to be Re = 6,430, as for the asymmetric array. As previously stated, the 4 thermocouples allowed the temperature to be determined in only 4 positions along the instrumented cylinder surface. The corresponding Nusselt number profiles shown in Figure 6.5, were therefore obtained by interpolation, assuming y-symmetry of the flow, and consequently, of the heat transfer field. Despite the small number of measurement locations the figure indicates

[3] Note that the corresponding Reynolds number based on the gap velocity is 7,845.

that the heat transfer rates are lower around the first row cylinder and they increase in subsequent rows. Rows 3 to 6 have similar Nu number distributions while the heat transfer rates measured in row 2 are lower than those measured in downstream rows for $\varphi \leq 30°$ and higher for larger circumferential angles.

The variation of the Nusselt number with Re for each measurement location around the first cylinder in steady flow is shown in Figure 6.6. The Reynolds number was varied in the range $1{,}608 < Re < 6{,}430$. It is interesting to note that although the heat transfer rates decrease linearly with Re, as expected, the Nu number variation is significantly steeper at the front stagnation point, $\varphi = 0°$, than at higher circumferential angles (the equations of the linear data fits are indicated in the figure). At $\varphi = 0°$ the Nusselt number decreases by about 67 % in the Reynolds number range investigated. At $\varphi = 25°$ the slope of the linear fit is slightly higher than that at $\varphi = 155°$ and $\varphi = 180°$. From Re = 6,430 to Re = 1,608 the Nusselt number decreases by about 60 % at $\varphi = 25°$, $\varphi = 155°$ and $\varphi = 180°$. This implies that the dependence of the Nusselt number on the Reynolds number is less pronounced for higher circumferential angles. Furthermore, the difference between the Nusselt numbers measured at different φ angles decreases substantially with Re. The relative difference between the Nu numbers at $\varphi = 0°$ and $\varphi = 180°$ decreases from 83 % at Re = 6,430 to 73 % at Re = 1,608. This implies that the dependence of the Nusselt number on the circumferential angle becomes weaker at lower Re.

Figures 6.7 shows the mean Nusselt number of the first cylinder at various Reynolds numbers in the in-line array in steady flow. The data were obtained from those in Figure 6.6 by averaging the local Nusselt numbers at the measurement locations for each Re. The data were interpolated by both a linear and a power fit. The corresponding equations are indicated in the figure. Note that, as indicated by the equation of the power fit of the steady flow data, the power index of the Reynolds number is equal to 0.5, in agreement with the data of other authors (the power index found in the literature vary from 0.5 to 0.6 for similar Reynolds numbers (Žukauskas, 1972)). The mean Nusselt number varies from $Nu_m = 67.6$ at Re = 6,430 to 35.7 at Re = 1,608.

The local Nusselt distribution around the first cylinder of the in-line array for various Re values is shown in Figure 6.8. It can be seen that by decreasing the Reynolds number, the dependence of the Nusselt number on Re becomes progressively weaker, particularly for $\varphi \geq 155°$. Furthermore, at low Re the dependence of Nu on φ is reduced. Note that the difference between the Nusselt numbers measured at $\varphi = 155°$ and $\varphi = 180°$ is equal to $\Delta Nu = 1.4$ at Re = 1,608 and to $\Delta Nu = 5.1$ at Re = 6,430. The Nusselt number variation is significantly steeper at lower circumferential angles, $\varphi \leq 25°$, and it increases with Re. At Re = 6,430, the difference between the Nusselt numbers measured at $\varphi = 0°$ and $\varphi = 25°$ is approximately 37.2.

Figure 6.9 shows a comparison between the Nusselt number distributions around the first cylinder in steady and pulsating flow (f_d = 10 Hz) at two different Reynolds numbers, 5,466 and 2,894, which correspond to the relative amplitude of pulsations A_o of 0.036 and 0.15 respectively. The figure shows that, as already observed in the asymmetric array, the pulsations enhance the heat transfer, at least over part of the tube periphery. It is noticeable that, as for the asymmetric array, an increase of the amplitude of pulsations corresponds to an increase in the heat transfer efficiency. Furthermore, this effect is more pronounced in the rear part of the cylinder, that is the Nu number increases with circumferential angle φ. Note that at Re = 5,466 the effect of pulsations can be noticed only for $\varphi > 100°$. At the lower Re, Re = 2,894, the Nu in pulsating flow is about 11 % higher than that in steady flow at the front stagnation point and 37 % at $\varphi = 180°$. It is interesting to notice that the Nusselt number measured at the lower Re at the rear stagnation point in pulsating flow is as high as that measured in steady flow at the higher Re.

Figure 6.10 shows a comparison of the local Nusselt number dependence on Re at different angular positions around the first elliptic cylinder of the in-line array between steady and pulsating flow (f_d = 10 Hz). The figure also gives the value of the relative amplitude of pulsations, A_o, at the various Reynolds numbers. It is interesting to notice that at the highest Re investigated, that is at the lowest A_o, no effect of pulsations can be observed at the front stagnation point and at $\varphi = 25°$. Only a very small effect of pulsations can be instead seen downstream of the separation point, i.e. at $\varphi = 155°$ and $\varphi = 180°$, where the Nu number in pulsating flow is slightly higher

than that in steady flow. It should be noted that at $\varphi = 0°$ and $\varphi = 25°$ the Nu in pulsating flow number becomes higher than that in steady flow for $Re \leq 4{,}800$ ($A_o \geq 0.042$) and $Re \leq 4{,}500$ ($A_o \geq 0.060$). The heat transfer augmentation from steady to pulsating flow increases with A_o. At lower Re the pulsating flow Nu, Nu_p[4], increases progressively with A_o. The heat transfer augmentation is slightly higher at at the front stagnation point than at 25°. The effect of pulsations is more evident, as already observed, in the rear part of the cylinder, $\varphi = 155°$ and $\varphi = 180$.

The local Nusselt numbers recorded along the circumference of each row of the asymmetric array were averaged and the arithmetic mean value of the Nusselt number, Nu_m, was so obtained. The mean values are shown in Figure 6.11 in comparison with those obtained in the in-line array. Two curves are shown for the in-line array: the first is obtained by averaging the local Nusselt numbers at the measurement points ($\varphi = 0°$, $\varphi = 25°$, $\varphi = 155°$ and $\varphi = 180°$) and the other by averaging the Nu numbers obtained by sampling at each 2° the interpolation curves shown in Figure 6.5. The cubic shape of the profile of the mean Nusselt number, Nu_m, against row depth in the asymmetric array shows that Nu_m increases from the first to the fourth row and then decreases down to the sixth row. The Nu_m in the in-line array instead increases from the first to the second and then it is fairly constant from the third to the sixth row, i.e. the entrance region is restricted to the first two rows. A similar trend was observed by Merker and Hanke (1986) for the shell-side of tube banks having oval shaped cylinders, although the entrance region extended up to the third row. Note that the heat transfer of the in-line array is considerably lower than that of the staggered array in agreement with the results of other authors for similar Reynolds numbers (Žukauskas, 1972). Žukauskas found that with an increase of Re, the heat transfer of the in-line arrays increases more rapidly and at high Re it approaches the heat transfer intensity of staggered arrays.

[4] Nu_p indicates the Nu number in pulsating flow as opposite to Nu_s, which indicates the Nu number in steady flow.

6.4 Conclusions

An experimental investigation was carried out on the heat transfer over circular and elliptic cylinders of an asymmetric and in-line array respectively in both steady and pulsating flow.

The heat transfer rates in the asymmetric array in steady flow are low around the first row cylinder and they increase in subsequent rows. Inner rows, i.e. rows 3 to 5, have similar Nu number distributions which implies that the entrance effects in the asymmetric arrangement are restricted to the first three rows only. The heat transfer rates at the exit of the bundle, that is row 6, are also similar to the rates measured in row 2.

A local minimum in the Nusselt number profile around the first row was observed downstream of the separation point ($\varphi \cong 135°$) which may be attributed to the presence of a stagnant region downstream of the separation point. The same minimum was detected also around downstream rows, but at slightly different locations along the circumferential length.

A comparison of the heat transfer rates between steady and pulsating flow clearly shows that the heat transfer is enhanced when the flow is pulsed. The flow conditions adopted were such that vortex shedding was promoted and locked at the pulsation frequency. The augmentation of the heat transfer can be partly attributed to the increased turbulence levels in pulsating flow (see Chapter 4) and partly to the forced convection in the boundary layer introduced by the pulsations, particularly under lock-on conditions (Karamercan and Gainer, 1979).

A comparison was made between Nu_p and Nu_s at the front stagnation point of the staggered array. It was observed that as the Reynolds number decreases and correspondingly the relative amplitude of the upstream pulsations, A_o, increases the Nusselt number in pulsating flow becomes progressively higher, by up to 40 % at Re = 2,251, than that in steady flow.

The local Nusselt number distribution in all rows of the in-line array with elliptic cylinders shows, despite the small number of measurement locations, that the heat transfer rates are low around the first row cylinder and they increase in subsequent rows with. Rows 3 to 6 have similar Nu number distributions while the heat transfer rates measured in row 2 are lower than those measured in downstream rows for $\varphi \leq 30°$ and higher for larger angles.

The Nusselt number dependence on Re was also investigated. It was observed that that although the heat transfer rates increase linearly with Re the Nu number variation is significantly steeper at the front stagnation point than at higher circumferential angles of the cylinders and that the dependency of the Nusselt number on φ becomes weaker at lower Re. The heat transfer augmentation due to pulsations increases with the relative amplitude of pulsations A_o as already observed in the asymmetric array. Finally, a comparison was made of the averaged local Nusselt numbers recorded in steady flow along the circumferential length between the asymmetric and the in-line array. It was found that the heat transfer of the in-line array is considerably lower than that of the staggered array in all rows, in agreement with the results of earlier studies for similar Reynolds numbers.

It may be concluded that the effect of pulsations on the heat transfer in tube bundles can be significant under certain circumstances. However, the mechanisms of heat transfer are not fully understood, as shown by the discrepancy in the data reported in the published literature (Cheng et al, 1997) and, although the present study has provided some insight as indicated earlier in this section, further work in this area is clearly needed.

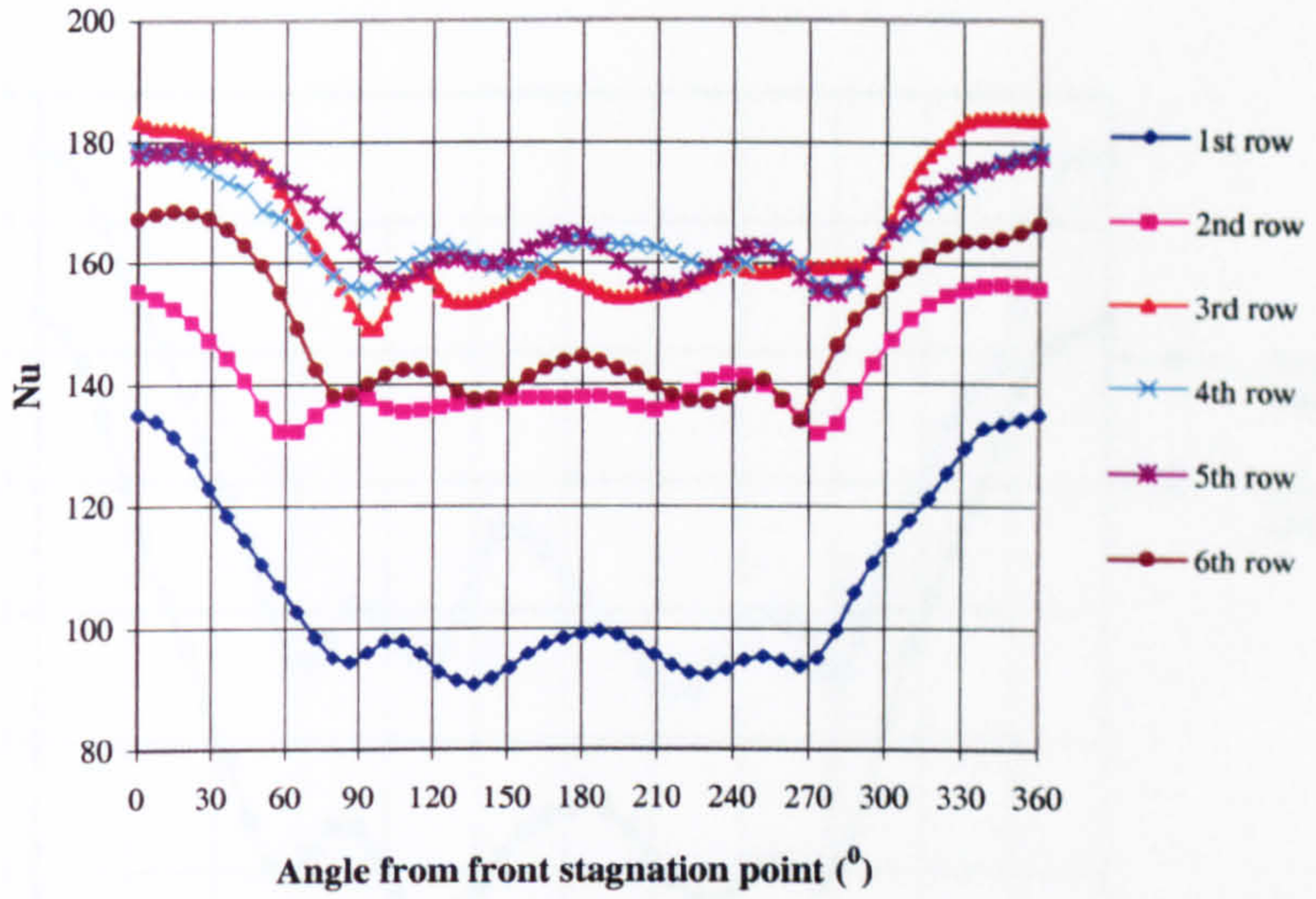

Figure 6.1. Comparison of the local Nu number distributions between different rows in steady flow in the asymmetric array (Re = 6,430).

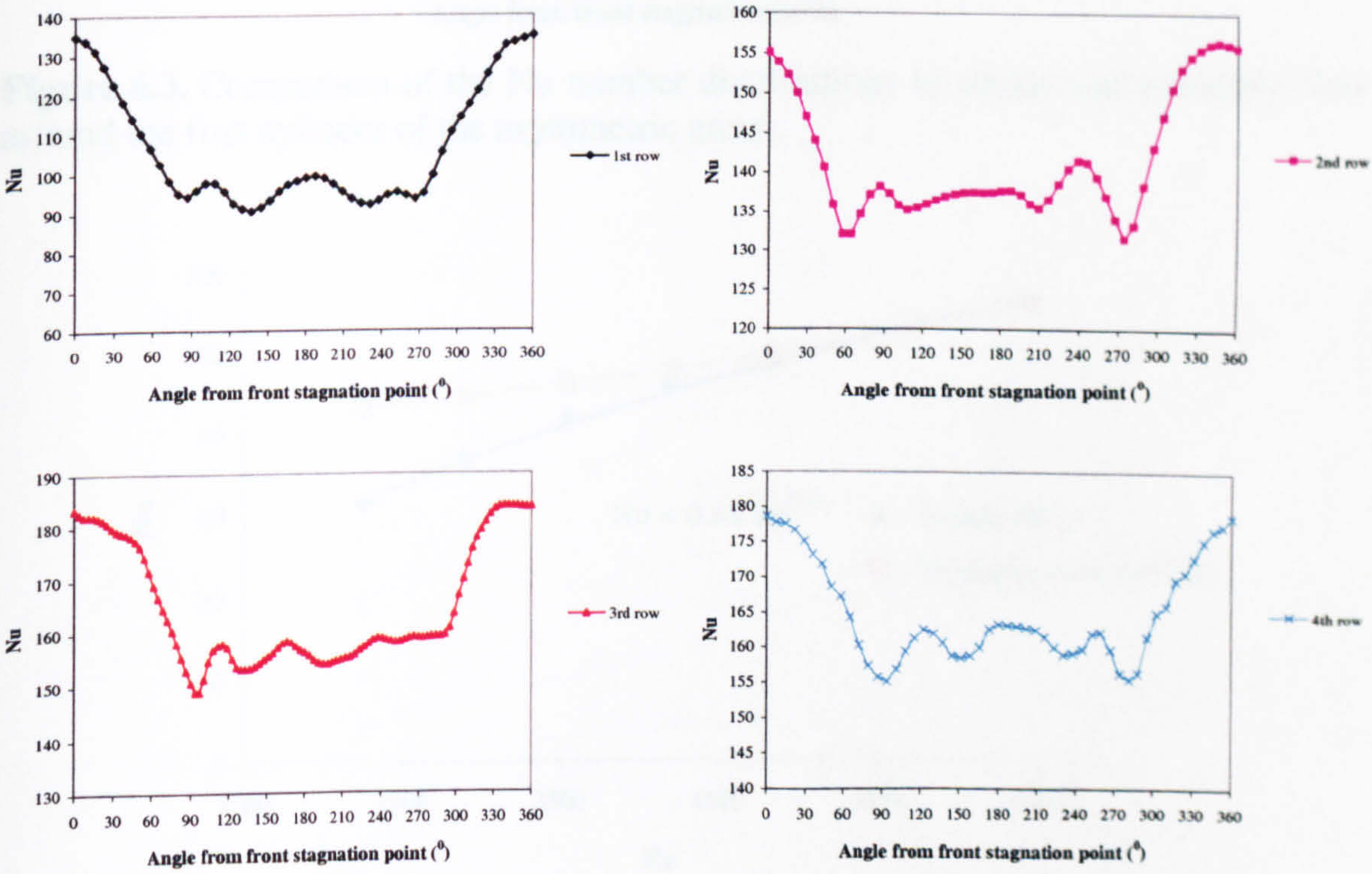

Figure 6.2. Nu number profiles around all row cylinders in steady flow in the asymmetric array (Re = 6,430).

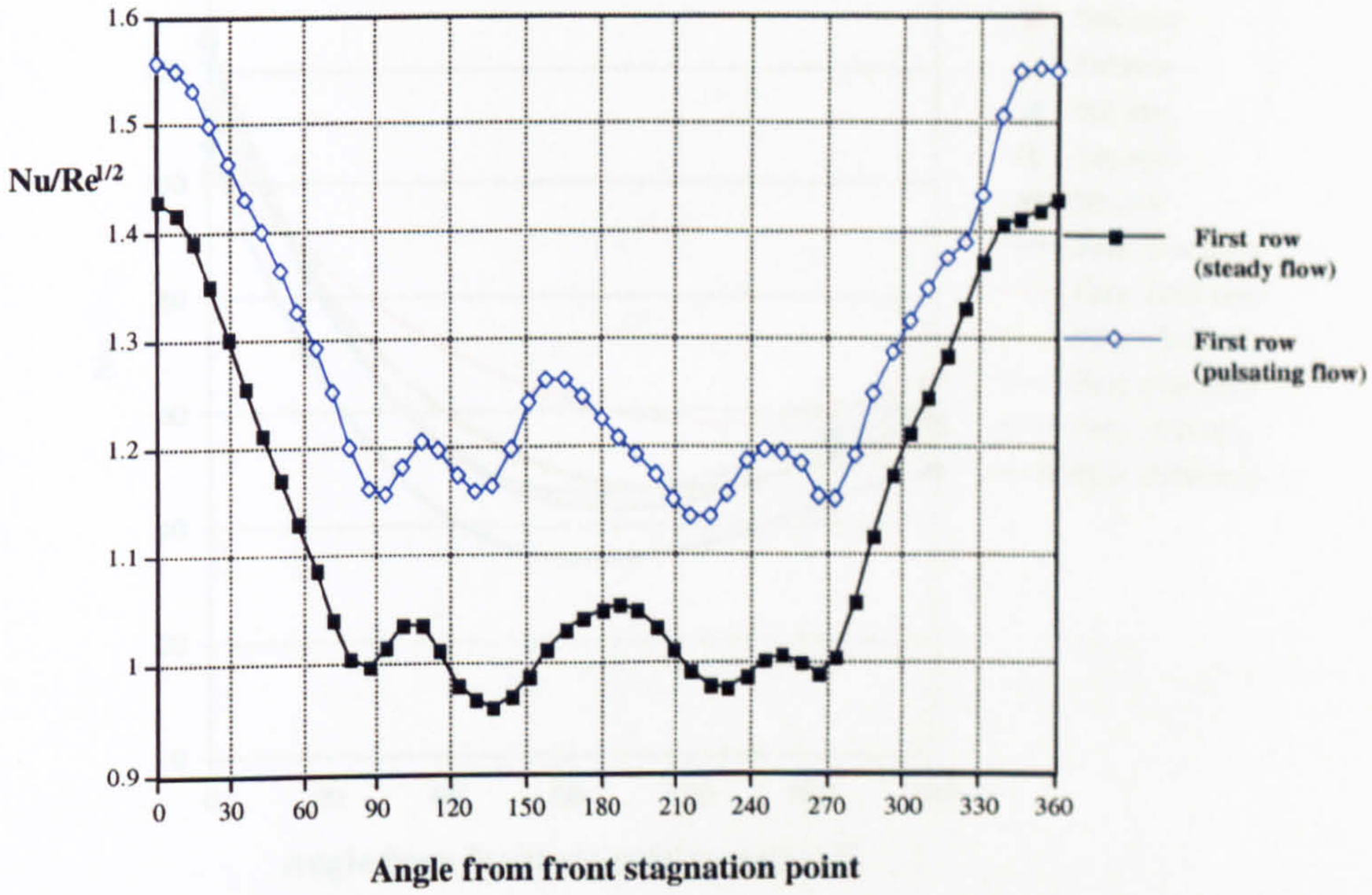

Figure 6.3. Comparison of the Nu number distributions in steady and pulsating flow around the first cylinder of the asymmetric array.

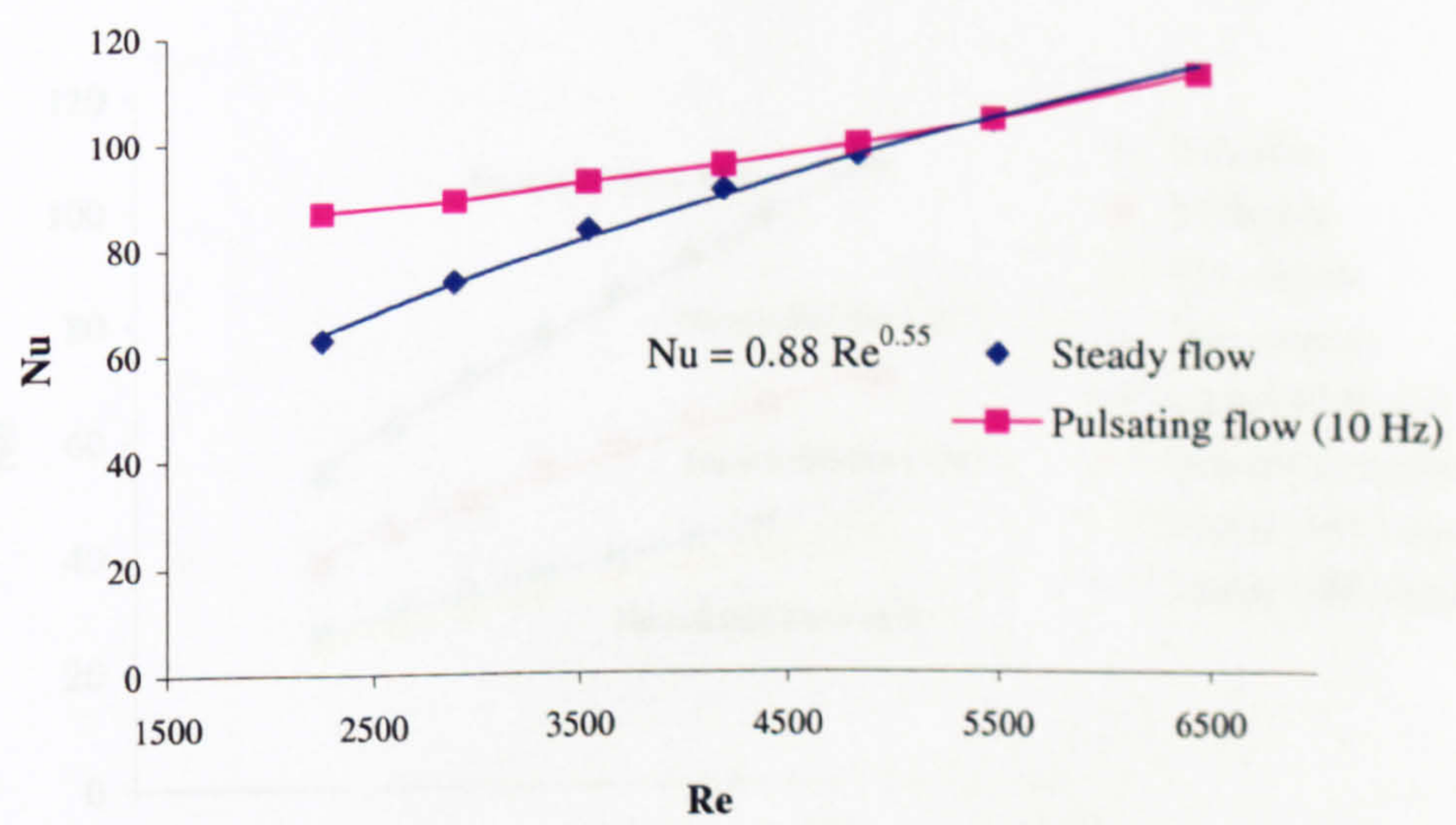

Figure 6.4. Comparison between the local Nusselt number in steady and pulsating flow (10 Hz) at the front stagnation point of the first cylinder at different amplitude of pulsations and dependence Nu-Reynolds number in steady flow in the asymmetric array.

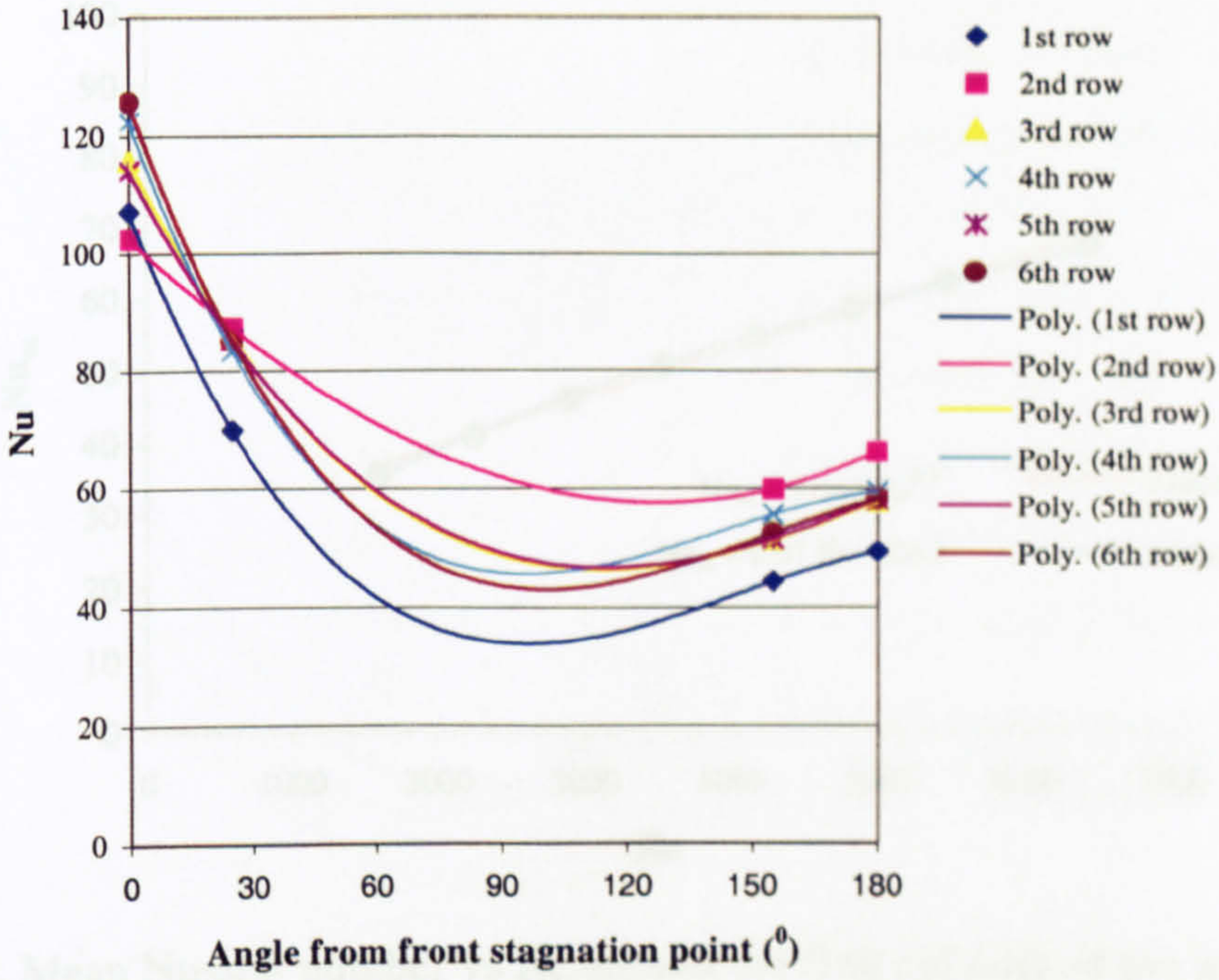

Figure 6.5. Variation of Nu number with the circumferential angle, φ, around all rows of the in-line array with elliptic cylinders (Re = 6,430).

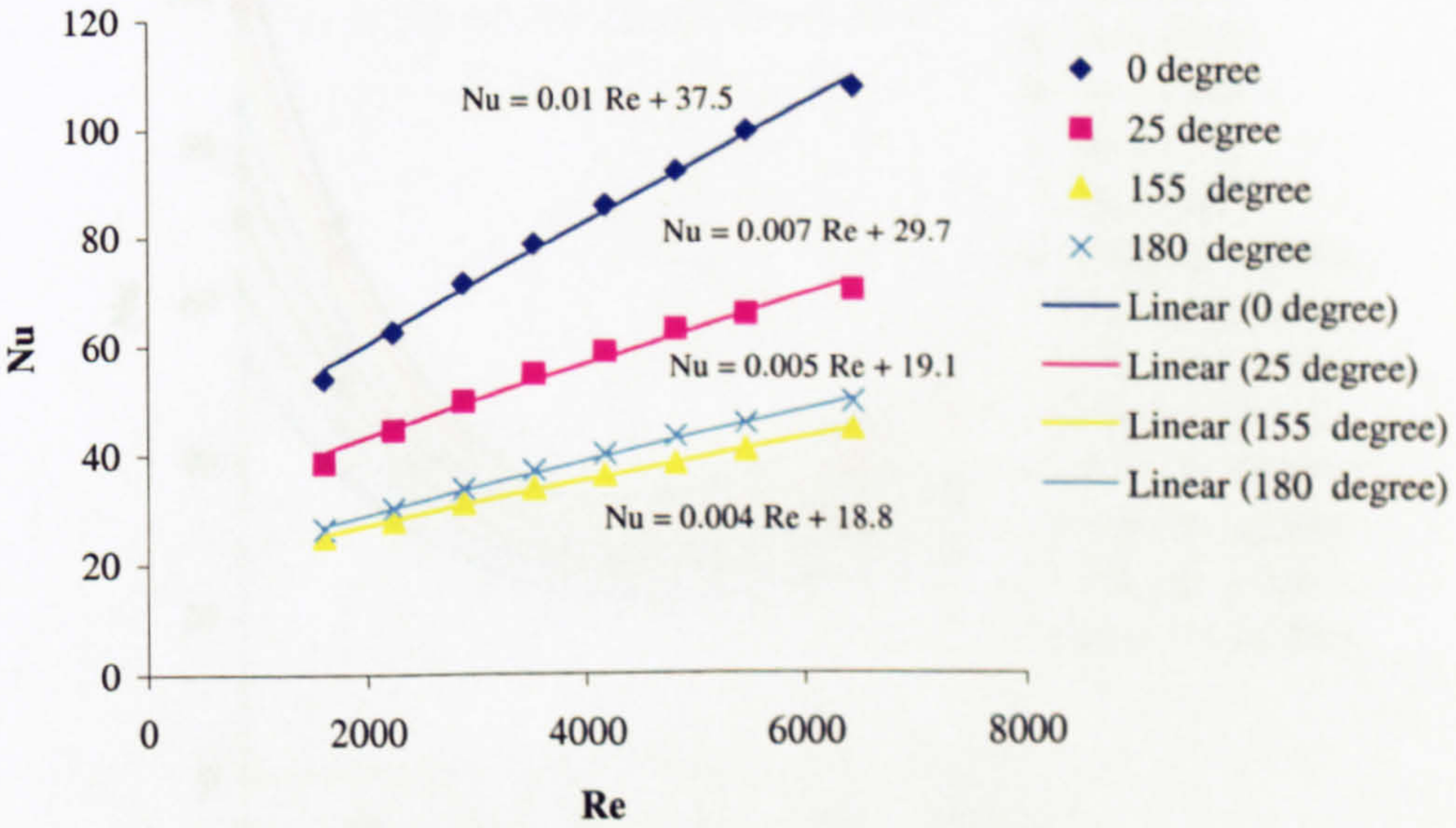

Figure 6.6. Variation of local Nusselt number with Re around the first cylinder of the in-line array in steady flow.

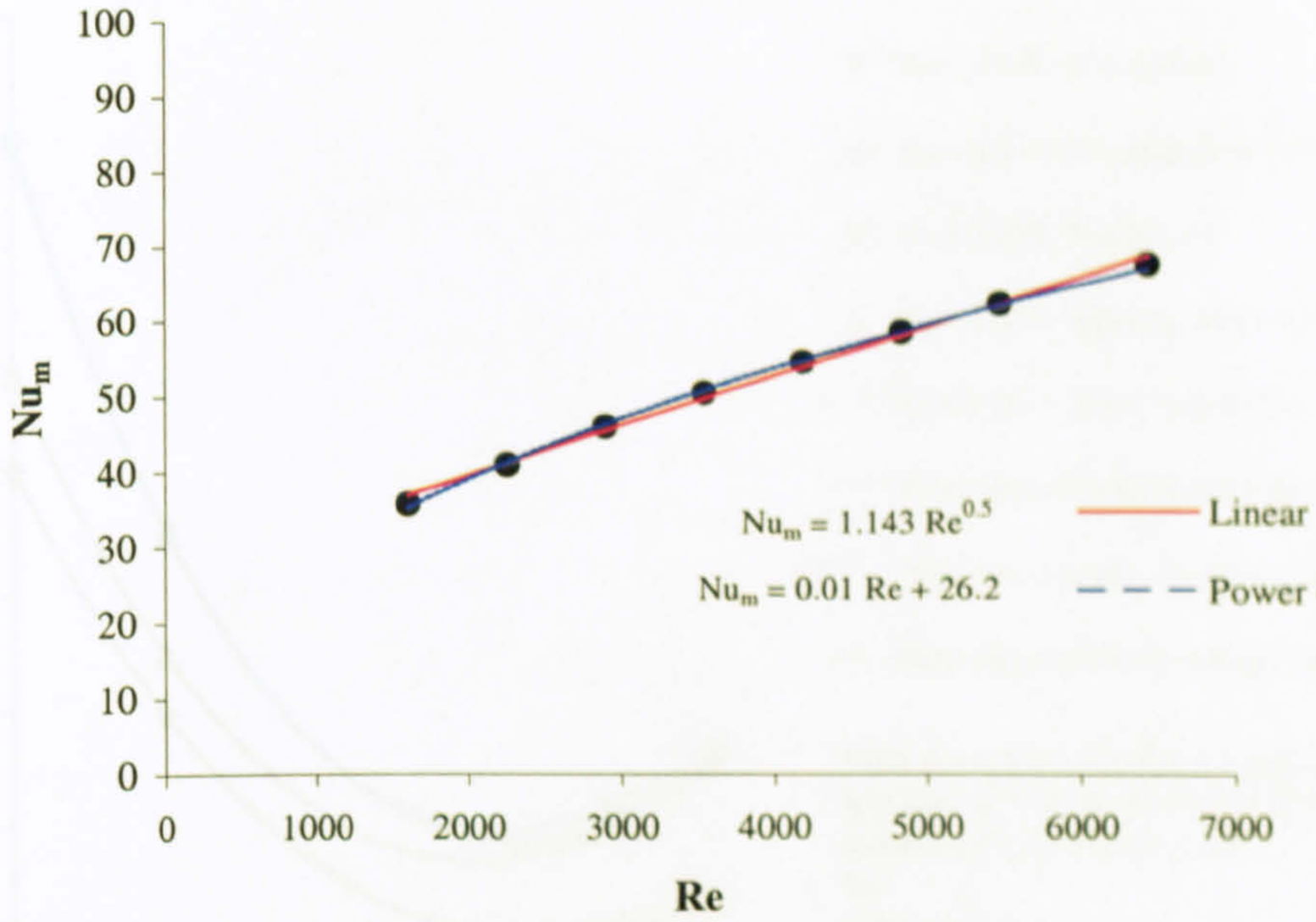

Figure 6.7. Mean Nusselt number vs Re around the first cylinder of the in-line array.

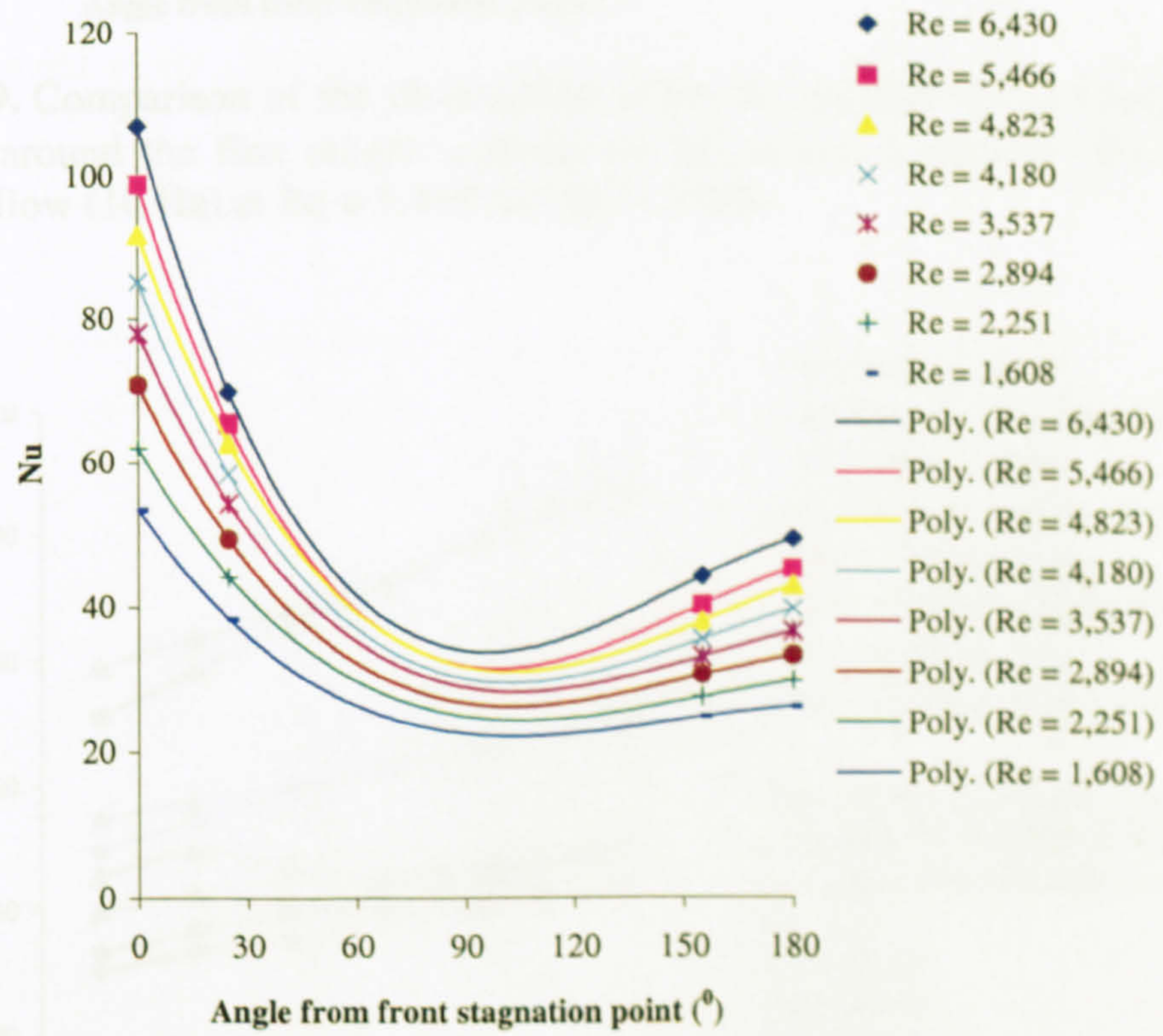

Figure 6.8. Nu number vs the circumferential angle, φ, around the first row of the in-line array at various Re.

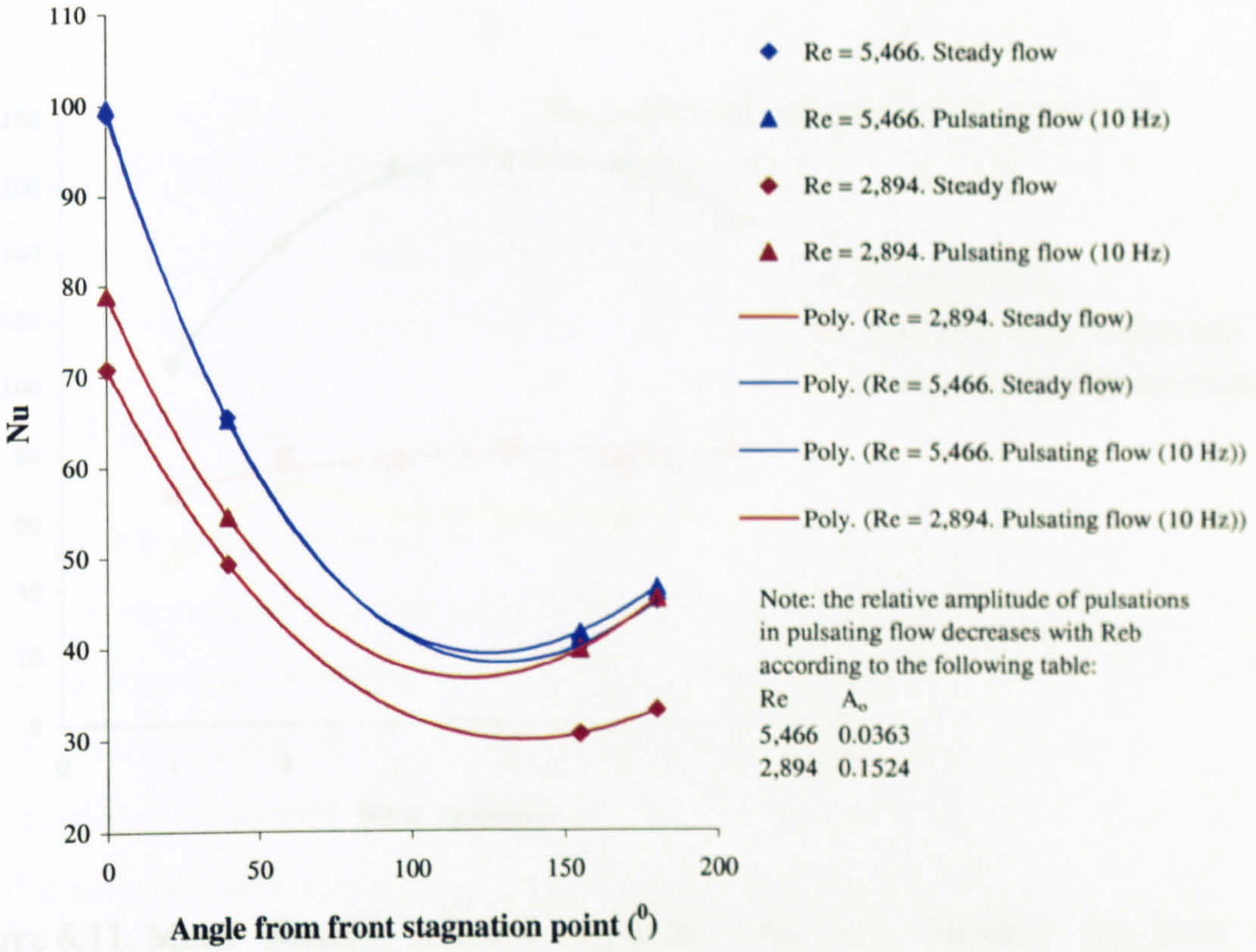

Figure 6.9. Comparison of the distribution of the Nu number vs the circumferential angle, φ, around the first elliptic cylinder of the in-line array between steady and pulsating flow (10 Hz) at Re = 5,466 and Re = 2,894.

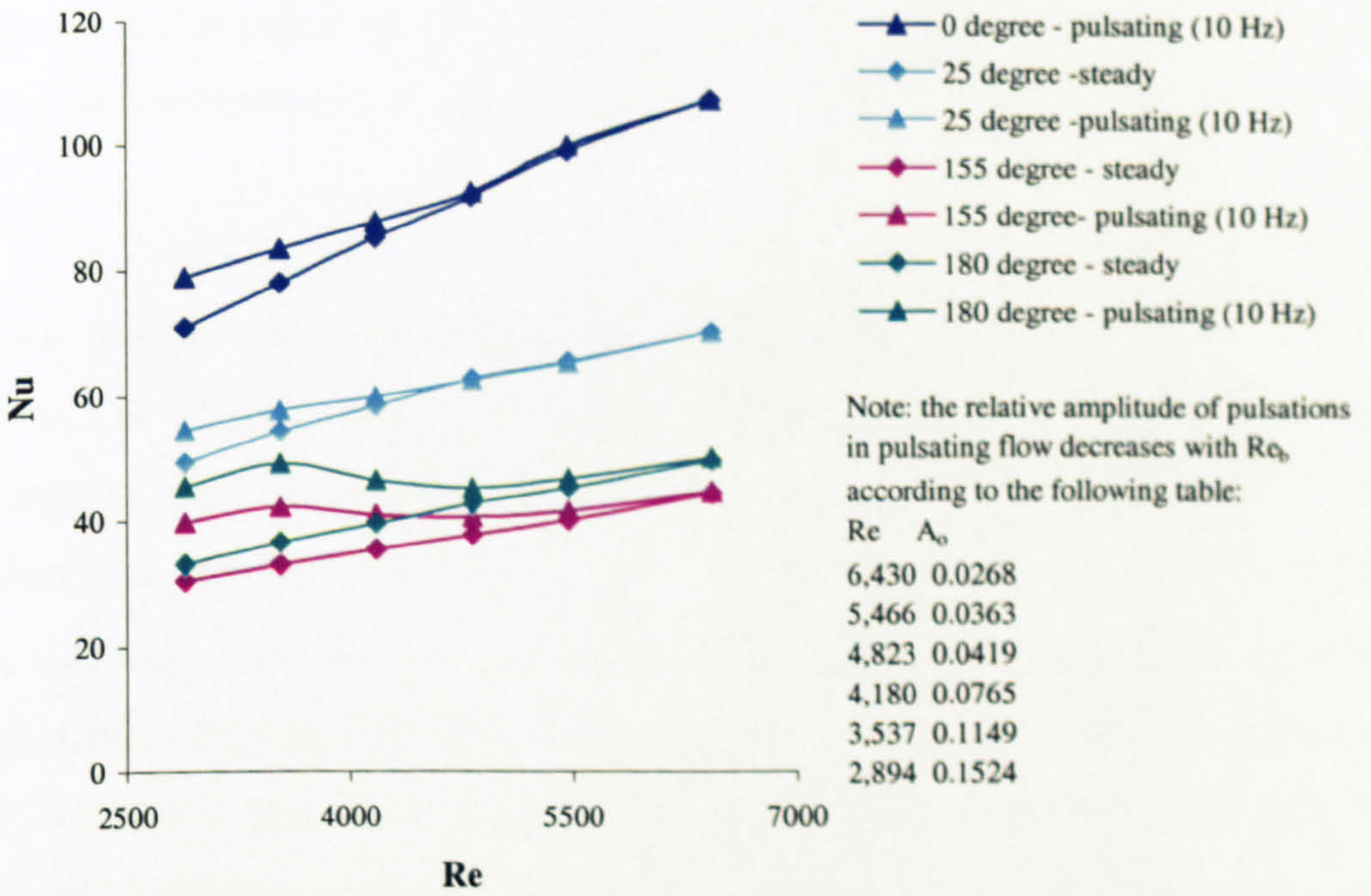

Figure 6.10. Local Nusselt number dependence on the Reynolds number at different angular position around the first elliptic cylinder of the in-line array.

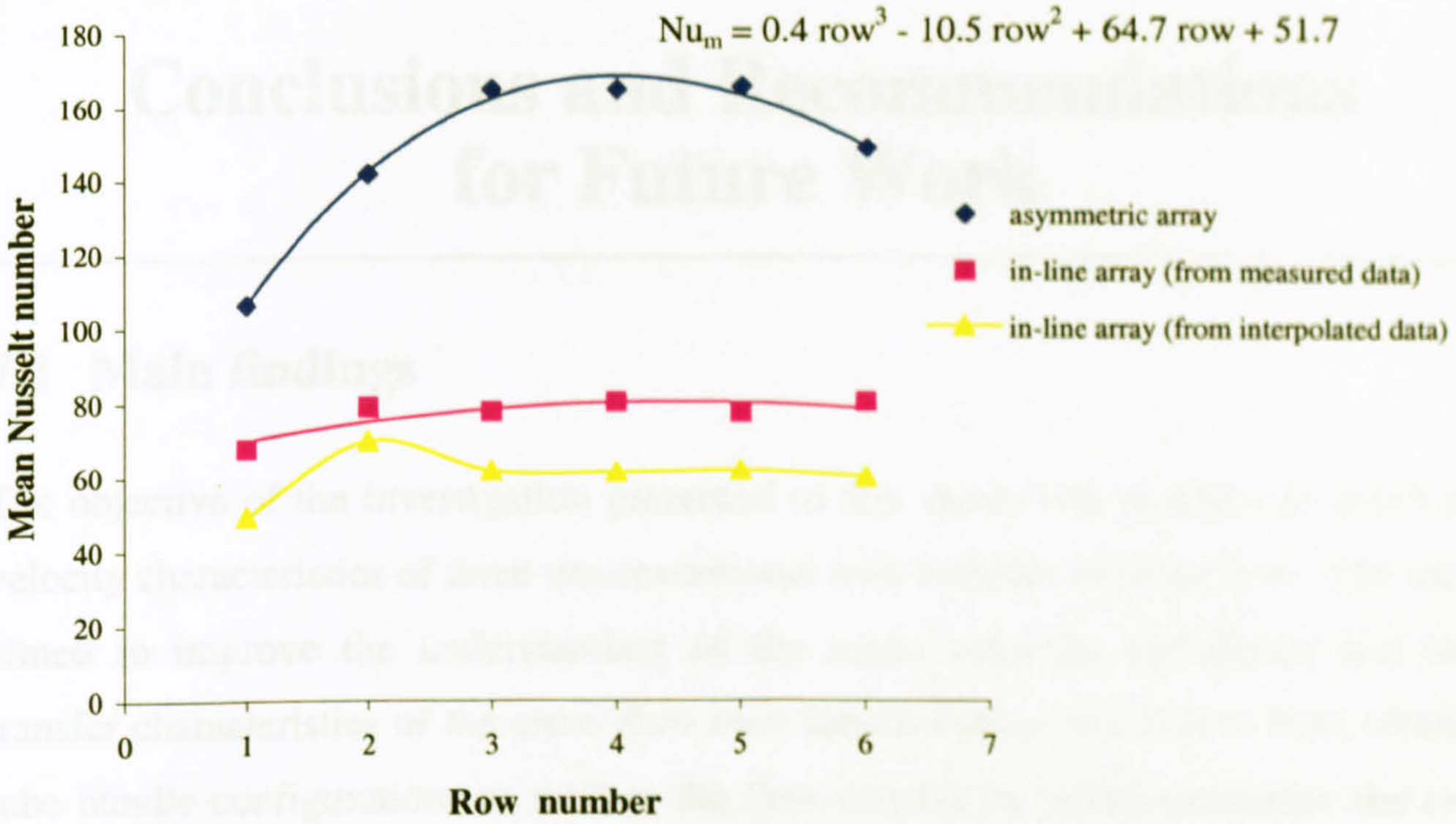

Figure 6.11. Mean Nusselt number variation with row number for both the asymmetric and the in-line array (Re = 6,430).

CHAPTER 7

Conclusions and Recommendations for Future Work

7.1 Main findings

The objective of the investigation presented in this thesis was to study in detail the velocity characteristics of three unconventional tube bundles in cross flow. The study aimed to improve the understanding of the mean velocity, turbulence and heat transfer characteristics of the cross-flow over tube bundles, and thus to help identify tube bundle configurations as well as the flow conditions which maximise the heat transfer and minimise fouling of the outer surface of the tubes.

Ensemble-averaged and time-resolved velocity measurements were taken using the laser Doppler anemometry (LDA) technique. Laser sheet flow visualisation was also employed to provide qualitative information on the flows under investigation. Surface temperature measurements in both the asymmetric test section with circular cylinders and the in-line one with elliptic cylinders were taken using a thermocouple measurement technique. All measurements were taken in both steady and pulsating flow.

The tube bundle models investigated comprised an in-line arrangement with elliptic cylinders, an asymmetric arrangement with circular cylinders and an in-line arrangement with drop-shaped cylinders. The in-line arrangement with elliptic cylinders had pitch ratios of $S_T/2b = 5.5$ and $S_L/2a = 1.6$, where 2b and 2a were the minor and major axes of the elliptic cross-section of the cylinders. The axis ratio of the cylinders, b:a, was 1:2. The elliptic cylinders had a major axis of 13 mm and a minor axis of 6.5 mm. These axes were chosen so that the circumferential length of the elliptic cylinders was the same as that of the circular ones employed in the asymmetric arrangement. The asymmetric arrangement, constructed by shifting the even rows in the in-line tube arrangement by one diameter in the positive transverse direction, had a longitudinal pitch ratio, S_L/d, of 2.1 and a transverse pitch ratio,

S_T/d, of 3.6. *The circular cylinders* were 10 mm in diameter. Finally, the in-line arrangement with drop-shaped tubes had a longitudinal pitch ratio, S_L/d_x, *of 1.6 and* a transverse pitch ratio, S_T/d_y, of 5.8, where d_x is the height of the drop-shaped cylinders and d_y the diameter of the bottom circular half of the cylinders. The drop-shaped cylinders were manufactured by joining half a cylinder with a parabolically-shaped one. The total cross-sectional longitudinal, d_x, and transversal lengths, d_y, of the cylinders were 13.08 mm and 6.16 mm respectively, the latter corresponding to *the diameter* of the semi-circular cylinder.

The main findings of this experimental study can be summarised as follows:

➢ The results showed that the in-line tube bundle with elliptic cylinders generates less turbulence than an equivalent (with the same longitudinal and transverse spacing) in-line array with circular tubes. The turbulence levels remain nearly constant along the flow passages indicating negligible interference between adjacent columns. The difference of the two r.m.s. components, u'/U_∞ and v'/U_∞, is near zero over the whole flow domain indicating that the turbulence might be assumed to be highly isotropic. On the contrary, the turbulence in the wake regions of the in-line arrangement with circular tubes was found to be highly anisotropic, especially downstream of the third and fourth rows (Balabani, 1996).

➢ The investigation carried out on the flow around the asymmetric array *with* circular cylinders showed that the tube bundle configuration investigated generates less turbulence than a staggered array (with the same longitudinal and transverse spacing) with circular tubes (Balabani, 1996). In the freestream the streamwise turbulence increases in the downstream direction from its upstream value up to $0.3U_\infty$. Values up to $0.5U_\infty$ are instead recorded in the wake of the first row. In contrast to what was observed in the in-line array with elliptic tubes, therefore, the interference between adjacent columns is not negligible. The turbulence is isotropic on the entrance of the bank ($v'/u' = 1$), but in the wakes of the downstream rows the anisotropy ($1 - v'/u'$) raises above 60 % with maximum values in the proximity of the downstream cylinders (80%), especially the third and fourth ones. This is in

agreement with the flow in the wake regions of the staggered array that was found to be highly anisotropic, especially in the wake regions.

➢ The experimental investigation on the in-line array with drop-shaped cylinders indicated that differences of turbulence levels between the in-line arrays with elliptic and drop-shaped cylinders respectively can be observed only in the cylinder wakes, particularly behind the first one. The magnitude of the r.m.s peak behind the first elliptic cylinder is up to 75 % higher than that observed behind the drop-shaped one.

➢ Time resolved measurements in the in-line array with elliptic tubes showed evidence of a weak vortex shedding activity. The correspondent Strouhal number, defined by the gap velocity and the minor axis of the elliptic cylinders, 2b, was found to be equal to 0.11. The only significant effect of the pulsations on the turbulence of the flow was observed in the wake of the first cylinder. The occurrence of lock-on of the natural vortex shedding at half of the superimposed pulsation frequency was observed in all rows. Behind the first row, where no vortex shedding activity was observed in steady flow, the superimposed pulsations triggered the shedding of vortices and its frequency locked at half of the driving frequency.

➢ A vortex shedding activity was detected in the asymmetric array with circular cylinders, but it is not as well defined as in the in-line array with elliptic cylinders respectively. The Strouhal number, defined by the gap velocity and the diameter of the circular cylinders, d, was found to be approximately equal to 0.22 in inner rows. The only significant effect of the pulsations on the turbulence of the flow was observed in the wake of the first cylinder. Lock-on of the natural vortex shedding at either the superimposed pulsation frequency or at half of it, depending on the relative amplitude of pulsations, was observed in all rows. Behind the first row, where no clear vortex shedding frequency could be determined (although, in contrast to what was observed in the in-line array with elliptic tubes, shed and convected vortices could be clearly distinguished) the superimposed pulsations triggered the shedding of vortices and its frequency locked at the driving frequency or at half of it.

➢ A vortex shedding activity could be observed behind all rows of the in-line array with drop-shaped tubes, but a well defined vortex shedding frequency was

detected only downstream of the second one. The Strouhal number was found to be equal to 0.16 in inner rows. The only significant effect of the pulsations on the turbulence of the flow was observed behind the first cylinder as in the in-line array with elliptic cylinders. Lock-on of the natural vortex shedding at either the superimposed pulsation frequency or at half of it depending on the reduced amplitude of pulsations upstream of the tube bundle was observed.

➢ The flow visualisation showed the lack of any significant vortex activity behind the first row of the in-line array with elliptic cylinders, and confirmed the occurrence of lock-on of the natural vortex shedding at half of the superimposed pulsation frequency. The flow visualisation study in the asymmetric array also confirmed the findings of the LDA measurements and in particular the lack of a well-defined and unique vortex shedding frequency. Furthermore, it showed a weak vortex activity behind the first row, but also the presence of a region close to the cylinder wall, which is almost stagnant resembling only partially the wake characteristics of the first cylinder of the in-line array with elliptic tubes. In that case, the flow in the wake at the first row was entirely stagnant and was characterised by the absence of vortex activity. The flow visualisation study in the in-line array with drop-shaped cylinders indicated the presence of an intense vortex activity even behind the first row, in contrast to what was observed in the in-line array with elliptic cylinders.

➢ The heat transfer characteristics of both the in-line and the asymmetric array with elliptic and circular cylinders respectively were investigated in both steady and pulsating flow. The heat transfer rates in the asymmetric array in steady flow are low around the first row cylinder and they increase in subsequent rows. Inner rows, i.e. rows 3 to 5, have similar Nu number distributions which implies that the entrance effects in the asymmetric arrangement are restricted to the first three rows only. The heat transfer rates at the exit of the bundle, that is row 6, are also similar to the rates measured in row 2.

➢ A local minimum in the Nusselt number profile around the first row was observed downstream of the separation point ($\varphi \cong 135°$) which may be attributed to the presence of a stagnant region downstream of the separation point. The same minimum was detected also around downstream rows, but at slightly different

locations along the circumferential length. A comparison of the heat transfer rates between steady and pulsating flow clearly shows that the heat transfer is enhanced when the flow is pulsed. However, it should be noted that the flow conditions adopted were such that vortex shedding was promoted and locked at the pulsation frequency. A comparison was made between Nu_p and Nu_s at the front stagnation point of the staggered array. It was observed that as the Reynolds number decreases and correspondingly the relative amplitude of the upstream pulsations, A_o, increases the Nusselt number in pulsating flow becomes progressively higher, by up to 40 % at Re = 2,251, than that in steady flow.

➢ The local Nusselt number distribution in all rows of the in-line array with elliptic cylinders shows, despite the small number of measurement locations, that the heat transfer rates are low around the first row cylinder and they increase in subsequent rows. Rows 3 to 6 have similar Nu number distributions while the heat transfer rates measured in row 2 are lower than those measured in downstream rows for $\varphi \leq 30°$ and higher for larger angles. The Nusselt number dependence on Re was also investigated. It was observed that that although the heat transfer rates increase linearly with Re the Nu number variation is significantly steeper at the front stagnation point than at higher circumferential angles of the cylinders and that the dependency of the Nusselt number on φ becomes weaker at lower Re. The heat transfer augmentation due to pulsations increases with the relative amplitude of pulsations A_o as already observed in the asymmetric array. Finally, a comparison was made of the averaged local Nusselt numbers recorded in steady flow along the circumferential length between the asymmetric and the in-line array. It was found that the heat transfer of the in-line array is considerably lower than that of the staggered array in all rows, in agreement with the results of earlier studies for similar Reynolds numbers.

7.2 Recommendations for future work

This thesis provides an extensive qualification of the flow fields generated by the novel tube bundles investigated in both steady and pulsating flow conditions as well as of the heat transfer characteristics of both the in-line and the asymmetric array with elliptic and circular cylinders respectively. However, there are some areas where further investigation is recommended in order to improve the understanding of tube bundle flows and heat transfer.

- Further development of fundamental studies of the flow and heat transfer over simple assemblies or single cylinders, particularly those of novel shape, will improve the understanding of more complicated tube bundle flows.

- The visualisation technique employed in this study provided fine details of the flow in individual wakes. However, visualisation of the global flow patterns, i.e. of the flow patterns in the array as a whole, was hindered by inhomogeneous lighting. Therefore, a more elaborated visualisation technique is required. Konstantinidis (2001) has suggested the use of multiple light or laser sources by means of mirrors.

- Surface temperature measurements around the elliptic cylinders of the in-line array were obtained with four thermocouples embedded on the wall of an electrically heated cylinder. However, single-point thermocouple measurements require a large number of sensors to resolve the temperature distribution around the cylinder surface and can be lengthy and time-consuming. Therefore, a simple cost-effective method, which allows fast and accurate measurements, is needed.

- Finally, as also observed by Balabani (1996), larger scale models in conjunction with refractive index matching will facilitate near wall measurements to be taken. These measurements will provide detailed and useful information on the development of the boundary layer. Furthermore, larger scale models are preferred for flow visualisation, as the resolution would be improved.

References

Andraka, C. E. and **Diller, T. E. (1985).** Heat transfer distribution around a cylinder in pulsating cross-flow. *Transactions of the ASME: Journal of Engineering for Gas Turbines and Power*, Vol. 107, pp. 976-982.

Armstrong, B. J., Barnes, F.H. and **Grant, I. (1986).** The effect of a perturbation on the flow over a bluff cylinder. *Physics of Fluids*, Vol. 29, No. 7, pp. 2095-2102.

Armstrong, B. J., Barnes, F. H. and **Grant, I. (1987).** A comparison of the structure of the wake behind a circular cylinder in a steady flow with that in a perturbed flow. *Physics of Fluids*, Vol. 30, pp. 19-26.

Balabani, S. (1996). An experimental investigation of the crossflow over tube bundles. PhD Thesis, King's College London, University of London.

Balabani, S. and **Yianneskis, M. (1996).** Vortex shedding and turbulence scales in staggered tube bundle flows. *Canadial Journal of Chemical Engineering*, Vol. 210, pp. 317-331.

Balachandar, S., Mittal, R. and **Najjar, F. M. (1997).** Properties of the mean recirculation region in the wakes of two dimensional bluff bodies. *Journal of Fluid Mechanics*, Vol. 351, pp. 167-199.

Barbi, C., Favier, D. P., Maresca, C. A. and **Telionis, D. P. (1986).** Vortex shedding and lock-on of a circular cylinder in oscillatory flow. *Journal of Fluid Mechanics*, Vol. 170, pp. 527-544.

Base, T. E., Patel, J. M. and **Valaitis, G. C. (1981).** Heat transfer from cylinders in unsteady flow. *Canadian Journal of Chemical Engineering*, Vol. 59, pp. 247-250.

Bendat, J. S. and **Piersol, A. G. (1971).** Random data; ananlysis and measurement procedures, Wiley-Interscience.

Bergeles, G., Yianneskis, M., Kravaritis, A., Balabani, S., Bouris-Burry, D. and **Itskos, S. (1996).** Effects of fouling on the efficiency of heat exchangers in lignite utility boilers. Final Report, Joule II Research Programme, Contract No. JOU2-CT2-0014.

Bergeles, G., Yianneskis, M., Grillot, J. M., Giannopoulos N., Balabani, S., Bouris, D., Castiglia, D., Konstantinidis, E., Papadakis, G. and **Tochon, P. (2000).** Fouling minimisation and process intensification in heat exchangers. Final Report, Joule III Research Programme, Contract No. JOU3-CT97-0064.

Buchhave, P., George, W. K. and **Lumley, J. L. (1979).** The measurement of turbulence with the Laser-Doppler anemometer. *Annual Review of Fluid Mechanics*, Vol. 11, pp. 443-503.

Castiglia, D., Balabani, S., Papadakis, G. and **Yianneskis, M. (2001).** An experimental and numerical study of the flow past elliptic cylinder arrays. Proceedings of IMechE, Part C, Vol. 215, pp.1287-1301.

Chen, Y. N. (1977). The sensitive tube spacing region of tube bank heat exchangers for fluid elasting coupling in crossflow. ASME Symposium Fluid Structure Interaction Phenomena in Pressure Vessel and Piping Systems (Eds. M. K. Au-Yang and S. J. Brown), 1977, pp. 1-18.

Chen, Y. N. (1984). Flow-induced vibrations of in-line heat exchangers. Symposium on Flow Induced Vibrations, 3 (eds. Païdoussis, M. P., Chenowth, J. M., Bernstein J. M.), New Orleans, 1984, pp. 163-170.

Cheng, C. H., Chen, H. N. and **Aung, W. (1997).** Experimental study of the effect of transverse oscillation on convection heat transfer from a circular cylinder. *Journal of Heat Transfer*, Vol. 119, pp. 474-482.

Cheung, R. S. W. (1989). An investigation of flow patterns inside inlet ports. PhD Thesis, King's College London, University of London.

Cooper, W. L., Yang, K. T. and **Nee, V. W. (1993).** Fluid mechanics of oscillatory and modulated flows and associated applications in heat and mass transfer - A Review. *Journal of Energy, Heat and Mass Transfer*, Vol. 15, pp. 1-19.

Durâo, D. F. G. and **Whitelaw, J. H. (1976).** The influence of sampling procedure on the velocity bias in turbulent flows. The Accuracy of Flow Measurements by Laser Doppler Methods, Proc. LDA-Symposium, Copenhagen 1975, pp. 138-149.

Durâo, D. F. G., Laker, J. and **Whitelaw, J. H. (1980).** Bias effects in laser Doppler anemometry. *J. Phys. E.: Sci. Instrum.*, Vol. 13, pp. 442-445.

Durst, F., Melling, A. and **Whitelaw, J. H. (1976).** Principles and practise of Laser-Doppler anemometry. Academic Press, London.

Fitz-Hugh, J. S. (1973). Flow induced vibration in heat exchangers. UKAEA/NPL International Symposium on Vibration Problems in Industry, Keswick, Paper No. 427.

Fitzpatrick, J. A. and **Donaldson, I. S. (1980).** Row depth effects on turbulence spectra and acoustic vibrations in tube banks. *Journal of Sound and Vibration*, Vol. 73, No 2, pp. 225-237.

George, W. K. (1975). Limitations to measuring accuracy inherent in the Laser Doppler signal. The Accuracy of Flow Measurements by Laser Doppler Methods, Proc. LDA-Symposium, Copenhagen 1975, pp. 20-64.

George, W. K. and **Lumley, J. L. (1973).** The laser-Doppler velocimeter and its application to the measurement of turbulence. *Journal of Fluid Mechanics*, Vol. 60, No. 2, pp. 321-362.

Gerrard, J. H. (1966). The mechanics of the formation region of vortices behind bluff bodies. *Journal of Fluid Mechanics*, Vol. 25, part 2, pp. 401-413.

Griffin, O. M. and **Ramberg, S. E. (1976).** Vortex shedding from a cylinder vibrating in-line with an incident uniform flow. *Journal of Fluid Mechanics*, Vol. 75, pp. 257-276.

Halim, M. S. (1988). Detailed velocity measurements of flow through staggered in-line tube banks in cross-flow using laser Doppler anemometry. PhD Thesis, University of Manchester.

Halim, M. S. and **Turner, J. T. (1986).** Measurements of cross flow development in a staggered tube bundle. 3rd Int. Symp. on Applications of Laser Techniques to Fluid Mechanics, Lisbon, paper 21.7.

Hinze, J. O. (1975). Turbulence, McGraw Hill.

Hooker, S. G. (1936). On the action of viscosity in increasing the spacing ration of a vortex street, Proceedings of the Royal Society of London, Ser. A, Vol. 154, pp. 67-89.

Karamercan, O. E. and **Gainer, J. (1979).** The effect of pulsations on heat transfer. *Ind. Eng. Chem. Fundam.*, Vol. 18, No. 1, pp. 11-15.

Katinas, V. and **Tumosa, A. (1992).** Heat transfer and fluid dynamics in asymmetric transverse flows over bundles of tubes in heat exchangers. In Recent Advances in Heat Transfer (Eds. B. Sundén and A. Žukauskas), Elsevier, pp. 532-540.

Kikuchi, Y., Suzuki, H., Kitagawa, M. and **Ikeya K. (2000).** Effect of pulsating Strouhal number on heat transfer around a heated cylinder in pulsating cross-flow. *JSME International Journal*, Vol. 43, pp. 250-257.

Kim, B. K., Borrel, G. J., Diller, T. E., Cramer, M. S. and Telionis, D. P. (1983). Pulsating flow and heat transfer over a circular cylinder. Proceedings of the Symposium on Non-Linear Problems in Energy Engineering, Argonne, Illinois, pp. 96-101.

Konstantinidis, E., Castiglia, D., Balabani, S. and Yianneskis, M. (2000). On the flow and vortex shedding characteristics of an in-line tube bundle in steady and pulsating crossflow. *Trans. IChemE*, Vol. 78, Part A, pp. 1129-1138.

Konstantinidis, E. (2001). Pulsating flow in cylinder arrays. PhD Thesis, King's College London, University of London.

Kotake S. and **Aoki I. (1984).** Heat transfer of a cylinder in large-amplitude oscillating wake flows. *International Journal of Heat and Mass Transfer*, Vol. 27, No.10, pp. 1903-1917.

Kresta, S. M. (1991). Characterisation, measurement and prediction of the turbulent flow in stirred tanks. PhD Thesis, McMaster University, U.S.A.

Lee, K. C. (1995). An experimental investigation of the trailing vortex structure and mixing characteristics of stirred vessels. PhD Thesis, King's College London, University of London.

Li, Q., Cheng, Z., Flechtner, U. and **Warnecke H. (1997).** Warmeubergang und Druckverlust auf der Außenseite in flüchtend angeordneten Rohrbündeln mit ellipsoiden Rohren. *Chemische Technik*, Vol. 49, pp. 183-185.

Lin, J.-C., Towfighi, J. and **Rockwell, D. (1995).** Instantaneous structure of the near-wake of a circular cylinder: on the effect of Reynolds number. *Journal of Fluids and Structures*, Vol. 9, pp. 409-418.

Ljungkrona, L., Norberg, C. and **Sunden, B. (1991).** Flow around two tubes in an in-line arrangement; flow visualisations and pressure measurements. Proc. of 2nd

World Conference on Experimental Heat Transfer, Fluid Mechanics, and Thermodynamics, pp. 333-340.

Melling, A. (1975). Investigation of flows in non-circular ducts and other configurations by laser Doppler anemometry. PhD Thesis, Imperial College, University of London.

Melling, A. (1977). Axisymmetric, turbulent flow in a motored reciprocating engine. Imperial College Mech. Eng. Dept. Report CHT/77/4, 1977.

Merker, G. P. and **Hanke, H. (1986a).** Measurements of local mass transfer and pressure distribution along the shell-side of oval-shaped tubes in cross flow heat exchangers. *International Journal of Heat and Mass Transfer*, Vol. 6, pp. 2721-2726.

Merker, G. P. and **Hanke, H. (1986b).** Heat transfer and pressure drop along the shell-side of tube banks having oval-shaped tubes. *Int. J. Heat Mass Transfer*, Vol. 29, No.12, pp. 1903-1909.

Merzkirch, W. (1987). Flow visualization, Academic Press.

Mittal R. and **Balachandar S. (1996).** Direct numerical simulation of flow past elliptic cylinders. *Journal of Computational Physics*, Vol. 124, pp. 351-367.

Mizushina, T., Maruyama, T. and **Hirasawa, H. (1974).** Structure of the turbulence in pulsating flows. *Journal of Chemical Engineering of Japan*, Vol. 8, No. 3, pp. 210-216.

Modi, V. J. and **Wiland, E. (1970).** Unsteady aerodynamics of stationary cylinders in subcritical flow. *AIAA Journal*, Vol. 8, No.10, pp. 1814-1821.

Modi, V. J. and **Dikshit, K. (1974).** Near-wakes of elliptic cylinders in subcritical flow. *AIAA Journal*, Vol. 13, No.4, pp. 490-497.

Moretti, P. M. (1993). Flow-induced vibrations in arrays of cylinders. *Annual Review of Fluid Mechanics*, Vol. 25, pp. 99-114.

Nair, M. T. and **Sengupta, T. K. (1997).** Onset of asymmetry: flow past circular and elliptic cylinders. *Int. Journal for Numerical Methods in Fluids*, Vol. 23, 1327.

Oengören, A. and **Ziada, S. (1995).** Vortex shedding, acoustic resonance and turbulent buffeting in normal triangle tube arrays. In Flow Induced Vibrations (Ed. Bearman), Balkema, Rotterdam, pp. 295-313.

Ota, T., Aiba, S., Tsuruta, T. and **Kaga, M. (1983).** Forced convection heat transfer from an elliptic cylinder of axis ratio 1:2. *Bulletin of JSME*, Vol. 26, No. 212, pp. 262-267.

Ota, T., Nishiyama, H. and **Taoka, Y. (1984).** Heat transfer and flow around an elliptic cylinder. *Int. Journal of Heat and Mass Transfer*, Vol. 27, No. 10, pp. 1771-1779.

Ota, T., Nishiyama, H., Kominami, J. and **Sato, K. (1986).** Heat transfer from two elliptic cylinders in tandem arrangement. *Journal of Heat Transfer*, Vol. 108, pp. 525-531.

Owen, P. R. (1965). Buffeting excitation of boiler tube vibration. *Journal of Mechanical Engineering Science*, Vol. 7, pp. 431-439.

Païdoussis, M. P. (1983). A review of flow-induced vibrations in reactors and reactor components. *Nuclear Engineering and Design*, Vol. 74, pp. 31-60.

Peacock, J., Jones, T., Tock, C. and **Lutz, R. (1998).** The onset of turbulence in physiological pulsatile flow in a straight tube. *Experiments in Fluids*, Vol. 24, pp. 1-9.

Rae, G. J. and **Wharmby, J. S. (1987).** Strouhal numbers for in-line arrays. Proc. Int. Conference on Flow Induced Vibrations, Bowness-on Windermere, England, 1987, Paper E4, pp. 233-242.

Roshko, A. (1961). Experiments on the flow past a circular cylinder at very high Re number. *Journal of Fluid Mechanics,* Vol. 10, No. 3, pp. 345-356.

Ruth, E. K. (1983). Experiments on a crossflow heat exchanger with tubes of lenticular shape. *Journal of Heat Transfer*, Vol. 105, pp. 571-575.

Savkar, S. D. (1977). A brief review of flow induced vibrations of tube arrays in cross-flow. *Transactions of the ASME: Journal of Fluids Engineering*, Vol. 99, pp. 517-519.

Scholten, J. W. and **Murray, D. B. (1998).** Heat transfer and velocity fluctuations in a staggered tube array. *International Journal of Heat and Fluid Flow*, Vol. 19, pp. 233-244.

Sharatchandra, M. C. and **Rhode, D. L. (1997).** Turbulent flow and heat transfer in staggered tube banks with displaced tube rows. *Numerical Heat Transfer*, Part A, 31, pp. 611-627.

Snarski, S. R. and **Jordan, S. A. (2001).** Fluctuating wall pressure on a circular cylinder in cross flow and the effect of angle of incidence. Proceedings of ASME FEDSM'01, Paper FEDSM2001-18262, New Orleans, Louisiana.

Stephan, K. and **Traub, D. (1986).** Influence of turbulence intensity on heat transfer and pressure drop in compact heat exchangers. In Heat Transfer 1986, Proceedings of the 8th international Heat Transfer Conference, San Francisco (Eds. C.L. Tien, V.P. Carey and J. K. Ferrell), Hemisphere Publishing, Vol. 6, pp. 2739-2744.

Strouhal, V. (1878). Uber eine besondere Art der Tonerregung. *Ann. Physik. Chem.*, Vol. 5, pp. 216-251.

Suen, K. O. (1992). Investigation of gas flow in motored high speed diesel engine by laser-Doppler anemometry. PhD Thesis, King's College London, University of London.

Sumner, D., Price, S. J. and **Paidoussis, M. P. (2000).** Flow-pattern identification for two staggered circular cylinders in cross-flow. *Journal of Fluid Mechanics*, Vol. 411, pp. 263-303.

Sung, H. J., Hwang, K. S. and **Hyun, J. M. (1994).** Experimental study on mass transfer from a circular cylinder in pulsating flow. *Int. Journal of Heat and Mass Transfer*, Vol. 37, No. 15, pp. 2203-2210.

Telionis, D. P., Gundappa, M. and **Diller, T. E. (1992).** On the organisation of flow and heat transfer in the near wake of a circular cylinder in steady and pulsating flow. *Transactions of the ASME: Journal of Fluids Engineering*, Vol. 114, pp. 348-355.

Traub, D. (1990). Turbulent heat transfer and pressure drop in plain tube bundles. *Chem. Eng. Process.*, Vol. 28, No 28, pp. 173-181.

Véret, C. (1987). Flow visualization IV. Proceeding of the 4th International Symposium on Flow Visualization, Hemisphere Publishing.

Weaver, D. S., Fitzpatrick, J. A. and **Elkashan, M. (1987).** Strouhal numbers for heat exchanger tube arrays in crossflow. *Transactions of the ASME, Journal of Pressure Vessel Technology*, Vol. 109, pp. 219-223.

Weaver, D. S. and **Fitzpatrick, J. A. (1988),** A review of cross-flow induced vibrations in heat exchangers tube arrays. *Journal of Fluid and Structures*, Vol. 2, pp. 73-93.

Weaver, D. S., Lian, H. Y. and **Huang, X. Y. (1991).** A study of vortex shedding in a normal triangular tube array. In Flow Induced Vibrations, I.Mech.E, Paper C416/091, pp. 511-515.

Weaver, D. S., Lian, H. Y. and **Huang, X. Y. (1993).** Vortex shedding in rotated square arrays. *Journal of Fluids and Structures*, Vol. 7, pp. 107-121.

Williamson, C. H. K. (1996). Vortex shedding in the cylinder wake. *Annual Review of Fluid Mechanics*, Vol. 28, pp. 477-539.

Wolochuk, M. C., Plesniak, M. W. and **Braun, J. E. (1996).** The effects of turbulence and unsteadiness on vortex shedding from sharp-edged bluff bodies. *Transactions of the ASME: Journal of Fluids Engineering*, Vol. 118, pp. 18-25.

Wung, T. S., Niethammer, J. E. and **Chen, C. J., (1986).** Measurements of heat - mass transfer and pressure drop for some non-standard arrays of tubes in crossflow. Heat Transfer 1986, Proc. 8th Int. Heat Transfer Conference, San Francisco (Eds. C.L. Tien, V.P. Carey and J. K. Ferrell), Hemisphere Publishing, pp. 1041-1046.

Yanta, W. J. (1973). Turbulence measurements with a laser-Doppler velocimeter. Naval Ordnance Labs, White Oak, Silver Spring, Maryland, Report NOLTR 73 - 94.

Yianneskis, M. (1982). Flow in reciprocating engine cylinders and curved ducts. PhD Thesis, Imperial College of Science and Technology, University of London.

Ziada, S. and **Oengöeren, A. (1991).** Vorticity shedding and acoustic resonance in an in-line tube bundle. Part one: vorticity shedding. In Flow Induced Vibrations. IMech.E., Paper C416/047, pp. 497-509.

Žukauskas, A. (1972). Heat transfer from tubes in crossflow. Advances in Heat Transfer (Eds. J.P. Hartnett and T.F. Irvine), Academic Press, Vol. 8, pp. 93-160.

Žukauskas, A. (1989). High-performance single-phase heat exchangers (Ed. J. Karni), Hemisphere Publishing, USA.